

# Characterisation and hydration of ye'elimite containing cements

THÈSE N° 7953 (2018)

PRÉSENTÉE LE 6 AVRIL 2018

À LA FACULTÉ DES SCIENCES ET TECHNIQUES DE L'INGÉNIEUR  
LABORATOIRE DES MATÉRIAUX DE CONSTRUCTION  
PROGRAMME DOCTORAL EN SCIENCE ET GÉNIE DES MATÉRIAUX

ÉCOLE POLYTECHNIQUE FÉDÉRALE DE LAUSANNE

POUR L'OBTENTION DU GRADE DE DOCTEUR ÈS SCIENCES

PAR

Frank BULLERJAHN

acceptée sur proposition du jury:

Prof. P. Muralt, président du jury  
Prof. K. Scrivener, Dr M. Ben Haha, directeurs de thèse  
Prof. E. Gartner, rapporteur  
Prof. T. Matschei, rapporteur  
Prof. P. Bowen, rapporteur



ÉCOLE POLYTECHNIQUE  
FÉDÉRALE DE LAUSANNE

Suisse  
2018





*Wenn der Wind der Veränderung weht,  
bauen die einen Mauern und die  
anderen Windmühlen.*

*Chinese proverb*



## **Preface**

The doctoral thesis was submitted to the École polytechnique fédérale de Lausanne (EPFL; Switzerland) for the degree of Philosophiae Doctor (PhD).

The thesis is financed by the HeidelbergCement AG and conducted in the HeidelbergCement Technology Center GmbH (HTC; Leimen, Germany) in collaboration with the Laboratory of Construction Materials (LMC) at EPFL. The thesis started in November 2013 and ended with the submission of the doctoral thesis in November 2017. It was followed by the private and public defence in the first quarter of 2018. The PhD candidate was fully employed at HTC during the project period. The academic supervisor from EPL was Prof. Karen L. Scrivener. The industrial co-supervisor was Dr. Mohsen Ben Haha (HTC).

The research was mainly carried out at the HTC with support of the employees of the analytical center. Part of the research was done at the EPFL with the technical and strong scientific support by Dr. Emmanuelle Boehm-Courjault and the Center of Microscopy of EPFL (EPFL-CIME).

Strong technical and scientific support was provided by Dr. Maciej Zajac, Dr. Jan Skocek (HTC) and Dr. Barbara Lothenbach (Eidgenössische Materialprüfanstalt EMPA) for the data analyses and especially the thermodynamic modelling.

Leimen, 08.02.2018

Frank Bullerjahn



## Acknowledgement

The presented work would not have been achieved without the help and support of a range of people. I would like to take the opportunity to express them my great gratitude.

First of all, I would like to acknowledge the supervision of Professor Karen Louise Scrivener, the head of the Laboratory of Construction Materials (LMC), EPFL. She was the one who guided me all the way with great patience, endurance and numerous us useful advices and constructive feedbacks. Thank you for your great support and teaching. I also like to thank you for the possibility to work in an international, multi-disciplinary team of so many brilliant scientists, most of whom become close friends. This thesis has been in all aspects an extraordinary experience. Thank you Karen!

Special thanks to my supervisor and dear friend Dr. Mohsen Ben Haha, team leader Scientific Coordination at HeidelbergCement AG. Thank you for creating this great opportunity to go the next step in my scientific carrier in one of the best laboratories of construction materials. You encouraged, guided and helped me all the time but you also provided me with constructive criticism when needed. You endured the reading each single version of each single draft and you always come up with good ideas afterwards. Thank you my friend!

Further, I like to express my gratitude to my colleagues and dear friends Dr. Maciej Zajac and Dr. Jan Skocek for their contribution, encouragement, help, and constructive discussions and feedback during my thesis. In this sense I would further like to thank Dr. Emmanuelle Boehm-Courjault, Dr. Pawel Durdzinski and Dr. Ruben Snellings for their strong support and friendship.

I would like to thank the members of the jury for the fruitful discussion, their very helpful comments and corrections; Prof. Paul Bowen, Prof. Ellis Gartner, Prof. Thomas Matschei and Prof. Paul Muralt.

I would like to thank the Schott-Schmalz-Stiftung and the HeidelbergCement AG for sponsoring my research. I greatly appreciate the opportunities and trust that I have experienced. In particular I like to thank my colleagues from the analytical center for the great support. Especially, I like to thank Nicolas John Spencer, Christopher Stabler and Anna Boehm.

My deepest gratitude goes to my family and my friends who supported and who encouraged me throughout this project. Especially, I like to thank my parents, my cousin Jette, my closest friends Chrischi and Gruni. All of you tried to understand and “share” my deep curiosity for grey powder.

Thanks to my colleague Dr. Anca Itul for her efforts to check and correct my spelling. Furthermore, I was very lucky to meet several generations of scientists in the LMC. Special thanks to all of you: Bizzo, Arnaud, Hadi, Élise, Berta, François, Alexandre, Julien, Franco, Luis, Lily, Aslam, John, Lionel, Aurelie, Xuerun, Mink, Wiola, Hamed, Cyrille, Chitvoranund, Hui, Yosra, Soja, Sui, Montini and Amélie. Great thanks to the fantastic organizers: Maude, Anne-Sandra and Marie-Alix.

I could only have accomplished this work with the great support and endurance of my precious girlfriend, partner and best friend Tatiana. Her support, love and understanding powered me all the way. This thesis is dedicated to her.

Leimen, February 08, 2018

Frank Bullerjahn



## Abstract

Calcium sulphoaluminate cements (CSA) with the main phase ye'elimite are a promising class of non-Portland cements which are gaining increasing interest from the cement industry. However, the hydration kinetics of CSA cements varies strongly, even for cements with similar composition and fineness. Understanding the origin of this variation was the main motivation for this thesis. Earlier studies indicated that the type and composition of ye'elimite was related to the different hydration kinetics. Iron-rich CSA cements often show faster hydration kinetics compared to those with low iron contents. The addition of easily soluble calcium sulphate such as gypsum mitigates this effect, resulting in a harmonization of the hydration sequences and kinetics. The literature reports that stoichiometric ye'elimite has an orthorhombic symmetry at ambient conditions, whereas a cubic symmetry is stabilised by the presence of minor elements such as iron. Thus, previous to this work, it was often assumed that there was a link between the presence of iron, the polymorphism of ye'elimite and the hydraulic reactivity. This thesis provides new insights into the effect of iron on the formation and hydration of different ye'elimite types, including the effect of gypsum and mayenite additions.

We found that ye'elimite is formed from the reaction of the intermediate calcium aluminates such as krotite with anhydrite. Iron primarily accelerates the formation of krotite and as a result also of ye'elimite. However, this leads to the faster decomposition of ye'elimite and as a result, mayenite starts to form.

The investigation of the ye'elimite hydration revealed five hydration periods. The onset and length of these periods is largely controlled by the solution composition. We could further show that two main hydration reactions occur. The first hydration reaction is the formation of ettringite, monocalcium aluminate decahydrate and amorphous aluminium hydroxide and occurs primarily during the initial and dormant period. The second hydration reaction is the formation of monosulphate and gibbsite-like aluminium hydroxide, occurring primarily during the acceleration and main hydration period. Increasing the water to binder ratio generally favours the first reaction. Gypsum accelerates the hydration and modifies the hydrates assemblage by favouring the formation of ettringite rather than that of monosulphate, independent of the type of ye'elimite used. We could simulate the hydration kinetics of iron-rich ye'elimite by blending stoichiometric ye'elimite with synthetic mayenite. Hence, it appears that the presence of mayenite explains the different kinetics.

We investigated the chemical shrinkage of neat ye'elimite and the effect of gypsum. The experiments revealed a transitory chemical expansion, during which bound water is released. This could be linked to the transformation and crystallization of previously formed metastable amorphous phases such as aluminium hydroxide. The transitory chemical expansion was followed by a recovery period when the shrinkage and the bound water contents returned to their original values. One possible explanation for this phenomenon is the swelling of the amorphous aluminium hydroxide.

*Keywords: ye'elimite, iron solid solution ye'elimite, mayenite, gypsum, hydration and kinetics periods*





## Zusammenfassung

Calciumsulfaluminat-basierte (CSA) Zemente, mit der Hauptphase Ye'elimit, sind eine vielversprechende Alternative zur Portlandzement und erlangen zunehmend an Bedeutung für die Zementindustrie. Jedoch variiert die Hydratationskinetik von CSA Zementen trotz vergleichbarer Zusammensetzung und Feinheit. Es war das Hauptanliegen der vorliegenden Arbeit die Ursachen für die variierende Hydratationskinetik zu bestimmen. In frühere Studien wurde ein Zusammenhang zwischen der Zusammensetzung von Ye'elimit und dessen hydraulischer Reaktivität hergestellt. Eisenhaltiger CSA reagiert schneller als solcher mit geringen Eisengehalten. Die Zugabe von Gips hebt diesen Effekt jedoch auf und führt zu einer Vereinheitlichung der Hydratationsabfolgen und der Kinetik. Frühere Arbeiten berichten das stochiometrischer Ye'elimit bei Umgebungsbedingung eine orthorhombische Symmetrie aufweist, wohingegen eine kubische Symmetrie bei Gegenwart von Nebenbestandteilen, zum Beispiel Eisen, stabilisiert wird. Daher wurde im Vorfeld zu dieser Arbeit oft ein Zusammenhang zwischen dem Gegenwart von Eisen, der Polymorphie von Ye'elimit und dessen hydraulischer Reaktivität hergestellt. Diese Arbeit liefert neue Einblicke über den Einfluss von Eisen auf die Bildung und Hydratation von verschiedenen Ye'elimiten, inklusive des Effekts der Zugabe von Gips und Mayenit.

Wir konnten zeigen, dass Ye'elimit durch die Reaktion von Calciumaluminat-Zwischenprodukten, wie Krotit und Mayenit, mit Anhydrit gebildet wird. Eisen beschleunigt vorrangig die Bildung von Krotit, was wiederum die Bildung von Ye'elimit begünstigt. Dies beschleunigt jedoch auch zu den Zerfall von Ye'elimit, wodurch die Bildung von Mayenit einsetzt.

Im Verlauf der Untersuchung der Hydratation von Ye'elimit konnten wir fünf Hydratationsstadien bestimmen. Der Beginn und die Dauer der einzelnen Stadien werden vor allem durch die Zusammensetzung der Lösung gesteuert. Wir konnten zeigen, dass im Wesentlichen zwei Haupthydratationsreaktionen ablaufen. Bei der zuerst einsetzenden Reaktion werden Ettringit, Monocalciumaluminat-Decahydrat und amorphes Aluminiumhydroxid gebildet. Diese Reaktionen laufen vorrangig während der Prä-Induktion und Induktionsperiode ab. Im Verlauf der darauffolgenden Beschleunigungs- und Haupthydratationsperiode setzt die zweite Reaktion ein, wobei vorwiegend Monosulfat und Gibbsit-artiges Aluminiumhydroxid gebildet werden. Die Erhöhung des Wasser zu Bindemittelverhältnis begünstigt im Allgemeinen die erste Reaktion. Die Zugabe von Gips beschleunigt die Hydratation und verändert die Zusammensetzung der Hydratphasen, durch die begünstigte Bildung von Ettringit anstelle von Monosulfat, unabhängig davon welcher Ye'elimittyp eingesetzt wurde. Wir konnten die Hydratationskinetik eines eisenreichen Ye'elimits durch die Zugabe von Mayenit zu stöchiometrischem Ye'elimit nachstellen. Dies scheint zu belegen, dass Mayenit die veränderte Hydratationskinetik verursacht.

Die Untersuchung des chemischen Schwindens von Ye'elimit allein und in Gegenwart von Gips zeigten eine vorübergehende chemische Expansion bei der gebundenes Wasser freigesetzt wird. Dies konnte durch die Umwandlung und Kristallisation von metastabilen Hydraten wie amorphem Aluminiumhydroxid erklärt werden. Jedoch werden die Ausgangswerte des Schwindens sowie des gebundene Wassers anschließend wieder erreicht. Wir vermuten daher, dass die Verfügbarkeit von freiem Raum sowie von Wasser das Quellen des amorphem Aluminiumhydroxid „Gels“ ermöglicht.

*Stichworte: Ye'elimit, eisenhaltiger Ye'elimit, Mayenit, Gips, Hydratationskinetik und –perioden*



## Publications

The PhD thesis includes the following peer-reviewed scientific conference and journal papers:

Conference papers

- I Iron solid solutions of ye'elimite - Effect on reactivity**  
Bullerjahn, Frank; Ben Haha, Mohsen; Scrivener, Karen Louise  
Proceedings of 14th International Congress on the Chemistry of Cement (ICCC); 2015
- II Iron solid solutions of ye'elimite - Effect on reactivity**  
Bullerjahn, Frank; Ben Haha, Mohsen; Scrivener, Karen Louise  
19. ibausil; 2015

Journal papers

- III Chemical shrinkage of ye'elimite with and without gypsum**  
Bullerjahn Frank, Skocek Jan, Ben Haha Mohsen, Scrivener Karen Louise  
*DRAFT under preparation*
- IV Hydration reactions of synthetic ye'elimite**  
Bullerjahn Frank, Boehm-Courjault Emmanuelle, Maciej Zajac, Ben Haha Mohsen, Scrivener Karen Louise  
*DRAFT under preparation*
- V Hydration of an iron solid solution ye'elimite and impact of mayenite**  
Bullerjahn Frank, Boehm-Courjault Emmanuelle, Maciej Zajac, Ben Haha Mohsen, Scrivener Karen Louise  
*DRAFT under preparation*

### Declaration of authorship

Frank Bullerjahn conducted most of the experiments and analyses presented in the thesis. He also wrote the main part of the thesis and the above-listed publications. Basic material analyses such as XRF, PSD,  $SSA_{BET}$  and ICP-OES were carried out by the laboratories of the research and technology center of the HeidelbergCement AG. The sample preparation and STEM-EDS analyses were done by Emmanuelle Boehm-Courjault with support of the Center of Microscopy of EPFL (EPFL-CIME). The thermodynamic modelling in paper IV and V was strongly supported by Maciej Zajac (HTC), Jan Skocek (HTC) and Barbara Lothenbach (Swiss Federal Laboratories for Materials Testing and Research, Laboratory for Concrete and Construction Chemistry, EMPA).

## Publications

An overview about the materials presented the publications is given in Table 1.1-1.

**Table 1.1-1 Overview of the materials used for the various papers of this PhD thesis**

Ye'elimité	Others	Synthesis campaign	Abbr. in article	Paper				
				I	II	III	IV	V
Y		S2	Cli_0.00	x	x			
0.05Fe-Y			Cli_0.05	x	x			
0.08Fe-Y			Cli_0.08	x	x			
Fe-Y			Cli_0.20	x	x			
0.40Fe-Y			Cli_0.40	x	x			
0.80Fe-Y			Cli_0.80					
Y		S3	Cli_0.00-1250		x			
			Y			x	x	x
Fe-Y			Cli_0.20-1250		x			
		Fe-Y						x
	Anhydrite		A	x				
	Gypsum		G	x		x		
	Mayenite		$C_{12}A_7$					x
	Quartz		Qz				x	x

## Glossary

The cement notation is used throughout the document:

$A = Al_2O_3$ ,  $C = CaO$ ,  $F = Fe_2O_3$ ,  $H = H_2O$ ,  $K = K_2O$ ,  $M = MgO$ ,  $N = Na_2O$ ,  $S = SiO_2$ ,  $\bar{S} = SO_3$  and  $Z = ZnO$ .

### Materials:

A	Anhydrite (calcium sulphate, $CaSO_4$ or $C\bar{S}$ )
BYF	Belite ye'elimite ferrite cement (belite > ye'elimite > ferrite content)
CAC	Calcium aluminate cement
CSA	Calcium sulphoaluminate cement (high ye'elimite content, typically > 50%)
G	Gypsum (calcium sulphate, $CaSO_4 \cdot H_2O$ or $C\bar{S}H_2$ )
PC	Portland cement
Qz	Quartz ( $SiO_2$ or $S$ )
Y	Stoichiometric ye'elimite ( $Ca_4Al_6O_{12}SO_4$ or $C_4A_3\bar{S}$ )
0.xxFe-Y	Range of iron solid solution ye'elimite with substitution level of $x$ in $C_4A_{3-x}F_x\bar{S}$ , with $x$ ranging from 0.00 to 0.80
Fe-Y	Iron solid solution ye'elimite with fixed value of $x = 0.20$ ( $C_4A_{2.8}F_{0.2}\bar{S}$ )

### General abbreviations:

ASTM	American Society for Testing and Materials
BW	Bound water
EPFL	ÉCOLE POLYTECHNIQUE FÉDÉRALE DE LAUSANNE
ETA	European technical approval
FW	Free water
GB	Guobiao (Chinese translation for national standard)
GOF	Goodness of fit
HTC	HeidelbergTechnology Center GmbH
Rwp	Weighted profile factor
w/b	Water to binder ratio, used for investigated systems in this thesis
w/c	Water to cement ratio, used when referring to PC, CSA and BYF cements
w/s	Water to solid ratio, used for blends of binder and inert quartz

## Glossary

### Methods and devices:

CS	Chemical shrinkage
FIB	Focused ion beam
GEMS	Gibbs Energy Minimization Software
ICC	Isothermal conduction calorimetry
ICP-OES	Inductively coupled plasma optical emission spectrometry
SSA <sub>BET</sub>	Specific surface area from N <sub>2</sub> absorption and using the BET-equation
SEM-EDS	Scanning electron microscopy coupled with energy-dispersive X-ray spectroscopy
BSE	Backscattered electron microscopy
HR-SEM	High resolution scanning electron microscope equipped with a field emission gun
STEM	Scanning Transmission electron microscopy analyses
PSD	Particle size distribution by laser diffraction
QXRD	Quantitative X-ray powder diffraction analysis coupled with the Rietveld refinement
TGA	Thermogravimetric analyses
Wt.%	Weight percentage

## Table of contents

<b>PREFACE</b>	<b>V</b>
<b>ACKNOWLEDGEMENT</b>	<b>VII</b>
<b>ABSTRACT</b>	<b>IX</b>
<b>ZUSAMMENFASSUNG</b>	<b>XI</b>
<b>PUBLICATIONS</b>	<b>XIII</b>
<b>GLOSSARY</b>	<b>XV</b>
<b>TABLE OF CONTENTS</b>	<b>XVII</b>
<b>1 GENERAL INTRODUCTION</b>	<b>1</b>
1.1 ALTERNATIVE BINDERS – REQUIREMENTS AND CONCEPTS	2
1.2 CONTEXT OF THE THESIS	3
1.3 MOTIVATION	4
1.4 RESEARCH APPROACH OF THE THESIS	5
1.5 OBJECTIVES	6
1.6 CONTENT OF THE THESIS	8
<b>2 LITERATURE REVIEW</b>	<b>9</b>
2.1 CALCIUM SULPHOALUMINATE CEMENT (CSA)	9
2.1.1 PRODUCTION – RAW MATERIALS AND PYRO-PROCESSING	10
2.1.2 CLINKER COMPOSITION	10
2.1.3 ANHYDROUS PHASES	11
2.2 MINERAL DISSOLUTION AND PRECIPITATION REACTIONS	13
2.2.1 CONCEPT OF UNDER- AND SUPERSATURATION	15
2.3 HYDRATION OF YE’ELIMITE	19
2.3.1 YE’ELIMITE - BASIC HYDRATION REACTIONS	19
2.3.2 HYDRATION SEQUENCES AND EFFECT OF ADDITIONS	20
2.3.3 FORMATION OF SOLID SOLUTION YE’ELIMITE AND HYDRAULIC REACTIVITY	21
2.4 THERMODYNAMIC MODELLING OF HYDRATION REACTIONS	22

<b>3</b>	<b>MATERIALS AND METHODS</b>	<b>25</b>
3.1	HYDRATED RESIDUES	25
3.2	OVERVIEW OF USED TECHNIQUES	26
3.3	BET SPECIFIC SURFACE AREA ( $SSA_{BET}$ ) AND PARTICLE SIZE DISTRIBUTION (PSD)	26
3.4	ISOTHERMAL CONDUCTION CALORIMETRY (ICC)	26
3.5	CHEMICAL SHRINKAGE (CS)	27
3.6	THERMOGRAVIMETRIC ANALYSES (TGA)	27
3.7	X-RAY FLUORESCENCE ANALYSES (XRF)	28
3.8	X-RAY POWDER DIFFRACTION (XRD)	28
3.9	HIGH RESOLUTION SCANNING ELECTRON MICROSCOPY ANALYSES (HR-SEM)	30
3.10	SEM WITH X-RAY ENERGY-DISPERSIVE SPECTROSCOPY (SEM-EDS)	30
3.11	SCANNING TRANSMISSION ELECTRON MICROSCOPY ANALYSES (STEM)	31
3.11.1	PREPARATION OF THE STEM SAMPLES BY FOCUSED ION BEAM (FIB)	31
3.12	SOLUTION CHEMISTRY BY INDUCTIVELY COUPLED PLASMA OPTICAL EMISSION SPECTROMETRY (ICP-OES)	31
3.13	HYDRATES SOLUBILITY AND THERMODYNAMIC MODELLING (SI)	31
3.14	SUSPENSION EXPERIMENTS	32
3.15	SUMMARY ABOUT POSSIBILITIES AND LIMITATIONS	33
<b>4</b>	<b>CLINKER SYNTHESIS AND CHARACTERISATION</b>	<b>37</b>
4.1	YE'ELIMITE SYNTHESIS	38
4.2	CLINKER CHARACTERISATION	40
4.2.1	MINERALOGICAL COMPOSITION	40
4.2.2	DETECTION LIMIT FOR MAYENITE IN YE'ELIMITE CLINKER	42
4.3	ANALYSIS OF MICROSTRUCTURE AND PHASE COMPOSITION OF SELECTED CLINKER	44
4.3.1	YE'ELIMITE FORMATION SCHEME – REACTION SEQUENCES	44
4.3.2	CLINKER AND PARTICLE MICROSTRUCTURE	46
4.3.3	THE FLUXING EFFECT OF IRON – IMPACT ON MICROSTRUCTURE	46
4.4	ELEMENTAL COMPOSITION OF YE'ELIMITE	48
4.5	DISCUSSION	52
4.5.1	FORMATION AND STABILITY OF STOICHIOMETRIC YE'ELIMITE AND IN THE PRESENCE OF IRON	52
4.5.2	FORMATION AND COMPOSITION OF FERRITES AND THE LIQUID PHASES	54
4.5.3	CALCIUM ALUMINATE PHASES	56
4.6	CONCLUSIONS	58



## Table of contents

<b>5</b>	<b>HYDRATION REACTIONS OF SYNTHETIC YE'ELIMITE</b>	<b>59</b>
<b>5.1</b>	<b>SUMMARY – EXPERIMENTS CARRIED OUT IN CHAPTER 5</b>	<b>61</b>
<b>5.2</b>	<b>SUMMARY - ANHYDROUS MATERIALS USED IN THE CHAPTERS 5, 6 AND 7</b>	<b>62</b>
<b>5.3</b>	<b>RESULTS</b>	<b>63</b>
<b>5.4</b>	<b>DISCUSSION OF RESULTS</b>	<b>66</b>
5.4.1	INITIAL AND DORMANT PERIOD – WHY DOES THE DISSOLUTION SLOW DOWN	66
5.4.2	ACCELERATION AND MAIN PERIOD – WHY DOES THE DISSOLUTION REACCELERATES	74
5.4.3	FINAL PERIOD	76
5.4.4	EFFECT OF W/B ON THE HYDRATION KINETICS IN PASTE	77
<b>5.5</b>	<b>GENERAL DISCUSSION</b>	<b>80</b>
5.5.1	HYDRATION SEQUENCES	80
5.5.2	WHY DOES THE DISSOLUTION SLOW DOWN AND WHY DOES IT ACCELERATE AGAIN	81
<b>5.6</b>	<b>CONCLUSIONS</b>	<b>83</b>
<b>6</b>	<b>EFFECT OF GYPSUM ON THE HYDRATION OF YE'ELIMITE AND THE CHEMICAL SHRINKAGE</b>	<b>85</b>
<b>6.1</b>	<b>SUMMARY OF EXPERIMENTS CARRIED OUT IN CHAPTER 6</b>	<b>86</b>
<b>6.2</b>	<b>EFFECT OF GYPSUM ON THE HYDRATION OF YE'ELIMITE</b>	<b>87</b>
6.2.1	EFFECT OF GYPSUM ON THE HYDRATION KINETICS	87
6.2.2	EFFECT OF WATER TO SOLID RATIO	87
6.2.3	EXPERIMENTS IN SUSPENSIONS	89
6.2.4	FORMED HYDRATES	91
6.2.5	HYDRATES STRUCTURE AND COMPOSITION	94
6.2.6	DISCUSSION	98
<b>6.3</b>	<b>CHEMICAL SHRINKAGE OF YE'ELIMITE ALONE AND WITH GYPSUM</b>	<b>99</b>
6.3.1	HYDRATES FORMED AND BOUND WATER CONTENT	100
6.3.2	SEM-EDS ANALYSES OF HYDRATED SAMPLES	103
6.3.3	MASS AND VOLUME BALANCE CALCULATIONS	105
6.3.4	DISCUSSION	106
<b>6.4</b>	<b>GENERAL DISCUSSION</b>	<b>108</b>
<b>7</b>	<b>HYDRATION OF AN IRON-RICH YE'ELIMITE AND EFFECT OF MAYENITE</b>	<b>111</b>
<b>7.1</b>	<b>SUMMARY – EXPERIMENTS CARRIED OUT IN CHAPTER 7</b>	<b>112</b>
7.1.1	HYDRATION KINETICS IN PASTES	113
7.1.2	EFFECT OF MAYENITE ON THE HYDRATION KINETICS OF NEAT YE'ELIMITE CLINKER	114
7.1.3	EFFECT OF MAYENITE ON THE HYDRATION KINETICS IN THE PRESENCE OF GYPSUM	116
<b>7.2</b>	<b>IMPACT OF MAYENITE ON THE SOLUTION COMPOSITION</b>	<b>117</b>
7.2.1	EXPERIMENTAL RESULTS	118
7.2.2	EFFECT OF MAYENITE ON THE HYDRATION KINETICS OF YE'ELIMITE ALONE AND WITH GYPSUM	121
<b>7.3</b>	<b>EFFECT OF IRON ONTO THE HYDRATES MICROSTRUCTURE AND COMPOSITION</b>	<b>122</b>
<b>7.4</b>	<b>DISCUSSION</b>	<b>127</b>

Table of contents

<b>8</b>	<b>SUMMARY OF THE FINDINGS, CONCLUSIONS AND PERSPECTIVES</b>	<b>129</b>
<b>8.1</b>	<b>INTRODUCTION</b>	<b>129</b>
<b>8.2</b>	<b>CLINKER SYNTHESIS AND CHARACTERISATION</b>	<b>130</b>
<b>8.3</b>	<b>HYDRATION REACTIONS OF SYNTHETIC YE'ELIMITE</b>	<b>131</b>
<b>8.4</b>	<b>EFFECT OF GYPSUM ON THE HYDRATION OF YE'ELIMITE</b>	<b>133</b>
<b>8.5</b>	<b>THE CHEMICAL SHRINKAGE EVOLUTION OF NEAT YE'ELIMITE AND WITH GYPSUM</b>	<b>134</b>
<b>8.6</b>	<b>HYDRATION OF AN IRON-RICH YE'ELIMITE AND EFFECT OF MAYENITE</b>	<b>135</b>
<b>8.7</b>	<b>GENERAL DISCUSSION</b>	<b>136</b>
<b>8.8</b>	<b>PERSPECTIVES</b>	<b>138</b>
	<b>REFERENCES</b>	<b>141</b>
	<b>LIST OF PUBLICATIONS</b>	<b>155</b>
	<b>ANNEX</b>	<b>157</b>
	<b>CURRICULUM VITAE</b>	<b>247</b>

# 1 General introduction

The worldwide most used cement type is Portland cement (PC). PC is one of the most cost- and energy-efficient building materials and on a unit basis the associated  $CO_2$  emissions are lower than for other building materials such as steel or wood [1] [2]. However, in sum it accounts for 5-8 % of the global manmade  $CO_2$  emissions [3] [4]. The basis of it is Portland cement clinker which is produced from the firing of a raw meal at a temperature of about 1450 °C. The raw meal is composed of limestone, clay and some correctives such as iron ore and silica sources. The decomposition of limestone is the main material-related “fossil”  $CO_2$  source. Including energy-related  $CO_2$  emissions, the manufacturing of 1t of cement clinker releases about 800 kg of  $CO_2$ . The clinker is ground together with calcium sulphate to produce the final cement. PC is mainly used in concrete, which is, beside processed water, the largest used man-made material worldwide by mass. Nowadays, no satisfactory alternative to replace PC exists. Thus, there is increasing demand for the development of environmental friendly binders. Using locally available materials can be a huge advantage as it reduced the  $CO_2$  emission related to materials transport.

Another important aspect to be considered when discussing the ecological impact of cement production is the embodied energy. Figure 1.1-1 gives a comparison between the embodied energy for the production of one ton of various building materials. The total consumed energy includes all associated energies for all production processes such as those for mining and processing of natural resources (raw materials for cement or steel production, aggregates and sand for concrete, etc.), transportation of goods and people and finally the manufacturing itself. By comparing the embodied production energy, it is clear that PC and explicitly PC concrete remain one of the most cost- and energy-efficient building materials. Nevertheless, the cement industry has to look for opportunities to reduce the embodied energy and the associated  $CO_2$  footprint even further, to compensate for the expected enormous growth in cement demand in the developing world.

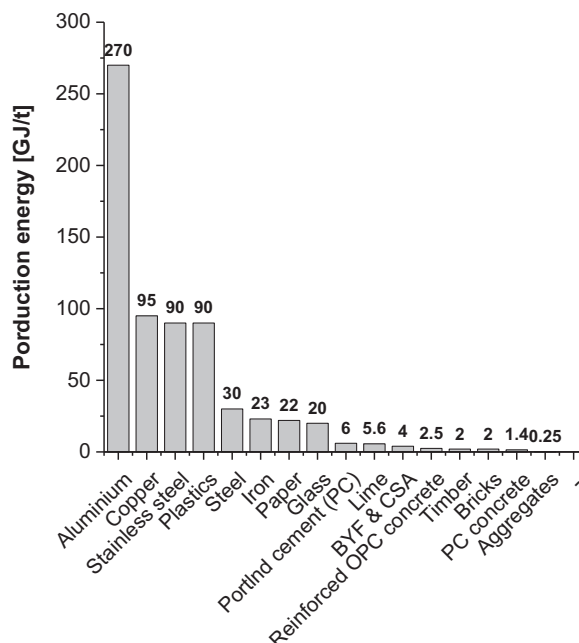


Figure 1.1-1 Embodied energy for the production of one ton of a specific building material (data adopted from [5] [6] [7]) including own presumed values for CSA and BYF (internal reports HC AG)

Such solutions may be based on the production of alternative binders such as calcium sulphoaluminate (CSA), especially belite-rich types sometimes referred to as belite ye'elinite ferrite (BYF). Despite all the efforts to produce environmental friendly "green" binders, the demand for a robust solution having similar properties as PC represents and remains one of the major challenges. This point will be further discussed in section 1.1 below and in Chapter 2.

## 1.1 Alternative binders – requirements and concepts

One important component, out of several solutions, to reduce the building materials-associated  $CO_2$  emissions is the development of low- $CO_2$  or so called "green" binders. These days there is an endless number of proposed novel and "green" binder concepts, including carbon-based glues [8], foams [9], (molten) sulphur concrete [10] and more "classical" solutions such as inorganic materials. For the purpose of this study, we only refer to those alternative binders which are based on inorganic cementitious materials that can be used for construction. To be considered as a real opportunity some basic requirements need to be met:

- Raw materials must be globally abundant, locally available (minimal transportation distances) and obtainable at low cost
- Quality of raw materials (composition) should be stable to allow maintaining a stable production
- Technical feasibility at industrial (production) scale
- New binder should have essentially a lower CaO demand in the final product(s)
- Possibility for the recycling of (its own) wastes and by-products "2<sup>nd</sup> life"

Even more important, is that the cement performance is stable. The material handling during preparation of concrete should be ideally similar to PC. Ultimately, the concrete should preferably behave similar or even better when compared to PC concrete with regard to e.g. the strength development, volume stability, surface quality and resistance to chemical or physical attacks. In the field of inorganic building materials, several technologies are currently under investigation by research institutes, industrial players and start-up companies which may fulfil some or even all of the points stated above. These building materials are:

- Calcium sulphoaluminate (CSA) type cements [11] [12]
- Geopolymers or alkali activated binders [13] [14]
- Hydrothermal binders [15] [16] [17]
- Binders requiring hardening by carbonation of magnesium or calcium based materials; Novacem [18], Solidia [19] and Calera [20] type binders or sequestered carbon cement
- Magnesium cements such as oxide [21], Sorel [22] [23] or silicate [24] ones

To substitute PC in a substantial amount and on global scale further aspects should be considered. The market not only demands a product with constant product properties but in addition, performance and durability data should be available. In the best case, the material (class) would be covered by already existing standards. CSA cements are a promising class of non-Portland cements [1] [11], with the main phase ye'elinite ( $C_4A_3\bar{S}$  or  $Ca_4Al_6O_{12}SO_4$ ), which fulfil most of the presented requirements. The subclass of BYF cements are of high interest. Their lower ye'elinite contents allow its production from lower quality bauxite (the main aluminium source) or industrial by-products to replace at least partly expensive bauxite sources.

Those materials offer a high potential for the construction industry for the following reasons:

- (1) Global availability and local accessibility of well-known virgin raw materials such as limestone, gypsum, bauxite and alumina-rich clay
- (2) Possibility of substitution of virgin raw materials by industrial by-products and wastes
- (3) Meaningful reduction of raw material and process related  $CO_2$  emissions
- (4) Mastered production technology and the possibility of using existing PC plants
- (5) Energy saving potential due to 200 °C up to 300 °C lower sintering temperature (fuel consumption) and friable clinker providing a soft and easy to grind material compared to PC
- (6) In general, known hydration processes and products, adjustable and comparable properties of its cement to PC
- (7) Existence of more than three decades of experiences in various applications and availability of durability data in some cases
- (8) Already existing standards and technical approvals for the use of CSA in some countries.  
However, so far not for structural applications.

The industrial feasibility as well as the above mentioned savings were already proven at industrial scale [11] [25] [26]. In the meantime, the HeidelbergCement AG successfully conducted two industrial BYF production trials in existing European PC cement plants. One of the produced clinkers is currently under investigation in the context of ECO-BINDER project [27] which is supported by the European Commission under the Energy Theme of Horizon 2020, Technological development Grant Agreement number 637138.

## 1.2 Context of the thesis

Stable product characteristics are of high importance for the development of robust cements which can be used for ready mix or pre-cast concrete applications. In what follows, we will highlight why it is important to understand the hydration kinetics and underlying reactions. This knowledge would enable the necessary development of needed admixtures such as retarders [28] [29] [30] [31] [32]. Figure 1.2-1 shows a comparison of the open time of cement mortars based on PC and CSA.

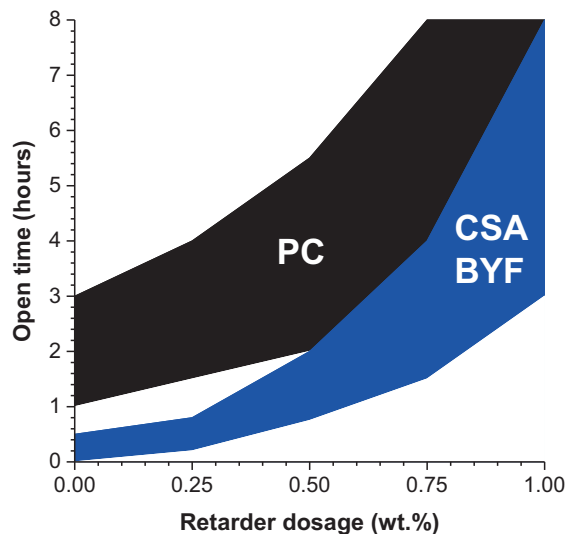


Figure 1.2-1 Open time of PC versus CSA depending on the retarder dosage

The open time known as workability and shown as mortar spread typically ranges from 1 to 3 hours for PC. On the contrary, CSA has an open time of minutes or seconds as a consequence of its faster hydration development. Extending the open time can only be achieved by the addition of a retarder. This is necessary for handling, placing and surface finishing of concrete. The use of a retarding agent has another beneficial feature. Figure 1.2-2 shows the mortar spread (a) and compressive strength evolution (b) of tested belite-rich CSA labelled “BYF” (BYF 2 also in Figure 1.4-2) with and without the use of 10 wt.% micronized natural anhydrite “10A” and of a retarder. The non-retarded binders start with a lower initial mortar spread and reveal a rapid drop afterwards. Additionally, the reached strength level is surprisingly low for both cements. The addition of a retarder resulted in a higher initial mortar spread, a longer open time and by far superior strength values. The addition of anhydrite alone had no retarding effect, but instead it boosted the early strength values.

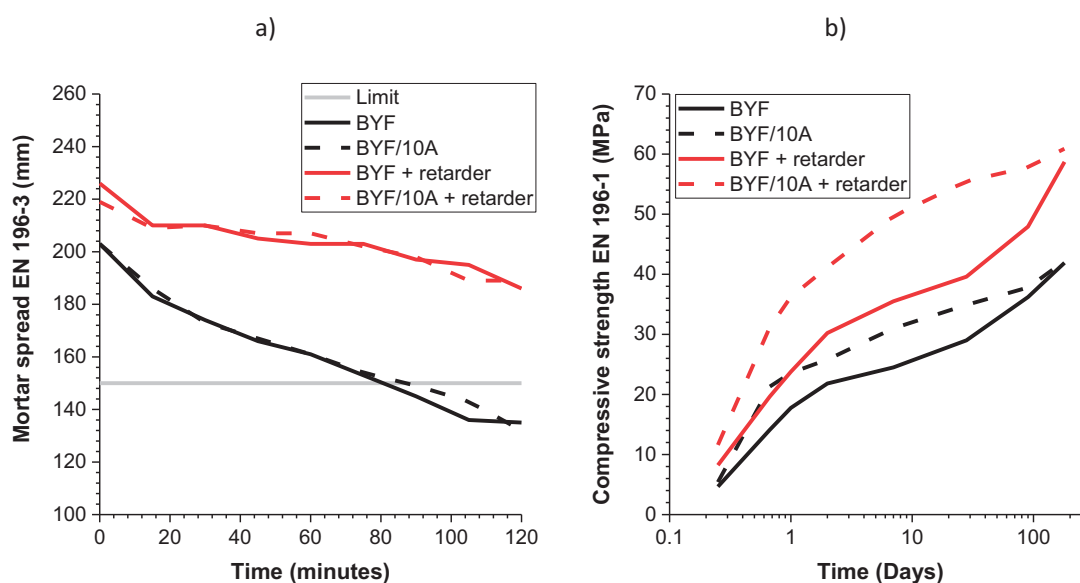


Figure 1.2-2 Open time of PC versus CSA depending on the retarder dosage (a); mortar spread (b) and compressive strength (c) development of BYF binders with and without retarder

### 1.3 Motivation

The results presented above highlight the importance of the understanding of the hydration reactions. This understanding would facilitate the production of durable concrete and the successful commercialisation of CSA and BYF binders. We reported earlier that CSA and BYF cements often exhibit different hydration kinetics and associated cement properties [33] [34], despite having similar characteristics in terms of chemical and mineralogical composition and fineness. The origin of these differences remains unknown. Most early age properties are primarily related to the hydration of ye’elimite. In an earlier work of us [34], we observed the correlation between the type of ye’elimite formed and the different reactivity of the cements. At room temperature, stoichiometric ye’elimite has an orthorhombic symmetry [35] [36], but often traces of cubic form are present in CSA and BYF clinkers as well [37]. The cubic symmetry seems to correlate with the iron content and the process conditions which cause the faster hydration [33] [34]. Later studies on synthetic ye’elimite confirmed these findings [38] [39]. However, the origin of the altered hydration kinetics remains unclear.

## 1.4 Research approach of the thesis

PC serves as a textbook example of a reliable, robust, stable and modern product. Figure 1.4-1 shows the rate of heat evolution of PC taken from three different cement plants and of synthetic tricalcium silicate ( $C_3S$ ). An important feature is the similar hydration pattern for the three cements, independent of their differences such as fineness or composition (not shown). Synthetic  $C_3S$  represents a good model system for PC [40] [41] [42] [43]. By analysing the cause of the onset, duration and end of the underlying reactions it was possible to gain important insights in the fundamental parameters controlling the hydration of PC [44] [45] [46]. This will be discussed in more detail in Chapter 2, section 2.2.

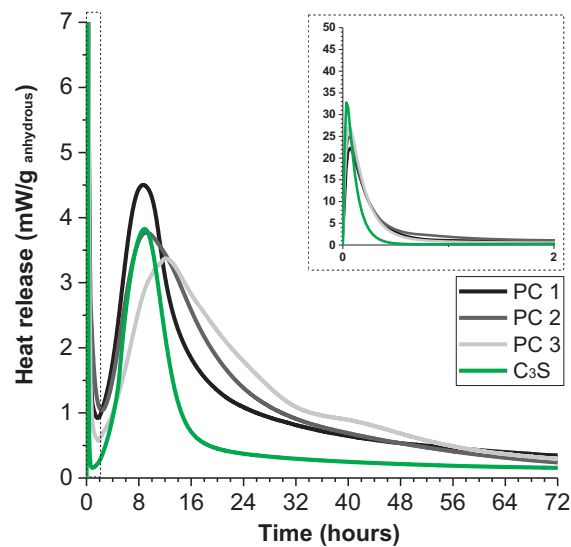
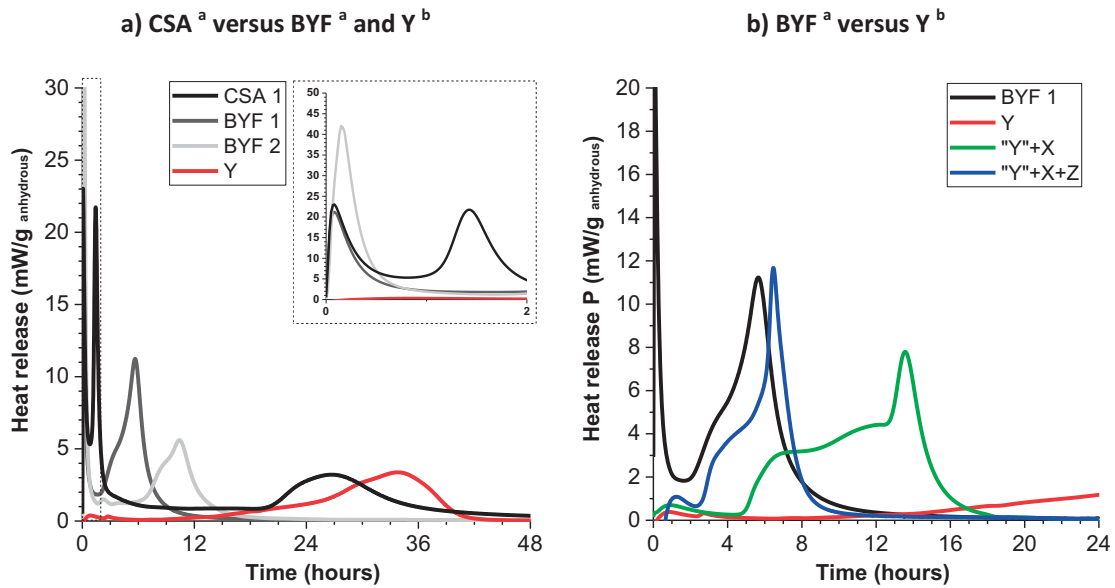


Figure 1.4-1 Rate of heat evolution from isothermal conduction calorimetry of PC and  $C_3S$  at 20 °C and w/c 0.5; calorimetry data for  $C_3S$  provided by Xerun Li

Applying a similar approach as for PC, we use synthetic ye'elimite as reference system for CSA and BYF. Figure 1.4-2 a) presents the heat release of CSA and BYF cements and of stoichiometric ye'elimite (normalized to ye'elimite content of 30% similar to that found in BYF). The BYF 1 and BYF 2 were produced during one industrial trial and had very similar compositions and fineness. In contrast to PC, the CSA and BYF cements reveal very different hydration kinetics. Also, the hydration of the synthetic ye'elimite (Y) (see Figure 1.4-2 b)) shows a different hydration pattern compared to that of CSA and BYF cements. This raises the question, whether we can use synthetic ye'elimite as a model system to explain the hydration reactions of CSA and BYF as discussed in the Chapters 5 to 7. The unknown components labelled as "X" in Figure 1.4-2 b) will be presented in section 6.2.5, summarizing the some of the findings of this thesis.



<sup>a</sup> CSA and BYF from industrial production, BYF samples have almost the same composition, tested at w/c 0.5

<sup>b</sup> Y synthesized at lab scale, tested at w/c 2 and measured data normalized to ye'elimite content of 30%

Figure 1.4-2 Rate of heat evolution from isothermal conduction calorimetry of CSA, BYF and Y at 20 °C

## 1.5 Objectives

The literature reports that stoichiometric ye'elimite has an orthorhombic symmetry at ambient conditions, whereas a cubic symmetry is stabilised by the presence of minor elements such as iron. Thus, previous to this work, it was often assumed that there was a link between the presence of iron, the polymorphism of ye'elimite and the hydraulic reactivity. The hydration of iron-rich ye'elimite proceeds faster compared to the stoichiometric one in most the cases and if no easily soluble calcium sulphate is added.

The objective of this thesis is to answer the following questions:

- i. To which extent can iron substitute aluminium in ye'elimite and what are the best conditions to form such solid solutions?
- ii. Does the formation of iron-bearing ye'elimite solid solution alter the hydration kinetics?
  - a. If it does, what causes the alteration of the hydration kinetics?
  - b. Which mechanism is altered and how?
- iii. iii. What are the hydration mechanisms for stoichiometric ye'elimite?

To answer these questions we synthesized stoichiometric ye'elimite and several (mainly) iron-bearing solid solutions. The anhydrous clinkers were fully characterised by QXRD, XRF, SEM-EDS and other methods. The results are presented in Chapter 4 and Annex part - IV.



## General introduction

Following the initial rapid reaction after contact with water, several other hydration stages were identified. This raises additional questions:

- i. Which phases are formed and how fast during each hydration stage?
- ii. What controls the duration and the advancement from one hydration period to another?
- iii. Are the formed phases stable or do they transform over time?
- iv. What is the effect of the water to cement and of the water to solid ratio on the kinetics?
- v. Can we compare the results from paste (static) and suspension (dynamic) experiments?
- vi. Why does the addition of gypsum results in similar hydration kinetics and sequences, independent of the ye'elimite type?

The related experimental results are presented in Chapter 5, 6 and the annex - part V.

We will demonstrate in Chapter 7 that the polymorphism alone cannot explain the different hydration kinetics. These observations led to the following questions:

- vii. Which mechanism(s) cause(s) the faster hydration kinetics of the iron-bearing solid solution ye'elimites? Possible hypotheses are:
  - a. Modification of the formed hydrates assemblage composition by iron
    - i. Formation iron-bearing of solid solutions of ettringite, monosulphate, aluminium hydroxide and others
    - ii. Formation of additional phases such as iron hydroxide or iron-bearing katoite ( $C_3(A,F)H_6$ )
  - b. Changes in the solution concentrations and in the mobility of species, affecting the dissolution rates
  - c. Unknown factor(s) such as the
    - i. Presence and / or reaction of so far not considered anhydrous phases
    - ii. Formation of unknown / not considered hydrates
- viii. What is the role of calcium sulphate?

**One of the key findings is the presence of mayenite in the iron-rich ye'elimite**, either as amorphous phase or as crystalline phase below XRD detection limit. This led to the next questions:

- ix. What causes the formation of mayenite?
- x. What is the detection limit of mayenite in ye'elimite clinkers?

All related experimental results are presented in Chapter 4 and annex - part IV. Based on these findings we can address the following questions:

- xi. What is the impact of mayenite on the hydration kinetics?
  - a. Can we simulate this effect using synthetic mayenite?
  - b. Which reactions or hydration periods are altered?

Outside of the initial scope of the thesis, we investigated the chemical shrinkage of neat ye'elimite and the impact of gypsum. The chemical shrinkage measurements indicated that a chemical expansion occurs for both binders. We carried out several supplementing investigations to assess the origin of the chemical expansion. The results of those are presented in Chapter 6 and the annex - part V.

## 1.6 Content of the thesis

This thesis is divided in 8 chapters and it is structured as follows:

Chapter 1 includes a general introduction with focus on the possibilities to reduce the  $CO_2$  emissions for the cement industry. It further presents the context and background, motivation and objectives as well as the experimental approach used in this study.

Chapter 2 presents a literature review summarizing the historical background and provides an overview regarding the production and composition of CSA, BYF and the main anhydrous phases present in this study. The hydration of ye'elimite is briefly introduced as well as the basic principles of mineral dissolution and precipitation. The concept of thermodynamic modelling is briefly described.

Chapter 3 details the applied characterisation methods, the sample preparation procedure for hydrated residues and the possibilities and limitations of the applied techniques.

Chapter 4 presents the results of the anhydrous characterisation, microstructural features and the determination of the elemental composition of the each synthesised ye'elimite polymorph. It also details the cause of the mayenite formation and its XRD detection limit.

Chapter 5 presents a general overview regarding the hydration kinetics and reactions of stoichiometric ye'elimite. It further provides insights into the dissolution and precipitation reactions during the first seconds and minutes, including the formation, composition and the morphologies of initial hydration products. The hydration pattern during the first 24 hours was divided into five stages for which we could determine some mechanisms for their onset and for their end. In a next step, the impact of the w/c ratio on the hydration kinetics of pastes was investigated.

Chapter 6 details the impact of gypsum on the hydration of ye'elimite and especially on the hydration stages. It provides insights into the dissolution and precipitation reactions, addressing the importance of the solution composition on the accelerated formation of ettringite and the corresponding dissolution of ye'elimite. It further includes the chemical shrinkage evolution of stoichiometric ye'elimite alone and in the presence of gypsum. This study revealed a transitory chemical expansion resulting from the recrystallization of aluminium hydroxide and the release of bound water.

Chapter 7 reveals the impact of synthetic mayenite on the hydration kinetics of stoichiometric and iron-rich ye'elimite in pastes and suspensions. Further, the effect of combined gypsum and mayenite additions was assessed. It further provides theoretical insights to explain the underlying mechanisms.

Chapter 8 summarizes the main findings, draws conclusions and identifies potential future research directions.

## 2 Literature review

### 2.1 Calcium sulphoaluminate cement (CSA)

The **historical development** of the CSA technology is briefly discussed here. The production and use of CSA clinkers and cements was originally described by Alexander Klein in the late 1950s, mainly for shrinkage compensation in PC-based concrete [47] [48]. This led to the invention of ASTM Type K cement (ASTM C845-04) based on the “Klein” compound which is ye’elimite. They were also used for other non-structural applications, such as repair mortars or rapid hardening additive for OPC [47] [11]. Further development was done in China under the brand name “Third Cement Series” [11] and resulted in the Chinese cement standard GB 20472-2006. Two main CSA types were differentiated which are sulphoaluminate “SAC” and ferroaluminate cements “FAC”. The standard was first published in 1981, revised in 2006 and includes three CSA classes [49]:

- Rapid hardening sulphoaluminate cement – R.CSA
- Low alkaline sulphoaluminate cement – L.CSA
- Self-stress sulphoaluminate cement – S.CSA

The important properties of CSA-based binders (see also annex – part II) can be summarized as follows:

- Additive for PC for the control of the setting time, early strength [11] [50] or for shrinkage compensation [11] [51]
- Good durability of CSA-based concrete with respect to
  - Sulphate resistance [30] [50] [52]
  - Resistance against sea water and sodium chloride [30] [50]
  - Resistance against carbonation [30] [53] [54]
- Normal workability and setting times when retarders are used [11] [29] [30]
- Reduced risk of efflorescence as no or little as portlandite is formed during hydration [55]
- Cold weather application [29] [56] and freeze-thaw resistance [57] [58]

CSA type cements were already intensively studied, developed and used in real applications over decades. Additionally, commercial products, standards and technical approvals exist already (additional information are available in the annex – part II) providing a “proof of concept” for this alternative binder type. Belite-rich CSA types sometimes referred to as belite ye’elimite ferrite (BYF) are gaining increasing interest. This is due to the potential to substitute expensive or  $CO_2$ -bearing virgin materials such as bauxite or limestone, respectively with industrial by-products and wastes [33] [59] [60] [61]. This would enable a significant cost reduction (e.g. for bauxite) and of  $CO_2$  emissions (e.g. from limestone). On the contrary, the use of industrial by-products and wastes could increase the content of minor elements such as iron, alkali, phosphor and heavy metals [33] [61]. Especially the iron content increases with the use of by-products and wastes.

### 2.1.1 Production – Raw materials and pyro-processing

CSA was historically produced from virgin raw materials such as limestone, bauxite and clay together with gypsum under oxidizing conditions [1] [12]. The optimal production temperature is around 1250°C [1] [12] [25] and strongly depends on the raw materials used and the formulation [33]. Strigáč et al. [62] emphasized that the type of raw material used has a strong impact on the clinker formation and composition as the main minerals ye'elimite, belite and ferrite can incorporate significant amounts of foreign elements. The optimal production temperature also depends on the probable formation of intermediate, unwanted phases. For example, Korndörfer [63] showed that the use of kaolin instead of bauxite as alumina source hinders the formation of ye'elimite within temperature range from 1000 °C to 1200 °C. This was caused by the formation of gehlenite ( $C_2AS$ ), which is an unwanted, intermediate phase. This phase is not hydraulically reactive but binds alumina and calcium which are in turn not anymore available for the reactive clinker phases. Sintering temperatures above 1250 °C would be needed to decompose gehlenite again. On the contrary, too high temperatures and / or dwell times should be avoided as this could lead also to the decomposition of ye'elimite [64]. Recently it was shown that elemental sulphur or sulphur-rich products can be used as alternative fuels for the production of CSA and BYF [65]. The combustion causes the oxidation of sulphur and formation of gaseous  $SO_2$ , which can react with phases such as lime, calcium aluminates and silicates to form anhydrite, ternesite and ye'elimite. The gaseous  $SO_2$  further stabilises sulphate-bearing phases at higher sintering temperatures [65] [66]. Another advantage is the significant reduction of process related  $CO_2$  emissions by replacing conventional hydrocarbon based fuels such as oil or coal by the elemental sulphur and its derivatives.

### 2.1.2 Clinker composition

The chemical composition of CSA clinkers covers a broad range in the system  $CaO - SiO_2 - Al_2O_3 - Fe_2O_3 - SO_3$  as shown in Table 2.1-1. CSA has lower  $CaO$  and  $SiO_2$  but far higher  $Al_2O_3$  and  $SO_3$  contents compared to PC or BYF. BYF falls into the ranges between PC and CSA, where the iron content is typically higher.

**Table 2.1-1 Typical compositional ranges of PC, CSA and BYF**

	PC (%)	CSA types(%)	BYF types (%)
<b><i>CaO</i></b>	<b>55 – 75</b>	<b>35 – 45</b>	<b>45 – 56</b>
<b><i>SiO<sub>2</sub></i></b>	<b>15 – 25</b>	<b>5 – 10</b>	<b>15 – 22</b>
<b><i>Al<sub>2</sub>O<sub>3</sub></i></b>	<b>2 – 6</b>	<b>25 – 35</b>	<b>15 – 25</b>
<b><i>Fe<sub>2</sub>O<sub>3</sub></i></b>	<b>0 – 6</b>	<b>0 – 9</b>	<b>2 – 12</b>
<b><i>SO<sub>3</sub></i></b>	<b>0.3 – 1.5</b>	<b>6 – 30</b>	<b>6 – 15</b>

The mineralogical phase assemblage of CSA and BYF in comparison to PC is shown in Table 2.1-2. Alite is the dominant phase in PC whereas CSA and BYF do not contain significant alite contents. Ye'elimite is the phase which determines the clinker and cement quality. Dicalcium silicate and ferrites are typically present as minor phases in PC or CSA, whereas they are the main phases of BYF. Additional information about the potential for the reduction of the emissions, the energy consumption or the clinker classification and cement properties can be found in in annex – part II.

Table 2.1-2 Comparison of typical compositional ranges of the mineralogical phase assemblages

	PC [%]	CSA types [%]	BYF types [%]
$C_3S$ (alite)	55 – 75	0 – 5	0 – 5
$C_2S$ (belite)	10 – 20	0 – 55	45 – 75
$C_3A$ , $CA$ , $C_{12}A_7$ , $CA_2$ (aluminates)	5 – 10	0 – 20	0 – 5
$C_4AF$ (ferrites)	5 – 10	0 – 30	2 – 40
$C_4A_3\bar{S}$ (ye'elimite)		45 – 75	20 – 45
<b>Cements</b>			
$C\bar{S} \cdot xH$ (calcium sulphates)	3 – 6	0 – 30	0 – 15
C & CH (free lime & portlandite)	0 – 2	0 – 25	0 – 1

### 2.1.3 Anhydrous phases

**Calcium sulphoaluminate** or **ye'elimite** ( $Ca_4Al_6O_{12}SO_4$ ) is a mineral belonging to the sodalite family. Ye'elimite is a pure aluminate sodalite which contains calcium instead of sodium. The sodalite group phases have the general formula  $M_{6+x}(TO_2)_{12}Y_x \cdot nH_2O$  (with  $x = 0 \leq x \leq 2$  and  $n = 0 \leq n \leq 8$ ) ([67] [68] [69]) with:  $M$  being low charged caged cations ( $M = Na^+, Ca^{2+}, Mg^{2+}$ ),  $T$  are tetrahedral coordinated framework-building cations ( $T = Si^{4+}, Al^{3+}, Fe^{3+}$ ) and  $Y$  are caged anions ( $Y = Cl^-, OH^-, SO_4^{2-}$ ). The charged balance is maintained by compensating the excess charge of the framework unit by the cage anions. The aluminate sodalite ye'elimite is characterized by a  $[Al_{12}O_{24}]^{12-}$  framework, together with one or more divalent, less monovalent, cation(s) and a tetrahedral shaped oxyanion  $SO_4^{2-}$ . The derived chemical general formula for ye'elimite would be accordingly:  $Ca_8[Al_{12}O_{24}](SO_4)_2$ . The arrangement of the framework is very flexible and can adopt its structure (e.g. rotation and tilting of the  $TO_4$  tetrahedra) and size in dependence of the present cage cations and anions. However, it needs to maintain the charge balance. The excess charge of the  $[Al_{12}O_{24}]^{12-}$  framework is balanced by caged  $Ca^{2+}$  and  $SO_4^{2-}$  [67] [68]. Stoichiometric ye'elimite has cubic symmetric at temperatures above 800 °C and undergoes a phase transition to an orthorhombic symmetry at room temperature [36] [70] [71]. Several research groups reported the possible stabilization of a pseudocubic symmetry by incorporating foreign ions such as iron [34] [35] [39] [72].

**Calcium aluminates** are forming the binary system  $CaO - Al_2O_3$  which contains several intermediate phases. The calcium aluminates tricalcium aluminate ( $C_3A$ ), **krotite** or monocalcium aluminate ( $CA$ ), **grossite** or monocalcium di-aluminate ( $CA_2$ ) and **mayenite** ( $C_{12}A_7$ ) are mainly of relevance for the cement industry. Tricalcium aluminate is the main aluminate phase present in PC. This phase will not be further addressed, as it is not present in most of the investigated synthesized clinkers. Krotite is the main phase of calcium aluminate cements "CAC" together with grossite and mayenite [73] [74] [75] [76]. These phases are typically only present as minor phases in CSA or BYF [33] [37]. Krotite has a wide stability field, can form large prismatic crystals and often contains iron [77]. Mayenite has a very narrow stability field, forms small crystallites which are further intermixed or embedded within other phases like krotite or ferrite [73] [78]. Several elements are known to stabilise mayenite. Those include iron [73] [77] [79] [80] [81], fluoride, chloride, cyanide, sulphide [82], magnesium [79] [81] and silica [79] [81] [83]. New types of commercial CACs are available which are mainly composed of amorphous mayenite glass [83] [84] [85] [86]. It is well known that the different aluminates hydrate with different rates depending on their calcium content [73]. Mayenite is by far more reactive than krotite but less reactive than tricalcium aluminate.

Pure krotite can have a dormant period ranging over tens of hours. Grossite reacts at a much slower rate than krotite. The addition of calcium sulphate, e.g. as gypsum, causes an acceleration of the krotite and retardation of the mayenite hydration. Grossite almost does not react within the first days of hydration.

The formation of the **calcium ferrites** starts with calcium ferrite (*CF*) at about 1000 °C, followed by dicalcium ferrite or srebrodolskite ( $Ca_2Fe_2^{3+}O_5$  or  $C_2F$ ) [87] [88]. By increasing the temperature above 1216 °C **srebrodolskite** starts to melt. In the presence of alumina the melting point of the ferrites decreases and wide ranges of solid solutions with the general formula  $Ca_2(Al_xFe_{2-x})O_5$ , with x from > 0 to below 1.40, can be formed. Raab [89] showed that srebrodolskite and **brownmillerite** can be formed already at 700 °C when using nano-sized raw mixes such as from sol-gel synthesis. The alumina-rich solid solutions are formed by dissolving of alumina into the liquid phase and the recrystallization of alumina-rich ferrites during cooling. The alumina can originate from the raw materials components or from intermediate clinker phases such as calcium aluminates [90]. Srebrodolskite has an orthorhombic primitive lattice, where the symmetry can be preserved to substitution levels of x up to about 0.6 [91] [92]. The further increase of the alumina concentrations causes the modification of the symmetry to an orthorhombic, body-centred phase [92] [93] such as brownmillerite (ideally  $Ca_2(Al, Fe^{3+})_2O_5$  or  $C_4AF$ ) [73]. It is generally accepted that the ferritic phase, written  $C_4AF$ , represents non-ideal solid solution which also contains additional elements such as alkalis, magnesium, silica, sulphur and phosphor [62] [91] [94]. Reducing conditions\* cause the partial substitution of  $Ca^{2+}$  by  $Fe^{2+}$  [89], where the  $Fe^{2+}/Fe^{3+}$  ratio correspond to the applied sintering temperature [95]. Clinkers with high  $Fe^{2+}/Fe^{3+}$  ratios had greenish to bluish colour where clinkers with low ratios had a dark brownish to black colour [95]. As for the aluminates it is general accepted knowledge that the ferritic phase hydrates with different rates, depending on the alumina over iron ratio and the presence of calcium sulphate [93] [96] [97] [98]. The alumina-rich phases hydrate faster than iron-rich ones and the presence of calcium sulphate causes a strong retardation of both.

\* Lack of oxygen in the gaseous atmosphere, i.e. low oxygen partial pressure, from e.g. incomplete oxidation of (hydro)carbon fuels, resulting in the formation of reducing agents such as C, CO or  $H_2$ : e.g.  $Fe_2O_3 (s) + CO (g) \leftrightarrow 2 FeO (s) + CO_2 (g)$

**Calcium sulphate** or **Anhydrite** ( $C\bar{S}$ ), as part of the clinker, is typically present as a minor phase in CSA [33] [37] and synthetic ye'elimite (see Chapter 0 and annex – part IV). It is present as anhydrite I, also called dead burnt anhydrite, which forms and is stable above 1180 °C [99]. Dead burnt anhydrite is known for its slow dissolution rate (annex – part V). Anhydrite is only stable till 1300 °C under oxidizing conditions (excess of oxygen in the gaseous atmosphere, i.e. high oxygen partial pressure). The decomposition process accelerates once the temperatures rise above 1300 °C. On the contrary, the decomposition of anhydrite starts from around 1100 °C under reducing conditions [100] [101] [102]. The decomposition of anhydrite causes the volatilization of sulphur and the formation of free lime such as e.g.:  $CaSO_4 (s) + CO (g) \leftrightarrow CaO (s) + SO_2 (g) + CO_2 (g)$ .

## 2.2 Mineral dissolution and precipitation reactions

The hydration of cement is in simple terms a dissolution-precipitation process [46]. The water is initially undersaturated with respect to the anhydrous phases and hydrates. Consequently, the anhydrous phase starts to dissolve. The dissolution is rapid at a high degree of undersaturation whereas it slows down when coming closer to point of equilibrium solubility of the dissolving phase [40]. The solution becomes increasingly enriched with dissolved ions, supersaturation with respect to specific hydrates is reached and in consequence the precipitation of the saturated hydrates may occur. The supersaturation and type of formed hydrates depend on the starting material chemistry, mineralogy, the dissolution and nucleation rates as well as other parameters such as the alkalinity and temperature of the solution. Additionally, it was recently discussed by Nicoleau et al. [103], that ongoing reactions such as the dissolution of a solid, changing of the solution composition and the formation of the hydrates are coupled. This means, any parameter that alters one of those variables, e.g. causing the accelerating or decelerating of a reaction, will also alter the others.

Why it is important to speak about the dissolution and precipitation? In simplified terms, because it determines the properties of the products. This ranges from the fresh, e.g. workability or rheology, to the hardened properties, e.g. strength development. It is absolutely critical to understand the fundamental hydration mechanisms. This is especially true for the development of alternative binders which have to be competitive to PC, not only from economic standpoints but even more from the performance characteristics. The basis for the understanding of the fundamental reaction mechanism is found in the three major questions [46]:

- At which rate does the system react? The reactions typically follow a kinetic path instead of forming directly the thermodynamic most stable hydrates. The overall hydration kinetics depend on the rate of the anhydrous dissolution and the formation of hydrates, as well as material specific properties such as particle and crystallite sizes, crystallography aspects (e.g. solid solutions, defects, etc.), morphologies, phase assemblages and distribution.
- What types of phases are formed and are they stable?
- How does the formed phase assemblage fill the available space, e.g. between the (left) anhydrous particles and that of which was formerly occupied by the anhydrous and free water? This does determine the type of the formed microstructure and in that respect the obtained macroscopic properties.

Especially for alumina-rich binders we have to address an additional question:

- Are the formed phases stable and what happens to e.g. the microstructure during transformation and recrystallization processes? Those questions include thermodynamic as well as kinetic drivers.

The general chronological order for the formation of hydrates can be given as follows (adopted from [104] and extended):

Exposure of a mineral to (highly) undersaturated aqueous solution → Mineral dissolution → Increase of solution concentrations → Aqueous complexation → Adsorption (surface complexation) → Absorption → Surface precipitation → Co-precipitation → Ion-diffusion → Crystal growth, transformation (via solution) and recrystallization



The above given reaction order is further visualized in Figure 2.2-1 below.

The hydration of cement typically results in the formation of metastable phase, followed by the progressive transformation to (more) stable hydrates. This especially is the case for alumina-rich binders such as calcium aluminate cements [73]. This is partially related to the formation of polymorphic compounds such as aluminium hydroxide. Aluminium hydroxide can precipitate in several crystal structures or as amorphous phase, where the different types can have also different properties such as the density, specific surface area or the amount of combined water. It is possible that only one of the polymorphs is thermodynamically stable under the given hydration conditions such as solution composition, temperature, pressure, etc.. The formation of metastable phases can be kinetically favoured and is usually followed by the transformation into more stable phase [105]. However, this process can be (infinitely) slow as e.g. it is the case for C-S-H, the main hydration product of PC. In addition, the stable hydrates tend to grow on expense of smaller crystallites to reduce the total (surface, interfacial) energy of the system. This process was noticed a long time ago by Ostwald who formulated his rule of stages, often referred to “Ostwald Rule of Stages” and followed by the so called “Ostwald ripening” [105] [106]. The process of the recrystallization typically includes the interaction of the formed solid with the aqueous solution and formed ion complexes. Overviews covering the geochemical theory of dissolution and the cement hydration in general were provided by Juilland [107], Scrivener and Nonat [46] and Scrivener et al. [108]. The role of the nucleation, growth and crystallisation process are of particular relevance to understand path from the anhydrous dissolution to the first (stable) nuclei and crystals. The interested readers are also invited to consult for example the work of Horn and Riegler [109], Kashchiev [110] and Cölfen [111].

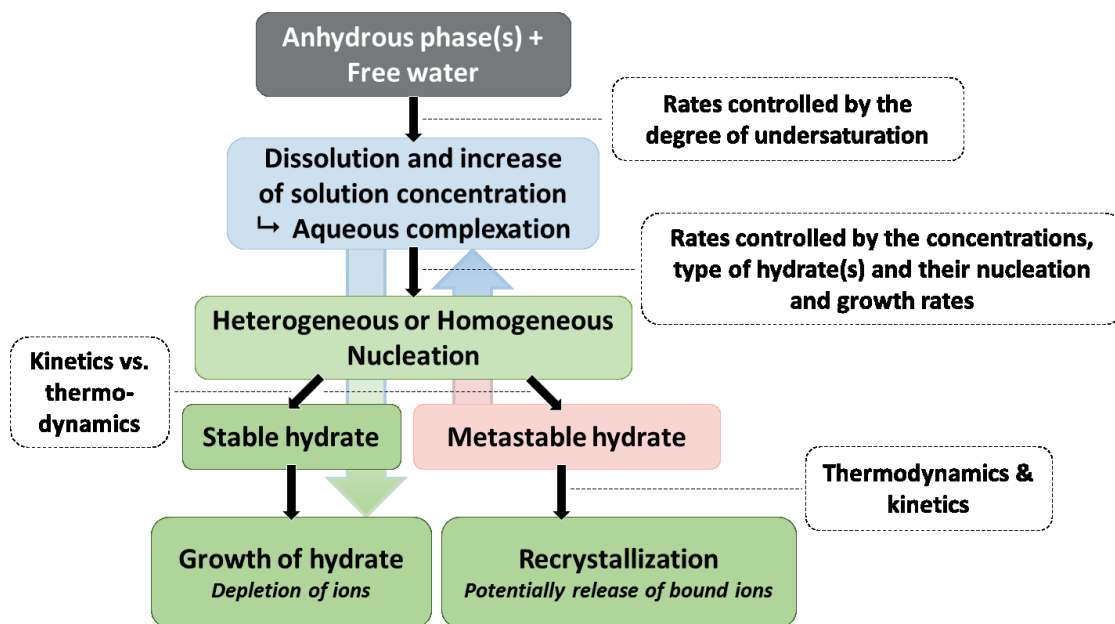


Figure 2.2-1 Simplified chronological order for the formation of hydrates



### 2.2.1 Concept of under- and supersaturation

An idealized scheme of the nucleation and growth process is shown in the Figure 2.2-2. The dissolution starts in pure water and proceeds subsequently within a solution containing several ions such as of  $Ca^{2+}$ ,  $Al(OH)_4^-$ ,  $OH^-$  and  $SO_4^{2-}$  in the case of ye'elimite. Supersaturation with respect to hydrates such as ettringite, monosulphate and aluminium hydroxide will be reached and their precipitation may occur. It is important to determine the driving force for the hydration rate, the dissolution, the precipitation or a combination of both. Literature reports that CSA and BYF cements react rapidly directly after contact with water causing the rise of the solution concentrations and the formation of amorphous, metastable phases. The rapid concentration increase in solution together with the rapid nucleation process may kinetically favour the formation of metastable phases.

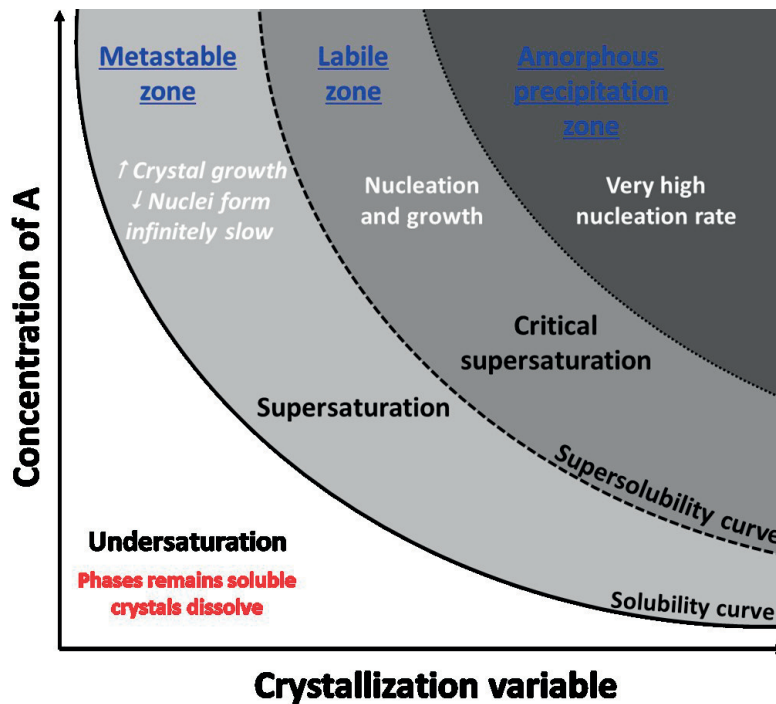


Figure 2.2-2 Idealized scheme of the nucleation and growth process (adopted from [112] and extended) together with the four major zones “Undersaturation”, “Saturation”, “Supersaturation” and “Amorphous precipitation”; crystallization variable such as concentration of B, temperature or pressure

Several parameters could influence the dissolution – precipitation rates such as:

- Modifying the solution chemistry (ionic strength) by adding selectively one of the elements or even further ones
- Changing the temperature, pH or the experimental setup such as low versus high-intensity mixing
- Adding further components (e.g. accelerators, retarders, complexing or chelating agents)
- Providing surface area as nucleation sites to reduce the activation energy barrier

Dissolution and nucleation processes are coupled reactions. Any factor favouring one of them, e.g. acceleration or retardation, will in turn alter both [113]. This opens the question, at which rates phases will dissolve, concentrations will be reached and the nucleation of hydrates will occur?

For example, is there any correlation between the reported rapid dissolution rate of ye'elimite, the consecutive increase of the  $Al(OH)_4^-$  concentration, and in the formation of amorphous aluminium hydroxide instead of gibbsite- or bayerite-like aluminium hydroxide [114]? Scrivener and Nonat [46] provided summary about the common understanding regarding the dissolution and precipitation mechanisms, covering the calcium silicate as well as calcium aluminate hydration. It is worth to briefly refresh what is known about the system  $CaO - Al_2O_3 - H_2O$  before going to the more complex system  $CaO - Al_2O_3(\pm Fe_2O_3) - SO_3 - H_2O$ . As stated by Scrivener and Nonat [46] we assume that the dissolution of all the anhydrous phases is globally congruent to maintain the charge and mass balance as present in the crystallographic structure. In the system  $CaO - Al_2O_3 - H_2O$  three variables have to be considered, namely the concentrations of  $Ca^{2+}$ ,  $Al(OH)_4^-$ , and  $OH^-$ .

Figure 2.2-3 is an extension of the idealized Figure 2.2-2, showing selected solubility curves of the hydrates monocalcium aluminate hydrate ( $CAH_{10}$ ), dicalcium aluminate hydrate ( $C_2AH_8$ ) and aluminium hydroxide types " $AH_3$ " (crystalline and amorphous). All hydrates are less soluble than the anhydrous phases such as ye'elimite or krotite, where aluminium hydroxide is typically always oversaturated. The lines with the labelling C:A= 1 and 3 ( $CaO / Al_2O_3$ ) indicate the evolution of the solution composition assuming the pure dissolution of the ideal calcium aluminates such krotite ( $CA$ ) and tricalcium aluminate ( $C_3A$ ). As the dissolution of krotite proceeds  $Al(OH)_4^-$  and  $Ca^{2+}$  will be released, where the concentrations will move along the line for C:A=1. It will intersect "X" only with the solubility curve of  $CAH_{10}$ , indicating that only this phase should form, which is typically not the case. The line C:A= 3 intersects first with the solubility curve of  $CAH_{10}$  followed by that of e.g.  $C_2AH_8$ . Theoretically both phases may form but  $CAH_{10}$  should form first.

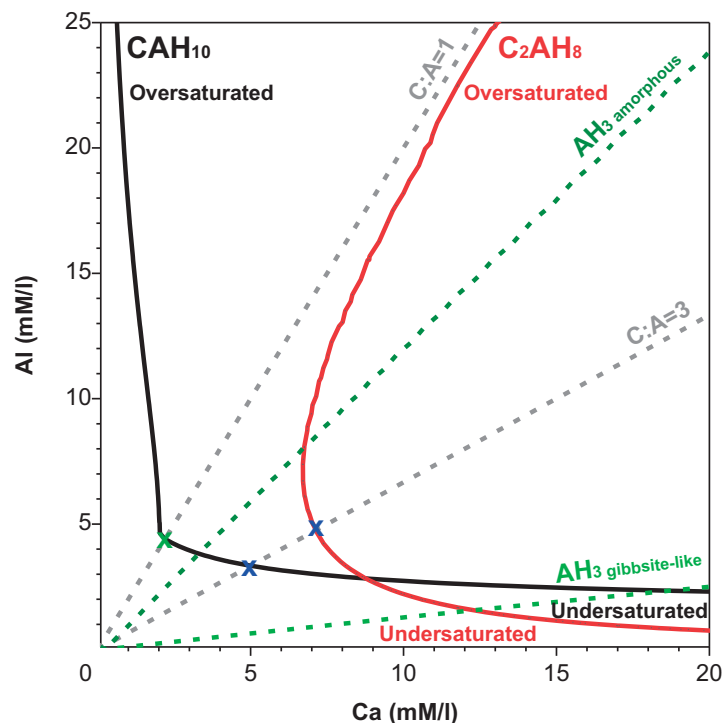


Figure 2.2-3 Selected solubility curves of  $CAH_{10}$  and  $C_2AH_8$  at 25 °C for the system  $CaO - Al_2O_3 - H_2O$  such as CAC; calculated with GEMS and using thermodynamic data from [115] and for amorphous  $AH_3$  from [116]; the dashed lines show the evolution of the solution for different of C/A ratios ( $CaO / Al_2O_3$ ) and "X" represents the intersects with the solubility lines of the selected hydrates

Figure 2.2-4 is an extension of Figure 2.2-3, showing the solubility curves of all reported hydrates in the system  $CaO - Al_2O_3 - H_2O$ . The theoretical ratio for C:A=2 " $C_2A$ " is plotted as well but this phase does not exist. Monocalcium aluminate hydrate ( $CAH_{10}$ ) and katoite ( $C_3AH_6$ ) should be the stable products in the sulphate-free system. However, typically neither  $CAH_{10}$  nor  $C_3AH_6$  are observed or form very slowly, suggesting that their formation and growth may be kinetically hindered even if thermodynamically preferred. Instead, the initial formation of metastable hydrates such as dicalcium aluminate hydrates  $C_2AH_8$  (from  $CA$  or  $C_{12}A_7$ ) or tetracalcium aluminate hydrates  $C_4AH_x$  (from  $C_3A$ ) occurs [73].  $C_3AH_6$  forms over time from the transformation of the metastable hydrates [73] [117] or by increasing the temperature [118] [119]. On the contrary, the formation of  $CAH_{10}$  is favoured at low temperatures around 5 °C, where its solubility increases rapidly with temperature, again favouring the formation of katoite [120].

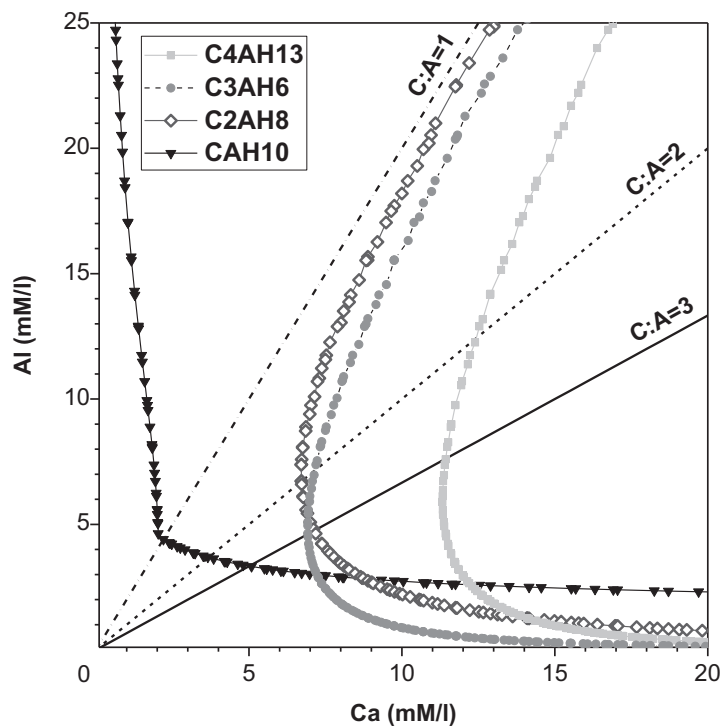


Figure 2.2-4 Solubility curves at 25 °C for the system  $CaO - Al_2O_3 - H_2O$  such as CAC; thermodynamic data from [115]

A fourth variable, namely  $SO_4^{2-}$ , has to be included in the system  $CaO - Al_2O_3 - SO_3 - H_2O$ . The solubility curves at a selected sulphate concentration of 0.02 mM/l are shown Figure 2.2-5 (a). The chosen sulphate concentration is representative for the early hydration period of ye'elimite. In addition, the line for dissolving stoichiometric ye'elimite, including the corresponding sulphate concentration, are those of sulphate-free calcium aluminates (C:A=1, 2 and 3) are shown.

Ye'elimite has a lower C:A ratio compared to krotite. Consequently, the line representing the congruent dissolution of ye'elimite intersects with all sulphate-free calcium aluminate, where again the first phase which is oversaturated is  $CAH_{10}$  followed  $C_2AH_8$ ,  $C_3AH_6$  and finally  $C_4AH_x$ . However, as sulphate is present in solution, ettringite and monosulphate are oversaturated shortly after  $CAH_{10}$  but before e.g.  $C_2AH_8$  and  $C_3AH_6$ . If supposedly present, the dissolution of the theoretical phase " $C_2A$ ", which is close to the composition of mayenite ( $C_{12}A_7$ ), would result in a further decrease of the  $Al/Ca$  ratio in solution compared to the dissolution of ye'elimite and krotite. Intersects with the solubility lines of all hydrates are shifted to lower alumina concentrations. Especially  $C_2AH_8$  and  $C_3AH_6$  become supersaturated at already relatively low alumina concentrations of about 6 and 7 mM/l compared to around 11 and 13 mM/l for ye'elimite. This can have a significant effect on the hydration kinetics as it is known that the nucleation of  $C_2AH_8$  is more easy and rapid compared e.g.  $CAH_{10}$  [73].

Another important aspect is the formation of gibbsite-like or amorphous aluminium hydroxide. The stability of amorphous relative to gibbsite-like aluminium hydroxide may in turn favour the formation of ettringite plus  $CAH_{10}$  rather than of monosulphate as lately reported [121]. The amorphous aluminium hydroxide has higher solubility relative to gibbsite-like type and is in equilibrium with the solution at higher aluminium ion concentration. This in turn enables the formation of ettringite and  $CAH_{10}$  rather than monosulphate. This effect is visualized in Figure 2.2-5. (b).

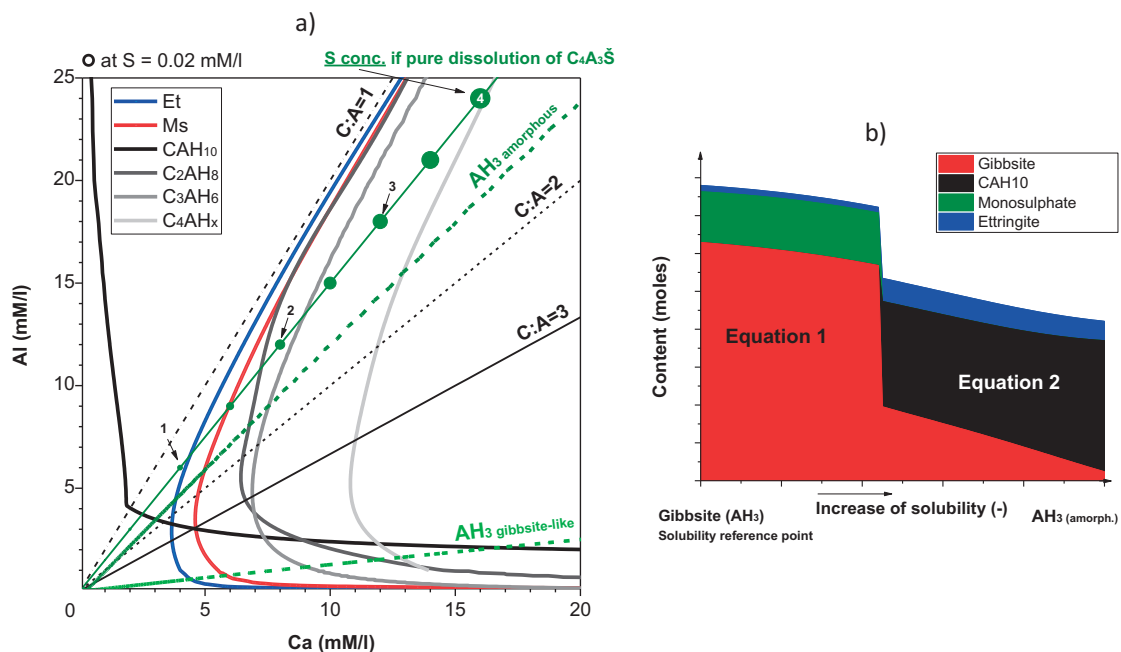


Figure 2.2-5 a) Solubility curves of selected phases at 25 °C for the system  $CaO - Al_2O_3 - SO_3 - H_2O$  such as CSA at a given sulphate concentrations of 0.02 mM/l; thermodynamic data from [115] [116]; b) Schematic representation of the impact of the aluminium hydroxide solubility on the potential phase assemblage (adopted from [121] [122]) of fully hydrated Y (including the minors), the following values were used in the calculations Gibbsite with  $\log K_{S0} = -1.12$  [115] and amorphous  $AH_3$  am with  $\log K_{S0} = 0.24$  [116]

## 2.3 Hydration of ye'elimite

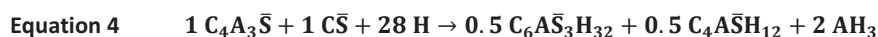
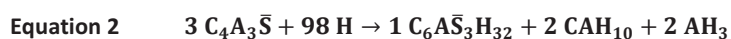
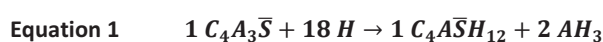
The fresh and hardened properties of CSA cement are typically controlled by the rapid dissolution of ye'elimite and the quantity and rate at which ettringite or monosulphate are formed. Therefore it is important to understand the parameters which control these reactions. Table 2.3-1 provides an idealized schematic overview about the anhydrous compositions, the ions in solutions and the hydrates assemblage. More details about the hydrates can be found in annex – part II and V.

Table 2.3-1 Idealized summary of the anhydrous phases, liberated ions and hydrates

Anhydrous	Liberated ions	Hydrates
$C_4A_3\bar{S}$	$Al(OH)_4^-$	Monosulphate, ettringite $CAH_{10}$ , $AH_3$ amorphous and $AH_3$ gibbsite-like
	$Ca^{2+}$	
	$SO_4^{2-}$	
	$OH^-$	
$C_4A_3\bar{S}$ $C\bar{S}H_2$	$Ca^{2+}$	Ettringite, $AH_3$ amorphous and $AH_3$ gibbsite-like ( $CAH_{10}$ , monosulphate)
	$SO_4^{2-}$	
	$Al(OH)_4^-$	
	$OH^-$	

### 2.3.1 Ye'elimite - Basic hydration reactions

Generally, the hydration reactions of ye'elimite are considered as shown in the simplified hydration reactions according to Equation 1 to Equation 4. The general order starts with the hydration of plain ye'elimite followed by the hydration of ye'elimite in the presence of calcium sulphate. Ideally, ye'elimite reacts in the presence of water to form monosulphate and gibbsite-like aluminium hydroxide (Equation 1). It also can lead to the formation of ettringite, metastable  $CAH_{10}$  and amorphous aluminium hydroxide (Equation 2). Ye'elimite reacts in the presence of two moles calcium sulphate to form ettringite and aluminium hydroxide (Equation 3). When calcium sulphate is depleted the formation of monosulphate becomes the dominant reaction. This is the case for the main investigated mix ratio in this thesis (Equation 4).



These are simplified equations. The stable phase assemblage may differ significantly, depending on the hydration kinetics and the stability of the formed phases. For example, the formation of metastable  $CAH_{10}$  was already reported for hydrated CSA [121] [123] and ye'elimite [124], where others reported the formation of  $C_3AH_6$  [125] [126].

CSA cements normally are used together with calcium sulphate to adjust the cement hydration reactions and products. The most common used calcium sulphate types are anhydrite and gypsum [11] [114] [127]. The addition of those promotes the formation of ettringite rather than of monosulphate. Table 2.3-2 shows the quantity of combined water per gram of ye'elimite for the reactions given above. Depending on the formed hydrates assemblages very different quantities of water can be bound per gram of ye'elimite. Any transformation from one phase assemblage to another could result in the release of bound water and / or a chemical expansion.

For example, the transformation of the product according to Equation 2 to the one according to Equation 1 would cause the release of about 29.3% combined water per gram of paste.

**Table 2.3-2 Combined water content**

Reaction	Combined water per 100 g paste		per 100 g of Y
	Vol.-%	Wt.-%	Wt.-%
Equation 1	58.10	34.70	<b>53.14</b>
Equation 4	64.32	40.33	<b>82.66</b>
Equation 2	71.57	49.09	<b>96.43</b>
Equation 3	67.75	43.68	<b>112.17</b>

### 2.3.2 Hydration sequences and effect of additions

Isothermal conduction calorimetry is a powerful tool to characterise the hydration kinetics of ye'elimite. The hydrations starts with the wetting of the anhydrous phases such as ye'elimite and the sulphate source (gypsum or anhydrite), during which a small quantity of those dissolve. This part of the hydration is typically an exothermic process as shown e.g. in Figure 1.4-2. The hydration typically slows down fast after the initial period reaching a dormant period. The initial crystalline detectable hydration products are ettringite together with amorphous aluminium hydroxide [128]. It was already reported that ettringite was formed from the hydration of neat ye'elimite, i.e. absence of calcium sulphate, where the origin of its formation remains unknown [38] [39]. Winnefeld and Lothenbach [121] proposed that the formation of amorphous aluminium hydroxide and its higher solubility maintains higher aluminium ion concentration in solution. This in turn enables the formation of  $CAH_{10}$  together with ettringite (e.g. reaction according to Equation 2).

The presence of calcium sulphate such as gypsum typically accelerates the hydration, where primarily the length of the initial and dormant period is shortened [39] [114] [121] [129]. In addition, a steadily higher heat release throughout the dormant period is observed in the presence of calcium sulphate [129]. The acceleration is caused by the steady formation of ettringite together with aluminium hydroxide [121] [114], until sulphate is depleted and the formation of monosulphate together with aluminium hydroxide becomes the dominant reaction [39] [130]. The origin of the onset, duration and end of the dormant period as well of the still high heat release remain unknown but seems to be linked to the formation of ettringite. The following onset of the acceleration, and with that of the main hydration period, is related to the reaccelerated ye'elimite dissolution and the continuous formation of ettringite, monosulphate together with aluminium hydroxide [114] [130]. Neither the heat flow during the dormant period nor the onset point of the acceleration period is affected by the calcium sulphate type [129]. This indicates that the reaction throughout this period maintains unchanged.

The onset of the monosulphate formation is typically visible as another maxima or (right hand) shoulder peak in the heat flow curves [129]. It was further reported that the formation of ettringite and or monosulphate continued after depletion of ye'elimite [131] [132]. The origin of the continuing formation was related to the reaction aluminium hydroxide with calcium and sulphate. Some argued, that this reaction could cause an expansion in a hardened CSA cement matrix [129] [133] [134]. The type of calcium sulphate such as gypsum or anhydrite also plays an important role. The dissolution kinetics of the anhydrite are much slower than those gypsum [135] [136] [137].

As a result, the formation of ettringite proceeds faster with gypsum. The use of anhydrite could cause an undersupply of calcium and sulphate ions during the main hydration period. Thus, the formation of ettringite could be temporarily hindered which favours the formation of AFm phases such as  $CAH_{10}$ ,  $C_4AH_x$ , monosulphate and sulphate-hydroxy solid solution AFm [129]. The addition of reactive lime sources such as free lime or portlandite causes the flash set originating from the instant formation of  $C_4AH_x$ . This is caused by the high calcium concentration which shifts the intersection of the ye'elimite line to the solubility lines of the sulphate-free calcium aluminate hydrates (as discussed in section 2.2.1). This effect cannot be controlled by the presence of calcium sulphate but last only until e.g. portlandite is depleted [129]. The compressive strength is strongly altered depending on the type of binder, plain clinker versus cements with calcium sulphate, and the type of addition. The plain clinker reaches the lowest early but the highest 28 d strength. Cements made with gypsum reach the highest early and moderate 28 d strength. Cements made with anhydrite reach a moderate early strength but the same or even superior strength 28 d when compared to those with gypsum [129]. This clearly demonstrates the importance of the correlation between the rapid hydration kinetics, the formed hydrates and of the microstructure evolution [129] [128]. However, several questions remain open.

- What causes the onset, duration and end of the different hydration period?
- What happens during the dormant period, e.g. continuous heat flow, when comparing neat clinker versus cements with the addition of calcium sulphate?
- What causes the different kinetics comparing similar materials?
- What is the impact of the rapid reaction on the phase and microstructure formation?
- Which hydrates are formed at which point of time, including sulphate-free calcium aluminate and if so, why (kinetics versus thermodynamics)?

The hydration of ye'elimite with and without additions presents a good model system for the CSA and even BYF. The underlying reactions and mechanisms which control the different hydration periods and kinetics will be presented in the Chapter 5, 6 and 7 (and annex – part V).

### 2.3.3 Formation of solid solution ye'elimite and hydraulic reactivity

The production and use of CSA cements is of high interest for the cement industry. The (fresh) properties of CSA such as open time, setting and early strength development are primarily related to the hydration of ye'elimite and therefore it is important to know the aspects controlling its reactivity. A first step to understand the hydration behaviour is to know the anhydrous clinker as several aspects such as the bulk chemistry and mineralogy, the clinker microstructure and the formation of solid solution may play a role. As mentioned before, ferroaluminate cements "FAC" are a sub class of CSA cements described in the Chinese cement standard GB 20472-2006 [11]. Several authors reported that the hydration of FAC proceeds faster and that the initial pH was higher compared to CSA cements with low iron content [11] [12]. Similarly, it was shown that the use of industrial by-products and wastes for the production of BYF result generally in an increase of the iron content [33], the formation of a cubic ye'elimite rather than an orthorhombic one and faster hydration kinetics [34]. Jansen et al. [39] investigated the hydration of a synthetic stoichiometry and of an iron-bearing solid solution ye'elimite. They also reported a faster hydration and higher initial pH for the iron-bearing ye'elimite. The origin of the faster hydration as well as of the higher initial pH remains unknown.



However, the hydration kinetics for both ye'elimite varieties are similar when calcium sulphate is added. Similarly, other authors report that gypsum accelerates the kinetics of both ye'elimite types by promoting the formation of ettringite [38] [39].

The formation of several solid solutions of ye'elimite were already described for several other elements such as Ba [138], Cr [139] [140], Cu [141], F [138] [140], Mg and Mn [138], P [138] [139], Sr [142], Ti and Zn [140]. However, the impact of the hydration kinetics and reactions of ye'elimite often remains unknown. This is of particular high relevance as typically all used raw materials for the clinker production do contain such minor elements, including iron. Furthermore, there is interest to use industrial by-products and wastes such as calcareous ashes, air cooled blast furnace slag, alumina salt slag, phosphor gypsum and steel slag as alternative raw materials to replace virgin raw materials such as limestone, bauxite, gypsum and iron ore [34] [59] [143]. The use of by-products and waste may cause the increase of the content of minor and trace elements such as alkali, magnesium, phosphate, chromium, copper and many others in the clinker. Ultimately, the formation of new phases, e.g. calcium potassium or sodium sulphate and of solid solutions of the main clinker phases, can occur [33]. As a result, the hydration of cements made from such clinkers becomes more complex.

## 2.4 Thermodynamic modelling of hydration reactions

As discussed earlier, the hydration of ye'elimite-rich binders is rather complex, partly due to the rapid reaction, the formation of metastable and often poorly crystalline to amorphous hydrates. Furthermore, the determination and quantification of the formed hydrates can be experimentally challenging. Thermodynamics are the driving force, among many other parameters, for the dissolution and precipitation of solids. Thermodynamic calculations of the equilibrium chemistry in heterogeneous systems can therefore provide a powerful tool to enable the indirect assessment of the hydration reactions and products. This is possible for systems for which self-consistent thermodynamic data sets are available. The basis for thermodynamic calculations is the knowledge about the solubility products  $K_{s0}$  of all involved components and the complex formation constants [144]. Hence, the chemical interactions between the solvent, the solids and gaseous phases, the species and complexes formed in solution can be considered simultaneously. This in turn, enables the prediction of equilibrium states and relative phase stability in these complex multi-component, multi-ions systems. In other words, thermodynamic modeling is an advanced mass balance approach which predicts the stable hydrate assemblages at given equilibrium conditions [144].

During the hydration of cement the formation of metastable phases can be kinetically favoured rather than that of the thermodynamic stable ones, usually followed by their transformation into more stable phases [105]. The software solutions offer possibilities to define the kinetics or the type of hydrates formed by e.g. restricting the dissolution (rate) of minerals, using mineral dissolution rates determined experimentally as input data, suppressing selected phases during the calculations and / or by using different solubility product data. This enables the prediction of those metastable phases and of the bulk phase assemblage at a given time or hydration degree. The hydration kinetics of the cement can be used as input parameter for the thermodynamic modelling of the hydration reactions. They can be measured by several methods including the isothermal conduction calorimetry, quantitative X-ray diffraction coupled with thermogravimetric analyses, dissolution experiment coupled with the analyses of the solution concentrations, SEM-EDS and image analyses and combinations thereof [114] [145] [146].



The deviation between the measured to calculated solution and solid composition could indicate for example the presence of unknown (not considered) phases, solid solutions, solution complexes / species or the impact of the kinetics.

Thermodynamic calculations were already successfully used for aluminate-rich cements such as CAC [122] or CSA / BYF [32] [114] [121]. Out of those, the free to use geochemical modelling program GEMS [147] provides a very powerful tool which already includes the thermodynamic data from the PSI-GEMS database [148] [149] and a cement specific data base [150] [151] and plenty of extensive tutorials. For example, Winnefeld and Lothenbach [114] could successfully link the dissolution of the anhydrous phases, the formation of hydration and the evolution of the solution composition of two different CSA cements with the thermodynamic prediction of the hydration reactions. As a result, the authors were able to predict correctly the formation of amorphous aluminium hydroxide for both CSA cements and of the metastable  $CAH_{10}$  for the one labelled "CSA-1". Finally, they could model the phase transformation, volume changes and the amorphous compositions. This shows the strength of combining experimental studies with the thermodynamic modelling of the hydration reactions. Once the developed thermodynamic model is robust and able to predict the hydration of cement, it allows the easy and fast parameter variation. Thus it could provide further insights into the effect of parameters such as the clinker composition, the application temperature or the water to cement ratio [114]. This advanced approach could simultaneously consider the thermodynamics and kinetics of the cement hydration [144].

Recently, Winnefeld and Lothenbach [121] reported the use of thermodynamic modelling to create ternary diagrams which could be used to directly assess the long-term composition and stability hydrates formed during the hydration of CSA, especially such cements containing belite. However, the modelling of the alumina-rich system remains challenging because of the presence of unknown quantities, of (sometimes) unknown phases and solids solutions. For example, Zajac et al. [152] investigated the hydration of alumina-rich binders based on OPC-metakaolin, CAC-limestone-anhydrite and CSA-anhydrite blends. The authors added the data for amorphous aluminium hydroxide, labelled "Al(OH)3(am)", into the thermodynamic cement specific database CEMDATA14 [115]. They used a higher solubility ( $\log K_{S0}$  of 0.24 from [116]) for Al(OH)3(am) compared with micro-crystalline Al(OH)3 ( $\log K_{S0} = -0.67$ ). The introduction of Al(OH)3(am) caused the change of the predicted phase assemblage for neat ye'elimite from monosulphate with gibbsite or micro-crystalline aluminium hydroxide to a mix of ettringite,  $CAH_{10}$  and Al(OH)3(am). This is related to the higher solubility of amorphous relative to gibbsite-like aluminium hydroxide and the resulting higher the aluminium ion concentration maintained in solution as discussed in section 2.2.1. The impacts on the ye'elimite hydration will be discussed in detail in the Chapters 5, 6 and 7.



### 3 Materials and methods

#### 3.1 Hydrated residues

**Hydrated residues for QXRD and TGA analyses** originated from the experiments carried out on pastes and suspensions. At chosen times the hydration of the samples was stopped by the solvent exchange method. For that purpose the hydrates solid residues were placed as received on a filter (blue ribbon filter based on cellulose ether, Whatman® grade 589/3) and a vacuum was applied to extract the aqueous solution. The filtrate was gently crushed ( $< 63\mu\text{m}$ ) if needed, immersed for 15 min in isopropanol, afterwards flushed once with petrol ether and finally dried at 20 °C for at least 24 hours in a desiccator, over silica gel (to capture any humidity) and by applying a medium vacuum (about -0.4 to -0.5 bar). The powder residue left on the filter was further characterised.

**SEM-EDS analyses of polished sections** were prepared by cutting slices of about 5 mm height from hydrated cement pastes. The slices were immersed for 48 hours in isopropanol. The samples were afterwards dried at 20 °C for at least 48 hours in a desiccator by applying a medium vacuum. Finally, the samples were epoxy resin impregnated and polished.

**Hydrated residues for HR-SEM (morphology and surface characterisation) and STEM-EDS (microstructure and phase composition) analyses** were prepared using the same conditions as for the experiments in suspensions (as described in section 3.1.4). For w/b 100, only 0.18 g of anhydrous sample was hydrated for (very) short periods. The small sample size was chosen to reduce the amount of water needed to realize a w/b of 100, to keep the time needed for the drying of the sample (at the end of the experiments) and with that the exposure to water, as short as possible. Gypsum was added to the solution, if present. The procedure needed only to be changed for the very short hydration period of 30 seconds. For that the anhydrous clinker was placed directly on the filter, followed by the flushing with the solution (distilled water or with the solution containing pre-dissolved gypsum). All other hydrated samples were transferred to a filter funnel after chosen periods and the remaining water was extracted by applying a vacuum. The time needed to extract the water was included in the hydration time. The samples were immediately transferred to isopropanol (isopropanol to solid ratio was greater than 1000) and kept for 5 minutes. Finally, the samples were dried and stored under medium vacuum (about -0.4 to -0.5 bar) and above a drying agent until the date of testing. Table 3.1-1 summarizes the mixing time total water exposure time.

Table 3.1-1 Sample preparation time and nomenclature

Sample	Time of mixing	Exposure to water [s]	Sample	Time of mixing	Exposure to water [s]
Y		30	Fe-Y		30
	10	90		10	90
	60	250		60	120
	300	420		300	420
	6 h	6 h		3 h	3 h
Y+G		30	Fe-Y+G		30
	10	150		10	
	300	420		300	
	4 h	4 h		3 h	3 h

### 3.2 Overview of used techniques

Table 3.2-1 gives an overview of the used techniques.

Characterisation	Method	Location	Analysed by
Chemical composition	XRF	HTC	Laboratory
	SEM-EDS	EPFL	Frank Bullerjahn
	SEM-EDS + QXRD	EPFL - HTC	Frank Bullerjahn
	STEM-EDS	EPFL	Emmanuelle Boehm-Courjault
Mineral composition	XRD	HTC	Frank Bullerjahn
	TGA	HTC	Frank Bullerjahn
Mass balance calculations	SEM-EDS + QXRD + TGA	HTC	Frank Bullerjahn
Hydration reactions and kinetics	Calorimetry	HTC	Frank Bullerjahn
	Chemical shrinkage	HTC	Frank Bullerjahn
	Reactor dissolution experiments	HTC	Frank Bullerjahn
	pH, conductivity	HTC	Frank Bullerjahn
	ICP-OES	HTC	Laboratory
	QXRD	HTC	Frank Bullerjahn
Physical characterisation	PSD, $SSA_{BET}$	HTC	Laboratory
Saturation indexes	Thermodynamic modelling	HTC	Maciej Zajac, Frank Bullerjahn and Jan Skocek

### 3.3 BET specific surface area ( $SSA_{BET}$ ) and particle size distribution (PSD)

The  $SSA_{BET}$  was determined by five-point N<sub>2</sub> absorption / desorption isotherm measurements using a NOVA Touch NT4LX-1 from Fa. Quantachrome using the BET-equation (BET = Brunauer, Emmett and Teller). The anhydrous samples were degassed for two hours at 110 °C under a medium vacuum prior to the measurement. Hydrated samples were degassed for 24 hours at 30 °C and applying a medium vacuum. The particle size distribution was determined by laser diffraction using a Malvern MasterSizer 2000 applying the Fraunhofer model. For that purpose the sample was dispersed / deagglomerated in isopropanol and using an ultrasonic device. The results are presented as cumulative and frequency volume distribution.

### 3.4 Isothermal conduction calorimetry (ICC)

The isothermal conduction calorimetry (ICC) enables the time resolved assessment of the released heat at constant temperature conditions and as a result the assessment of the hydration kinetics. All materials (clinker, cement and water) were stored for at least 24 hours at 20 °C ± 1 °C to ensure thermal equilibrium within the calorimeter. Cement pastes were prepared (~4g anhydrous plus additional water) by external mixing for 30 seconds with 2500 U/min using a laboratory Vortex shaker (VF2, Janke and Kunkel Labortechnik). For each measurement a vial of water is measured as a blank and to apply a correction for the baseline drift. The continuous data collection was done on a TAM AIR calorimeter from TA instruments. The results are presented as the rate of heat liberation (P in mW/G) and the integrated cumulative heat (Q in J/g).

### 3.5 Chemical shrinkage (CS)

The principle was developed by Le Chatelier [153] and provides the time resolved assessment of the hydration reactions at constant temperature. This is done by measuring the volume differences between the reactants and the hydration products under saturated conditions. The results are expressed as integrated cumulative shrinkage (CS in  $\text{cm}^3/\text{g}$ ). The dilatometric technique was used as described in [154] [155]. For that purpose about 20 ml of paste with a w/b of 2 was mixed using the same shaker and conditions as for calorimetry. The pastes were then rapidly transferred to glass vials (sample height around 10 mm). The samples were knocked gently 25 times to release entrapped air bubbles. Afterwards, the vials were filled up carefully with water using a pipette so as not to disturb the cement paste. After filling the glass bottle with water, a graduated pipette was inserted through the lid and water was injected carefully to reach a level of about 1 ml (accuracy of reading of about 0.01 ml). Coloured liquid paraffin (1-(Methylamino)anthraquinone;  $\text{C}_{15}\text{H}_{11}\text{NO}_2$ ; CAS Number 82-38-2) was placed on top to avoid evaporation and to better read the level. The coloured liquid paraffin has to be filtered through a 0.45  $\mu\text{m}$  filter before its use. Measurements were made by controlling the level of the paraffin oil level regularly (more frequently at early ages and only three times per day after 48 hours of hydration). The data collection, if not stated otherwise, started 1 hour after the sample preparation to allow the equilibration of the sample, the measured value after 1 hour is the reference or zero value. Always five samples per material were measured. During each experiment a blank sample was additionally measured to check the base line drift. No drift was measured throughout any of the experiments.

### 3.6 Thermogravimetric analyses (TGA)

The mass changes through constant heating were recorded with a thermobalance. The observed mass loss is related to the decomposition of minerals and the release of water and other gaseous species such as  $\text{CO}_2$  or  $\text{SO}_2$ . Thermogravimetric analyses were done on raw materials to verify the purity, e.g. of materials like calcite and gibbsite, and on hydrated samples to determine the composition qualitatively. The phase quantification by TGA was not applicable as peaks of several phases overlap. In addition, the presence of unidentified phases, e.g. not XRD detectable, with an unknown composition cannot be excluded. The amount of bound water (BW) was determined on the residues after the solvent exchange. The weight loss before and after the solvent exchanges was also measured to control the measured BW content. The results are presented as the weight loss over temperature and the 1<sup>st</sup> order derivative of the weight loss expressed. TGA measurements were carried out using a Netzsch STA 449 F3 "Jupiter" device and always  $30 \pm 2$  mg of powder. The powder samples were placed in open platinum crucibles (Pt/Rh 85  $\mu\text{l}$ : # 399.205). The measured temperature range was from 30 °C to 1050 °C, applying a heating rate of 10 K/min and continuous purging with  $\text{N}_2$ . The data were analysed using the Netzsch Proteus Software. Several hydrated samples were repeatedly measured as well after several periods of storage under a medium vacuum to determine the deviation from one to another. The observed deviation of the total mass loss was lower than 1 wt.%.

### 3.7 X-ray fluorescence analyses (XRF)

X-ray fluorescence spectrometry was applied to determine the quantitative elemental main oxide composition of the investigated materials using the Axios device from PANalytical. Preparation of the fused beads: About 1.0 g of the sample is heated for 10 minutes at  $1050\text{ °C} \pm 10\text{ °C}$  to determine the loss of ignition. The residue of thermal treated sample is stored in a desiccator to reach about  $20\text{ °C}$ . After cooling, the sample is mixed in the ratio 1:9 with a  $\text{Li}_2\text{B}_4\text{O}_7 / \text{LiBO}_2$  mix and  $\text{LiF}$  as fluxing agents. The mix is transferred to a platinum crucible and 2 drops of a 5%  $\text{LiBr}$ -solution are added. The final sample is heated in total for 6 minutes at  $1050\text{ °C}$ . After the first 3 minutes the crucible is removed from the muffle furnace and the sample is carefully mixed manually by swirling and returned to the muffle furnace for additional 3 minutes. Afterwards the melt is transformed to the bead form and cooled down with a fan.

### 3.8 X-ray powder diffraction (XRD)

The qualitative and quantitative mineralogical composition of clinkers and hydrated cement pastes were examined using the X-ray powder diffraction (XRD) analysis coupled with the Rietveld refinement (QXRD). All samples were prepared from fine powders (max. particle size of about  $20\text{ }\mu\text{m}$ , typically around  $10\text{ to }15\text{ }\mu\text{m}$ ) and using the back-loading method. The XRD patterns of the samples were obtained at room temperature using a Bruker D8 Advance in a  $\theta$ - $2\theta$  configuration with a monochromatic  $\text{CuK}\alpha$  radiation ( $\lambda = 1.54059\text{ \AA}$ ) and equipped with the LYNXEYE (1D) detector. The generator settings were 40 kV and 40 mA. We used fixed divergence ( $0.29^\circ$ ), primary and secondary sollar ( $4^\circ$ ) slits. The measurement range was  $5^\circ$  to  $70^\circ$   $2\theta$  with a step-size of approximately  $0.02^\circ$ . Continuous rotation was applied during the data acquisition. DIFFRACplus EVA search/match software and the PDF-2 database (release 2010) were used for qualitative spectra evaluations. The Topas 4.2 software package was used for quantitative Rietveld analysis [156]. The following parameters typically were refined but constraint: specimen displacement, background (Chebychev using 3 coefficients for anhydrous and 5 for the hydrated samples), scale factors, unit cell parameters, crystallite size  $L$  and for selected phases (e.g. ettringite and monosulphate) preferred orientation. Rietveld analyses were carried out only on dry samples, e.g. anhydrous or stopped hydrated samples, by using the internal and external standard method [157] [158]. The refinement results of the anhydrous samples were used to constrain the parameters for the refinement and quantification of the hydrated samples. For the external standard method a slice of quartzite rock was used as secondary standard and calibrated against NIST corundum. The external standard was always measured at the same day and using the same measurement conditions as for the sample. For the internal standard method, the (anhydrous or stopped) samples were blended with zincite ( $10\text{ wt.}\% \text{ ZnO}$ ). The used  $\text{ZnO}$  was 100% crystalline when cross-checked with the external standard method. Within this thesis the term X-ray amorphous includes all non-detectable material like gelatinous and poorly (micro-) crystalline phases. The quantitative phase composition of cement pastes was normalised to the amount of weight anhydrous solids, taking into account the amount of chemical bound water deduced by the TGA and using Equation 5 or Equation 6.

**Equation 5** Expressed per 100 g paste:  $m_i = m_{i\text{ QXRD}} * (1 + H_2O_{BW}) / (1 + w/c)$

**Equation 6** Expressed per 100 anhydrous:  $m_i = m_{i\text{ QXRD}} * (1 + H_2O_{BW})$

## Materials and methods

Where,  $m_i$  is the normalized quantity of phase  $i$ ;  $m_{i\ QXRD}$  is the quantity of  $i$  determined from the Rietveld analyses,  $w/c$  is the applied water to cement ratio and  $H_2O_{BW}$  amount of bound water on ignited basis according to Equation 7.

$$\text{Equation 7 } H_2O_{BW} = (100 - BW) * (100/BW)$$

The used crystallographic structures for the Rietveld refinements are summarized in Table 3.8-1.

**Table 3.8-1 Structures used for the Rietveld refinements**

Name	Abbreviation & Grouping	Formula	Oxides (sulphides)	Cement notation	Reference
<b>Main clinker phases</b>					
Ye'elimite ortho.	Y-o	$Ca_4Al_6O_{12}SO_4$	$4CaO \cdot 3Al_2O_3 \cdot SO_3$	$C_4A_3\bar{S}$	[36]
Ye'elimite cubic	Y-c			$C_4A_3-xF_x\bar{S}$	[72]
Tricalcium aluminate	Aluminates	$Ca_3Al_2O_6$	$3CaO \cdot Al_2O_3$	$C_3A$	[159]
Krotite		$CaAl_2O_4$	$CaO \cdot Al_2O_3$	$CA$	[78]
Mayenite		$Ca_{12}Al_{14}O_{33}$	$12CaO \cdot 7Al_2O_3$	$C_{12}A_7$	[160]
Grossite		$CaAl_4O_7$	$CaO \cdot 2Al_2O_3$	$CA_2$	[161]
Brownmillerite	Ferrites	$Ca_4Al_2Fe_2O_{10}$	$4CaO \cdot Al_2O_3 \cdot Fe_2O_3$	$C_4AF$	[162]
Srebrodolskite		$Ca_2Fe_2O_5$	$2CaO \cdot Fe_2O_3$	$C_2F$	[163]
Anhydrite	A	$CaSO_4$	$CaO \cdot SO_3$	$C\bar{S}$	[164]
Gypsum	G	$CaSO_4 \cdot 2H_2O$	$CaO \cdot SO_3 \cdot H_2O$	$C\bar{S}H_2$	[165]
<b>Minor clinker phases</b>					
Corundum	Minors	$Al_2O_3$	$Al_2O_3$	$A$	[166]
Maghemite		$Fe_2O_3$	$Fe_2O_3$	$F$	[167]
Wuestite		$FeO$	$FeO$		
Free lime		$CaO$	$CaO$	$C$	[168]
Periclase		$MgO$	$MgO$	$M$	[169]
Spinel		$MgAl_2O_4$	$MgO \cdot Al_2O_3$	$MA$	[170]
Magnesioferrite		$MgFe_2O_4$	$MgO \cdot Fe_2O_3$	$MF$	[171]
Wollastonite		$CaSiO_3$	$CaO \cdot SiO_2$	$CS$	[172]
Glauberite		$Na_2Ca(SO_4)_2$	$Na_2O \cdot CaO \cdot 2SO_3$	$CNS_2$	[173]
Jasmondite		$Ca_{11}(SiO_4)_4O_2S$	$10CaO \cdot 4SiO_4 \cdot CaS$		[174]
<b>Hydrates</b>					
Ettringite	Et	$Ca_6Al_2(OH)_{12}(SO_4)_3 \cdot 26H_2O$	$6CaO \cdot Al_2O_3 \cdot 3SO_3 \cdot 32H_2O$	$C_6A\bar{S}_3H_{32}$	[175]
Monosulphate	Ms	$Ca_4Al_2(OH)_{12}(SO_4) \cdot 6H_2O$	$4CaO \cdot Al_2O_3 \cdot SO_3 \cdot 12H_2O$	$C_4A\bar{S}H_{12}$	[176]
Gibbsite	$AH_3$	$Al(OH)_3$	$Al_2O_3 \cdot 3H_2O$		[177]
Bayerite				$AH_3$	[178]
<b>Standards</b>					
Quartz	Qz	$SiO_2$	$SiO_2$	$S$	[179]
Zincite		$ZnO$	$ZnO$	$Z$	[180]

The obtained refinements of the anhydrous samples were used as starting models for the quantification of the hydrated samples. Using this approach it is possible to constrain selected parameters such as for the crystal lattice which enables a more stable refinement. Rietveld analysis of such complex mineralogical compositions could result in errors up to 3% by the total mass of sample [37].

The sample preparation procedure such as the solvent exchange can reduce the amount of XRD detectable hydrates. Recent study systematically investigated the impacts arising from the chosen procedure [181]. All investigated protocols damaged to a certain extent the hydrates. The use of isopropanol, as done in this thesis, is one of the least harmful methods to preserve the phase, especially for ettringite and monosulphate [182]. Own testes showed that the detected ettringite and aluminium hydroxide contents were slightly reduced by about 5 to 10%, whereas the amount of monosulphate decreased by about 10 to 20% for stopped powder compared to fresh slices (not polished). However, the damaging effect varies and correlates with the sample age [182], where the effect is typically reduced with longer curing periods.

### 3.9 High resolution scanning electron microscopy analyses (HR-SEM)

The scanning electron microscopy is a quite powerful technique to identify the type, structure and potentially interaction of formed hydrates as well as morphological changes of the anhydrous particles and the resulting changes of the hydration kinetics [40] [43]. In that respect, the morphologies of the anhydrous starting materials as well as of the hydrated products were characterised by HR-SEM. A FEI Sirion SFEG microscope equipped with a field emission gun (tungsten crystal thermionic emitter) and an in-lens ultra-high resolution detector was used. Low accelerating voltages of 1-2 kV were applied. The measurements were done on very small quantities of powder which was dispersed on a carbon tape. The samples were carbon coated to avoid the surface charging. A Cressington carbon coater was used and applying both a tilt and rotation during the coating process. The coating thickness was controlled by a gold shutter and adjusted to 15 to 20 nm.

### 3.10 SEM with X-Ray energy-dispersive spectroscopy (SEM-EDS)

Backscattered electron image together with EDS analysis were carried out on polished sections anhydrous and hydrated samples in a FEI Quanta 200 SEM equipped with a tungsten thermionic filament and a Bruker XFlash EDS detector. The number of counts, set to 50000, was set as target instead of the measurement time. A set of standards was recovered under the same measurement conditions as used the sample analyses. A calibration was carried out against a copper standard always after starting the analyses of the new sample or latest after 4 hours of running the device. The matrix effect was corrected by the "phi-rho-Z" method. Based on these analyses it is possible to follow and describe the formation and development of the cement paste microstructure as well as its elemental composition [183]. For that purpose all samples were epoxy resin impregnated and polished down to 1  $\mu\text{m}$ , using diamond sprays and petrol as a lubricant. The embedded sample was polished on SiC paper # 1200 (Struers) to expose the surface. Afterwards, the polishing was done in about 6 to 10 hours depending on the sample where successively finer grades of the diamond spray were used. The order of polishing steps was 30 to max. 45 minutes at 9 micron, 2 to 3 hours at 3 micron and 2 to 3 hours at 1 micron. The samples as well as the polishing disc were cleaned each hour by placing them in isopropanol and in an ultra-sonic bath for 3 minutes. The polished sections were stored under a medium vacuum in a desiccator for at least 24 hours. The samples were coated with a  $\approx 30$  nm carbon film prior to the experiment. The analyses were done under high vacuum conditions ( $\approx 5 \times 10^{-5}$  Pa) and an accelerating voltage of 15 kV to ensure a good compromise between spatial resolution and excitation. The working distance was kept always constant at 12.5 mm. Backscattered electron images (BSE) were used for the allocation of the measurements points.



### 3.11 Scanning Transmission electron microscopy analyses (STEM)

We used the scanning transmission electron microscopy (STEM) mode in which the electron probe is focused into a small probe and scanned over the thin sample. The generated signal is detected at any point of the specimen. Two different detectors were used: bright field (BF) and high angle annular dark field (HAADF) ones. X-ray energy-dispersive spectroscopy (TEM-EDX) was also carried out in this mode to determine the composition of the hydrates. A FEI Tecnai Osiris microscope equipped with a Bruker Nano XFlash EDX detector was used, operating at 80 kV and at low current; these parameters aiming at preserving the hydrates microstructure.

#### 3.11.1 Preparation of the STEM samples by Focused Ion Beam (FIB)

Powders were first mixed with a special TEM hard resin (Gatan G2 epoxy). This mixture was centrifuged in a tube at 15000 rpm during 15 minutes in order to have a high density of particles at the bottom of the tube and only a small part of resin. After polymerization of the resin at 80 °C for 12 hours, a slice of about 700 microns thick and 4 mm diameter was cut in the bottom of the tube. This slice was cut as a semi-disc and was then polished on both sides until reaching a thickness of 20 to 30 microns. It was then glued on a copper half-ring of 3 mm of outer diameter and 1.5 mm of inner diameter, to ensure mechanical resistance while handling the sample. 2 windows of  $5 \times 10 \mu\text{m}^2$  were thinned down in each sample by FIB to about 100-150 nm of thickness to achieve the electron transparency needed for STEM analyses.

### 3.12 Solution chemistry by inductively coupled plasma optical emission spectrometry (ICP-OES)

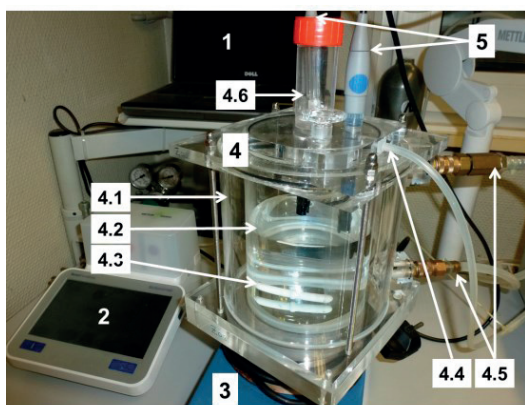
At chosen points of time 10 to 15 ml solution was taken, filtered (0.45  $\mu\text{m}$  Nylon filters) and immediately acidified with a 65%  $\text{HNO}_3$  (ratio solution to acid was 1:1). The high concentration of acid was necessary to avoid the precipitation of solids such alumina gel. The solution samples were taken directly from the reactor (see 3.14) for the suspension experiments carried out at w/b 100. For those carried out at w/b 40, the solution was taken from the set of additional batch samples. The samples were stored at 5 °C till the measurement. The solution composition was measured within at least 24 hours for Al, Ca, Fe, K, Na, S and Si (ICP-OES, Varian Vista Pro with CCD-detector). A part of the extracted untreated solution was immediately measured for the conductivity and the pH.

### 3.13 Hydrates solubility and thermodynamic modelling (SI)

The saturation indexes at equilibrium conditions were calculated using GEMS (“Gibbs Energy Minimization Software” for Geochemical Modeling) [147]. The software package includes thermodynamic databases [148] [149] with the cement-specific data sets [115] [150] [151]. This method requires basic information like the cement chemistry or mineralogy, the solution composition, dissolution kinetics (e.g. from ICC, CS, QXRD and TGA) and phase specific solubility. More details can be found in the annex – part III.

### 3.14 Suspension experiments

Double-walled, water-jacketed and sealed reactors were build (material = Plexiglas; total volume = 1100 ml), to follow dissolution reactions in suspensions. The temperature was controlled by a thermostatic bath with external water circulation. All experiments were conducted at 23 °C  $\pm$ 0.2 if not specified otherwise. The reactor was kept sealed and flushed with N<sub>2</sub> throughout the experiment to avoid carbonation. The continuous data acquisition of the conductivity, pH and temperature were done using a SevenExcellence S475A from Mettler Toledo, equipped with conductivity (Cond Inlab 731-ISM, precision  $\pm$  0.01 mS/cm) and pH (Inlab Expert Pro-ISM, precision  $\pm$  0.05 pH units; XEROLYT® EXTRA polymer based reference electrolyte) electrodes. The data were logged constantly with a recording interval of 2 seconds (for measurements periods of 24 hours) or 30 seconds (for measurements periods to 16 days). Both electrodes are equipped with a temperature sensor (precision  $\pm$  0.1 °C). The measured values are recorded and automatically corrected for the reference temperature of 25 °C. The electrodes were calibrated against standards (three point pH and single point conductivity calibration) before each measurement. In addition, the conductivity and pH of fresh prepared KOH reference solutions was regularly measured to cross check the calibration results. The suspension was stirred at a fixed speed of 600 r/min throughout all experiments. All experiments were carried out at least with double determinations. Always ultrapure demineralised water and water to binder ratios (w/b) from 40 to 1000 were used. The suspensions were made by adding 20 g down to 0.08 g of Y to 800 ml of water.



- 1 = PC for data collection
- 2 = SevenExcellence (S475A Mettler Toledo)
- 3 = Magnetic mixing plate
- 4 = Reactor
- 4.1 = Outer chamber for water circulation for temperature control
- 4.2 = Inner "reaction" chamber
- 4.3 = Magnetic stirrer
- 4.4 = Nitrogen injection point
- 4.5 = Port external water circulation for temperature control
- 4.6 = Gas exit
- 5 = Electrodes

Technical drawing

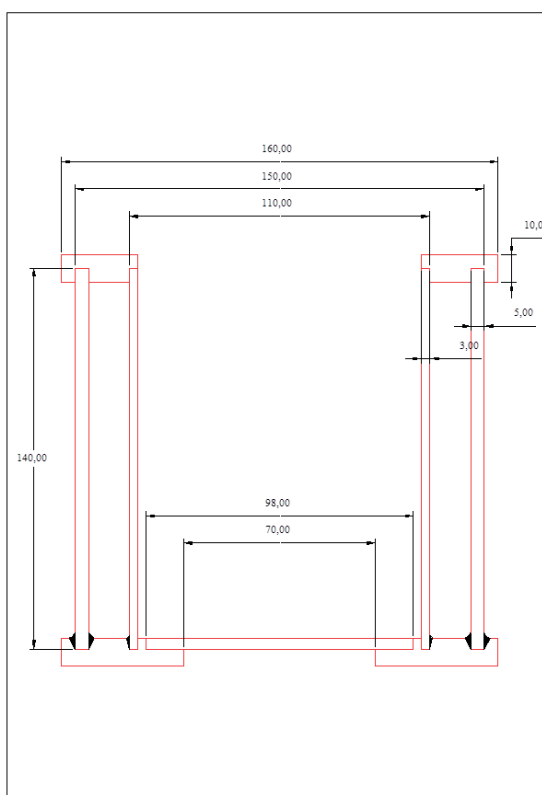


Figure 3.14-1 Photograph of a reactor, including the detailed description, and the technical drawing

### 3.15 Summary about possibilities and limitations

Table 3.15-1 provides a short overview about the possibilities and limitations of the individual methods and to highlight the possibility and need to use at least two different but complementary methods. The by far most applied technique to monitor the hydration process is isothermal conduction calorimetry, as it is easy to handle, very sensitive but also reliable. However, several other complementary techniques such as chemical shrinkage, insitu QXRD, electron microscopy, dissolution experiments (solution evolution  $\pm$  solids) and others are increasingly used to gain further insights in the hydration process. By using complementary methods it is possible to very and cross check obtained results and to potentially assess new phenomena. For example, ICC and CS measurements of the same material should provide a very similar evolution with regard to the integrated cumulative heat versus the cumulative of the measured shrinkage. In addition, the CS would provide further insights into features such as volume changes. QXRD results could be cross checked by e.g. TGA, mass balance calculations based on QXRD+TGA (i.e. for BW and total chemistry) or even IC, ICC and XRF measurements. This could be helpful to e.g. asses the amorphous phase composition.

**Table 3.15-1 Overview regarding the possible output and the limitations of the methods used thought out this study**

Method	Output	Limitations
BET	<ul style="list-style-type: none"> <li>- Total available surface area, i.e. including porosity, will be assessed</li> <li>- Possible to obtain a correlation between the observed reaction rate and the available surface area like during high temperature synthesis (e.g. rate of mineral formation at given temperature and / or time) or during the hydration of a mineral</li> </ul>	<ul style="list-style-type: none"> <li>- A quantitative physical parameter to be determined</li> <li>- Very sensitive to the sample preparation and type especially in the case of hydrates</li> </ul>
PSD	<ul style="list-style-type: none"> <li>- Full particle size distribution as the sum of each fraction can be determined</li> <li>- With knowledge about material properties the surface area can be calculated</li> <li>- Possible to obtain a correlation between the observed reaction rate and the PSD, i.e. either during high temperature synthesis (e.g. rate of mineral formation at given temperature and / or time) or during the hydration of a mineral</li> </ul>	<ul style="list-style-type: none"> <li>- Outcome can vary depending on the used type of model, assumed particle shape (typically spheres) and transparency</li> <li>- Sensitive to sample preparation, measurement mode, e.g. dry or wet, and the type of used dispersion media</li> </ul>
ICC	<ul style="list-style-type: none"> <li>- Time resolved assessment of the released heat at constant temperature conditions providing information about the reaction rates</li> <li>- The heat release can be calculated (e.g. for DoH by QXRD) and compared to the measured one</li> </ul>	<ul style="list-style-type: none"> <li>- Mainly qualitative information</li> <li>- Several reactions can overlap resulting e.g. in a "single" maximum</li> <li>- Very material specific (w/c, type of binder, temperature, ...)</li> </ul>

## Materials and methods

CS	<ul style="list-style-type: none"> <li>- Time resolved assessment of the hydration reaction at constant temperature conditions by the volume differences between the reactants and the hydration products providing information about the reaction rates and volume changes</li> <li>- Results can be connected to observed physical phenomena as the total volume changes are measured</li> <li>- The shrinkage can be calculated (e.g. for DoH by QXRD) and compared to the measured one</li> </ul>	<ul style="list-style-type: none"> <li>- Several reactions can overlap</li> <li>- Very material specific (w/c, type of binder, temperature, ...)</li> <li>- Little is known for CSA</li> <li>- Hydrates and phase assemblage composition often not well known or easy to determine</li> </ul>
TGA	<ul style="list-style-type: none"> <li>- Determination of total mass loss and potential for separation of e.g. of water from carbonate</li> <li>- Determination of BW content</li> <li>- Qualitative identification of hydrates, even for such which are not (well) detectable by QXRD like <math>AH_3</math></li> </ul>	<ul style="list-style-type: none"> <li>- The transformation / decomposition reactions of various phases overlap</li> <li>- Can be very specific for the type of material and the sample preparation (type of binder, sample mass, shape of crucible, heating rate, method to stop the hydration, ...)</li> </ul>
- XRF	<ul style="list-style-type: none"> <li>- Quantitative composition (for the calibrated) main oxides can be determined</li> </ul>	<ul style="list-style-type: none"> <li>- Volatile elements can be lost during the preparation of the fused beads</li> </ul>
QXRD	<ul style="list-style-type: none"> <li>- Identification and quantification of crystalline phases</li> <li>- Use of indirect methods to quantify even X-ray amorphous fraction</li> <li>- Time resolved phase evolution (anhydrous and hydrates) possible providing information about the reaction rates</li> <li>- The knowledge of the reaction degree of the anhydrous and of the quantity of formed hydrates enable mass balance calculations to derive the theoretical composition of the X-ray amorphous fraction</li> </ul>	<ul style="list-style-type: none"> <li>- Signals of several reactants and products strongly overlap</li> <li>- Very sensitive to the applied methodology for stopping of hydration</li> <li>- Dependent on the user skills</li> <li>- Can be very specific for the type of material and the sample preparation (type of binder, back- versus frontloading, method to stop the hydration, Rietveld refinement strategy, used structure models, ...)</li> <li>- Very material specific (w/c, type of binder, temperature, ...) – as a result, very different extents of hydration can be measured and results cannot be linked directly to physical phenomena</li> <li>- Several phases can be present as poorly crystalline and (partly) amorphous</li> <li>- Spottiness and preferred orientation effects can occur</li> <li>- The quantification can reach high relative errors</li> </ul>

## Materials and methods

SEM	<ul style="list-style-type: none"> <li>- Characterisation of phase morphology and composition</li> <li>- Characterisation of the composition and development of the microstructure (phase distribution, elemental composition, etc.)</li> </ul>	<ul style="list-style-type: none"> <li>- Sample preparation (stopping of hydration, polishing, etc.) and measurement conditions (vacuum, etc.) alter the sample</li> <li>- Significant intermixing of phases and separation signals is difficult</li> <li>- An interaction volume is measured</li> <li>- Beam damages of e.g. hydrates can occur</li> <li>- Time consuming and assessment of very small areas</li> </ul>
STEM	<ul style="list-style-type: none"> <li>- Characterisation of phase morphology and composition</li> <li>- Higher accuracy for EDS and morphological analyses compared to SEM</li> <li>- Characterisation of the composition and development of the microstructure (i.e. distribution of phases, elemental composition, etc.)</li> </ul>	<ul style="list-style-type: none"> <li>- Same as for SEM except that pure phases can be measured due to the use of thin sections</li> </ul>
DR	<ul style="list-style-type: none"> <li>- Time resolved assessment of the dissolution and precipitation reactions at constant temperature conditions providing information about the reaction rates</li> <li>- Several signals can be measured and experimental set-ups are possible</li> <li>- Can be easily supplemented with other methods such as ICP-OES, QXRD, TGA, SEM-EDS, etc.</li> <li>- Very well controlled conditions</li> </ul>	<ul style="list-style-type: none"> <li>- Very little is known for CSA to appoint or differentiate reactions</li> <li>- Several reactions can overlap</li> <li>- Strong dependence on method and material (reactor geometry, w/c, binder type, temperature, mixing speed, etc.)</li> <li>- Only qualitative information without the use of other methods</li> </ul>
ICP-OES	<ul style="list-style-type: none"> <li>- Quantitative determination of the element concentration in solution</li> </ul>	<ul style="list-style-type: none"> <li>- Only information about the total element concentration but not about the type of species</li> <li>- Our results indicate that the correct determination of the alumina concentration is very sensitive to the applied sample preparation procedure</li> </ul>
SI	<ul style="list-style-type: none"> <li>- Existing software like GEM-PSI (link) can be used</li> <li>- Enables prediction of hydration reactions and of potential intermediate and final phase assemblages</li> <li>- Results can be connected to observed physical phenomena as besides phase assemblages also volume changes can be predicted</li> </ul>	<ul style="list-style-type: none"> <li>- Need for “basic” information about the cement composition (chemistry and mineralogy) and dissolution kinetics (e.g. from QXRD and TGA)</li> <li>- Detailed studies needed to gather data needed for the calculation of (meta-) stable phase assemblages</li> <li>- Not only thermodynamics but kinetics play an important role</li> <li>- Heterogeneous materials and reactions</li> </ul>



## 4 Clinker synthesis and characterisation

The results presented in this chapter were partly reported in peer-reviewed conference and journal papers:

- 19. Internationale Baustofftagung (ibausil); 16. - 18.09.2015 Weimar, Germany
  - o Title: Iron solid solutions of ye'elimite - Effect on reactivity [184]
- 14<sup>th</sup> International Congress on the Chemistry of Cement (ICCC); 13. - 16.10.2015 Beijing, China
  - o Title: Iron solid solutions of ye'elimite - Effect on reactivity [185]

---

<b>4 CLINKER SYNTHESIS AND CHARACTERISATION .....</b>	<b>37</b>
<b>4.1 YE'ELIMITE SYNTHESIS .....</b>	<b>38</b>
<b>4.2 CLINKER CHARACTERISATION .....</b>	<b>40</b>
4.2.1 MINERALOGICAL COMPOSITION.....	40
4.2.2 DETECTION LIMIT FOR MAYENITE IN YE'ELIMITE CLINKER .....	42
<b>4.3 ANALYSIS OF MICROSTRUCTURE AND PHASE COMPOSITION OF SELECTED CLINKER.....</b>	<b>44</b>
4.3.1 YE'ELIMITE FORMATION SCHEME – REACTION SEQUENCES .....	44
4.3.2 CLINKER AND PARTICLE MICROSTRUCTURE.....	46
4.3.3 THE FLUXING EFFECT OF IRON – IMPACT ON MICROSTRUCTURE.....	46
<b>4.4 ELEMENTAL COMPOSITION OF YE'ELIMITE.....</b>	<b>48</b>
<b>4.5 DISCUSSION .....</b>	<b>52</b>
4.5.1 FORMATION AND STABILITY OF STOICHIOMETRIC YE'ELIMITE AND IN THE PRESENCE OF IRON .....	52
4.5.2 FORMATION AND COMPOSITION OF FERRITES AND THE LIQUID PHASES.....	54
4.5.3 CALCIUM ALUMINATE PHASES .....	56
<b>4.6 CONCLUSIONS .....</b>	<b>58</b>

---

This chapter presents details regarding the synthesis protocols on the clinker mineral formation, elemental phase composition and microstructure.

We have discussed in Chapter 1, section 1.2 that the hydration kinetics of CSA cements varies strongly, even for cements with similar composition and fineness. The literature reports that stoichiometric ye'elimite has an orthorhombic symmetry at ambient conditions, whereas a cubic symmetry is stabilized by the presence of iron [35]. In earlier studies, the different hydration kinetics were related to the type and composition of ye'elimite, where iron-rich solid solution ye'elimite shows a faster reaction [34]. Thus, previous to this work, it was often assumed that there was a link between the presence of iron, the polymorphism and the hydraulic reactivity. The impact of iron is particularly of importance for BYF clinker, as they are often produced using iron-bearing industrial by-products as raw materials. Understanding the origin of this variation was the main motivation for this work. One key aspect is the impact of iron on the formation and composition of the ye'elimite clinker. The objectives of this part of the thesis are to investigate the role of iron on the clinker formation. This includes the bulk mineralogical composition of the bulk, the level of iron-substitution in ye'elimite and the impact of iron on the microstructure. For that purpose, we synthesised stoichiometric ye'elimite and mainly iron-bearing solid solutions by varying the raw materials treatment, the raw mix composition and the sintering protocol. The bulk chemistry and mineralogy, microstructure and elemental phase composition of the clinkers was assessed by XRF, QXRD and SEM-EDS ( $\pm$ STEM-EDS) analyses.

#### 4.1 Ye'elimite synthesis

A summary of the synthesis campaigns and the investigated parameters is shown in Table 4.1-1.

**Table 4.1-1 Set of samples, investigated parameters and respective sample nomenclature in brackets**

Investigated parameters for series		
S1	S2	S3
Formation solid solutions Sintering temperatures ranging from 1100 to 1300°C	Formation iron-bearing solid solutions	Using optimized raw materials and mix preparation for the production of about 1 kg batches
Nomenclature		
	with x in $C_4A_{3-x}F_x\bar{S}$	
	0.00 (Y)	
$C_4A_3\bar{S}$ (Y)	0.05 (0.05Fe-Y)	Y
$C_4A_{2.8}F_{0.2}\bar{S}$ (Fe-Y)	0.08 (0.08Fe-Y)	Fe-Y
$N_{0.2}C_{3.8}A_{2.8}F_{0.2}\bar{S}$ (Na-Fe-Y)	0.20 (Fe-Y)	
	0.40 (0.40Fe-Y)	
	0.80 (0.80Fe-Y)	



### Clinker synthesis and characterisation

The synthesis protocols for the different campaigns are shown in Table 4.1-2. The quantity of applied sintering cycles as well as the achieved mineralogy is presented in Table 4.2-1. The raw materials composition, the raw mix designs and the achieved mix compositions as well as the particle size distributions of all ground clinkers are reported in the annex – part IV.

**Table 4.1-2 Raw mix and clinker production protocol**

S1	S2	S3
<b>Targeted clinker composition</b>		
100% ye'elimité	95% ye'elimité & 5% anhydrite	95% ye'elimité & 5% anhydrite
<b>Alumina oxide and calcium sulphate used</b>		
As received	As received	Ground to d90 < 40 µm
<b>Materials homogenization and grinding</b>		
Suspension using isopropanol		Suspension using water
1) Suspension for 2 minutes in ultrasonic bath a) Drying for 24 hours at 110 °C  2) Suspension for 1 minute in a planetary ball mill (PBM) a) Drying for 24 hours at 110 °C	1) Suspension for 4 hours in a roller bock a) Drying for 24 hours at 60 °C  2) Grinding of suspension for 1 minute in a VDM a) Drying for 24 hours at 60 °C	1) Suspension for 2 minutes in a planetary ball mill (PBM) a) Drying for 24 hours at 110 °C
<b>Sintering procedure</b>		
Powders gently compacted in corundum crucible using a pestle		
Open crucible	Crucible covered with a lid	
Sintering for 1 hour directly at targeted temperature	Heating from 20 °C to 900 °C with a heating rate of 5 °C/min Sample was kept for 1 hour at 900 °C Heating to target temp. with a heating rate of 10 °C/min	
	<u>Dwell time at target temp.</u> 1 hour	<u>Dwell time at target temp.</u> 3 hours for Y 2 hours for Fe-Y
Clinker cooling - At air and placed on a steel plate		
<b>Intermediate grinding</b>		
Dry powder for 1 minute in VDM before sintering repetition	none	
<b>Sintering repetitions</b>		
3 times <sup>a</sup>	1 to 3 times <sup>b</sup>	1 time
<b>Sintering temperatures (°C)</b>		
1100		
1150		
1200		
1250		X
1300	X	

<sup>a</sup> 5 wt.% of extra anhydrite was added before 3<sup>rd</sup> sintering as a high loss of SO<sub>3</sub> occurs due to the volatilization of sulphur

<sup>b</sup> Target to reach a minimum content of 90% ye'elimité

## 4.2 Clinker characterisation

### 4.2.1 Mineralogical composition

The main phases identified by QXRD are ye'elimite, krotite (often referred to monocalcium aluminate) and anhydrite. Depending on the raw mix preparation and clinker production protocol, several other minor phases were present. Y refers to the stoichiometric ye'elimite whereas Fe-Y refers to  $C_4A_{2.8}F_{0.2}\bar{S}$  which is present in all three campaigns. Various iron-bearing solid solutions were prepared for the series 2 (S2). The samples are labelled hereafter 0.xFe-Y, where x stands for the level of iron substitution in  $C_4A_{3-x}F_x\bar{S}$  (e.g. 0.05Fe-Y for  $C_4A_{2.95}F_{0.05}\bar{S}$ ). From the results of S1 and S2 it was found that the fineness, especially of the  $Al_2O_3$  source, proves a major impact on the formation of ye'elimite over the (persistence of) intermediate calcium aluminate phases (see also annex – part IV, Table 8.8-14 and Table 8.8-15). As a result, all raw materials for S3 were used with a minimum fineness of the  $d_{90} < 40 \mu m$  (according to laser diffraction). Table 4.2-1 shows the quantitative composition determined of the clinkers (no amorphous phase detected).

Table 4.2-1 Mineralogical composition of the clinker from Rietveld analysis of XRD; n.d. = not detected; + = traces

Target composition	S1			S2						S3			
	100% Y			95% Y + 5% $C\bar{S}$						95% Y + 5% $C\bar{S}$			
	Y	Fe-Y	Na-Fe-Y	Y	0.05 Fe-Y	0.08 Fe-Y	Fe-Y	0.4 Fe-Y	0.8 Fe-Y	Y	Fe-Y		
$C_4A_{3-x}F_x\bar{S}$ with $x_{target} =$	0	0.2	0.2	0	0.05	0.08	0.2	0.4	0.8	0	0.2		
Sintering temperature (°C)	1300			1300						1250			
Sintering repetitions (-)	3	3	3	3	2	2	1	1	2*	1	1		
				[%]									
Ye'elimite ortho. $C_4A_3\bar{S}$	96.9	35.0	19.7	93.7	90.9	46.7	24.9	19.2	n.d.	87.9	traces		
Ye'elimite cubic $C_4A_{3-x}\bar{S}$	n.d.	59.3	73.2	n.d.	n.d.	46.6	67.7	70.5	78.6	n.d.	93.9		
Mayenite $C_{12}A_7$	n.d.	0.8	0.5	n.d.	n.d.	0.5	0.6	1.4	1.7	n.d.	0.6		
Krotite $CA$	n.d.	n.d.	n.d.	3.1	2.1	0.6	n.d.	n.d.	1.9	5.1	0.2		
Grossite $CA_2$	n.d.	n.d.	n.d.	n.d.	n.d.	n.d.	n.d.	n.d.	n.d.	0.3	n.d.		
Brownmillerite $C_4AF$	n.d.	2.7	5.6	n.d.	n.d.	n.d.	n.d.	2.3	1.4	n.d.	n.d.		
Srebrodolskite $C_2F$	n.d.	n.d.	n.d.	n.d.	n.d.	n.d.	n.d.	n.d.	4.3	n.d.	n.d.		
Maghemite $F$	n.d.	n.d.	n.d.	n.d.	n.d.	n.d.	0.8	1.3	2.5	n.d.	0.3		
Wuestite FeO	--	n.d.	n.d.	n.d.	n.d.	n.d.	n.d.	n.d.	0.8	n.d.	n.d.		
Anhydrite $C\bar{S}$	2.7	2.2	n.d.	2.2	6.1	5.0	5.7	5.0	5.9	6.7	5.0		
Glauberite $CNS_2$	n.d.	n.d.	0.7	n.d.	n.d.	n.d.	n.d.	n.d.	n.d.	n.d.	n.d.		
Jasmundite $Ca_{11}(SiO_4)_4O_2S$	--	n.d.	0.3	n.d.	n.d.	n.d.	n.d.	n.d.	n.d.	n.d.	n.d.		
Periclase $M$	0.4	n.d.	n.d.	0.2	0.2	0.2	0.3	0.3	n.d.	n.d.	n.d.		
Spinel $MA$	n.d.	n.d.	n.d.	0.8	0.7	0.4	n.d.	n.d.	n.d.	n.d.	n.d.		
Wollastonite $CS$	n.d.	n.d.	n.d.	n.d.	n.d.	n.d.	n.d.	n.d.	2.8	n.d.	n.d.		

\* minor changes of composition after 2<sup>nd</sup> sintering (slightly reduced ye'elimite content but formation of srebrodolskite, maghemite and mayenite over krotite, wustite and calcium ferrite [CF])

All other results as indicated by Table 4.1-2, including a detailed assessment of the impact of the sintering temperature on the clinker formation and hydration kinetics, are summarized in the annex – part V. All clinkers had high ye'elimite contents. Only orthorhombic ye'elimite was detected in the absence of iron. The addition of iron favours the formation the cubic type over the orthorhombic one and increasing additions enhanced the formation of ye'elimite.

Several minor phases such as krotite, grossite (often referred to monocalcium di-aluminate) and brownmillerite (representing a solid solution between  $C_6A_2F$  to  $C_6AF_2$ ) were found. The formation of mayenite was only detected in iron-containing clinkers. Figure 4.2-1 shows sections of the XRD patterns of the clinkers produced throughout the several campaigns. The addition of iron enables the formation of iron-bearing solid solutions of ye'elimite. This is revealed by several aspects. The reflections slightly shift to lower 2Theta angles, i.e. increasing d-spacing, as a result of the isomorphous substitution of  $Al^{3+}$  (0.535 Å) by the larger  $Fe^{3+}$  ion (0.645 Å). All strong peaks of the cubic and orthorhombic form overlap but the representative reflections of the orthorhombic structure decrease in intensity and almost disappear whereas the reflections of the higher symmetry cubic cell are maintained. These observations are consistent with earlier studies [35] [39] [72] [186].

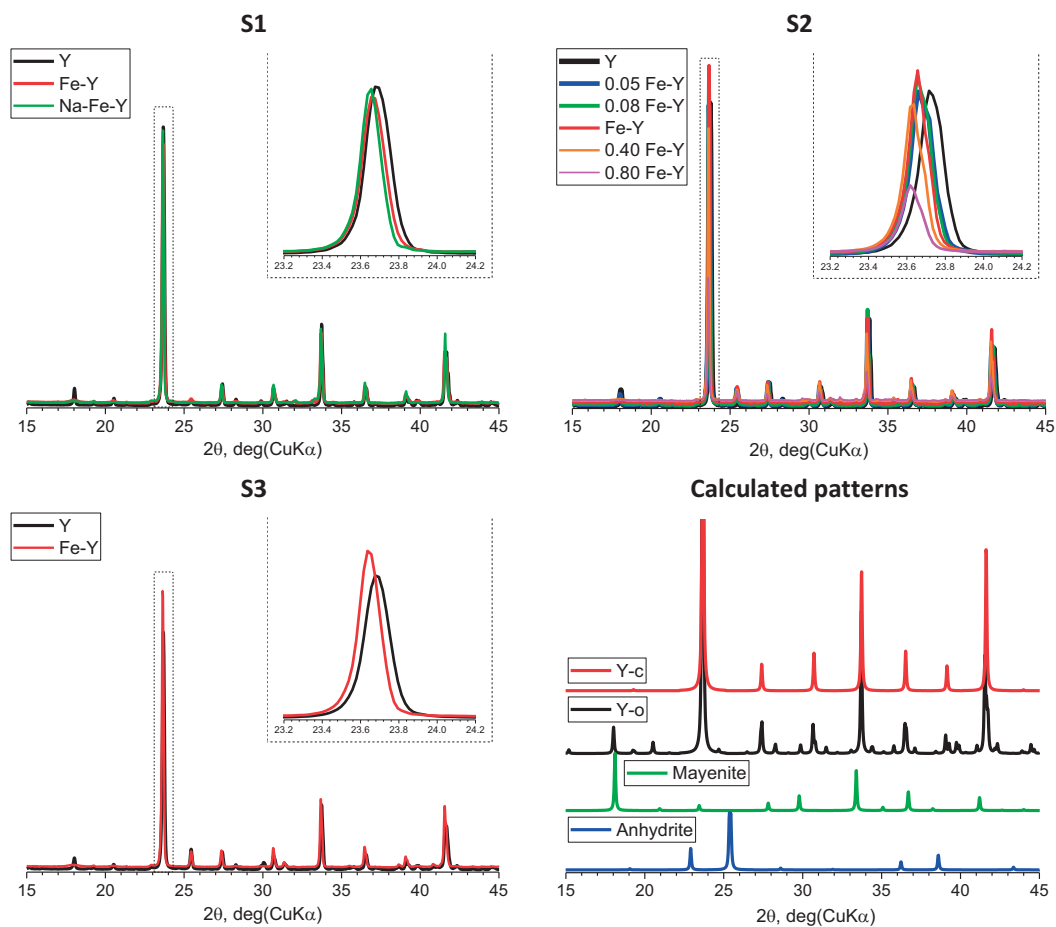


Figure 4.2-1 XRD plot of the synthesised ye'elimite (as measured) including a zoomed section and calculated XRD patterns for orthorhombic (Y-o) [36], cubic (Y-c) ye'elimite [72] and mayenite [160]; # =  $C\bar{S}$

For comparison to the synthetic ye'elimite, the calculated patterns of cubic and orthorhombic ye'elimite, mayenite and anhydrite are presented. The differentiation and quantification of orthorhombic and cubic ye'elimite is difficult as the patterns of both are overlapping but possible as the orthorhombic form has extra reflections due to its lower symmetry. The differentiation of both types depends on the presence or absence, sharpness and intensity of those reflections, i.e. peaks. But the representative reflections of the orthorhombic structure are also overlapping with those of mayenite complicating its determination and quantification.

The choice of the starting model of ye'elimite for the quantifications has only a limited impact on the determined total ye'elimite quantity. Comparing the results for refinements using the orthorhombic or cubic one and with combination of both only causes marginable differences below  $\pm 2\%$  of ye'elimite.

Figure 4.2-2 shows a zoomed section highlighting this effect. The peak doublet (or triplet when including the shoulder to higher  $2\theta$  angles) of the orthorhombic structure is shifted to lower angles and is poorly resolved with increasing iron additions. The increasing iron incorporation corresponds to the increase of the cell volume ranging from about  $1555.15 \text{ \AA}^3$  to  $1560.96 \text{ \AA}^3$  (ortho) and  $779.15 \text{ \AA}^3$  to  $781.76 \text{ \AA}^3$  (pseudo-cubic) but is within the limits of experimental error. This is consistent to the findings of Schmidt [186], there was no linear correlation between the cell volume and the determined chemistry. Another parameter that affects the unit cell volume is the sintering temperature. It was shown by several authors that higher temperatures causes an expansion of the unit cell volume of synthetic stoichiometric and solid solution ye'elimite [72] [187] [36]. The same was found by De la Torre et al. [188] for BYF clinker produced at lab-scale. Therefore, the determination of the composition of the solid solutions formed by QXRD and coupled Rietveld analyses was not applicable. Finally, the increase of the background signal is caused by the increase of the iron content and the resulting fluorescence of iron atoms when using  $\text{Cu K}\alpha_1$  radiation. Despite all the mentioned difficulties, we included mayenite throughout the Rietveld calculations as STEM-EDS analyses indicate its presence in the iron-rich clinkers. All other phases reveal characteristic and separated reflections and are detectable at even very low contents such as 0.2%.

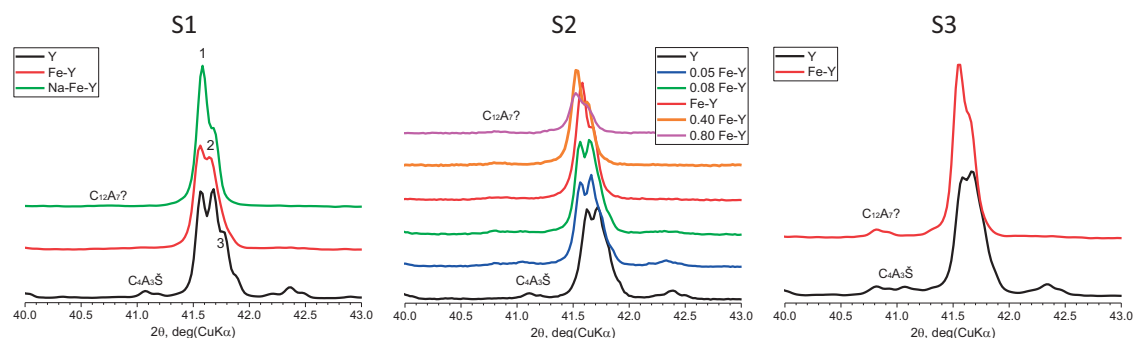


Figure 4.2-2 Zoomed sections of  $\gamma$ -shifted patterns showing the shift and weakening of the triplet of stoichiometric orthorhombic ye'elimite with increasing iron incorporation

#### 4.2.2 Detection limit for mayenite in ye'elimite clinker

The XRD detectable quantities of mayenite are typically below 1%. It is also possible that a part of mayenite is present in an amorphous form [83] [85] [95]. We synthesised crystalline mayenite and prepared mixes with ye'elimite clinkers to assess the potential detection limit. A new batch of Y, produced according to approach for the S3 series (see annex – part V, Table 8.8-18), was used for this study. From the sample Fe-Y of the S3 series there was enough material available. The synthetic mayenite ( $\text{C}_{12}\text{A}_7$ ) was produced by sintering a stoichiometric raw mix, composed of calcite and gibbsite powder, four times for 2 hours at  $1300 \text{ }^\circ\text{C}$  following fast cooling at air and intermediate grinding steps. The raw mix (as suspension with water) and the (intermediate) clinker (as dry powder) were ground for one minute in a planetary ball mill. The clinker is composed of about 97.5% mayenite, 1.9% tricalcium aluminate and 0.6% krotite. No amorphous phase was detected.

## Clinker synthesis and characterisation

The results of the quantification of the Y and Fe-Y mixes with mayenite are presented in Table 4.2-2. No mayenite was detected in the neat Y and therefore the results are the same. The mix with 0.5 wt.% reveals only in marginable differences, by means of the resulting compositions, Rwp and GOF values, when refining with and without mayenite. Profound misfits, consistent with the increasing weighted profile R-factor (Rwp) and goodness of fit (GOF or  $\chi^2$ ) values, are observable for mixes with 4.0 wt.%. The Fe-Y clinker seems to contain already traces of mayenite. As for Y, only marginable differences are observed for low mayenite additions up to 2 wt.%. At higher levels a significant misfits occur if mayenite is not included during the refinement. It is important to note that the Fe-Y clinker contains also traces of orthorhombic ye'elinite type according to initial Rietveld analyses but was not included during these refinements. This causes the slight higher Rwp and GOF values obtained for Fe-Y compared to Y.

**Table 4.2-2 Rietveld results of Y or Fe-Y -  $C_{12}A_7$  mixes; using the orthorhombic (Y) and cubic (Fe-Y) structure**

Target mayenite Content (wt.%)	Y refined without $C_{12}A_7$					Y refined with $C_{12}A_7$					
	$C_4A_3\bar{S}$ -o	$C\bar{S}$	CA	F	Rwp / GOF	$C_4A_3\bar{S}$ -o	$C\bar{S}$	CA	F	$C_{12}A_7$	Rwp / GOF
	(%)					(%)					
0.0	95.2	3.4	1.4	n.d.	7.22 / 2.23	95.2	3.4	1.4	n.d.	0.0	7.22 / 2.23
0.5	95.4	3.3	1.3	n.d.	7.12 / 2.21	95.0	3.3	1.3	n.d.	0.4	7.04 / 2.19
1.0	95.4	3.3	1.3	n.d.	7.23 / 2.24	94.5	3.3	1.4	n.d.	0.8	6.97 / 2.16
2.0	95.6	3.4	1.9	n.d.	7.78 / 2.41	94.1	3.2	1.1	n.d.	1.6	6.90 / 2.14
4.0	96.2	2.9	0.9	n.d.	9.54 / 2.96	92.5	3.1	0.9	n.d.	3.5	6.79 / 2.11
8.0	94.5	2.8	2.7	n.d.	12.81 / 3.93	89.1	2.9	1.1	n.d.	6.9	6.74 / 2.07
	Fe-Y refined without $C_{12}A_7$					Fe-Y refined with $C_{12}A_7$					
	$C_4A_3\bar{S}$ -c	$C\bar{S}$	CA	F	Rwp / GOF	$C_4A_3\bar{S}$ -c	$C\bar{S}$	CA	F	$C_{12}A_7$	Rwp / GOF
	(%)					(%)					
0.0	94.4	5.0	0.4	0.2	7.40 / 2.77	94.0	5.0	0.3	0.3	0.4	7.37 / 2.76
0.5	94.1	5.0	0.6	0.3	7.43 / 2.79	93.6	5.0	0.2	0.3	0.9	7.33 / 2.76
1.0	94.2	4.9	0.6	0.3	7.50 / 2.84	93.3	4.7	0.3	0.3	1.4	7.27 / 2.75
2.0	94.0	4.9	0.9	0.2	7.80 / 2.93	92.4	4.8	0.2	0.2	2.4	7.21 / 2.71
4.0	93.6	4.6	1.6	0.2	8.59 / 3.20	90.6	4.7	0.4	0.2	4.1	7.07 / 2.64
8.0	92.4	4.6	2.8	0.2	10.90 / 4.04	87.0	4.6	0.6	0.2	7.6	7.26 / 2.69

Figure 4.2-3 shows the difference plots between the observed and calculated patterns from the Rietveld analyses of selected mixes. Consistent with the increasing Rwp and GOF values, the visual misfit becomes only evident with increasing mayenite additions around 2 wt.%. Based on the given results we assume a QXRD detection limit for mayenite of about 2%.

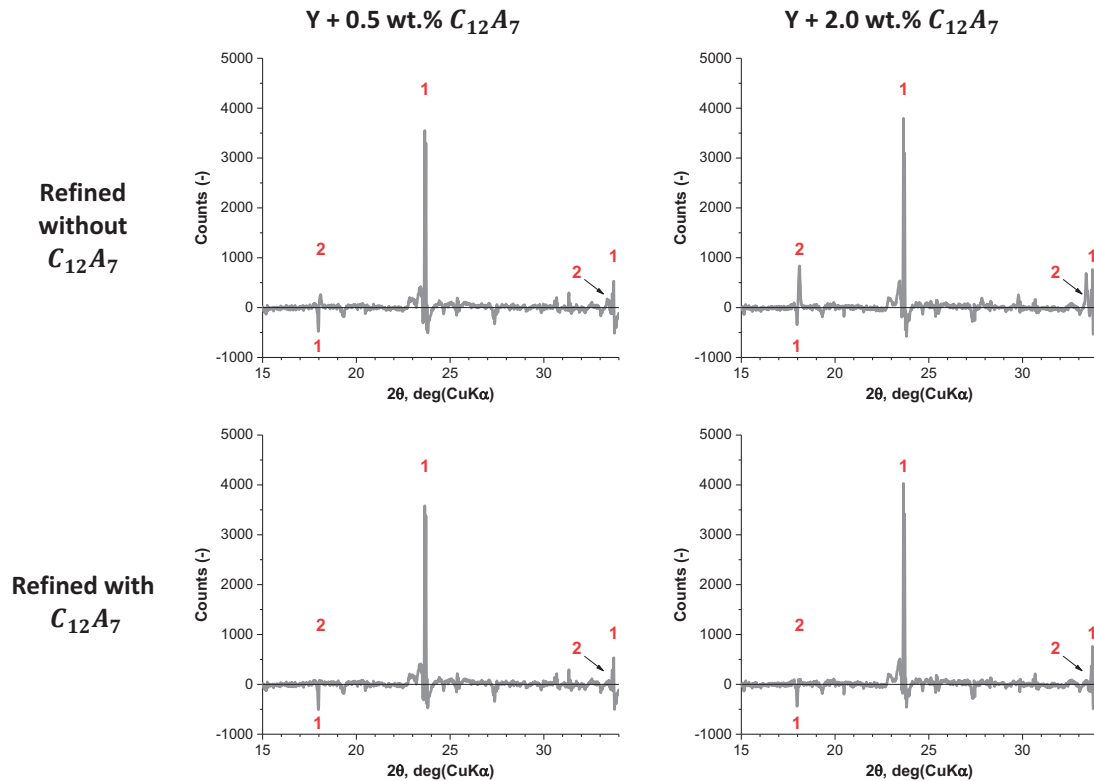


Figure 4.2-3 Difference plots of selected mixes from Rietveld analyses; 1 =  $C_4A_3\bar{S} - o$  and 2 =  $C_{12}A_7$  position of peak(s); measured peak intensity at 23.65 2Th Degrees of about 510000 counts (-)

### 4.3 Analysis of microstructure and phase composition of selected clinker

#### 4.3.1 Ye'elinite formation scheme – Reaction sequences

An idealized scheme its formation sequence of ye'elinite is shown in Figure 4.3-1 and complemented with a micrograph and elemental maps of synthetic Y (S1). Opposing gradients of alumina, calcium and sulphate are present through the Y particle. The alumina content is the highest in the center and decrease to the outer zone. The highest calcium and sulphate concentration is present in the middle or outer zones and both are absent in the center of the particle. This indicates that the initial reaction occurs between aluminium oxide (A) and calcium oxide or lime (C), to form aluminates phases as intermediate products. The used aluminium oxide contains traces of iron which is incorporated into ye'elinite. Magnesium oxide, present in the used calcium carbonate, is exclusively enriched in the calcium aluminates layer. Silicon is present as minor element in the used calcium carbonate and gypsum and thus, is appears (enriched) in the same area originally occupied by those materials.



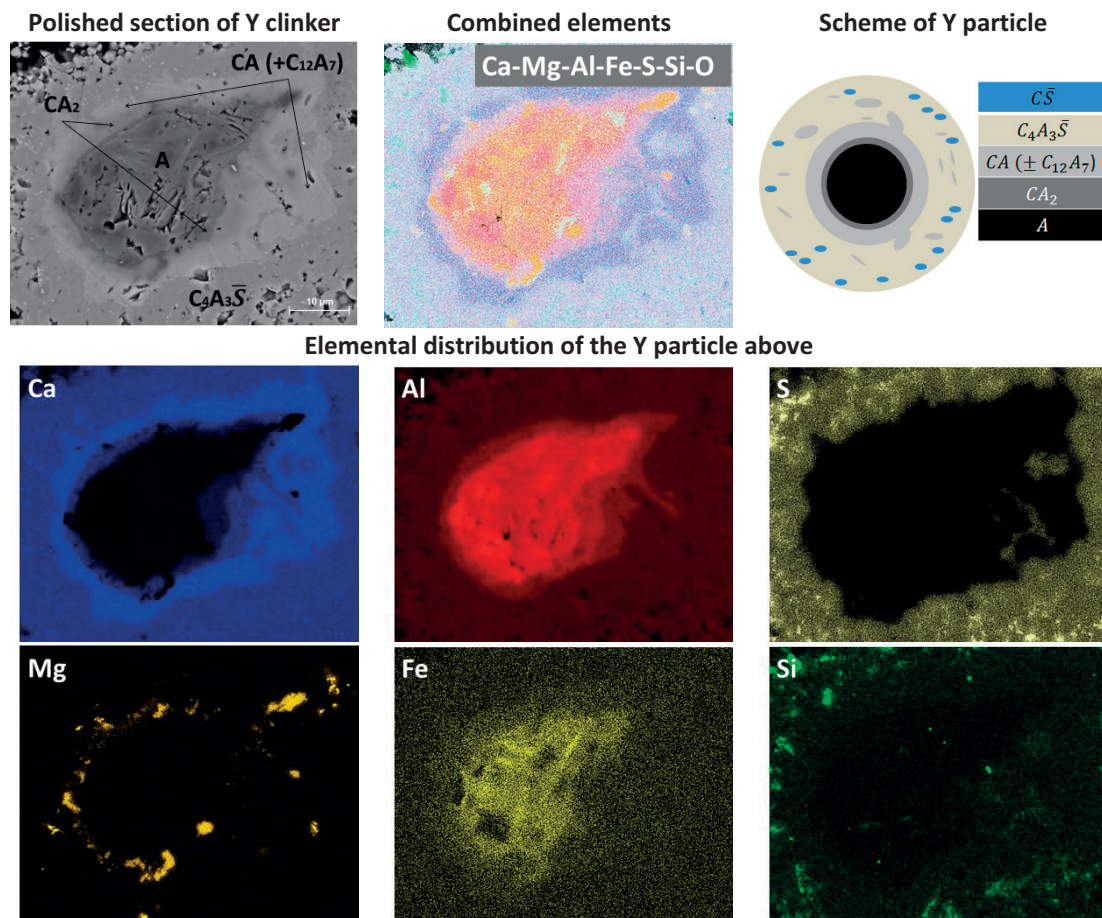
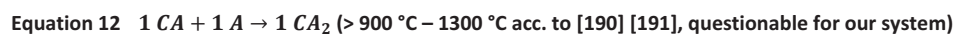
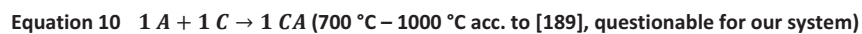
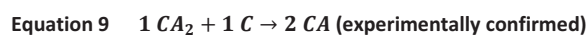


Figure 4.3-1 (Top) Scanning electron micrograph of a polished section of Y and scheme of Y particle formed from anhydrous starting materials; (bottom) element distribution; Na equally distributed (not presented)

The reaction sequences leading to formation ye'elimite are represented by the idealized Equation 8 to Equation 14. Aluminium oxide ( $A$ ) reacts with lime ( $C$ ) to form intermediate grossite ( $CA_2$ ) in the temperature range of 700 °C to 1000 °C [189]. The grossite reacts  $C$  to form a layer of krotite ( $CA$ ). The formed krotite can react with lime to form (traces of) mayenite ( $C_{12}A_7$ ). The formation of mayenite may originate from local heterogeneities due to the not perfect raw mix homogeneity. Finally, krotite and mayenite further react with anhydrite ( $C\bar{S}$ ) to form ye'elimite.



The described formation sequences were also proven experimentally, as shown in Table 8.8-14 and Table 8.8-15 (annex – part IV). A similar reaction sequence was already described by Bergman [87] for the formation of ferritic phases from solid state reactions between  $C$  and  $F$ .

### 4.3.2 Clinker and particle microstructure

SEM micrographs of polished sections and fractured powder samples of Y and Fe-Y (S3) are shown in Figure 4.3-2. Both clinkers reveal a porous microstructure, where the iron-rich clinker seems to be slightly less porous consistent to findings in similar studies [185] [192]. The crystals have a well-developed morphology as shown by the well visible polyhedral grains of an average size around 1 micron. The iron-rich solid solutions tend to be on average bigger and with a less well-developed morphology. The microstructure and the shape of the particles in both samples resemble a ceramic sintering product formed by solid state reactions from which melt were almost absent. The bright spots in the sample Fe-Y consist mainly of  $C_2F$  but sometimes of a solid solution magnesium ferrite - spinel  $[M(F, A)]$  and an iron-rich  $C_2(A, F)$ , according to SEM-EDS analyses. However, the presence of these phases was not confirmed by QXRD analyses indicating that the overall amounts are either below the detection limit or present in amorphous state.

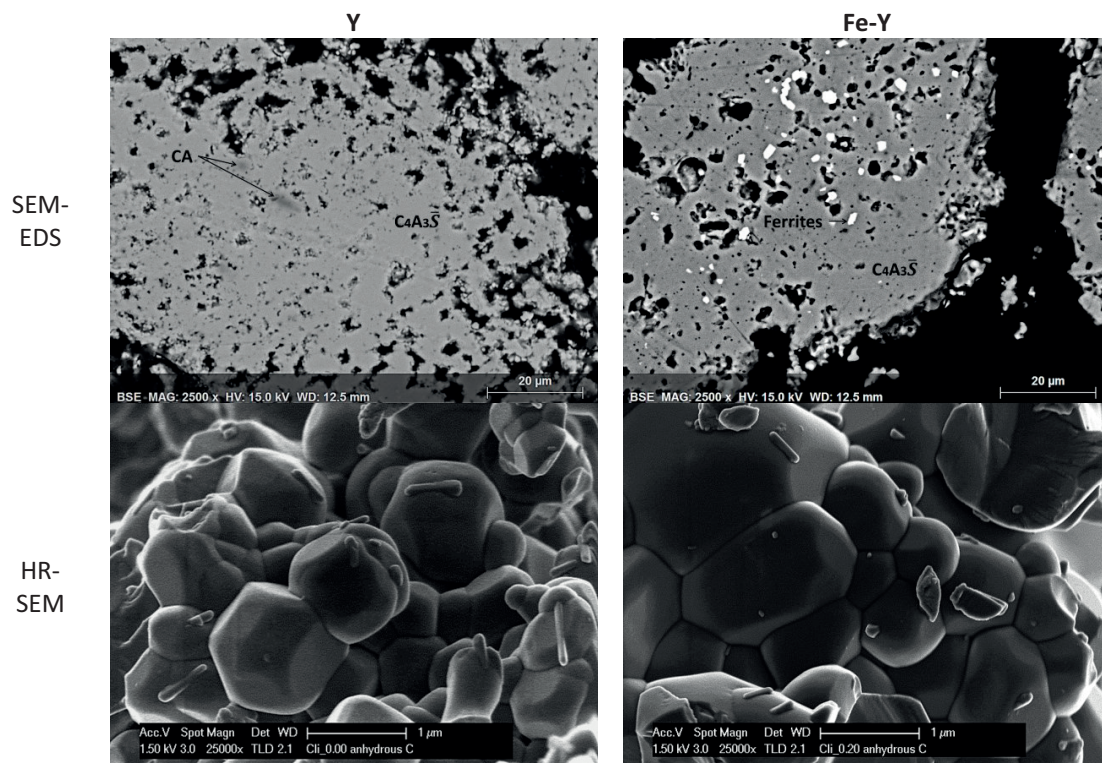
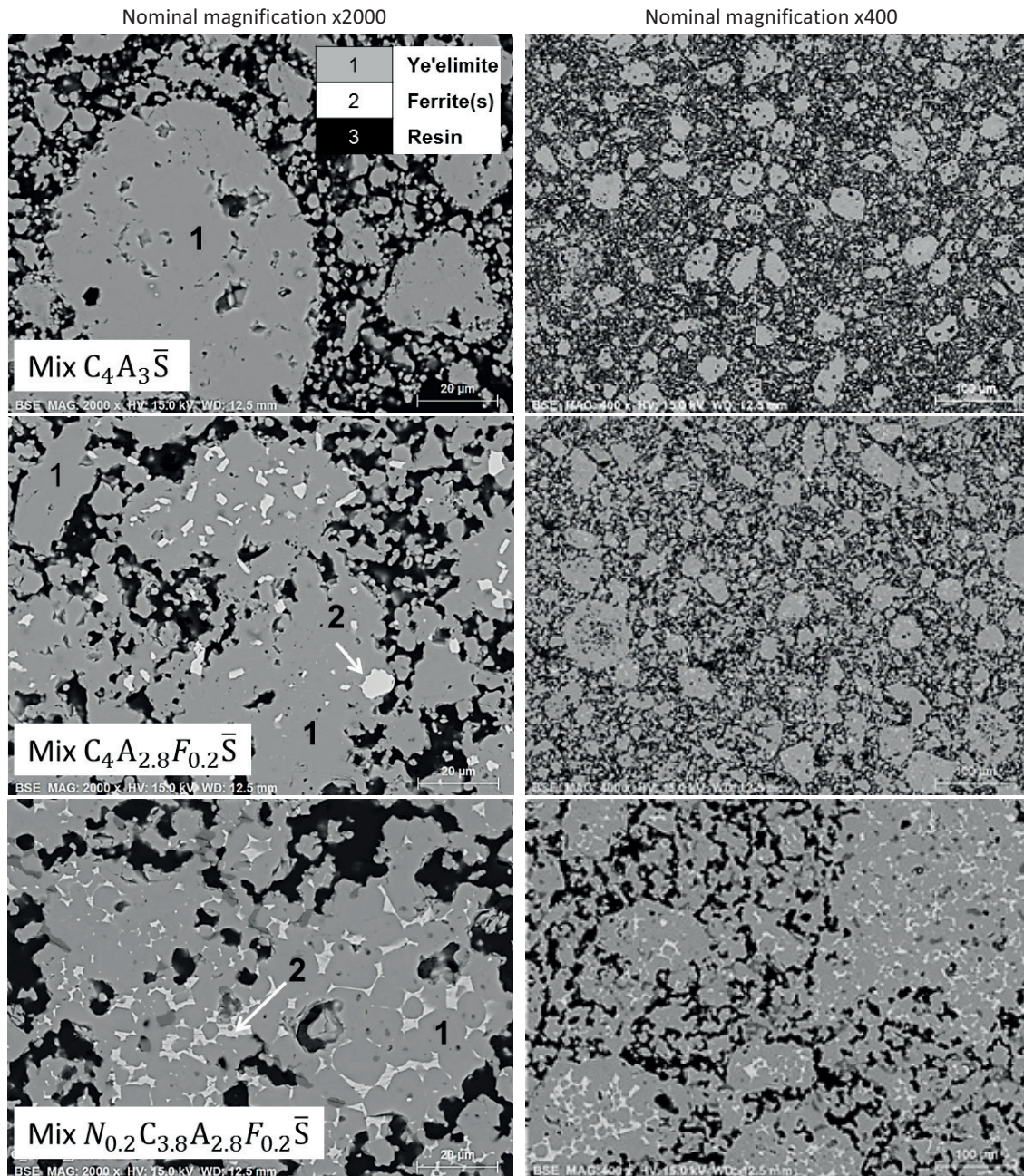


Figure 4.3-2 Scanning electron micrograph of a polished sections (top) and fractured powder samples (bottom) of Y and Fe-Y (from S3)

### 4.3.3 The fluxing effect of iron – Impact on microstructure

As mentioned above, Y can be almost exclusively formed by solid state reactions. The addition of iron, alone and with additional sodium, has a fluxing and mineralizing effect which primarily accelerates the formation krotite and grossite followed by its depletion due to the formation of ye'elimite. The impact of the liquid phase on the clinker microstructure is highlighted in Figure 4.3-3. The formation of a liquid phase is indicated by the enhanced nodulizing, the denser microstructure and reduced porosity (supported by  $SSA_{BET}$  analyses Table 8.8-13, annex part IV). The addition of sodium to the iron-rich sample increases the quantity of the liquid phase and seems to reduce its viscosity. This seems to cause the formation of particles or nodules composed of rounded ye'elimite crystals embedded within a matrix of a ferritic phase.





The formation of a liquid phase, as shown earlier by Touzo et al. [193] and Zupančič et al. [187], results from the relatively low melting points of calcium ferrite phases [87]. The ferritic phases such as srebrodolskite ( $C_2F$ ) and brownmillerite ( $C_4AF$ ) can be formed as primary and secondary phases. Primary ones are formed from the raw materials or probably from the crystallisation of a liquid phase and are already detectable in the samples produced at 1100 °C. Secondary ferritic phases are formed from the decomposition of iron-bearing ye'elinite, formation of an intermediate liquid phase [193] and the resulting crystallisation of it during cooling.

#### 4.4 Elemental composition of ye'elimite

To assess the elemental composition of the ye'elimite formed, SEM-EDS analyses on polished sections were done. In a first step only ye'elimite particles were analysed by placing measurement points randomly by hand on ye'elimite particles. In the case of Y up to 0.08 Fe-Y about 300 to 600 points were collected. For the samples with higher iron additions up to 1000 points were collected as often some inhomogeneous areas with high iron enrichment were observed. In a second set of experiments 6 frames were collected including a raster of 200 points per frame (only for the samples of the S3). The following elements were quantified from the measured spectra: main Al, Ca, Fe, S and minors Si, Na, K, Mg. Two selected results for Y and Fe-Y (S3) series are presented in 2D plots of the given atomic ratios (see Figure 4.4-1).

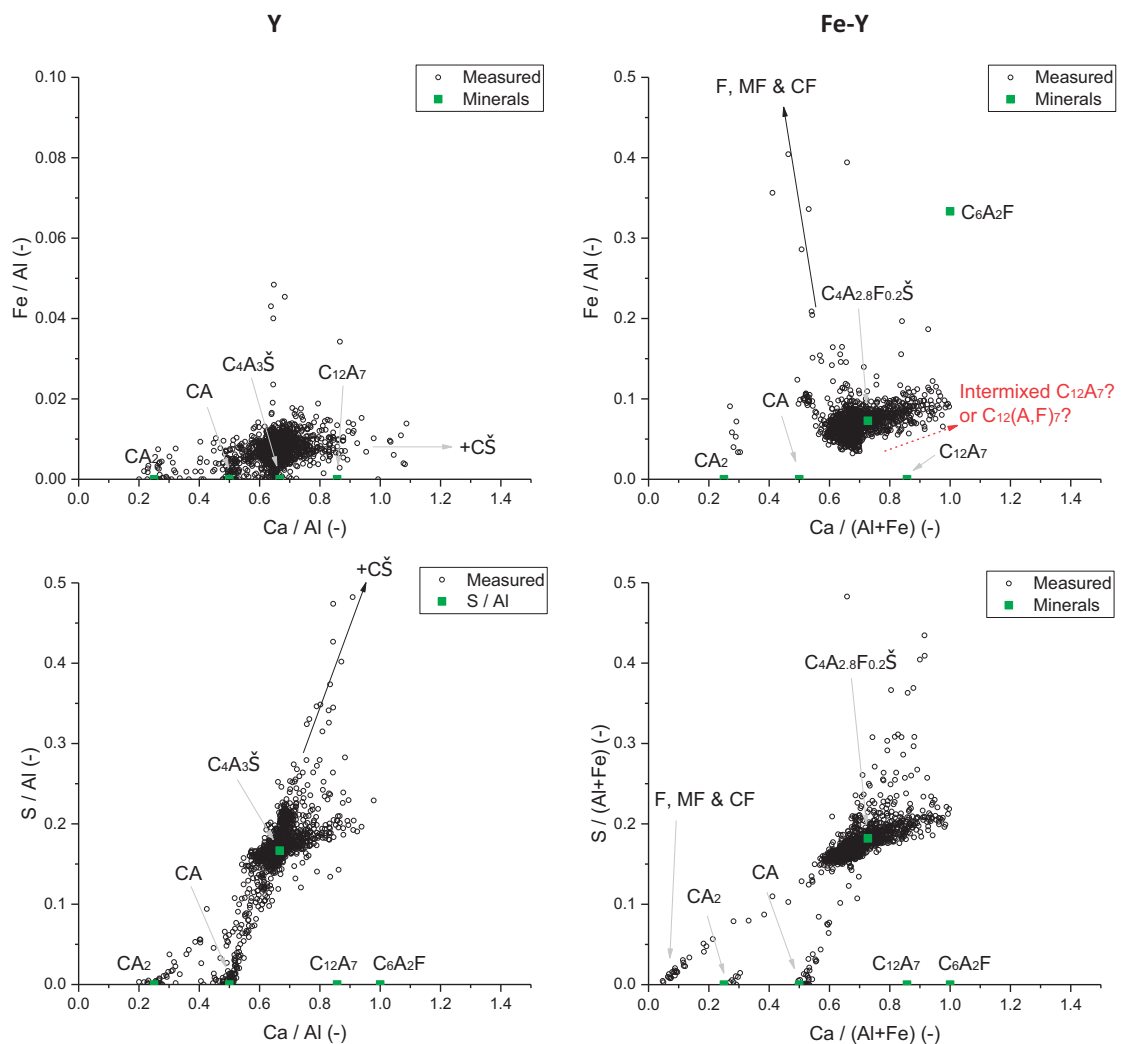


Figure 4.4-1 Atomic ratios of Fe/Al over Ca/Al (top) including a zoomed section and S/Al over Ca/Al (bottom) in the Y and Fe-Y samples of S3; F = maghemite, MF = magnesioferrite, CF = calcium ferrite

The majority of data points are located in a cluster around the composition of ye'elimite. Two additional clusters are present around the composition of krotite and grossite. These clusters are less pronounced in the Fe-Y sample compared to Y. Furthermore, anhydrite from the raw materials is present and intermixed with ye'elimite in Y. On the contrary, at least one calcium-rich phases such as mayenite or brownmillerite are intermixed with ye'elimite in Fe-Y. This result indicates the partial localised decomposition of ye'elimite, volatilization of sulphur and formation of krotite and lime. The formed lime may further react with the aluminate and ferrite phases to form e.g. mayenite and / or ferrite.

To calculate the elemental composition of synthesised solid solutions of ye'elimite, various measures had to be applied. A clear distinction of the several aluminate phases and ye'elimite by their respective grey levels was not possible. To enable a proper determination of the elemental composition, a set of elemental filters based on atomic ratios were used. In this way the analyses of minor phases such as grossite, krotite or anhydrite, which are often intermixed or embedded with(in) the ye'elimite particles (e.g. see Figure 4.3-1), could be removed.

Table 4.4-1 Set of filters based on atomic ratios (-)

Ca / (Al+Fe)		S / Ca		S / (Al+Fe)		Fe / Al depending on x	
>	<	>	<	>	<	>	<
0.60	0.80	0.20	0.30	0.10	0.23	0.00	0.20

The corrected data was used to calculate the composition of the (solid solution) ye'elimite. The results were normalized to 16 atoms of oxygen for ye'elimite ( $Ca_4Al_6O_{12}SO_4$ ) to facilitate comparison among different samples as done in other studies [62] [193]. Note that to calculate these compositions; we assume that each element is bound to the corresponding number of oxygens to form electrically neutral oxides. Such a procedure provides an improved accuracy over using the oxygen content determined by EDS. Emitted X-rays from oxygen have a relatively low energy and meaningful portion of it can be easily absorbed by the specimen and the detector window resulting. The composition of the ferritic phase was assessed whenever possible (to reach 10 atoms of oxygen). Unfortunately, we cannot assess the oxidation state and in that respect valence state of iron by SEM-EDS which may lead to errors in the results. For example, it is well known that  $Fe^{2+}$  can substitute for  $Ca^{2+}$  in calcium ferrites [89] and probably in ye'elimite as well. For reasons of simplicity and lack of experimental data we assumed that the valence state of iron is exclusively  $Fe^{3+}$ , only the substitution of  $Al^{3+}$  by  $Fe^{3+}$  was taken into account.

The results are presented in Table 4.2-2 together with the achieved substitution degree and calculated molecular weight of the solid solution ye'elimite (molecular weight of stoichiometric ye'elimite is 610.3 g/mol). The determined elemental phase compositions were used for the later presented mass balance calculations.



Table 4.4-2 Calculated elemental compositions (atomic form) of the produced ye'elimite clinkers throughout several campaigns, results were normalized for 16 atoms of oxygen

$C_4A_{3-x}F_x\bar{S}$	Calculated compositions	Target Fe (-)	Achieved Fe (-) [%]	Mol. Wt. (g/mol)
<b>S1</b>				
Y	$Ca_{4.06}Mg_{0.08}Na_{0.02}Al_{5.91}Fe_{0.01}Si_{0.03}S_{1.02}O_{16}$	--	--	612.3
Fe-Y	$Ca_{4.02}Mg_{0.09}Na_{0.02}Al_{5.63}Fe_{0.24}Si_{0.04}S_{1.00}O_{16}$	0.40	0.24 [60%]	617.6
0.2Na-Fe-Y	$Ca_{3.98}Mg_{0.08}Na_{0.14}Al_{5.65}Fe_{0.23}Si_{0.04}S_{0.99}O_{16}$	0.40	0.23 [57%]	618.3
<b>S2</b>				
Y	$Ca_{3.84}Mg_{0.16}Na_{0.05}Al_{5.99}Fe_{0.01}Si_{0.11}S_{0.92}O_{16}$	--	--	610.4
0.05Fe-Y	$Ca_{3.91}Mg_{0.15}Na_{0.04}Al_{5.90}Fe_{0.09}Si_{0.06}S_{0.93}O_{16}$	0.10	0.09 [91%]	614.0
0.08Fe-Y	$Ca_{3.87}Mg_{0.16}Na_{0.03}Al_{5.85}Fe_{0.15}Si_{0.08}S_{0.92}O_{16}$	0.16	0.15 [94%]	615.2
Fe-Y	$Ca_{3.85}Mg_{0.15}Na_{0.03}Al_{5.69}Fe_{0.29}Si_{0.10}S_{0.92}O_{16}$	0.40	0.29 [73%]	618.7
0.4Fe-Y	$Ca_{4.01}Mg_{0.13}Na_{0.02}Al_{5.54}Fe_{0.47}Si_{0.05}S_{0.91}O_{16}$	0.80	0.47 [59%]	627.4
0.8Fe-Y	$Ca_{3.99}Mg_{0.01}Na_{0.01}Al_{5.47}Fe_{0.55}Si_{0.03}S_{0.97}O_{16}$	1.60	0.55 [31%]	626.7
<b>S3</b>				
Y	$Ca_{4.01}Mg_{0.02}Al_{5.99}Fe_{0.05}Si_{0.03}S_{0.95}O_{16}$	--	--	612.9
Fe-Y	$Ca_{4.01}Mg_{0.03}Al_{5.67}Fe_{0.39}Si_{0.03}S_{0.94}O_{16}$	0.40	0.39 [97%]	622.9

The samples from S2 were, despite the intensive cleaning of all devices, contaminated with a raw meal used for the production of synthetic glass. This explains the measurable higher contents of *Mg*, *Na*, and *Si*. The sample 0.8Fe-Y was prepared following the same protocol but in another facility. As a result, the quantified contents of *Mg*, *Na*, and *Si* are lower and within the error of the applied technique. An almost full substitution was only achieved for 0.05Fe-Y, 0.08Fe-Y (S2) and Fe-Y (S3) and generally decreases with increasing iron contents. The maximum achieved substitution of *A* by *F*, *x* in  $C_4A_{3-x}F_x\bar{S}$ , was about 0.27 (about 7.2 wt.%  $Fe_2O_3$ ) for the sample 0.80Fe-Y, which indicate a trend to the value of about 0.34 reported by Touzo et al. [193].

In addition to SEM-EDS, the anhydrous particles of Y and Fe-Y (S3) are characterized by STEM-EDS analyses of the anhydrous particles (present in the hydrated samples after 30 seconds of hydration, see Chapter 5). The results are presented in Table 4.4-3 and are consistent with the SEM-EDS analyses. A few areas of the Fe-Y anhydrous particles have *Ca* / *Al* ratios of about 0.80 which is close to that of mayenite of about 0.86.

Table 4.4-3 Elemental ratios of ye'elimite measured by SEM-EDS and STEM-EDS (anhydrous residues); bulk = all measured data

	<i>Ca</i> / <i>Al</i> [-]			<i>S</i> / <i>Al</i> [-]			<i>Fe</i> / <i>Al</i> [-]			STEM $\Sigma$ of measured areas
	SEM		STEM	SEM		STEM	SEM		STEM	
	Ye'elimite	$\emptyset$ bulk		Ye'elimite	$\emptyset$ bulk		Ye'elimite	$\emptyset$ bulk		
Y	0.669	0.654	0.665	0.159	0.165	0.151	0.008	0.007	0.010	40
$C_4A_3\bar{S}$	0.667			0.167			--			
Fe-Y	0.707	0.742	0.740	0.166	0.184	0.164	0.069	0.113	0.065	50
$C_4A_{2.8}F_{0.2}\bar{S}$	0.714			0.179			0.071			

The impact of the sintering temperature on the formation and substitution of A by F in  $C_4A_{3-x}F_x\bar{S}$  was reported earlier [140] [194] [187]. The optimum temperature for the formation of iron-rich  $C_4A_{3-x}F_x\bar{S}$  or even  $C_4F_3\bar{S}$  is reported to be about 1100 °C. On the contrary it is about 1200 °C to 1250 °C to reach the highest ye'elimite content together with separate calcium ferritic phases. Such investigations were not within the scope of this study. Additionally, it is very likely that other elements such as *Na, K, Mg, Ti, Cr, Si, P, F* or *Cl* would further alter elemental composition of solid solution ye'elimite and in consequence the kinetics of formation and decomposition as well the hydraulic reactivity. Such systems should be studied, also in correlation to the sintering parameters and ultimately, to assess the impact on the hydraulic reactivity of ye'elimite.

As mentioned in section 4.3.3 and highlighted in Figure 4.3-3, the S1 clinkers show clear indication of the decomposition of ye'elimite into the iron-based liquid phase, which is exacerbated in the presence of sodium. This is due to the relatively high applied sintering temperature of 1300 °C, the formation of a liquid phase promoting the raw mix burnability and the three-time repetition of the sintering. We were able to collect sufficient data to calculate the ferritic phase composition(s). The measured atomic *Al / Fe* ratio of the ferritic phase is about 0.35 for Fe-Y and 0.73 for 0.2Na-Fe-Y. The increasing Al contents further strengthened the assumption that ye'elimite starts to decompose.

Mass balance calculations are applied using the ye'elimite compositions from SEM-EDS and the QXRD analyses to calculate the bulk chemistry. This enables the cross checking and validation of the individual analyses. The comparisons of the calculated and measured chemical composition of Y and Fe-Y (S3) are shown in Table 4.4-4 as one example. The calculated and measure compositions are almost identical which indicates that the analytical results are reasonably good.

**Table 4.4-4 Comparison of the measured (XRF) and calculated (mass balance calculations based on QXRD and SEM-EDS) chemical clinker composition of by; n.d. = not detected**

	Y			Fe-Y		
	Calculated	measured	Difference	calculated	measured	Difference
<i>SiO<sub>2</sub></i>	0.22	0.20	-0.02	0.27	0.20	0.07
<i>Al<sub>2</sub>O<sub>3</sub></i>	47.12	47.78	0.66	43.98	43.84	0.15
<i>TiO<sub>2</sub></i>	n.d.	0.00	0.00	n.d.	0.00	0.00
<i>MnO</i>	n.d.	0.00	0.00	n.d.	0.00	0.00
<i>Fe<sub>2</sub>O<sub>3</sub></i> (%)	0.56	0.65	-0.09	4.97	5.26	-0.29
<i>CaO</i>	36.81	36.87	-0.06	36.31	36.29	0.02
<i>MgO</i>	0.12	0.10	0.02	0.17	0.10	0.07
<i>K<sub>2</sub>O</i>	n.d.	0.01	-0.01	n.d.	0.01	-0.01
<i>Na<sub>2</sub>O</i>	n.d.	0.00	0.00	n.d.	0.00	0.00
<i>SO<sub>3</sub></i>	14.86	14.37	0.49	14.31	14.29	0.02
<i>P<sub>2</sub>O<sub>5</sub></i>	n.d.	0.02	-0.02	n.d.	0.02	-0.02

## 4.5 Discussion

### 4.5.1 Formation and stability of stoichiometric ye'elimite and in the presence of iron

Literature reports that stoichiometric ye'elimite undergoes a cubic to orthorhombic temperature dependent phase transformation [35] [36] [70] [72], where the onset of the transformation appears at 711 K  $\pm$  5 during heating [70] versus about 742 K  $\pm$  5 during cooling [35] [36] [70]. The partial substitution of  $Al^{3+}$  by  $Fe^{3+}$  within the crystal structure of ye'elimite stabilises the cubic symmetry during cooling [35] [39] [72] [186]. Consistent with the study of Zhang et al. [195] we could show that the formation of ye'elimite is accelerated at all temperature in the presence of iron (see Y and Fe-Y of S1 after the first sintering cycle, Chapter 12, section 12.7.2, Table 12.7-4 and 12.7-5). Our SEM analyses of polished and fractured samples studied here indicate that stoichiometric ye'elimite mainly forms by solid-state reactions, via the reaction of anhydrite with intermediate calcium aluminate phases consistent with earlier findings [196]. The addition of iron has a fluxing and a mineralizing effect probably due to the melting of ferritic phases around 1200 °C [87] [187]. The liquid phase acts as a glue to bind particles and as a transportation media for dissolved elements [193]. This for example leads to the observed more densified microstructure of Fe-Y compared to Y and even more pronounced densification when sodium is also present. The mineralizing effect may occur due to the substitution of  $Al^{3+}$  by  $Fe^{3+}$  [64] [187] [195] which seem to promote the growth of particles. However, iron seem to primarily accelerate the formation of the intermediate calcium aluminate phases already at lower sintering temperature such as 1100 °C as shown in Table 4.5-1. The presence of those intermediate phases is obligatory, as they react further with anhydrite to form ye'elimite. Thus, any reaction that accelerates the formation of the calcium aluminate favours the formation of ye'elimite. The positive impact of iron on the formation of the calcium aluminate and ye'elimite seem inversed at 1300 °C.

**Table 4.5-1 Selected results from the mineralogical composition of the clinkers from the first series (S1) Table 8.8-14 and Table 8.8-15 (see annex – part IV);  $\Sigma C_4A_3\bar{S}$  = ortho. + cubic type; n.d. = not detected**

	1 <sup>st</sup> sintering at 1100 °C		1 <sup>st</sup> sintering at 1150 °C		1 <sup>st</sup> sintering at 1200 °C		1 <sup>st</sup> sintering at 1250 °C		1 <sup>st</sup> sintering at 1300 °C	
	Y	Fe-Y	Y	Fe-Y	Y	Fe-Y	Y	Fe-Y	Y	Fe-Y
$\Sigma C_4A_3\bar{S}$	14.4	17.2	20.4	25.5	18.8	79.0	37.8	79.6	89.4	78.9
$\Sigma C_{12}A_7 + CA$ + $CA_2$	17.6	29.7	25.7	32.3	27.6	13.8	26.4	8.6	5.3	13.9
$\Sigma C_4AF + C_2F$	n.d.	10.5	n.d.	10.4	n.d.	3.5	n.d.	7.3	n.d.	3.5
$\Sigma A + F + C$ + $C\bar{S}$	67.2	42.0	53.3	31.5	52.9	3.7	35.3	4.5	5.0	3.7
<i>Minors</i>	0.8	0.6	0.6	0.3	0.7	n.d.	0.5	n.d.	0.3	n.d.

The use of SEM-EDS enabled us to successfully determine the elemental composition of ye'elimite and the level of substitution of  $Al^{3+}$  by  $Fe^{3+}$ . On the contrary to earlier findings [35] [39] [72], the indirect determination of the  $Al^{3+}$  by  $Fe^{3+}$  substitution in ye'elimite via QXRD the lattice volume evolution or by mass balance calculations was not accurate. Most of the minor phases, including mayenite and ferrites, are below the detection limit but in contrast, visible in the SEM micrographs. The determination of the increasing cell volume of ye'elimite due to the partial substitution of  $Al^{3+}$  (0.535 Å) by the larger  $Fe^{3+}$  (0.645 Å) could also not be used as other minor elements such as silicon or magnesium were incorporated into the crystal lattice as well. Moreover, we can neither exclude that the iron is present in several oxidation states, which would alter the results, nor that the applied sintering temperature and cooling procedure affect the cell volume [36] [72] [187].

The maximum value of  $x$  in  $C_4A_{3-x}F_x\bar{S}$  measured by SEM-EDS analyses was about 0.27 (about 7.2 wt.%  $Fe_2O_3$ ) for the sample 0.80Fe-Y, which is close to the values of 0.32 to 0.34 reported by Zupančič et al. [187] and Touzo et al. [193]. Substitution levels of  $Al^{3+}$  by  $Fe^{3+}$  above 90% of the target were only achieved for 0.05Fe-Y and 0.08Fe-Y of the S2 series but not for Fe-Y. Using an optimized raw mix preparation procedure it was also possible to achieve more than 90% in the Fe-Y sample of the S3 series. The observation of the morphological changes by the incorporation of iron is consistent with the study of Zupančič et al. [187]. The authors found that the presence of iron as hematite ( $F$ ) or calcium ferrite ( $CF$ ), led to the formation of more rounded particles and a denser clinker microstructure. The authors attributed this to the impact of the formation of a liquid phase and its interaction with ye'elimite. This assumption is strengthened by our findings.

The calculated chemical compositions of almost all ye'elimite samples, except for S1, are close to the theoretical values (4 for  $Ca$ , 6 for  $\Sigma(Al + Fe)$  and 1 for  $S$ ), in agreement to the QXRD evaluations and to complementary studies [62] [193] [197]. The calculated bulk clinker chemistry, based on QXRD and SEM-EDS analyses, further validates the results of the individual analytical methods. In contrast to the study of Idrissi et al. [192] no high  $Ca$  deficiency was found. In [192] the measured average formulas were obtained directly from the SEM-EDS measurements instead of filtering the results and calculating the atoms per formula unit. By recalculating the presented data, one will reach  $Ca$  contents ranging from around 3.7 to 4.3,  $\Sigma(Al + Fe)$  from 5.5 to 6.6 and  $S$  from 0.8 to 1.1. This indicates that ye'elimite was not measured as pure phase but was intermixed with calcium aluminate and calcium ferrites. With regard to S1: too high sintering temperatures and many cycles (total sintering time of 3 hours) caused the decomposition of ye'elimite, volatilisation sulphur and formation of secondary phases such as calcium aluminates and ferrites in S1. These phases were finely intermixed or embedded within the ye'elimite and the applied filters were not sufficient to provide accurate results.

Based on the findings presented here we can formulate the following hypothesis: the mineralizing and the fluxing effect of iron leads to an increasing rate of formation of solid solution ye'elimite. The solid solution ye'elimite seems to possess a lower thermal stability compared to the stoichiometric one. Actually it is not clear what causes the lower thermal stability. One possibility is that the lower thermal stability is due to changing crystal structure. Another aspect could be the related to the faster formation of the solid solution ye'elimite. As it is faster formed, ye'elimite particles are longer exposed to the sintering temperature and may start to decompose again beside the still ongoing formation from the not yet reacted raw materials.

An idealized scheme of the hypotheses is shown in Figure 4.5-1. It highlights the points for the Y and Fe-Y from the S3 series. Our hypothesis is supported by the findings of the comparative studies from Li et al. [64] and Zhang et al. [195]. The authors studied the formation and decomposition kinetics of ye'elimite from tricalcium aluminate and anhydrite. They found that already 1% of  $Fe_2O_3$  ( $x = 0.05$  in  $C_4A_{3-x}F_x\bar{S}$ ) reduces the formation and decomposition activation energies by about 20% ( $184 \pm 25$  kJ/mol) and 34% ( $523 \pm 17$  kJ/mol), respectively, compared to stoichiometric ye'elimite ( $231 \pm 42$  kJ/mol and  $792 \pm 64$  kJ/mol). This means ye'elimite would form faster at similar conditions but also starts faster to decompose again.

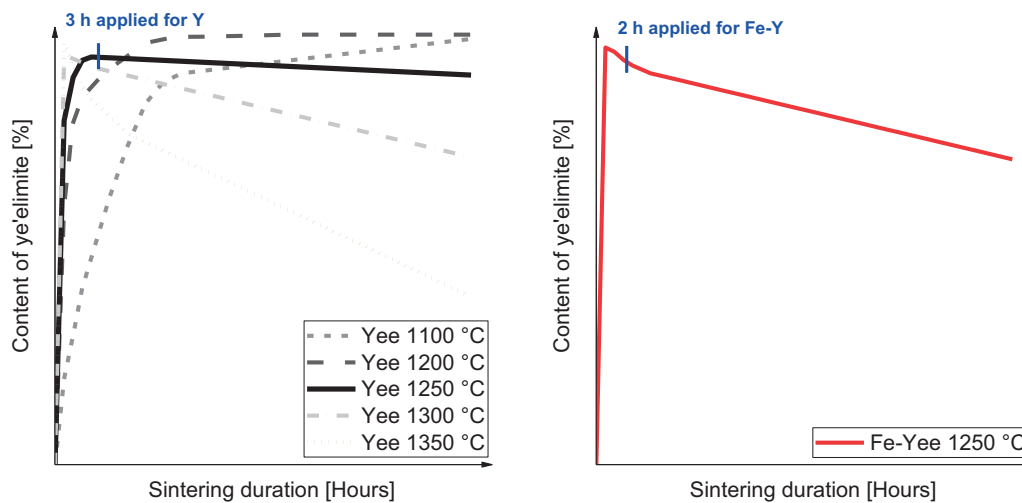
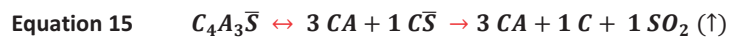


Figure 4.5-1 Proposed scheme of the ye'elimite formation depending of the applied sintering temperature and duration; the scheme is adopted from the findings of Li et al. [64] and Zhang et al. [195]

The decomposition of ye'elimite causes the formation of secondary phases such as mayenite, krotite, and ferrite. The formation of mayenite ( $Ca / Al$  ratio  $\sim 0.86$ ) depends on the availability of excess free lime ( $C$ ). This is not the case for the synthesis of a “Ca deficient” ye'elimite ( $C_4A_3\bar{S}$  with a  $Ca / Al$  ratio  $\sim 0.66$ ) which should form according to Equation 13 (see section 4.2.2). Therefore we assume that the decomposition of ye'elimite follows Equation 15. At least a part of anhydrite starts to decompose which in consequence lead to the partial volatilization of  $SO_2$  and the formation of free lime. The fate of iron is not included for reasons of simplicity. The validity of this reaction sequence was experimentally proven for stoichiometric ye'elimite by Puertas et al. [198].



#### 4.5.2 Formation and composition of ferrites and the liquid phases

As shown in Table 4.2-2 under section 4.4, the achieved level of substitution of  $Al^{3+}$  by  $Fe^{3+}$  in ye'elimite ranges from about 31% up to 97%. The remaining or free iron is present as maghemite ( $Fe_2O_3$ ) (see Table 4.2-1 under section 4.2.1). No magnetic particle where detectable which excludes the presence of magnetite ( $Fe_3O_4$ ). Traces of several calcium-bearing ferrites and of a magnesium ferrite ( $MF$ ) were rarely detected or only found during the SEM-EDS analyses like for Fe-Y of the S3 series. This indicates over all very low contents of these phases. Primary ferritic phases are formed from the reaction of the raw materials. The formation of secondary ferrites is the consequence of the decomposition of Fe-bearing ye'elimite. The composition of the ferritic phase can be close to the composition of  $C_6A_2F$  but tends in general to iron-rich members such as  $C_6AF_2$ ,  $C_2F$  or even  $CF$  and  $CF_2$ . This is consistent to the findings by other researchers [62] [187] [193]. The magnesium ferrite is a complex solid solution which further contains calcium and aluminium. The presence of these minor phases was only revealed by SEM-EDS measurements but not by QXRD. The formation of spinel-type phases, e.g.  $MA$ ,  $MF$  and various heterogeneous solid solutions, was already described for CSA type clinkers [197] [199]. One major condition for the formation is the absence of  $SiO_2$  which would alternatively promotes the formation of members of the melilite group. The formation of the magnesium ferrite or of spinel depends obviously on the availability of magnesium oxide.



The formation of a liquid phase is typically related to the presence of iron and is of particular importance in the field of cement production. The liquid phase should have two effects; it should enhance the mass transport between solids via the liquid phase and it should enable the nodulization leading to the formation of a denser microstructure [187] [193] [200]. Consistently, the presence of a liquid phase is revealed experimentally in SEM micrographs by the denser microstructure and reduced porosity (supported by  $SSA_{BET}$  analyses, see section 4.2.2). The addition of sodium (S1) seems to decrease the viscosity and increase the quantity of the liquid phase. On the contrary, it is well known that alkali metal oxides such as potassium and sodium oxide are known as network modifiers [201] which increase the viscosity of a liquid phase but reduces the surface tension [202] [203]. In that regard they are typically used to decrease the melting point of synthetic glass, slags and coal ashes during production [204] [205]. However, in our case sodium decreases the melting point of the ferrites and it seems also the viscosity of the liquid phase, which may be the dominant factor here. This is consistent to earlier findings regarding the combined effect of alkali and iron [206] [207]. Additionally, one has to consider the impact of the presence of sulphate which may cause the phase separation and formation of a second *Alkali* –  $CaO$  –  $SO_3$  melt [208] [209]. In that respect, the formation of glauberite ( $CNS_2$ ) was observed in the sodium-rich ye'elimite clinker (S1). Similar effects can be observed in the case of the phase assemblage, melting point and viscosity of the ferritic liquid present in OPC clinker [210] [211].

Comprehensive summaries of the impacts of several minor elements on the OPC clinker phase formation and microstructure, including the liquid phase, are summarized by Klemm and Skalny [212], Viswanathan and Gosh [213], Johansen and Bhatti [214]. The aspects mentioned above may explain the observed nodulizing and densification of ye'elimite clinkers with increasing iron contents. Consistent with earlier observations [202] [203], the addition of sodium decreases not only the formation temperature of the liquid phase and but also increases the quantity. Furthermore, ye'elimite particles become rounded and are embedded within a matrix of the ferritic liquid phase. Zupančič et al. [187] related the rounding of ye'elimite to the initiated decomposition or dissolution, which would be supported by the differences in the ferritic phase composition determined by us experimentally (see section 4.4). Another important aspect regarding the composition and viscosity of the ferritic liquid phase is the content of dissolved sulphate. It is well known in the cement industry but not without controversy, that sulphate reduces the surface tension and viscosity of the liquid phase which enhances the wetting and nodulization [215] [216]. However, other authors observed an increased liquid phase viscosity due to the presence of sulphate [217] [218]. Generally speaking, the lower viscosity of the liquid phase may enhance the mass transfer between the solid and liquid fraction which may promote the faster formation but also faster decomposition of ye'elimite. This assumption is strengthened by the results shown in Figure 4.3-3 (section 4.3.3) and Figure 4.5-1 above. The impact of sodium on the thermal stability of ye'elimite is not known.

Finally, in the study of Touzo et al. [193] all analysed ferrites were free of sulphate. The authors reported that the liquid phase facilitates the formation of ye'elimite but that sulphate is not well retained and tends to volatile. In contrast, within this study the ferritic phases typically contain around 0.6% to 0.9% sulphate which is in a similar range as measured by Strigác et al. [62]. The observed differences are very probable related to the differences in the experimental set-up. In the study of Touzo et al. [193] mixtures of synthetic  $C_4A_3\bar{S}$  and  $C_2F$  were prepared, followed by a sintering at 1325 °C. After sintering, the elemental composition of the produced clinker was assessed and a significant volatilization of sulphur ( $SO_2$ ) was observed.

In complementary studies on the thermal stability of anhydrite [101] [102] it was shown that under oxidizing conditions the volatilization of sulphur following the decomposition of anhydrite starts from around 1100 °C. Increasing temperatures accelerates this process and the decomposition becomes rapid at above 1300 °C. Slightly reducing conditions profoundly decreases the thermal stability of anhydrite even at temperatures far below 1300 °C. Within the present study we used an excess of calcium sulphate (added as anhydrite) as well as a lower sintering temperature of 1250 °C compared to 1330 °C used by Touzo et al. [193]. The crucibles were covered with lids and as a result, the  $SO_2$  partial pressure should be higher and as result, the loss of sulphur should be minimized. It is very probable that under the conditions used by Touzo et al. [193], the ferrites are either not incorporating sulphur from the beginning (at the moment that ye'elimite starts to dissolve into the melt or decompose to calcium aluminates and anhydrite) or they represent the first phases starting to decompose, releasing the bound sulphur and recrystallize during cooling from the melt.

#### 4.5.3 Calcium aluminate phases

The calcium aluminates krotite and grossite are the main phases present in commercial CACs, representing the binary system  $CaO - Al_2O_3$ . The ratio between krotite and grossite in CAC depends mainly on the ratio of calcium oxide over aluminium oxide in the raw mix [75] [76]. Dodecalcium hepta-aluminate or also known as mayenite may occur as minor phase in CAC. Mayenite is also known as a minor phase present in OPC (occasionally) and CSA or BYF (typical). We have shown that iron promotes the formation of clinker minerals such as ye'elimite and the intermediate calcium aluminates. Especially, the intermediate phase krotite is formed much faster, also at lower synthesis temperatures such as 1100 °C (see also annex, part IV, Table 8.7-12 and 8.7-13). In krotite, a substitution level up to 5 wt.% of aluminium by iron has been reported [77] [78]. Thus we assume that iron has, besides the fluxing, a mineralizing effect which could explain our experimental observations.

Similarly literature reports that mayenite is a non-stoichiometric phase which is stabilized by the incorporation of an excess of oxygen [219] or hydroxide [220] [221]. Several other elements can be incorporated into the crystal lattice of mayenite as well. In the context of ionic conductors, Eufinger et al. [82] provided a good summary about known solid solutions of mayenite containing. They also successfully investigated the high temperature solid state synthesis of mayenite substitute with fluoride, chloride, cyanide and sulphide replacing the hydroxide. Other studies investigated the synthesis and characteristics of mayenite doped with silica [79] [83] and magnesium [79]. In the work of Galuskin et al. [81] the natural analogues of many of the synthetic solid solutions are reported. One element of particular interest is iron. Iron-bearing solid solutions of mayenite were already prepared and the results indicated that iron may have a stabilising, i.e. mineralizing, effect [73] [77] [79] [80] [81] which is consistent to our findings. The formation of mayenite was strongly promoted in the presence of iron at low sintering temperatures such as 1100 °C (see also annex, part IV Table 8.7-12 and 8.7-13).

Clinker synthesis and characterisation

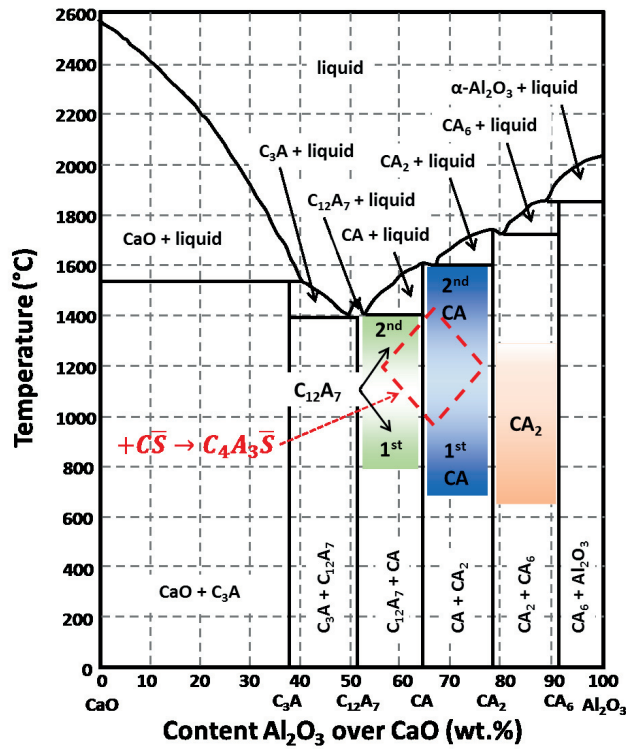


Figure 4.5-2 Phase diagram of the system  $CaO - Al_2O_3$  in air of ordinary humidity adopted from [73] and extended for the temperature ranges for the intermediated clinker phases, presented in colour bars, adopted from [79] [189] and including  $CA_2$  [190] [191] (extend range based on our findings)

## 4.6 Conclusions

The main findings can be summarized as follows:

- Ye'elimite is formed from the reaction of the intermediate calcium aluminates with anhydrite
- Several primary and secondary calcium aluminates and ferritic phases are formed
  - Primary from the raw materials and secondary from the decomposition of ye'elimite
- Iron has a fluxing and mineralizing effect
  - Enables or enhance the formation of a liquid phase
  - Accelerates the formation of intermediate (solid solution) calcium aluminates and thus of the solid solution ye'elimite
  - Potentially reduces the thermal stability of ye'elimite probably by
    - Its faster formation and longer residence time at the sintering temperature
    - Lowering the formation and decomposition activation energies
- The decomposition of ye'elimite and volatilization of sulphur causes the formation of secondary mayenite and lead to an increase of the  $A / F$  ratio and in the ferritic phases
- SEM-EDS analyse provided a powerful technique which revealed the
  - The densification of the microstructure in the presence of iron
  - Presence of several minor phases which are below the XRD detection limit
  - Maximum value of  $x$  in  $C_4A_{3-x}F_x\bar{S}$  of about 0.27 (7.2 wt.%  $Fe_2O_3$ ) where the (almost) full incorporation can be easily achieved around 0.05 to 0.10 (5 wt.%)

The fluxing effect causes an enhanced nodulization, the densification of the microstructure, which promotes the mass transport of elements and thus the mineral formation. Especially, the intermediate phase krotite is formed faster and at lower synthesis temperatures such as 1100 °C. Hence it enables the faster ye'elimite formation. This effect is enhanced in the presence of sodium. Those results indicate that formation rate of krotite one of the key aspects to control the formation rate of ye'elimite. These findings can be directly applied for the production of CSA and BYF clinkers. For example, using a higher fineness of the calcium and aluminium sources as well as a good homogenization it could be feasible to optimize the production of such clinkers, e.g. enabling the reduction of the sintering temperature and / or the dwell time.

The partial substitution of  $Al^{3+}$  by  $Fe^{3+}$  within the crystal structure of ye'elimite stabilizes the cubic form to ambient temperature. However, using the same synthesis conditions, we observed the faster decomposition of the solid solution ye'elimite. It may originate from the incorporation of iron and the modification of the crystal structure. Another possibility could be related to the improved clinker burnability and faster ye'elimite formation in the presence of iron. Due to its faster formation, ye'elimite is also exposed for a longer period to the sintering temperature. Consequently, a fraction of ye'elimite may start to decompose. The decomposition of ye'elimite led than to the volatilization of sulphur and the formation of secondary phases such as mayenite, krotite and ferrites. The results of individual methods were checked successfully for plausibility by comparison to complementary analyses. For example, we carried out mass balance calculations by combining SEM-EDS and QXRD analysis to calculate the bulk chemical composition and to compare those results were compared to the measured XRF. Finally, the determination of the substitution level of alumina by iron was successfully done using SEM-EDS analyses. On the contrary, the indirect determination via QXRD alone and / or by applying mass balance calculations was not accurate.

## 5 Hydration reactions of synthetic ye'elimite

The results of this chapter will be reported in peer reviewed journal(s):

- Cement and Concrete Research
  - Title: Hydration reactions of synthetic ye'elimite
    - Draft under preparation

---

<b>5</b>	<b><u>HYDRATION REACTIONS OF SYNTHETIC YE'ELIMITE</u></b>	<b>59</b>
<hr/>		
<b>5.1</b>	<b>SUMMARY – EXPERIMENTS CARRIED OUT IN CHAPTER 5</b>	<b>61</b>
<b>5.2</b>	<b>SUMMARY - ANHYDROUS MATERIALS USED IN THE CHAPTERS 5, 6 AND 7</b>	<b>61</b>
<b>5.3</b>	<b>RESULTS</b>	<b>63</b>
<b>5.4</b>	<b>DISCUSSION OF RESULTS</b>	<b>66</b>
5.4.1	INITIAL AND DORMANT PERIOD – WHY DOES THE DISSOLUTION SLOWS DOWN	66
5.4.2	ACCELERATION AND MAIN PERIOD – WHY DOES THE DISSOLUTION REACCELERATES	74
5.4.3	FINAL PERIOD	76
5.4.4	EFFECT OF W/B ON THE HYDRATION KINETICS IN PASTE	77
<b>5.5</b>	<b>GENERAL DISCUSSION</b>	<b>80</b>
5.5.1	HYDRATION SEQUENCES	80
5.5.2	WHY DOES THE DISSOLUTION SLOW DOWN AND WHY DOES IT ACCELERATE AGAIN	81
<b>5.6</b>	<b>CONCLUSIONS</b>	<b>83</b>

---

This chapter presents the results of experiments neat stoichiometric ye'elimite clinker carried out in pastes and suspensions covering water to binder (w/b) ratios from 0.5 to 1000. The experiments in paste were done for w/b ratios from 0.5 to 40. The experiments in paste were carried out suspensions with w/b ratios from 40 to 1000. Finally, a thorough comparison between the experiments carried out in paste and suspension is given.

In general, it is widely accepted that hydration of ye'elimite is primarily responsible for the early properties of CSA and BYF cements. The main hydration products are ettringite, monosulphate and poorly crystalline or amorphous phases such aluminium hydroxide. Rarely the formation of different calcium aluminate hydrates is reported as well. It is often reported that the hydration kinetics varies strongly, even for cements with similar composition and fineness. The objective of this chapter is to characterise and understand the mechanisms operating at the different hydration stages of ye'elimite.

For that the dissolution of anhydrous phases, evolution of the solution composition and the resulting formation, composition and morphology of the hydrates were investigated. Two sets of experiments were carried out. The first was carried out on paste samples with water to cement ratios from 0.5 to 40. Mainly isothermal conduction calorimetry was used to assess the hydration kinetics. In this experimental set, quartz was used to allow the preparation of pastes with high water to binder ratios but avoiding or minimizing the bleeding or the sedimentation. The calorimetry measurements were supplemented by thermogravimetric analyses (TGA) and quantitative X-ray powder diffraction (QXRD) to determine the composition of the formed hydration products. The second series of experiments were done in diluted suspensions with water to cement ratios from 40 to 1000. In this set of experiments simultaneously the hydration kinetics and reactions were assessed qualitatively and quantitatively by measuring the specific electrical conductivity, pH and the solutions compositions. These results were further supplemented by TGA, QXRD, high resolution scanning electron microscopy analyses (HR-SEM) and scanning transmission electron microscopy (STEM) analyses.

## 5.1 Summary – Experiments carried out in Chapter 5

Y clinker from the S3 series was used. The experiments were made in pastes and suspension in order to investigate the impact of the water to binder (w/b) ratio, the availability of surface area (Qz filler) and the evolution of the phase assemblage and solution concentrations. The experiments which were carried out are summarised in Table 5.1-1. Not all results are included in this chapter but available in the annex – part V.

Table 5.1-1 Experimental matrix

		Paste ± Qz		Suspension	
		w/b 0.5 - 40	w/b 40 - 1000	w/b 40	w/b 100
Calorimetry	Continuous measurement 0 - 48 h	x			
QXRD + TGA	Single sample at the end	x			x
	Samples taken during 24 h			x	
Mass balance calculations	All	x		x	x
Conductivity and pH	Continuous measurement 0 - 24 h		x	x	x
ICP-OES	Samples taken during 24 h			x	x
HR-SEM	Samples taken during 7 min				x
STEM-EDS	Samples taken during 6 h				x
Modelling	Samples taken during 24 h			x	x

Two sets of **paste samples** were prepared by external mixing for 30 seconds with 2500 U/min using a laboratory Vortex shaker (VF2, Janke and Kunkel Labortechnik). First, neat binder pastes were prepared with w/b ratios from 0.5 to 10. For the second set of experiments, the binder was consecutively replaced by inert quartz filler (Qz) to reach w/b ratios from 1.11 to 40 keeping the maximum water to solid (w/s) ratio of 2. The compositions of the blends with quartz are shown in Table 5.1-2.

Table 5.1-2 Binder compositions; w / s = water to solid ratio, w/b water to cement ratio

	Y	Qz	w/s	w/b
	[%]			
w/b 0.5	100	0	0.5	0.5
w/b 1	100	0	1	1
w/b 1.11	90	10	1	1.11
w/b 2	100	0	2	2
w/b 2.22	90	10	2	2.22
w/b 5	40	60	2	5
w/b 7.5	26.65	73.35	2	7.5
w/b 10	20	80	2	10
w/b 20	10	90	2	20
w/b 40	5	95	2	40

## 5.2 Summary - Anhydrous materials used in the Chapters 5, 6 and 7

The ye'elimite clinkers Y (investigated in Chapter 5, 6 and 7) and Fe-Y (investigated in Chapter 6 and 7) from the S3 series were investigated. Mayenite (investigated in Chapter 7) was produced by sintering the mix four times for 2 hours at 1300 °C following intermediate grinding steps. The mineralogy, from Rietveld analysis of XRD, of the produced clinkers is presented in Table 5.2-1. The effects of gypsum (p.a. Merck) and quartz (p.a. Merck) additions were investigated in all following chapters (investigated in Chapter 5 [Qz], 6 [G and G+Qz] and 7 [G, Qz and G+Qz]).

Table 5.2-1 Quantitative phase composition of materials used; n.d. = not detected

		Y	Fe-Y	$C_{12}A_7$	G	Qz
		[%]				
Orthorhombic ye'elimite (Y)	$C_4A_3\bar{S}$	87.9	traces	n.d.	n.d.	n.d.
Cubic iron-rich ye'elimite (Fe-Y)	$C_4A_{2.8}F_{0.2}\bar{S}$	n.d.	93.9	n.d.	n.d.	n.d.
Tricalcium aluminate	$C_3A$	n.d.	n.d.	1.9	n.d.	n.d.
Mayenite	$C_{12}A_7$	n.d.	0.6	97.5	n.d.	n.d.
Krotite	$CA$	5.1	0.3	0.6	n.d.	n.d.
Grossite	$CA_2$	0.3	n.d.	n.d.	n.d.	n.d.
Maghemite	$F$	n.d.	0.3	n.d.	n.d.	n.d.
Anhydrite	$C\bar{S}$	6.7	5.0	n.d.	n.d.	n.d.
Gypsum	$C\bar{S}H_2$	n.d.	n.d.	n.d.	100.0	n.d.
Quartz	$S$	n.d.	n.d.	n.d.	n.d.	100.0

All materials were ground in a planetary ball mill to a target  $d_{90} < 40\text{-}\mu\text{m}$ . The achieved particle size distributions are shown in Figure 5.2-1. Fe-Y was slightly coarser which is supported by the lower  $SSA_{\text{BET}}$  value of  $0.96\text{ m}^2/\text{g}$  compared to Y  $1.16\text{ m}^2/\text{g}$ . The  $SSA_{\text{BET}}$  of mayenite, gypsum and quartz was  $1.04\text{ m}^2/\text{g}$ ,  $1.13\text{ m}^2/\text{g}$  and  $1.22\text{ m}^2/\text{g}$ .

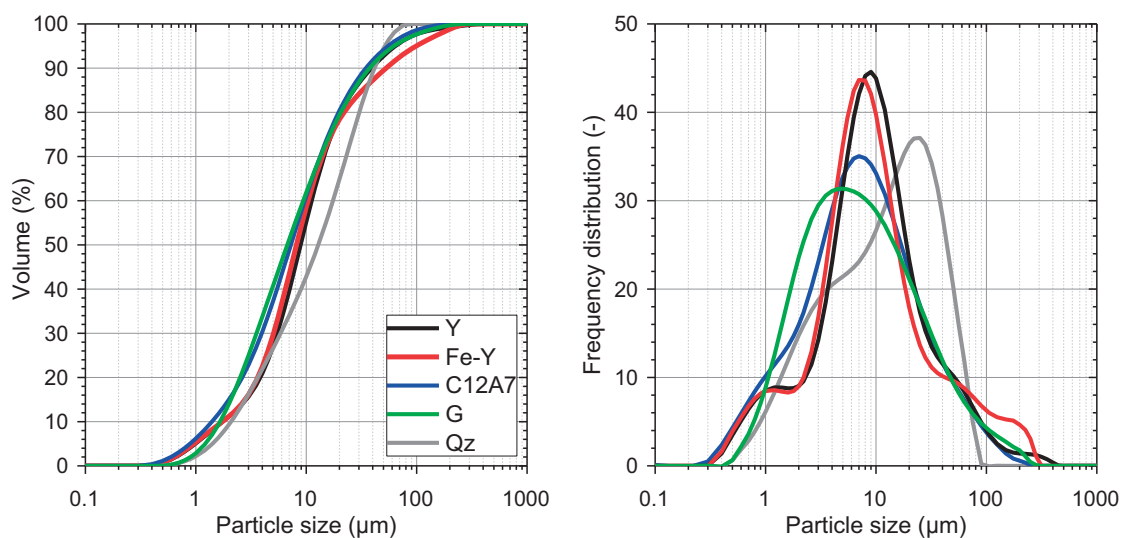


Figure 5.2-1 Particle size distribution of starting materials



### 5.3 Results

Figure 5.3-1 shows a summary of the results from the experiments in suspensions. The tests are primarily based on the continuous measurement of the conductivity and the pH (both temperature corrected), supplemented by spot analyses of the solution and the solid residue composition.

The solid black line (Figure 5.3-1 (a)) presents the conductivity, which provides qualitative information about the dissolution of the anhydrous phase and the precipitation of hydrates. This is due to the fact that cations and anions in solution such as of  $Ca^{2+}$ ,  $Al(OH)_4^-$ ,  $OH^-$  and  $SO_4^{2-}$  can carry an applied electric current. Conductivity is a material an “intrinsic” property of the material, e.g. in our case of the suspension. However, it provides “only” qualitative information, as it measures the combined effect of all ions in solution, i.e. the ionic strength. The increase of the conductivity is somewhat proportional to the anhydrous dissolution (e.g. neglecting the potential formation of ion pairs or complexes), which presents the source of liberated ions. The precipitation of hydrates causes the consumption of ions from solution and thus the decrease of the conductivity. However, the measured conductivity depends on several factors such as the concentration, mobility of ions, valence of ions and the temperature. The grey line represents the pH, which presents a direct quantitative measurement of the  $H^+$  or  $H_3O^+$  concentration.

Figure 5.3-1 (b) presents the measured concentrations at given times. In addition, the theoretical values for Ca and S are shown, which were derived from mass balance calculations based on the measured Al concentration and assuming the congruent dissolution of ye'elimite. The measured concentrations follow well the evolution of the conductivity up to about 160 minutes of hydration. The evolution starts to deviate afterwards, indicating a change of the hydration mechanism.

The dissolution of the anhydrous phases together with the formation of the hydrates is shown in Figure 5.3-1 (c). The dissolution of ye'elimite corresponds well to the evolution of the conductivity. The formation of the hydrates follows a more complex pattern. Initially only an X-ray amorphous phase is formed and this phase maintains to be the dominant fraction throughout the entire experiment. All the studied hydrated samples were characterised after stopping the hydration by solvent exchange. This may have damaged the hydrates, especially at early hydration ages. The first XRD detectable (crystalline) hydrate after about 70 minutes of hydration is ettringite, followed by monosulphate and gibbsite-like aluminium hydroxide after about 200 minutes.

Based on the sum of the given results, we defined five hydration stages and two main hydration reactions, which will be described in detail throughout this Chapter. A brief summary can be given as follow. During the first period, ye'elimite rapidly dissolves followed by the slowdown of the dissolution. The rise of the conductivity, pH and the measured solution concentrations follow well the dissolution of ye'elimite. The second period was set, during which the hydration of ye'elimite almost stops and only ettringite continuous to form. The third period is highlighted by the re-acceleration of the ye'elimite dissolution and profound changes in the solution composition, e.g. especially the drop of the sulphate concentration and the increase of the pH. The fourth period is represented by the rapid and full hydration of all anhydrous phases, which was also revealed by the evolution of the conductivity and pH. The fifth period is characterized by the continuous slow increase of the conductivity and pH as well as the crystallization of monosulphate and gibbsite-like aluminium hydroxide.

Hydration reactions of synthetic ye'elinite

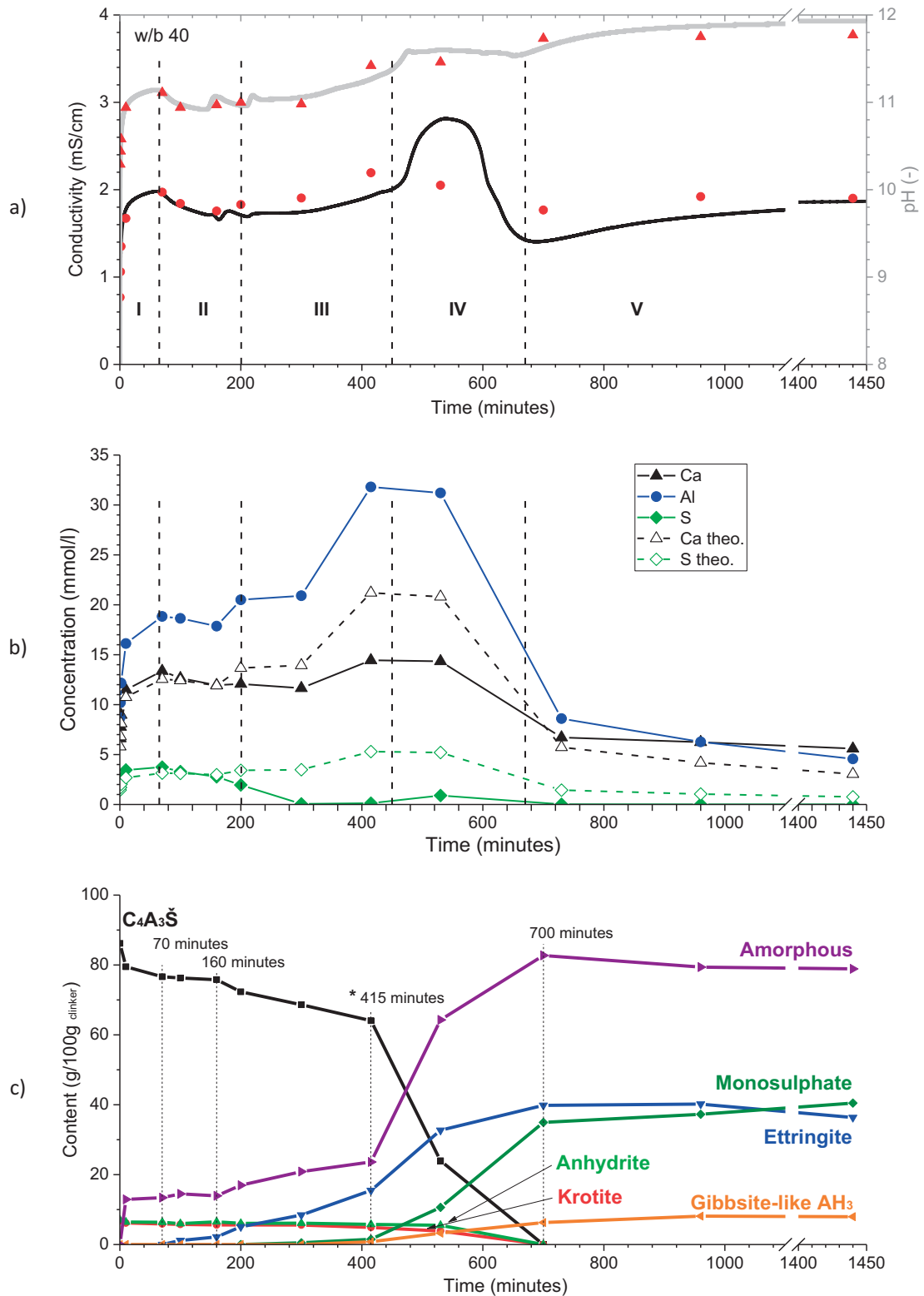


Figure 5.3-1 a) Conductivity [●] and pH [▲] measurements including the spot experiments at 23 °C for w/b 40 for the hydrated residues; b) evolution of solution composition (spot samples), including the calculated Ca and S concentrations (dashed lines) derived from the Al concentration and c) normalized phase assemblage of the spot samples determined by QXRD and TGA analyses

The five defined hydration stages can be summarized as follows:

Stage I: Initial period

Ye'elimite dissolves rapidly during the first seconds to minutes after contact with water. This is followed by the fast slowdown of the kinetics. No crystalline phases were detected by XRD but an amorphous phase was formed. HR-SEM micrographs (see section 5.4.1) reveal that the initial hydration products are precipitating onto the anhydrous grains (as a "layer") and that needle-like ettringite is embedded in this phase. The reached degree of hydration (DoH) is approximately 11%. Neither the hard burnt anhydrite nor krotite had reacted to a measureable extent. The slowdown of the ye'elimite dissolution occurred within seconds and before the formation of the layer. Contrary, the increase of the solution concentrations coincides with the slowdown.

Stage II: Induction or Dormant period

During this period, the content of ye'elimite remains almost unchanged, while ettringite continues to form slowly. The length of this period seems to be controlled by the nucleation and growth rate of ettringite. This causes the continuous consumption of sulphate ions from solution. Again, neither the hard burnt anhydrite nor krotite had reacted to a measureable extent. The sulphate concentration drops fast between 160 to 200 minutes. The reached DoH is about 12% after 160 minutes and 16% after 200 minutes, marking the end of the dormant and the onset of the acceleration period.

Stage III: Acceleration period

The beginning of the acceleration period is revealed by several aspects. The sulphate ion concentration starts to fall, whereas the pH increases, causing the acceleration of the ye'elimite dissolution. At the same time the formation of monosulphate and gibbsite-like aluminium hydroxide start to form. Additionally, the dissolution of ye'elimite as well as the formation of the hydrates continuously accelerates. The reached DoH is about 26% at the end of this period, which is around 415 minutes. Both, the hard burnt anhydrite and krotite starts to react. The depletion of sulphate ions corresponds to the increasing pH values due to the increasing hydroxyl ion concentrations. The increasing pH may contribute to the acceleration of the dissolution and precipitation kinetics.

Stage IV: Main hydration period

The main hydration period is marked by the rapid dissolution of ye'elimite and the formation of monosulphate, ettringite and the X-ray amorphous phase. A DoH of about 70% is reached at the conductivity peak maximum. The near complete depletion of all clinker phases, i.e. DoH 100%, was reached at the point at which the conductivity drops to its minimum. Sulphate is not detected in solution, except at 530 minutes, even when ye'elimite and the hard burnt anhydrite dissolved. This indicates that the formation of monosulphate and ettringite proceed at a similar rate as the anhydrous dissolution.

Stage V: Final period

During this period, monosulphate and gibbsite-like aluminium hydroxide continues to form, where the content of ettringite and the amorphous phases decreases. This indicates that the recrystallization and transformation of metastable hydrates occurs.

## 5.4 Discussion of results

### 5.4.1 Initial and dormant period – Why does the dissolution slow down

Figure 5.4-1a shows the evolution of the conductivity during the first five minutes of the hydration of Y at w/b ratios from 40 to 1000. We assumed that pure dissolution occurs at a high water to binder ratio such as 1000 and that the increase of the conductivity is proportional to the ion concentration in solution. If correct, the dissolution of Y should provide a linear increase of the conductivity. However, a linear increase was only observed for very short periods from 15 to 140 seconds for w/b 40 and 1000, respectively. This indicates that the period of pure dissolution is as short as about 15 seconds in the case of Y at w/b 40. We further tried to assess whether or not this was really a period of pure dissolution. For that we back-calculated the theoretical slopes based on the determined value at w/b 1000. The results of these calculations are shown in Figure 5.4-1b. The measured and calculated values start to deviate already from w/b 800, indicating that pure dissolution never occurred under the given conditions at lower w/b. The deviation was even more pronounced at lower w/b ratios. This brings us to the following question. What causes the slowdown in the dissolution: hindered dissolution or precipitation? To assess the nature of the hydration reactions, we have chosen the w/b ratios of 40 and 100 for two main reasons:

- 1) The w/b ratio of 40 presents the bridge to the experiments carried out in pastes.
- 2) At w/b 100 the hydration sequences are similar to those observed at w/b 40, where the length of the period of the almost linear increase is extended to about 30 seconds. Moreover, we can investigate the impact of the w/b ratio on the ye'elimite hydration.

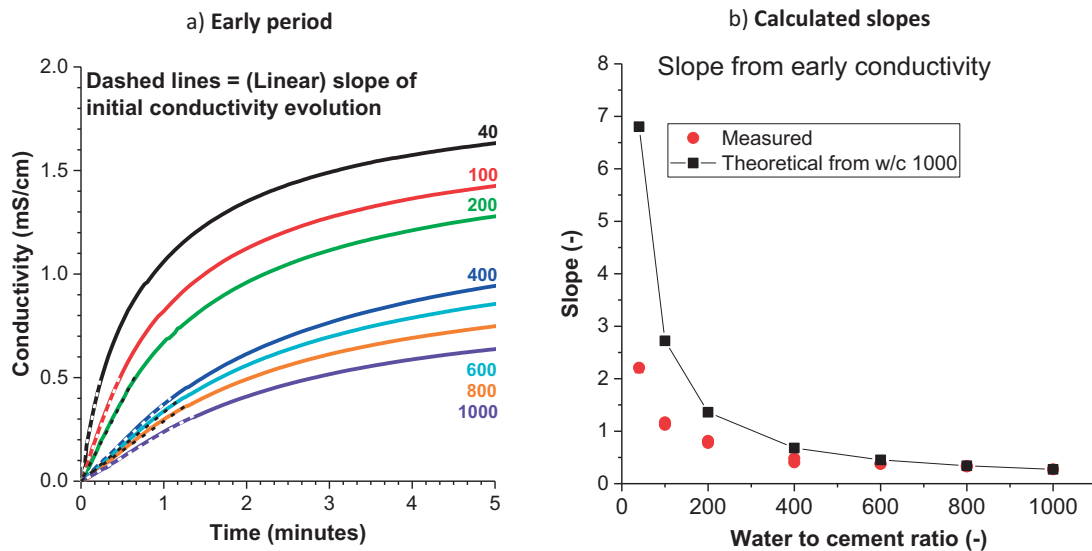


Figure 5.4-1 Conductivity evolution of neat Y during the first 2 minutes of hydration (a) and theoretical and measured (double determination) slope of the dissolution rate using w/b 1000 as reference point (b)

The comparison of the tests done at w/b 40 and 100 are shown in Figure 5.4-2. The results demonstrate that the hydration follows the same reaction sequences, only with different kinetics. Therefore, we assume that results obtained at w/b 40 can be supplemented with the samples obtained at w/b 100.

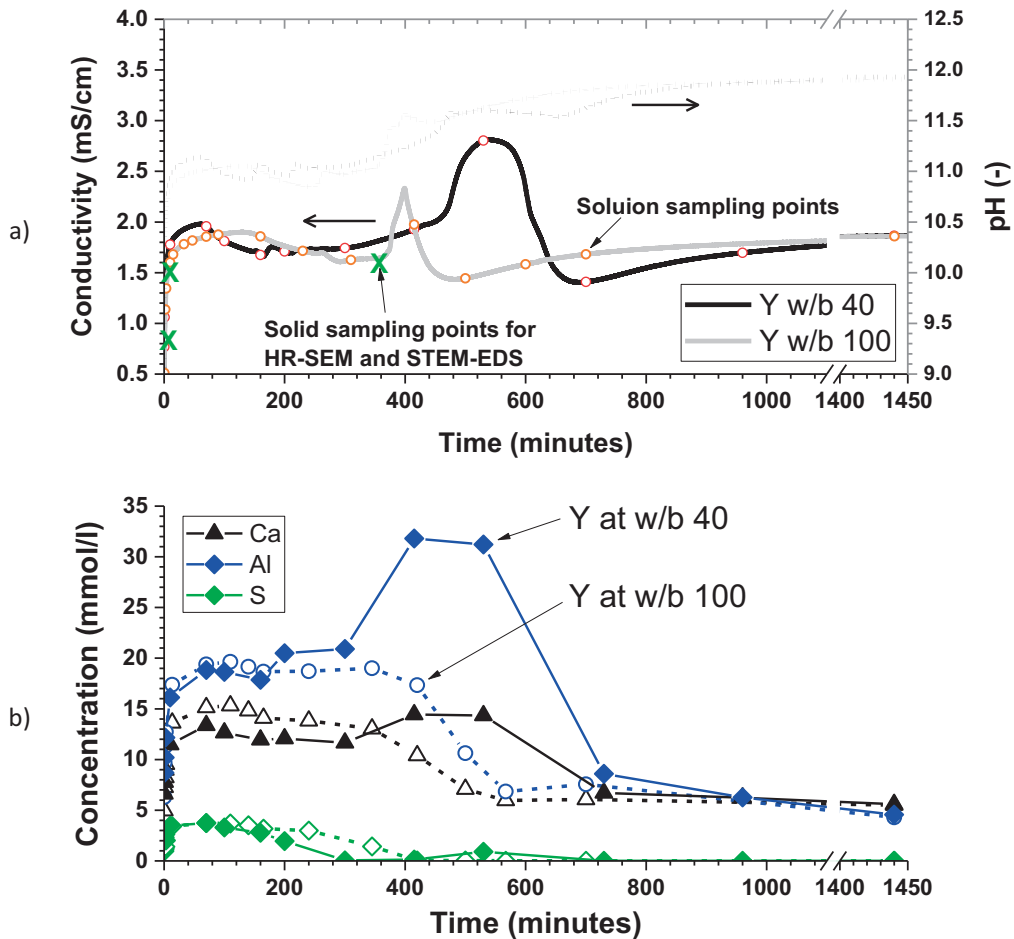


Figure 5.4-2 Comparison of the steady evolution of the conductivity, pH (a) and the concentrations measured on spot samples (b) of Y at w/b 40 (solid line & filled symbols) and 100 (dashed line & empty symbols); "X" represents the sampling points for HR-SEM and STEM-EDS analyses

Figure 5.4-3 (logarithmic scale) presents the evolution of the conductivity and of the element concentrations in solution highlighting the initial and dormant period. The solution composition and the conductivity follow a similar trend during these periods. The solution concentration increases fast until 10 minutes of hydration and afterwards much slower. At the same time the dissolution of ye'elinite slows down or even stops (as shown in Figure 5.3-1), indicating that the reached concentrations affect its dissolution. We calculated the theoretical concentrations of *Ca* and *S* from the measured *Al* concentration from the measured *Al* concentration by mass balance, i.e. according to the composition ye'elinite. The calculated ratios of *Al*, *S* and *Ca* in solution are almost identical to the ratios in ye'elinite up to approximately 70 minutes of hydration. This indicates that either only congruent dissolution occurs or that a phase is precipitating with a composition close to that of the dissolving ye'elinite. The hydration reaction seems to be changed from 70 to 200 minutes as the measured and calculated concentration does not match anymore. Additionally, the conductivity decreases, indicating the precipitation of hydrates.

Hydration reactions of synthetic ye'elimité

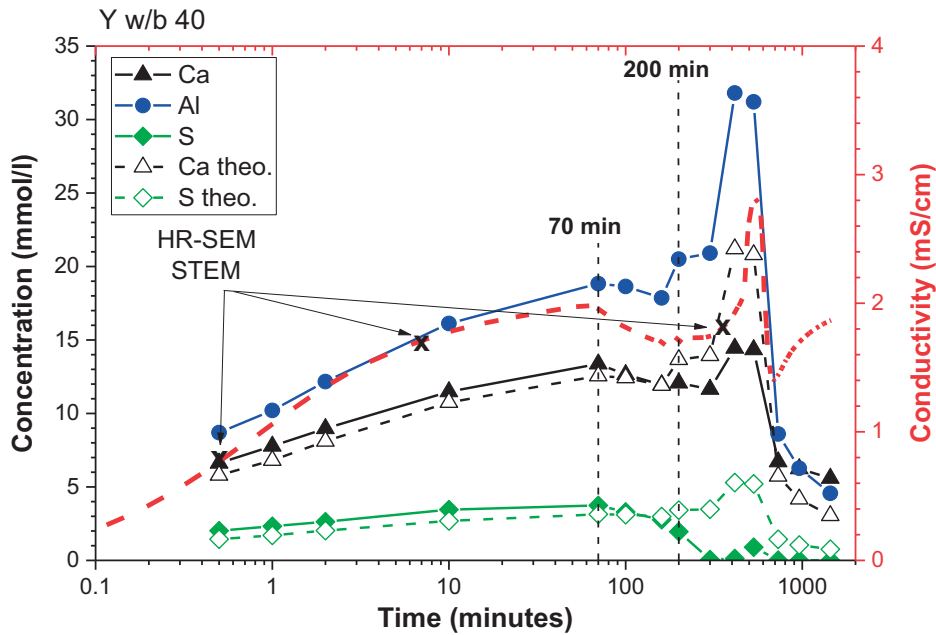


Figure 5.4-3 Evolution of the conductivity (continuous measurement) and concentration (spot samples), including the calculated Ca and S concentrations (dashed lines) derived from the Al concentration by mass balance calculations

We used the thermodynamic modelling, based on the measured solution concentrations, to calculate the saturation indices with respect to the different phases. The results are presented in Figure 5.4-4. Ettringite, all three aluminium hydroxide types and  $CAH_{10}$  are instantly oversaturated. They stay oversaturated throughout the entire experiment except the amorphous aluminium hydroxide type, which becomes undersaturated after passing the main conductivity peak. Monosulphate was initially undersaturated and becomes oversaturated only after 10 minutes. Moreover, we see a clear shift of the chemical equilibria after sulphate ions got depleted from solution. At this point the aluminium ion concentration increases, the saturation indices of ettringite decreases, whereas that of monosulphate and sulphate-free calcium aluminates rises. A new equilibrium between monosulphate and ettringite is established, which in turn seems to control the aluminium ion concentration. Gypsum was undersaturated throughout the entire experiment.

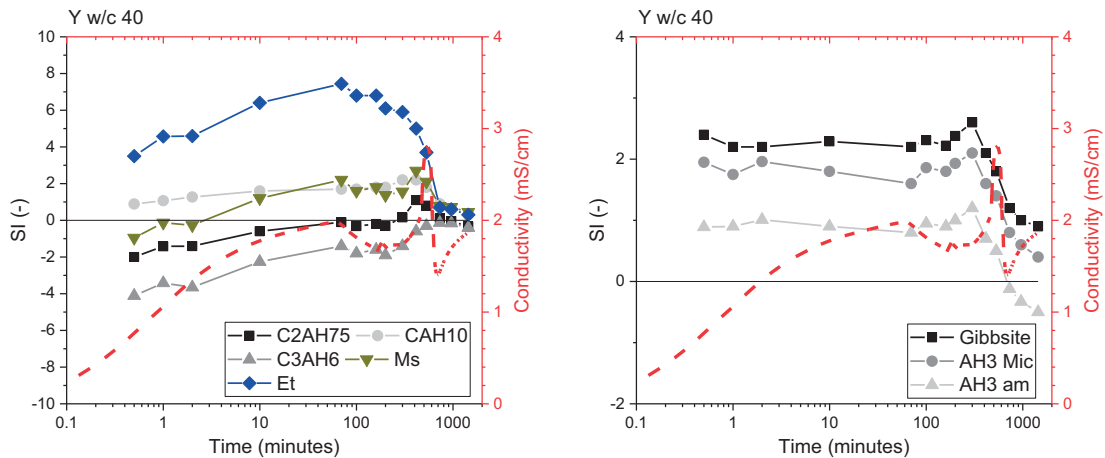


Figure 5.4-4 Calculated saturation indices from the respective solution concentrations measured for the spot samples; the following values were used in the calculations AH3 Gibbsite with  $\log K_{S0} = -1.12$ , AH3 Mic with  $\log K_{S0} = -0.67$  both from [115] and AH3 am with  $\log K_{S0} = 0.24$  [116]; Ms = monosulphate and Et = ettringite

Contrary to the predictions from thermodynamic modelling, no crystalline detectable hydrates were detected during the initial hydration period as shown in Figure 5.3-1 (c). Instead an X-ray amorphous phase was formed. We used HR-SEM and STEM-EDS to assess the type and composition of the initially formed hydrates for Y hydrated at w/b of 100. The higher w/b was chosen to slow down enough the hydration but stay as close as possible to the w/b of 40. Moreover, we took the samples during the same hydration periods as present at w/b 40.

The morphological characterisation results are shown in Figure 5.4-5. As early as 30 seconds of hydration an instant precipitation of globules-like hydrates on the surface of the anhydrous particles was observed. This indicates that the released ions were not able to diffuse fast enough away from the dissolving ye'elimite particles. This is related to the fact, that the concentrations increased to fast and supersaturation of several hydrates such as amorphous aluminium hydroxide or ettringite was instantly reached. In addition we note that the hydration proceeded faster along grain boundaries. After 420 seconds of hydration almost all anhydrous particles were covered with a "layer" of hydrates, which appears to be composed of several phase including ettringite. The thickness of the layer varied between 20 and 50 nm.

The remaining parts from the covered anhydrous particles were partly empty, indicating a continuous dissolution of ye'elimite. The layer of hydrates fills the space which was originally occupied by the anhydrous phases. Upon hydration a gap was formed between the layer and the anhydrous grain. This space was only marginally filled by hydrates. The presence of such "hollow layers" was firstly described by Hadley [222]. Similar features were observed for hydrating CSA [223] and OPC-CSA mixtures [86]. Once again, this indicates that the layer does not inhibit the further dissolution of ye'elimite.

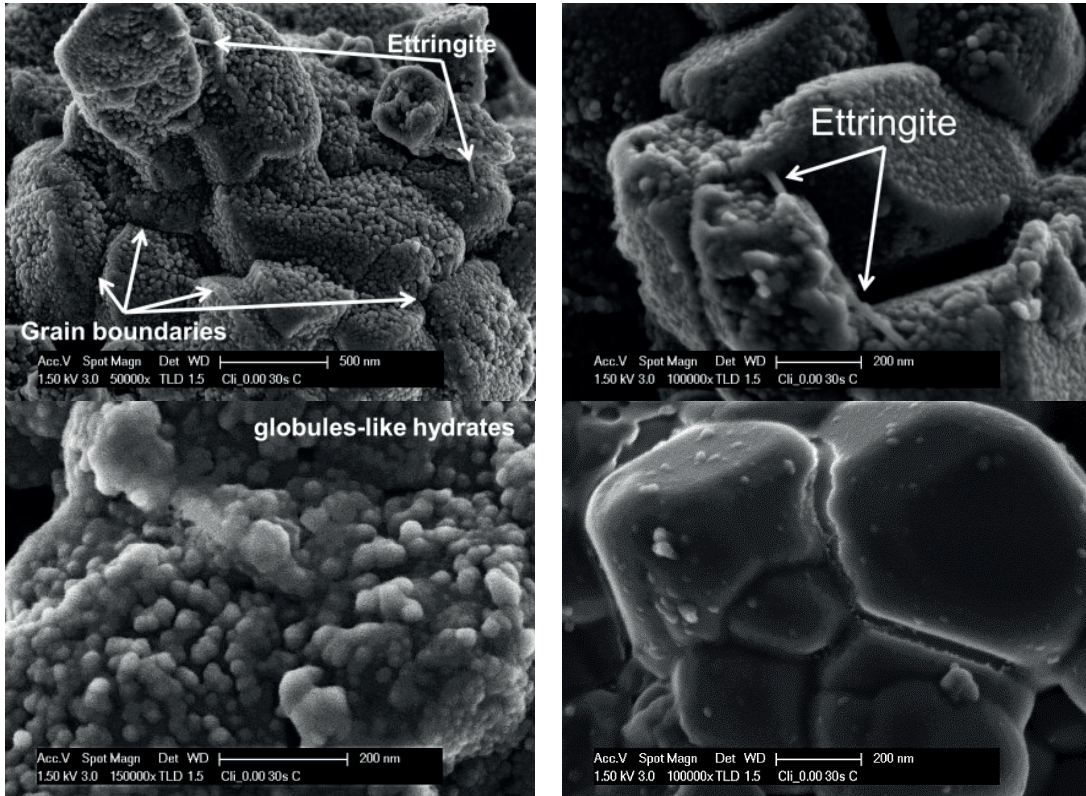
The results demonstrate that at no point of our experiments pure dissolution occurred (even at w/b of 100), which is consistent to findings shown in Figure 5.4-1. Hence, the well matching evolution of the measured and calculated Ca and S concentrations up to about 160 minutes of hydration, indicates that the X-ray amorphous phase should have a bulk chemical composition close to that of the dissolving ye'elimite. To determine whether this is the case, the analyses were supplemented with STEM-EDS analyses.

Additionally, the correlation between the rapid dissolution of an aluminium-rich anhydrous phase, the rapid increase of the solution concentrations and ultimately, in the instant formation of a layer or shell of hydrates was reported for sulphate-free calcium aluminates such as mayenite. For example, Raab [95] and You et al. [83] carried out experiments on crystalline, poorly crystalline and even amorphous mayenite. The hydration of poorly crystalline or amorphous mayenite proceeds by far faster compared to crystalline one. The rapid increase of the solution concentration caused the formation of dense layers of hydrates covering the anhydrous particles. On the contrary, the slower hydration crystalline mayenite resulted in the formation of well grown hydrates and particle surfaces which remains accessible. You et al. [83] even differentiated a dense inner layer of a gelatinous phase and a porous outer layer composed of a mixture of metastable  $C_2AH_8$  and  $AH_3$ .



Hydration reactions of synthetic ye'elimité

Y at 23 °C and w/b 100 after 30 seconds of hydration



Y at 23 °C and w/b 100 after 420 seconds of hydration

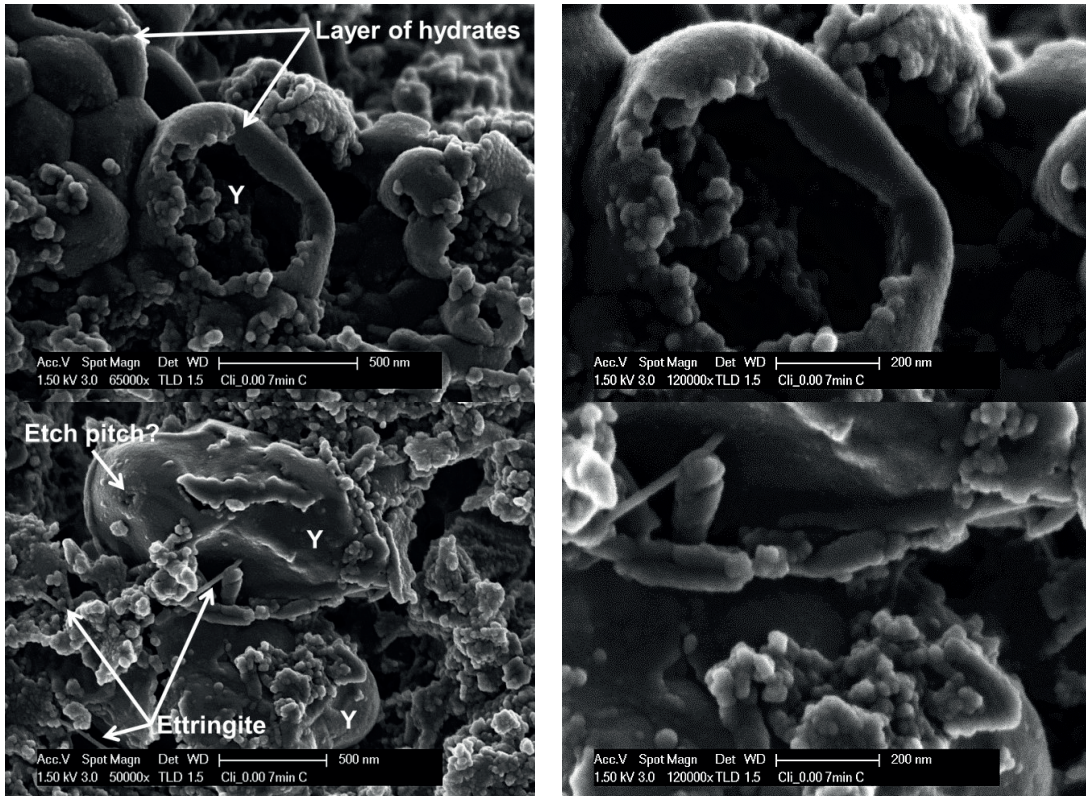


Figure 5.4-5 Morphological characterization of the hydrated ye'elimité at 23 °C and a w/b ratio of 100



As for the HR-SEM analyses, the layer of hydrates was observed after 420 seconds. The structure and composition of the hydrates, determined by STEM-EDS, are shown in Figure 5.4-6 and Table 5.4-1. The composition of the hydrates layer is close to that of ye'elimite, which supports the findings of the solution analyses and highlights their accuracy. The present porous structure of the hydrates is most likely a result from the unavoidable beam damaging and dehydration throughout the sample preparation and analyses.

Besides the hydrates layer, we noticed a foil-like calcium aluminate hydrate (probably  $CAH_{10}$ ) that is formed in the available space. The foil-like hydrates have an atomic  $Ca / Al$  ratio close to that of  $CAH_{10}$  ( $Ca / Al = 0.50$ ). The determined lower  $Ca / Al$  ratio of about 0.34 indicates that the foil-like calcium aluminate hydrate is either intermixed with aluminium hydroxide or its composition would be close to  $CA_{1.6}H_x$ , where the value of  $x$  remains unknown. Similar compositions of the foil-like hydrates were determined in other samples and different ages (see Table 5.4-2 in Chapter 5, Table 7.3-1 in Chapter 7 and annex – part V). Thus we assume that the composition is representative.

The sum of all results presented so far, indicates that the early hydration period follows the reaction according to Equation 2, e.g. neat ye'elimite reacts with water to form ettringite,  $CAH_{10}$  and amorphous aluminium hydroxide (see Chapter 2). It seems that the formation of this metastable phase assemblage is favoured by the rapid dissolution of ye'elimite and the corresponding increasing solution concentrations. The fast increase of the solution concentrations, especially of aluminium, favours the precipitation of amorphous rather than crystalline aluminium hydroxide [122] [224]. This effect may be enhanced by the presence of sulphate ions which are known to cause its faster nucleation but impeding its crystallisation [225] [226]. The amorphous type has higher solubility product relative to gibbsite-like type and is in equilibrium with the solution at higher aluminium ion concentration. This in turn enables and favours the formation of ettringite and  $CAH_{10}$  [121].

Table 5.4-1 Atomic ratios of the hydrated areas determined by STEM-EDS

Sample	In layer-like hydrates		Number of measured areas
	$Ca / Al$ [–]	$S / Al$ [–]	
<b>Anhydrous Y</b>	<b>0.65</b>	<b>0.16</b>	
100% Y after 420 seconds	0.65	0.13	18
	In foil-like hydrates		
100% Y after 420 seconds	0.34	0.07	1

Furthermore, the continuous formation of ettringite, e.g. such as observed during the dormant period, typically depends on the presence of additional calcium sulphate, which is not present in our case. It is possible that the hard-burnt anhydrite, sometimes referred to dead burnt or insoluble anhydrite, present as minor phase in the Y clinker enables the formation of ettringite. However, our analyses indicate that anhydrite did not react at that time and the presence of  $CAH_{10}$  further strengthens our assumption that the hydration follows the reaction stated above. The impact of hard burnt anhydrite was also tested initially. For that, we produced hard burnt anhydrite by tempering gypsum for two hours at 1100°C. Blends of ye'elimite with this anhydrite were tested by calorimetry. The results confirmed that had burnt anhydrite did not alter the early hydration reactions of ye'elimite. In addition, the dissolution rate to that of gypsum, middle (G 2 hours at 700 °C) and hard burnt anhydrite were compared in suspension. Hard burnt anhydrite dissolves very slowly compared to the two other materials (see Figure 8.8-56, Figure 8.8-61 and Figure 8.8-62; annex - part V).

Hydration reactions of synthetic ye'elinite

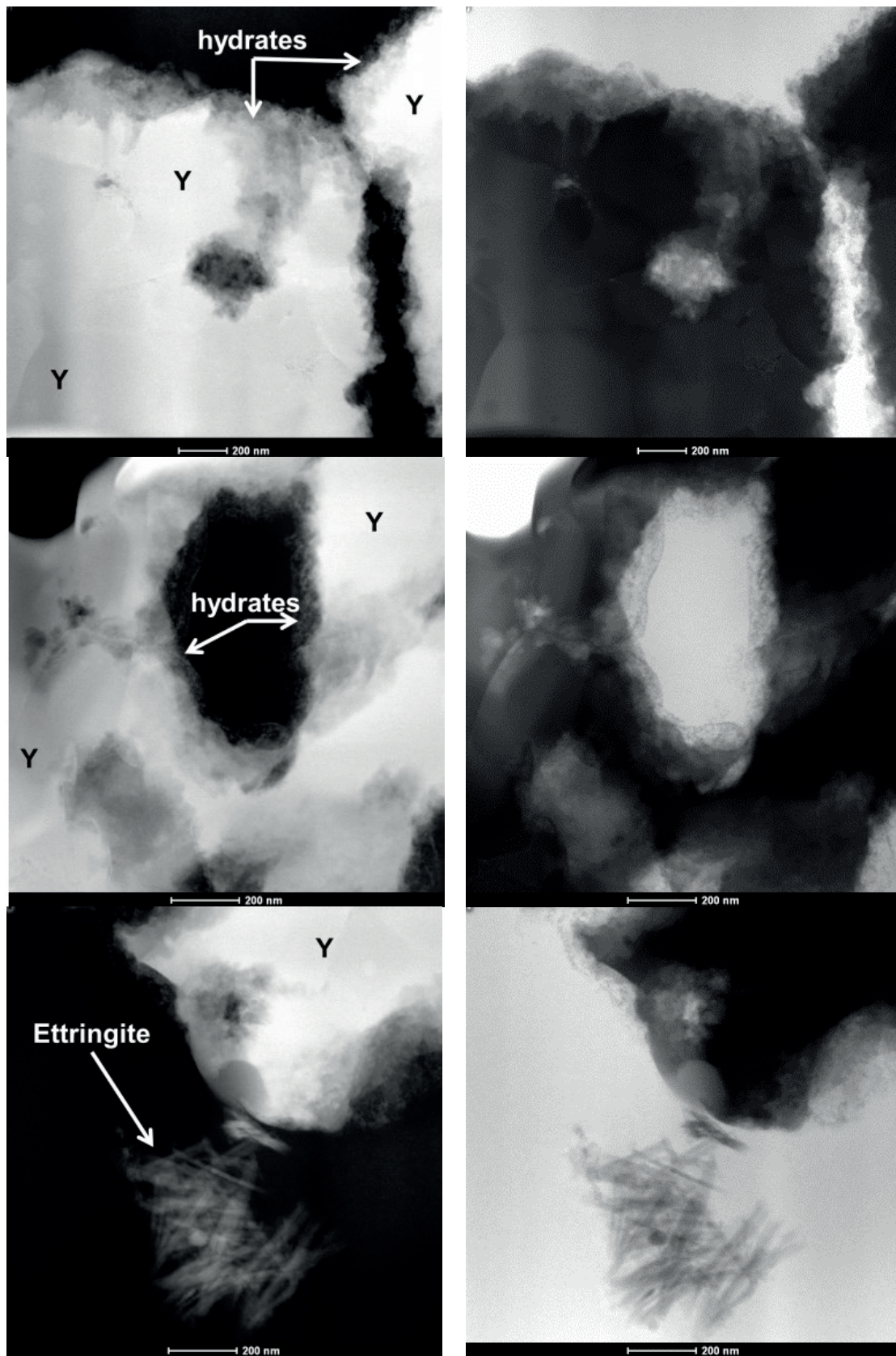


Figure 5.4-6 STEM images (up: HAADF image and down: BF image) of ye'elinite after 7 minutes of hydration at 23 °C and a w/b ratio of 100; Y = anhydrous ye'elinite particles

Throughout the initial stage only amorphous phases were detected by XRD, which may be partly related to the solvent exchange procedure. Traces of ettringite were firstly detected by XRD after 70 minutes and continue to form throughout the dormant period. Thermal analyses were made to supplement the XRD measurements and to potentially determine qualitatively which hydrates were formed. The results are shown in Figure 5.4-7. The first two samples collected after 10 and 70 minutes of hydration, revealed a weight loss from approximately 60 °C up to 250 °C. The phases known to decompose within this temperature range are  $CAH_{10}$  [117] [227], amorphous aluminium hydroxide [224] [228] and ettringite. From about 160 minutes on a right-hand shoulder peak, ranging from about 140 to 300 °C, starts to form and becomes relatively strong at 200 minutes. This peak seems to originate from the dehydration of monosulphate [229], which would indicate the onset of a new hydration period.

A detailed overview about various thermogravimetric analyses of typical solids formed in cementitious materials can be found in the book of Scrivener et al. [230].

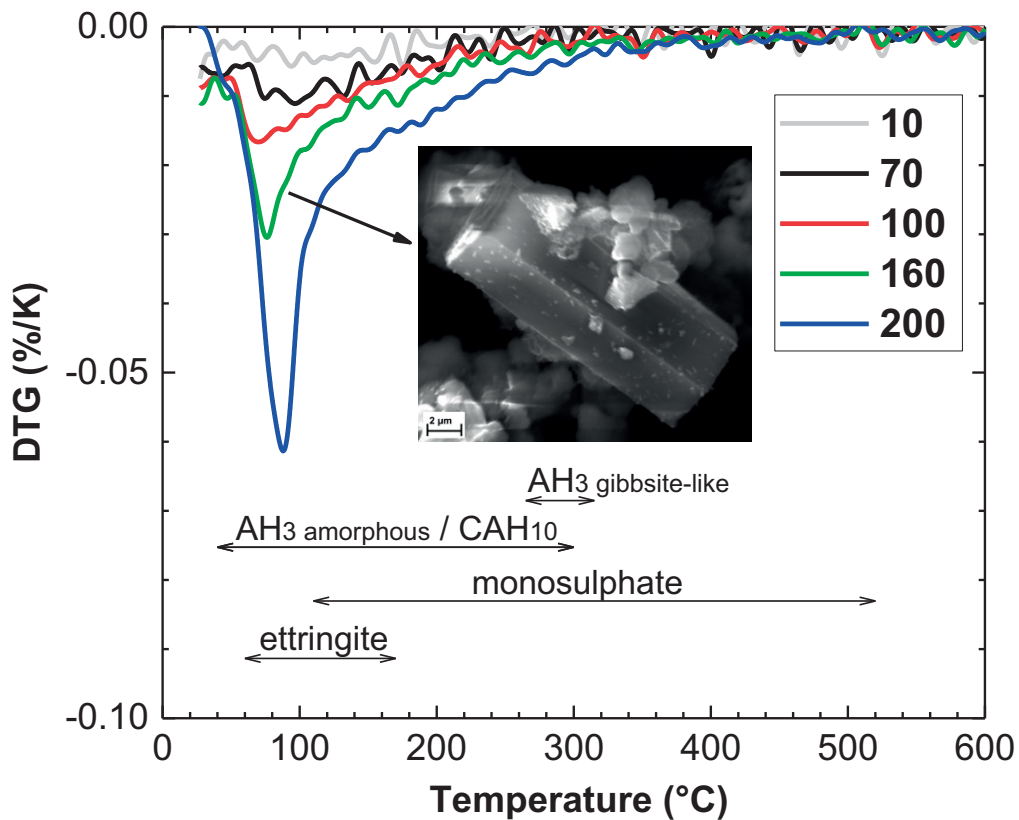


Figure 5.4-7 Differential thermogravimetric analyses of samples hydrated at 23 °C and a w/b of 40 for samples collected after 10 to 200 minutes of hydration including a SEM micrograph showing a idiomorphic prismatic ettringite crystal detected after 160 minutes

#### 5.4.2 Acceleration and main period – Why does the dissolution reaccelerates

The acceleration period starts between 160 to 200 minutes. It is marked by the restarting ye'elimite dissolution, the almost linear drop of the sulphate ion concentrations, the increase of the conductivity and the pH. The calculated and measured concentrations start to deviate profoundly. This indicates that the precipitation of one or more phases occur, which have a bulk chemical composition different to that of ye'elimite. Most likely, this relates partly to onset of the monosulphate and gibbsite-like aluminium hydroxide formation according to Equation 1.

The increase of the pH coincides with the decreasing sulphate concentration and is caused by the increase in hydroxyl ion concentrations. At the same period of time, the consecutive rapid ye'elimite dissolution and monosulphate formation is initiated. Thus we assume that the rising pH favours both reactions. A similar accelerating effect of the pH on the hydration of ye'elimite and CSA was already shown for the addition of *KOH* [130] or *NaOH* [231].

The STEM-EDS analyses of the hydrates formed during the acceleration period are shown in Figure 5.4-6 and Table 5.4-2. The layer of hydrates and the foil-like  $CAH_{10}$  and ettringite were still present after 6 hours. In addition, well crystallized monosulphate was formed. Ettringite, monosulphate and the foil-like  $CAH_{10}$  were mainly formed in the available space. The sum of all results indicates that the onset of the acceleration period is triggered by the drop of the sulphate concentration and potentially by the rising pH. A higher pH may have further promoted the formation and stability of monosulphate rather than of ettringite.

**Table 5.4-2 Atomic ratios of the hydrated areas determined by STEM-EDS**

Sample	In layer-like hydrates		Number of measured areas
	$Ca / Al [-]$	$S / Al [-]$	
<b>Anhydrous Y</b>	<b>0.65</b>	<b>0.16</b>	
100% Y 6 hours	0.60	0.15	14
	In foil-like hydrates		
100% Y 6 hours	0.31	0.07	5



Hydration reactions of synthetic ye'elinite



Figure 5.4-8 STEM images (up: HAADF image and down: BF image) of Y after 6 hours of hydration at 23 °C and a w/b ratio of 100; dotted red line indicates the surface of the anhydrous; Y = anhydrous ye'elinite particles

The formation of monosulphate, beside ettringite, accelerates measurably after 415 minutes of hydration by both XRD (Figure 5.3-1c) and TG analyses (Figure 5.4-9). In addition, gibbsite-like  $AH_3$  was first time clearly detected by XRD and TGA (from its characteristic weight loss at 290 °C). After about 415 minutes of hydration, ye'elimite starts to dissolve rapidly.

This represents the **onset of the main hydration period**. High ettringite, monosulphate and amorphous phase contents were formed, reaching a maximum at 700 minutes of hydration. At the same time the near complete depletion of all clinker phases occurs, marking the end of the main hydration period.

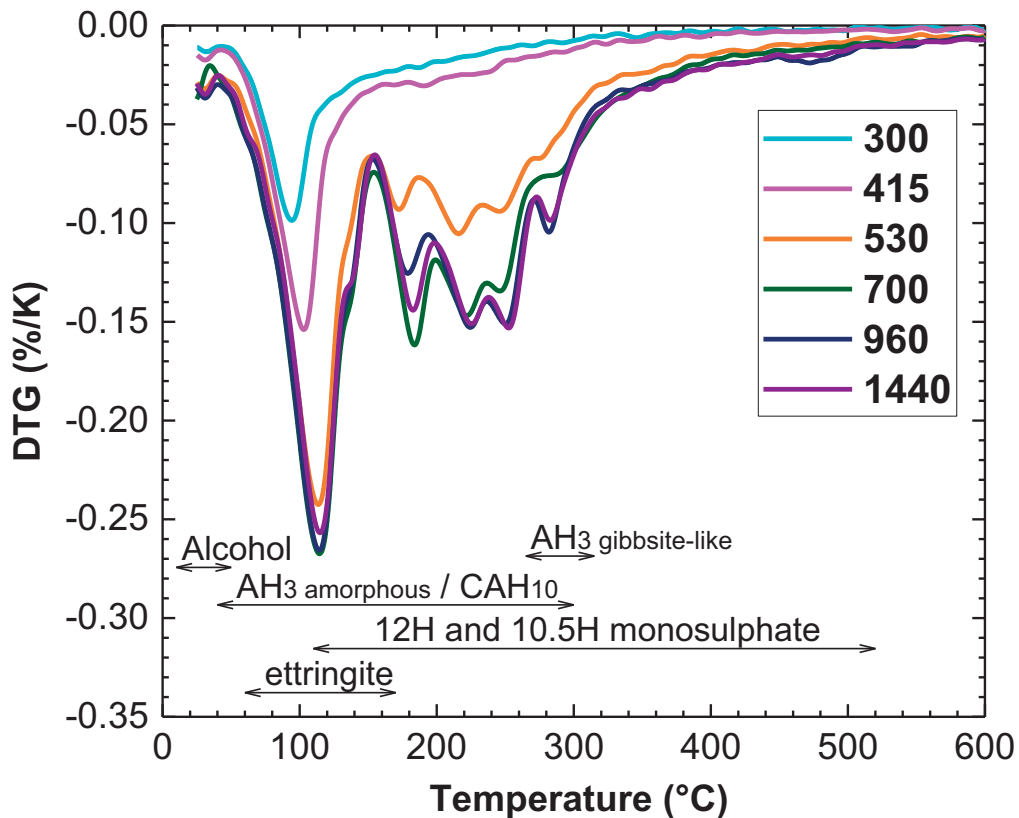


Figure 5.4-9 Differential thermogravimetric analyses of samples hydrated at 23 °C and a w/b of 40 for samples collected after 300 to 1440 minutes of hydration, covering the acceleration, main and final hydration period

### 5.4.3 Final period

During the final period, a transformation and redistribution of hydrates is observed. The quantity of monosulphate and gibbsite-like aluminium hydroxide continues to rise, while the ettringite and amorphous content decreases. Also the ionic concentration of the solution drops as a result of the depletion of all anhydrous phases and continues nucleation and growth of hydrates. The saturation indices of all hydrates are close to zero except for the amorphous aluminium hydroxide, which becomes undersaturated. This indicates that the dissolution of this phase may occur, whereas the growth, the recrystallization and potentially transformation of other formed hydrates continues. The pH continues to increase slowly which is caused by the increase of hydroxyl ion and decrease of aluminium concentrations.

#### 5.4.4 Effect of w/b on the hydration kinetics in paste

So far, we were able to explain the general ye'elimite hydration pattern in suspension (dynamic experimental conditions), but the question that remains is if this knowledge can be applied to the paste samples (static experimental conditions). The experiments in suspension are primarily providing information about the development of the conductivity and pH, the ionic strength, of the solution. On the contrary, the experiments in paste are based on isothermal conduction calorimetry, providing qualitative information (non-specific measurements as it does not differentiate between the types of reaction) about the heat released from the dissolution and precipitation reactions.

A special approach was used in order to evaluate the comparability of both experimental set-ups and to assess the effect of the w/b ratio on the hydration kinetics. Ye'elimite was gradually replaced by ground inert quartz filler (Qz) to increase the w/b but maintaining maximum water to solid (w/s) ratio of 2. One additional set of samples without quartz filler was prepared for w/b ratios from 0.5 to 10 to check for the filler effect [232]. The composition of the formed phase assemblages is available in the annex part V, Figure 8.8-10 to Figure 8.8-20.

Figure 5.4-10 compares the heat evolution for the calorimetry of the Y-Qz paste sample at w/b 40 to the conductivity recorded for suspensions at the same w/b. Both measurements show a similar sequence of effects, but at different rates. Most likely, the continuous stirring of the suspensions caused the acceleration of hydration. Due to the similar curve profiles, e.g. similar sequence of events, we concluded that the hydration mechanisms for both systems are similar.

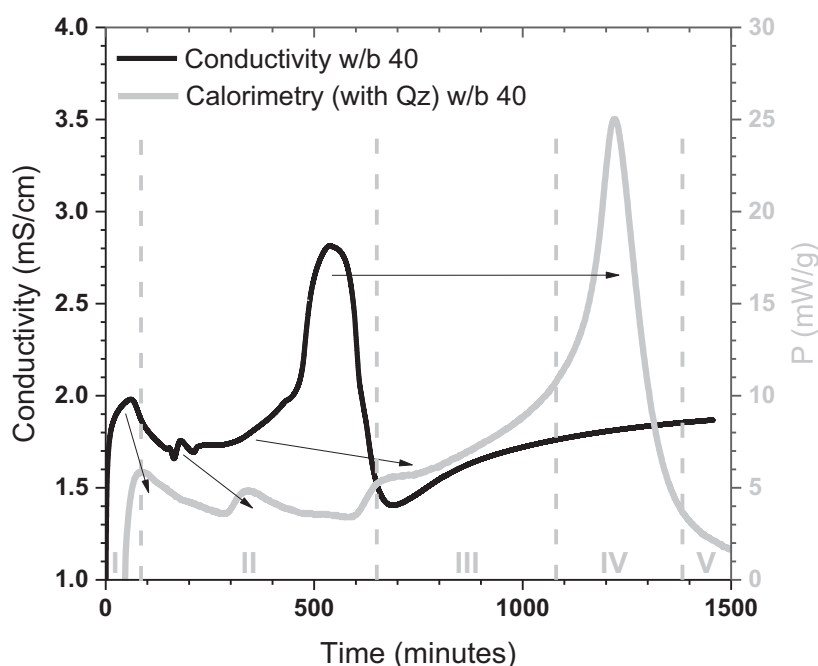


Figure 5.4-10 Comparison of Y hydrated at w/b 40 as paste and as suspension; peak I and peak II are explained below

Figure 5.4-11 presents calorimetry results for selected w/b ratios. The hydration kinetics were slightly decelerated for w/b ratio 1. The addition of quartz resulted in the acceleration towards the original value, due to the filler effect. Higher w/b ratios generally accelerate the hydration, particularly in the presence of the quartz filler. Additionally, a broad (left hand) shoulder peak (labelled "Acceleration period" in Figure 5.4-11 (b)) was noticed in the samples prepared with high w/b ratios.

The general shape of the curves for Y with Qz at high w/b, is similar to that of binders composed of ye'elimite "Y" and calcium sulphate "CS" with a molar CS / Y ratio below 2 [130]. In such case, the main heat release peak (e.g. labelled "Main hydration peak" in Figure 5.4-11 (b)) coincides to the point of the sulphate depletion. This marks the onset of the rapid ye'elimite dissolution and formation of primarily monosulphate together with some ettringite. Consistent to our findings in suspensions, the hydration reaction seems to change from the formation of primarily ettringite to monosulphate as main sulphate-bearing hydrate.

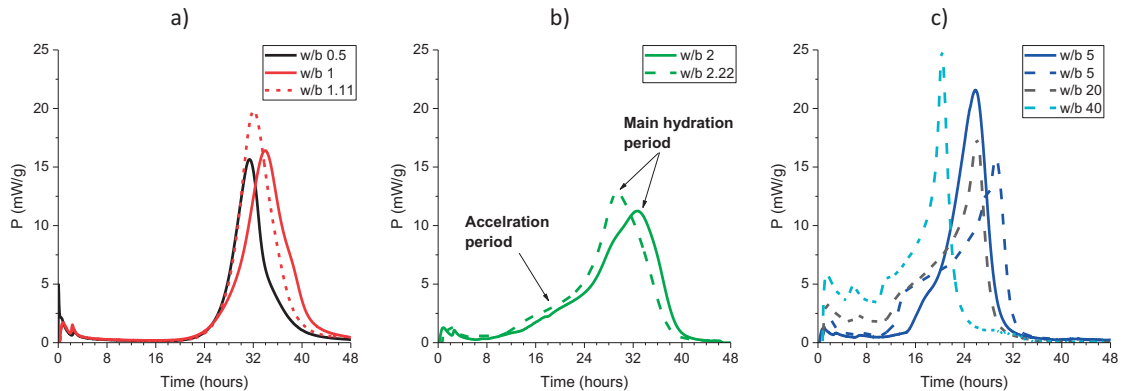


Figure 5.4-11 Rate of heat evolution of Y with and without quartz at several w/b ratios; the solid line depicts the neat clinker while the dashed line represents blends with quartz

Figure 5.4-12 gives the calorimetry results of Y at w/b of 1, of Y with quartz (Y+Qz) at w/b of 5 and an idealized schematic representation of the hydration reactions determined in suspension.

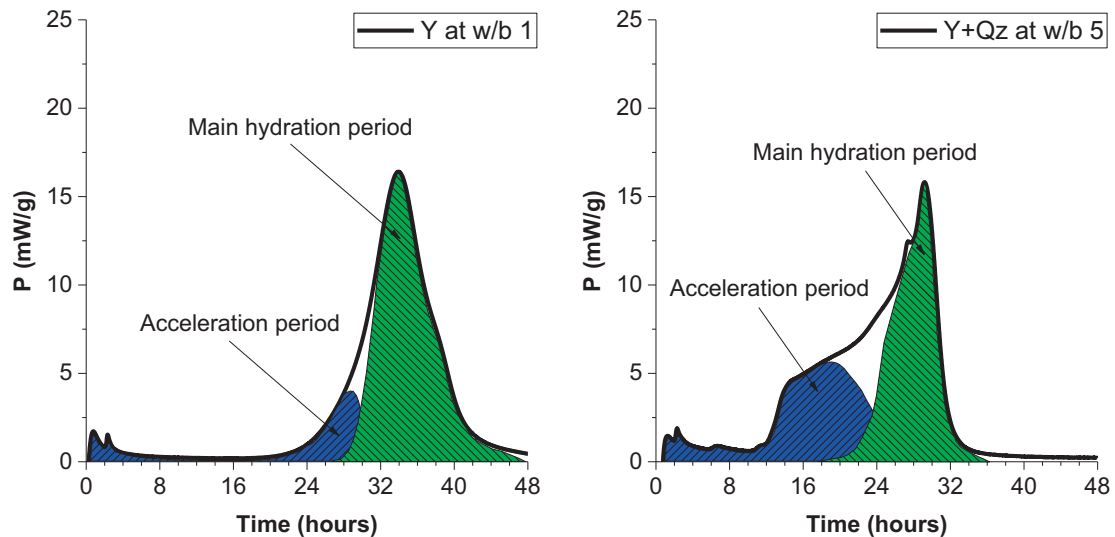


Figure 5.4-12 Simplified schematic representation for the rate of heat evolution for Y with and without quartz for the underlying reactions; blue = primarily the formation of ettringite, CAH<sub>10</sub> and amorphous aluminium hydroxide; green = primarily the formation of monosulphate and gibbsite-like aluminium hydroxide

The water to binder and water to solid ratio proves a strong impact on the hydration kinetics and on the formed type of hydrates. Increasing both ratios strongly promote the formation of ettringite together with amorphous aluminium hydroxide and CAH<sub>10</sub> rather than monosulphate and gibbsite-like aluminium hydroxide. This may partly relate to the availability of nucleation sites. As a result, the dormant period is shortened by the faster depletion of sulphate ions from solution.



We actually assume that the rapid dissolution of ye'elimite and in consequence the increase of the solution concentrations, especially of aluminium, caused the formation of the amorphous phase. This was potentially further promoted by increasing the water to binder ratio. A similar phenomenon was already reported for the hydration of krotite [233]. The rapid hydration of krotite result in the formation of a metastable amorphous phase (gel) which slowly crystallizes with time to poorly crystalline  $CAH_{10}$ . This phase further slowly converts to katoite and gibbsite and / or bayerite. The transformation rate of the intermediate metastable phases accelerates by increasing the applied water to solid ratio [74]. Overall, the hydration kinetics of neat ye'elimite and even some of the hydration products is reminiscent to that of krotite ( $CA$ ), despite the presence and impact of sulphate.

Additionally, an endothermic reaction was sometimes measured during the first hour of hydration as shown in Figure 5.4-13. The intensity of the endothermic peak correlates well with the increased w/b ratio used and to the replacement level of binder by quartz. Based on the results presented before, we actually assume that the peak originates from the precipitation of the amorphous phase such as the aluminium hydroxide. However, it should be noted that those results are obtained, by normalizing the measured heat release to the amount of anhydrous binder. Quartz, used to replace ye'elimite and to maintain a constant w/s ratio of 2, presents the largest quantity of the investigated paste. The measured heat was therefore very low (close to the detection limit) at e.g. high w/b ratios such as 20 or 40. The normalization to per gram of anhydrous ye'elimite will therefore multiply any analytical contribution or error such as the baseline drift or even small temperature differences between the sample and the device.

It is further important to remind the reader that all materials had the same temperature as the calorimeter. For example, the signal would be also endothermic in the case that the temperature of the materials would be lower than that of the calorimeter. However, such an artefact would cause only a linear increase of the signal, which was not observed in our case. The signal starts at zero followed by the decrease and recovery. This clearly indicates an ongoing chemical reaction.

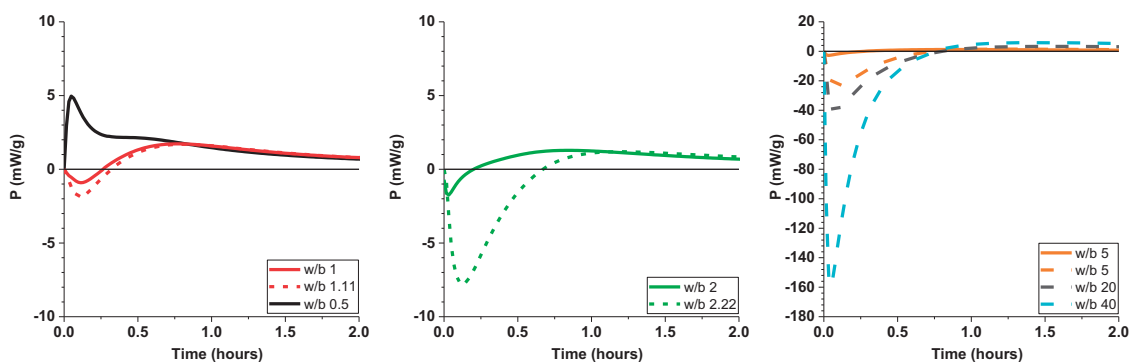
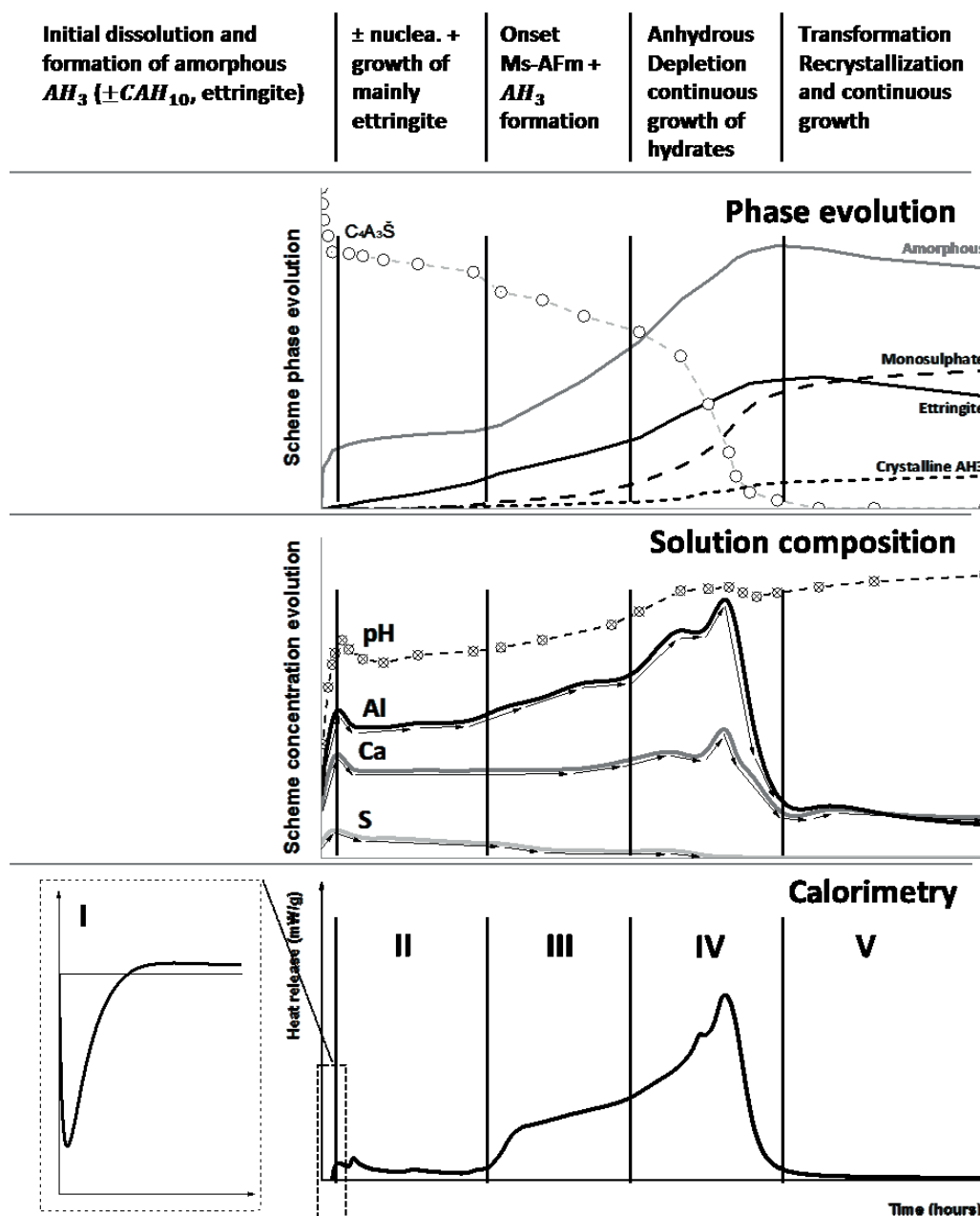


Figure 5.4-13 Early age rate of heat evolution of Y with and without quartz at several w/b ratios from Figure 5.4-12

## 5.5 General discussion

### 5.5.1 Hydration sequences

We could derive an idealized scheme for the evolution of the hydration kinetics, solution composition, phase assemblages and hydration periods, based on the results obtained in suspension and paste. This schematic representation is shown in in Figure 5.5-1. Each stage and the underlying hydration reactions are described below.



- Stage I: Initial period:
  - Wetting and rapid dissolution of a small quantity ye'elimite
  - Formation of mainly amorphous hydrates such as aluminium hydroxide and foil-like calcium aluminate hydrate (probably  $CAH_{10}$ ) together with traces of ettringite
  - Presence of an endothermic peak for neat clinker probably from the precipitation of amorphous aluminium hydroxide
  - Slowdown coincides with the increase of the solution concentrations
- Stage II: Induction or dormant period:
  - Slow or almost no dissolution of ye'elimite but continuing formation of ettringite
  - Slow but constant drop of the sulphate concentration and increase of the pH
  - The length of the dormant period correspond to the continuing slow formation of ettringite and the resulting decrease of mainly the sulphate ion concentration
- Stage III: Acceleration period
  - Drop of sulphate ion concentration below a critical level
  - Faster increase of pH and aluminium ion concentration
  - (Re-) Acceleration of the dissolution of ye'elimite
  - Onset of the monosulphate and gibbsite-like aluminium hydroxide formation
  - General acceleration of the formation of hydrates
- Stage IV: Main hydration period including the deceleration phase
  - Rapid ye'elimite dissolution and formation of monosulphate and ettringite, potentially favoured by the rising pH
  - Continuous formation ( $\pm$  crystallisation) of gibbsite-like aluminium hydroxide
  - Depletion of all anhydrous phases
  - The duration of this period seems to depend equally on the rate of the ye'elimite dissolution and the formation of monosulphate and ettringite. Interestingly, the formation of monosulphate and ettringite seems to proceed as fast as the dissolution of ye'elimite, as the sulphate concentration was always below the detection limit
- Stage V: Final hydration period
  - Equilibration stage during which the concentrations are low in solution and the pH being relatively high (e.g. around 12)
  - The transformation, (re)crystallization and growth of hydrates such as monosulphate and gibbsite-like aluminium hydroxide occurs

### 5.5.2 Why does the dissolution slow down and why does it accelerate again

The slowdown could be potentially related to the increase of the **solution concentrations**, which could be explained by the dissolution theory from geochemistry. The degree of undersaturation is high directly after the addition of water. Hence, the rate of dissolution is high. Already within seconds after contact with water, a measureable quantity of ye'elimite dissolves, causing increasing the ionic concentrations in solution. Next, a slowdown of the kinetics is observed. Most likely, the slowdown in kinetics is caused by the increase of the solution concentrations, especially of aluminium and sulphate over calcium ions, which limit the further anhydrous dissolution. Ye'elimite is potentially in equilibrium with the given solution composition.

This assumption is strengthened by the fact that the slowdown of the dissolution and the consecutive onset of the dormant period seems to be more or less independent from the applied w/b ratio but correspond to the given solution composition. One important aspect that needs to be noted is the lack of sulphate during the main hydration period, even when ye'elimite dissolves rapidly, compared to the relatively high sulphate concentration during the initial and the dormant period. These results suggest that the precipitation of monosulphate and ettringite proceeds as fast as the dissolution of ye'elimite depleting instantly all liberated sulphate ions. On the contrary, during the dormant period the slow decrease of the sulphate concentration (no dissolution of ye'elimite within the method accuracy) corresponds to the slow formation of ettringite. In that respect, Damidot concluded in his work [234] that high aluminium ion concentrations at given calcium and sulphate ion concentrations could limit the nucleation rate of ettringite, as primarily the supersaturated domain of  $CAH_{10}$  and amorphous aluminium hydroxide is reached. This in turn should slow down the hydration kinetics but favours the growth of ettringite. This seems to be consistent to our findings, as demonstrated by the well crystallized ettringite formed during the dormant period (see Figure 5.4-7). On the contrary, ettringite formed during the acceleration and main period forms clusters of fine, needle-like shaped crystals (see also annex – part V, starting from Figure 8.8-65).

Another cause may be the potential **absorption of sulphate on reactive dissolution sites**. The slowdown of the  $C_3A$  dissolution rate in the presence of sulphate is caused by the absorption of sulphate ions on reactive dissolution sites [45] [235]. A similar mechanism may cause the slowdown of the ye'elimite dissolution. For example, the drop of the sulphate concentration and the resulting acceleration of the hydration coincide with the onset of the monosulphate formation. However, one should keep in mind the important differences between the hydration of ye'elimite ( $C_4A_3\bar{S}$ ) and  $C_3A$ . Sulphate is a part of the crystal structure of ye'elimite and will be always released together with calcium and aluminium during the dissolution.  $C_3A$  does not contain sulphate and may dissolve into a solution containing sulphate ions. Moreover, the dissolution of  $C_3A$  ( $Ca / Al = 1.50$ ) liberates by far less aluminium and more calcium [235] compared to ye'elimite (i.e.  $Ca / Al = 0.67$ ). Hence, the hydration kinetics and composition of the hydrates assemblage are different. Therefore, for the time being it remains unclear whether this mechanism is present or not.

Another hypothesis which may explain these experimental results is the **protective layer, barrier or membrane theory**. The rapid dissolution of ye'elimite caused the rapid increase of the solution concentrations and ultimately, in the instant precipitation of amorphous phases covering the anhydrous grains. Several authors speculated that such an amorphous layer provides a diffusion barrier which would slowdown the dissolution of cementitious materials [120] [236] [237] [238] [239]. They argued that the hydration products form less permeable membrane on the anhydrous particles surface, limiting the diffusion or transport of water and ions. The recrystallization or dissolution of the metastable phase(s) forming the layer would expose fresh anhydrous surfaces to the solution, which in turn would result in the reacceleration of the dissolution. **We strongly doubt for several reasons that such a mechanism, if present at all, profoundly alter the hydration of ye'elimite.** The slowdown of dissolution occurred after seconds and before the formation of the layer of hydrates. Furthermore, the formed Hadley grains prove the continuous dissolution of ye'elimite and the layer seems to be rather soft as it was easily damaged during the preparation of the HR-SEM samples. The friable nature of the layer or shell should be of high relevance for the experiments carried out in suspension.

The samples were stirred continuously at 600 r/min, which should result in the abrasion of any formed shell or layer. Thus, fresh surfaces should be steadily exposed no dormant period should be observed. However, a dormant period was still present. Hence, the layer of hydrates cannot explain the slowdown of the dissolution process.

## 5.6 Conclusions

This work investigated the hydration reactions and kinetics of neat stoichiometric ye'elimite. For that we developed a research approach to assess the hydration reactions and kinetics along two main axes. One set of experiments was carried out in suspension. In this setup we assessed the evolution of the solution composition (conductivity, pH and concentrations), the rate of the anhydrous dissolution and the hydrates formation as well as their composition. A second set of experiments was done in paste, where the impact of the water to binder and water to solid ratio was varied. By this we were able to identify two major hydration reactions and to define five hydration periods. The evolution of the solution composition, especially the sulphate ion concentration and the pH, seems to be the main controlling parameter, causing the slowdown or acceleration as well as the type of hydration reaction. Furthermore, the hydration sequences and periods detected in the suspension experiments were also found in the paste samples. Thus we could successfully link the results from experimental set-ups. This is especially of relevance, as calorimetry measurements of paste samples are commonly used to assess the hydration kinetics of ye'elimite based binders such as CSA or BYF.

The experiments in paste typically show a single main hydration peak. However, this peak represents at least two overlapping precipitation reactions, beside the continuing dissolution of ye'elimite. The nucleation and growth of ettringite,  $CAH_{10}$  and amorphous aluminium hydroxide presents the first reaction and starts directly after the contact with water. It almost exclusively proceeds till the end of the dormant but remains throughout the acceleration and main hydration period. The steady formation of ettringite during the dormant period causes the depletion of sulphate ions from solution. This led to the increase of the pH and to the acceleration of the hydration. At the same time the onset of the main hydration reaction, i.e. the formation of monosulphate and gibbsite-like aluminium hydroxide, occurs. Increasing the w/b ratio, especially the presence of nucleation sites provided by the inert quartz filler, enhanced the formation of ettringite,  $CAH_{10}$  and amorphous aluminium hydroxide, causing the faster depletion of sulphate ions from solution. Thus, the onset of the monosulphate formation occurs earlier.

These findings offer new insights into the hydration of ye'elimite-rich binders. The dissolution of the anhydrous phases, the formation of metastable hydrates and the different hydration periods could be successfully linked with the evolution of the solution. This knowledge could be used to improve the thermodynamic predictions of the hydration reactions and ultimately, the performance and stability of CSA and BYF concrete.



## 6 Effect of gypsum on the hydration of ye'elimite and the chemical shrinkage

The results of this chapter will be reported in peer reviewed journal(s):

- Cement and Concrete Research
  - o Title: Chemical shrinkage of ye'elimite alone and with gypsum
    - Draft under preparation

### CONTENTS

---

<b>6</b>	<b>EFFECT OF GYPSUM ON THE HYDRATION OF YE'ELIMITE AND THE CHEMICAL SHRINKAGE .....</b>	<b>85</b>
<b>6.1</b>	<b>SUMMARY OF EXPERIMENTS CARRIED OUT IN CHAPTER 6 .....</b>	<b>86</b>
<b>6.2</b>	<b>EFFECT OF GYPSUM ON THE HYDRATION OF YE'ELIMITE .....</b>	<b>87</b>
6.2.1	EFFECT OF GYPSUM ON THE HYDRATION KINETICS .....	87
6.2.2	EFFECT OF WATER TO SOLID RATIO .....	87
6.2.3	EXPERIMENTS IN SUSPENSIONS .....	89
6.2.4	FORMED HYDRATES .....	91
6.2.5	HYDRATES STRUCTURE AND COMPOSITION .....	94
6.2.6	DISCUSSION .....	98
<b>6.3</b>	<b>CHEMICAL SHRINKAGE OF YE'ELIMITE ALONE AND WITH GYPSUM .....</b>	<b>99</b>
6.3.1	HYDRATES FORMED AND BOUND WATER CONTENT .....	100
6.3.2	SEM-EDS ANALYSES OF HYDRATED SAMPLES .....	103
6.3.3	MASS AND VOLUME BALANCE CALCULATIONS .....	105
6.3.4	DISCUSSION .....	106
<b>6.4</b>	<b>GENERAL DISCUSSION.....</b>	<b>108</b>

---

This chapter presents details regarding the effect of gypsum on the hydration of ye'elimite. Additionally, we investigated the chemical shrinkage of ye'elimite with and without gypsum.

It is generally accepted that the hydration of CSA cements is primarily controlled by the reaction of ye'elimite. The addition of calcium sulphate accelerates the hydration and modifies the phase assemblage, promoting the formation of ettringite rather than of monosulphate [114] [121]. In addition, earlier studies have shown that the hydration kinetics for stoichiometric and iron-rich ye'elimite are similar when calcium sulphate is added [38] [39]. The objective of the first part of the chapter is to characterise and understand the effect of gypsum on the hydration of stoichiometric and solid solution ye'elimite. We followed the same experimental approach as presented in Chapter 5, for the characterisation of the hydration reactions and periods.

The second part of the chapter focuses on the characterisation of the chemical shrinkage evolution of ye'elimite. We tried to relate the chemical shrinkage evolution to the formed phase assemblage. The measurement of the chemical shrinkage enables simultaneously the investigation of the hydration kinetics as well as of the overall volume changes in the system. This is because water molecules present in liquid water occupy more space than those bound in hydrates. For that we selected two systems, neat ye'elimite and a ye'elimite with the addition of gypsum (22% gypsum). We chose these two binders as they represent simplified references for complex CSA cement types. The chemical shrinkage measurements were supplemented by TGA, QXRD and SEM-EDS analyses. Finally, we combined the experimental results from chemical shrinkage measurements with those of TGA and QXRD analyses to carry out mass and volume balance calculations to assess the composition of the amorphous phase.

## 6.1 Summary of experiments carried out in Chapter 6

The effect of gypsum and of the water to binder (w/b) ratio on the hydration was investigated using a binder composed of 78% Y (from S3 series) or Fe-Y (from S3 series) with 22% gypsum (G). The experiments which were carried out are summarised in Table 5.1-1. The results which are not explicitly shown in this chapter can be found in the annex – part V.

Table 6.1-1 Experimental matrix; Qz = quartz

		Paste (+ Qz) w/b 0.5 - 40	Paste w/b 2	Suspension w/b 100
Calorimetry	Continuous measurement 0 - 48 h	x	x	
Chemical shrinkage	0 - 28 d		x	
QXRD + TGA	Single sample at the end	x		x
	Samples taken during 28 d		x	
Mass (+ volume) balance calculations	All	x	x	x
Conductivity and pH	Continuous measurement 0 - 24 h			x
ICP-OES	Samples taken during 24 h			x
SEM-EDS	Samples taken during 28 d		x	
HR-SEM	Samples taken during 7 min			X
STEM-EDS	Samples taken during 6 h			X
Modelling	Samples taken during 24 h			x



## 6.2 Effect of gypsum on the hydration of ye'elinite

### 6.2.1 Effect of gypsum on the hydration kinetics

Figure 6.2-1 shows the isothermal conduction calorimetry results for neat Y, neat Fe-Y and of both clinkers with additional gypsum. The instant dissolution of gypsum liberates extra calcium and sulphate to solution, causing the instant oversaturation and precipitation of ettringite [39] [128]. The hydration slows down after the initial stage reaching a dormant period in all four samples. The duration of this dormant period can vary significantly depending on the binder type used. Figure 6.2-1 demonstrates that Y and Fe-Y have different kinetics, whereas the binders with gypsum reveal similar kinetics and sequences, independent on the ye'elinite type used. Moreover, the duration of the dormant period is shortened and the heat flow maintains at a higher level compared to the neat clinkers. The origin of the onset, duration and end of the dormant period as well as of the higher heat release will be presented in the following sections. The origin of the endothermic peak in the case of neat clinkers is related to the precipitation of amorphous phases such as aluminium hydroxide (as discussed in Chapter 5). This endothermic peak is absent in the samples containing gypsum, indicating that the formation of ettringite, which is exothermic, overlaps and covers this reaction.

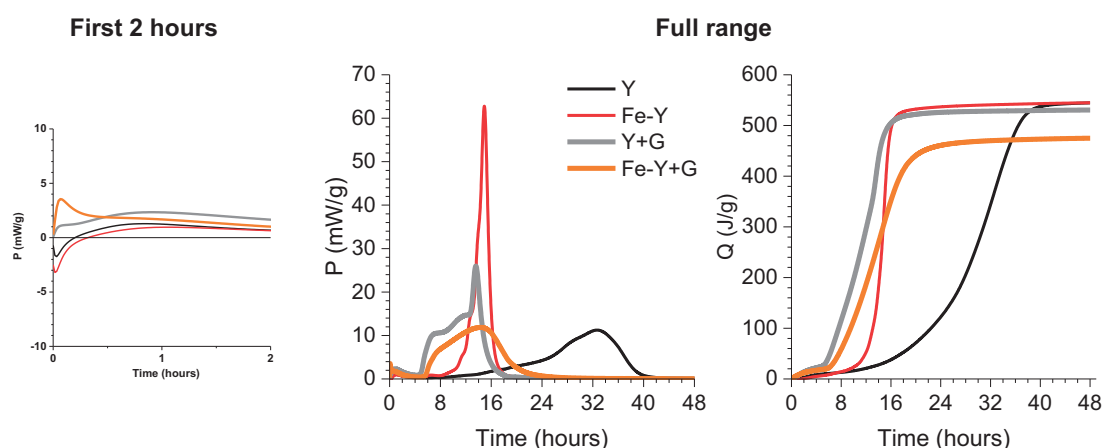


Figure 6.2-1 Rate of heat evolution and cumulative heat of neat Y, Fe-Y and both with gypsum at a w/b 2

### 6.2.2 Effect of water to solid ratio

Figure 6.2-2 shows the rate of heat evolution and the cumulative heat of Fe-Y+G at all tested w/b ratios. In these series of experiments Fe-Y was used instead of Y, due to the lack of available Y clinker. This was possible as both materials show very similar hydration kinetics and sequences. An increased w/b and w/s ratio accelerates the hydration kinetics. The first exothermic (at low w/b) or endothermic (at high w/b) peak occurred at around 1 to 3 hours of hydration. Even at high w/b supersaturation of amorphous aluminium hydroxide is instantly reached and its nucleation (which is probably endothermic) occurs. It follows the dormant period. A second maximum appears with increasing w/b ratios. This represents the point of sulphate depletion and the onset of monosulphate formation [130]. For water to binder ratio above 7.5, the peaks start to merge again with further increasing w/b ratios, where only a single one was left at w/b 40. Based on the findings presented in Chapter 5, we assume that the high w/b and the presence nucleation sites promote the nucleation of ettringite. Moreover, the increase of the water to binder ratio led to the increase of the cumulative heat release, which corresponds to the higher hydration degree (Chapter 5).

Effect of gypsum on the hydration of ye'elimite and the chemical shrinkage

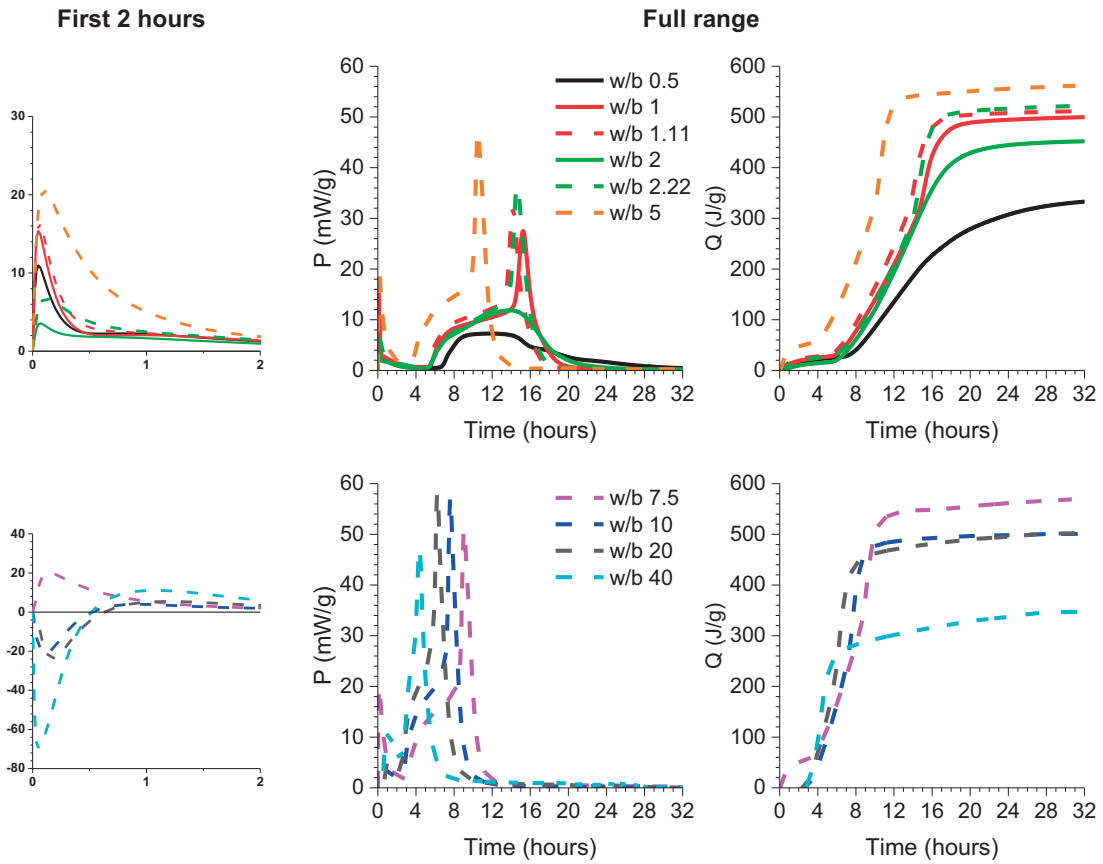


Figure 6.2-2 Rate of heat evolution and cumulative heat of 78% Fe-Y with 22% G at varying w/b but fix w/s ratio of 2; the solid line depicts the neat cement while the dashed line represents blends with quartz

We presented in Chapter 1, Figure 1.4-2 (b) the isothermal conduction calorimetry results of several BYF and CSA cements. We further plotted that of synthetic Y with various additions labelled "X" and "Z". Figure 6.2-3 presents the updated graph. We could relatively well simulate the complex hydration pattern of industrial BYF cement, by blending Fe-Y with gypsum and quartz. By substituting a part of the binder with inert quartz filler we reach the same effective water to ye'elimite ratio as in the BYF cement. It is plausible that e.g. belite has a similar role in BYF at the early hydration.

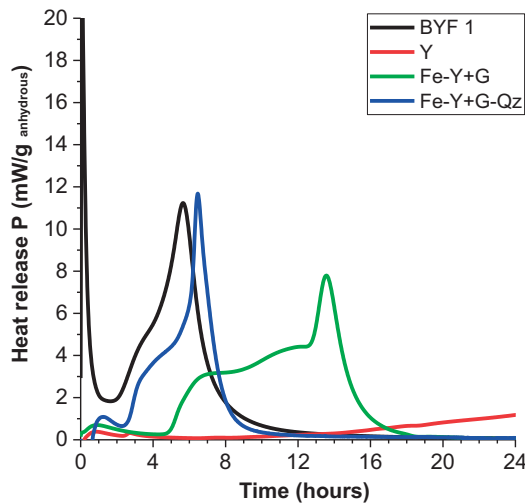


Figure 6.2-3 Rate of heat evolution of a BYF cement, Y and blends of 78% Fe-Y with 22% gypsum (G) and quartz (Q)

### 6.2.3 Experiments in suspensions

Figure 6.2-4 presents the evolution of the conductivity and pH in suspension at w/b of 100. During the first minutes of hydration, both Y+G and Fe-Y+G show a relatively similar evolution in terms of pH and conductivity. Initially a steep increase of the conductivity and the pH is present and lasts until 4 minutes for (Fe-Y+G) and 10 minutes for (Y+G). During this period slightly higher values for calcium and aluminium ions are reached for Fe-Y+G. No clear distinction between hydration periods was possible, e.g. as done for neat clinker, by the evolution of the conductivity or pH. This is due to the rapid dissolution of some gypsum, where the remaining one presents a calcium and sulphate buffer, keeping both concentrations high in solution. The fall of the conductivity and rise of pH presents the point of the depletion of solid gypsum. The small hump marks the continuing ye'elimite dissolution.

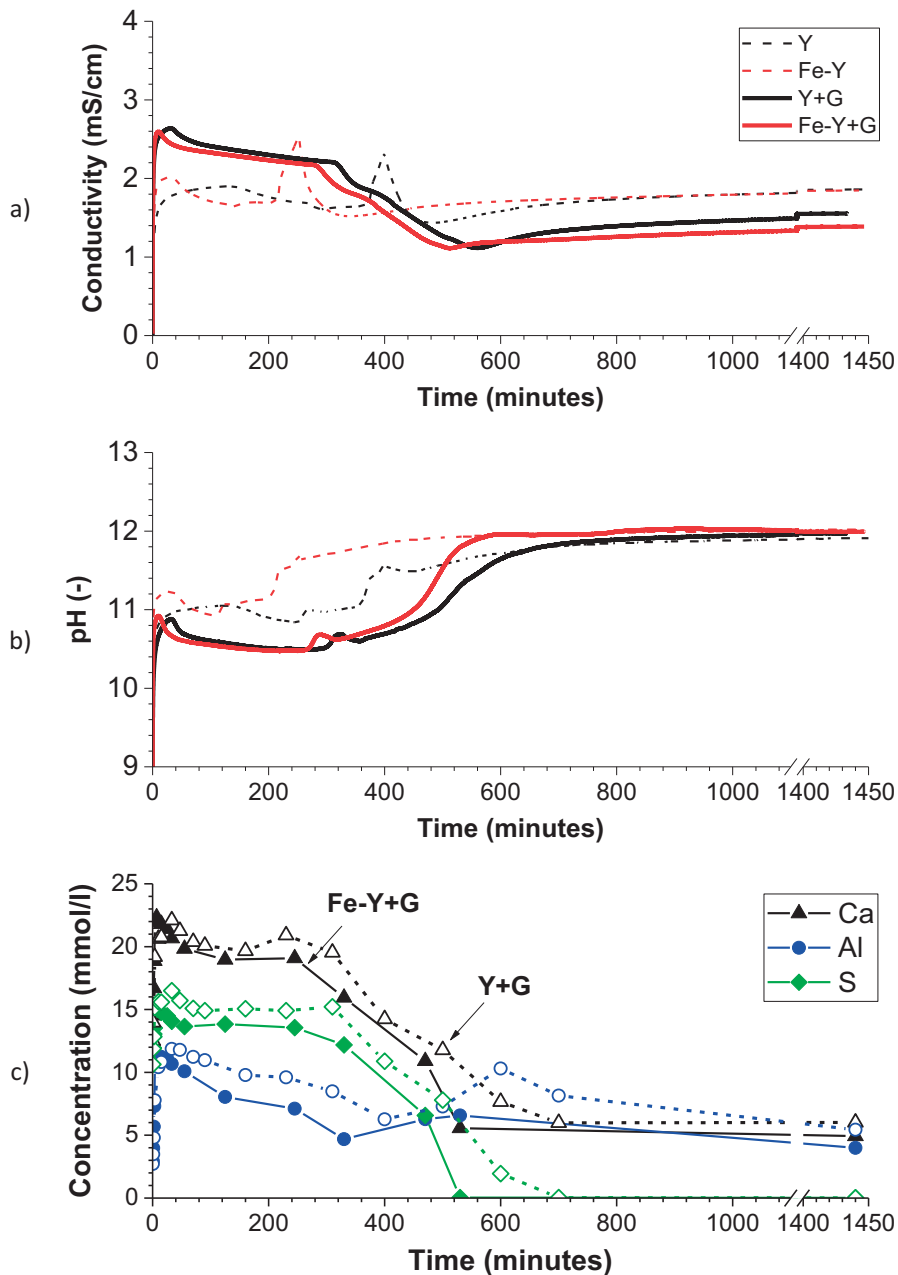


Figure 6.2-4 Evolution of the conductivity (a), pH (b) and solution concentration (c) of Y, Fe-Y, Y+G and Fe-Y+G at w/b 100

Another possibility to plot the results is in logarithmic scale, which enables the better assessment of the early hydration period. This is shown in Figure 6.2-5 for the conductivity and the concentrations in solution. We note that the concentrations of calcium and sulphate are by far higher and of aluminium lower in the presence of gypsum compared to the concentrations measured during the hydration of neat Y (Chapter 5). After the maximum is reached, there is a steady slow decrease of all concentrations. We assume this is caused by the simulations steady dissolution of primarily gypsum (with some ye'elimite), buffering the steady nucleation and growth of ettringite and aluminium hydroxide. This is indicated by the stronger decrease of the aluminium ion concentration compared to those of calcium and sulphate. The sharp drop of the calcium and sulphate at about 300 minutes represents the point of the gypsum depletion, which coincides with the continuing ye'elimite dissolution and the onset of the monosulphate formation. The pH increases due to the higher hydroxyl ion concentrations to maintain electron neutrality, i.e. establishing equilibrium conditions.

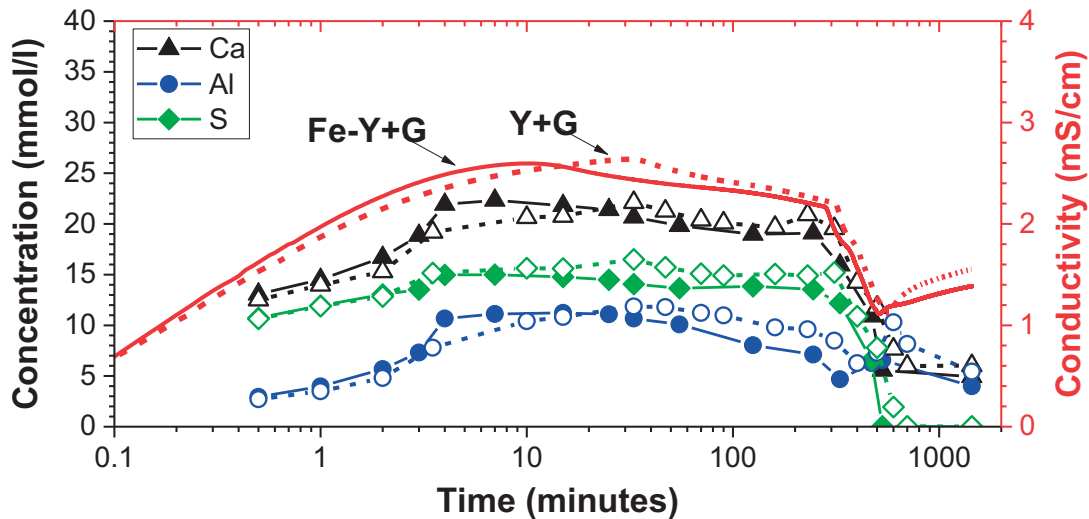


Figure 6.2-5 Evolution of the conductivity and of the solution composition for Y+G (dashed line and empty symbols) and Fe-Y+G (solid line and symbols) at w/b 100; Fe was always below the detection limit

Figure 6.2-6 shows a plot of the measured solution concentrations and the hydrates solubility lines at two selected sulphate concentrations. The chosen sulphate concentrations are representative for the measured ones at different hydration ages. Instantly, a high calcium and sulphate concentration is reached, whereas the aluminium ion concentration is “suppressed” compared to the results obtained for neat ye'elimite. For example, the  $Ca / Al$  ratio in solution measured for neat Y as well as Fe-Y were always about 0.7 to 0.8 during the initial until main hydration period, and reached about 1.1 to 1.2 at the end of the experiment. On the contrary, the  $Ca / Al$  ratio in solution for Y-G and Fe-Y+G varied initially from 2.5 to 4, maintain relatively stable around 1.8 to 2.2 during the main hydration period and reached values of about 1.1 to 1.2 only after the gypsum depletion. The alumina concentrations seems to be constrained to lower levels compared to neat Y, corresponding to the formation of ettringite. This is consistent with our findings, showing that the measured solution concentrations are located around the solubility curve of ettringite at the given sulphate concentrations and move along until about 300 minutes. At this stage the depletion solid gypsum occurs, which provided the initial calcium and sulphate buffer to the solution.

Once gypsum is depleted and the sulphate ion concentrations fall to zero, a new chemical equilibrium between ettringite and monosulphate is reached, e.g. explaining also the increase of the aluminium ion concentration. From that point on, the hydration follows the same evolution as that of the neat ye'elimite, i.e. points are located in the stability field between  $CAH_{10}$  and ettringite.

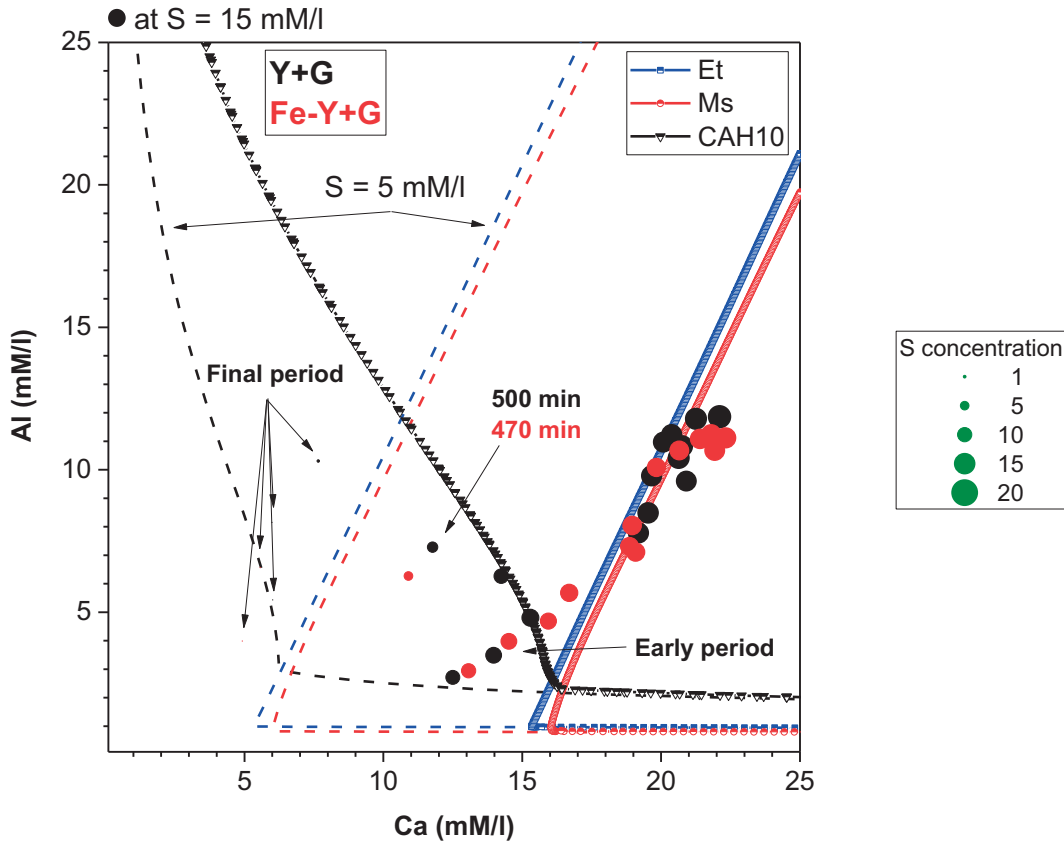


Figure 6.2-6 Solubility curves at 25 °C for the system  $CaO - Al_2O_3 - SO_3 - H_2O$  at fix sulphate concentrations of 5 mM/l (a) and 15 mM/l (b) and measured concentrations of ● Y+G and ● Fe-Y+G at w/b 100

#### 6.2.4 Formed hydrates

The quantitative phase composition, determined by QXRD and TGA analysis of dried powders (after the solvent exchange), for the hydrated neat Y, Fe-Y and with gypsum at a w/b ratio of 100 is shown in Figure 6.2-7a. It should be noted that the applied solvent exchange protocol can damage the hydrates such as ettringite or monosulphate. Both these techniques would result in an increase of the amorphous content. The nature and the quantity of hydrates formed after 24 hours of hydration is almost identical for both samples containing gypsum. Ettringite is the main XRD detectable hydrate formed. Additionally, traces of poorly crystalline gibbsite were also observed. For the plain hydrated clinker samples there is an almost equal mix of XRD detectable ettringite and monosulphate formed. Figure 6.2-7b gives the correlation between the amount of amorphous phases formed after 24 hours of hydration and the specific surface area of the anhydrous materials. We note that the hydrated samples including iron have a higher quantity of amorphous phases formed which corresponds to a higher specific surface area. It remains unknown what causes this. However, this can be an artefact related to the experimental techniques used during the sample preparation. However, for reasons discussed in what follows, we assume that this is at least partly related to the presence of iron.

Effect of gypsum on the hydration of ye'elimite and the chemical shrinkage

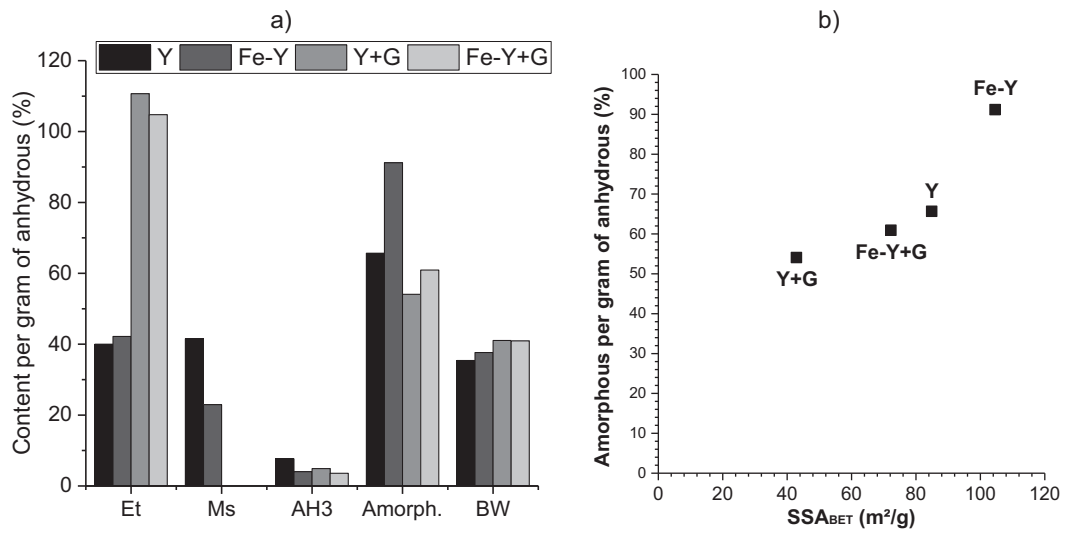


Figure 6.2-7 Hydrates formed after 24 hours of hydration at w/b 100 and bound water (BW) content for neat ye'elimite clinkers and with the addition of gypsum; Et = ettringite and Ms = monosulphate

The results of the thermogravimetric analyses for the hydrated Y, Fe-Y with and without the addition of gypsum at a w/b ratio of 100 are shown in Figure 6.2-8. The curves are almost identical for Y+G and Fe-Y+G, which further indicate the positive impact of gypsum not only on the hydration kinetics but also on the formed hydrates. In the presence of gypsum, ettringite forms as the main hydrate. This is consistent with the XRD findings. In addition, traces of monosulphate and aluminium hydroxide were also identified.

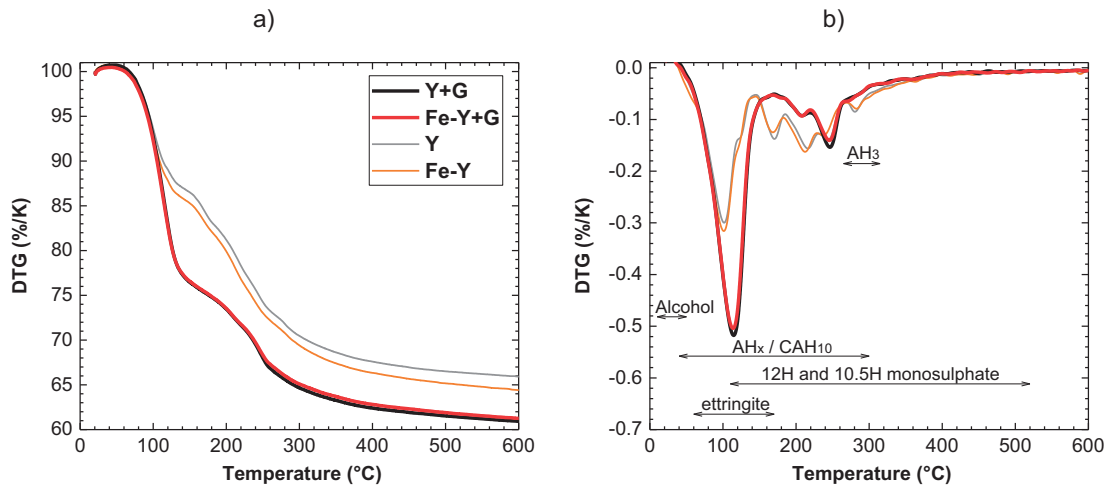


Figure 6.2-8 Formed hydrates after 24 hours at w/b 100 and bound water content; Et = ettringite and Ms = monosulphate

Figure 6.2-9 gives a fragment of the diffraction pattern of hydrated binders after 24 hours of reaction at w/b of 100. The slightly higher background for the Fe-Y-based samples is related to the iron fluorescence, resulting from the interaction with the used copper X-ray source. STM-EDS analyses demonstrate that iron is incorporated into ettringite and monosulphate (see section 6.2.5 below) However, no measureable peak shift, which would indicate the potential substitution of aluminium by iron in the crystal structures of ettringite or monosulphate, was observed in any of the hydrated samples. But we note the presence of measurably higher quantities of monosulphate in a lower hydration state stabilized as 10.5 Ms for the hydrated Fe-Y sample compared to Y. This points to a higher sensitivity of the iron-containing solid solution monosulphate to the applied solvent exchange procedure. On the contrary, almost identical patterns are observed in the binders containing gypsum with ettringite being the dominant hydrate. This indicates, together with the STM-EDS analyses, that the impact of iron on the crystallinity and stability is less strong for ettringite compared to monosulphate.

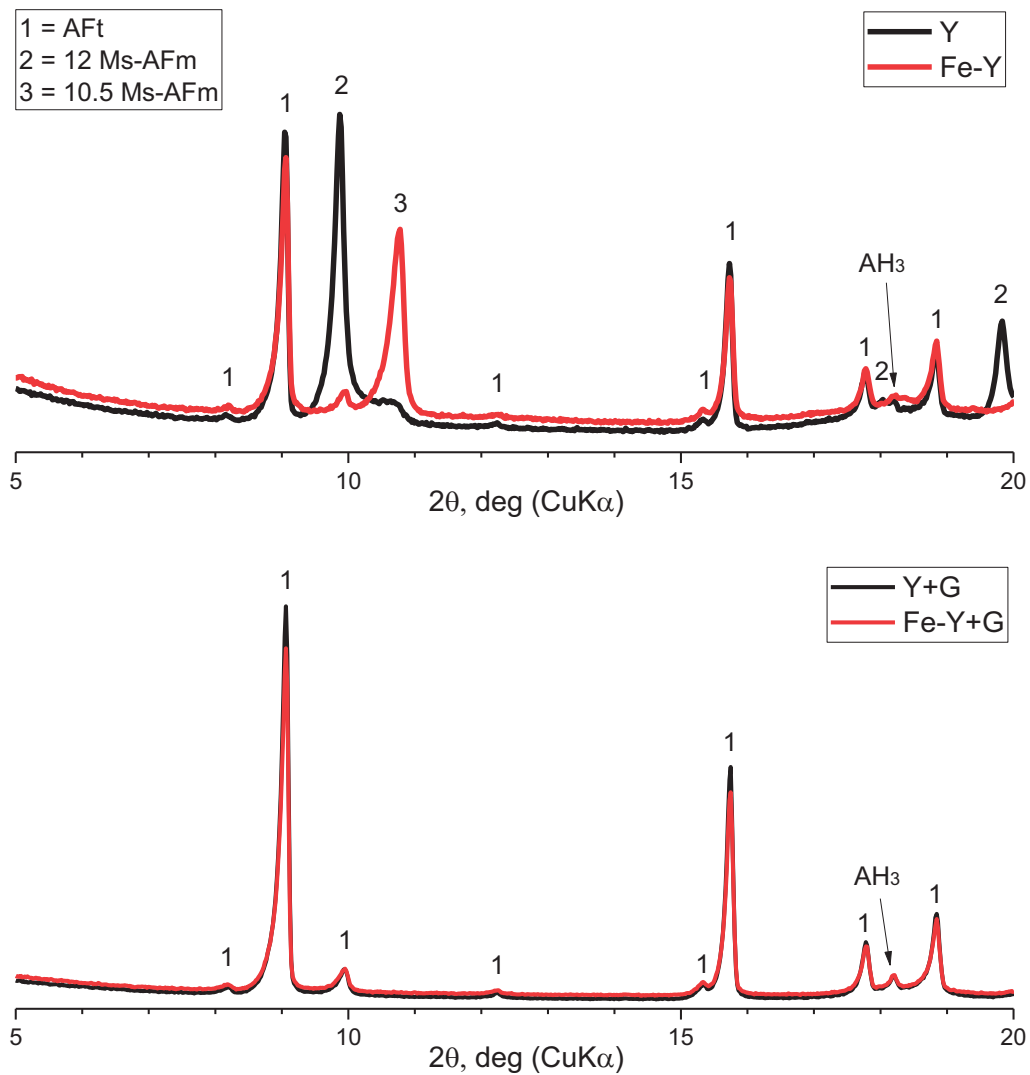


Figure 6.2-9 Fragmented diffraction pattern of hydrated binders after 24 hours of reaction at w/b 100, measurements of dry powders after solvent exchange

### 6.2.5 Hydrates structure and composition

Figure 6.2-10 to Figure 6.2-12 shows HR-SEM and STEM micrographs of Y+G hydrated for 30 seconds, 7 minutes and 4 hours at w/b 100. Additional results for Fe-Y+G samples are available in the annex – part V (see to Figure 8.8-42 to Figure 8.8-44). HR-SEM micrographs of the hydrated ye'elimite particles reveal clear evidence of the ongoing ye'elimite dissolution already after 30 seconds of hydration. The dissolution sites remind etch pitches reported for hydrating tricalcium silicate ( $C_3S$ ) [40] [107]. Comparing the extent of the dissolution of ye'elimite in Y+G and the coverage with hydrates to that of neat Y (as shown in Chapter 5) at given hydration times, it seems that gypsum reduces the dissolution rate of ye'elimite during the first seconds and minutes of hydration. The formation of clusters of globules-like hydrates is observed, whereby the majority of the available surface of the anhydrous particles is not yet covered. This is still the case even after 7 minutes of hydration. Ettringite is already formed after 30 seconds of hydration and continues to form and grow afterwards. Ettringite is always intermixed with the globules-like hydrates, which is probably aluminium hydroxide. These intermixed hydrates start to form even some bigger clusters.

In accordance with the HR-SEM, STEM-EDS analyses of the Y+G samples (Fe-Y+G in annex – part V) were carried out. The analyses reveal that a layer of hydrates is already present after 7 minutes of hydration. Ettringite is mainly embedded within this layer. As for the neat Y, the layer of hydrates seems not to hinder the continuing hydration, as indicated by the presented in Figure 6.2-4. In addition, the space between the shell and anhydrous grain is more filled with hydrates compared to the samples of neat Y. Table 6.2-1 presents the bulk composition of the formed hydrates layer determined by STEM-EDS. The layer of hydrates has a composition close to that of the used anhydrous ye'elimite, which is surprisingly very similar to the composition derived for those present in the hydrated neat Y. Again, the porous structure of the hydrates is very probable a result of the unavoidable beam damaging, i.e. dehydration, occurring throughout the sample preparation and analyses.

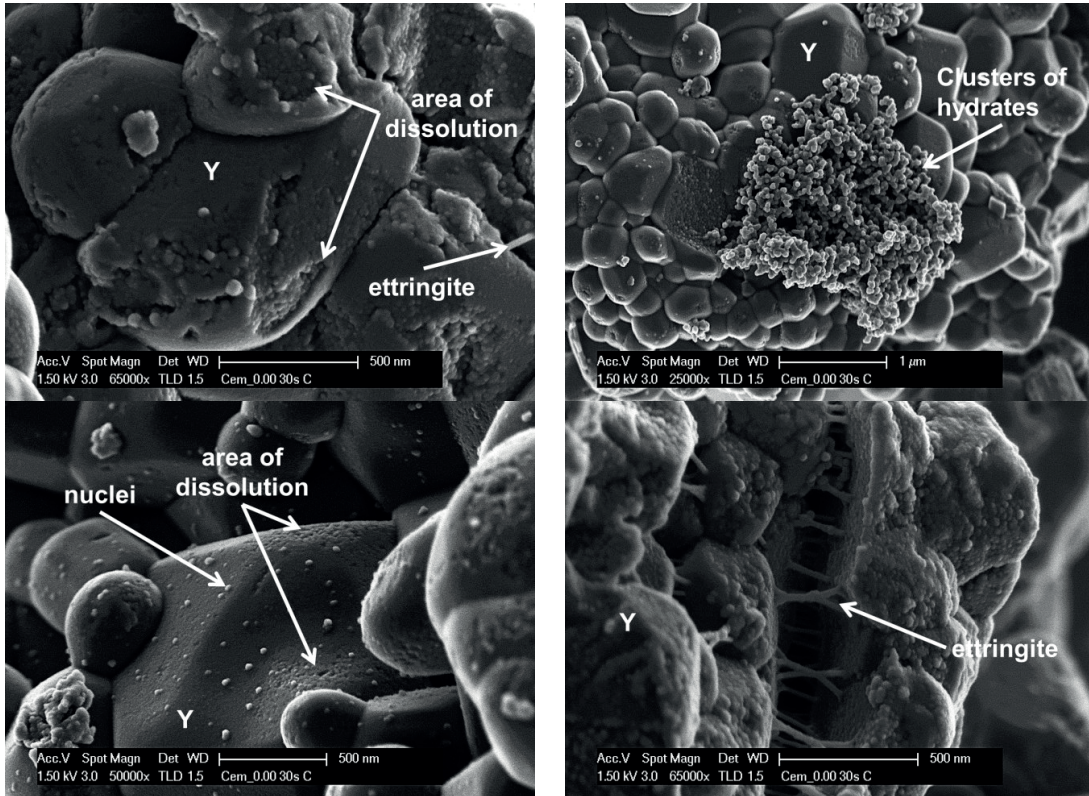
A profoundly altered composition of the shell-like product was found for the Fe-Y+G samples. The layer is profoundly enriched in iron, whereas aluminium seems to be “leached” after 7 minutes of hydration. This effect is less pronounced in the sample hydrated for 3 hours. We assume that the continuing hydration of ye'elimite and the formation of additional hydrates “dilute” this effect.

**Table 6.2-1 Atomic ratios of the hydrated areas determined by STEM-EDS in the Y+G and Fe-Y+G sample**

Sample	In layer-like hydrates			Number of measured areas
	$Ca / Al$ [–]	$S / Al$ [–]	$Fe / Al$ [–]	
<b>Anhydrous Y</b>	<b>0.65</b>	<b>0.16</b>	<b>0.005</b>	
Y+G 7 minutes	0.62	0.14	0.02	33
Y+G 4 hours	0.69	0.19	0.02	29
<b>Anhydrous Fe-Y</b>	<b>0.69</b>	<b>0.16</b>	<b>0.07</b>	
Fe-Y+G 7 minutes	0.97	0.21	0.49	32
Fe-Y+G 3 hours	0.70	0.17	0.16	30



Y+G at 23 °C and w/b 100 after 30 seconds of hydration



Y+G at 23 °C and w/b 100 after 420 seconds of hydration

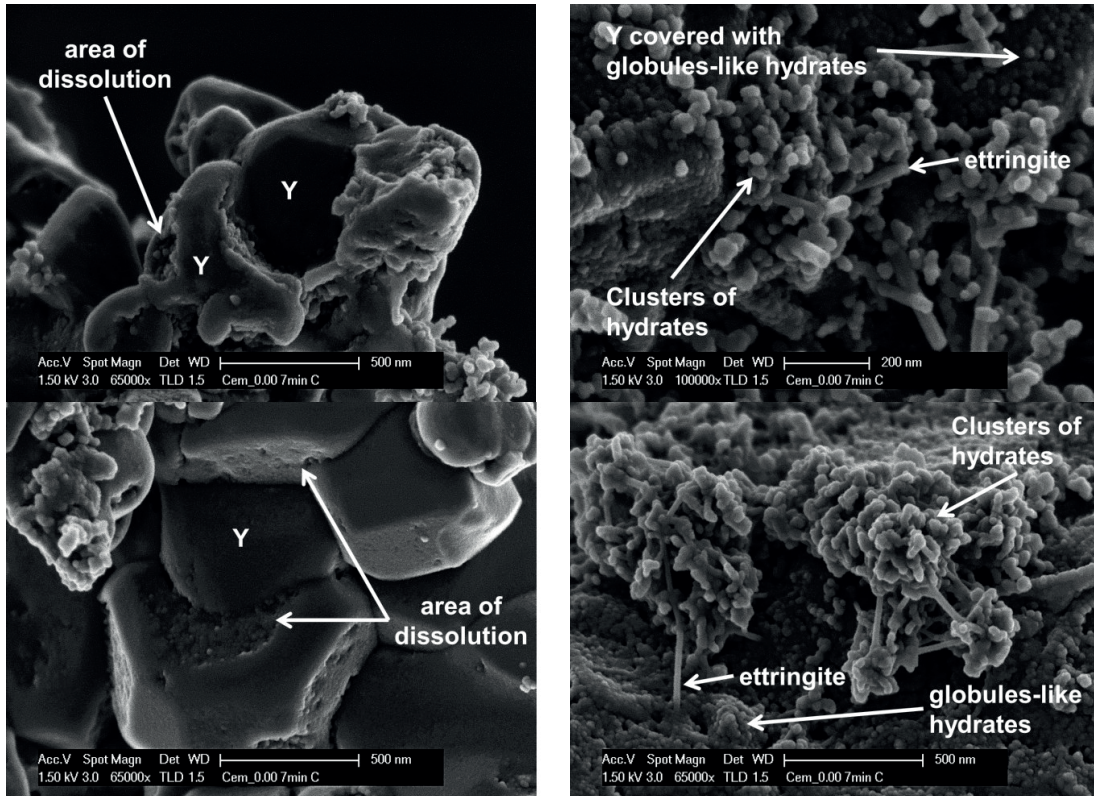


Figure 6.2-10 Morphological characterization of the hydrated ye'elimite at 23 °C and a w/b ratio of 100



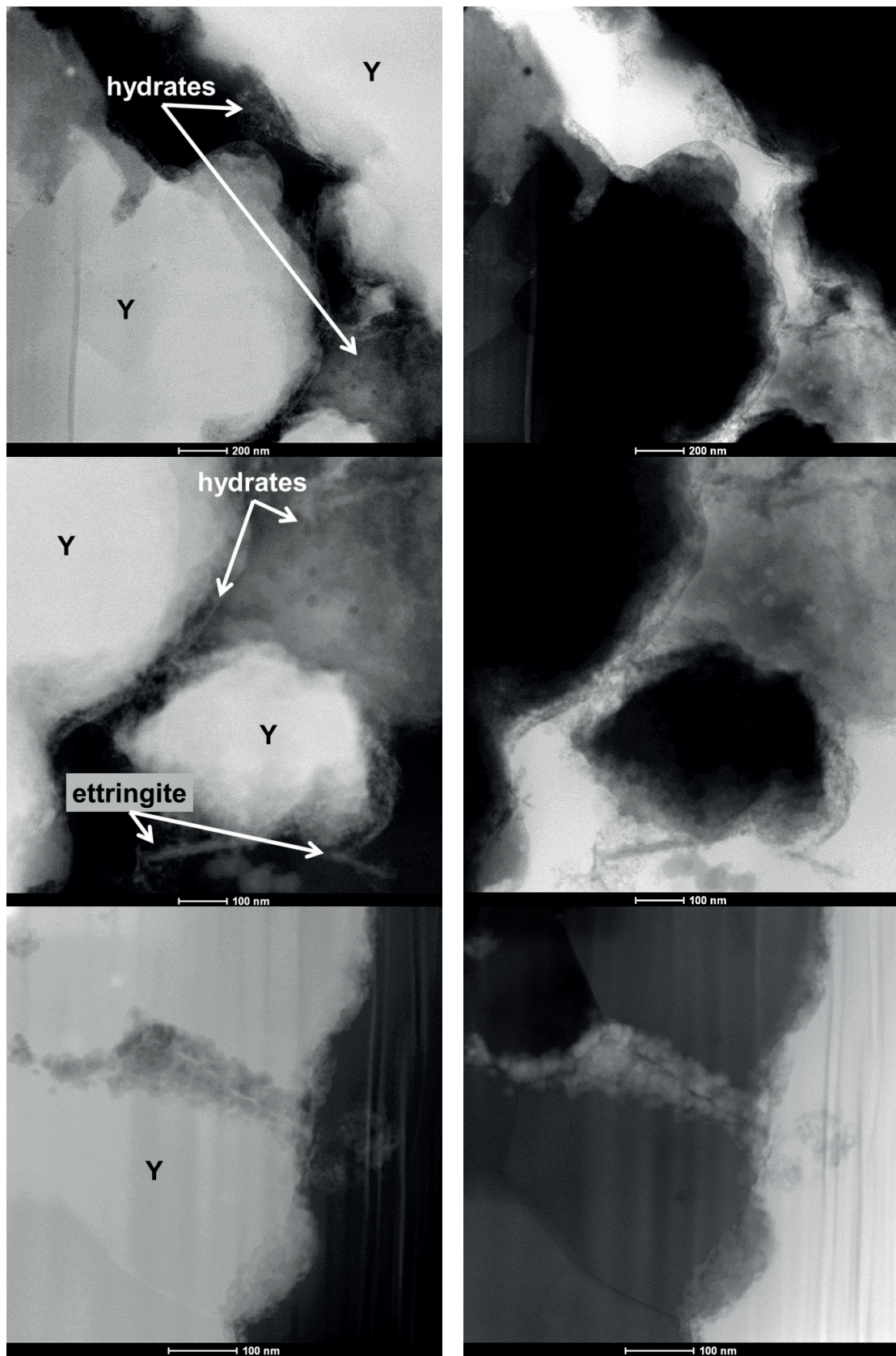


Figure 6.2-11 STEM images (up: HAADF image and down: BF image) of Y+G after 7 minutes of hydration at 23 °C and a w/b ratio of 100; Y = anhydrous ye'elimite particles; hydrates = mix of phases including ettringite



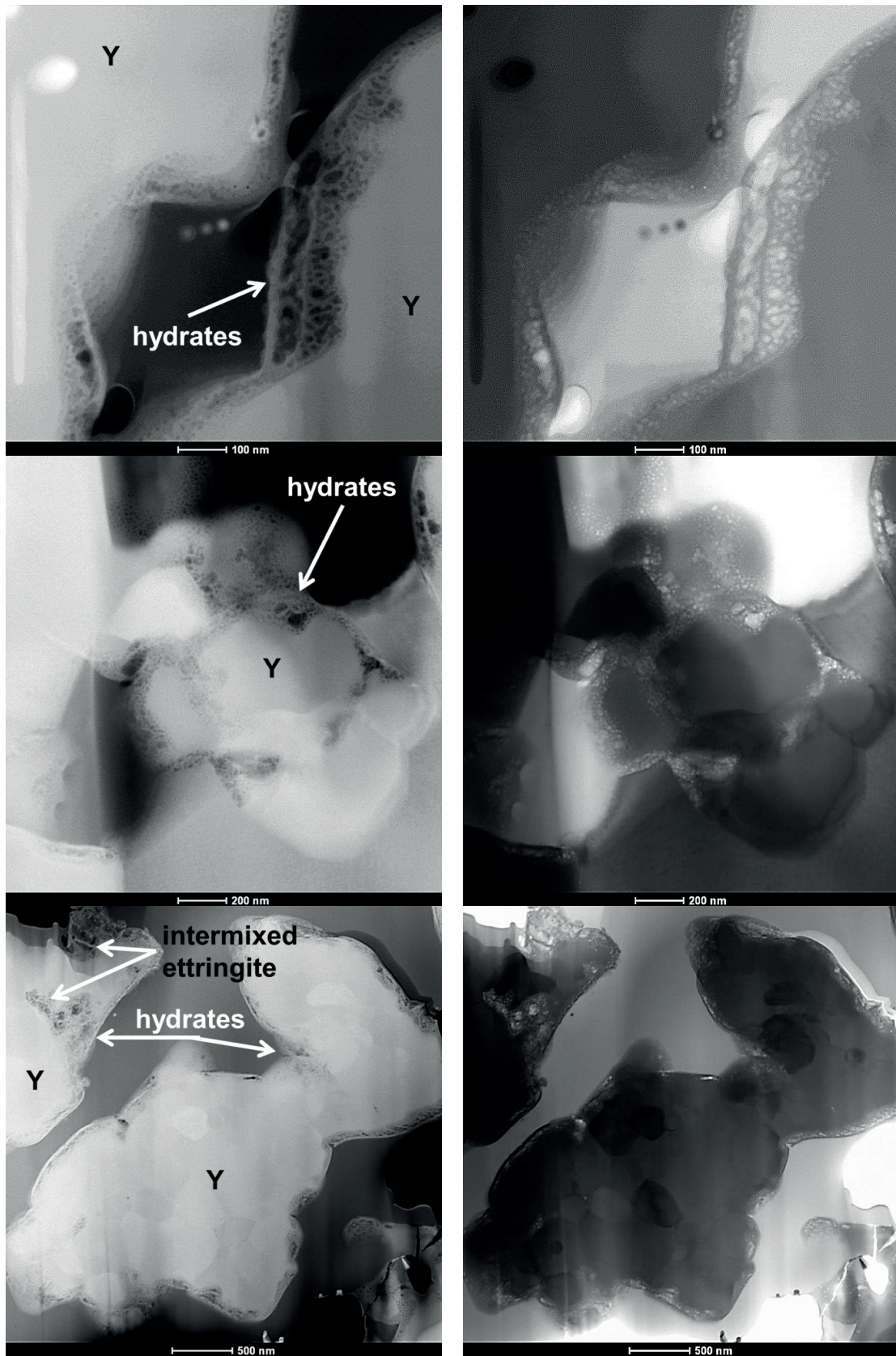


Figure 6.2-12 STEM images (up: HAADF image and down: BF image) of Y+G after 4 hours of hydration at 23 °C and a w/b ratio of 100; Y = anhydrous ye'elimite particles; hydrates = mix of phases including ettringite

### 6.2.6 Discussion

Considering the results obtained above, several aspects regarding the hydration kinetics need to be pointed out. First, the presence of gypsum clearly leads to similar hydration sequences and hydration kinetics in paste, independent of the composition and modification of the ye'elimite. The experiments in suspension showed that gypsum dissolves rapidly, causing high concentrations of calcium and sulphate ions, whereas the aluminium ion concentration is relatively low compared to the neat ye'elimite clinker (see Chapter 5). As a result, ettringite is instantly highly oversaturated which favours its instant precipitation. Consequently, the aluminium ion concentration stays low in solution. The evolutions of the calcium and sulphate ion concentrations are buffered by the steady dissolution of primarily solid gypsum (together with some ye'elimite). This means that all ions consumed by the reaction to form e.g. ettringite are replaced by the dissolution of an equivalent amount of anhydrous phases. In general, the evolution of the solution concentrations indicates that precipitation of ettringite continues as long as the high calcium and sulphate ion concentrations are maintained. On the contrary, the aluminium ion concentration steadily decreases throughout the "dormant" period until 300 minutes of hydration, highlighting the slower ye'elimite dissolution. The following sharp drop of the calcium and sulphate ion concentration marks the point of the solid gypsum depletion and coincides with the increase of the pH. The following short increase of the aluminium concentration indicates the ongoing (maybe accelerating) ye'elimite dissolution. A new chemical equilibrium between ettringite and monosulphate is reached.

By linking these findings to the experiments in paste, we conclude that the higher heat release during the dormant period is caused by the steady dissolution of ye'elimite and gypsum and simultaneously, the nucleation and growth of ettringite. Similar results for the hydration sequences and the formation of hydrates were reported in the literature [39] [114] [130] for synthetic ye'elimite and commercial CSA cements. The distinction between different hydration periods, as done for neat ye'elimite (Chapter 5), was not possible as the solution composition is buffered by the steady dissolution gypsum (+ ye'elimite). Increasing w/b - w/s ratios and the addition gypsum promote the steady nucleation and growth of ettringite. Thus, the steady consumption of ions from solution provides the driving force for the continuing and fast dissolution of the anhydrous phases. Those results are supported by the findings of Jansen et al. [240]. The authors showed that the presence of filler generally enhances the rate of the ettringite formation. In addition, he showed that the formation slows down but continues during the dormant period. Once the sulphate is depleted from the system (i.e. the solid gypsum and the sulphate ions in solution), monosulphate starts to form rapidly. For our case, this corresponds to the second heat peak release from the calorimetric curves. However, Jansen et al. [240] have shown that this peak can be present even if the amount of gypsum should be sufficient to form exclusively ettringite during all hydration stages. The second peak was not related to the formation of monosulphate, but "secondary" ettringite, even if gypsum has been already depleted. The time gap observed between the release of sulphate, from gypsum and ye'elimite dissolution, and the formation of the required quantities of ettringite able to bind the released sulphate can be explained by the presence of a metastable amorphous aluminium hydroxide. Jansen et al. [240] have shown that the recrystallization or transformation of the amorphous aluminium hydroxide resulted in the release of bound water and potentially of ab- or adsorbed sulphate. This led to a "secondary" formation of ettringite.

Our HR-SEM and STEM-EDS analyses of hydrated Y in the presence of gypsum indicate that the dissolution rate of ye'elimite is slowed down during the initial hydration period. However, as for neat Y a layer of hydrates was found with a bulk chemical composition close to that of the used anhydrous ye'elimite type. The formation of ettringite indicate that the hydration that the hydration follows the expected hydration path, i.e. ye'elimite react with gypsum and water to form ettringite and aluminium hydroxide. Contrary to the hydration of neat Y, we did not observe the formation of a foil-like calcium aluminate hydrate ( $CAH_{10}$ ) as long gypsum was present. In general, the lower reached aluminium concentration together with the higher calcium and sulphate ion concentration favours the formation of ettringite and aluminium hydroxide, whereas the formation of  $CAH_{10}$  and potentially amorphous aluminium hydroxide is reduced or even suppressed.

The low mobility of iron in the solution caused its instant precipitation and a strong enrichment in the initial hydrates layer, in the case of hydrating Fe-Y. It is probably that the instant precipitation of such an iron-rich layer, which also contains some aluminium, calcium and sulphate alter the solution composition and potentially provides additional nucleation sites. This in turn may partly contribute to the observed slightly faster hydration kinetics of Fe-Y+G compared to Y+G. However, the formed microstructure and type of formed hydrates is almost identical in both samples, independent of the ye'elimite type used. This demonstrates that it is possible to formulate cements with similar hydration kinetics and microstructural features by the addition of gypsum. The effect that is caused by the presence of iron can be mitigated or even suppressed. Moreover, this highlights the need to determine and understand the underlying hydration reactions.

### 6.3 Chemical shrinkage of ye'elimite alone and with gypsum

Figure 6.3-1 gives the measured and calculated chemical shrinkage progression of Y and Y+G. The evolution of the chemical shrinkage indicates a faster hydration for Y+G compared to Y, which is consistent with the isothermal conduction calorimetry data. The nearly complete hydration of Y was reached after 2 days, while Y+G has reached similar hydration degree already after 1 day. We continued the chemical shrinkage measurements up to 28 days. The results revealed a transient decrease or "expansion" at around 5 days for Y+G and at 11 days for Y. The addition of gypsum shifts the expansion to earlier periods and reduces its level profoundly. In order to understand the underlying phenomena, we calculated the evolution of the chemical shrinkage based on the degree of hydration "DoH" (see section 6.3.1) and assuming the hydration reaction according to Equation 1 for Y and Equation 2 for Y+G (equations provided in Chapter 2). The densities of phases used for the mass and volume balance calculations are summarized in Table 6.3-1.

Table 6.3-1 Density of the phases used for the calculations

Phase	Density g/cm <sup>3</sup>	Reference	Phase	Density g/cm <sup>3</sup>	Reference
Ye'elimite	2.607	[241]	Ettringite	1.778	[241]
Mayenite	2.690	[73]	Monosulphate Ms14H	1.986	[242]
Krotite	2.980	[73]	Monosulphate Ms12H	2.008	[242]
Grossite	2.860	[73]	Monocalcium aluminate Decahydrate	1.720	[73]
Anhydrite	2.968	[241]	Gibbsite	2.421	[241]



The level of the calculated chemical shrinkage matches the experimental data. The calculated chemical shrinkage continuously increases as it is direct proportional to the hydration degree. Hence, this cannot explain the non-monotonous development observed experimentally. The transitory chemical expansion was followed by a recovery period when the shrinkage increased reaching higher values compared to the initial ones. The recovery of the shrinkage suggests that the hydration continued and / or a phase assemblage with higher density developed over time.

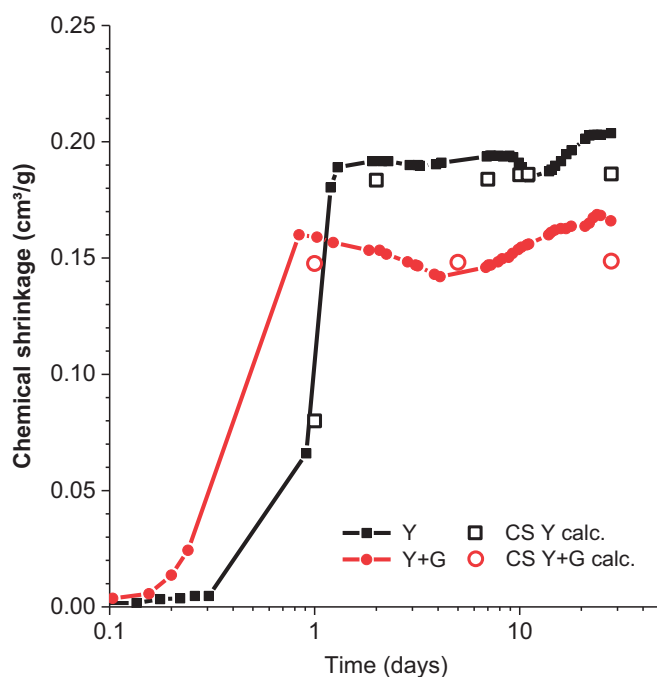


Figure 6.3-1 Measured and calculated chemical shrinkage, according to stoichiometric reactions, for Y and Y+G at w/b 2; the standard deviation between 5 samples was in average about 0.003 cm<sup>3</sup>/g

### 6.3.1 Hydrates formed and bound water content

The quantitative phase assemblage evolution determined by QXRD for ye'elimite hydrated at w/b 2 with (a) and without (b) the addition of gypsum is presented in Figure 6.3-2. It is important to note that traces of ye'elimite were detectable in both samples until 28 days of hydration, even at the applied w/b of 2. In contrast to the chemical shrinkage investigations for which the measurements were initiated after 1 hour after mixing, the QXRD and TGA analyses were started after 15 minutes. Already at this period of time, about 2% of ye'elimite was dissolved in the case of Y and about 6% of ye'elimite in the case Y+G. This means that the level of chemical shrinkage is slightly underestimated. No crystalline hydrates were detected by means of XRD but instead an amorphous material. It should be noted again that the applied solvent exchange protocol may cause some damage to the hydrates such as ettringite or monosulphate, resulting in their (partial) amorphisation. During the first 24 hours, the plain Y reached a DoH of 30% compared to almost 100% for Y+G. The main hydration products in Y were crystalline detectable hydrates such as ettringite, monosulphate and an amorphous phase. For Y+G it was almost exclusively ettringite and an amorphous phase. We derived the theoretical composition (dashed bars) of the fully hydrated binder by mass balance calculations. The content of ettringite is always close to the expected value. The detected quantities of monosulphate and aluminium hydroxide are by far lower, but reach in sum with the amorphous phase the expected level. This indicates the accuracy of the Rietveld analyses.

Effect of gypsum on the hydration of ye'elimite and the chemical shrinkage

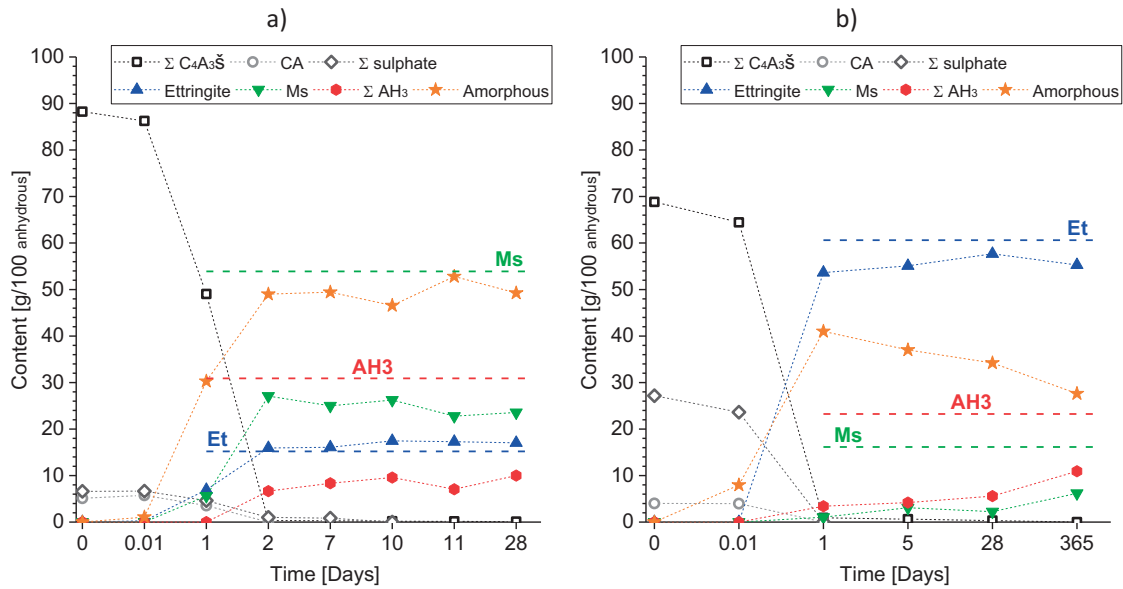


Figure 6.3-2 Hydrates assemblages of Y (a) and Y+G (b) at various hydration ages;  $\Sigma AH_3$  stands for the sum of quantified gibbsite and bayerite, Ms = monosulphate; the assumed relative error for each phase is about  $\pm 5\%$ .

Almost full hydration of Y was reached for after 2 days of hydration. Monosulphate was the main crystalline hydrate, followed by ettringite and traces of crystalline aluminium hydroxide (gibbsite and bayerite). The quantities of crystalline hydrates remained unchanged till about 7 to 11 days, during which primarily the monosulphate and amorphous phase contents vary. In contrast to the neat Y, the sample Y+G reached nearly complete hydration already after 1 day, with ettringite being the main crystalline detectable hydrate. The formation of monosulphate and primarily gibbsite-like aluminium hydroxide was only detected after 5 days. The content of ettringite remained almost constant up to 365 days, where the quantity of monosulphate and crystalline aluminium hydroxide almost doubled at the expense of the amorphous fraction. As stated before, the solvent exchange protocol can damage the hydrates such as ettringite or monosulphate [182]. Figure 6.3-3 presents a comparison of a fresh (untreated) slice and of a stopped powder.

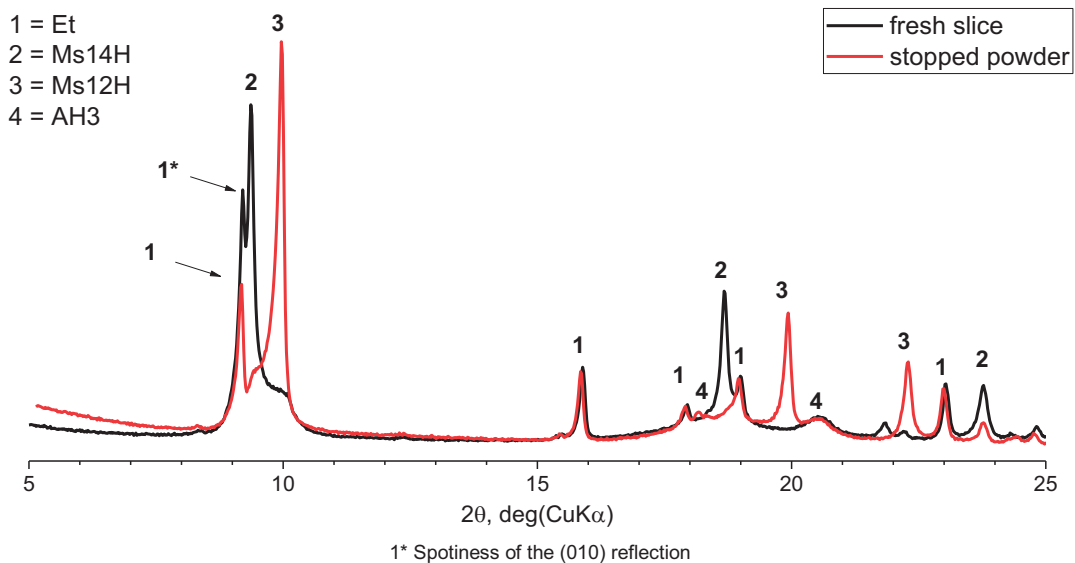


Figure 6.3-3 Fragmented diffraction patterns of hydrated Y as fresh slice or powder, after the solvent exchange, after 48 hours of reaction at w/b 2; Ms = monosulphate in a hydration state of 12 (12H) or 14 (14H) [242]



The diffractograms show that the hydration state of monosulphate is altered by the solvent exchange method, where the other hydrates such as ettringite or aluminium hydroxide are only slightly changed. The higher intensity of the (010) reflection labelled "1\*" of ettringite is related to the spottiness of the sample, e.g. the face of a large ettringite crystal exposed to the surface. All other reflections are almost identical by means of shape and intensity. Thus the quantification results are very similar for both samples. The detected ettringite and aluminium hydroxide contents were slightly reduced by about 5%, whereas the amount of monosulphate decreased by about 10%.

The evolution of the bound water (BW) content of both ye'elimite samples are shown in Figure 6.3-4. Plain Y reaches a maximum BW content of about 38.7% at 7 days. This is followed by a drop to 36.3% (difference of about 6%) and then it continuously increases until the end of the experiment. The sample Y+G reaches the highest BW content of around 42.2% at 1 day, followed by a drop to 41.1% (difference of about 3%) and a continuous increase until the end of the experiment. The timing of the observed decrease of the BW content correlates with that of the measured chemical expansion.

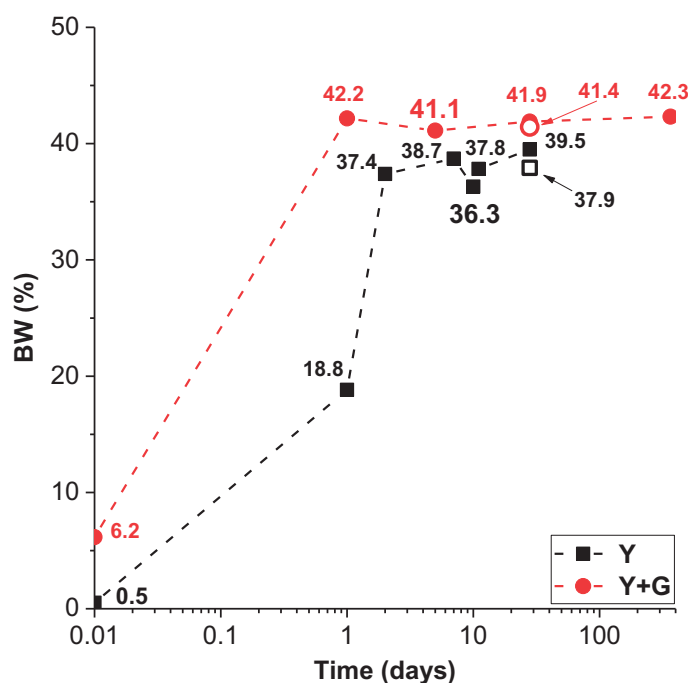


Figure 6.3-4 Evolution of bound water (BW) water per g of binder of Y  $\square$  and Y+G  $\circ$  represent the measured weight loss of the samples after finalisation of the respective chemical shrinkage measurement, i.e. 28 days (see also Figure 6.3-5)

Figure 6.3-5 presents the results of the TGA analyses for Y and Y+G at several hydration ages. Consistent to QXRD, we determined a mix of ettringite, monosulphate and gibbsite-like as well as amorphous aluminium hydroxide. In the case of Y+G, the hydrate assemblage consists almost entirely of ettringite with only traces of monosulphate and gibbsite-like aluminium hydroxide. Moreover, a shift of the ettringite peak maximum to higher decomposition temperatures is present, whereas the onset temperature remains the same. This is a result of the higher amounts of ettringite present. It is important to note that by SEM-EDS we further identified  $CAH_{10}$  in both samples. This phase decomposes over the same temperature range as ettringite [117] [227]. The decomposition of amorphous aluminium hydroxide covers an even broader range [224] [228] [243], starting from 60 °C to 100 °C.

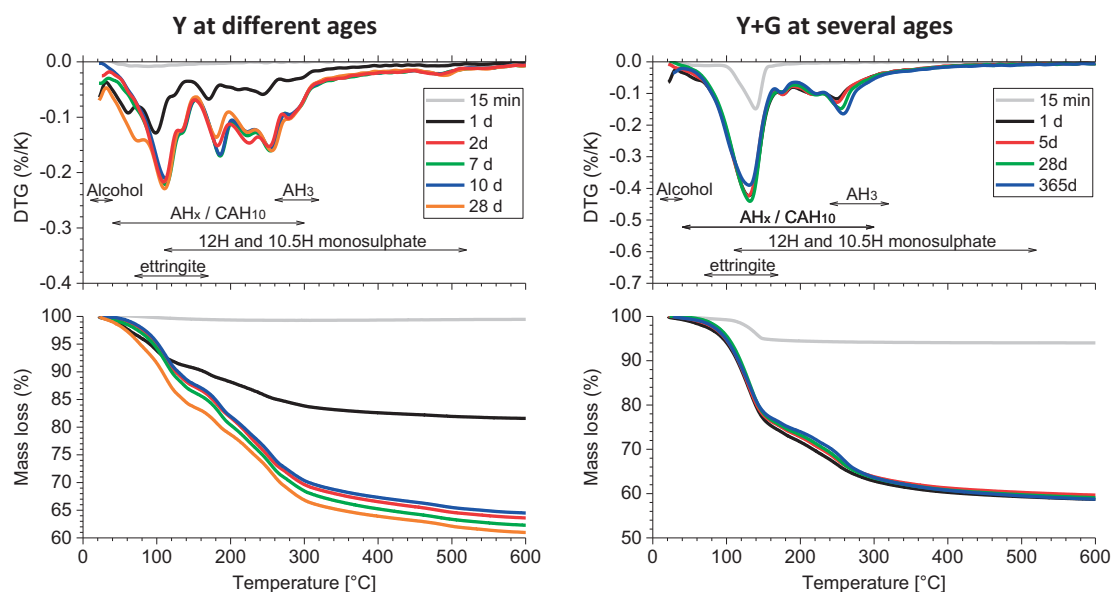


Figure 6.3-5 Differential thermogravimetric analysis (top) and mass loss (bottom) of Y and Y+G at several hydration ages;  $AH_x$  = amorphous aluminium hydroxide, hydration state of monosulphate with 12 or 10.5 water (H)

### 6.3.2 SEM-EDS analyses of hydrated samples

Figure 6.3-6 shows SEM micrographs of hydrated Y and Y+G samples after 28 days of hydration. The micrographs reveal a dense microstructure, with hydrates completely filling the space even at  $w/b$  2. Some anhydrous ye'elimite can be identified (bright areas). This is consistent to the XRD results. Additionally, some cracks were identified. The cracking is caused by the drying of the sample and the high vacuum used during the SEM-EDS analyses. We could distinguish two different fractions of hydrates, based on the two different areas identified. One is showing a bright grey level and the other one a dark grey level. This is consistent to other SEM studies on ye'elimite [129] and CSA [114].

Atomic ratio plots of the hydrated samples at several hydration ages are presented in Figure 6.3-7. Most points originate from mixtures of phases within the interaction volume rather than single phases. The plots indicate the presence of ettringite, monosulphate and aluminium hydroxide, which is consistent with the QXRD and TGA analyses. The presence of  $CAH_{10}$  was also supported by the SEM-EDS results. Based on the results, the bright grey level areas represents a mix of ettringite, monosulphate and  $CAH_{10}$ , intermixed with some aluminium hydroxide. The dark grey level area corresponds mainly to the aluminium hydroxide. Almost all measurement showed the presence of sulphur and occasionally of calcium in the aluminium hydroxide. This supports the reported affinity between aluminium hydroxide and sulphate.

The micrographs show a “better” separation of the bright and the dark grey level areas, indicating the separation between aluminium hydroxides and the other hydrates. Furthermore, it is also plausible that the high sulphate concentration originating in the gypsum dissolution, caused the formation of an aluminium hydroxide solid solution that contains sulphur.

Effect of gypsum on the hydration of ye'elimite and the chemical shrinkage

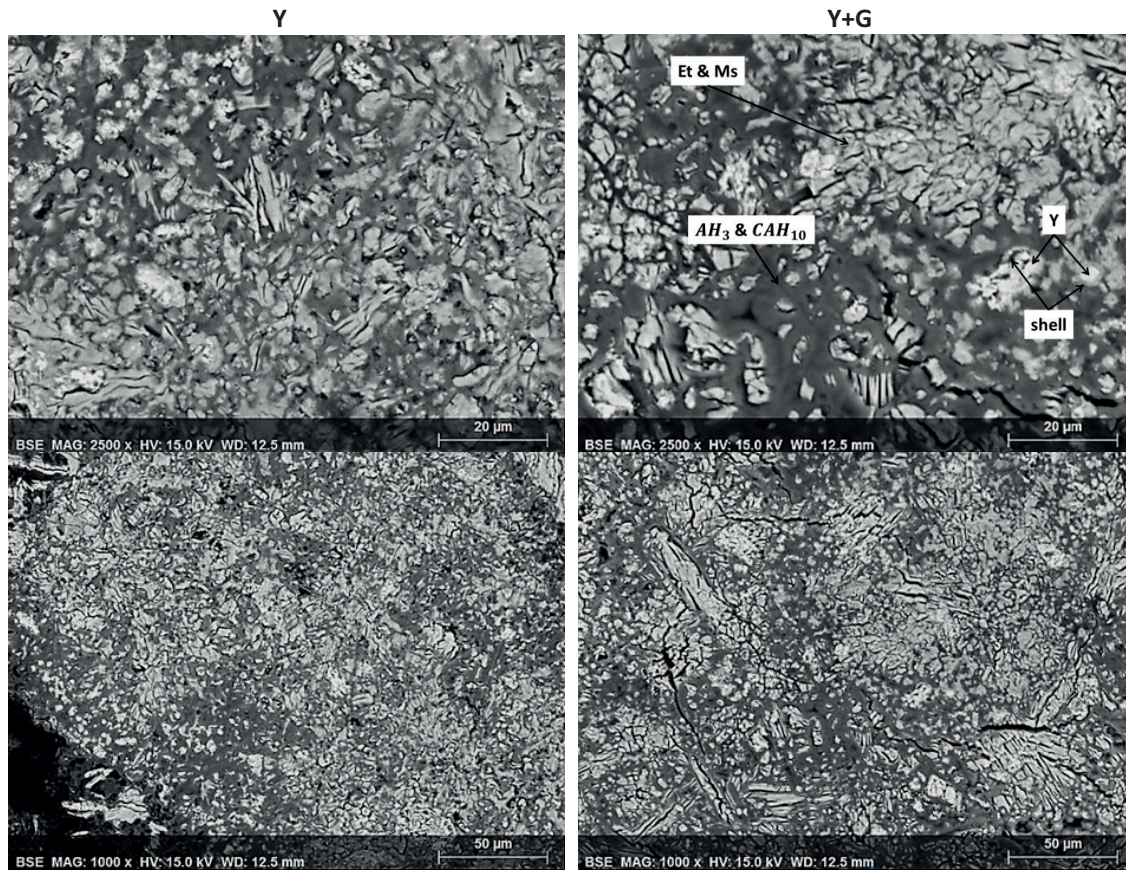


Figure 6.3-6 BSE micrograph of hydrated Y and Y+G after 28 days of hydration at w/b of 2; Et = ettringite, Ms= monosulphate, shell = layer of formed hydrates

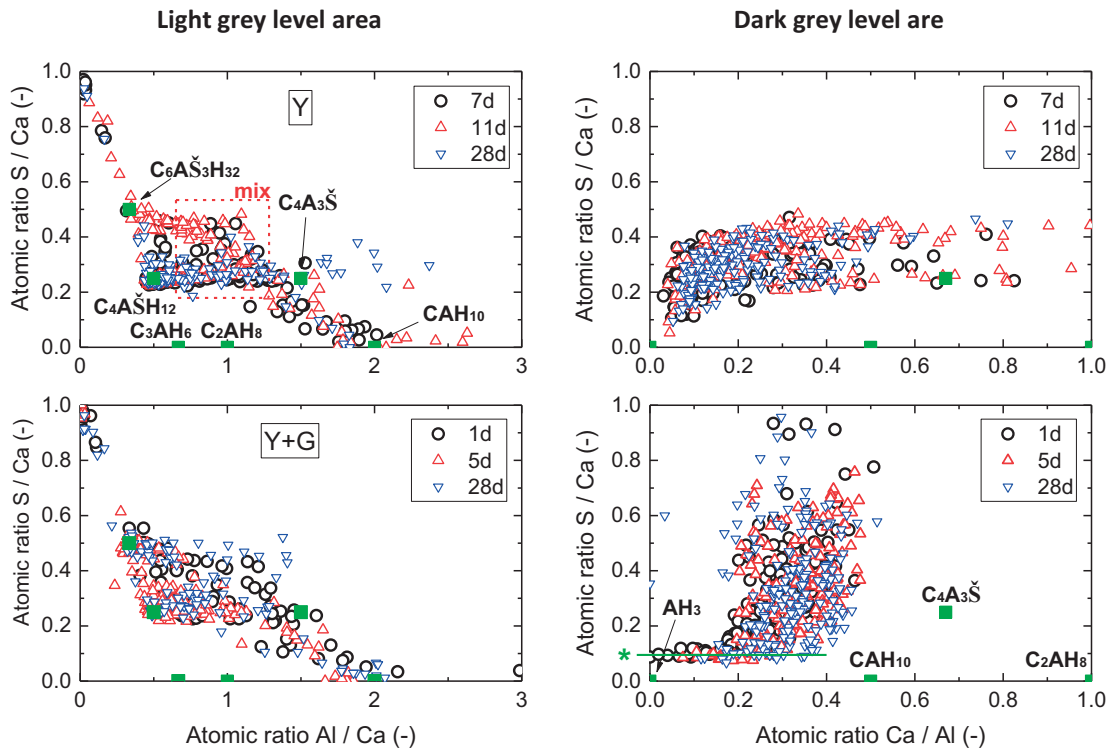


Figure 6.3-7 S/Ca over Al/Ca atomic-% ratios of the hydrated Y and Y+G; \* = S/Ca threshold ~ 0.10

### 6.3.3 Mass and volume balance calculations

To assess the chemical composition of the hydrate assemblage mass balance calculations based on TGA (bound and free water content) and QXRD data (quantity of crystalline phases and the amorphous fraction) were carried out. It is important to note that a part of the crystalline hydrates such as ettringite and monosulphate were damaged by the solvent exchange procedure during the sample preparation for TGA and XRD analysis. But the extent of the detected damage remains unknown.

The results indicated that the amounts of calcium and sulphur present in the amorphous phase were stable throughout the whole period considered for our experiments. The quantity of aluminium exhibit a minor but continuous drop and the water content varied significantly. Next, we calculated the density of the amorphous phase. This was done by assuming the formation of monosulphate for Y and ettringite for Y+G together with aluminium hydroxide and  $CAH_{10}$ . We have selected monosulphate or ettringite for Y and Y+G as those hydrates present the dominant crystalline phase in the respective binder. The calculations were carried out done using two approaches:

- First, by back-calculating the density of the amorphous phase from the measured chemical shrinkage ( $\rho_{CS}$ ) and based on the amounts of phases determined by QXRD-TGA. For that we used the densities given in Table 6.3-1. An average value, e.g. fitting best at all sample ages, for the density of amorphous aluminium hydroxide  $\emptyset \rho AH_3 \text{ amorphous}$  was calculated.
- Secondly, by forward-calculating the density based on the predicted mineralogical composition of the amorphous phase. In this second approach, the density of the amorphous  $AH_3$  ( $\rho AH_3 \text{ amorphous}$ ) was different among each sample and corresponded to the lowest value between the predicted and measured chemical shrinkage for all ages.

Table 6.3-2 shows the calculated densities of the amorphous phase at each hydration age,  $\rho_{CS}$  and the best fitting calculated average density of  $AH_3 \text{ amorphous}$ . The results provide, within the error of the applied methodology, similar density values for the amorphous phase. This indicates the consistency between the measured (chemical shrinkage and quantitative hydrates assemblage) and predicted data (mass and volume balance calculations).

Table 6.3-2 Calculated density ( $\text{g}/\text{cm}^3$ ) of the X-ray amorphous fraction X from the measured chemical shrinkage ( $\rho_{CS}$ ) and the determined hydrates assemblage composition ( $\rho_X$ )

		Y					
		1 d	2 d	7 d	10 d	11 d	28 d
$\rho_{CS}$		1.79	2.01	2.03	2.25	2.22	2.00
		With $\emptyset \rho AH_3 \text{ amorphous}$					2.55 $\text{g}/\text{cm}^3$
$\rho_X$		2.03	2.04	2.04	2.09	2.13	2.01
		With varying $\rho AH_3 \text{ amorphous}$					
		Y+G					
		1 d	5 d	28 d	365 d		
$\rho_{CS}$		1.79	1.84	1.81	--		
		With $\rho AH_3 \text{ amorphous}$			1.94 $\text{g}/\text{cm}^3$		
$\rho_X$		1.79	1.75	1.82	1.82		
		With varying $\rho AH_3 \text{ amorphous}$					

Most likely, the amorphous phase for Y is a mix of aluminium hydroxide and monosulphate which would explain the relative high calculated density of  $\emptyset \rho AH_3 \text{ amorphous}$  of about 2.25  $\text{g}/\text{cm}^3$ .



The lower calculated density  $\rho_{AH_3 \text{ amorphous}}$  of about 1.94 g/cm<sup>3</sup> for Y+G fit to a mixture of aluminium hydroxide,  $CAH_{10}$  and ettringite.

In general, the calculated densities of  $AH_3 \text{ amorphous}$  are within the ranges known for existing aluminium hydroxide types such as bayerite ( $\beta - Al(OH)_3$ ,  $\rho$  around 2.53 g/cm<sup>3</sup>) and gibbsite ( $\gamma - Al(OH)_3$ ,  $\rho$  around 2.40 g/cm<sup>3</sup>). For Y+G, the calculated densities of  $AH_3 \text{ amorphous}$  are closer to those of a mix of ettringite and  $CAH_{10}$ . Cuesta et al. [244] recently reported the formation of two types of aluminium hydroxide for the hydration of synthetic ye'elimite. One type was a gibbsite-like variety and the other one was an amorphous form, labelled "type 1"  $(CaO)_{0.04}(Al_2O_3)_3 \cdot 2.3H_2O$ , with a density of about 1.48 g/cm<sup>3</sup>. The presence of two types of aluminium hydroxide may occur here as well and would fit to the calculated density.

#### 6.3.4 Discussion

The chemical shrinkage measurements indicated that a chemical expansion occurs for both binders. The expansion seems to be caused by the partial release of the combined water. However, the chemical expansion observed was transitory, as the shrinkage returned to its original value afterwards. To assess the origin of the expansion several hydrated samples at different ages were investigated. The resulting hydration degree of the anhydrous phases was used to calculate the chemical shrinkage. The calculated shrinkage was found to increase continuously as it scales up to the ye'elimite hydration degree. Hence, the non-monotonous development observed experimentally cannot be explained. Moreover, the measured shrinkage values were always higher compared to the calculated values, except during the expansion period. This indicates that formed hydrates undergo a transformation reaction causing the release of bound water, followed by another reaction, which causes the uptake of water. This recovery started and proceeds even as all anhydrous phases are fully depleted. The transitory chemical expansion, followed by the increase of shrinkage values to the original ones, could neither be explained by the evolution of the anhydrous phases nor by the crystalline hydrates. A possible explanation could be that a gelatinous phase such as aluminium hydroxide starts to swell, once free space and water becomes available.

Aluminium hydroxide is one of the main constituents of the amorphous phase. It is known that it can be present in several varieties and at different hydration states. There have been extensive studies in the field of geochemistry, soil and applied clay science on the formation, composition and stability of aluminium (oxy-) hydroxides. In these studies, the term "gelatinous" is often used to refer to a non-crystalline, precursor form with high water content. As this gelatinous material crystallises, water is released [245] [246]. The type of the aluminium hydroxide formed, either amorphous or crystalline, depends on several aspects which will be highlighted in the following.

Factors which typically favour the formation of an amorphous form are high aluminium concentrations, high nucleation rates [224] [226], a pH below 11 [228] [243] or 10 [226], low temperatures and short curing times [228] [243]. The presence of sulphate ions leads to the faster nucleation of an amorphous aluminium hydroxide and sulphate ions seem to impede its crystallisation [225] [226] [247]. The reason for this is not yet known, but could be related the formation of solid solutions and the presence of sulphate ions in the structure. The impact of sulphate on the formation and crystallisation of the aluminium hydroxide was also observed in this study.

SEM-EDS and QXRD analyses indicated that the presence of gypsum had an impact on the composition, crystallization and growth of the amorphous aluminium hydroxide. Despite the fact that the crystalline fraction of alumina hydroxide did not considerably change after 7 days for the Y sample, it continuously increased in the case of Y+G. Thus, we assume that presence of gypsum may cause initially the precipitation of a sulphur-rich solid solution of amorphous aluminium hydroxide or the precipitating amorphous aluminium hydroxide with absorbed and / or adsorbed sulphate species onto its surface. Independent which mechanisms may be present, sulphate is released again into the solution as soon as its concentration drops below a critical value. In parallel, the crystallization of the aluminium hydroxide starts. This assumption is supported by the findings of Jansen et al. [240], who have shown that the recrystallization or transformation of the amorphous aluminium hydroxide, labelled "AH<sub>7</sub>", resulted in the release of bound water and potentially of ab- or adsorbed sulphate. This led to a "secondary" formation of ettringite. The composition of AH<sub>7</sub> was derived indirectly by mass balance calculations based on insitu hydration studies using QXRD and <sup>1</sup>H-TD NMR measurements. However, this high water content is rather questionable.

Several of the conditions found to favour the formation of amorphous aluminium hydroxide in the geochemical studies cited above also exist in hydrating ye'elimite-based binder such as CSA. CSA cements hydrate rapidly after contact with water, causing a rapid increase of solution concentrations. During the early hydration period, the pH of hydrating CSA system is about 10.0 to 10.5 [32] [114] and there is typically sulphate present in solution, even without the addition of extra gypsum. Other studies [32] report pH values of 8.5 in the presence of some admixtures. Therefore it is foreseeable that aluminium hydroxide is mainly present as amorphous phase. It can be also anticipated that this amorphous aluminium hydroxide will crystallise over time.

Other phases of particular relevance are the sulphate-free calcium aluminate hydrates. Calcium aluminate hydrates are often metastable and undergo phase transformation processes [73]. In Chapter 5 we reported that the rapid dissolution of ye'elimite resulted in the formation of foil-like CAH<sub>10</sub>. CAH<sub>10</sub> is a metastable phase, which is known to transform over time towards a thermodynamically more stable phase assemblage. This transformation causes the release of bound water, which may cause an expansion as described in Chapter 2 (see Table 2.3-2). Literature also reports the formation of water-rich C-A-H gel in hydration CAC, followed by its conversions to CAH<sub>10</sub> and the release of bound water [248] [249]. Especially the rapid hydration of krotite (the main phase of CAC and with a C / A ratio in the range of ye'elimite), results in the formation of amorphous calcium aluminate hydrates gel. Typically, also other metastable phases such as C<sub>2</sub>AH<sub>8</sub> or C<sub>4</sub>AH<sub>x</sub> are formed in the beginning. In general, all those phases convert over time to stable ones such as C<sub>3</sub>AH<sub>6</sub> and crystalline AH<sub>3</sub>, where a part of the bound water is released [248] [249].

The sulphate-bearing calcium aluminate hydrates such as monosulphate or ettringite can be present in different hydration stages as well. Bergold et al. [250] reported that a metastable water-rich monosulphate type is formed initially, labelled "AFm 16H" originating from the hydration of C<sub>3</sub>A in the presence of sulphate. The authors assumed that AFm 16H gradually dissolves and another monosulphate type with less water, "AFm 14H" (labelled Ms14 by us), precipitates. However, it is also possible that AFm 16H recrystallizes to AFm 14H which would cause the release of two moles water. It was further shown by Baquerizo et al. [242], that in the higher hydration state of monosulphate such as Ms14 is stable under saturated conditions over 20 °C and that once it dehydrates to the lower hydration state of Ms12 it does not rehydrate again.

As we have shown, monosulphate is mainly present as Ms14 in the fresh samples, whereas it is Ms12 and Ms10.5 in the stopped sample. It remains unknown whether Ms14 recrystallizes over time even under saturated conditions as during the chemical shrinkage measurements. However, as monosulphate represents one of the main hydration products for the Y sample, even such small changes may contribute to the measured chemical expansion. For example, the transformation from Ms14 to Ms12 would result in an expansion of about 4.4 g/cm<sup>3</sup> (using the densities provided by Baquerizo et al. [242]) and a water release of about 5.5 wt.%. This may explain the higher measured expansion and water release for Y compared to Y+G.

We could demonstrate that the transitory chemical expansion is linked with the recrystallization of previously formed amorphous phases. However, we can only speculate that the recovery is linked to the swelling of the amorphous aluminium hydroxide. The addition of gypsum can reduce the extent of the expansion. SEM micrographs show that even for tested high w/b of 2, the space was completely filled and that aluminium hydroxide is virtually the dominant phase, binding everything together. The chemical expansion and the release of bound water created space and enabled the access to water, which in turn led to the swelling of potentially amorphous “gelatinous” aluminium hydroxide still present in the system.

#### 6.4 General discussion

In this chapter, we investigated the impact of gypsum on the hydration and on the chemical shrinkage of ye'elimite. First, the addition of gypsum causes a harmonization of the hydration kinetics for Y and Fe-Y, which is important and beneficial for the development of robust and stable CSA or BYF cements. Gypsum further accelerates the hydration and modifies the hydrates assemblage by favouring the formation of ettringite rather than monosulphate. The heat release measurements indicated that in the presence of gypsum complete hydration was reached within 24 hours, whereas in the absence of gypsum it took 40 hours to reach the same hydration degree. Furthermore, the calorimetric measurements in paste have revealed a steady higher heat release during the dormant period in the presence of gypsum compared to the neat ye'elimite. The higher w/b and w/s ratios promote the steady formation of ettringite, where the solution composition is buffered by the continuing dissolution of the anhydrous phases.

The experiments carried out in diluted suspensions were done to assess the impact of gypsum in more detail. The rapid dissolution of gypsum leads to a strong increase of the calcium and sulphate ions and decrease of the aluminium ion concentrations compared to the ye'elimite clinker. These conditions favour the fast formation of ettringite and keep the aluminium ion concentrations in solution low. The evolution of the calcium and sulphate ion concentrations are buffered by the steady dissolution of solid gypsum. In general, the evolution of the solution concentrations indicates that precipitation of ettringite continues as long as the high calcium and sulphate ion concentrations are maintained. On the contrary, the aluminium ion concentration steadily decreases throughout the “dormant” period. This indicates that the dissolution rate is lower than the precipitation of ettringite. Once the sulphate is depleted (e.g. gypsum and form solution), the hydration follows the same sequences as for neat ye'elimite.

The chemical shrinkage analysis revealed a transitory chemical expansion which was followed by the recovery of shrinkage to its maximum values and eventually surpassing it. The chemical expansion could be linked to the recrystallization of previously formed amorphous phases, mainly that of aluminium hydroxide. The recrystallization causes the release of combined water. In addition, is possible the hydration state of other phases such as monosulphate and  $CAH_{10}$  changes over time, which could lead to the release of bound water as well. The recovery of the shrinkage suggests that the hydration continued and / or a phase assemblage with higher density developed over time. Most likely, the shrinkage recovery is related to the water uptake and swelling of the amorphous "gelatinous" aluminium hydroxide. The understanding of the origin of the chemical shrinkage and expansion is of high importance for the development of CSA and BYF based cements. For example, Morin et al. [251] reported the presence of a strength plateau in several BYF cements after the depletion of ye'elimite, while other anhydrous phases like belite and ferrite continued to react. The origin of the strength plateau remains unclear as it is not related to any slowdown of the reaction. It is possible that a transformation reaction or a chemical expansion occurs in parallel to the ongoing hydration of e.g. belite.





## 7 Hydration of an iron-rich ye'elimate and effect of mayenite

The results of this chapter will be reported in peer reviewed journal(s):

- Cement and Concrete Research
  - o Title: Hydration of an iron-rich ye'elimate and effect of mayenite
    - Draft under preparation

### CONTENTS

---

<b>7</b>	<b>HYDRATION OF AN IRON-RICH YE'ELIMATE AND EFFECT OF MAYENITE .....</b>	<b>111</b>
<b>7.1</b>	<b>SUMMARY – EXPERIMENTS CARRIED OUT IN CHAPTER 7 .....</b>	<b>112</b>
7.1.1	HYDRATION KINETICS IN PASTES.....	113
7.1.2	EFFECT OF MAYENITE ON THE HYDRATION KINETICS OF NEAT YE'ELIMATE CLINKER.....	114
7.1.3	EFFECT OF MAYENITE ON THE HYDRATION KINETICS IN THE PRESENCE OF GYPSUM.....	116
<b>7.2</b>	<b>IMPACT OF MAYENITE ON THE SOLUTION COMPOSITION.....</b>	<b>117</b>
7.2.1	EXPERIMENTAL RESULTS.....	118
7.2.2	EFFECT OF MAYENITE ON THE HYDRATION KINETICS OF YE'ELIMATE ALONE AND WITH GYPSUM.....	121
<b>7.3</b>	<b>EFFECT OF IRON ONTO THE HYDRATES MICROSTRUCTURE AND COMPOSITION .....</b>	<b>122</b>
<b>7.4</b>	<b>DISCUSSION.....</b>	<b>127</b>

---

Understanding the origin the different hydration kinetics of stoichiometric and iron-rich solid solution ye'elimite is the main motivation for the work presented in this chapter.

Chapters 2 and 4 report the impact of minor elements especially of iron on the formation and reactivity of CSA and BYF cements. The incorporation of iron into ye'elimite results in the stabilisation of a pseudo-cubic symmetry at ambient temperatures. However, the thermal stability was decreased compared to stoichiometric ye'elimite. Consequently, the iron-bearing solid solution ye'elimite starts to decompose yielding mayenite, whereas the stoichiometric ye'elimite remains stable under similar conditions. Previous to this work, it was often assumed that there was a link between the presence of iron, the polymorphism of ye'elimite and the hydraulic reactivity. The objective of this chapter is to characterise and understand the correlation between the substitution of aluminium by iron within the crystal structure of ye'elimite, the polymorphism and the hydraulic reactivity. We further tried to assess the effect of mayenite on the hydration mechanisms of ye'elimite at the different hydration stages determined earlier. For this purpose, the hydration kinetics at varying w/b ratios were studied in pastes and supplemented by experiments in suspension. The experiments carried out in suspensions enable the characterisation of the dissolution of the anhydrous phases, the evolution of the solution composition and the resulting composition and morphology of the hydrates formed.

## 7.1 Summary – Experiments carried out in Chapter 7

The Y and Fe-Y clinker from the S3 series were used. Two sets of experiments were carried out on blends of neat Y and Fe-Y clinker with the addition of 0.5%, 1% and 2 % mayenite and in the presence of gypsum. Similar to the case of stoichiometric ye'elimite from Chapter 5, the investigations were conducted in pastes and in suspensions in order to evaluate the effect of the water to binder (w/b) ratio, the availability of surface area and the evolution of the phase assemblage as well as the solution concentrations. The experiments are summarised in Table 7.1-1. The most relevant results are reported in this chapter. Other results can be found in the annex – part V.

Table 7.1-1 Experimental matrix

		Paste ± Qz	Suspension	
		w/b 0.5 - 40	w/b 40	w/b 100
Calorimetry	Continuous measurement 0 - 48 h	x		
Conductivity and pH	Continuous measurement 0 - 24 h		x	x
QXRD + TGA	Single sample at the end	x		x
	Samples taken during 24 h		x	
Mass balance calculations	All	x	x	x
ICP-OES	Samples taken during 24 h		x	x
Modelling	Samples taken during 24 h		x	x
HR-SEM	Samples taken during 7 min			x
STEM-EDS	Samples taken during 3 h			x
SEM	Samples taken during 24 h	x		

### 7.1.1 Hydration kinetics in pastes

It is often reported that the iron-rich solid solution ye'elimite hydrates faster compared to stoichiometric one. This is shown in Figure 7.1-1 together with a simplified scheme highlighting two of the five defined hydration periods presented in Chapter 5. Not only are the dormant period but as well the acceleration and main hydration period shortened for Fe-Y compared to Y. It is important to understand what causes those differences and how is this related to the formation of iron-rich solid solution ye'elimite. To obtain first insights, we compared the hydration kinetics of the two ye'elimite types at water to binder ratios ranging from 0.5 to 40, similar to the approach presented in section 5.4.4. The composition of the formed phase assemblages is available in the annex part V, Figure 8.8-10 to Figure 8.8-20.

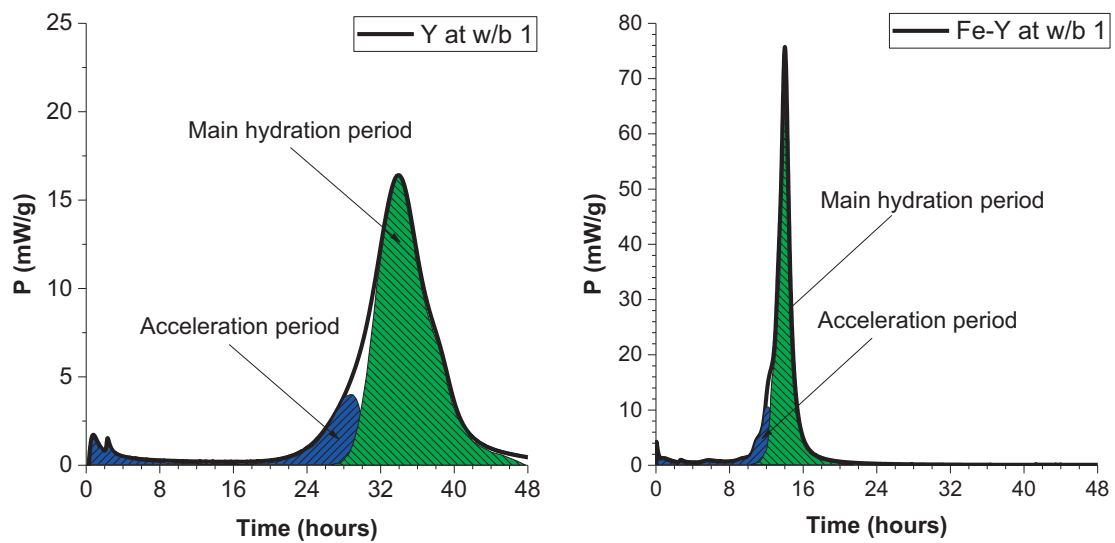


Figure 7.1-1 Rate of heat evolution Y, Fe-Y and scheme for the underlying reactions; blue = primarily the formation of ettringite,  $CAH_{10}$  and amorphous aluminium hydroxide; green = primarily the formation of monosulphate and gibbsite-like aluminium hydroxide

Figure 7.1-2 shows the results from calorimetry measurements for the neat Y and Fe-Y clinker at several w/b ratios. For w/b ratios up to 5, the dormant and the acceleration period are shorter for Fe-Y compared to Y. However, at higher w/b ratios such as 10 to 40 the hydration rates are almost identical. This demonstrates that the hydration kinetics and sequences are altered.

For example, we observe only a single sharp peak on the calorimetry curves for the Fe-Y at lower w/b ratios. On the contrary, this peak starts to broaden at high w/b ratios such as 10, forming a left-hand shoulder which indicates the acceleration period. The former main hydration peak is shifted from about 14 hours at w/b 1 to 22 hours at w/b 40 for Fe-Y. The fact that the differences seen at low w/b disappear at higher w/b, suggests that the polymorphism (alone) cannot explain the features observed. Furthermore, in some cases no acceleration was detected for solid solution ye'elimite even when the cubic form was present [184]. The other main difference, beside the polymorphism, between both clinkers is the **presence of mayenite in the Fe-Y** clinker which may explain the experimental results.

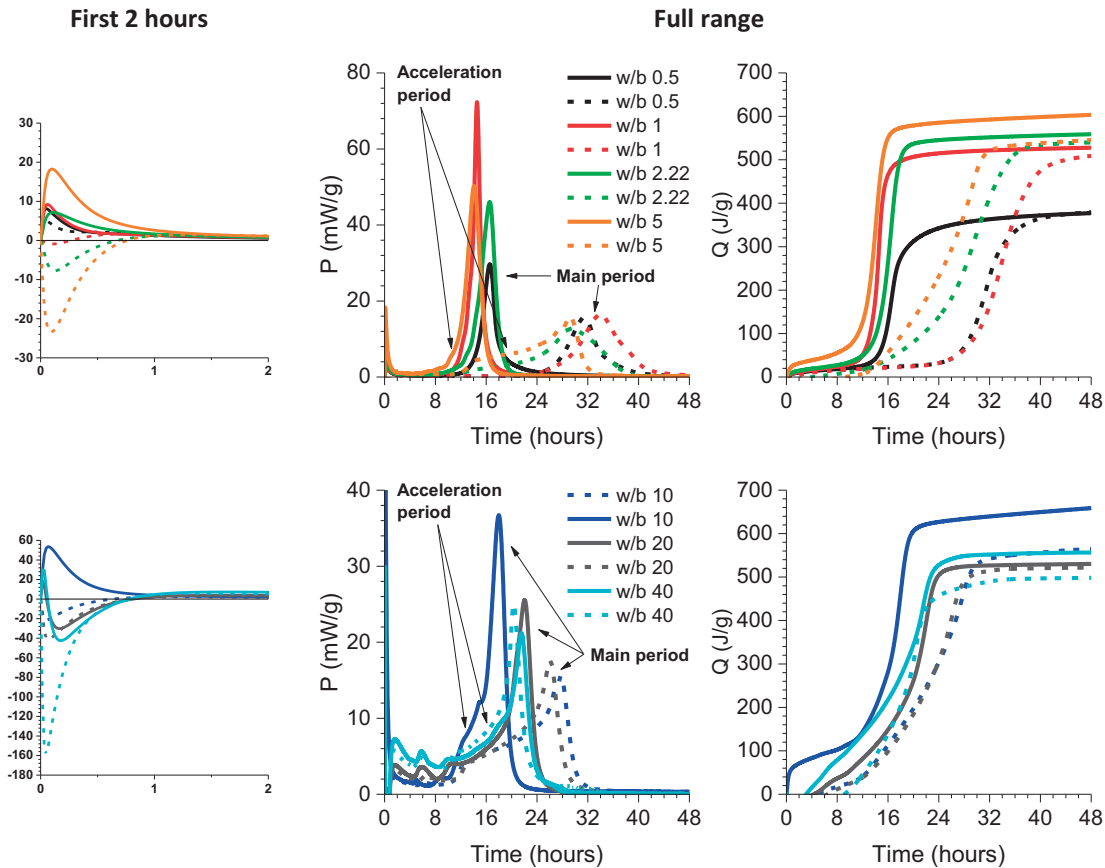


Figure 7.1-2 Rate of heat evolution and cumulative heat release for hydrating Y and Fe-Y; continuous line = Fe-Y and dashed line = Y; marking the duration of the two main reactions for Y

### 7.1.2 Effect of mayenite on the hydration kinetics of neat ye'elimite clinker

The hydration kinetics of Y and Fe-Y were analysed at a w/b ratio of 0.5 and 2, and with the addition of 0.5, 1 and 2 wt.% synthetic mayenite. The results are presented in Figure 7.1-3 and Figure 7.1-4. It must be noted that for the purpose of these investigations fine ground mayenite was added to the ye'elimite samples, whereas the mayenite present in the Fe-Y clinker is embedded in the ye'elimite particles. Therefore, we assume that the accessibility of mayenite can be different.

The hydration kinetics of Y are sensitive to the amount of mayenite and to the w/b ratio used. Only an exothermic peak was observed in the mayenite containing samples during the first 30 minutes of hydration, where the intensity rises with increasing mayenite additions. The impact on the main hydration peak is more complex. At a mayenite dosage of 0.5 wt.% and a w/b ratio of 0.5 a marginal acceleration of the hydration kinetics occurred. On the contrary, the addition of 0.5 wt.% mayenite had almost no impact at a w/b of 2. Already the addition of 1 wt.% mayenite was sufficient to perfectly match the hydration pattern of Fe-Y at both tested w/b ratios. Additionally, a small peak appears between 6 to 9 hours that becomes more visible with increased mayenite dosage. The cumulative heat release gives higher values for samples prepared with a w/b ratio of 2 compared to those prepared with a w/b ratio of 0.5. This is due to the higher hydration degree and is in line with what was reported by us in [33] (see also annex – part V) as at the lower w/b ratios the hydration is limited by the lack of water and space.

Hydration of an iron-rich ye'elimite and effect of mayenite

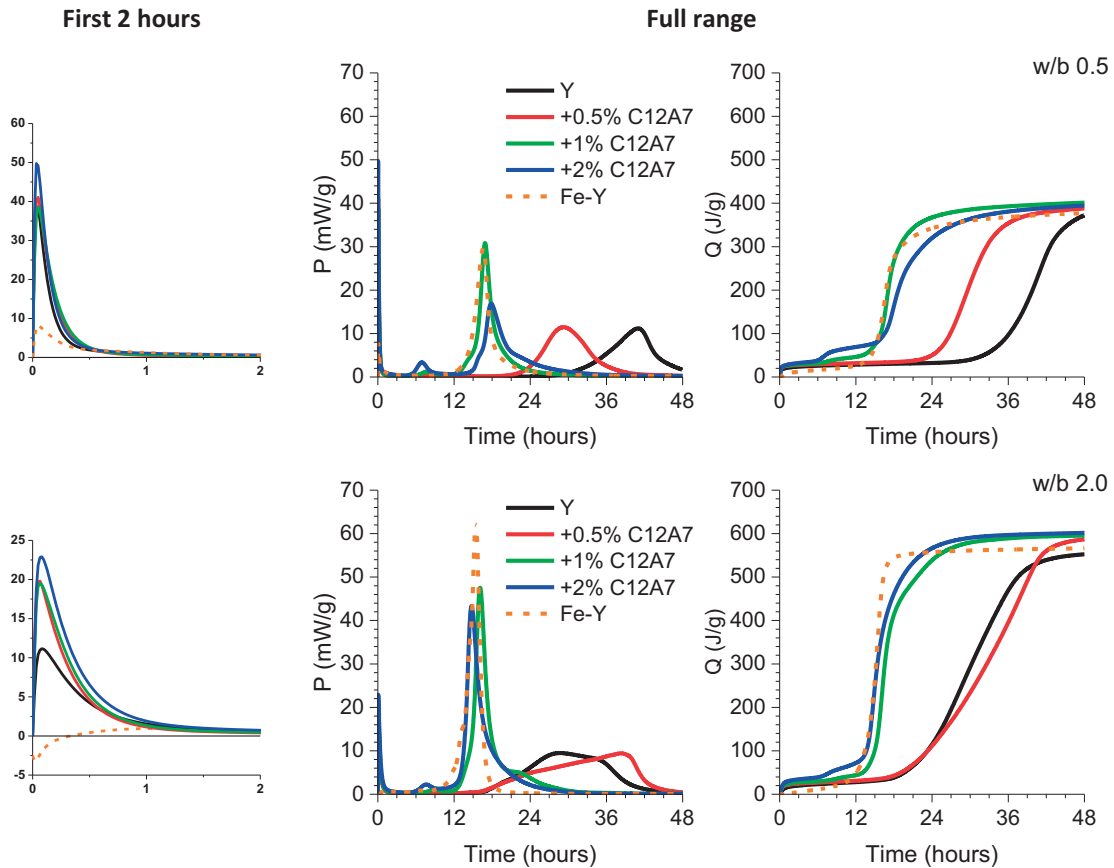


Figure 7.1-3 Rate of heat evolution and cumulative heat release of Y and Y with the addition of 0.5 to 2 wt.% mayenite ( $C_{12}A_7$ ) at a w/b of 0.5 and 2; dashed line = Fe-Y tested for the respective w/b ratio

Figure 7.1-4 gives the incremental and cumulative heat release for the addition of mayenite to Fe-Y. The data show that the addition of mayenite slightly retards the hydration kinetics, regardless of the w/b used. The effect was somewhat similar to what was observed for the addition of 2 wt.% mayenite to Y for a w/b of 0.5 compared to the addition of 1 wt.%. The deceleration of the reaction leads a longer dormant and to an extended acceleration period.

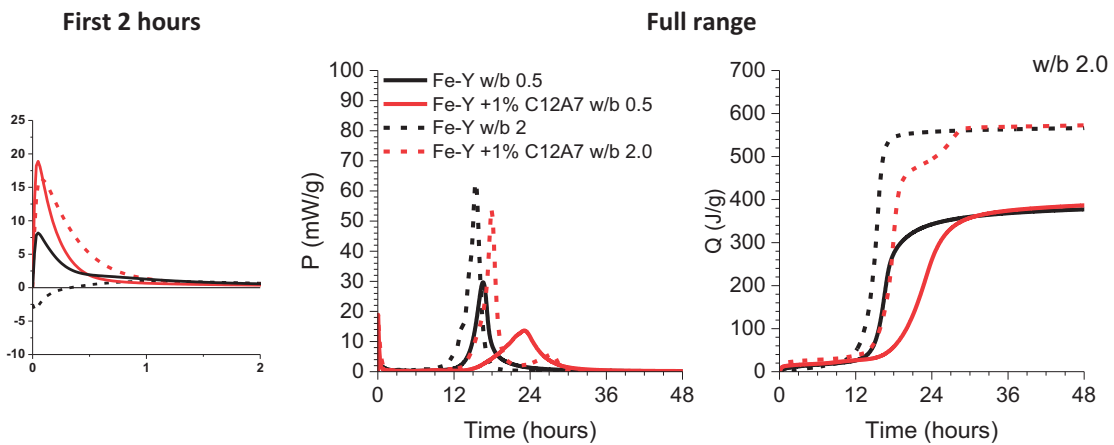


Figure 7.1-4 Rate of heat evolution and cumulative heat release of Fe-Y and Fe-Y with 1 wt.% mayenite ( $C_{12}A_7$ ) at w/b 0.5 (continuous line) and at w/b 2 (dashed line)

Our results indicate that the addition of 1% mayenite to the neat Y clinker was sufficient to replicate a similar hydration pattern to the Fe-Y clinker, where the mayenite is formed from the decomposition of ye'elimite. We assume that the rapid dissolution of mayenite causes higher calcium and aluminium concentrations in solution, and thus a higher oversaturation with respect to ettringite rather than of monosulphate. With this in mind we conclude that the polymorphism is not (primarily) responsible for the different hydration kinetics observed.

### 7.1.3 Effect of mayenite on the hydration kinetics in the presence of gypsum

The effect of mayenite on the hydration kinetics of ye'elimite in the presence of gypsum was tested using binders composed of 64% Fe-Y clinker and 36% gypsum with 1% mayenite. Similar to the previous investigations, all the tests were carried out at w/b of 0.5 and of 2. A ye'elimite to gypsum molar ratio of 2 was chosen to ensure sufficient gypsum is available to form just ettringite and aluminium hydroxide, i.e. to avoid monosulphate. The results presented in Figure 7.1-5 demonstrate that the retarding effect of mayenite on the hydration of Fe-Y clinker could be fully mitigated by the addition of gypsum. Additionally, the simultaneous presence of mayenite and of gypsum shortens the dormant period marginally by 1 hour for both w/b ratios investigated.

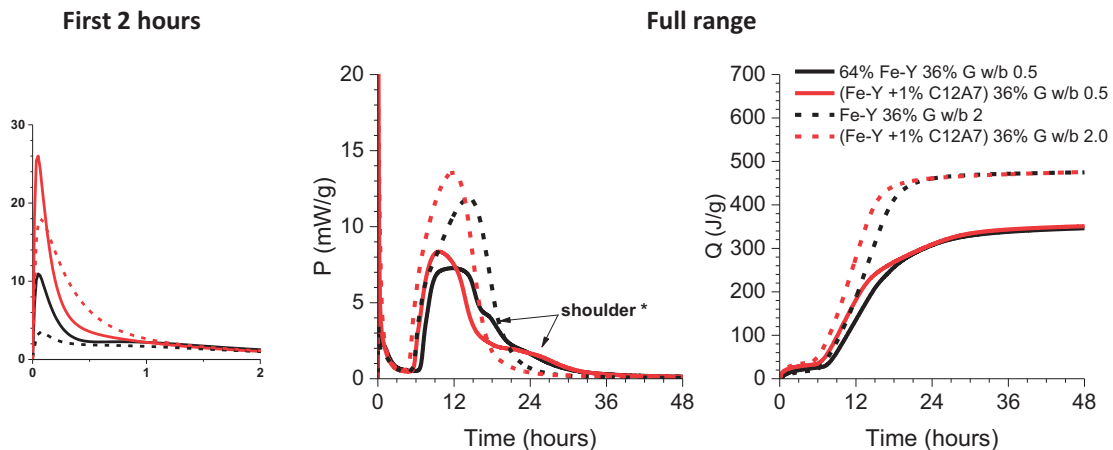


Figure 7.1-5 Rate of heat evolution and cumulative heat of Fe-Y+G and Fe-Y+G with 1 wt.% mayenite ( $C_{12}A_7$ ) at a w/b 0.5 (solid line) and 2 (dashed line)

The formation of second peak or more precisely a right-hand side shoulder can be observed. This shoulder peak is shifted to earlier times in the presence of mayenite resulting in a full overlapping with the main hydration peak. Jansen et al. [39] [240] found that during this period, the metastable amorphous aluminium hydroxide transforms to a gibbsite-like type, and the bound sulphate is released, which enables the second period of the ettringite formation. The hydration of mayenite accelerates the sulphate depletion, e.g. from solution and gypsum depletion, which in turn shifts the onset of the transformation of the amorphous aluminium hydroxide to an earlier period.



## 7.2 Impact of mayenite on the solution composition

We studied the hydration of Fe-Y in more detail (following the methodology used for Y in Chapter 5), to understand the impact of present mayenite on the dissolution and precipitation reactions. Figure 7.2-1 shows the solubility curves at two selected sulphate ion concentrations of 0.02 mM/l and 3.5 mM/l. The concept was briefly discussed in Chapter 2. Generally, higher sulphate ion concentrations shift the solubility lines of the sulphate-free calcium aluminate hydrates to higher calcium ion concentrations, where the slope remains almost the same. We further include the trendline for dissolution of mayenite. This phase has a lower  $Al / Ca$  ratio than ye'elimite. Thus, it intersects with the solubility lines for ettringite, monosulphate and the sulphate-free calcium aluminate hydrates at lower aluminium ion concentrations. Oversaturation levels, with respect to those hydrates, will be reached faster, favouring their precipitation. As a result, the hydration kinetics may be accelerated. Especially the faster formation of ettringite or monosulphate would result in the earlier depletion of sulphate ions from solution and consequently, the earlier onset of the acceleration period.

The formation of sulphate-free calcium aluminate such as  $C_2AH_8$  or  $C_3AH_6$  is rather unlikely. For pure ye'elimite, high aluminium ion (24 mM/l) and calcium ion (16 mM/l) concentrations would be needed to reach the solubility line of  $C_2AH_8$  at a sulphate concentration of 3.5 mM/l. For  $C_3AH_6$  even higher aluminium ions concentrations of about 28 mM/l (calcium about 18 mM/l) would be needed. However, these values are profoundly reduced if mayenite is present. The intersects for  $C_2AH_8$  and  $C_3AH_6$  are shifted to aluminium ion concentrations around 13 mM/l (calcium about 11 mM/l) and 15 mM/l (calcium about 13 mM/l), respectively. This can have a significant effect on the hydration kinetics as  $C_2AH_8$  nucleates more easily and rapid compared e.g.  $CAH_{10}$  [73]. As the dissolution and nucleation processes are coupled reactions, any factor favouring one of them will in turn cause the acceleration of both [113].

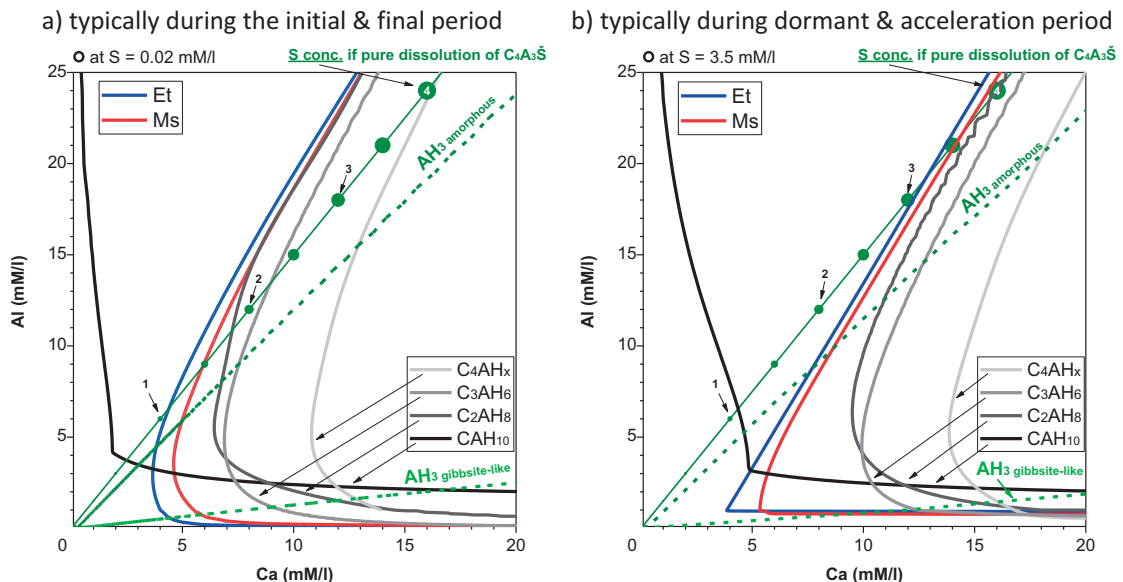


Figure 7.2-1 Solubility curves at 25 °C for the system  $CaO - Al_2O_3 - SO_3 - H_2O$  at a sulphate concentrations of 0.02 mM/l (a) and 3.5 mM/l (b)

7.2.1 Experimental results

Figure 7.2-2 presents the evolution of the pH, the conductivity and the element concentrations in solution of Y and Fe-Y at two different w/b ratios. The hydration sequences are similar for both ye'elimite types and applied w/b ratios but the kinetics are different. Fe-Y hydrates always faster compared to Y which is also shown by the higher initial pH and conductivity signal. The evolutions of the concentrations are very similar at both tested w/b ratios.

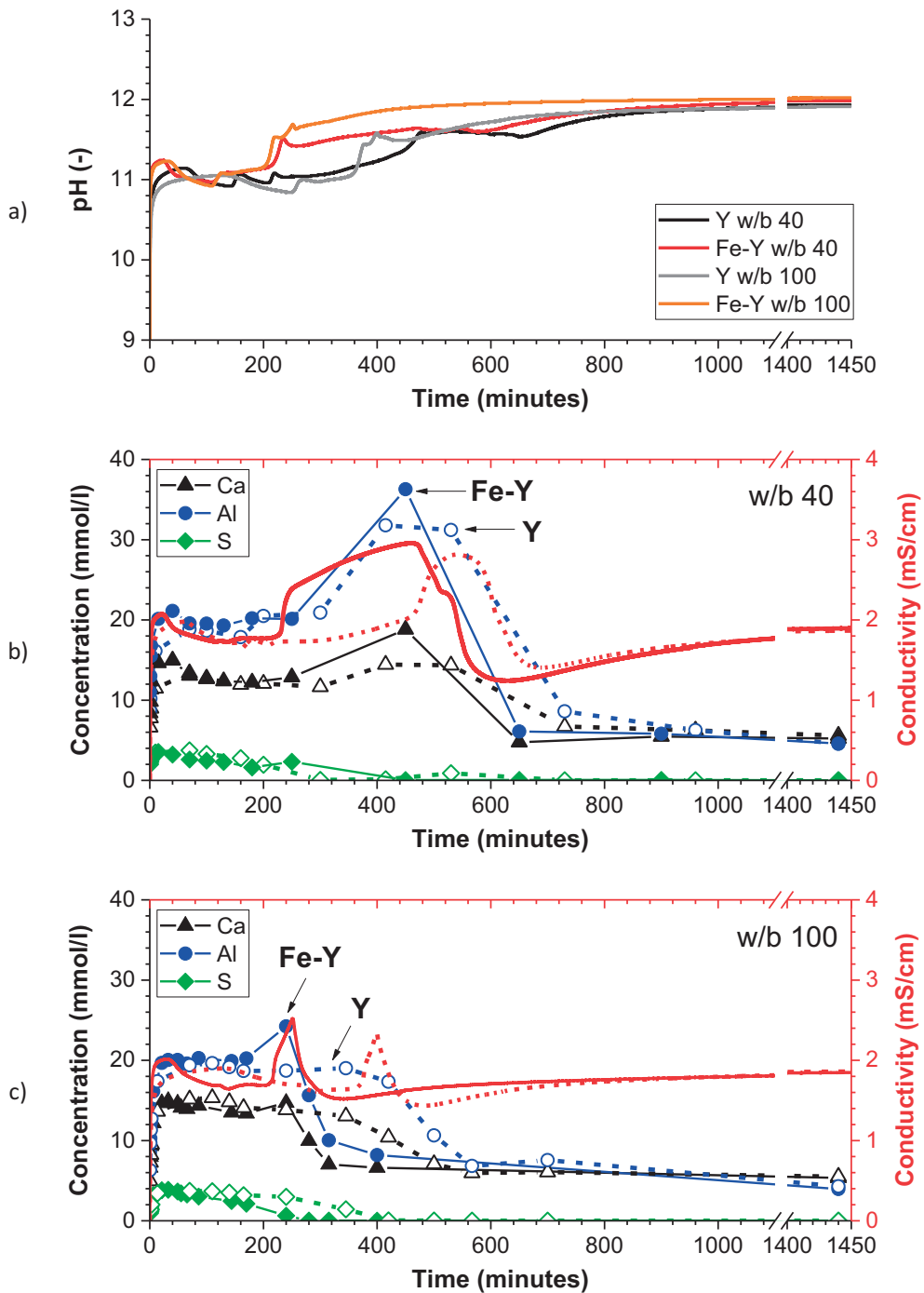


Figure 7.2-2 Evolution of the pH (a), the conductivity and solution composition for Y and Fe-Y at w/b 40 (b) and 100 (c); Fe always below detection limit

To highlight the differences during the early period, the same data is plotted in logarithmic scale in Figure 8.8-25. During the first minutes of hydration Fe-Y reveals higher calcium and aluminium ion concentrations compared to the Y samples (highlighted for w/b 40), whereas the concentration of sulphate is almost identical. The concentration of iron was always below the detection limit, indicating its instant precipitation. The concentrations are almost identical with the onset of the dormant period. The origin and mechanisms behind each hydration period were presented in discussed in Chapter 5. We will focus here the comparison between Y and Fe-Y.

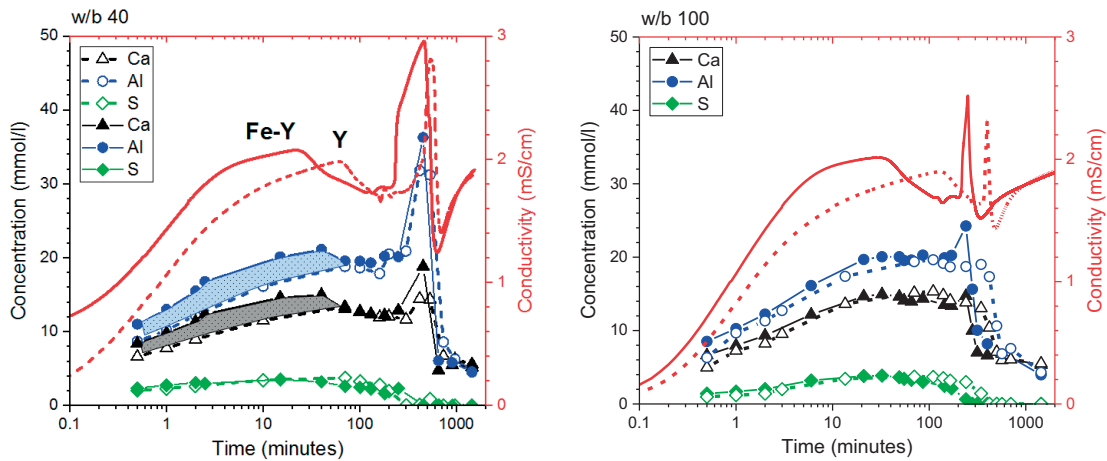


Figure 7.2-3 Evolution of the conductivity and the solution composition for Y (dashed line and empty symbols) and Fe-Y+G (continuous line and filled symbols)

The higher initial concentrations of calcium and aluminium for Fe-Y strengthens our hypothesis that the rapid dissolution of mayenite, i.e. a sulphate-free calcium aluminate, alters the solution composition and with that the hydration kinetics. The higher initial calcium and aluminium ion concentrations promote the formation of ettringite, causing the faster depletion of sulphate ions from solution and thus, the dormant period is shortened.

Figure 7.2-4 present the updates solubility curves from Figure 7.2-1 with the measured concentrations presented in Figure 7.2-3. Generally, the measured concentrations fall in between the solubility line of amorphous aluminium hydroxide and that of “dissolving” ye’elimite. It was shown in Chapter 5 that instantly after the contact with water the precipitation of hydrates is initiated. This first hydrate phase is X-ray amorphous and has a bulk chemical composition close to that of the dissolving ye’elimite type, with a slight enrichment of aluminium (or iron in the case of Fe-Y, see section 7.3).

The measured solution compositions are perfectly in line with those results. The solubility line of amorphous aluminium hydroxide in never passed (except during the final period), which demonstrates that it is always oversaturated. This keeps the aluminium ion concentration in solution high and in turn favours the formation of ettringite and monocalcium aluminate hydrate rather than of monosulphate. Only the samples taken during the equilibration hydration period show a steady depletion of aluminium from solution (see Figure 7.2-5), due to which the amorphous aluminium hydroxide type becomes undersaturated and as a results, may dissolve.

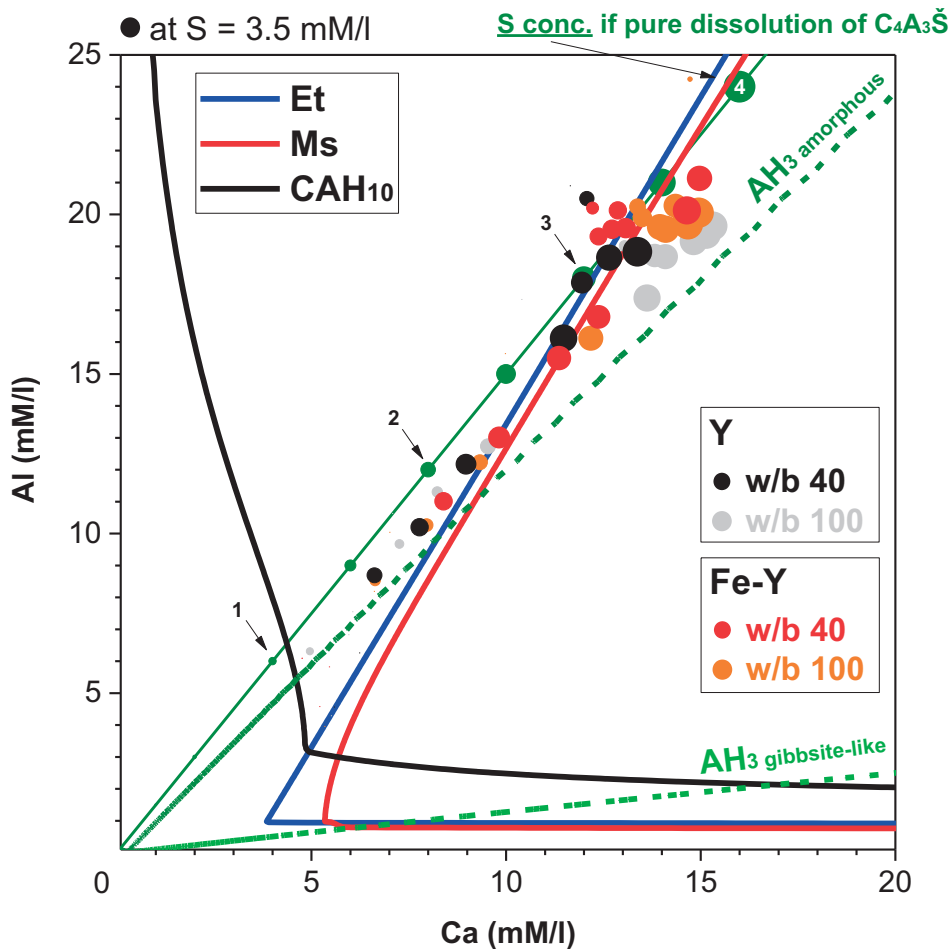


Figure 7.2-4 Solubility curves at 25 °C for the system  $CaO - Al_2O_3 - SO_3 - H_2O$  at a sulphate concentration of 3.5 mM/l; ● Y and ● Fe-Y

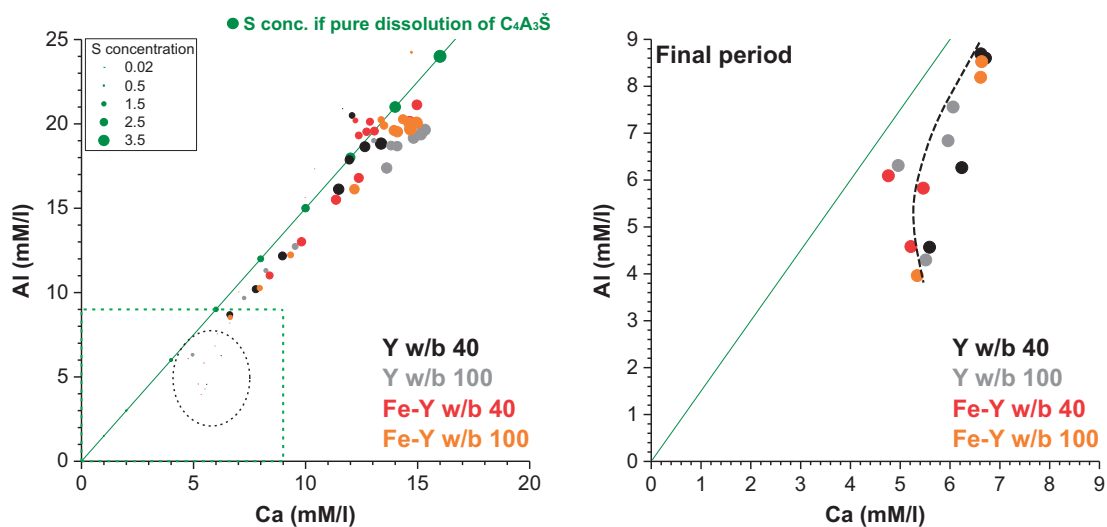


Figure 7.2-5 Calculated versus measured (● Y and ● Fe-Y) solution concentrations

7.2.2 Effect of mayenite on the hydration kinetics of ye'elimite alone and with gypsum

The impact of the addition of synthetic mayenite to stoichiometric ye'elimite at high a high w/b ratio was tested in suspension at w/b 100 by following the evolution of the conductivity and pH. The faster initial reaction, the higher pH value for Fe-Y during the initial period as well as the shortening of the dormant period could be very well reproduced.

However, the length of the acceleration period is extended and the main hydration peak is shifted to later times. The retardation of the main hydration peak was also observed for Y with 2 wt.% or Fe-Y with 1 wt.% mayenite in the paste samples. The origin of the retardation remains unknown. A hypothesis could be, that the faster depletion of sulphate ions by the precipitation of ettringite alters the  $Al / Ca$  ratio in solution. As ettringite uses more calcium than is released by the dissolution of ye'elimite, the aluminium ion concentration should increase over calcium. This in turn may shift the solution composition towards the solubility curves of amorphous aluminium hydroxide,  $CAH_{10}$  and away from monosulphate. However, their formation and growth may be kinetically hindered. Additionally, literature reports that sulphate ions cause the faster nucleation of an amorphous aluminium hydroxide [223] [224] [246]. Thus, due to its absence, i.e. depleted from solution, the nucleation rate is reduced which in turn may explain the longer duration of the acceleration period.

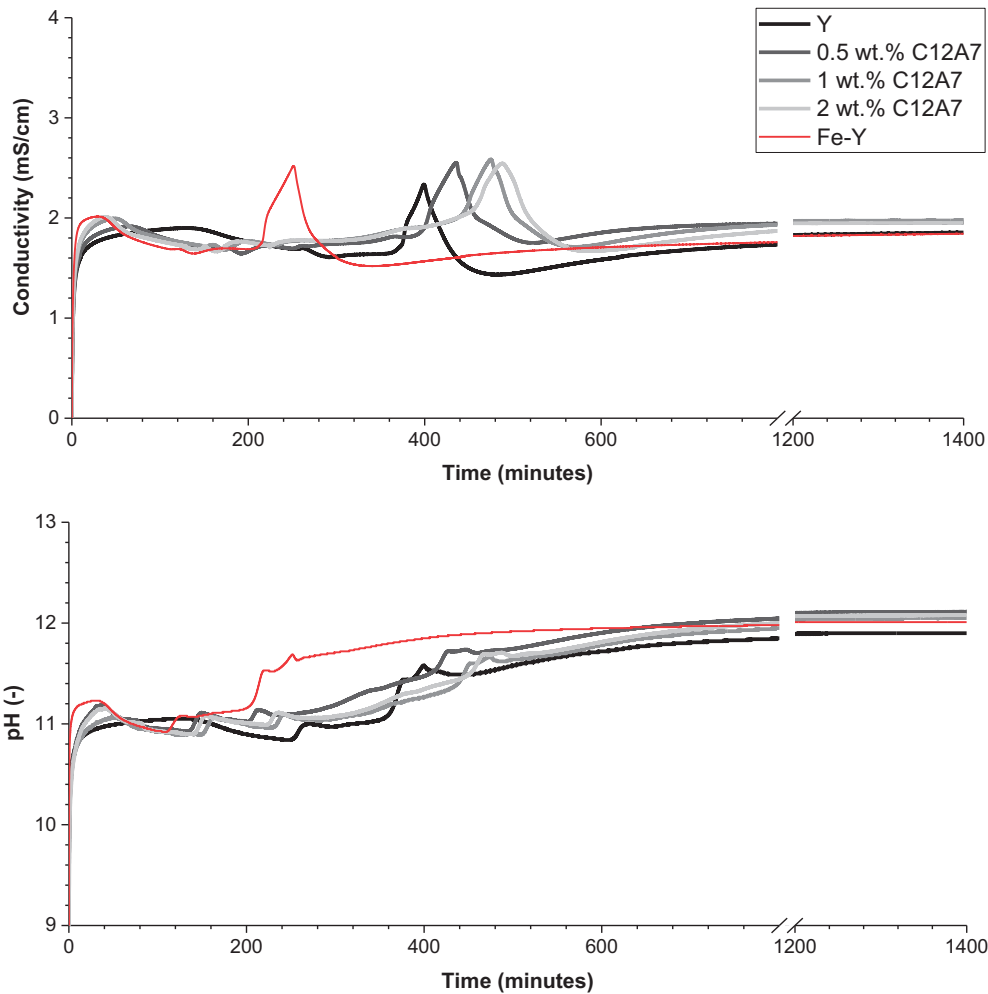


Figure 7.2-6 Evolution of the conductivity and pH of Y and Y with 0.5, 1 and 2 wt.% mayenite at w/b 100, Fe-Y for comparison

The impact of mayenite in the presence of gypsum is shown in Figure 7.2-7. Almost identical curves, for both the conductivity and pH evolution compared to the Fe-Y+G sample, could be simulated by the addition of 1 wt.% mayenite to Y+G. Especially, the shape of the initial period was well captured as shown by the almost full overlap with the Fe-Y+G curve. Those findings confirm the results from the experiments carried out in pastes at w/b 0.5 and 2.

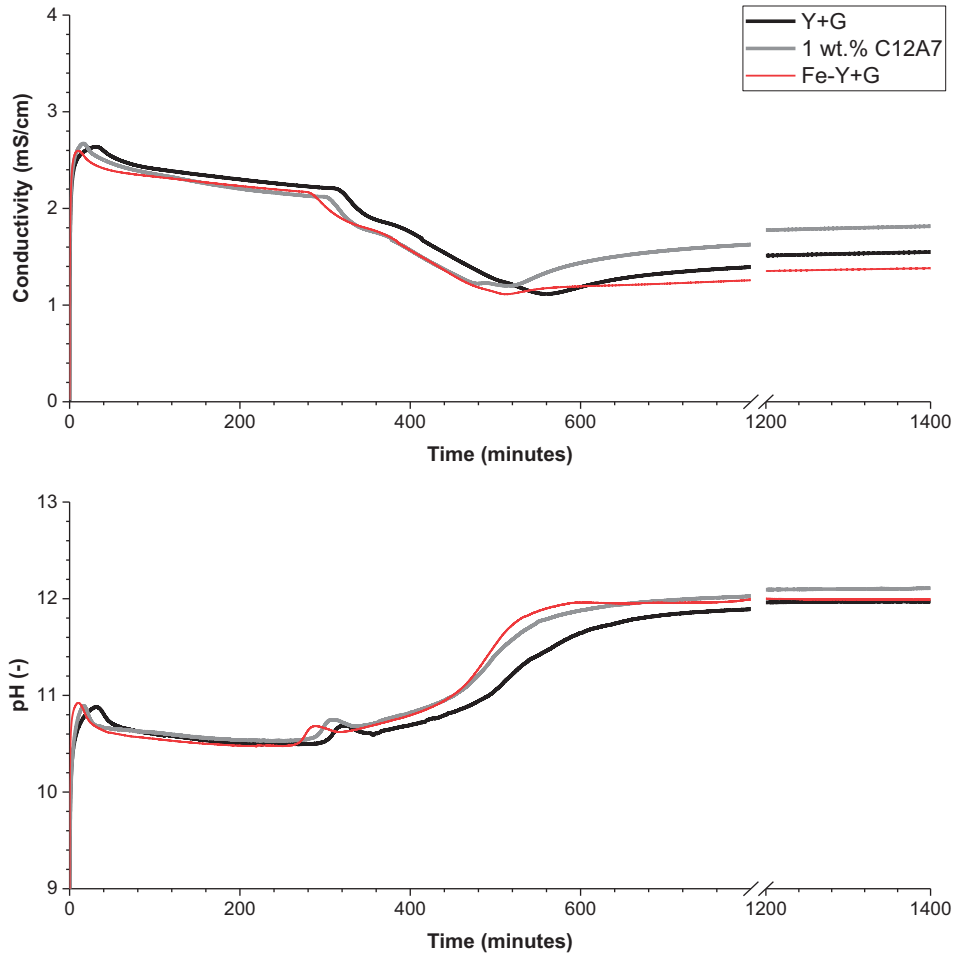


Figure 7.2-7 Evolution of the conductivity and pH of Y+G with the addition 1 wt.% synthetic mayenite at w/b 100, Fe-Y+G for comparison

### 7.3 Effect of iron onto the hydrates microstructure and composition

Figure 7.3-1 shows STEM-EDS micrographs of Fe-Y hydrated for 7 minutes and 3 hours at w/b 100. First, we often observed an enrichment of iron along grain boundaries of the anhydrous Fe-Y particles. Secondly, a layer of hydrates is instantly formed, similar to the findings for Y (Chapter 5), and this layer is enriched in iron. The enrichment of iron is very probably related to the low mobility of iron in the given solution composition. Table 7.3-1 presents the bulk composition of the formed hydrates in the Fe-Y samples. The results for Y are shown for comparison. The HR-SEM micrographs of Fe-Y hydrated at w/b 100 reveal very similar features as for Y and are therefore not presented here. They are available in the annex – part 5, Figure 8.8-28 to Figure 8.8-31.

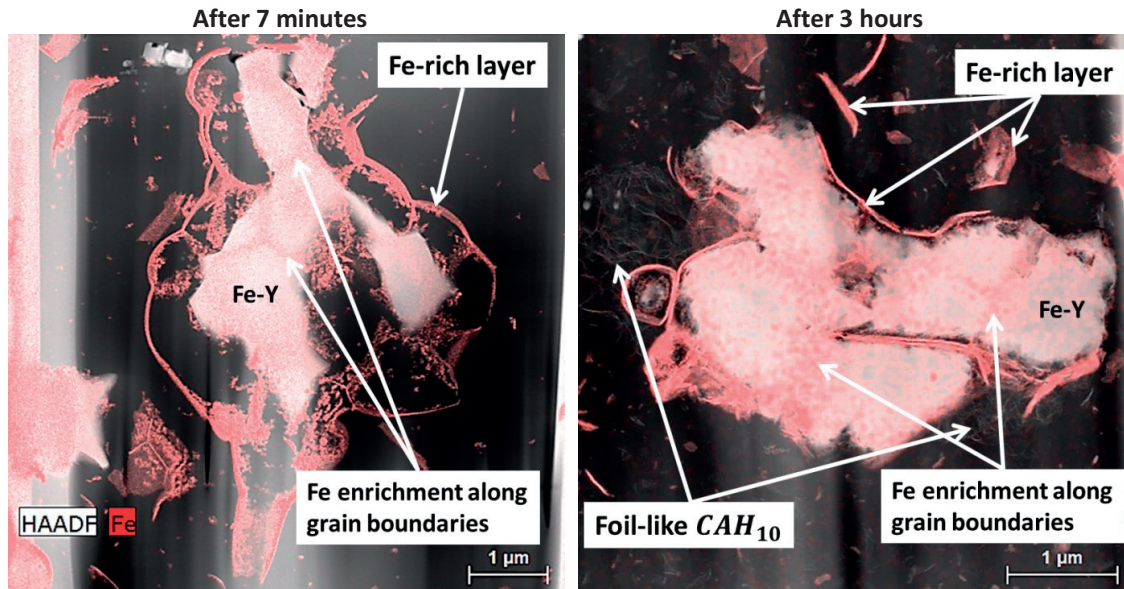


Figure 7.3-1 STEM-EDS micrograph of Fe-Y hydrated at w/b 100 for 7 minutes and 6 hours

The formed layer after 7 minutes of hydration has a different composition than the used iron-rich solid solution ye'elimite. The  $S / Al$  ratio is reduced by half and the  $Fe / Al$  ratio is increased. However, the compositions are closer after 3 hours of hydration, which is probably related to the higher hydration degree reached. The foil-like calcium aluminate hydrate has a similar composition in all samples, which indicates that the formation of iron-bearing solid solutions is limited.

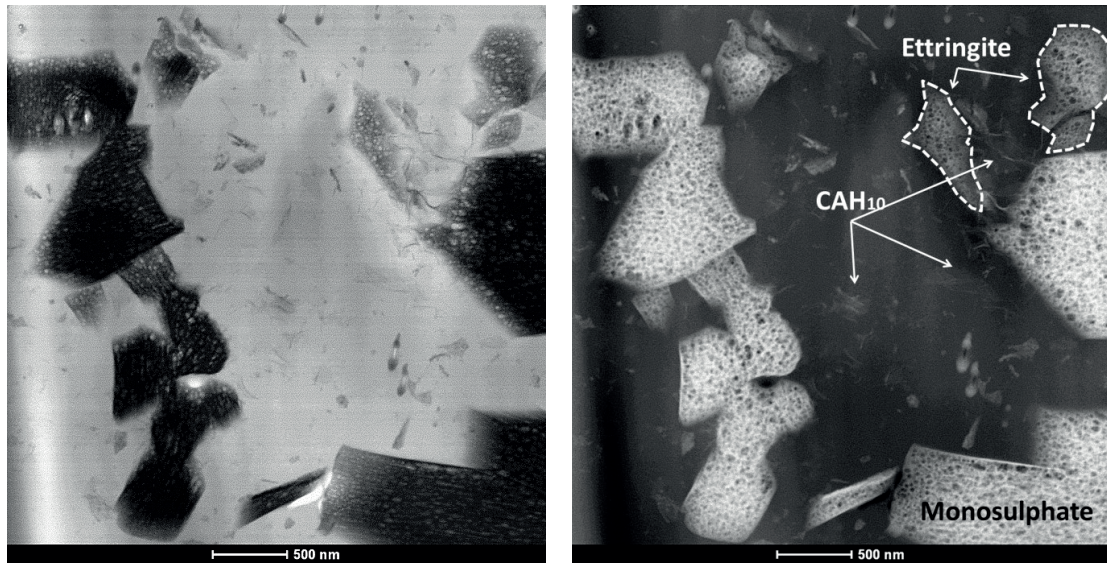
Table 7.3-1 Mean atomic ratios determined by STEM-EDS of the solid residues of Y and Fe-Y hydrated at w/b 100; n.d. = not detected

Sample	In layer-like hydrates			Number of measured areas
	$Ca / Al [-]$	$S / Al [-]$	$Fe / Al [-]$	
<b>Anhydrous Y</b>	<b>0.65</b>	<b>0.16</b>	<b>0.005</b>	
Y 7 min	0.65	0.13	0.03	18
Y 6 hours	0.60	0.15	0.04	14
<b>Anhydrous Fe-Y</b>	<b>0.69</b>	<b>0.16</b>	<b>0.07</b>	
Fe-Y 7 min	0.71	0.08	1.57	11
Fe-Y 3 hours	0.75	0.17	0.40	30
<b>In foil-like hydrates – potentially <math>CAH_{10}</math></b>				
Y 7 min	0.34	0.07	0.022	1
Y 6 hours	0.31	0.07	0.012	5
Fe-Y 7 min				n.d.
Fe-Y 3 hours	0.37	0.10	0.09	3

Figure 7.3-2 shows STEM-EDS micrographs elemental maps derived by analyses presenting the composition of ettringite and monosulphate. The large hexagonal particles present have a composition very close to that of monosulphate ( $C_4A\bar{S}H_{12}$ ). Only the highlighted particles in upper right corner reveal a composition close to that of ettringite  $C_6A\bar{S}_3H_{32}$ . The determined  $Fe / Al$  ratios for monosulphate and ettringite were about 0.02 to 0.04 and 0.08 to 0.11, respectively. This in turn would give a  $Al$  by  $Fe$  substitution of about 2-4% ( $C_4A_{1-x}F_x\bar{S}H_{12}$ ) and 7-10% ( $C_6A_{1-x}F_x\bar{S}_3H_{32}$ ), respectively. The worn-out parts of the shell are spread over the sample matrix. A second area is shown in Figure 7.3-4 Figure 7.3-2.



Area 1



Area 2

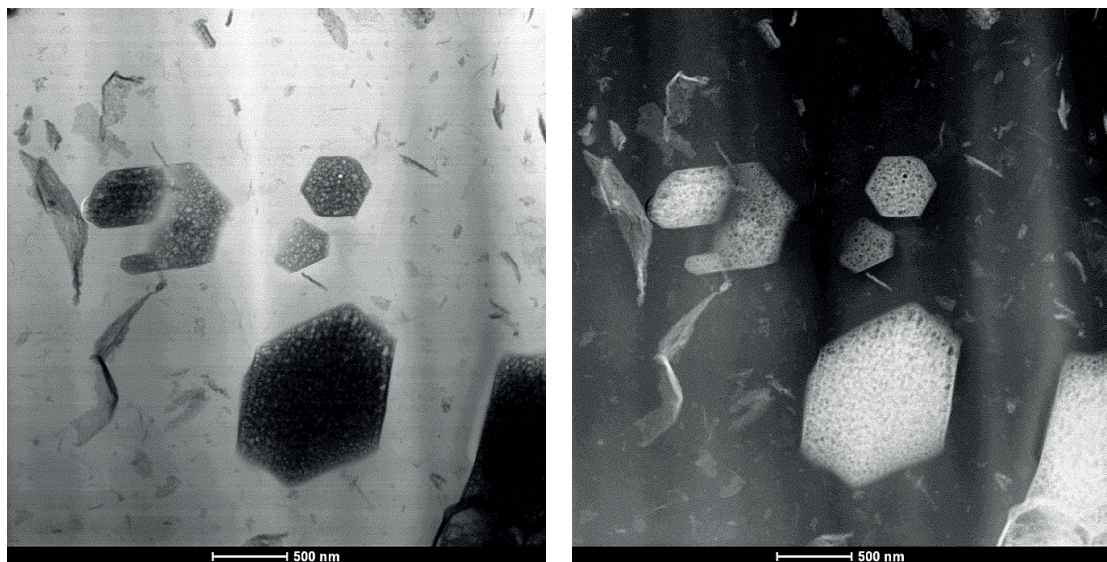


Figure 7.3-2 STEM-EDS micrographs of Fe-Y after 3 hours of hydration

The distributions of the main present elements are shown in Figure 7.3-3 and Figure 7.3-4. It can be clearly seen that iron is incorporated into monosulphate and ettringite. On the contrary, the foil-like calcium aluminate hydrate shows hardly any incorporation of iron (above the background noise). The iron-rich particles present the worn-out shell or hydrates layer formed initially.



Hydration of an iron-rich ye'elimite and effect of mayenite

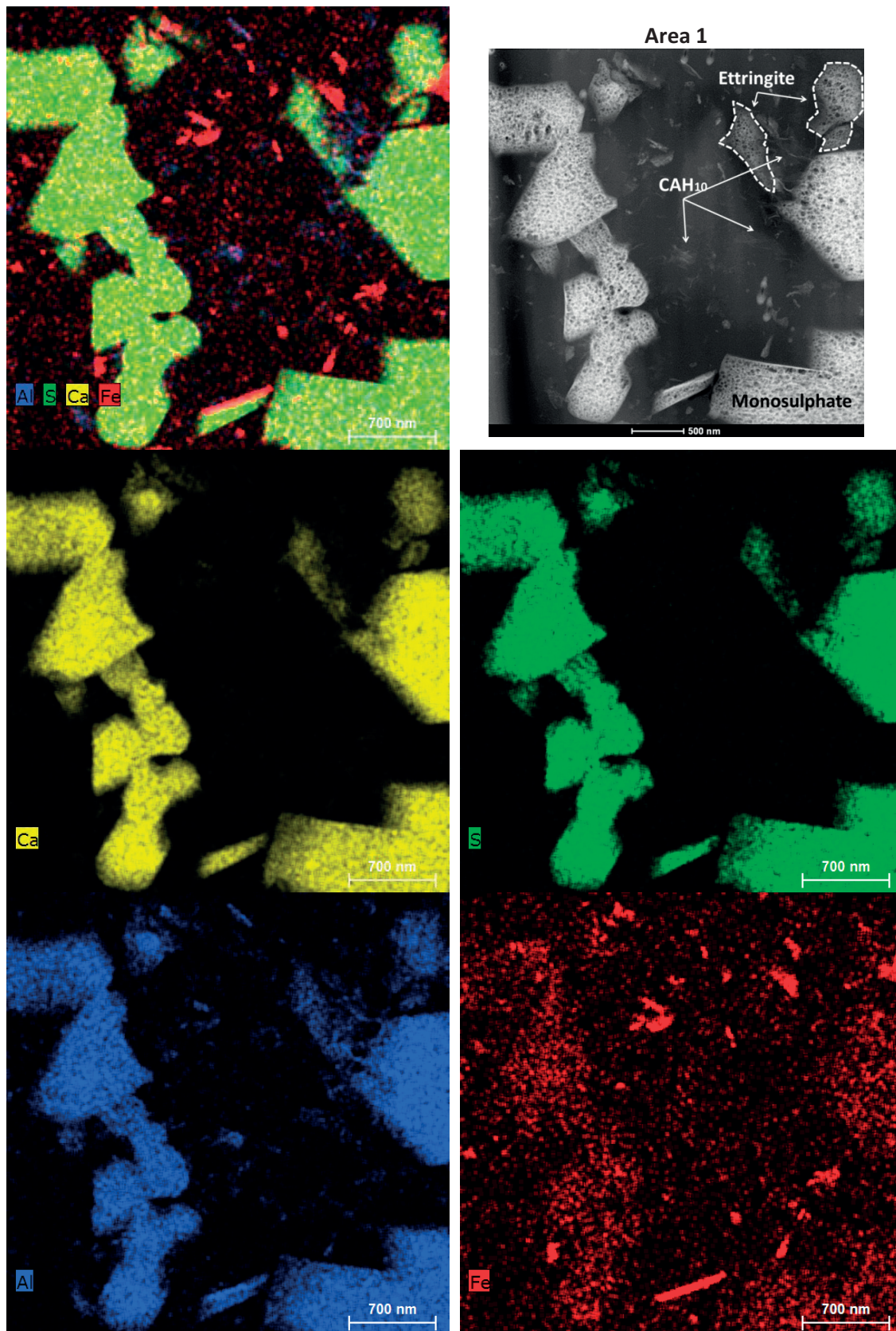


Figure 7.3-3 STEM-EDS micrographs of area 1 with the elemental distribution of *Ca*, *S*, *Al* and *Fe* of Fe-Y after 3 hours of hydration

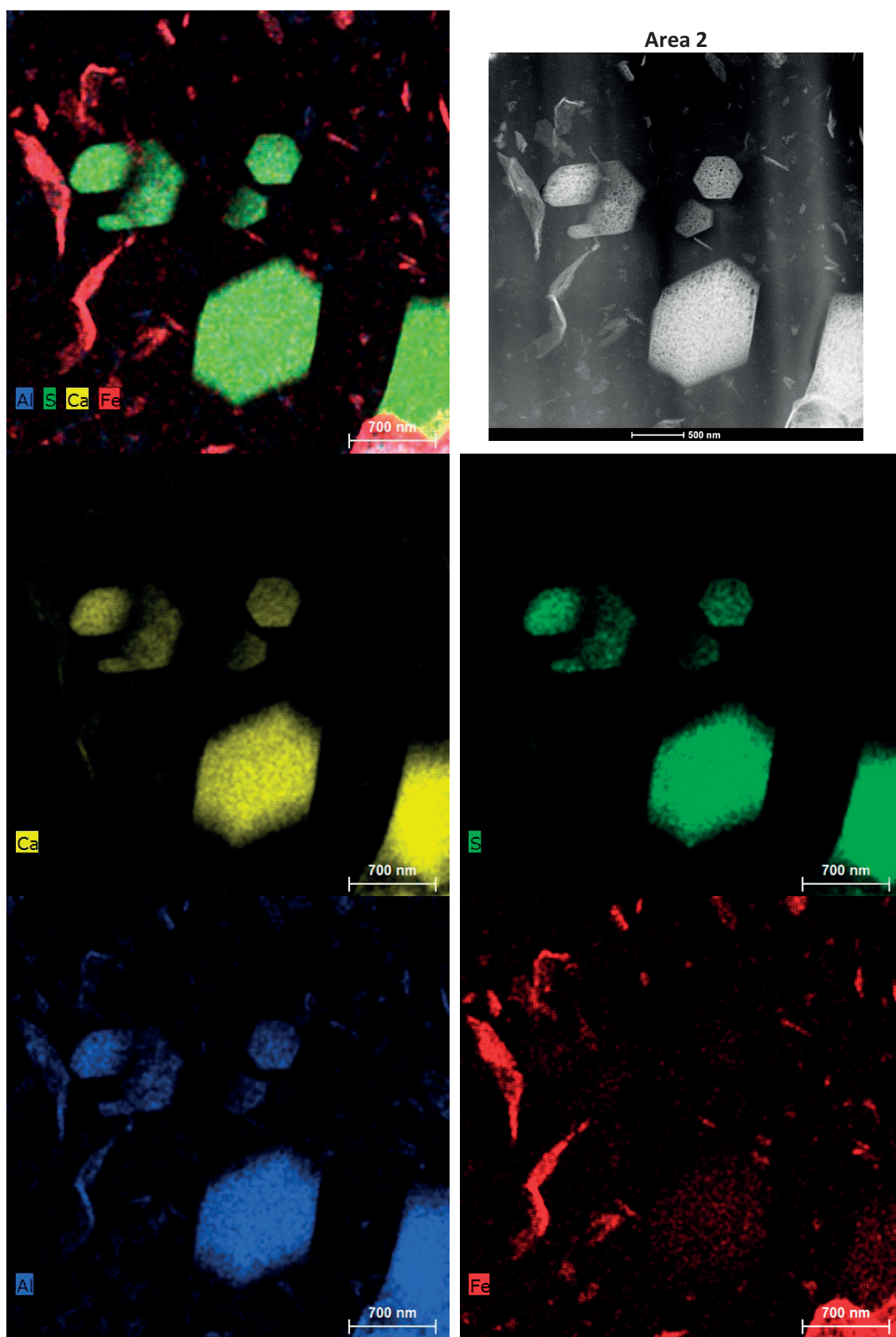


Figure 7.3-4 STEM-EDS micrographs of area 2 with the elemental distribution of *Ca*, *S*, *Al* and *Fe* of Fe-Y after 3 hours of hydration

## 7.4 Discussion

This work investigated the hydration kinetics of stoichiometric and an iron solid solution ye'elimite with the addition of mayenite in pastes and suspensions. We further investigated the effect of the combined addition of mayenite and gypsum to ye'elimite. We were able to reconstruct the hydration kinetics of Fe-Y by blending Y with mayenite. In Chapter 5 we have shown that the relative high solution concentrations of aluminium and sulphate ions over calcium ions control the onset and duration of the dormant period. In Chapter 6 we showed that the addition of gypsum profoundly increases the calcium and sulphate compared to the aluminium ion concentrations. These conditions favour and accelerate the formation of ettringite, which led to the shortening of the dormant period.

We have shown in section 7.1.1 that the different hydration kinetics the two ye'elimite types could be mitigated by increasing the water to binder ratio. The higher w/b and the availability promote the formation of ettringite, indicating that the length of this period is primarily controlled by the precipitation of hydrates rather than the dissolution rate of ye'elimite. Thus, the polymorphism cannot explain these differences or has only a little impact. On the contrary, we could perfectly reconstruct the hydration kinetics (paste) of iron-rich ye'elimite by blending stoichiometric ye'elimite with only 1 wt.% of synthetic mayenite. The addition of mayenite to Fe-Y strengthened, similarly to Y samples, the initial hydration reactions but caused the retardation of the main hydration reaction.

The rapid dissolution of synthetic or secondary mayenite (e.g. from the thermal decomposition of ye'elimite) proceeds during the first seconds to minutes of hydration. This is shown by e.g. the higher heat release (paste), the high pH (suspension), the greater aluminium and calcium concentrations (suspension). The hydration of mayenite alters the  $Al/Ca$  and  $Al/S$  ratios, promoting the faster formation of ettringite and depletion of sulphate from solution. In general, the depletion of sulphate from solution, the increase of the pH and the shortening of the dormant period are correlated. It actually seems that the polymorphism of ye'elimite has only a little impact. This reaction is followed by the rapid ye'elimite dissolution and onset of the monosulphate formation. Our results somewhat match the higher pH and the faster reaction found for iron-rich CSA, i.e. FAC, [11] [12] or synthetic (solid solution) ye'elimite [39].

Not all hydration periods are equally altered by the presence of mayenite. The length of the initial period, dormant and acceleration period are shortened in the presence of mayenite when testing paste samples. On the contrary, the duration of the dormant and acceleration period is lengthening when testing samples in suspension. The origin of the retarding effect of mayenite additions at high w/b ratios remains unknown. We can only speculate that the lack of sulphate ions reduces the nucleation rate of amorphous aluminium hydroxide and thus, causes the longer duration of the acceleration period.

It is also now possible to explain why the addition of gypsum causes an acceleration and harmonisation (i.e. similar sequences) of the hydration reactions. Almost identical hydration patterns for Y+G or Fe-Y+G with mayenite were observed in pastes and even in suspensions. The rapid dissolution of gypsum leads to a rapid increase of the calcium and sulphate ion concentration, whereas that of aluminium is decreased (see Figure 6.2.3 in Chapter 6). Those conditions favour the formation of ettringite [234], which keeps the aluminium ion concentration in solution low.



The dissolution of mayenite provides calcium and aluminium ions to a sulphate-rich solution, which further promotes the initial ettringite formation. However, the nucleation and growth of ettringite seem to be the main kinetic driver as long sulphate is available in solution, e.g. provided by the dissolution of gypsum. A similar impact of mayenite on the hydration of calcium aluminates alone and in the presence of gypsum is already known. Gosselin [22] has analysed the hydration of neat krotite and in the presence of mayenite. He could show that the concentration of calcium compared to aluminium ions was higher in the presence mayenite and that the dormant period was shortened. Similarly, the presence of mayenite causes the acceleration of the hydration kinetics for CAC clinker [95] [252] [253] [254], whereas formulations with calcium sulphate could reach reasonable long open times [255].

The low mobility of iron in solution, e.g. for the dissolution of iron-rich solid solution ye'elimite, resulted in another important difference compared to the hydration of stoichiometric ye'elimite. Iron was never detected in solution but instead was found to be highly enriched in the layer or "shell" of hydrates, covering the anhydrous particles. The formation of iron-rich areas is consistent to the finding by Zhang and Glasser [133] about the low mobility of iron in hydrating CSA. The composition of the iron-rich phase(s) and its impact on the hydration kinetics remains unknown. However, some information can be obtained from research done on the hydration of the calcium ferrites. Literature reports that the hydration of neat brownmillerite ( $C_4AF$ ) resulted in the formation of a gelatinous layer of hydrates is formed, which covers the anhydrous particles [256]. The authors claimed that the diffusion through the formed gelatinous hydrates layer is the rate limiting process. In a complementary study, the composition of the gelatinous iron-rich layer was investigated by X-ray absorption spectroscopy among other methods [257]. The authors found that the layer was composed of iron-bearing katoite ( $C_3(A,F)H_6$ ) and iron hydroxide ( $FH$ , i.e. goethite) besides various calcium aluminate hydrates. On the contrary, ettringite was formed in the presence of sulphate, where the ettringite was intermixed within the gelatinous iron hydroxide layer [93] [96]. However, the impact of the formed layer and its composition on the hydration kinetics remains to be speculations.

Our study provides very important insights to better understand the hydration of ye'elimite-rich binders, especially in the presence of minor phases such as mayenite. By knowing the parameters which cause the presence or absence of mayenite (Chapter 4), it is now possible to adjust the composition of CSA and BYF clinkers and cements according to the targeted application. For example, if fast setting and high early strength is required for applications such as shotcrete, pre-cast concrete or repair mortars, a CSA or BYF clinker with mayenite could be used together with a less soluble calcium sulphate such as hard burnt anhydrite. The formation of mayenite could be provoked by e.g. increasing the iron content in the raw materials and / or by increasing the sintering temperature or duration. On the opposite, if a long open time is targeted, the sintering duration or temperature should be optimized and strictly controlled to avoid the formation of mayenite, especially if iron-rich raw materials are used. Otherwise, gypsum could be added to mitigate the effect of mayenite. By combining all those measures it is possible to produce cements with stable and uniform features.

## 8 Summary of the findings, conclusions and perspectives

### CONTENTS

---

<b>8</b>	<b>SUMMARY OF THE FINDINGS, CONCLUSIONS AND PERSPECTIVES .....</b>	<b>129</b>
<b>8.1</b>	<b>INTRODUCTION.....</b>	<b>129</b>
<b>8.2</b>	<b>CLINKER SYNTHESIS AND CHARACTERISATION .....</b>	<b>130</b>
<b>8.3</b>	<b>HYDRATION REACTIONS OF SYNTHETIC YE'ELIMITE .....</b>	<b>131</b>
<b>8.4</b>	<b>EFFECT OF GYPSUM ON THE HYDRATION OF YE'ELIMITE .....</b>	<b>133</b>
<b>8.5</b>	<b>THE CHEMICAL SHRINKAGE EVOLUTION OF NEAT YE'ELIMITE AND WITH GYPSUM .....</b>	<b>134</b>
<b>8.6</b>	<b>HYDRATION OF AN IRON-RICH YE'ELIMITE AND EFFECT OF MAYENITE .....</b>	<b>135</b>
<b>8.7</b>	<b>GENERAL DISCUSSION.....</b>	<b>136</b>
<b>8.8</b>	<b>PERSPECTIVES .....</b>	<b>138</b>

---

### 8.1 Introduction

This thesis was developed along three main axes: the study of the impact of iron on the formation of solid solution ye'elimite; the hydration of stoichiometric ye'elimite alone and in the presence of gypsum, including the impact of the water to binder and water to solid ratio; and the comparison to the hydration the solid solution ye'elimite, including the effect of mayenite.

We discussed in Chapter 1 and 2 the demands and challenges for alternative binder concepts such as CSA and BYF. One of the major requirements is that the cement performance is stable. The material handling during preparation of concrete should be ideally similar to PC and the new binder should behave the same or even better with regard to e.g. the strength development, volume stability, surface quality and resistance to chemical or physical attacks. CSA and BYF cements with the main phase ye'elimite are a promising class of non-Portland cements which fulfil most of the requirements. However, the hydration kinetics of CSA and BYF cements vary strongly, even for cements with similar composition and fineness. Understanding the origin this variation was the main motivation for this thesis.

Earlier studies indicated that the type and composition of ye'elimite was related to the different hydration kinetics. Iron-rich CSA and BYF clinkers and cements often show faster hydration kinetics, higher initial pH and early strength compared to those with low iron contents. The addition of easy soluble calcium sulphate such as gypsum mitigates this effect, resulting in a harmonization of the hydration sequences and kinetics. The literature reports that stoichiometric ye'elimite has an orthorhombic symmetry at ambient conditions, whereas a cubic symmetry is stabilised by the presence of minor elements such as iron. Thus, previous to this work, it was often assumed that there was a link between the presence of iron, the polymorphism of ye'elimite and the hydraulic reactivity.

## 8.2 Clinker synthesis and characterisation

The effect of iron on the formation of stoichiometric and solid solution ye'elimite was studied in Chapter 0. Stoichiometric ye'elimite has an orthorhombic symmetry at ambient temperature. The maximum substitution value of  $x$  in  $C_4A_{3-x}F_x\bar{S}$  found was about 0.27 (7.2 wt.%  $Fe_2O_3$ ), where the optimum, e.g. achieving the near complete incorporation of all added iron, was around 0.10 (5 wt.%). The substitution of aluminium by iron preserved the cubic symmetry to ambient temperatures.

Ye'elimite is formed from the reaction of the intermediate calcium aluminates such as krotite and mayenite with anhydrite. Iron promotes the formation of a liquid phase, causing an enhanced nodulization, densification of the microstructure, which promotes the mass transport of elements and thus the mineral formation. Especially, the intermediate phase krotite is formed faster, which in turn enables the faster ye'elimite formation.

Ye'elimite containing iron seems to possess a lower thermal stability compared to the stoichiometric one and starts to decompose if the sintering temperature is too high and / or dwell time is too long. It was reported that a liquid phase facilitates the volatilisation of sulphate. This may contribute to the decomposition. First, the calcium sulphate dissolves into the ferritic liquid phase a part is lost by the volatilization. Second, the iron-rich ye'elimite is formed faster and thus is exposed longer to the sintering temperature. The decomposition of ye'elimite led to the volatilization of sulphur and the formation of secondary phases such as mayenite, krotite and ferrites. The XRD detectable quantities of mayenite are typically below 1% in the solid solution ye'elimite clinker. It is possible that a part of mayenite is present in an amorphous form. Blends of stoichiometric or solid solution ye'elimite with synthetic mayenite were prepared to determine the detection limit for mayenite. The limit was found to be around 2 %.

These findings can be directly applied for the production of CSA and BYF clinkers. For example, using a higher fineness of the calcium and aluminium sources as well as a good homogenization it could be feasible to optimize the production of such clinkers, e.g. enabling the reduction of the sintering temperature and / or the dwell time. Additionally, the decomposition of ye'elimite could be avoided or minimized even for iron-rich mixes by proper adjustment of the process conditions.



### 8.3 Hydration reactions of synthetic ye'elimite

To understand the effect of iron and the solid solution ye'elimite on the hydration, we first studied the dissolution and precipitation reactions of stoichiometric ye'elimite. These results are presented in Chapter 5. By carrying out experiments in pastes suspensions at several water to binder (w/b) ratios, we could define five hydration periods and formulate hypotheses for their onset and end.

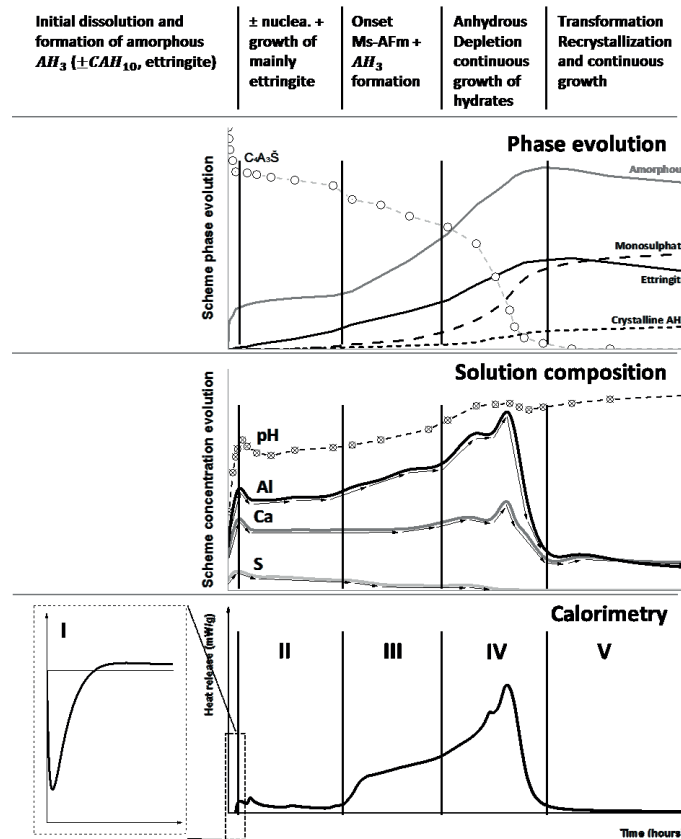


Figure 8.3-1 Idealized hydration scheme for ye'elimite and the corresponding hydration stages from section 0

**Stage I:** The initial period is marked by the wetting and rapid dissolution of a small quantity ye'elimite and the formation of primarily an amorphous phase. The first distinguishable hydration products are ettringite (HR-SEM, STEM and XRD), foil-like monocalcium aluminate decahydrate ( $CAH_{10}$ ) (HR-SEM and STEM) and aluminium hydroxide (TGA). During the first minutes of hydration a layer of hydrates forms around the anhydrous particles, but this is not believed to be responsible for the slowdown in reaction. The slowdown of the ye'elimite dissolution within seconds, already before the layer of amorphous phases is formed. Therefore the slowdown is believed to be due to the decrease in undersaturation caused by the rapidly increasing solution concentrations. It could be that ye'elimite is in equilibrium with the solution. Another cause may be the absorption of sulphate on reactive dissolution sites of ye'elimite, blocking its dissolution for given calcium and aluminium concentrations. However, this contradicts the accelerating effect of gypsum on the hydration.

**Stage II:** The dissolution of ye'elimite almost stops, whereas the formation of ettringite slowly continues. The rate of the ettringite formation seems to control the length of the dormant period. Its length corresponds to the slow continuous sulphate depletion resulting from the steady formation and growth of ettringite. The pH starts to increase slowly but steadily.

**Stage III:** Once the concentration of sulphate ions decreases enough (in the gypsum-free sample), the onset of the acceleration period occurs. At this stage the ye'elimite dissolution as well as the formation of hydrates accelerates. Additionally, monosulphate together with gibbsite-like aluminium hydroxide start to form. The drop and depletion of sulphate ions concentration corresponds to rising pH values due to the increasing hydroxyl ion concentrations to maintain electron neutrality in solution (new equilibrium conditions established). The increasing pH may contribute to the acceleration of the kinetics. It is important to note that according to the QRXD analyses neither the hard burnt anhydrite nor the krotite had reacted to any measurable extent till this period.

**Stage IV:** The main hydration period is marked by the rapid dissolution of ye'elimite and the formation of monosulphate, ettringite and the X-ray amorphous phase. The pH continues to rise and the near complete depletion of all clinker phases are observed. Sulphate is not detected in solution, even when ye'elimite and the hard burnt anhydrite dissolved. This indicates that the nucleation and growth of monosulphate and ettringite proceed at a similar rate as the ye'elimite dissolution. In general, the duration of this period seems to depend equally on the rate of the ye'elimite dissolution and the formation of monosulphate as well as ettringite.

**Stage V:** The final or equilibration and transformation period starts after the near complete depletion of all clinker phases. A slow and steady decrease of the aluminium ion concentration occurs. At the same time monosulphate and aluminium hydroxide continue to form, primarily from the amorphous phase and ettringite.

The hydration sequences and periods detected in the suspension experiments were also found in the paste samples. Thus we could successfully link the results from experimental set-ups. This is especially of relevance, as calorimetry measurements of paste samples are commonly used to assess the hydration kinetics of ye'elimite based binders such as CSA or BYF.

The experiments in paste typically show a single main hydration peak. However, this peak represents at least two overlapping precipitation reactions, beside the continuing dissolution of ye'elimite. This can be seen by increasing the w/b ratio together with the addition of inert quartz filler. The first reaction is the precipitation reaction of ettringite,  $CAH_{10}$  and amorphous aluminium hydroxide which starts directly after the contact with water and remains until the main hydration peak. This reaction causes the depletion of sulphate ions from solution in the gypsum-free sample, and the onset of the main reaction, which is the formation of monosulphate and gibbsite-like aluminium hydroxide. Increasing the w/b ratio, especially the presence of nucleation sites provided by the inert quartz filler, enhanced the formation of ettringite,  $CAH_{10}$  and amorphous aluminium hydroxide. This caused the faster depletion of sulphate ions, and thus the acceleration of the kinetics by the earlier onset of the monosulphate formation.

These findings offer new insights into the hydration of ye'elimite-rich binders. The dissolution of the anhydrous phases, the formation of metastable hydrates and the different hydration periods could be successfully linked with the evolution of the solution. This knowledge could be used to improve the thermodynamic predictions of the hydration reactions and ultimately, the performance and stability of CSA and BYF concrete.

#### 8.4 Effect of gypsum on the hydration of ye'elimite

The impact of gypsum on the hydration of stoichiometric and iron-rich ye'elimite was studied in the first part of Chapter 0. Gypsum additions lead to the harmonisation of the hydration kinetics at all applied w/b ratios, ranging from 0.5 over 40 (paste) to 100 (suspensions), independent of the ye'elimite type used. Gypsum accelerates the hydration and modifies the hydrates assemblage by favouring the formation of ettringite rather than monosulphate.

The rapid dissolution gypsum leads to a strong increase of the calcium and sulphate ion and decrease of the aluminium ion concentrations compared to the ye'elimite clinker (Chapter 5). These conditions favour the fast formation of ettringite, which keeps the aluminium ion concentrations in solution low. The evolutions of the calcium and sulphate ion concentrations are buffered by the steady dissolution of gypsum. In general, the evolution of the solution concentrations indicates that precipitation of ettringite continues as long as the high calcium and sulphate ion concentrations are maintained. On the contrary, the aluminium ion concentration steadily decreases throughout the "dormant" period. It is followed by the sharp drop of the calcium and sulphate ion concentration, at the point of gypsum depletion. Again the pH increases with the decreasing sulphate ion concentration. The following short increase of the aluminium ion concentration indicates the faster ye'elimite dissolution. Monosulphate starts to form. The distinction between different hydration periods, as done for ye'elimite alone (Chapter 5), was not possible in the suspension experiments due to a steady change in solution concentrations. However, they are clearly visible in paste.

Using the results from the suspension experiments, we could assess the hydration kinetics measured in paste. The continuous higher heat release throughout the dormant period in Y+G and Fe-Y+G pastes compared to neat Y and Fe-Y could be explained by the steady dissolution of gypsum and ye'elimite, and the continuous formation of ettringite. The increasing the w/b and w/s ratios, strongly accelerate the hydration kinetics. Based on our findings presented in the Chapters 5 and 0, we were able to link the acceleration to the faster nucleation and growth of ettringite. Thus, gypsum will be depleted faster by the formation of ettringite, and the lower sulphate concentration in solution allows the continuing dissolution of ye'elimite. The point of the gypsum depletion detected in the suspension experiments, corresponds to the second heat peak release from the calorimetric curves.

The results presented in the first part of Chapter 0 showed that it is possible to formulate stable cements with similar hydration kinetics by the addition of gypsum. The effect that is caused by the presence of iron can be mitigated or even suppressed.

## 8.5 The chemical shrinkage evolution of neat ye'elimite and with gypsum

We investigated the chemical shrinkage of neat ye'elimite and the impact of gypsum in the second part of Chapter 0. The chemical shrinkage measurements indicated that a chemical expansion occurs for both binders. The expansion seems to be caused by the transformation of hydrates and the related release of the combined water. However, the chemical expansion observed was transitory, as the shrinkage and the bound water contents returned to their original values. The non-monotonous development observed experimentally cannot be explained by the evolution of the crystalline detectable phases, including the anhydrous phases and hydrates. We assume, that the chemical expansion is linked to the transformation and recrystallization of metastable amorphous phases such as aluminium hydroxide and  $CAH_{10}$ , which causes the release of combined water. In addition, it is possible the hydration state of monosulphate changes over time from e.g. a type with 16 molecules of bound water down to one with 12. The formation of metastable phases is kinetically favoured by the high solution concentrations, especially of aluminium ions, during the hydration and is typically followed by the transformation into more stable phases.

SEM micrographs show that even for the applied high w/b ratio, the space was completely filled and that aluminium hydroxide is the main volume filling phase. In the case of the hydration of neat Y, monosulphate is intermixed with aluminium hydroxide. A better phase separation is evident in binders with gypsum. One possible reason for the high space filling potential could be the low densities of the phases such as amorphous aluminium hydroxide [244] and  $CAH_{10}$ .

The subsequent increase of shrinkage values to the original ones, could not be explained by the evolution of the anhydrous phases or the crystalline hydrates. One possible explanation is the swelling of the amorphous aluminium hydroxide "gel". We assume that the chemical expansion and the release of the bound water create free space. The availability of space and water enables the uptake of water (e.g. by ad- or absorption) and consequently, the swelling of the not yet crystallized amorphous aluminium hydroxide.

Understanding the cause of the chemical expansion could help to potentially correlate it with other experimental observations such as the presence of a strength plateau for CSA and BYF based cements. Furthermore, we could show that the chemical expansion could be significantly reduced by the addition of gypsum.

## 8.6 Hydration of an iron-rich ye'elimite and effect of mayenite

As discussed in Chapters 5 and 6, polymorphism alone cannot explain the different hydration kinetics of stoichiometric ye'elimite (Y) and the iron-bearing solid solution (Fe-Y). First, the observed effect could be mitigated and even suppressed by increasing the w/b and w/s ratio. Secondly, in some cases no acceleration was detected for solid solution ye'elimite even when the cubic form was present. In Chapter 4 it was shown that mayenite was formed in the iron-rich ye'elimite clinker. In Chapter 7 we then investigated the impact of mayenite additions to neat Y, Fe-Y and to blends with gypsum. We could simulate the hydration kinetics of Fe-Y in paste by blending Y with synthetic mayenite. This also gives higher initial pH, the higher initial calcium and aluminium ion concentration as well as the almost identical hydration for Y and Fe-Y pattern at w/b ratios from 7.5 to 40. It therefore appears that the presence of small quantities of mayenite, rather than polymorphism, explains the different kinetics.

The dissolution of mayenite, even if present in traces, proceeds during the first seconds to minutes of hydration. This was shown by the higher heat release (paste) as well as the higher aluminium and calcium ion concentrations (suspension). These conditions favour the fast nucleation and growth of ettringite, which is supported by the faster depletion of sulphate ions from solution. This also causes the higher initial pH for Fe-Y compared to Y, the earlier depletion of sulphate ions from solution and consequently, onset of the monosulphate formation. However, the effect of mayenite also depends on the added quantity ( $\pm$  accessibility). Too high additions of mayenite retarded the onset of the main hydration period, especially for Fe-Y. This retarding effect was less strong for the experiments carried out in paste compared to those in suspension. The addition of gypsum fully mitigates the retarding effect by accelerating the formation of ettringite.

The low mobility of iron in solution, e.g. for the dissolution of iron-rich solid solution ye'elimite, resulted in the precipitation of iron-rich hydrates which are intermixed in the layer or "shell", covering the anhydrous particles. The composition of the iron-rich phase(s) and its impact on the hydration kinetics remains unknown.

## 8.7 General discussion

The formation ye'elimite containing clinkers and the hydration of cements made thereof is a very challenging field of research for several reasons. The mineralogical composition of CSA and BYF cements is often quite complex, partly due to the fact that the clinkers are formed under non-equilibrium conditions. Furthermore, plenty of the formed minor phases are hydraulic reactive which alters the overall hydration. Such hydraulic reactive phases include for example calcium silicates, calcium aluminates, calcium ferrite, (calcium) alkali sulphates and other minor phases such as periclase of free lime. In addition, ye'elimite typically forms solid solutions, which further alter the hydration kinetics. These effects are amplified when using industrial by-products and wastes to replace virgin raw materials for the clinker production. CSA and BYF cements often exhibit different hydration kinetics and associated cement properties despite having similar characteristics in terms of chemical and mineralogical composition and fineness. The origin of these differences remains unknown. The same applies at least partly for the underlying hydration reactions. Thus, the measured performance in cement such as e.g. the strength development or volume stability often cannot be linked directly with the formed phase assemblage and its evolution. In that regard, little is known regarding the formation, composition and stability of one of the main hydration products, namely the amorphous phase(s). Understanding the origin of the different hydration kinetics, including the characterisation of the formed products, was the main motivation for this work.

We could show that the clinker formation, microstructure as well as the composition and stability of ye'elimite is altered in the presence of iron. The partial replacement of aluminium by iron in the raw mixes resulted in an improved clinker burnability, as shown by the faster phase formation at all tested temperatures. This includes the faster formation of intermediate calcium aluminates, which further react with calcium sulphate to form iron-bearing ye'elimite. As reported earlier, stoichiometric ye'elimite has an orthorhombic symmetry at ambient conditions, whereas a cubic symmetry is stabilised by iron. However, a fraction of the iron-rich solid solution ye'elimite starts to decompose during the applied sintering period. The decomposition results in the volatilization of sulphur and the formation secondary phases such as krotite, mayenite and calcium ferrite. Our findings suggest that at least in the case of mayenite a part of it is present as an X-ray amorphous phase. This demonstrates that equilibrium conditions were not reached under the given experimental conditions.

By studying the hydration of the stoichiometric and solid solution ye'elimite in paste and suspensions we could determine two main hydration reactions, define five periods and the main controlling parameters. The onset, duration and end of each period seem to be controlled by the solution composition. The hydration reactions and sequences are the same for stoichiometric and iron-rich solid solution ye'elimite but the kinetics vary. The differences in kinetics could be mitigated and even suppressed by increasing the w/b ratios in paste. Furthermore, in some cases no acceleration was detected for iron-rich solid solution ye'elimite, even when the cubic form was present. That demonstrates that the polymorphism alone cannot explain the differences. This brings us to the impact of the minor phases such as mayenite. We could reconstruct the hydration kinetics of iron-rich ye'elimite by blending stoichiometric ye'elimite with only 1 wt.% of synthetic mayenite. It therefore appears that the presence of small quantities of mayenite, rather than polymorphism, explains the different kinetics.



The effect of mayenite was explained by its rapid dissolution and the altered solution composition, favouring the nucleation and growth of ettringite. However, the addition of mayenite to the iron-rich solid solution ye'elimite caused the retardation of the main hydration peak. A similar retardation of the main peak was observed at very high water to binder ratios even for stoichiometric ye'elimite and with small mayenite additions. The addition of gypsum always led to a harmonization of the hydration sequences and kinetics, independent of the ye'elimite type, the presence of mayenite or the change of the w/b – w/s ratio. This is due to the fact that gypsum dissolves rapidly, causing instantly high calcium and sulphate ion concentrations, whereas the aluminium ion concentration is kept on a relatively low level.

The assessment of the different hydration kinetics of stoichiometric and iron-bearing solid solution ye'elimite was a challenging task. Only by applying a multi-method approach and by connecting different material related aspects (e.g. the raw materials, clinker formation and hydration reactions), we were able to link the effect of iron to the observed variations in the kinetics. With the obtained insights we are now able to investigate in more detail complex materials such as CSA and BYF. Following studies need to address several aspects such as the materials history, process conditions and clinker composition (comprising the microstructure and elemental mineral composition), to correctly address the (origin of different) hydration reactions and performance characteristics. This includes detailed knowledge about the composition and treatment of the raw materials and raw mixes (e.g. fineness, and distribution within size fractions, homogeneity, presence of fluxes and mineralisers, etc.) as well as the thermal history (e.g. sintering temperature, dwell times,  $O_2$  and  $SO_2$  partial pressure, clinker cooling, etc.).

## 8.8 Perspectives

We have shown that iron affects the ye'elimite formation and stability. However, **ye'elimite is formed** from the reaction of the intermediate calcium aluminates such as **krotite with anhydrite**. The presence of **iron** mainly **accelerates the formation of krotite**. But information is incomplete as to what extent iron alters the formation rate and stability of ye'elimite. To better understand this it would be interesting to **synthesize stoichiometric krotite and iron-bearing solid solutions**. These phases **can** then be **used as components for the direct synthesis of ye'elimite** without intermediate phases, but including the effect of the sintering temperature and time. By doing so all ye'elimite types should have the same thermal history and thus, it would be possible to better understand the role of iron on the formation rate and stability of ye'elimite.

Besides iron, several other **minor elements** such as alkali, boron, chrome, manganese, titanium, phosphate and many others are reported for CSA and BYF as well. It is possible that some of these elements affect the **formation, composition, stability and hydraulic reactivity of ye'elimite** in the same way as iron. Additional systematic studies are needed to better understand those impacts, to be able to control or at the best avoid any negative impact such as the decomposition of ye'elimite, the volatilization of sulphur and the resulting formation of secondary phases. Such studies would lay the basis to investigate the even more complex reactions and interactions, when using industrial by-products and waste for the production of CSA and BYF clinkers. Additionally, it is well known that several **minor phases** such as free lime, periclase, alkali sulphates and others can be present in such clinkers, depending on the choice of raw materials and the process conditions. These minor phases can affect the hydration reactions. For example, we briefly investigated the impact of **free lime** on the hydration kinetics in pastes and suspensions (see annex – a part V; Figure 8.8-57 to Figure 8.8-59 and Figure 8.8-64). These experiments revealed some interesting **similarities** to the **retarding effect of mayenite** alone, or the acceleration when **added together with gypsum**. It would be of high industrial relevance to better understand those “similarities” which would enable the preparation of strategies, e.g. in the case free lime is present in the clinker, to maintain a stable cement quality.

It was shown in this thesis that the evolution of the solution composition is the main factor determining the onset and duration of the hydration stages. The understanding of the effect of the solution composition on the dissolution precipitation reactions is therefore of high importance. For example, it would be good to develop **methods**, or determine **parameters** enabling the **measurement of anhydrous dissolution** and resulting **nucleation (rate) of the hydrates**. Several **starting solutions**, containing already e.g. aluminium, calcium or sulphate ion in different concentrations, could be prepared to study their impact on both, the **dissolution of ye'elimite** and the resulting **precipitation reactions**. Additionally, it would be also worth to check what would happen, if these ions are **added during the different hydration stages**. Would it be possible to retard or accelerate a reaction by increasing for example the aluminium or sulphate ion concentration? The obtained data could be implemented in thermodynamic databases such as used for GEMS to enable a better prediction of the hydration reactions. Another target could be, to minimize or even suppress the formation of metastable phases such as amorphous aluminium hydroxide and  $CAH_{10}$  to avoid any crystallization or transformation reaction. For example, the literature reports that **sulphate** ions cause the faster nucleation of an **amorphous aluminium hydroxide** but impede its crystallisation. On the contrary, **tartaric acid** is typically used to slow down or even **suppress** the nucleation of aluminium hydroxide.

It would be important to understand how different **ions** such as aluminium, calcium, sulphate **interact** in solution (formation of ion complexes, etc.), how the **concentrations** (e.g. representing different hydration periods) affect the interactions and what the effect of admixtures such as retarders is. The use of retarders such as borax, citrate, gluconate or tartrate was already reported for CSA and BYF cements. However, their working mechanisms, efficiency and effect on the formation of the metastable hydrates remain poorly understood.

Another interesting study would be the **effect of the temperature** on the dissolution and precipitation reactions, especially with regard to the observed **chemical expansion at 20 °C**. We could link the chemical expansion to the transformation and recrystallization of previously formed amorphous phases such as aluminium hydroxide, which causes the release of combined water. Similar studies could be repeated at **different temperatures such as 5, 40 or even 60 °C**. This could provide further insight in the composition and stability of the formed hydrates. Based on this, the **relationship** between the **time-temperature history**, the **crystallinity**, **hydration state**, **transformation rates**, **densities** and **bound water contents** of hydrates and the subsequent space filling potential could be further investigated, including the **microstructural evolution**. This may also clarify whether a part of the chemical expansion is related to other phases such as **monosulphate** and its change of the hydration state. Such study is not only important to gain fundamental insights in the hydration of ye'elimite-rich binders, but is also of relevance for other alumina-rich binders and the application of such binders in different environments.

The amorphous phase(s) form one of the main hydration products of ye'elimite-rich binders. The characterisation of **their chemical and mineralogical composition** would enable a higher precision when studying the hydration of e.g. CSA or BYF. This in turn may further enable a better determination and quantification of the metastable phases. This knowledge would be needed to measure any transformation and recrystallization process and to detect the parameters which cause their onset and rate. In that regard, some of the **experiments** carried out in this thesis should be **repeated using insitu methods**, e.g. avoiding the solvent exchange protocol. This would allow us to follow the hydration reactions, including any transformation causing e.g. a chemical expansion, without the formation of experimental artefacts resulting from the damaging of the hydrates. Further work should also focus on the **microstructural evolution of hydrating cement**, including the further assessment of the mechanisms of the chemical expansion and the impact of the (selected) filler additions such as quartz or e.g. limestone providing extra nucleation sites. The **effect of iron** (and its low mobility in the pore solution of hydrating ye'elimite, CSA and BYF) on the **nucleation, growth, composition and crystallinity of hydrates** should be further studied as well. It was shown, that monosulphate, formed in the Fe-Y samples, was damaged more profoundly by the solvent exchange method than in the Y samples. It would be important to understand the origin of this.

Finally, it is **desirable** to transfer the collected **results** and **knowledge** to **industrial scale**. This can be done by working with synthetic, model CSA and BYF cements obtained by e.g. blending ye'elimite with other phases such as belite, mayenite, ferrite and different calcium sulphates such as anhydrite and gypsum. It can be even supplemented by investigating the impact of e.g. **retarders on the selected phases or combinations of them**. Those experiments can be compared to the results obtained with CSA and BYF cements produced on industrial scale. Applying the knowledge we gained throughout this thesis, we are now able to develop clinker and cement compositions for dedicated applications.

### Summary of the findings, conclusions and perspectives

For example, if fast setting and high early strength is required for applications such as shotcrete, pre-cast concrete or repair mortars, a CSA or BYF clinker with mayenite could be used together with a less soluble calcium sulphate such as hard burnt anhydrite. The formation of mayenite could be provoked by e.g. increasing the iron content in the raw materials and / or by increasing the sintering temperature or duration. On the contrary, if a long open time is targeted, the sintering duration or temperature should be optimized and strictly controlled to avoid the formation of mayenite, especially if iron-rich raw materials are used. Otherwise, gypsum could be added to mitigate the effect of mayenite.

References

- [1] E. Gartner, "Industrially interesting approaches to "low-CO<sub>2</sub>" cements," *Cement and Concrete Research*, no. Vol. 34, pp. 1489-1498, 2004.
- [2] K. L. Scrivener, J. M. Vanderley und E. M. Gartner, „Eco-efficient cements: Potential economically viable solutions for a low-CO<sub>2</sub> cement-based materials industry," United Nations Environment Program (UNEP), 2016.
- [3] J. G. J. Olivier, G. Janssens-Maenhout und J. A. H. W. Peters, „Trends in global CO<sub>2</sub> emissions; 2012 Report," PBL Netherlands Environmental Assessment Agency, The Hague, Netherlands, 2012.
- [4] G. Habert, „Environmental impact of Portland cement production," in *Eco-efficiency of Portland Cement Concrete*, Cambridge, United Kingdom, Woodhead Publishing Limited, 2013, p. 3–25.
- [5] V. U. o. Wellington, „Victoria University of Wellington School of Architecture Te Kura Waihanga," Victoria University of Wellington, [Online]. Available: <http://www.victoria.ac.nz/architecture/centres/cbpr/resources/>. [Zugriff am 30 06 2017].
- [6] N. R. M. C. Association, „Concrete CO<sub>2</sub> Fact Sheet "2PCO<sub>2</sub>",“ National Ready Mixed Concrete Association (NRMCA), Silver Spring, USA, 2008.
- [7] M. A. G. Stumpf, M. P. Kulakowski, L. B. Breitenbach und F. Kirch, „A case study about embodied energy in concrete and structural masonry buildings," *Revista de la Construcción*, Bd. 13, Nr. 2, pp. 9-14, 2014.
- [8] R. N. J. Comans, E. Zuiver, P. A. Geelhoed und D. Hoede, „Characterisation of leaching properties of C-FIX products and components," ENC-Clean Fossil Fuels Environmental Risk Assessment, Netherlands, 2003.
- [9] A. F. T. Inc., „AMC Foam Technologies Inc.," [Online]. Available: <http://www.amcfoam.com/index.html>. [Zugriff am 03 09 2017].
- [10] M. A. Samarai, M. Laquerbe und A. Al-Hadithi, „Sulphur sand mixes as building material," *Materials and Structures*, Bd. 18, Nr. 1, pp. 57-65, 1985.
- [11] L. Zhang, M. Su und Y. Wang, „Development of the use of sulfo- and ferroaluminate cements in China," *Advances in Cement Research*, Bd. 11, Nr. 1, pp. 15-21, 1999.
- [12] P. K. Mehta, „Investigations on energy-saving cements.," *World Cement Technology*, Bd. 11, Nr. 4, pp. 166-177, 1980.
- [13] P. Duxson, A. Fernández-Jiménez, J. L. Provis, G. C. Lukey, A. Palomo und J. S. J. Deventer, „Geopolymer technology: the current state of the art," *Journal of Materials Science*, Bd. 42, pp. 2917-2933, 2007.
- [14] C. Li, H. Sun und L. Li, „A review: The comparison between alkali-activated slag (Si+Ca) and metakaolin (Si+Al) cements," *Cement and Concrete Research*, Bd. 40, pp. 1341-1349, 2010.
- [15] E. I. Al-Wakeel und S. A. El-Korashy, „Reaction mechanism of the hydrothermally treated CaO-SiO<sub>2</sub>-Al<sub>2</sub>O<sub>3</sub> and CaO-SiO<sub>2</sub>-Al<sub>2</sub>O<sub>3</sub>-CaSO<sub>4</sub> systems," *JOURNAL OF MATERIALS SCIENCE*, Bd. 31, pp. 1909-1913, 1996.
- [16] M. Achtenbosch, U. Dewald, E. Nieke und G. Sardemann, „New calcium hydrosilicate-based cements: Cempliment - a Technology Assessment," *Zement Kalk Gips*, Bd. 6, pp. 48-57, 2016.
- [17] T. Link, F. Bellmann, H. M. Ludwig und M. Ben Haha, „Reactivity and phase composition of Ca<sub>2</sub>SiO<sub>4</sub> binders made by annealing of alpha-dicalcium silicate hydrate," *Cement and Concrete Research*, Bd. 67, pp. 131-137, 2015.
- [18] M. Achtenbosch, C. Kupsch, E. Nieke und G. Sardemann, „Sind „Green Cements“ die Zukunft? Erste systemanalytische Abschätzungen Teil 1: Novacem®," KIT Scientific Publishing, Karlsruhe, Germany, 2011.
- [19] V. Atakan, S. Sahu, S. Quinn, X. Hu und N. DeCristofaro, „Why CO<sub>2</sub> matters - advances in a new class of cement," *Zement Kalk Gips International*, Bd. 3, pp. 1-4, 2014.
- [20] M. S. Imbabi, C. Carrigan und S. McKenna, „Trends and developments in green cement and concrete technology," *International Journal of Sustainable Built Environment*, Bd. 1, Nr. 2, pp. 194-216, 2012.
- [21] C. Du, „A Review of Magnesium Oxide in Concrete," *Concrete international*, Bd. 27, Nr. 12, pp. 45-50, 2005.
- [22] S. Sorel, „ Sur un nouveau ciment magnésien (On a new magnesium cement),," *Comptes Rendus Hebdomadaires des Séances de l'Académie des Sciences*, Bd. 65, pp. 102-104, 1876.
- [23] A. S. Wagh, *Chemically Bonded Phosphate Ceramics*, Oxford, United Kingdom: Elsevier, 2004.
- [24] T. Zhang, C. Cheeseman und L. Vandeperre, „Development of low pH cement systems forming

- magnesium silicate hydrate (M-S-H),“ *Cement and Concrete Research*, Bd. 41, pp. 439-442, 2011.
- [25] C. D. Popescu, M. Muntean und J. H. Sharp, „Industrial trial production of low energy belite cement,“ *Cement & Concrete Composites*, Bd. 25, pp. 689-693, 2003.
- [26] A. Poget, „Aether™ Lower Carbon Cements,“ Alma Consulting Group, [Online]. Available: <http://www.aether-cement.eu/>. [Zugriff am 01 09 2017].
- [27] Dappolonia, „ECO-BINDER,“ Dappolonia, [Online]. Available: <http://www.ecobinder-project.eu/en/>. [Zugriff am 01 09 2017].
- [28] B. W. A. Ost, B. Schiefelbein und J. M. Summerfield, „Very high early strength cement“. US Patent US 3860433 A, 30 05 1972.
- [29] J. Ambroise und J. Péra, „Use of calcium sulfoaluminate cement to improve strength of mortars at low temperature,“ in *Concrete Repair, Rehabilitation and Retrofitting II*, London, UK, Taylor & Francis Group, 2009, pp. 881-885.
- [30] K. Quillin, „Performance of belite-sulfoaluminate cements,“ *Cement and Concrete Research*, Bd. 31, pp. 1341-1349, 2001.
- [31] E. Bescher, M. Sambol, E. K. Rice und J. D. Mackenzie, „Determination of water-to-cement ratio in freshly mixed rapid-setting calcium sulfoaluminate concrete using 2.45 GHz microwave radiation,“ *Cement and Concrete Research*, Bd. 34, Nr. 5, pp. 807-812, 2004.
- [32] M. Zajac, J. Skocek, F. Bullerjahn und B. H. Mohsen, „Effect of retarders on the early hydration of calcium-sulpho-aluminate (CSA) type cements,“ *Cement and Concrete Research*, Bd. 84, pp. 62-75, 2016.
- [33] F. Bullerjahn, M. Zajac und M. Ben Haha, „CSA raw mix design: Effect on clinker formation and reactivity,“ *Materials and Structures*, Bd. 48, Nr. 12, pp. 3895-3911, 2015.
- [34] F. Bullerjahn, D. Schmitt und M. Ben Haha, „Effect of raw mix design and of clinkering process on the formation and mineralogical composition of (ternesite) belite calcium sulphoaluminate ferrite clinker,“ *Cement and Concrete Research*, Bd. 59, pp. 87-95, 2014.
- [35] O. Andac und F. P. Glasser, „Polymorphism of calcium sulphoaluminate (Ca<sub>4</sub>Al<sub>6</sub>O<sub>16</sub>•SO<sub>3</sub>) and its solid solutions,“ *Advances in Cement Research*, Bd. 6 (22), pp. 57-60, 1994.
- [36] A. Cuesta, A. G. De la Torre, E. R. Losilla, V. K. Peterson, P. Rejmak, A. Ayuela, C. Fronters und M. A. G. Aranda, „Structure, Atomistic Simulations, and Phase Transitions of Stoichiometric Ye'elimite,“ *Chemistry of Materials*, Bd. 25, pp. 1680-1687, 2013.
- [37] G. Álvarez-Pinazo, A. Cuesta, M. Garcia-Mate, I. Santacruz, E. R. Losilla, A. G. De la Torre, L. León-Reina und M. A. G. Aranda, „Rietveld quantitative phase analysis of Ye'elimite-containing cements,“ *Cement and Concrete Research*, Bd. 42, pp. 960-971, 2012.
- [38] A. Cuesta, G. Álvarez-Pinazo, S. G. Sanfélix, I. Peral, M. A. G. Aranda und A. G. De la Torre, „Hydration mechanisms of two polymorphs of synthetic ye'elimite,“ *Cement and Concrete Research*, Bd. 63, pp. 127-136, 2014.
- [39] D. Jansen, A. Spies, J. Neubauer und F. Goetz-Neunhoeffer, „Studies on the early hydration of two modifications of ye'elimite with sulfate,“ *Cement and Concrete Research*, Bd. 91, pp. 106-116, 2017.
- [40] P. Juilland, E. Gallucci, R. Flatt und K. Scrivener, „Dissolution theory applied to the induction period in alite hydration,“ *Cement and Concrete Research*, Bd. 40, Nr. 6, pp. 831-844, 2010.
- [41] L. Nicoleau, E. Schreiner und A. Nonat, „The Di- and Tricalcium Silicate Dissolutions,“ *Cement and Concrete Research*, Bd. 47, pp. 14-30, 2013.
- [42] L. Nicoleau, E. Schreiner und A. Nonat, „Ion-specific effects influencing the dissolution of tricalcium silicate,“ *Cement and Concrete Research*, Bd. 59, pp. 118-138, 2014.
- [43] P. Juilland und E. Gallucci, „Morpho-topological investigation of the mechanisms and kinetic regimes of alite dissolution,“ *Cement and Concrete Research*, Bd. 76, pp. 180-191, 2015.
- [44] B. Lothenbach, T. Matschei, G. Möschner und F. P. Glasser, „Thermodynamic modelling of the effect of temperature on the hydration and porosity of Portland cement,“ *Cement and Concrete Research*, Bd. 38, Nr. 1, pp. 1-18, 2008.
- [45] J. W. Bullard, H. M. Jennings, R. A. Livingston, A. Nonat, G. W. Scherer, J. S. Schweitzer, K. L. Scrivener und J. J. Thomas, „Mechanisms of cement hydration,“ *Cement and Concrete Research*, Bd. 41, Nr. 12, pp. 1208-1223, 2011.
- [46] K. L. Scrivener und A. Nonat, „Hydration of cementitious materials, present and future,“ *Cement and*

- Concrete Research*, Bd. 41, pp. 651-665, 2011.
- [47] A. Klein und G. E. Troxell, „Studies of Calcium Sulfoaluminate Admixtures for Expansive Cements,“ *Proceedings of American Society for Testing Materials (ASTM)*, Bd. 58, pp. 986-1008, 1958.
- [48] A. Klein, „Calciumaluminosulfate and expansive cements containing same“. US Patent 3, 155, 526, 1963, 03 11 1963.
- [49] L. C. v. Nes-Blessing, „Classification of Calcium Sulfoaluminate Cements and the differences between them,“ in *ibausil*, Weimar, Germany, 2012.
- [50] F. P. Glasser und L. Zhang, „High-performance cement matrix based on Calcium-Sulfoaluminate-belite composition,“ *Cement and Concrete Research*, Bd. 21, pp. 1881-1886, 2001.
- [51] J. Péra und J. Ambroise, „New applications of Calcium Sulfoaluminate Cement,“ Institut National des Sciences Appliquées de Lyon, Lyon, France, 2004.
- [52] E. Dan und I. Janotka, „CHEMICAL RESISTANCE OF PORTLAND CEMENT, BLAST- FURNACE SLAG PORTLAND CEMENT AND SULPHOALUMINATE-BELITE CEMENT IN ACID, CHLORIDE AND SULPHATE SOLUTION: SOME PRELIMINARY RESULTS,“ *Ceramics – Silikáty*, Bd. 47, Nr. 4, pp. 141-148, 2003.
- [53] C. W. Hargis, B. Lothenbach, C. J. Müller und F. Winnefeld, „Carbonation of calcium sulfoaluminate mortars,“ *Cement and Concrete Composites*, Bd. 80, pp. 123-134, 2017.
- [54] L. Zhang und F. P. Glasser, „Investigation of the microstructure and carbonation of CSA-based concretes removed from service,“ *Cement and Concrete Research*, Bd. 35, pp. 2252-226, 2005.
- [55] J. H. Sharp, C. D. Lawrence und R. Yang, „Calcium sulfoaluminate cements-low-energy cements, special cements or what?,“ *Advances in Cement Research*, Bd. 11, Nr. 1, pp. 3-13, 1999.
- [56] W. Kurdowskie, C. M. George und F. P. Sorrentino, „Special cements,“ in *Proceedings of the VIIIth International Congress on the Chemistry of Cement*, Rio de Janeiro, Brazil, 1986.
- [57] I. Janotka und L. Krajčič, „Resistance to freezing and thawing of mortar specimens made from sulphoaluminate-belite cement,“ *Bulletin Materials Science*, Bd. 23, Nr. 6, pp. 521-527, 2000.
- [58] K. Quillin, „Low-CO2 Cements based on Calcium Sulfoaluminate,“ Building Research Establishment "bre", Watford, UK, 2010.
- [59] J. Beretka, B. de Vito, L. Santoro, N. Sherman und G. L. Valenti, „Utilisation of industrial wastes and by-products for the synthesis of special cements,“ *Resources, Conservation and Recycling*, Bd. 9, pp. 179-190, 1993.
- [60] N. Sherman, J. Beretka, L. Santoro und G. L. Valenti, „Long-term behaviour of hydraulic binders based on calcium sulfoaluminate and calcium sulfosilicate,“ *Cement and Concrete Research (CCR)*, Bd. 25, pp. 113-126, 1995.
- [61] C. A. Luz, J. C. Rocha, M. Cheriaf und J. Pera, „Valorization of galvanic sludge in sulfoaluminate cement,“ *Construction and Building Materials*, Bd. 23, pp. 595-601, 2009.
- [62] J. Strigác, M. T. Palou, J. Krištin und J. Majling, „Morphology and chemical composition of minerals inside the phase assemblage C – C2S – C4A3s - C4AF – Cs relevant to sulphoaluminate belite cements,“ *Ceramics – Silikáty*, Bd. 44 (1), pp. 26-34, 1999.
- [63] J. Korndörfer, „ntersuchungen zur Herstellung eines hydraulischen Bindemittels auf der Basis eines Rückstandes des Bergbaus von lateritischen Erzen,“ Martin-Luther-Universität Halle-Wittenberg, Halle Saale, Germany, 2000.
- [64] X. Li, Y. Zhang, X. Shen, Q. Wang und Z. Pan, „Kinetics of calcium sulfoaluminate formation from tricalcium aluminate, calcium sulfate and calcium oxide,“ *Cement and Concrete Research*, Bd. 55, pp. 79-87, 2014.
- [65] T. Hanein, I. Galan, F. P. Glasser, S. Skalamprinos, A. Elhoweris, M. S. Imbabi und M. N. Bannerman, „Stability of ternesite and the production at scale of ternesite-based clinkers,“ *Cement and Concrete Research*, Bd. 98, pp. 91-100, 2017.
- [66] M. W. Pryce, „Calcium sulphosilicate in lime-kiln wall coating,“ *Mineralogical Magazine*, Bd. 38, 1972.
- [67] W. Depmeier, „Aluminate sodalite  $\text{Ca}_8[\text{Al}_{12}\text{O}_{24}](\text{WO}_4)_2$  at room temperature,“ *Acta Crystallogr.*, Bd. 40, pp. 226-231, 1984.
- [68] W. Depmeier, „Structure of cubic aluminate sodalite  $\text{Ca}_8[\text{Al}_{12}\text{O}_{24}](\text{WO}_4)_2$  in comparison with its orthorhombic phase and with cubic  $\text{Sr}_8[\text{Al}_{12}\text{O}_{24}](\text{CrO}_4)_2$ ,“ *Acta Crystallogr.*, Bd. 44, pp. 201-207, 1988.
- [69] J. Homeyer, Kristallchemische Untersuchungen zur Einlagerung der Gastspecies  $[\text{Na}_4\text{N}_3]^{3+}$  in Sodalith



- und Cancrinit und  $[X_3(H_2O)_4]_3$  (X = Na, Li, K, Rb) in Sodalith: Synthese, Struktur und thermisches Verhalten, Universität Hannover: Fachbereich Geowissenschaften und Geographie, 2001.
- [70] D. Kurokawa, S. Takeda, M. Colas, T. Asaka, P. Thomas und K. Fukuda, „Phase transformation of  $Ca_4[Al_6O_{12}]SO_4$  and its disordered crystal structure at 1073 K,“ *Journal of Solid State Chemistry*, Bd. 215, pp. 265-270, 2014.
- [71] C. W. Hargis, J. Moon, B. Lothenbach, F. Winnefeld, H.-R. Wenk und P. J. M. Monteiro, „Calcium Sulfoaluminate Sodalite ( $Ca_4Al_6O_{12}SO_4$ ) Crystal Structure Evaluation and Bulk Modulus Determination,“ *Journal of the American Chemical Society*, Bd. 97, Nr. 3, pp. 892-898, 2014.
- [72] A. Cuesta, A. De la Torre, E. R. Losilla, I. Santacruz und M. A. Aranda, „Pseudocubic Crystal Structure and Phase Transition in Doped Ye'elimite,“ *Crystal Growth and Design*, Bd. 14, pp. 5158-5163, 2014.
- [73] P. Hewlett, *LEA's Chemistry of Cement and Concrete 4th edition*, Elsevier Science & Technology Books, 2004.
- [74] J. G. Griffin, *Calcium Aluminates: Synthesis, Characterization and Hydration Behaviour*, Denton Texas, USA: North Texas State University, 1984.
- [75] K. L. Scrivener und H. F. W. Taylor, „Microstructural development in pastes of a calcium aluminate cement,“ in *Proceedings of the International Symposium on Calcium Aluminate Cements*, Queen Mary and Westfield College, University of London, R. J. Mangabhai, 1990, pp. 41-51.
- [76] K. L. Scrivener und A. Capmas, „Calcium ALuminate Cements,“ in *Lea's - The Chemistry of Cement and Concrete 4th edition*, London, Arnold P. C. Hewlett, 1998, pp. 709-778.
- [77] T. D. Robson, „The Chemistry of Calcium Aluminates and their relating Compounds,“ in *Proceedings of the 5th International Symposium on the Chemistry of Cement*, Tokyo, Japan, 1968.
- [78] W. Hörkner und H. K. Müller-Buschbaum, „Crystal-structure of  $CaAl_2O_4$ ,“ *Inorg. Nuclear Chem.*, Bd. 38, p. 983-984, 1976.
- [79] S. N. Ude, *The synthesis and Crystal Chemistry of  $Ca_{12}Al_{14}O_{33}$  doped with  $Fe_2O_3$* , University of Tennessee, Knoxville, 2010.
- [80] H. Boysen, I. Kaiser-Bischoff, M. Lerch, S. Berendts, A. Börger, D. M. Trots, M. Hoelzel und A. Senyshyn, „Structures and properties of variously doped Mayenite investigated by neutron and synchrotron powder diffraction,“ *Zeitschrift für Kristallographie*, Bd. 30, pp. 323-328, 2009.
- [81] E. V. Galuskin, F. Gfeller, I. O. Galuskina, T. Armbruster, R. Bailau und V. V. Sharygin, „Mayenite supergroup, part I: Recommended nomenclature,“ *European Journal of Mineralogy*, Bd. 27, pp. 99-111, 2015.
- [82] J.-P. Eufinger, A. Schmidt, M. Lerch und J. Janek, „Novel anion conductors - conductivity, thermodynamic stability and hydration of anion-substituted mayenite-type cage compounds  $C_{12}A_7:X$  (X = O, OH, Cl, F, CN, S, N),“ *Physical Chemistry Chemical Physics*, Bd. 17, pp. 6844-6857, 2015.
- [83] K.-S. You, J.-W. Ahn, K.-H. Lee und S. Goto, „Effects of crystallinity and silica content on the hydration kinetics of  $12CaO \cdot 7Al_2O_3$ ,“ *Cement and Concrete Composites*, Bd. 28, Nr. 2, pp. 119-123, 2006.
- [84] E. Sakai, Y. Nikaido, T. Itoh und M. Daimon, „Ettringite formation and microstructure of rapid hardening cement,“ *Cement and Concrete Research*, Bd. 34, pp. 1669-1673, 2004.
- [85] H.-G. Park, S.-K. Sung, C.-G. Park und J.-P. Won, „Influence of a  $C_{12}A_7$  mineral-based accelerator on the strength and durability of shotcrete,“ *Cement and Concrete Research*, Bd. 38, Nr. 3, pp. 379-385, 2004.
- [86] G. Le Saoût, B. Lothenbach, A. Hori, T. Higuchi und F. Winnefeld, „Hydration of Portland cement with additions of calcium sulfoaluminates,“ *Cement and Concrete Research*, Bd. 43, pp. 81-94, 2013.
- [87] B. Bergman, „Solid-State Reactions between  $CaO$  Powder and  $Fe_2O_3$ ,“ *Journal of the American Ceramic Society*, Bd. 69, Nr. 8, pp. 608-611, 1986.
- [88] Y. Wang und J. Deng, „An investigation into cement  $CaO-SiO_2-Al_2O_3-Fe_2O_3-SO_3$  system,“ in *8th International Congress on the Chemistry of Cement*, Rio de Janeiro, Brazil, 1986.
- [89] B. Phillips und A. Muan, „Phase Equilibria in the system  $CaO$ -iron Oxide in air at 1 atm  $O_2$  pressure,“ *Journal of the American Ceramic Society*, Bd. 41, Nr. 11, pp. 445-454, 1958.
- [90] T. F. Newkirk und R. D. Thwaite, „Pseudoternary System Calcium Oxide-Monocalcium Aluminate ( $CaO-Al_2O_3$ )-Dicalcium Ferrite ( $2CaO \cdot Fe_2O_3$ ),“ *Journal of Research of the National Bureau of Standards*, Bd. 61, Nr. 4, pp. 233-245, 1958.
- [91] B. V. Chesnokov und L. F. Bazhenova, „Srebrodolskite  $Ca_2Fe_2O_5$  - a new mineral,“ *Zapiski Vsesoyuznogo*

## Summary of the findings, conclusions and perspectives

- Mineralogicheskogo Obshchestva*, Bd. 114, Nr. 2, pp. 195-199, 1985.
- [92] K. Fukuda und H. Ando, „Determination of the Pcmn/lbm2 phase boundary at high temperatures in the system  $\text{Ca}_2\text{Fe}_2\text{O}_5\text{-Ca}_2\text{Al}_2\text{O}_5$ “, *Journal of the American Ceramic Society*, Bd. 85, pp. 13000-1303, 2002.
- [93] A. Emanuelson und S. Hansen, „Distribution of iron among ferrite hydrates“, *Cement and Concrete Research*, Bd. 27, Nr. 8, pp. 1167-1177, 1997.
- [94] K. Kolovos, S. Tsvilis und G. Kakali, „The effect of foreign ions on the reactivity of the  $\text{CaO-SiO}_2\text{-Al}_2\text{O}_3\text{-Fe}_2\text{O}_3$  system“, *Cement and Concrete Research*, Bd. 32, pp. 463-469, 2002.
- [95] B. Raab, Synthese und Charakterisierung nanoskaliger hydraulisch hochreaktiver Phasen des Portland- und Tonerdezements, Naturwissenschaftlich Fakultät III der Martin-Luther-Universität Halle-Wittenberg : Martin-Luther-Universität Halle-Wittenberg , 2010.
- [96] A. Emanuelson, E. Henderson und S. Hansen, „Hydration of ferrite  $\text{Ca}_2\text{AlFeO}_5$  in the presence of sulphates and bases“, *Cement and Concrete Research*, Bd. 26, Nr. 11, pp. 1689-1694, 1996.
- [97] L. Black, C. Breen, J. Yarwood, J. Phipps und G. Maitland, „In situ Raman analysis of hydrating C3A and C4AF pastes in presence and absence of sulphate“, *Advances in Applied Ceramics*, Bd. 105, Nr. 4, pp. 209-2016, 2006.
- [98] M. Collepardi, S. Monosi und G. Moriconi, „Tetracalcium aluminoferrite hydration in the presence of lime and gypsum“, *Cement and Concrete Research*, Bd. 9, pp. 431-437, 1979.
- [99] B. d. Gipsindustrie, Gipsdatenbuch, Berlin, Germany: Bundesverband der Gipsindustrie e.V., 2003.
- [100] J. Bensted und S. P. Varma, „Infrared Spectroscopy Studies of Calcium Sulphate heated to High Temperatures“, *Zeitschrift für Naturforschung*, Bd. 26 b, pp. 690-693, 1971.
- [101] A. R. Nielsen, M. B. Larsen, P. Glarborg und K. Dam-Johansen, „High-temperature release of  $\text{SO}_2$  from calcined cement raw materials“, *Energy & Fuels*, Bd. 25, pp. 2917-2966, 2011.
- [102] A. Hoteit, E. Bouquet, C. Schönnenbeck und P. Gilot, „Sulfate decomposition from circulating fluidized bed combustors bottom ash“, *CHEMICAL ENGINEERING SCIENCE*, Bd. 62, Nr. 23, pp. 6827-6835, 2007.
- [103] L. Nicoleau, A. Nonat und D. Daval, „Rate-limiting reaction of C3S hydration - A reply to the discussion “A new view on the kinetics of tricalcium silicate hydration” by E. Gartner“, *Cement and Concrete Research*, Bd. In Press, pp. 1-5, 2017.
- [104] J. Bruno, D. Bosbach und A. Navrotsky, Chemical Thermodynamics of Solid Solutions of Interest in Radioactive Waste Management - A State-of-the-Art Report, Paris, France: OECD Publishing, 2007.
- [105] Z. Kolar, J. J. M. Binsma und B. Subotić, „The formation of orthorhombic  $\text{BaF}_2$  by precipitation from aqueous solutions and its transformation into cubic  $\text{BaF}_2$ “, *Journal of Crystal Growth*, Bd. 76, Nr. 2, pp. 408-412, 1986.
- [106] H. A. Van Straten, B. T. W. Holtkamp und P. L. De Bruyn, „Precipitation from supersaturated aluminate solutions: I. Nucleation and growth of solid phases at room temperature“, *Journal of Colloid and Interface Science*, Bd. 98, Nr. 2, pp. 342-362, 1984.
- [107] P. Juilland, „Early Hydration of Cementitious Systems“, ÉCOLE POLYTECHNIQUE FÉDÉRALE DE LAUSANNE (EPFL), Lausanne, Switzerland, 2009.
- [108] K. L. Scrivener, P. Juilland und P. J. M. Monteiro, „Advances in understanding hydration of Portland cement“, *Cement and Concrete Research*, Bd. 78, Nr. A, pp. 38-56, 2015.
- [109] D. Horn und J. Rieger, „Organic Nanoparticles in the Aqueous Phase-Theory, Experiment, and Use“, *Angewandte Chemie International Edition*, Bd. 40, pp. 4330-4361, 2001.
- [110] D. Kashchiev, Nucleation - Basic Theory with Applications, Amsterdam, Netherlands: Elsevier Ltd, 2000.
- [111] H. Cölfen und M. Antonietti, Mesocrystals and Nonclassical Crystallization, New Jersey, United States: John Wiley & Sons, Ltd, 2008.
- [112] J. M. Garcia-Ruiz, „Nucleation of protein crystals“, *Journal of Structural Biology*, Bd. 142, pp. 22-31, 2003.
- [113] L. Nicoleau und A. Nonat, „A new view on the kinetics of tricalcium silicate hydration“, *Cement and Concrete Research*, Bd. 86, pp. 1-11, 2016.
- [114] F. Winnefeld und B. Lothenbach, „Hydration of calcium sulfoaluminate cements – Experimental findings and thermodynamic modelling“, *Cement and Concrete Research*, Bd. 40, pp. 1239-1247, 2010.
- [115] EMPA, „Thermodynamic data for hydrated solids in Portland cement system ( $\text{CaO-Al}_2\text{O}_3\text{-SiO}_2\text{-CaSO}_4\text{-CaCO}_3\text{-Fe}_2\text{O}_3\text{-MgO-H}_2\text{O}$ )“, 09 05 2017. [Online]. Available:

<https://www.empa.ch/de/web/s308/cemdata>. [Zugriff am 28 09 2017].

- [116] C. B. Bahn, K. Ě. Kasza, W. J. Shack, K. Natesan und P. Klein, „Evaluation of precipitates used in strainer head loss testing: Part III. Long-term aluminum hydroxide precipitation tests in borated water,“ *Nuclear Engineering and Design*, Bd. 241, p. 1914–1925, 2011.
- [117] B. Pacewska und M. Nowacka, „Studies of conversion progress of calcium aluminate cement hydrates by thermal analysis method,“ *Journal of Thermal Analysis and Calorimetry*, Bd. 117, Nr. 2, p. 653–660, 2014.
- [118] C. Gosselin, E. Gallucci und K. L. Scrivener, „Influence of self heating and Li<sub>2</sub>SO<sub>4</sub> addition on the microstructural development of calcium aluminate cement,“ *Cement and Concrete Research*, Bd. 40, Nr. 10, pp. 1555-1570, 2010.
- [119] M. U. Okoronkwo und F. P. Glasser, „Compatibility of hydrogarnet, Ca<sub>3</sub>Al<sub>2</sub>(SiO<sub>4</sub>)<sub>x</sub>(OH)<sub>4</sub>(3–x), with sulfate and carbonate-bearing cement phases: 5–85 °C,“ *Cement and Concrete Research*, Bd. 83, pp. 86-96, 2016.
- [120] A. D. Capmas, D. Ménérier-Sorrentino und D. Damidot, „Effect of temperature on setting time of calcium aluminate cements,“ in *Calcium Aluminate Cements - Proceedings of the International Symposium*, Printed in Great Britain at the University Press, Cambridge, R. J. Mangabhaii, 1990.
- [121] F. Winnefeld und B. Lothenbach, „Phase equilibria in the system Ca<sub>4</sub>Al<sub>6</sub>O<sub>12</sub>SO<sub>4</sub> - Ca<sub>2</sub>SiO<sub>4</sub> - CaSO<sub>4</sub> - H<sub>2</sub>O referring to the hydration of calcium sulfoaluminate cements,“ *RILEM Technical Letters*, pp. 10-16, 2016.
- [122] B. Lothenbach, L. Pelletier-Chaignat und F. Winnefeld, „Stability in the system CaO–Al<sub>2</sub>O<sub>3</sub>–H<sub>2</sub>O,“ *Cement and Concrete Research*, Bd. 42, Nr. 12, p. 1621–1634, 2012.
- [123] S. Berger, C. C. D. Coumes, P. Le Bescop und D. Damidot, „Influence of a thermal cycle at early age on the hydration of calcium sulphoaluminate cements with variable gypsum contents,“ *Cement and Concrete Research*, Bd. 41, pp. 149-160, 2011.
- [124] C. W. Hargis, A. P. Kirchheim, P. J. M. Monteiro und E. M. Gartner, „Early age hydration of calcium sulfoaluminate (synthetic ye'elimite, C<sub>4</sub>A<sub>3</sub>S) in the presence of gypsum and varying amounts of calcium hydroxide,“ *Cement and Concrete Research*, Bd. 48, pp. 105-115, 2013.
- [125] I. Kaprálik und F. Hanic, „Phase relations in the subsystem C<sub>4</sub>A<sub>3</sub>S-CsH<sub>2</sub>-CH-H<sub>2</sub>O of the system CaO-Al<sub>2</sub>O<sub>3</sub>-Cs-H<sub>2</sub>O Referred to Hydration of Sulphoaluminate Cement,“ *Cement and Concrete Research*, Bd. 19, pp. 89-102, 1989.
- [126] J. Wang, „Hydration mechanism of cements based on low-CO<sub>2</sub> clinkers containing belite, ye'elimite and calcium alumino-ferrite,“ PhD thesis Université Lille 1, Lille, France, 2010.
- [127] H. Beltagui, G. Jen, M. Whittaker und M. S. Imbabi, „The influence of variable gypsum and water content on the strength and hydration of a belite-calcium sulphoaluminate cement,“ *ADVANCES IN APPLIED CERAMICS*, Bd. 116, Nr. 4, pp. 199-206, 2017.
- [128] F. Winnefeld, M. Ben Haha und B. Lothenbach, „Hydration mechanisms of calcium sulfoaluminate cements assessed by scanning electron microscopy and thermodynamic modelling,“ in *13th International Congress on the Chemistry of Cement*, Madrid, Spain, 2011.
- [129] F. Winnefeld und S. Barlag, „Influence of calcium sulfate and calcium hydroxide on the hydration of calcium sulfoaluminate clinker,“ *Zement Kalk Gips International*, Bd. 12, pp. 42-53, 2009.
- [130] F. Winnefeld und S. Barlag, „Calorimetric and thermogravimetric study on the influence of calcium sulfate on the hydration of ye'elimite,“ *Journal Thermal Analysis and Calorimetry*, Bd. 101, Nr. 3, pp. 949-957, 2009.
- [131] V. Kasselouri, P. Tsakiridis, C. Malami, B. Georgali und C. Alexandridou, „A Study on the Hydration Products of a Non-Expansive Sulfoaluminate Cement,“ *Cement and Concrete Research*, Bd. 25, Nr. 8, pp. 1726-1736, 1995.
- [132] M. T. Palou und J. Majling, „Hydration in the system C<sub>4</sub>A<sub>3</sub>S-CsH<sub>2</sub>-CH-H,“ *Journal of Thermal Analysis*, Bd. 46, pp. 557-563, 1996.
- [133] L. Zhang und F. P. Glasser, „Hydration of calcium sulfoaluminate cement at less than 24 h,“ *Advances in Cement Research (ACR)*, Bd. 14, Nr. 4, pp. 141-155, 2002.
- [134] I. Wang und F. P. Glasser, „Hydration of sulphoaluminate cements,“ *Advances in Cement Research*, Bd. 8, pp. 134-147, 1996.
- [135] J. Majling, R. Znášik, A. Gabrišová und S. Svetík, „The influence of anhydrite reactivity upon hydration of calcium sulphoaluminate cement clinker,“ *Thermochimica Acta*, Bd. 92, Nr. C, pp. 349-352, 1985.

### Summary of the findings, conclusions and perspectives

- [136] S. Sahu, V. Tomková, J. Majling und J. Havlica, „Influence of particle sizes of individual minerals on the hydration process in the system C2S-C4A3s-Cs,“ *Cement and Concrete Research*, Bd. 23, Nr. 3, pp. 693-699, 1993.
- [137] S. Sahu, J. V. Havlica, J. Tomková und J. Majling, „Hydration behaviour of sulphoaluminate belite cement in the presence of various calcium sulphates,“ *Thermochimica Acta*, Bd. 175, Nr. 1, pp. 45-52, 1991.
- [138] J. Chang, X. Cheng, F. Liu, L. Lu und B. Teng, „Influence of fluorite on the Ba-bearing sulphoaluminate cement,“ *Cement and Concrete Research*, Bd. 31, pp. 213-216, 2001.
- [139] M. Y. Benarchid, J. Rogez, A. Diouri, A. Boukhari und J. Aride, „Formation and hydraulic behaviour of chromium-phosphorus doped calcium sulfoaluminate cement,“ *Thermochimica Acta*, Bd. 433, pp. 183-186, 2005.
- [140] Y. Li, X. Liu, X. Niu und L. Song, „Influence of minor oxides on formation and decomposition of mineral calcium sulfoaluminate ( $3\text{CaO}\cdot 3\text{Al}_2\text{O}_3\cdot \text{CaSO}_4$ ),“ *Materials Research Innovations*, Bd. 11, Nr. 2, pp. 92-94, 2007.
- [141] S. Ma, X. Shen, Y. Huang und B. Zhong, „Effect of CuO on the formation mechanism of Calcium Sulphoaluminate,“ *Journal of Wuhan University of Technology Material Science*, pp. 518-521, 2008.
- [142] Y. G. Wang, H. Q. Ye, K. H. Kuo, X. J. Feng, S. Z. Long und G. L. Lao, „High-resolution electron diffraction of the twinning and intergrowth in  $\text{Ca}_4\text{Al}_6\text{So}_{16}$  and  $\text{Ca}_3\text{SrAl}_6\text{SO}_{16}$ ,“ *Journal of Material Science*, Bd. 26, pp. 6325-6330, 1991.
- [143] G. Belz, J. Beretka, M. Marrocoli, L. Santoro, N. Sherman und G. L. Valenti, „Use of fly ash, blast furnace slag and chemical gypsum for the synthesis of calcium sulphoaluminate-based cements,“ *Special Publication, ACI*, Bd. 153, pp. 513-530, 1995.
- [144] B. Lothenbach, „Thermodynamic equilibrium calculations in cementitious systems,“ *Materials and Structures*, Bd. 43, pp. 1413-1433, 2010.
- [145] M. Ben Haha, K. De Weerd und L. Barbara, „Quantification of the degree of reaction of fly ash,“ *Cement and Concrete Research*, Bd. 40, pp. 1620-1629, 2010.
- [146] T. Matschei, B. Lothenbach und F. P. Glasser, „Thermodynamic properties of Portland cement hydrates in the system  $\text{CaO}-\text{Al}_2\text{O}_3-\text{SiO}_2-\text{CaSO}_4-\text{CaCO}_3-\text{H}_2\text{O}$ ,“ *Cement and Concrete Research*, Bd. 37, Nr. 10, pp. 1379-1410, 2007.
- [147] D. A. Kulik, T. Wagner, S. V. Dmytrieva, G. Kosakowski, F. F. Hingerl, K. V. Chudnenko und U. R. Berner, „GEM-Selektor geochemical modeling package: revised algorithm and GEMS3K numerical kernel for coupled simulation codes,“ *Computational Geosciences*, Bd. 17, Nr. 1, pp. 1-24, 2012.
- [148] T. Thoenen und D. Kulik, „Nagra/PSI chemical thermodynamic database 01/01 for GEMS-selektor (V.2-PSI) geochemical modelling code,“ <http://gems.web.psi.ch/doc/pdf/TM-44-03-04-web.pdf> PSI, 2013.
- [149] W. Hummel, U. Berner, E. Curti, F. Pearson und T. Thoenen, „Nagra/PSI Chemical Thermodynamic Data Base 01/01, USA also published as Nagra Technical Report NTB 02-16,“ in *Universal Publishers/uPUBLISH.com*, Wettingen, Switzerland 2002, 2002.
- [150] B. Lothenbach und F. Winnefeld, „Thermodynamic modelling of the hydration of Portland cement,“ *Cement and Concrete Research*, Bd. 36, p. 209–226, 2006.
- [151] T. Matschei, B. Lothenbach und F. Glasser, „Thermodynamic properties of Portland cement hydrates in the system  $\text{CaO}-\text{Al}_2\text{O}_3-\text{SiO}_2-\text{CaSO}_4-\text{CaCO}_3-\text{H}_2\text{O}$ ,“ *Cement and Concrete Research*, Bd. 37, pp. 1379-1410, 2007.
- [152] M. Zajac, S. Hoock, C. Stabler und M. Ben Haha, „Effect of hydration kinetics on properties of compositionally similar binders,“ *Cement and Concrete Research*, p. 12, 2017.
- [153] H. Le Chatelier, „Sur les changements de volume qui accompagnent le durcissement des ciments,“ *Bulletin Société de l'Encouragement pour l'Industrie Nationale*, Bd. 5, Nr. 5, pp. 54-57, 1900.
- [154] M. Geiker und I. Knudsen, „Chemical shrinkage of Portland cements,“ *Cement and Concrete Research*, Bd. 12, pp. 603-610, 1982.
- [155] A. C-1608-07, *Standard test method for chemical shrinkage of hydraulic cement paste*, ASTM International, 2007.
- [156] B. AXS, *Topas V: general profile and structure analysis software for powder diffraction data*, Karlsruhe: Bruker AXS, 2008.

- [157] D. Jansen, The hydration of an Ordinary Portland Cement (OPC) and the influence of selected polymers: A mineralogical study using an external standard method for quantitative X-ray diffraction, Friedrich-Alexander-Universität Erlangen-Nürnberg, 2011.
- [158] E. J. Mittemeijer und U. Welzel, Modern Diffraction Methods, Weinheim, Germany: Wiley-VCH Verlag GmbH & Co. KGaA, 2012.
- [159] R. Berliner und P. b. West, „Neutron powder diffraction investigation of model cement compounds,“ *Cement and Concrete Research*, Bd. 27, Nr. 4, pp. 551-575, 1997.
- [160] H. Bartl und T. Scheller, „Zur Struktur des  $(\text{CaO})_{12}(\text{Al}_2\text{O}_3)_7$ ,“ *Neues Jahrbuch für Mineralogie*, Bd. 35, pp. 547-552, 1970.
- [161] V. A. Efremov, S. I. Gutnikov und A. A. Kartashov, „Average grossite crystal structure,“ *Personal communication to Crystallography Open Database (COD)*, 2012.
- [162] A. A. Colville und S. Geller, „The crystal structure of brownmillerite,  $\text{Ca}_2\text{FeAlO}_5$ ,“ *Acta Crystallographica*, Bd. 27, Nr. Sec. B, pp. 2311-2315, 1971.
- [163] D. Grier und G. McCarthy, „ICDD Grant-in-Aid,“ *North Dakota State Univ., Fargo, ND, USA.*, 1993.
- [164] A. Kirfel und G. Will, „Charge density in anhydrite,  $\text{CaSO}_4$ , from X-ray and neutron diffraction measurements,“ *Acta Crystallographica*, Bd. 36, Nr. Sec. B, pp. 2881-2890, 1980.
- [165] B. B. Pedersen und D. Semmingsen, „Neutron diffraction refinement of the structure of gypsum,  $\text{CaSO}_4 \cdot 2\text{H}_2\text{O}$ ,“ *Acta Crystallographica B*, Bd. 38, pp. 1074-1077, 1982.
- [166] n. Ishizawa, T. Miyata, I. Minato, F. Marumo und S. Iwai, „A structural investigation of  $\alpha\text{-Al}_2\text{O}_3$  at 2170 K,“ *Acta Crystallographica*, Bd. B36, pp. 228-230, 1980.
- [167] H. S. Shin, „A study on the structure of maghemite ( $\gamma\text{-Fe}_2\text{O}_3$ ). I. Rietveld analysis of powder XRD patterns,“ *Journal of the Korean Ceramic Society*, Bd. 35, Nr. 10, pp. 1113-1119, 1998.
- [168] I. Oftedal, *Z. Phys. Chem.*, Bd. 128, Nr. 154, 1927.
- [169] R. M. Hazen, „Effects of temperature and pressure on the cell dimension and X-ray temperature factors of periclase,“ *American Mineralogist*, Bd. 61, pp. 266-271, 1976.
- [170] T. Yamanaka und Y. Takéuchi, „Order-disorder transition in  $\text{MgAl}_2\text{O}_4$  spinel at high temperatures up to 1700 °C,“ *Zeitschrift fuer Kristallographie*, Bd. 165, Nr. 1-4, pp. 65-78, 2010.
- [171] H. S. C. O'Neil, H. Annersten und D. Virgo, „The temperature dependence of the cation distribution in magnesioferrite ( $\text{MgFe}_2\text{O}_4$ ) from powder XRD structural refinements and Moessbauer spectroscopy,“ *American Mineralogist*, Bd. 77, pp. 725-740, 1992.
- [172] Y. Ohashi, „Polysynthetically-twinned structures of enstatite and wollastonite,“ *Physics and Chemistry of Minerals*, Bd. 10, Nr. 5, p. 217-229, 1984.
- [173] G. Cocco, E. Corazza und C. Sabelli, „The crystal structure of glauconite,  $\text{CaNa}_2(\text{SO}_4)_2$ ,“ *Zeitschrift fuer Kristallographie, Kristallgeometrie, Kristallphysik, Kristallchemie*, Bd. 122, pp. 175-184, 1965.
- [174] L. S. Dent Glasser und C. K. Lee, „The structure of jasmundite,  $\text{Ca}_{22}(\text{SiO}_4)_8\text{O}_{45}\text{S}_2$  Locality: Ettringer Feld lava flow, Bellerberg volcano, Mayen, Eifel, Germany,“ *Acta Crystallographica*, Bd. Section B, Nr. 37, pp. 803-806, 1981.
- [175] F. Goetz-Neunhoeffler und J. Neubauer, „Refined ettringite ( $\text{Ca}_6\text{Al}_2(\text{SO}_4)_3(\text{OH})_{12} \cdot 26\text{H}_2\text{O}$ ) structure for quantitative X-ray diffraction analysis,“ *Powder Diffraction*, Bd. 21, Nr. 01, pp. 4-11, 2006.
- [176] R. Allmann, „Refinement of the hybrid layer structure hexahydroxaluminocalcium hemisulfate trihydrate  $[\text{Ca}_2\text{Al}(\text{OH})_6]^+ [(1/2 \text{SO}_4 \cdot 3\text{H}_2\text{O})^-]$ ,“ *Neues Jahrbuch für Mineralogie Monatshefte*, pp. 136-144, 1977.
- [177] H. Saalfeld und M. Wedde, „Refinement of the crystal structure of gibbsite,  $\text{Al}(\text{OH})_3$ ,“ *Zeitschrift für Kristallographie*, Bd. 139, pp. 129-135, 1974.
- [178] R. Rothbauer, F. Zigan und H. O'Daniel, „Verfeinerung der struktur des bayerits,  $\text{Al}(\text{OH})_3$ ,“ *Zeitschrift für Kristallographie*, Bd. 125, pp. 317-331, 1967.
- [179] Y. Le Page und G. Donnay, „Refinement of the crystal structure of low-quartz,“ *Acta Crystallographica B*, Bd. 32, pp. 2456-2459, 1976.
- [180] J. Albertsson, S. C. Abrahams und A. Kvik, „Atomic displacement, anharmonic thermal vibration, expansivity and pyroelectric coefficient thermal dependence in  $\text{ZnO}$ ,“ *Acta Crystallographica*, Bd. 45, pp. 34-40, 1989.



## Summary of the findings, conclusions and perspectives

- [181] I. Galan, H. Beltagui, M. García-Maté, F. P. Glasser und M. S. Imbabi, „Impact of drying on pore structures in ettringite-rich cements,“ *Cement and Concrete Research*, Bd. 84, pp. 85-94, 2016.
- [182] R. Snellings, „X-ray powder diffraction applied to cement,“ in *A Practical Guide to Microstructural Analysis of Cementitious Materials*, Boca Raton, United States, Taylor & Francis, 2016, pp. 107-176.
- [183] K. L. Scrivener, „Backscattered electron imaging of cementitious microstructures: understanding and quantification,“ *Cement and Concrete Composites*, Bd. 26, Nr. 8, pp. 935-945, 2004.
- [184] F. Bullerjahn, M. Ben Haha und K. L. Scrivener, „Iron solid solutions of ye'elimite - Effect on reactivity,“ in *19. ibausil*, Weimar, Germany, 2015.
- [185] F. Bullerjahn, M. Ben Haha und K. L. Scrivener, „Iron solid solutions of ye'elimite - Effect on reactivity,“ in *Proceedings of 14th ICCO*, Beijing, China, 2015.
- [186] R. Schmidt, Untersuchung zur Verwertung und Beseitigung industrieller mineralischer Reststoffe aus der Rauchgasreinigung, Martin-Luther-Universität Halle-Wittenberg: Mathematisch-Naturwissenschaftlich-Technische Fakultät, 2000.
- [187] N. Zupančič, D. Kolar, D. Sušnik und Z. Samardžija, „Role of Fe<sub>2</sub>O<sub>3</sub> on formation kinetics and microstructure of calcium sulfoaluminoferrite C<sub>4</sub>(A,F)<sub>3</sub>s,“ *British Ceramic Transactions*, Bd. 93, Nr. 6, pp. 219-223, 1994.
- [188] A. G. De la Torre, A. J. M. Cuberos, G. Alvarez-Pinazo, A. Cuesta und M. A. G. Aranda, „In situ powder diffraction study of belite sulfoaluminate clinkering,“ *Journal of Synchrotron Radiation*, Bd. 18, pp. 506-514, 2011.
- [189] W. Kurdowski, *Cement and Concrete Chemistry*, Netherlands: Springer, 2014.
- [190] Y. Suzuki, N. Kondo und T. Ohji, „In Situ Synthesis and Microstructure of Porous CaAl<sub>4</sub>O<sub>7</sub> Monolith and CaAl<sub>4</sub>O<sub>7</sub>/CaZrO<sub>3</sub> Composite,“ *Journal of the Ceramic Society of Japan*, Bd. 109, Nr. 3, pp. 205-209, 2001.
- [191] P. Shrimali, Studies on phase formation in high alumina cement by varying manufacturing parameter and effect of those phases in refractory castable, National Institute of Technology Rourkela: Department of Ceramic Engineering, 2013.
- [192] M. Idrissi, A. Diouri, D. Damidot, J. M. Greneche, M. Alami Talbi und M. Taibi, „Characterisation of iron inclusion during the formation of calcium sulfoaluminate phase,“ *Cement and Concrete Research*, Bd. 40, pp. 1314-1319, 2010.
- [193] B. Touzo, K. Scrivener und F. P. Glasser, „Phase compositions and equilibria in the CaO-Al<sub>2</sub>O<sub>3</sub>-Fe<sub>2</sub>O<sub>3</sub>-SO<sub>3</sub> system, for assemblages containing ye'elimite and ferrite Ca<sub>2</sub>(Al,Fe)O<sub>5</sub>,“ *Cement and Concrete Research*, Bd. 54, pp. 77-86, 2013.
- [194] V. Makhmudova, M. Iskandarova, Y. Ivanova, G. Chernev und N. Ruziev, „Synthesis and properties of sulphoferrite calcium clinkers and low temperature cements on their basis,“ *Journal of the Uni. Chem. Techn. and Metallurgy*, Bd. 46 (2), pp. 151-154, 2011.
- [195] Y. Zhang, X. Shen und X. Li, „Kinetics of calcium sulfoaluminate with 1% iron oxide by isothermal and isoconversional methods,“ *Advances in Cement Research*, pp. 1-11, 2017.
- [196] M. M. Ali, S. Gopal und S. K. Handoo, „Studies on the Formation kinetics of Calcium Sulphoaluminate,“ *Cement and Concrete Research*, Bd. 24, Nr. 4, pp. 715-720, 1994.
- [197] E. V. Sokol, S. N. Kokh, Y. Vapnik, V. Thiery und S. A. Korzhova, „Natural analogs of belite sulfoaluminate cement clinkers from Negev Desert, Israel,“ *American Mineralogist*, Bd. 99, p. 1471-1487, 2014.
- [198] F. Puertas, M. T. Blanco Varela und S. Giménez Molina, „Kinetics of the thermal decomposition of C<sub>4</sub>A<sub>3</sub>s in air,“ *Cement and Concrete Research*, Bd. 25, Nr. 3, pp. 572-580, 1995.
- [199] M. Gallardo, J. M. Almanza, D. A. Cortés, J. C. Escobedo und J. I. Escalante-García, „Synthesis and mechanical properties of a calcium sulfoaluminate cement made from industrial wastes,“ *Materials de Construcción*, Bd. 64, Nr. 315, p. 8, 2014.
- [200] A. GHOSH, T. K. BHATTACHARYA, B. MUKHERJEE, H. S. TRIPATHI und S. K. DAS, „Effect of Fe<sub>2</sub>O<sub>3</sub> on the densification and properties of lime,“ *Ceramics - Silikáty*, Bd. 47, Nr. 2, pp. 70-74, 2003.
- [201] W. H. Zachariasen, „The Atomic Arrangement in Glass,“ *Journal of the American Chemical Society*, Bd. 54, Nr. 10, p. 3841-3851, 1932.
- [202] Y. M. Butt, V. V. Timashev und A. P. Ozokin, „The mechanism of clinker formation process and ways of modification of clinker structure,“ in *6th International Congress on Chemistry of Cement (ICCC)*, Moscow, Russia, 1974.

- [203] V. V. Timashev, „The kinetics of clinker formation. The structure and composition of clinker and its phases,“ in *7th International Congress on the Chemistry of Cement (ICCC)*, Paris, France, 1980.
- [204] M. Muhammadiéh, Beitrag zur Ermittlung des Ansatzbildungspotenzials von Braunkohlen in Dampferzeugern, Technische Universität Bergakademie Freiberg: Fakultät für Maschinenbau, Verfahrens- und Energietechnik, 2007.
- [205] P. Wang und M. Massoudi, „Slag Behavior in Gasifiers. Part I: Influence of Coal Properties and Gasification Conditions,“ *Energies*, Bd. 6, pp. 784-806, 2013.
- [206] A. Zawada, „Der strukturelle Einbau von Eisenionen in Alkali- Erdalkalisilikat- und Alumosilikatgläsern sowie die Charakterisierung der Eigenschaften der Gläser,“ Der Technischen Universität Bergakademie Freiberg, Freiberg, Germany, 2002.
- [207] D. J. Min und S. M. Jung, „Current status of slag design in metallurgical processes,“ in *Advances in Molten Slags, Fluxes, and Salts: Proceedings of the 10th International Conference on Molten Slags, Fluxes and Salts (MOLTEN16)*, Seattle, USA, Springer International Publishers, 2016, pp. 17-28.
- [208] Y. B. Pliego-Cuervo und F. P. Glasser, „The role of Sulphate in Cement Clinkering Reactions: Phase formation in the system CaO-Al<sub>2</sub>O<sub>3</sub>-Fe<sub>2</sub>O<sub>3</sub>-SiO<sub>2</sub>-CaSO<sub>3</sub>-K<sub>2</sub>SO<sub>4</sub>,“ *Cement and Concrete Research*, Bd. 9, pp. 573-581, 1979.
- [209] Y. B. Pliego-Cuervo und F. P. Glasser, „The role of sulfates in Cement Clinkering Reactions: Phase formation and Melting in the System CaO-CaSiO<sub>2</sub>-CaSO<sub>4</sub>-K<sub>2</sub>SO<sub>4</sub>,“ *Cement and Concrete Research*, Bd. 7, pp. 477-482, 1977.
- [210] W. R. Eubank und R. H. Bogue, „Preliminary Study on Portions of the Systems Na<sub>2</sub>O-CaO-Al<sub>2</sub>O<sub>3</sub>-Fe<sub>2</sub>O<sub>3</sub> and Na<sub>2</sub>O-CaO-Al<sub>2</sub>O<sub>3</sub>-Fe<sub>2</sub>O<sub>3</sub>-SiO<sub>2</sub>,“ *Journal of Research of the National Bureau of Standards*, Bd. 40, pp. 225-234, 1948.
- [211] L. J. Beyers, G. A. Brooks, B. Blanpain und F. Verhaeghe, „Effects of structure on the thermodynamic and transport properties of Na<sub>2</sub>O-CaO-SiO<sub>2</sub>-FeO-Fe<sub>2</sub>O<sub>3</sub> melts,“ in *Advances in Molten Slags, Fluxes, and Salts: Proceedings of The 10th International Conference on Molten Slags, Fluxes and Salts (MOLTEN16)*, Washington, USA, 2016.
- [212] W. A. Klemm und J. Skalny, „Mineralizers and Fluxes in Clinkering Process,“ *Cement Research Progress (American Ceramic Society)*, pp. 259-280, 1976.
- [213] V. N. Viswanathan und S. N. Gosh, „Mineralizers and Fluxes in Clinkerization,“ in *Advances in Cement Technology*, Oxford, United Kingdom, Pergamon Press, 1983, pp. 177-202.
- [214] V. Johansen und J. I. Bhatti, „Fluxes and Mineralizers in Clinkering Process,“ in *Innovations in Portland Cement Manufacturing*, Portland Cement Association, 2004, pp. 369-402.
- [215] S. Horkoss, R. Lteif und T. Rizk, „Calculation of the C<sub>3</sub>A Percentage in High Sulfur Clinker,“ *International Journal of Analytical Chemistry*, pp. 1-5, 2010.
- [216] I. Maki, „Formation and microscopic textures of Portland cement clinker minerals, part 1,“ *Cement Wapno Beton*, Bd. 2, pp. 65-85, 2006.
- [217] T. Tsuboi, T. Ito, Y. Hokinous und Y. Matsuzaki, „The influence of MgO, SO<sub>3</sub> and ZnO on the sintering of Portland Cement Clinker,“ *Zement-Kalk-Gips*, Bd. 25, Nr. 9, pp. 426-431, 1972a.
- [218] T. Tsuboi und T. Ogawa, „Microscopic studies of clinker for evaluating the sintering process,“ *Zement-Kalk-Gips*, Bd. 25, Nr. 6, pp. 292-294, 1972b.
- [219] J. Imlach, L. D. Glasser und F. Glasser, „Excess oxygen and the stability of 12CaO\*7Al<sub>2</sub>O<sub>3</sub>,“ *Cement and Concrete Research*, Bd. 1, pp. 57-61, 1971.
- [220] R. W. Nurse, J. H. Welch und A. J. Majumdar, „The 12CaO-7Al<sub>2</sub>O<sub>3</sub> Phase in the CaO-Al<sub>2</sub>O<sub>3</sub> System,“ *Transactions of the British Ceramic Society*, Bd. LXIV, pp. 323-332, 1965.
- [221] V. K. Singh und F. P. Glasser, „High temperature reversible moisture uptake in calcium aluminate Ca<sub>12</sub>Al<sub>14</sub>O<sub>33-x</sub>(OH)<sub>2x</sub>,“ *Ceramics International*, Bd. 14, Nr. 1, pp. 59-62, 1988.
- [222] D. W. Hadley, „The nature of the paste-aggregate interface,“ Purdue University, West Lafayette, 1972.
- [223] I. A. Chen, C. W. Hargis und M. C. Juenger, „Understanding expansion in calcium sulfoaluminate-belite cements,“ *Cement and Concrete Research*, Bd. 42, pp. 51-60, 2012.
- [224] A. Violante und P. M. Huang, „Formation mechanism of aluminium hydroxide polymorphs,“ *Clays and Clay Minerals*, Bd. 41, Nr. 5, pp. 590-597, 1993.
- [225] P. H. Hsu, „Aluminum hydroxides and oxyhydroxides,“ in *Minerals in Soil Environments*, S. S. S. Am., Hrsg.,



- Madison, WI, J.B. Dixon and S.B. Weed, 1989, pp. 99-143.
- [226] K. P. Prodromou und A. S. Pavlatou-Ve, „Formation of aluminium hydroxides as influenced by aluminium salts and bases,“ *Clay and Clay minerals*, Bd. 43, Nr. 1, pp. 111-115, 1995.
- [227] A. N. Christensen, T. R. Jensen, B. Lebech, J. C. Hanson, H. J. Jakobsen und J. Skibsted, „Thermal decomposition of monocalcium aluminate decahydrate (CaAl<sub>2</sub>O<sub>4</sub>·10H<sub>2</sub>O) investigated by in-situ synchrotron X-ray powder diffraction, thermal analysis and <sup>27</sup>Al, 2H MAS NMR spectroscopy,“ *Dalton Transactions - The international journal for inorganic, organometallic and bioinorganic chemistry*, pp. 455-462, 2008.
- [228] T. Sato, „Preparation of Gelatinous Aluminium Hydroxide,“ *Zeitschrift für anorganische und allgemeine Chemie*, Bd. 391, pp. 69-78, 1972.
- [229] L. G. Baquerizo, T. Matschei, K. L. Scrivener, M. Saeidpour und L. Wadsö, „Hydration states of AFm cement phases,“ *Cement and Concrete Research*, Bd. 73, p. 143-157, 2015.
- [230] B. Lothenbach, P. Durdzinski und K. De Weerd, „Thermogravimetric analysis,“ in *A Practical Guide to Microstructural Analysis of Cementitious Materials*, Boca Raton, United States, Taylor & Francis Group, 2016, pp. 177-211.
- [231] M. J. Sánchez-Herrero, A. Fernández-Jiménez und A. Palomo, „C<sub>4</sub>A<sub>3</sub>Š hydration in different alkaline media,“ *Cement and Concrete Research*, Bd. 46, pp. 41-49, 2013.
- [232] T. Oey, A. Kumar, J. W. Bullard, N. Neithalath und G. Sant, „The Filler Effect: The Influence of Filler Content and Surface Area on Cementitious Reaction Rates,“ *Journal of the American Ceramic Society*, Bd. 96, Nr. 6, pp. 1978-1990, 2013.
- [233] F. Guirado, S. Galí und J. S. Chinchón, „The thermal decomposition of hydrated alumina cement (CAH<sub>10</sub>),“ *Cement and Concrete Research*, Bd. 28, Nr. 3, pp. 381-390, 1998.
- [234] D. Damidot, „Calculation of critically supersaturated domains with respect to ettringite in the CaO-Al<sub>2</sub>O<sub>3</sub>-CaSO<sub>4</sub>-H<sub>2</sub>O system at 20°C,“ in *12th International Congress on the Chemistry of Cement*, Montreal, Canada, 2007.
- [235] H. Minard, S. Garrault, L. Regnaud und A. Nonat, „Mechanisms and parameters controlling the tricalcium aluminate reactivity in presence of gypsum,“ *Cement and Concrete Research*, Bd. 37, pp. 1418-1426, 2007.
- [236] S. Goto, K. S. You, K. Ioku und H. Fujimori, „Amorphous Layers Controlling the Rate of Hydration of Cement Minerals,“ *Journal of the Ceramic Society of Japan*, Bd. 112, pp. 1308-1310, 2004.
- [237] J. Havlica und D. Roztocka, „Hydration kinetics of calciumaluminate phases in the presence of various ratios of Ca<sup>2+</sup> and SO<sub>4</sub><sup>2-</sup> ions in liquid phase,“ *Cement and Concrete Research*, Bd. 23, pp. 294-300, 1993.
- [238] W. Lan und F. P. Glasser, „Hydration of calcium sulphoaluminate cements,“ *Advances in Cement Research*, Bd. 8, Nr. 3, pp. 127-134, 1996.
- [239] J.-B. Champenois, C. Cau Dit Coumes, A. Poulesquen, P. Le Bescop und D. Damidot, „Beneficial use of a cell coupling rheometry, conductimetry, and calorimetry to investigate the early age hydration of calcium sulfoaluminate cement,“ *Rheol Acta*, Bd. 52, pp. 177-187, 2013.
- [240] D. Jansen, A. Spies, D. Ectors, F. Goetz-Neunhoeffler und J. Neubauer, „Hydration of ye’elimite, the role of free water and sulfate during hydration,“ in *2nd International Conference on the Chemistry of Construction Materials (ICCCM)*, Munich, Germany, 2016.
- [241] M. Balonis und F. P. Glasser, „The Density of Cement Phases,“ *Cement and Concrete Research*, Bd. 39, pp. 733-739, 2009.
- [242] L. G. Baquerizo, T. Matscheia, K. L. Scrivener, A. Thorell und L. Wadsö, „Methods to determine hydration states of minerals and cement hydrates,“ *Cement and Concrete Research*, Bd. 65, p. 85-95, 2014.
- [243] T. Sato, „The Thermal Transformation of Gelatinous Aluminium Hydroxide,“ *Zeitschrift für anorganische und allgemeine Chemie*, Bd. 391, pp. 167-173, 1972.
- [244] A. Cuesta, A. De la Torre, I. Santacruz, P. d. S. Trtik, D. A. Julio, M. Holler und M. Aranda, „Chemistry and Mass Density of Aluminum Hydroxide Gel in Eco-Cements by Ptychographic X-ray Computed Tomography,“ *The Journal of Physical Chemistry*, Bd. 121, pp. 3044-3054, 2017.
- [245] K. Wefers und C. Misra, „Oxides and Hydroxides of Aluminum; Alcoa Technical Paper No. 19,“ *Aluminium Company of America (Alcoa)*, p. 100, 1987.

- [246] G. Lefèvre, M. Duc, P. Lepeut, R. Caplain und Michel Fédoroff, „Hydration of  $\gamma$ -Alumina in Water and its Effects on Surface Reactivity,“ *Langmuir*, Bd. 18, pp. 7530-7537, 2002.
- [247] H. De Hek, R. J. Stol und P. L. De Bruyn, „Hydrolysis-Precipitation Studies of Aluminium(III) Solutions 3.The Role of the Sulfate Ion,“ *Journal of Colloid and Interface Science*, Bd. 64, Nr. 1, pp. 72-89, 1978.
- [248] R. N. Edmonds und A. J. Majumdar, „The hydration of monocalcium aluminate at different temperatures,“ *Cement and Concrete Research*, Bd. 18, Nr. 2, pp. 311-320, 1988.
- [249] A. Rettel, R. Seydel, W. Gessner, J. P. Bayoux und A. Capmas, „Investigations on the influence of alumina on the hydration of monocalcium aluminate at different temperatures,“ *Cement and Concrete Research*, Bd. 23, Nr. 3, pp. 387-398, 1993.
- [250] S. T. Bergold, F. Goetz-Neunhoeffler und J. Neubauer, „Interaction of silicate and aluminate reaction in a synthetic cement system: Implications for the process of alite hydration,“ *Cement and Concrete Research*, Bd. 93, pp. 32-44, 2017.
- [251] V. Morin, P. Termkhajornkit, B. Huet und G. Pham, „Impact of quantity of anhydrite, water to binder ratio, fineness on kinetics and phase assemblage of belite-ye'elinite-ferrite cement,“ *Cement and Concrete Research*, Bd. 99, pp. 8-17, 2017.
- [252] P. Barret und D. Bertrandie, „ Hydration of aluminate cements,“ in *Engineering Foundation Conference*, Durham, United Kingdom, 1994.
- [253] C. Parr, F. Simonin, B. Touzo, C. Wöhrmeyer, B. Valdelièvre und A. Namba, „The Impact of Calcium Aluminate Cement Hydration upon the Properties of Refractory Castables,“ *Technical Paper - Reference: TP-GB-RE-LAF-043*, pp. 1-17, 2004.
- [254] A. Capmas, D. Sorrentino und D. Damidot, „Effect of temperature on setting time of calcium aluminate cements,“ in *Proceedings of the International Symposium on Calcium Aluminate Cements*, London, UK, 1990.
- [255] H. Uchikawa und S. Uchida, „The hydration of  $11\text{CaO}\cdot 7\text{Al}_2\text{O}_3\cdot \text{CaF}_2$  at 20 °C,“ *Cement and Concrete Research*, Bd. 2, pp. 681-695, 1972.
- [256] M. Fukuhara, S. Goto, K. Asaga, M. Daimon und R. Kondo, „Mechanisms and kinetics of C4AF hydration with gypsum,“ *Cement and Concrete Research*, Bd. 11, Nr. 3, pp. 407-414, 1981.
- [257] J. Rose, A. Bénard, S. E. Mrabet, A. Masion, I. Moulin, V. Briois, L. Olivi und J. Y. Bottero, „Evolution of iron speciation during hydration of C4AF,“ *Waste Management*, Bd. 26, pp. 720-724, 2006.
- [258] G. Habert, C. Billard, P. Rossi, C. Chen und N. Roussel, „Cement production technology improvement compared to factor 4 objectives,“ *Cement and Concrete Research*, Bd. 40, pp. 820-826, 2010.
- [259] M. Schneider, „Process technology for efficient and sustainable cement production,“ *Cement and Concrete Research*, Bd. 78, Nr. A, pp. 14-23, 2015.
- [260] J. Ruppert und V. Hoenig, „Development of State of the Art Techniques in Cement Manufacturing: Trying to Look Ahead,“ European Cement Research Academy (ECRA), A-2016/2305, Dusseldorf Germany and Geneva Switzerland, 2017.
- [261] J. Bhatti, „Role of Minor Elements on Cement Manufacture and Use,“ *Research and Development Bulletin RD109T*, Bd. 1990, p. 48, 1995.
- [262] D. Herfort, G. K. Moir, V. Johansen, F. Sorrentino und H. Bolio Arceo, „The chemistry of Portland cement clinker,“ *Advances in Cement Research*, Bd. 22, Nr. 4, pp. 187-194, 2010.
- [263] E. Menéndez, F. P. Glasser, B. Aldea, C. Andrade und Y. C. Zimmermann, „Effects of the incorporation of aluminum fluoride mineralizers in Portland cement clinker phases,“ 15 10 2015. [Online]. Available: <http://www.regainmaterials.com/about/publications/effects-of-the-incorporation-of-aluminium-fluoride-mineralizers-in-portland-cement-clinker-phases>. [Zugriff am 91 09 2017].
- [264] D. Stephan, R. Mallmann, D. Knöfel und R. Härdtl, „High intakes of Cr, Ni, and Zn in clinker Part II. Influence on the hydration properties,“ *Cement and Concrete Research*, Bd. 29, pp. 1959-1967, 1999.
- [265] E. W. Gartner und H. Hirao, „A review of alternative approaches to the reduction of CO<sub>2</sub> emissions associated with the manufacture of the binder phase in concrete,“ *Cement and Concrete Research*, Bd. 78, Nr. A, pp. 126-142, 2015.
- [266] A. Alaoui, A. Feraille, A. Dimassi und V. H. Nguyen, „Experimental study of sulfoaluminate concrete based materials,“ in *CONSEC'07*, Tours, France, 2007.
- [267] T. A. Ragozina, „Reaction of calcium sulphate with aluminate at 1200 °C,“ *Zurnal prikladnoj chimii (Zh.*

## Summary of the findings, conclusions and perspectives

- Prikl. Khim.*) [Journal of applied Chemistry of USSR], pp. 1682-1684, 1957.
- [268] N. Fukuda, „Constitution of Sulfo Aluminous Clinker,“ *Bulletin of the Chemical Society of Japan*, Bd. 34, pp. 138-139, 1961.
- [269] P. E. Halstead und A. E. Moore, „The composition and crystallography of an anhydrous calcium aluminosulphate occurring in expanding cement,“ *Journal of Applied Chemistry*, Bd. 12, pp. 413-417, 1962.
- [270] A. P. Osokin, Y. R. Krivoborodov und N. F. Dyukova, „Sulfoferrite cements,“ 9th ICCS New Dehli, 1992.
- [271] H. Pöllmann, S. Stöber und R. Schmidt, „Synthesis and characterization of Sulfoaluminate (Belite) cements from industrial residues,“ *Proceedings of the First International Conference on Sulphoaluminate Cement: Materials and Engineering Technology - Wuhan University of Technology Press*, pp. 366-384, 2013.
- [272] D. Chen, X. Feng und S. Long, „The influence of ferric oxide on the properties of  $3\text{CaO}\cdot 3\text{Al}_2\text{O}_3\cdot \text{CaSO}_4$ ,“ *Thermochimica Acta*, Bd. 215, pp. 157-169, 1993.
- [273] A. Cuesta, G. Álvarez-Pinazo, S. G. Sanfélix, I. Peral, M. A. G. Aranda und A. G. De la Torre, „Hydration mechanisms of two polymorphs of synthetic ye'elimite,“ *Cement and Concrete Research*, Bd. 63, pp. 127-136, 2014.
- [274] R. Kondo, „The Synthesis and Crystallography of a Group of New Compounds Belonging to the Hauyne Type Structure,“ *Journal of the Ceramic Association of Japan*, Bd. 73, pp. 1-8, 1965.
- [275] H. Saalfeld und W. Depmeier, „Silicon-free compounds with sodalite structure,“ *Krist. Tech.*, Bd. 7, pp. 229-232, 1972.
- [276] M. E. Brenchley und M. T. Weller, „Synthesis and structure of sulfide aluminate sodalites,“ *Journal of Materials Chemistry*, Bd. 2, pp. 1003-1005, 1992.
- [277] P. Zhang, Y. Chen, L. Shi, G. Zhang, W. Huang und J. Wu, „The crystal structure of  $\text{C}_4\text{A}_3\text{S}$ ,“ in *Proceeding of 9th International Congress on the Chemistry of Cement*, New Delhi, India, 1992.
- [278] I. Krstanovi, A. Radakovi und L. J. Karan, „X-ray Powder Data for  $\text{Ca}_4\text{Al}_6\text{O}_{12}\text{SO}_4$ ,“ *Powder Diffraction*, Bd. 7, Nr. 1, pp. 47-48, 1992.
- [279] N. J. Calos, C. H. L. Kennard, A. K. Whittaker und R. L. Davis, „Structure of Calcium Aluminate Sulfate  $\text{Ca}_4\text{Al}_6\text{O}_{16}\text{S}$ ,“ *Journal of Solid State Chemistry*, Bd. 119, pp. 1-7, 1995.
- [280] E. C. Posnjak, „The system  $\text{CaSO}_4\text{-H}_2\text{O}$ ,“ *American Journal of Science*, Bd. 35, pp. 247-272, 1938.
- [281] W. A. Deer, R. A. Howie und J. Zussman, *Rock-forming minerals*, Vol. 5: Non-Silicates 2nd Edition, London, United Kingdom: William Clowes & Sons, 1963.
- [282] Z. Hasratningsih, „Phase and strength changes of gypsum in the dental lost wax method,“ Department of prosthetic dentistry, University of Sydney, Sydney, Australia, 1987.
- [283] J. Bensted und S. Prakash, „Investigation of the calcium sulphate–water system by infrared spectroscopy,“ *Nature*, Bd. 219, pp. 60-61, 1968.
- [284] G. Azimi, V. G. Papangelakis und J. E. Dutrizac, „Modelling of calcium sulphate solubility in concentrated multi-component sulphate solutions,“ *Fluid Phase Equilibria*, Bd. 260, pp. 300-315, 2007.
- [285] ITALCEMENTI S.P.A., „ETA-13/0520 ALICEM. Rapid hardening Calcium Sulphoaluminate based Cement,“ Fraunhofer IRB, 13 06 2013. [Online]. Available: <https://www.baufachinformation.de/ALICEM/bzp/126675>. [Zugriff am 17 09 2017].
- [286] Buzzi Unicem Spa, „ETA 13/0417 "Next SR03". Schnellerhärtender Zement auf Basis von Calciumaluminatsulfat,“ Fraunhofer IRB, 21 06 2013. [Online]. Available: <https://www.baufachinformation.de/Next-SR03/bzp/130016>. [Zugriff am 17 09 2017].
- [287] Buzzi Unicem Spa, „ETA 13/0418 "Next SL05 NF". Rapid hardening calcium sulphoaluminate based cement,“ Fraunhofer IRB, 21 06 2013. [Online]. Available: <https://www.baufachinformation.de/Next-SL05-NF/bzp/130018>. [Zugriff am 17 09 2017].
- [288] VICAT, „ETA-16/0850 ALPENAT R<sup>2</sup>. Calcium Sulphoaluminate based Cement,“ Fraunhofer IRB, 07 12 2016. [Online]. Available: <https://www.baufachinformation.de/ALPENAT-R%C2%B2/bzp/145690>. [Zugriff am 17 09 2017].
- [289] A. E. Moore und H. F. W. Taylor, „Crystal structure of Ettringite,“ *Acta Crystallographica*, Bd. 26, pp. 386-393, 1969.
- [290] I. Chartschenko, K. Volke und J. Stark, „Untersuchungen über den Einfluß des pH-Wertes auf die

## Summary of the findings, conclusions and perspectives

- Ettringitbildung," *Wissenschaftliche Zeitschrift der Hochschule für Architektur und Weimar*, Bd. 39, Nr. 1, pp. 171-176, 1993.
- [291] E. Henderson, X. Turillas und P. Barnes, „Stability and Microstructure of Calcium Sulphoaluminate Hydrates Present in Hydrated Cement Pastes, Using in Situ Synchrotron Energy-Dispersive Diffraction," *Journal of Material Science*, Bd. 30, pp. 3856-3862, 1995.
- [292] C. J. Warren und E. J. Reardon, „The solubility of Ettringite at 25 °C," *Cement and Concrete Research*, Bd. 24, Nr. 8, pp. 1515-1524, 1994.
- [293] G. Renaudin, Y. Filinchuk, J. Neubauer und F. Goetz-Neunhoeffler, „A comparative structural study on wet and dry ettringite," *Cement and Concrete Research*, Bd. 40, pp. 370-375, 2010.
- [294] L. G. Baquerizo, T. Matschei und K. L. Scrivener, „Impact of water activity on the stability of ettringite," *Cement and Concrete Research*, Bd. 79, pp. 31-44, 2016.
- [295] H. Pöllmann, H. J. Kuzel und R. Wenda, „Compounds with ettringite structure," *Neues Jahrbuch für Mineralogie Abhandlungen*, Bd. 160, Nr. 2, pp. 133-158, 1989.
- [296] H. Pöllmann, „Immobilization of pollutants in waste disposals by forming storing up mineral reservoirs," in *10th International Congress for Applied Mineralogy*, Pretoria, South Africa, 1991.
- [297] G. Möschner, B. Lothenbach, J. Rose, A. Ullrich, R. Figi und R. Kretzschmar, „Solubility of Fe-ettringite (Ca<sub>6</sub>[Fe(OH)<sub>6</sub>]<sub>2</sub>(SO<sub>4</sub>)<sub>3</sub>·26H<sub>2</sub>O)," *Geochimica et Cosmochimica Acta*, Bd. 72, Nr. 1, pp. 1-18, 2008.
- [298] G. Möschner, B. Lothenbach, F. Winnefeld, A. Ullrich, R. Figi und R. Kretzschmar, „Solid solution between Al-ettringite and Fe-ettringite (Ca<sub>6</sub>[Al<sub>1-x</sub>Fe<sub>x</sub>(OH)<sub>6</sub>]<sub>2</sub>(SO<sub>4</sub>)<sub>3</sub>·26H<sub>2</sub>O)," *Cement and Concrete Research*, Bd. 39, Nr. 6, pp. 482-489, 2009.
- [299] B. Dilnesaa, E. Wieland, B. Lothenbach, R. Dähn und K. Scrivener, „Fe-containing phases in hydrated cements," *Cement and Concrete Research*, Bd. 58, pp. 45-55, 2014.
- [300] H.-J. Kuzel, „Ersatz von Al<sup>3+</sup> durch Cr<sup>3+</sup> und Fe<sup>3+</sup> in 3CaO·Al<sub>2</sub>O<sub>3</sub>·CaCl<sub>2</sub>·nH<sub>2</sub>O und 3CaO·Al<sub>2</sub>O<sub>3</sub>·CaSO<sub>4</sub>·nH<sub>2</sub>O," *Zement Kalk Gips*, Bd. 21, Nr. 12, pp. 493-499, 1968.
- [301] A. Mesbah, M. François, C. Cau-dit-Coumes, F. Frizon, Y. Filinchuk, F. Leroux, J. Ravoux und G. Renaudin, „Crystal structure of Kuzel's salt 3CaO·Al<sub>2</sub>O<sub>3</sub>·1/2CaSO<sub>4</sub>·1/2CaCl<sub>2</sub>·11H<sub>2</sub>O determined by synchrotron powder diffraction," *Cement and Concrete Research*, Bd. 41, pp. 504-509, 2011.
- [302] T. Scholten, Untersuchungen an sulfatischen Klinkerphasen CO<sub>2</sub>-armer Zemente, Technische Universität Clausthal: Fakultät für Natur- und Materialwissenschaften, 2017.
- [303] F. Bullerjahn, E. Boehm-Courjault, M. Zajac, M. Ben Haha und K. L. Scrivener, „Hydration reactions of synthetic ye'elimite," *Cement and Concrete Research*, 2018.
- [304] L. J. Parrot und D. C. Killoh, „Prediction of cement hydration," *British Ceramic Proceedings*, Bd. 35, pp. 41-53, 1984.
- [305] B. Lothenbach, T. Matschei, G. Möschner und F. P. Glasser, „Thermodynamic modelling of the effect of temperature on the hydration and porosity of Portland cement," *Cement and Concrete Research*, Bd. 38, pp. 1-18, 2008.

## List of publications

### JOURNAL PAPERS

- 
- 2016 ***Effect of retarders on the early hydration of calcium-sulpho-aluminate (CSA) type cements***  
Maciej Zajac, Jan Skocek, Frank Bullerjahn, Mohsen Ben Haha  
Cement and Concrete Research Vol. (84), 2016; pp 62-75
- 2014 ***CSA raw mix design: Effect on clinker formation and reactivity***  
Bullerjahn F., Zajac M., Ben Haha M.  
Materials and Structures Vol. (48) Issue 12, 2014, pp 3895–3911
- 2014 ***The role of the alumina content of slag, plus the presence of additional sulfate on the hydration and microstructure of Portland cement-slag blends***  
Whittaker M., Zajac M., Ben Haha M., Bullerjahn F., Black L.  
Cement and Concrete Research Vol. (66), pp 91-101
- 2014 ***Effect of raw mix design and clinking procedure on the formation and mineralogical composition of (ternesite) belite calcium sulfoaluminate ferrite clinker***  
Bullerjahn F., Ben Haha M., Schmitt D.  
Cement and Concrete Research Vol. (59), pp 87-95
- 2011 ***Use of Layered Double Hydroxides (LDH) of the hydrotalcite group as reservoir minerals for nitrate in soils – Examination of the chemical and mechanical stability***  
Witzke, T & Torres-Dorante, L.O.; Bullerjahn, F.; Pöllmann, H  
Minerals as Advanced Materials II, pp 131-145
- 2011 ***Untersuchungen zur Verbesserung der chemischen Stabilität eines Bodenadditivs auf LDH-Basis durch Coating***  
Bullerjahn, F.; Witzke, T.; Pöllmann, H. & Torres-Dorante, L.O.  
Hallesches Jahrbuch für Geowissenschaften Vol. 31, pp 34

### CONFERENCE PAPERS

- 
- 2015 ***Iron solid solutions of ye'elimite - Effect on reactivity***  
Bullerjahn F., Ben Haha M., Scrivener K. L.  
ibausil in Weimar, Germany
- 2015 ***Effect of retarders on the early performance of CSA-type cement***  
Skocek J., Zajac M., Bullerjahn F., Ben Haha M.  
ibausil in Weimar, Germany
- 2015 ***Iron solid solutions of ye'elimite - Effect on reactivity***  
Bullerjahn F., Ben Haha M., Scrivener K. L.  
14th International Congress on the Chemistry of Cement (ICCC) in Beijing, China
- 2015 ***On the reactivity of ternesite***  
Ben Haha M., Bullerjahn F., Zajac M.  
14th International Congress on the Chemistry of Cement (ICCC) in Beijing, China
- 2015 ***Effect of raw mix design and of clinking process on the formation and mineralogical composition of (ternesite) belite calcium sulfoaluminate ferrite clinker***  
Bullerjahn F. and Ben Haha M  
14th International Congress on the Chemistry of Cement (ICCC) in Beijing, China

## List of publications

- 2013 ***Effect of raw mix design and clinkering procedure on the formation and mineralogical composition of calcium sulphoaluminate clinker compositions***  
Bullerjahn F., Ben Haha M., Schmitt D.  
1st ICCCM, October 07 - 09, 2013, Berlin/Germany
- 2013 ***Assessment of the effect of belite content on the hydration mechanisms of calcium sulphoaluminate cements***  
Ben Haha M., Bullerjahn F., Zajac M., Schmitt D.  
1st ICCCM, October 07 - 09, 2013, Berlin/Germany
- 2012 ***Belite calcium sulfoaluminate ternesite (BCT) – A new environmentally friendly binder***  
Ben Haha M., Bullerjahn F., Zajac M., Schmitt D.  
Concrete Innovation Conference (CIC) in Oslo, Norway
- 2012 ***CSA Zement - Eigenschaften, Anwendung und Performance***  
Bullerjahn F.  
5th "HeidelbergCement Bauchemie Tage" April 19 - 20, 2012, Münster/Germany



## Annex

## Annex part I

**List of figures**

Figure 1.1-1 Embodied energy for the production of one ton of a specific building material (data adopted from [5] [6] [7]) including own presumed values for CSA and BYF (internal reports HC AG)	1
Figure 1.2-1 Open time of PC versus CSA depending on the retarder dosage	3
Figure 1.2-2 Open time of PC versus CSA depending on the retarder dosage (a); mortar spread (b) and compressive strength (c) development of BYF binders with and without retarder	4
Figure 1.4-1 Rate of heat evolution from isothermal conduction calorimetry of PC and C3S at 20 °C and w/c 0.5; calorimetry data for C3S provided by Xerun Li	5
Figure 1.4-2 Rate of heat evolution from isothermal conduction calorimetry of CSA, BYF and Y at 20 °C	6
Figure 2.2-1 Simplified chronological order for the formation of hydrates	14
Figure 2.2-2 Idealized scheme of the nucleation and growth process (adopted from [112] and extended) together with the four major zones “Undersaturation”, “Saturation”, “Supersaturation” and “Amorphous precipitation”; crystallization variable such as concentration of B, temperature or pressure	15
Figure 2.2-3 Selected solubility curves of CAH10 and C2AH8 at 25 °C for the system CaO – Al2O3 – H2O such as CAC; calculated with GEMS and using thermodynamic data from [115] and for amorphous AH3 from [116]; the dashed lines show the evolution of the solution for different of C/A ratios (CaO /Al2O3) and “X” represents the intersects with the solubility lines of the selected hydrates	16
Figure 2.2-4 Solubility curves at 25 °C for the system CaO – Al2O3 – H2O such as CAC; thermodynamic data from [115]	17
Figure 2.2-5 a) Solubility curves of selected phases at 25 °C for the system CaO – Al2O3 – SO3 – H2O such as CSA at a given sulphate concentrations of 0.02 mM/l; thermodynamic data from [115] [116]; b) Schematic representation of the impact of the aluminium hydroxide solubility on the potential phase assemblage (adopted from [121] [122]) of fully hydrated Y (including the minors), the following values were used in the calculations Gibbsite with log $KS_0 = -1.12$ [115] and amorphous AH3 am with log $KS_0 = 0.24$ [116]	18
Figure 3.14-1 Photograph of a reactor, including the detailed description, and the technical drawing	32
Figure 4.2-1 XRD plot of the synthesised ye’elimite (as measured) including a zoomed section and calculated XRD patterns for orthorhombic (Y-o) [36], cubic (Y-c) ye’elimite [72] and mayenite [160]; # = CS	41
Figure 4.2-2 Zoomed sections of $\gamma$ -shifted patterns showing the shift and weakening of the triplet of stoichiometric orthorhombic ye’elimite with increasing iron incorporation	42
Figure 4.2-3 Difference plots of selected mixes from Rietveld analyses; 1 = C4A3S – o and 2 = C12A7 position of peak(s); measured peak intensity at 23.65 2 $\theta$ Degrees of about 510000 counts (-)	44
Figure 4.3-1 (Top) Scanning electron micrograph of a polished section of Y and scheme of Y particle formed from anhydrous starting materials; (bottom) element distribution; Na equally distributed (not presented)	45
Figure 4.3-2 Scanning electron micrograph of a polished sections (top) and fractured powder samples (bottom) of Y and Fe-Y (from S3)	46
Figure 4.3-3 Scanning electron micrograph of a polished section of Y, Fe-Y and Na-Fe-Y clinkers of the S1 series	47
Figure 4.4-1 Atomic ratios of Fe/Al over Ca/Al (top) including a zoomed section and S/Al over Ca/Al (bottom) in the Y and Fe-Y samples of S3; F = maghemite, MF = magnesioferrite, CF = calcium ferrite	48

<i>Figure 4.5-1 Proposed scheme of the ye'elimite formation depending of the applied sintering temperature and duration; the scheme is adopted from the findings of Li et al. [64] and Zhang et al. [195]</i>	54
<i>Figure 4.5-2 Phase diagram of the system CaO – Al<sub>2</sub>O<sub>3</sub> in air of ordinary humidity adopted from [73] and extended for the temperature ranges for the intermediated clinker phases, presented in colour bars, adopted from [79] [189] and including CA2 [190] [191] (extend range based on our findings)</i>	57
<i>Figure 5.2-1 Particle size distribution of starting materials</i>	62
<i>Figure 5.3-1 a) Conductivity [●] and pH [▲] measurements including the spot experiments at 23 °C for w/b 40 for the hydrated residues; b) evolution of solution composition (spot samples), including the calculated Ca and S concentrations (dashed lines) derived from the Al concentration and c) normalized phase assemblage of the spot samples determined by QXRD and TGA analyses</i>	64
<i>Figure 5.4-1 Conductivity evolution of neat Y during the first 2 minutes of hydration (a) and theoretical and measured (double determination) slope of the dissolution rate using w/b 1000 as reference point (b)</i>	66
<i>Figure 5.4-2 Comparison of the steady evolution of the conductivity, pH (a) and the concentrations measured on spot samples (b) of Y at w/b 40 (solid line &amp; filled symbols) and 100 (dashed line &amp; empty symbols); “X” represents the sampling points for HR-SEM and STEM-EDS analyses</i>	67
<i>Figure 5.4-3 Evolution of the conductivity (continuous measurement) and concentration (spot samples), including the calculated Ca and S concentrations (dashed lines) derived from the Al concentration by mass balance calculations</i>	68
<i>Figure 5.4-4 Calculated saturation indices from the respective solution concentrations measured for the spot samples; the following values were used in the calculations AH3 Gibbsite with log KS0 = – 1.12, AH3 Mic with log KS0 = – 0.67 both from [115] and AH3 am with log KS0 = 0.24 [116]; Ms = monosulphate and Et = ettringite</i>	68
<i>Figure 5.4-5 Morphological characterization of the hydrated ye'elimite at 23 °C and a w/b ratio of 100</i>	70
<i>Figure 5.4-6 STEM images (up: HAADF image and down: BF image) of ye'elimite after 7 minutes of hydration at 23 °C and a w/b ratio of 100; Y = anhydrous ye'elimite particles</i>	72
<i>Figure 5.4-7 Differential thermogravimetric analyses of samples hydrated at 23 °C and a w/b of 40 for samples collected after 10 to 200 minutes of hydration including a SEM micrograph showing a idiomorphic prismatic ettringite crystal detected after 160 minutes</i>	73
<i>Figure 5.4-8 STEM images (up: HAADF image and down: BF image) of Y after 6 hours of hydration at 23 °C and a w/b ratio of 100; dotted red line indicates the surface of the anhydrous; Y = anhydrous ye'elimite particles</i>	75
<i>Figure 5.4-9 Differential thermogravimetric analyses of samples hydrated at 23 °C and a w/b of 40 for samples collected after 300 to 1440 minutes of hydration, covering the acceleration, main and final hydration period</i>	76
<i>Figure 5.4-10 Comparison of Y hydrated at w/b 40 as paste and as suspension; peak I and peak II are explained below</i>	77
<i>Figure 5.4-11 Rate of heat evolution of Y with and without quartz at several w/b ratios; the solid line depicts the neat clinker while the dashed line represents blends with quartz</i>	78
<i>Figure 5.4-12 Simplified schematic representation for the rate of heat evolution for Y with and without quartz for the underlying reactions; blue = primarily the formation of ettringite, CAH10 and amorphous aluminium hydroxide; green = primarily the formation of monosulphate and gibbsite-like aluminium hydroxide</i>	78
<i>Figure 5.4-13 Early age rate of heat evolution of Y with and without quartz at several w/b ratios from Figure 5.4-12</i>	79
<i>Figure 5.5-1 Idealized hydration scheme per gram of ye'elimite and the corresponding hydration stages</i>	80
<i>Figure 6.2-1 Rate of heat evolution and cumulative heat of neat Y, Fe-Y and both with gypsum at a w/b 2</i>	87
<i>Figure 6.2-2 Rate of heat evolution and cumulative heat of 78% Fe-Y with 22% G at varying w/b but fix w/s ratio of 2; the solid line depicts the neat cement while the dashed line represents blends with quartz</i>	88
<i>Figure 6.2-3 Rate of heat evolution of a BYF cement, Y and blends of 78% Fe-Y with 22% gypsum (G) and quartz (Q)</i>	88

<i>Figure 6.2-4 Evolution of the conductivity (a), pH (b) and solution concentration (c) of Y, Fe-Y, Y+G and Fe-Y+G at w/b 100</i>	89
<i>Figure 6.2-5 Evolution of the conductivity and of the solution composition for Y+G (dashed line and empty symbols) and Fe-Y+G (solid line and symbols) at w/b 100; Fe was always below the detection limit</i>	90
<i>Figure 6.2-6 Solubility curves at 25 °C for the system CaO – Al<sub>2</sub>O<sub>3</sub> – SO<sub>3</sub> – H<sub>2</sub>O at fix sulphate concentrations of 5 mM/l (a) and 15 mM/l (b) and measured concentrations of ● Y+G and ● Fe-Y+G at w/b 100</i>	91
<i>Figure 6.2-7 Hydrates formed after 24 hours of hydration at w/b 100 and bound water (BW) content for neat ye’elimite clinkers and with the addition of gypsum; Et = ettringite and Ms = monosulphate</i>	92
<i>Figure 6.2-8 Formed hydrates after 24 hours at w/b 100 and bound water content; Et = ettringite and Ms = monosulphate</i>	92
<i>Figure 6.2-9 Fragmented diffraction pattern of hydrated binders after 24 hours of reaction at w/b 100, measurements of dry powders after solvent exchange</i>	93
<i>Figure 6.2-10 Morphological characterization of the hydrated ye’elimite at 23 °C and a w/b ratio of 100</i>	95
<i>Figure 6.2-11 STEM images (up: HAADF image and down: BF image) of Y+G after 7 minutes of hydration at 23 °C and a w/b ratio of 100; Y = anhydrous ye’elimite particles; hydrates = mix of phases including ettringite</i>	96
<i>Figure 6.2-12 STEM images (up: HAADF image and down: BF image) of Y+G after 4 hours of hydration at 23 °C and a w/b ratio of 100; Y = anhydrous ye’elimite particles; hydrates = mix of phases including ettringite</i>	97
<i>Figure 6.3-1 Measured and calculated chemical shrinkage, according to stoichiometric reactions, for Y and Y+G at w/b 2; the standard deviation between 5 samples was in average about 0.003 cm<sup>3</sup>/g</i>	100
<i>Figure 6.3-2 Hydrates assemblages of Y (a) and Y+G (b) at various hydration ages; ΣAH<sub>3</sub> stands for the sum of quantified gibbsite and bayerite, Ms = monosulphate; the assumed relative error for each phase is about ±5%.</i>	101
<i>Figure 6.3-3 Fragmented diffraction patterns of hydrated Y as fresh slice or powder, after the solvent exchange, after 48 hours of reaction at w/b 2; Ms = monosulphate in a hydration state of 12 (12H) or 14 (14H) [242]</i>	101
<i>Figure 6.3-4 Evolution of bound water (BW) water per g of binder of Y □ and Y+G O represent the measured weight loss of the samples after finalisation of the respective chemical shrinkage measurement, i.e. 28 days (see also Figure 6.3-5)</i>	102
<i>Figure 6.3-5 Differential thermogravimetric analysis (top) and mass loss (bottom) of Y and Y+G at several hydration ages; AH<sub>x</sub> = amorphous aluminium hydroxide, hydration state of monosulphate with 12 or 10.5 water (H)</i>	103
<i>Figure 6.3-6 BSE micrograph of hydrated Y and Y+G after 28 days of hydration at w/b of 2; Et = ettringite, Ms= monosulphate, shell = layer of formed hydrates</i>	104
<i>Figure 6.3-7 S/Ca over Al/Ca atomic-% ratios of the hydrated Y and Y+G; * = S/Ca threshold ~ 0.10</i>	104
<i>Figure 7.1-1 Rate of heat evolution Y, Fe-Y and scheme for the underlying reactions; blue = primarily the formation of ettringite, CAH<sub>10</sub> and amorphous aluminium hydroxide; green = primarily the formation of monosulphate and gibbsite-like aluminium hydroxide</i>	113
<i>Figure 7.1-2 Rate of heat evolution and cumulative heat release for hydrating Y and Fe-Y; continuous line = Fe-Y and dashed line = Y; marking the duration of the two main reactions for Y</i>	114
<i>Figure 7.1-3 Rate of heat evolution and cumulative heat release of Y and Y with the addition of 0.5 to 2 wt.% mayenite (C12A7) at a w/b of 0.5 and 2; dashed line = Fe-Y tested for the respective w/b ratio</i>	115
<i>Figure 7.1-4 Rate of heat evolution and cumulative heat release of Fe-Y and Fe-Y with 1 wt.% mayenite (C12A7) at w/b 0.5 (continuous line) and at w/b 2 (dashed line)</i>	115
<i>Figure 7.1-5 Rate of heat evolution and cumulative heat of Fe-Y+G and Fe-Y+G with 1 wt.% mayenite (C12A7) at a w/b 0.5 (solid line) and 2 (dashed line)</i>	116
<i>Figure 7.2-1 Solubility curves at 25 °C for the system CaO – Al<sub>2</sub>O<sub>3</sub> – SO<sub>3</sub> – H<sub>2</sub>O at a sulphate concentrations of 0.02 mM/l (a) and 3.5 mM/l (b)</i>	117

Figure 7.2-2 Evolution of the pH (a), the conductivity and solution composition for Y and Fe-Y at w/b 40 (b) and 100 (c); Fe always below detection limit	118
Figure 7.2-3 Evolution of the conductivity and the solution composition for Y (dashed line and empty symbols) and Fe-Y+G (continuous line and filled symbols)	119
Figure 7.2-4 Solubility curves at 25 °C for the system $\text{CaO} - \text{Al}_2\text{O}_3 - \text{SO}_3 - \text{H}_2\text{O}$ at a sulphate concentration of 3.5 mM/l; ● Y and ● Fe-Y	120
Figure 7.2-5 Calculated versus measured (● Y and ● Fe-Y) solution concentrations	120
Figure 7.2-6 Evolution of the conductivity and pH of Y and Y with 0.5, 1 and 2 wt.% mayenite at w/b 100, Fe-Y for comparison	121
Figure 7.2-7 Evolution of the conductivity and pH of Y+G with the addition 1 wt.% synthetic mayenite at w/b 100, Fe-Y+G for comparison	122
Figure 7.3-1 STEM-EDS micrograph of Fe-Y hydrated at w/b 100 for 7 minutes and 6 hours	123
Figure 7.3-2 STEM-EDS micrographs of Fe-Y after 3 hours of hydration	124
Figure 7.3-3 STEM-EDS micrographs of area 1 with the elemental distribution of Ca, S, Al and Fe of Fe-Y after 3 hours of hydration	125
Figure 7.3-4 STEM-EDS micrographs of area 2 with the elemental distribution of Ca, S, Al and Fe of Fe-Y after 3 hours of hydration	126
Figure 8.3-1 Idealized hydration scheme for ye'elimite and the corresponding hydration stages from section 0	131
Figure 8.8-1 Global cement production until 2015 and prediction for 2050 based on the data from the World Business Council for Sustainable Development (WBCSD); <a href="https://www.wbcscement.org/">https://www.wbcscement.org/</a> (checked 07-2017)	167
Figure 8.8-2 Order of hydraulic reactivity and CaO phase content	174
Figure 8.8-3 Particle size distribution (PSD) of the used raw materials (left) and the prepared mixes (right); ar = used as received	183
Figure 8.8-4 Cumulative volume distribution (top) and frequency distribution (bottom) of the PSD of the ground clinkers (left) and a comparison of chosen raw mixes and clinkers (right)	184
Figure 8.8-5 PSD of the ground clinkers (left) and a comparison of chosen raw mixes and clinkers (right)	185
Figure 8.8-6 Plot of the $\text{Al}_2\text{O}_3 / \text{Fe}_2\text{O}_3$ ratio in C4A3 – xF <sub>x</sub> S (left); Dotted trend line = $\text{Al}_2\text{O}_3 / \text{Fe}_2\text{O}_3$ ratio of 3, values determined by SEM-EDS analysis (including data for various CSA and BYF from pilot and industrial scale)	187
Figure 8.8-7 Mineralogical composition of targeted stoichiometric (left) and an iron-rich solid solution ye'elimite "C4A2.8F0.2S" (right) composition, applying different temperature and sintering dwell time; samples from [304] and evaluated by myself	188
Figure 8.8-8 SEM micrographs of the ye'elimite clinkers from the S2 series	189
Figure 8.8-9 SEM micrographs of the Na-Fe-Y from the 2013 series and BYF clinker produced at industrial scale	190
Figure 8.8-10 Rate of heat evolution (left and middle) and cumulative heat (right) of hydrating Y and blends containing quartz expressed per gram of clinker; solid line = neat clinker and dashed line = blend with quartz	192
Figure 8.8-11 Rate of heat evolution (left and middle) and cumulative heat (right) of hydrating Fe-Y and blends containing quartz expressed per gram of clinker; solid line = neat clinker and dashed line = blend with quartz	193
Figure 8.8-12 Hydration degree of Y and Fe-Y versus the cumulative heat	193
Figure 8.8-13 Measured versus targeted Qz content in paste; error bar represent the relative error of 5%	194
Figure 8.8-14 Normalized phase assemblage per gram of anhydrous and without Qz	194
Figure 8.8-15 Normalized phase assemblage per gram of anhydrous and without Qz	195
Figure 8.8-16 Normalized TGA analysis of Y and Fe-Y with Qz at w/b from 0.5 to 2 after 2 days of hydration	195
Figure 8.8-17 Normalized TGA analysis of Y and Fe-Y with Qz at w/b from 5 to 40 after 2 days of hydration	196

## Annex

<i>Figure 8.8-18 Comparison of the normalized TGA analysis of Y (solid line) and Fe-Y (dashed line)</i>	196
<i>Figure 8.8-19 XRD plot of Y and Fe-Y blends with Qz filler</i>	197
<i>Figure 8.8-20 Normalized phase assemblage per gram of anhydrous and without Qz</i>	198
<i>Figure 8.8-21 Evolution of the phase assemblage of the spot samples for Y [305] (left) and Fe-Y (right) at w/b 40 and of the continuous measured conductivity; Et = ettringite and Ms = monosulphate</i>	199
<i>Figure 8.8-22 Differential thermogravimetric analyses for Y [305] (left) and Fe-Y (right) at w/b of 40</i>	200
<i>Figure 8.8-23 Mass balance analyses for Y (top) and Fe-Y (bottom) at w/b of 40</i>	201
<i>Figure 8.8-24 Evolution of the conductivity and pH; □ = sampling points</i>	202
<i>Figure 8.8-25 Evolution of the conductivity (continuous measurement) and concentration (spot samples) including the calculated Ca and S concentrations (dashed lines) for Y (left) and Fe-Y (right) at w/b 100, solubility products from [117] and for AH3am was log K<sub>SO</sub> of 0.24 from [118]</i>	203
<i>Figure 8.8-26 Morphological characterization of the hydrated Y at 23 °C and a w/b ratio of 100</i>	204
<i>Figure 8.8-27 Morphological characterization of the hydrated Y at 23 °C and a w/b ratio of 100</i>	205
<i>Figure 8.8-28 Morphological characterization of the hydrated Fe-Y at 23 °C and a w/b ratio of 100</i>	206
<i>Figure 8.8-29 Morphological characterization of the hydrated Fe-Y at 23 °C and a w/b ratio of 100</i>	207
<i>Figure 8.8-30 Morphological characterization of the hydrated Fe-Y at 23 °C and a w/b ratio of 100</i>	208
<i>Figure 8.8-31 Morphological characterization of the hydrated Fe-Y at 23 °C and a w/b ratio of 100</i>	209
<i>Figure 8.8-32 STEM images (HAADF) of Y after 7 minutes of hydration at 23 °C at w/b 100</i>	210
<i>Figure 8.8-33 STEM images (HAADF) of Fe-Y after 7 minutes of hydration at 23 °C at w/b 100</i>	211
<i>Figure 8.8-34 STEM images (HAADF and BF image) of Y after 7 minutes of hydration at 23 °C at w/b 100</i>	212
<i>Figure 8.8-35 STEM images (HAADF and BF image) of Fe-Y after 7 minutes of hydration at 23 °C at w/b 100</i>	213
<i>Figure 8.8-36 STEM images (HAADF and BF image) of Fe-Y after 7 minutes of hydration at 23 °C at w/b 100</i>	214
<i>Figure 8.8-37 STEM micrographs (HAADF and BF image) of Y after 6 hours of hydration at 23 °C and w/b 100</i>	216
<i>Figure 8.8-38 STEM micrographs (HAADF and BF image) of Y after 6 hours of hydration at 23 °C and w/b 100</i>	217
<i>Figure 8.8-39 STEM micrographs (HAADF and BF image) of Fe-Y after 3 hours of hydration at 23 °C and w/b 100</i>	218
<i>Figure 8.8-40 STEM micrographs (HAADF and BF image) of Fe-Y after 3 hours of hydration at 23 °C and w/b 100</i>	219
<i>Figure 8.8-41 Evolution of the conductivity (continuous measurement) and concentration (spot samples) including the calculated Ca and S concentrations (dashed lines) for Y (left) and Fe-Y (right) at w/b 100, solubility products from [117] and for AH3am was log K<sub>SO</sub> of 0.24 from [118]</i>	220
<i>Figure 8.8-42 Morphological characterization of the hydrated Fe-Y+G at 23 °C and a w/b ratio of 100</i>	221
<i>Figure 8.8-43 STEM images (up: HAADF image and down: BF image) of Y+G after 7 minutes of hydration at 23 °C and a w/b ratio of 100; Y = anhydrous ye'elimite particles; hydrates = mix of phases including ettringite</i>	222
<i>Figure 8.8-44 STEM images (up: HAADF image and down: BF image) of Y+G after 4 hours of hydration at 23 °C and a w/b ratio of 100; Y = anhydrous ye'elimite particles; hydrates = mix of phases including ettringite</i>	223
<i>Figure 8.8-45 Chemical composition of the crystalline detectable hydrates assemblage derived by the mass balance calculations for Y and Y+G in paste ; FW = free water and BW = chemically bound water; X = quantity of amorphous fraction; S = SO<sub>3</sub>; A = Al<sub>2</sub>O<sub>3</sub> and C = CaO</i>	224
<i>Figure 8.8-46 Chemical composition of the amorphous fraction X in paste</i>	224
<i>Figure 8.8-47 Calculated mineralogical composition of X in Y and Y+G over time</i>	225
<i>Figure 8.8-48 XRD plot of Y and Y+G at w/b 2 after 28 days of hydration</i>	226
<i>Figure 8.8-49 Differential thermogravimetric analysis (top) and weight loss (bottom) and of Y (left) and Y+G (right) after 28 days of hydration; samples taken after the completion of the chemical shrinkage measurements</i>	226
<i>Figure 8.8-50 Backscattered electron micrographs (BSE) of hydrated y and Y+G</i>	227



## Annex

<i>Figure 8.8-51 Measured chemical shrinkage of Fe-Y with and without G at w/b 2; the standard deviation between 5 samples was in average about 0.003</i>	228
<i>Figure 8.8-52 Particle size distribution (top) and rate of heat evolution and cumulative heat at w/b 2 (bottom)</i>	229
<i>Figure 8.8-53 PSD (left) and SSABET versus PSD (right)</i>	230
<i>Figure 8.8-54 Rate of heat evolution (top) and cumulative heat (bottom) of the sieved fractions</i>	231
<i>Figure 8.8-55 Particle size distribution (top), rate of heat evolution and cumulative heat (bottom)</i>	232
<i>Figure 8.8-56 Rate of heat evolution (left and middle) and cumulative heat (right) of hydrating Y, Fe-Y and Na-Fe-Y from S1 as neat clinker (top), cement with 2M hard burnt anhydrite, 2 h at 1100 °C (middle) and 2M gypsum (bottom) at w/b 1</i>	233
<i>Figure 8.8-57 Rate of heat evolution (left and middle) and cumulative heat (right) of neat clinkers (top) and cements with gypsum (bottom) at a w/b ratio of 2</i>	234
<i>Figure 8.8-58 Rate of heat evolution (left and middle) and cumulative heat (right) of cements with gypsum (top), gypsum and portlandite (middle) and with middle burnt anhydrite, 2 h at 700 °C (bottom) at a w/b ratio of 2</i>	235
<i>Figure 8.8-59 Rate of heat evolution (left and middle) and cumulative heat (right) of hydrating Y (top) and Fe-Y (bottom) as neat clinker or cement with 2M gypsum with and without 1 wt.% portlandite (CH) at w/b 2,</i>	236
<i>Figure 8.8-60 Evolution of the conductivity of Y and Fe Y with (bottom) and without (top) gypsum at w/b ratios from 40 to 1000</i>	237
<i>Figure 8.8-61 Evolution of the early conductivity of several calcium sulphates at w/b ratios from 100 to 1000 up to 30 minutes (top) and during the first minute (bottom)</i>	238
<i>Figure 8.8-62 Evolution of the early conductivity of Y at different calcium sulphates dosages (top) and measured and calculated slope values during the first seconds to minutes for the linear increase of the conductivity (bottom)</i>	238
<i>Figure 8.8-63 Evolution of the conductivity (top) and pH (bottom) of Y and Fe-Y with the addition of gibbsite [AH3] (left) and goethite [FH] (right); dashed lines represent the five hydration stages for plain Y</i>	239
<i>Figure 8.8-64 Evolution of the conductivity (top) and pH (bottom) of Y and Fe-Y with the addition of gibbsite [AH3] (left) and goethite [FH] (right) at w/b 100; dashed lines represent the five hydration stages</i>	240
<i>Figure 8.8-65 Rate of heat evolution Fe-Y+Qz with and without gypsum at w/b 2.22 and 20 (w/s 2)</i>	240
<i>Figure 8.8-66 SEM micrographs; AFm = mixtures of Ms-AFm and e.g. CAH10 (often traces of AH3), Et = ettringite, G = gypsum and Qz = quartz</i>	241
<i>Figure 8.8-67 SEM micrographs; AFm = mixtures of Ms-AFm and e.g. CAH10 (often traces of AH3), Et = ettringite and Qz = quartz</i>	242
<i>Figure 8.8-68 SEM micrographs; AFm = mixtures of Ms-AFm and e.g. CAH10 (often traces of AH3), Et = ettringite and Qz = quartz</i>	243
<i>Figure 8.8-69 SEM micrographs; AFm = mixtures of Ms-AFm and e.g. CAH10 (often traces of AH3)</i>	244
<i>Figure 8.8-70 Rate of heat evolution (left) and cumulative heat (right) of cements</i>	245



## List of tables

Table 1.1-1 Overview of the materials used for the various papers of this PhD thesis	xiv
Table 2.1-1 Typical compositional ranges of PC, CSA and BYF	10
Table 2.1-2 Comparison of typical compositional ranges of the mineralogical phase assemblages	11
Table 2.3-1 Idealized summary of the anhydrous phases, liberated ions and hydrates	19
Table 2.3-2 Combined water content	20
Table 3.1-1 Sample preparation time and nomenclature	25
Table 3.2-1 Material characterization	26
Table 3.8-1 Structures used for the Rietveld refinements	29
Table 3.15-1 Overview regarding the possible output and the limitations of the methods used thought out this study	33
Table 4.1-1 Set of samples, investigated parameters and respective sample nomenclature in brackets	38
Table 4.1-2 Raw mix and clinker production protocol	39
Table 4.2-1 Mineralogical composition of the clinker from Rietveld analysis of XRD; n.d. = not detected; + = traces	40
Table 4.2-2 Rietveld results of Y or Fe-Y - C12A7 mixes; using the orthorhombic (Y) and cubic (Fe-Y) structure	43
Table 4.4-1 Set of filters based on atomic ratios (-)	49
Table 4.4-2 Calculated elemental compositions (atomic form) of the produced ye'elimite clinkers throughout several campaigns, results were normalized for 16 atoms of oxygen	50
Table 4.4-3 Elemental ratios of ye'elimite measured by SEM-EDS and STEM-EDS (anhydrous residues); bulk = all measured data	50
Table 4.4-4 Comparison of the measured (XRF) and calculated (mass balance calculations based on QXRD and SEM-EDS) chemical clinker composition of by; n.d. = not detected	51
Table 4.5-1 Selected results from the mineralogical composition of the clinkers from the first series (S1) Table 8.8-14 and Table 8.8-15 (see annex – part IV); $\Sigma$ C4A3S = ortho. + cubic type; n.d. = not detected	52
Table 5.1-1 Experimental matrix	61
Table 5.1-2 Binder compositions; w / s = water to solid ratio, w/b water to cement ratio	61
Table 5.2-1 Quantitative phase composition of materials used; n.d. = not detected	62
Table 5.4-1 Atomic ratios of the hydrated areas determined by STEM-EDS	71
Table 5.4-2 Atomic ratios of the hydrated areas determined by STEM-EDS	74
Table 6.1-1 Experimental matrix; Qz = quartz	86
Table 6.2-1 Atomic ratios of the hydrated areas determined by STEM-EDS in the Y+G and Fe-Y+G sample	94
Table 6.3-1 Density of the phases used for the calculations	99
Table 6.3-2 Calculated density (g/cm <sup>3</sup> ) of the X-ray amorphous fraction X from the measured chemical shrinkage ( $\rho_{CS}$ ) and the determined hydrates assemblage composition ( $\rho_X$ )	105
Table 7.1-1 Experimental matrix	112
Table 7.3-1 Mean atomic ratios determined by STEM-EDS of the solid residues of Y and Fe-Y hydrated at w/b 100; n.d. = not detected	123
Table 8.8-1 Cement composition versus performance (data taken from [12]) tested in mortar according to ASTM C109; n.d. = not determined	169
Table 8.8-2 Raw material related emission of CO <sub>2</sub> related to the production of stoichiometric phases and using CaCO <sub>3</sub> and others; adopted from Gartner [1]	170
Table 8.8-3 Comparison of the raw meal CO <sub>2</sub> emission and energy demand of producing PC and BYF, modified from [265] and including data from [25]	170
Table 8.8-4 Overview of existing ye'elimite structures; adopted from [186]	172

## Annex

<i>Table 8.8-5 CSA family (typical ranges)</i>	173
<i>Table 8.8-6 Summary of parameters</i>	178
<i>Table 8.8-7 Theoretical reaction of ye'elimite during cement hydration</i>	179
<i>Table 8.8-8 Example for the starting composition used for the mass balance calculation</i>	180
<i>Table 8.8-9 Example of the calculated composition of the bulk sample</i>	180
<i>Table 8.8-10 Example of the calculated composition of the amorphous phase</i>	181
<i>Table 8.8-11 Raw mix designs</i>	182
<i>Table 8.8-12 Measured chemical composition of the raw materials (for all synthesis campaigns) and the produced raw mixes in g/100g; L.o.I = loss of ignition at 1050 °C; * = out of calibration range</i>	183
<i>Table 8.8-13 Specific surface area of the ground clinkers</i>	185
<i>Table 8.8-14 Mineralogical composition of stoichiometric ye'elimite as a function of the applied temperature</i>	186
<i>Table 8.8-15 Mineralogical composition of iron-bearing ye'elimite as a function of the applied temperature</i>	186
<i>Table 8.8-16 Mineralogical composition of sodium-iron-bearing ye'elimite as a function of the applied temperature</i>	187
<i>Table 8.8-17 Minimum and maximum minor elements contents present in synthetic phases and industrial clinker minerals; n.d. = not determined</i>	191
<i>Table 8.8-18 Mineralogy of the sieved fractions</i>	230
<i>Table 8.8-19 Mineralogical composition of CSA and BYF clinker; n.d. = not detected</i>	245

**List of equations**

Equation 1	$1 C4A3S + 18 H \rightarrow 1 C4ASH12 + 2 AH3$	19
Equation 2	$3 C4A3S + 98 H \rightarrow 1 C6AS3H32 + 2 CAH10 + 2 AH3$	19
Equation 3	$1 C4A3S + 2 CS + 38 H \rightarrow 1 C6AS3H32 + 2 AH3$	19
Equation 4	$1 C4A3S + 1 CS + 28 H \rightarrow 0.5 C6AS3H32 + 0.5 C4ASH12 + 2 AH3$	19
Equation 5	Expressed per 100 g paste: $m_i = m_i QXR D * (1 + H2OBW)/(1 + w/c)$	28
Equation 6	Expressed per 100 anhydrous: $m_i = m_i QXR D * (1 + H2OBW)$	28
Equation 7	$H2OBW = 100 - BW * (100/BW)$	29
Equation 8	$1 C + 2 A \rightarrow CA2$ (870 °C – 1100 °C, experimentally confirmed)	45
Equation 9	$1 CA2 + 1 C \rightarrow 2 CA$ (experimentally confirmed)	45
Equation 10	$1 A + 1 C \rightarrow 1 CA$ (700 °C – 1000 °C acc. to [189], questionable for our system)	45
Equation 11	$7 CA + 5 C \rightarrow C12A7$ (870 °C – 1100 °C, experimentally confirmed)	45
Equation 12	$1 CA + 1 A \rightarrow 1 CA2$ (> 900 °C – 1300 °C acc. to [190] [191], questionable for our system)	45
Equation 13	$3 CA + 1 CS \rightarrow 1 C4A3S$ (experimentally confirmed)	45
Equation 14	$1 C12A7 + 5 A + 4 CS \rightarrow 4 C4A3S$ (of minor relevance)	45
Equation 15	$C4A3S \leftrightarrow 3 CA + 1 CS \rightarrow 3 CA + 1 C + 1 SO2$ (†)	54
Equation 16	without background correction: $R_p = \sum_i  y_{io} - y_{ic}  \sum_i y_{io}$	177
Equation 17	with background correction: $R_p = \sum_i  y_{io} - y_{ic}  \sum_i  y_{io} - y_{ib} $ ; with the background intensity $y_{ib}$	177
Equation 18	without background correction: $R_{wp} = \sum_i w_i (y_{io} - y_{ic})^2 \sum_i w_i (y_{io})^2$	177
Equation 19	with background correction: $R_{wp} = \sum_i w_i (y_{io} - y_{ic})^2 \sum_i w_i (y_{io} - y_{ib})^2$	177
Equation 20	$R_{exp} = (N - P) \sum_i w_i (y_{io})^2$	177
Equation 21	$GOF = \sum_i w_i (y_{io} - y_{ic})^2 (N - P) = \chi^2 = [R_{wp} R_{exp}]^2$	177
Equation 22	$\Delta G(p, T) = U + pV - TS = \Delta H - T\Delta S$	177
Equation 23	$\Delta G(p, T) = -RT \ln K$	178
Equation 24	$nA + mB \rightarrow oC$ where $K = [A]^n \cdot [B]^m [C]^o$	178
Equation 25	$Ca6[Al(OH)6]2(SO4)2 \cdot 26 H2O \leftrightarrow 6 Ca2 + +2 Al(OH)4 - +3 SO42 - +4 OH - +26 H2O$	178
Equation 26	$KSP = [Ca2+]^6 \cdot [AlOH4-]^2 \cdot [SO42-]^3 \cdot [OH-]^4 \cdot [H2O]^{26}$	178
Equation 27	$\log \gamma_i = -A \cdot Z_i^2 \cdot I + I - 0.24 \cdot I$	178
Equation 28	$CS_m = V_H + V_m - V_{hydrates}$ ;	179
Equation 29	$V_{hydrates} = h(M_h U_h M_m U_m p h)$ ;	179
Equation 30	$CS_\alpha = m C S_m a m w m$	179
Equation 31	$V C S_m = V_{shrinkage} Mass C4A3S = 115.26 \text{ cm}^3 / \text{mol} / 610.25 \text{ g/mol} = 0.1889 \text{ cm}^3 / \text{g}$ for $C4A3S$	180
Equation 32	$3 C4ASH12 + 4 AH3 + 44 H \leftrightarrow C6AS3H32 + 6 CAH10 \approx -5.2 \text{ vol.-% decrease}$	228
Equation 33	$3 C4ASH12 + 1 AH3 + 17 H \leftrightarrow C6AS3H32 + 3 C2AH8 \approx -3.9 \text{ vol.-% decrease}$	228
Equation 34	$C4ASH14 \leftrightarrow C4ASH12 + 2 H \approx 4.4 \text{ vol.-% increase}$	228
Equation 35	$3 CAH10 \rightarrow C3AH6 + 2 AH3 + 18 H \approx 2.5 \text{ vol.-% increase}$	228
Equation 36	$6 CAH10 \rightarrow 3 C2AH8 + 3 AH3 + 27 H \approx 4.5 \text{ vol.-% increase}$	228
Equation 37	$C4AH13 + AH3 \rightarrow C3AH6 + CAH10 \approx 2.3 \text{ vol.-% increase}$	228
Equation 38	$3 C2AH8 \rightarrow 2 C3AH6 + AH3 + 9 H \approx -4.3 \text{ vol.-% decrease}$	228
Equation 39	$AH3 + x \rightarrow AH3 + x H \approx \text{unknown volume increase}$	228



## Annex part II - SoA

### *CO<sub>2</sub> footprint associated with cement industry*

The carbon footprint of the cement industry will continue to grow despite the increasing efforts to reduce raw materials and process related CO<sub>2</sub> emissions during the production of OPC. This is simply related to the fact that the global cement demand will continue to grow as shown in Figure 8.8-1. The main drivers for this development are mainly India and several developing countries in Africa and South America. The prediction of the evolution of the global cement demand is of particular interest, considering the global CO<sub>2</sub> uptake or binding potential.

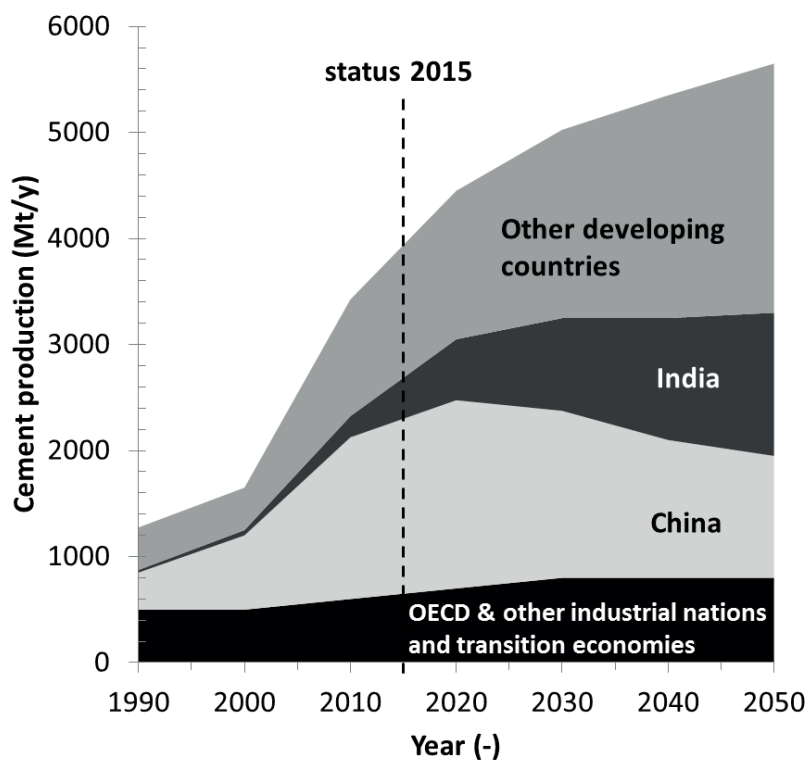


Figure 8.8-1 Global cement production until 2015 and prediction for 2050 based on the data from the World Business Council for Sustainable Development (WBCSD); <https://www.wbcscement.org/> (checked 07-2017)

### ***Process optimization***

Various measures are already implemented or under testing in modern cement plants to reduce the specific (fuel) energy consumption and / or to capture and potentially reuse emissions wherever possible: Various measures are already undertaken and under continuous improvement [258] [259] [260] like for example:

- Conventional and advanced energy and emission reduction options for clinker production like improving the thermal efficiency of kilns by oxyfuel and waste heat recovery technologies
- Modernizing and or optimizing installations like heat exchanger or burner, etc. to increase the kiln capacity of existing plants simultaneously with the reduction of the specific energy consumption per tonne of clinker
- Use of fluxes and mineralizers to potentially decrease the specific energy consumption and enhance the clinker reactivity
- Increasing the share of alternative raw materials and fuels, including biomass, sewage sludge as well as the use of e.g. solar and wind energy
- Developing Carbon Capture and Storage (CCS) and / or Carbon Capture and Reuse (CCR) technologies, including “Power-to-gas” (i.e. formation of  $CH_4$ ) and “Power-to-liquid” (i.e. formation of  $CH_3OH$ ) approaches
- Optimizing existing and introducing novel grinding technologies, including the use of grinding aids
- Optimizing the grinding procedures of raw materials (e.g. grindability and fineness versus burnability), clinker and cement, supplementary cementitious materials, including separate grinding to adjust the optimum PSD according to the targeted hydration behaviour

Despite all the efforts most technologies or approach are lacking a real applicability due to too high costs and / or limited environmental benefits [259]. Another aspect, related to the use of fluxes, mineralizers, alternative or waste fuels and raw materials, is the increase of the sum of minor and traces elements in the final clinker. Such “contaminants” can be incorporated into the cement phases forming broad ranges of solid solution [261] [262] which may lead to a decreasing clinker and cement quality [263] [264]. The decreasing quality mainly results from the presence of too high contents of potentially several minor constituents like heavy metals, chloride, fluorine and phosphate which in sum can affect the clinker mineral formation and mineral reactivity. To compensate for this drawback more energy needs to be invested for the finer grinding of the cement and / or by the higher cement dosage in concrete. Both measures would again nullify the initial environmental benefit.

Due to the before mentioned factors, strong limitations in further efficiency and costs improvements are obvious. Another opportunity to optimize processes is on the construction site. The use of advanced cement and concrete technology like low clinker and / or ultrahigh performance concrete [265] could offer some potential to measurably reduce process related  $CO_2$  emissions of OPC. Such solutions are already implemented when possible and economically feasible and reasonable. However, such approaches are often lacking suitable materials or skills of the users and / or would in consequence result in too high costs (for special admixtures and on-site support by experts). Another drawback is related to the lower fire resistance and in that regard, limitations regarding fire safety regulations.



### ***Belite-containing CSA***

Belite-rich (dicalcium silicate,  $Ca_2SiO_4$  or  $C_2S$ ) CSA-type clinkers gained increasing interest as they can be produced from industrial wastes and by-products [56] [59] [60] [63]. The advantages of using BYF, beside energy and  $CO_2$  savings, are the lower dependence on expensive bauxite, the higher flexibility for the use of silica- and iron-rich by-products or wastes and the broader range of clinker compositions which can be produced. The cement industry is working on the industrial production and commercialisation of those clinker types [27] [26]. For example, Mehta [12] provided compositional ranges of BYF cements and their reasonable good strength development (see Table 8.8-1).

**Table 8.8-1 Cement composition versus performance (data taken from [12]) tested in mortar according to ASTM C109; n.d. = not determined**

		Rapid hardening		Normal hardening	Slow hardening	
<b>Mineralogical composition (%)</b>						
Belite	$C_2S$	25	30	45	50	65
Ye'elimite	$C_4A_3\bar{S}$	20	20	20	10	10
Ferrite	$C_2(AF)$	40	30	15	30	15
Anhydrite	$C\bar{S}$	15	20	20	10	10
<b>Compressive strength development (MPa)</b>						
	1 d	34.8	28.3	9.5	5.6	5.2
	3 d	36.9	33.8	19.3	7.6	8.9
	7 d	37.4	37.7	27.4	11.7	12.4
	28 d	n.d.	n.d.	49.8	14.1	14.5
	90 d	n.d.	n.d.	n.d.	21.4	22.4
	120 d	51.8	53.8	86.2	n.d.	n.d.

Over the period of years several names and acronyms were used to label such CSA and belite-rich CSA clinkers:

- Calcium sulphoaluminate "CSA" and sulphoaluminate cement clinker "SCC"
- Belite sulphoaluminate "BSA" or belite calcium sulphoaluminate (ferrite) "BCSA(F)"
- Belite ye'elimite ferrite "BYF" and belite ye'elimite ternesite "BYT"
- Belite calcium sulphoaluminate ternesite "BCT" or "Ternocem®"
- Calcium sulphoaluminate belite "CSAB" or Sulphoaluminate belite "SAB"
- Sulphoaluminate cement "SAC" and ferroaluminate cement "FAC"
- (Belite) Alite calcium sulphoaluminate (ferrite) "(B)ACSA(F)"

### Energy and CO<sub>2</sub> savings by CSA and BYF

The environmental benefits of the CSA / BYF technologies can be mainly summarized as follow:

- Ye'elimite releases during its synthesis only about 37 % of the CO<sub>2</sub> compared to alite [25] and a part of calcium is originating from the added calcium sulphate
- The firing temperature takes place at about 200 °C lower than for PC clinker [25]
- Industrial by-products and wastes can be used primary raw materials [59] [63]
- The clinkers are easy to grind [25]
- For similar raw material related CO<sub>2</sub> savings, for example comparing slag or fly as Portland composite with BYF cements, a similar final but by far superior early age strength can be achieved [25] [60]

Other major phases, typically present in BYF clinkers, are calcium silicates like belite and ternesite as well as calcium ferrites like brownmillerite and srebrodolskite. Many different minor (reactive and inert) phases could be present as well, depending on various parameters like for example the raw mix design (amounts, types and composition of materials), targeted clinker compositions also in correlation to the process conditions [12] [34]. When comparing the clinker minerals and their associated CO<sub>2</sub> footprint it becomes obvious that the combination of ye'elimite, belite (ternesite) and brownmillerite offers high potential for CO<sub>2</sub> saving compared to PC (see Table 8.8-2).

**Table 8.8-2 Raw material related emission of CO<sub>2</sub> related to the production of stoichiometric phases and using CaCO<sub>3</sub> and others; adopted from Gartner [1]**

		g CO <sub>2</sub> /g phase	Reduction of % CO <sub>2</sub> /g phase
Alite	$C_3S$	<b>0.578</b>	<b>Reference</b>
Belite	$C_2S$	0.511	11.6
Wollastonite	$CS$	0.379	34.5
Ternesite	$C_5S_2\bar{S}$	0.366	36.7
Ye'elimite	$C_4A_3\bar{S}$	0.216	62.6
Krotite	$CA$	0.279	51.8
Mayenite	$C_{12}A_7$	0.381	34.1
Tricalcium aluminate	$C_3A$	0.489	15.4
Brownmillerite	$C_4AF$	0.363	37.4

A comparison of PC and BYF cement ( $C_4A_3\bar{S}$  53%;  $C_2S$  18%;  $C\bar{S}$  12% and  $C_4AF$  15%) was done by Alaoui et al. [266] and revealed the high potential for energy and CO<sub>2</sub> savings (see Table 8.8-3). Those assumptions were supported by industrial scale trial results [25].

**Table 8.8-3 Comparison of the raw meal CO<sub>2</sub> emission and energy demand of producing PC and BYF, modified from [266] and including data from [25]**

Parameters	PC	BYF
CO <sub>2</sub> emitted per ton clinker	535 kg/t	305 kg/t (-43%)
Specific heat consumption during clinkering <sup>1</sup>	3.845 GJ/t <sup>3</sup>	3.305 GJ/t (-14%)
Energy for crushing and grinding <sup>3</sup>	45-50 kWh/t	20-30 kWh/t (-40%)
Compressive Strength [MPa] 28d w/z 0.5, ~3000 Blaine	40-70	30-60

### **Anhydrous phases (extended)**

**Ye'elimite** also called calcium sulphoaluminate or the Klein's phase ( $Ca_4Al_6O_{12}SO_4$  or  $C_4A_3\bar{S}$ ) is a mineral belonging to the sodalite family. Ye'elimite represents a special pure aluminate sodalite which further contains mainly calcium instead of sodium. Ragozina [267] prepared the first synthetic ye'elimite by sintering a mixture of tricalcium aluminate and gypsum at 1200 °C within the composition ranges of 1.3 – 3.6 (CA) · 1 C $\bar{S}$ . Klein and Troxell [47] synthesised ye'elimite from reagent grade materials (portlandite, calcite, gypsum, aluminium sulphate) and using a sintering temperature of 1350 °C. Based on their analyses and mass balance calculations they proposed a composition in-between  $C_5A_2\bar{S}$  to  $C_9A_4\bar{S}_3$ . The term Klein's phase, when referring to ye'elimite or CSA, was founded. The exact stoichiometry of ye'elimite was later correctly identified by Fukuda [268]. Based on the stoichiometry, Halsted and Moore [269] allocated ye'elimite within the sodalite group. The first use of ye'elimite-bearing clinkers as hydraulic cement was described and patented by Klein and Troxel [47] [48]. The cage-like structure is formed from a framework of corner-linked  $TO_4$  tetrahedra. Those form four-member-rings in (100) and six-member-rings in (111) direction [67] [68] in which sodium is typically present as the cage cation. The sodalite group can be presented by the general formula  $M_{6+x}(TO_2)_{12} \cdot Y_x \cdot nH_2O$  (with  $x = 0 \leq x \leq 2$  and  $n = 0 \leq n \leq 8$ ) (see Homeyer [69] and Depmeier [67] [68]) with:

$M$  are large and low charged caged cations;  $M = Na^+, K^+, Fe^+, Mn^+, Zn^+, Li^+, Ca^{2+}, Mg^{2+}, Fe^{2+}, Cd^{2+}, Ag^{2+}, etc.$ ,

$T$  are tetrahedral coordinated framework-building cations;  $T = P^{5+}, Si^{4+}, Ge^{4+}, Al^{3+}, Fe^{3+}, B^{3+}, Ga^{3+}, Be^{2+}, etc.$  and

$Y$  are caged anions;  $Y = Cl^-, OH^-, Br^-, J^-, SO_4^{2-}, CrO_4^{2-} etc.$

The aluminate sodalite ye'elimite is characterized by a  $[Al_{12}O_{24}]^{12-}$  framework [67] [68], together with one or more divalent, potentially also some monovalent, cation(s) and a tetrahedral shaped oxyanion  $SO_4^{2-}$ . The derived chemical general formula for ye'elimite would be accordingly:  $Ca_8[Al_{12}O_{24}](SO_4)_2$ . The arrangement of the framework is very flexible and can adopt its structure (e.g. by rotation and tilting of the  $TO_4$  tetrahedra) and size in dependence of the size of the cage cations and anions [67] [68] but needs to maintain the charge balance. The excess charge of the  $[Al_{12}O_{24}]^{12-}$  framework is balanced by caged  $Ca^{2+}$  and  $SO_4^{2-}$ .

Iron can substitute the alumina within the crystal structure of ye'elimite forming a broad composition range of iron-bearing solid solutions [184] [185] [193]. The extent of the substitution of  $Al^{3+}$  by  $Fe^{3+}$  within the crystal lattice of ye'elimite and the temperature range(s) of stability remain a matter of debate. Previous investigations reported the formation of  $C_4F_3\bar{S}$  in a temperature range of 1100 to 1150 °C [194] or 950 to 1205 °C [270]. Other groups did not observe the existence of a  $C_4F_3\bar{S}$  phase and reported a maximum isomorphous substitution within a solid solution  $C_4A_{3-x}F_x\bar{S}$  of  $A$  by  $F$  of 1.3% up to 10.3% corresponding to  $x$  between 0.05 and 0.40 [62] [185] [193] [271], or even up to 25% ( $x \sim 1.05$ ) [192] [272]. Synthetic ye'elimite has orthorhombic symmetry at room temperature [35] [36]. The partial substitution of  $Al^{3+}$  by  $Fe^{3+}$  within the crystal structure stabilizes the (pseudo-) cubic symmetry at ambient temperatures [35] [39] [72]. In a recent paper [273] the effect of the formation of a complex solid solution of ye'elimite;  $Ca_{3.8}Na_{0.2}Al_{5.6}Fe_{0.2}Si_{0.2}\bar{S}$ , on the polymorphism was investigated confirming the earlier findings.

Stoichiometric ye'elimite reveals phase transitions starting from the cubic symmetric at high temperatures to an orthorhombic symmetry at room temperature [36] [70] [71]. Several research groups reported the possible stabilization of a pseudocubic symmetry by incorporating foreign ions [34] [35] [39] [72]. Table 8.8-4 provides an overview about existing structures. A real cubic symmetry, independent of doping, can only be maintained at temperatures above 800 °C [70] [72].

Table 8.8-4 Overview of existing ye'elimite structures; adopted from [186]

Symmetry	Space group	Lattice parameter	Reference	Year
Cubic	I 4 <sub>1</sub> 32	$a_o = 18.390 \text{ \AA}$	Halstead and Moore [269]	1962
Cubic	I 23	$a_o = 9.190 \text{ \AA}$	Kondo [274]	1965
Cubic	I $\bar{4}$ 3m	$a_o = 9.205 \text{ \AA}$	Saalfeld & Depmeier [275]	1972
Cubic	I $\bar{4}$ 3m	$a_o = 9.022 \text{ \AA}$	Brenchley & Weller [276]	1992
Tetragonal	P $\bar{4}$ c2	$a_o = 13.031 \text{ \AA}$ $c_o = 9.163 \text{ \AA}$	Zhang et al. [277]	1992
Tetragonal	P 4 <sub>1</sub> & P 4 <sub>1</sub> 22	$a_o = 13.030 \text{ \AA}$ $c_o = 9.161 \text{ \AA}$	Krstanovi et al. [278]	1992
Orthorhombic	P cc2	$a_o = 13.028 \text{ \AA}$ $b_o = 13.037 \text{ \AA}$ $c_o = 9.161 \text{ \AA}$	Calos et al. [279]	1995
Orthorhombic	P cc2	$a_o = 13.025 \text{ \AA}$ $b_o = 13.025 \text{ \AA}$ $c_o = 9.155 \text{ \AA}$	Cuesta et al. [36]	2013
Cubic	I $\bar{4}$ 3m	$a_o = 9.243 \text{ \AA}$	Kurokawa et al. [70]	2014
Cubic	I $\bar{4}$ 3m	$a_o = 9.197 \text{ \AA}$	Cuesta et al. [72]	2014

**Anhydrite** ( $C\bar{S}$ ) is typically present as a minor phase in CSA and BYF [33] [37] clinkers as well as in synthetic ye'elimite (Chapter 4 and annex – part IV). Originally, Posnjak [280] proposed a nomenclature based on Greek prefixes;  $\alpha - CaSO_4$ ,  $\beta - CaSO_4$  and  $\gamma - CaSO_4$ , in the order of the higher to the lowest (stability) temperatures. As this order was debated to contradict the general mineralogical usage of the Greek prefixes [281], it was proposed to use the labels anhydrite I, II and III [282].

Anhydrite III, also called “soluble anhydrite”, is the metastable low temperature phase, i.e. formed above 100 °C, and presents the most soluble type [99] [283]. Anhydrite III further can be differentiated as  $\beta -$  and  $\alpha -$ anhydrite where both forms are have an orthorhombic lattice. The solubility at 20 °C in water is about 8.8 g/l and 6.7 g/l for the  $\beta -$  and  $\alpha -$ anhydrite. Anhydrite II is the stable and less soluble type which is formed at calcination temperature above 200 °C [99]. It has an orthorhombic lattice and a solubility of about 2.7 g/l.

For the present study anhydrite I, i.e.  $\alpha - CaSO_4$ , is the most important type as it is typically present up to about 5% in the synthetic ye'elimite clinkers. Anhydrite I is only formed and stable above 1180 °C [99] and has a trigonal lattice. So far no information about its solubility was found. The reason therefore is likely to be linked to the reduced dissolution rate and the solubility of gypsum which is about 2.2 g/l. Generally speaking, it is well known that the solubility of anhydrite decreases, with one exception, by increasing the calcination temperature [284]. The results presented in Chapter 5 and annex – part V support this, as the anhydrite does not participate, i.e. dissolve, up to about 4 to 6 hours of hydration. One can assume that the solubility of anhydrite I dissolve too slowly and its solubility basically equals the one of gypsum.

Another important aspect of anhydrite is its thermal stability which was investigated by several researchers [100] [101] [102]. Nielsen et al. [101] and Hoteit et al. [102] could show the correlation between the thermal stability of anhydrite and the composition of the gaseous atmosphere. The authors could show that anhydrite is relatively stable under oxidizing conditions till about 1300 °C. Contrary, the decomposition of anhydrite starts from around 1100 °C under reducing conditions. Increasing temperatures always accelerates the decomposition process. The decomposition of anhydrite always goes hand in hand with the volatilization of sulphur and the formation of free lime.

### ***SoA – Cement classes and properties***

The classification of CSA clinker types is shown in Table 8.8-5.

Table 8.8-5 CSA family (typical ranges)

CSA		BY(T)F	
Ye'elimite > belite	Ye'elimite > 45%	Belite (± ternesite) > Ye'elimite	Belite (± ternesite) > 45%
Sulphoaluminate	Sulphoaluminate ferrite	Belite sulphoaluminate	Belite sulphoaluminate ferrite
Belite 0-30%	Belite 15-30%	Ye'elimite 20-45%	Ye'elimite 20-45%
Ferrite < 5%	Ferrite 15-40%	Ferrite < 10%	Ferrite ~ 10-40%
ACSA			
Ye'elimite > alite	Alite > ye'elimite		
PC – Sulphoaluminate			
Alite 10-30	Alite 30-60		
Ye'elimite 30-60%	Ye'elimite 5-20%		

Several types of CSA / BYF are already on the market or under investigation by the cement industry. Regarding commercial available products the following producers are known:

- Tangshan Polar Bear Building Materials Co. Ltd: CSA-based products
  - Several CSA clinker types (SAC and FAC) with and without calcium sulphate
  - Compositions in accordance to the Chinese standard GB 20472-2006
- (Former) Italcementi S.p.A. “**i.tech® ALI PRE / ALI CEM**”: CSA-based products
  - CSA ± with calcium sulphate and PC; ETA available [285]
- Buzzi Unicem S.p.A. “**Next**”: CSA-type
  - CSA ± with calcium sulphate and PC; ETAs available [286] [287]
- Vicat “**Alpenat®**”: BYF-type
  - BYF ± with calcium sulphate; ETA available [288]
- Caltra Nederland B.V. “**BeliCem® / Calumex®**”: CAS and BYF-based products
  - CSA / BYF ± portlandite and calcium sulphate as additive for PC
- CTS Cement “**Rapid Set®**”: BYF-based products
  - BYF ± with calcium sulphate and PC
- Bluey Technologies Pty Ltd. “**BluCem®**”: CSA-type

Several cement companies are working on the development of the clinker production, formulation of cements and the use in concrete. Those are:

- (Former) Lafarge “**Aether**®”: BYF-types
  - Several patents filled
- HeidelbergCement “**Ternocem**®”: BYF-types
  - Several patents filled
- Cemex: CSA-types
  - One patent filled

The **compressive strength** of CSA / BYF cements is typically controlled by the used clinker type and the blending with calcium sulphate. The rate of ettringite formation, and in that respect its subsequent impact on general hydration reactions and kinetics, is dependent on the rate of the calcium sulphate dissolution [136]. Other related parameters are the applied w/c ratio [12] [50] and on the use of admixtures like retarders [32]. The strength gains during the early hours of hydration is controlled by the dissolution of ye’elimite and (added) calcium sulphate which in consequence results in the massive and rapid formation of ettringite together with poorly crystalline aluminium hydroxide [50] [114] [133]. On the contrary, the strength gain is initially lower in the absence of calcium sulphate, as the main hydrates are monosulphate and poorly crystalline aluminium hydroxide [32] [114]. The optimum calcium sulphate content, with regard to the strength development and volume stability, for CSA and BYF based cements depend mainly on the quantity of ye’elimite. CSA cements develop a high early compressive strength but show a relatively low or even no further increase. Several authors attributed this to the fast consumption of free water, the filling of the free space with hydrates and in consequence, significant quantities of unreacted phases like belite, ferrite, anhydrite and even ye’elimite persist intermixed in the hydrated microstructure [50]. The hydration belite and the ferrite phases strongly depends on the applied water to cement ratio and the amount of added calcium sulphate [127] [251]. Belite typically starts to react already during the first twenty four hours of hydration [32] [33] but contributes typically measurably to the cement performance from seven days of hydration or often even only after twenty eight days on [114]. The contribution of the ferritic phases depends on the applied w/c ratio and sulphate content but typically occurs mainly after twenty eight or even ninety days of hydration [32].

### ***Hydration kinetics of aluminat e phases***

The calcium aluminates, including ye’elimite, hydrate at different rates, where the hydraulic reactivity decreases as the content of calcium oxide decreases. This order of the hydraulic reactivity and the respective calcium content of the phases is shown in below Figure 8.8-2.

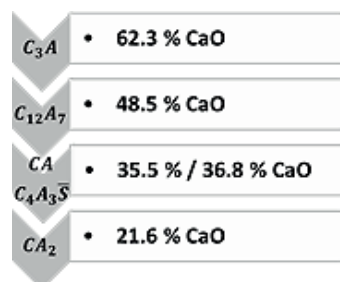


Figure 8.8-2 Order of hydraulic reactivity and CaO phase content



## Hydrates

**Ettringite**, often referred to alumina ferric oxide tri-sulphate using the abbreviation **Aft**, is a well-known phase for the cement industry. It is almost always present in hydrated cement and often the fresh properties of mortar and concrete are related to the formation of this phase. Ettringite is a member of the hydrated calcium aluminate family with the formula  $Ca_6[Al(OH)_6]_2(SO_4)_2 \cdot 26 H_2O$  ( $C_6A\bar{S}_3H_{32}$ ). Ettringite has a trigonal symmetry [175] [289]. The morphology comprises hexagonal prisms ranging from thick elongated, well defined tabular forms, over ideal short to elongated, six-sided and hexagonal prisms to clusters of fibrous- or needle-like crystals. The morphology depends on several parameters such as the solution concentrations, the formation rate, pH [290] [291] [292], or the water content [293]. The structure of ettringite is based on the columns and channels [289]. The columns are composed of alternating groups of edge-sharing  $Al(OH)_6$  octahedra and triangular groups of  $CaO_8$  polyhedra. Each calcium atom is coordinated with from four water molecules and four  $OH^-$  ions, giving the cylindrical shape. Both groups are connected via the  $OH^-$  ions. The empirical formula of such a column is  $[Ca_3Al(OH)_6 \cdot 12 H_2O]^{3+}$  and they are aligned in parallel to the c-axis. Sulphate ions and zeolitic water fill the channels in-between the columns [175]. The zeolitic water is only loosely bound and can be easily removed [294]. Due to this open structure with “filled channels”, the composition of ettringite is very variable and several solid solutions are known. The double charged sulphate anion can be partially substituted by e.g.  $CO_3^{2-}$ ,  $CrO_4^{2-}$ ,  $ClO_4^-$  and others [295] [296]. Literature also reports the substitution of aluminium by iron [297] [298] [299].

**Monophases**, often referred to alumina ferric oxide mono- using the abbreviation **AFm**, is another family of phases also very well-known for the cement industry [73]. Especially the member monosulphate, often referred monosulphate or monosulphoaluminate and labelled “Ms-AFm”, is of importance. Monosulphate and other AFm phases are typically formed at later hydration ages once sulphate is depleted. Monosulphate has a trigonal symmetry and typically precipitates with a hexagonal plate-like morphology. The general formula is  $C_4AX_2H_n$  being X a monovalent anion (e.g.  $OH^-$ ,  $NO_3^-$  and  $ClO_4^-$ ) or half a divalent anion (e.g.  $SO_4^{2-}$  and  $CO_3^{2-}$ ) [242] [300] [301]. AFm-phases belong to the family of lamellar or layered double hydroxides. The main layers are composed of positive charged  $[Ca_2Al(OH)_6]^+$  units where the negatively charged interlayers are filled with the anions and interlayer water. The substitution each third calcium atom by the smaller alumina atoms distorts the structure of the main layer and in consequence allows each calcium atom to coordinate with the oxygen atom of the interlayer water together with its six coordinated  $OH^-$  groups [73] [229]. The interlayer water is only loosely bound and can be easily removed [229]. Different anions can be simultaneously present in the interlayer. In the case of monosulphate several solid solutions are known where the carbonate-, namely monocarboaluminate and hemicarbo-aluminate, and chloride-bearing ones, namely monochloride or Friedel’s salt, are most common ones. Another AFm phase of particular interest is monocalcium aluminate decahydrate  $CAH_{10}$  ( $[CaAl_2(OH)_8 \cdot (H_2O)_2] \cdot 1.84 H_2O$ ).  $CAH_{10}$  is a metastable hydrate which typically occurs as one of the main initial hydration products of alumina-rich cements like CAC and synthetic clinker phases [73] [120].  $CAH_{10}$  has a hexagonal symmetry. It was often described a hexagonal platelet-like crystals where so far not micrographs, e.g. of fractured surfaces which could reveal the morphology, are reported to the best of our knowledge.

Several types of **aluminium hydroxides** are known where the two main types can be differentiated, namely oxy-hydroxides and tri-hydroxides. The group of oxy-hydroxides included diaspore  $\alpha - AlO(OH)$  ( $\rho$  around  $3.38 \text{ g/cm}^3$ ) and boehmite  $\gamma - AlO(OH)$  ( $\rho$  around  $3.03 \text{ g/cm}^3$ ). The group of tri-hydroxides includes gibbsite  $\gamma - Al(OH)_3$  ( $\rho$  around  $2.40 \text{ g/cm}^3$ ), bayerite ( $\alpha - Al(OH)_3$  ( $\rho$  around  $2.53 \text{ g/cm}^3$ ), and nordstrandite ( $\beta - Al(OH)_3$ ). Recently, Cuesta et al. [244] recently reported the formation of an aluminium hydroxide gel (i.e. type 1  $(CaO)_{0.04}(Al_2O_3)_3 \cdot 2.3H_2O$ ), with a density of about  $1.48 \text{ g/cm}^3$  in hydrated synthetic ye'elimite. Aluminium hydroxide which is formed during the hydration of alumina-rich cements like CAC, CSA and BYF is typically amorphous, sometimes called "alumina" gel [114] [122]. Further information are provided in Chapter 6

### ***Hydrates – Crystallinity, (meta)stability and hydration states***

The rapid hydration of ye'elimite may cause the formation of several metastable hydrates and in consequence a phase assemblage and matrix prone to transformation and recrystallization reactions. Such reactions may increase the sensitivity of the matrix to volume changes, cracking and others. Metastable phases are of higher energy than the stable ones (typically gel-like, nano or microcrystalline phases with higher a specific surface area and higher surface energy) which in consequence creates the driving forces for the transformation (via dissolution) to stable phases. This process is called "Ostwald ripening" or "Ostwald Rule of Stages" [106]. The onset and rate of such transformation depends on various parameters like the solution concentrations, pH, time and temperature. The following points have to be considered regarding the aspects like crystallinity, morphology and the thermodynamic stability of the formed hydrates in hydrated alumina-rich cements:

- Rapid dissolution and in consequence rapid increase of solution concentrations
- Alkalinity
- Temperature
- Water vapour pressure in correlation with the temperature
- Potential impact of carbonation

## Annex part III - Analytical methods

The **quantitative X-ray diffraction** (QXRD) is based on the Rietveld refinement during which several “least squares refinements” are done to reach the best possible fit between the measured and calculated pattern. This is achieved by changing iteratively the e.g. crystal structure and global profile (e.g. background, zero shift and sample displacement) parameters. Several indices exist to express the quality of the fit between observed and calculated patterns. Values which are commonly used are the reliability factors (R-factors). Several R-factors can be used like the unweighted profile R-factor ( $R_p$ ), the weighted profile R-factor ( $R_{wp}$ ) and the expected R-factor ( $R_{exp}$ ). These values compare the observed ( $y_{io}$ ) and calculated ( $y_{ic}$ ) intensities at any given measurement point.

**Equation 16** without background correction:  $R_p = \frac{\sum_i |y_{io} - y_{ic}|}{\sum_i y_{io}}$

**Equation 17** with background correction:  $R_p = \frac{\sum_i |y_{io} - y_{ic}|}{\sum_i |y_{io} - y_{ib}|}$ , with the background intensity  $y_{ib}$

**Equation 18** without background correction:  $R_{wp} = \sqrt{\frac{\sum_i w_i (y_{io} - y_{ic})^2}{\sum_i w_i (y_{io})^2}}$

**Equation 19** with background correction:  $R_{wp} = \sqrt{\frac{\sum_i w_i (y_{io} - y_{ic})^2}{\sum_i w_i (y_{io} - y_{ib})^2}}$

**Equation 20**  $R_{exp} = \sqrt{\frac{(N-P)}{\sum_i w_i (y_{io})^2}}$

The values N and P represent the sum of measurement points and of refined parameters, respectively. Another parameter to express the quality of the refinement is the goodness of fit (GOF or  $\chi^2$ ).

**Equation 21**  $GOF = \sqrt{\frac{\sum_i w_i (y_{io} - y_{ic})^2}{(N-P)}} = \chi^2 = \left[ \frac{R_{wp}}{R_{exp}} \right]^2$

Despite the numerical presentation of the quality of the fit, the difference between the observed and calculated pattern is typically also presented in a graph. This further helps to assess the quality of a refinement by visual inspection and to determine whether e.g. other (minor) phases are present or wrong structural models are used.

**Thermodynamic modelling** is a powerful tool to understand the dissolution of minerals, including cement phases, and to predict the formation of the solution composition and of the hydrates. The basis for the thermodynamic calculation is the minimisation of the free enthalpy ( $G$ ) or Gibbs free energy in the system according to Equation 22. This process described the driving force or measure of voluntariness for a process to start.

**Equation 22**  $\Delta G_{(\rho,T)} = U + \rho V - TS = \Delta H - T\Delta S$

where  $U$  is the internal energy,  $\rho$  is the pressure,  $V$  is the volume,  $H$  is the enthalpy,  $T$  is the temperature and  $S$  is the entropy.

- $\Delta G < 0$  Favourable or spontaneous reaction
- $\Delta G = 0$  In equilibrium
- $\Delta G > 0$  Unfavourable or non-spontaneous reaction (forced process)

Annex

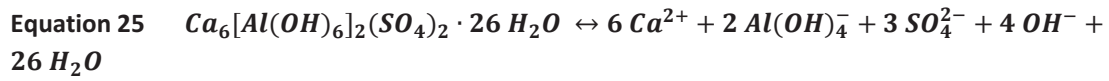
As mentioned above, GEMS also accounts the impacts the interactions of the ionic species which is based on the chemical potential ( $\mu_i$ ) and the number of particles ( $N_i$ ) involved. By including these factors one would derive the generalized equation below.

**Equation 23**  $\Delta G_{(\rho,T)} = -RT \ln K$

where  $K$  is the equilibrium constant and is based on the mass action law for chemical reactions:

**Equation 24**  $nA + mB \rightarrow oC$  where  $K = \frac{[A]^n \cdot [B]^m}{[C]^o}$

As an example, we can express the dissolution or formation reaction of ettringite as follows:



Following the equation given above, the solubility product " $K_{SP}$ " is:

**Equation 26**  $K_{SP} = [Ca^{2+}]^6 \cdot [Al(OH)_4^-]^2 \cdot [SO_4^{2-}]^3 \cdot [OH^-]^4 \cdot [H_2O]^{26}$

The given equation for the solubility product of ettringite already highlights the strong impact of the ion species. The activity calculations and corrections for the ion interactions are based on the Davies Equation shown below:

**Equation 27**  $\log \gamma_i = -A \cdot Z_i^2 \cdot \left( \frac{\sqrt{I}}{1+\sqrt{I}} - 0.24 \cdot I \right)$

Where  $\gamma_i$  is the activity coefficient for ion "i",  $A$  is a water and temperature dependent constant,  $Z$  is the charge of the specific ion and  $I$  is the ionic strength of the solution at a given concentration. The ion activity products (IAP) of the hydrates can be calculated from the activities obtained by Equation 17. The summary of the parameters is shown in Table 8.8-6.

Table 8.8-6 Summary of parameters

Reaction		$Ca_4Al_6SO_{16} + 12H_2O \rightarrow 4 Ca^{2+} + 6 Al(OH)_4^- + 1 SO_4^{2-}$
Solubility product	Ks	$[Ca^{2+}]^4 \cdot [Al(OH)_4^-]^6 \cdot [SO_4^{2-}]^1$
Ionic activity product (incl. activities)	IAP	$\{Ca^{2+}\}_{actual}^4 \cdot \{Al(OH)_4^-\}_{actual}^6 \cdot \{SO_4^{2-}\}_{actual}^1$
Activity coefficients	$\gamma$	$\{x\} = [x] \cdot \gamma_x$
Saturation index	SI	$\log(IAP/K_s)$
Effective saturation	SI <sub>eff</sub>	$\frac{1}{n} \cdot \log\left(\frac{IAP}{K_s}\right)$

with n = number of species

[ ] concentrations; { } activities

The **calculation** of the theoretical **chemical shrinkage** is based on the determined degree of hydration (DoH) of the anhydrous clinker minerals. The DoH is based on QXRD and TGA analyses as explain in more detail in section. Mass balance calculations are used to distribute the elements, e.g. from the dissolution of the anhydrous clinker phases, to a selected hydrate assemblages which can include ettringite, monosulphate,  $CAH_{10}$ ,  $C_3FH_6$  and  $AH_3$ . Knowing the densities ( $\rho$ ) of the anhydrous phases and the hydration products, the chemical shrinkage can be calculated (see Equation 28 to Equation 30).

$$\text{Equation 28} \quad CS_m = V_H + V_m - V_{hydrates};$$

Where:  $CS_m$  is the chemical shrinkage of the mineral or cement (m),

$V_H$  and  $V_m$  are the specific volumes of water and the phases, respectively and

$V_{hydrates}$  is the volume of hydrates per g of consumed mineral according to Equation 29

$$\text{Equation 29} \quad V_{hydrates} = \sum h \left( \frac{M_h U_h}{M_m U_m \rho_h} \right);$$

Where the sum of all hydration products (h) is calculated using:

$U_h$  and  $M_h$  represent the stoichiometric coefficient and the molar masses of the individual phases and

$\rho_h$  is the density of the formed hydrate.

Finally, to calculate the chemical shrinkage for each DoH the quantities of released elements were calculated, i.e. assuming the stoichiometric compositions of the phases (i.e.  $C_4A_3\bar{S}$ ,  $C_4A_{2.8}F_{0.2}\bar{S}$ ,  $CA$  and  $C\bar{S}$ ) and fully distributed between the hydrates. Knowing the hydrates assemblage the chemical shrinkage can be calculated accordingly.

$$\text{Equation 30} \quad CS(\alpha) = \sum_m CS_m \alpha_m w_m$$

Where: the DoH of a specific anhydrous phase is represented as  $\alpha_m$  and  $w_m$  is the initial weight of the phase.

A simplified example for the theoretical full hydration of ye'elimite:

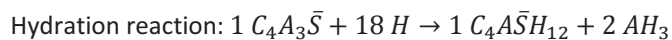


**Table 8.8-7 Theoretical reaction of ye'elimite during cement hydration**

	Mol. Wt. (g/mol)	Density (g/cm <sup>3</sup> )	Mol. Vol. (cm <sup>3</sup> /mol)	
<b>Reactants</b>				
1 $C_4A_3\bar{S}$	610.25	2.61	233.81	
18 $H$	324.28	1.00	324.28	
<u>Sum</u>	<u>934.53</u>		<u>558.09</u>	= $V_{reactants}$
<b>Products</b>				
1 $C_4A\bar{S}H_{12}$	622.52	1.99	312.82	
2 $AH_3$	312.01	2.40	130.01	
<u>Sum</u>	<u>934.53</u>		<u>442.83</u>	= $V_{products}$
			115.26	= $V_{shrinkage} \approx 20.7\%$ of reactants

The difference between  $V_{reactants}$  and  $V_{products}$  represents the volume of shrinkage, i.e.  $V_{shrinkage}$  expressed in  $\text{cm}^3/\text{mol}$ . By further relating the calculated shrinkage volume to the original mass of solids it is possible to derive the chemical shrinkage according to Equation 31:

$$\text{Equation 31 } V_{CS_m} = \frac{V_{shrinkage}}{\text{Mass}_{C_4A_3\bar{S}}} = \frac{115.26 \text{ cm}^3/\text{mol}}{610.25 \text{ g/mol}} = 0.1889 \text{ cm}^3/\text{g} \text{ for } C_4A_3\bar{S}$$

Accordingly, Equation 30 can be expressed as  $CS(\alpha) = 0.1889 \cdot \alpha_{C_4A_3\bar{S}} \cdot w_{C_4A_3\bar{S}}$ .

**Mass balance, phase assemblage, volume and density calculations** were based on the determined phase assemblage at a given hydration degree (see Table 8.8-8 and Table 8.8-9).

Table 8.8-8 Example for the starting composition used for the mass balance calculation

Oxides	Mol. Wt. g/mol	Phases	Mol. Wt. g/mol	Oxide composition g/100g					
				C	A	F	$\bar{S}$	S	H
$CaO$ (C)	56.1	$C_4A_3\bar{S}$ (Y)	610.3	36.8	50.1		13.1		
$Al_2O_3$ (A)	101.9	$C_4A_2.8F_{0.2}\bar{S}$ (Fe-Y)	621.8	36.1	45.9	5.1	12.9		
$Fe_2O_3$ (F)	159.7	$CA$ (-)	158.0	35.5	64.5				
$SO_3$ ( $\bar{S}$ )	80.0	$CA_2$ (-)	260.0	21.6	78.4				
$SiO_2$ (S)	60.1	$C_{12}A_7$ (-)	1386.6	48.5	51.5				
$H_2O$ (H)	18.0	$C\bar{S}$ (-)	136.1	41.2			58.8		
		$C_6A\bar{S}_3H_{32}$ (Et)	1255.1	26.8	8.1		19.1		45.9
		$C_4A\bar{S}H_{12}$ (Ms)	622.5	36.0	16.4		12.9		34.7
		$AH_3$ (-)	78.0		65.3				34.6
		$S$ (Qz)	60.1						100

A simplified example for Y at w/b 0.5 and after 48 hours of hydration: for the composition of the X-ray amorphous and crystalline not detectable (ACn) fraction.

Table 8.8-9 Example of the calculated composition of the bulk sample

	Starting composition - Y at w/b 0.5				Hydrated composition after 48 hours of hydration				
	Mineralogy		Composition		Mineralogy		Composition		
	Paste composition Wt.%	Normalized g/100g	Oxides g/100g		Paste composition Wt.%	Normalized g/100g	Oxides g/100g	Diff.	
Y	87.9	58.6	C	24.6	19.5	13.0	C	13.2	11.5
CA	5.1	3.4	A	31.7	3.0	2.0	A	11.6	20.1
$CA_2$	0.3	0.2	$\bar{S}$	10.3	0.0		$\bar{S}$	6.9	3.4
$C\bar{S}$	6.7	4.5	H	33.3	4.8	3.2	H	14.4	19.0
Et					16.3	10.9			
Ms					14.4	9.6			
$AH_3$					3.1	2.1			
ACn					80.9	53.9			
H	50.0	33.3			8.0	5.3			
<b>Total</b>	<b>150.0</b>	<b>100.0</b>			<b>150.0</b>	<b>100</b>		<b>46.1</b>	<b>53.9</b>



The difference (Diff.) represents the chemical composition of the amorphous fraction (ACn).

**Table 8.8-10 Example of the calculated composition of the amorphous phase**

	Normalized ACn composition			
	With H	Without H	With H	Without H
	g/100g		Mol/100g	
C	21.2	32.7	0.4	0.6
A	37.3	57.7	0.4	0.6
S	6.3	9.8	0.1	0.1
H	35.2		2.0	
<b>Total</b>	<b>100.0</b>	<b>100.0</b>		

The results of such calculations are visualized in Figure 8.8-20, Figure 8.8-23 and Figure 8.8-45 to Figure 8.8-47.

## Annex part IV – Anhydrous clinkers

**Raw materials and mixes:** Only reagent grade materials from Merck KGaA were used throughout the study. For S1 and S2, gypsum from Bernd Kraft was used, which did contain some magnesium oxide impurities. For the series S3 very pure gypsum from Merck was used. In case of S1 and S2, the gypsum was tempered for 2 hours at 700 °C to produce anhydrite which was afterwards used as raw material. For S3 the reagent grade gypsum was used as received. The raw mix designs are presented in Table 8.8-11.

**Table 8.8-11 Raw mix designs**

	$CaCO_3$	$Al_2O_3$	$Fe_2O_3$	$CaSO_4$	$CaSO_4 \cdot 2H_2O$	$Na_2SO_4$
	(wt.%)					
<b>S1</b>						
Y	38.34	39.06		22.60		
Fe-Y	37.78	35.92	4.02	22.28		
Na-Fe-Y	33.92	34.56	3.87	19.78		7.87
<b>S2</b>						
Y	38.34	39.06		22.60		
0.05Fe-Y	38.20	38.27	1.02	22.52		
0.08Fe-Y	38.12	37.79	1.62	22.47		
0.2Fe-Y	37.78	35.92	4.02	22.28		
0.4Fe-Y	37.24	32.88	7.92	21.95		
0.8Fe-Y	36.21	27.05	15.41	21.34		
<b>S3</b>						
Y	36.39	37.07			26.54	
Fe-Y	35.89	34.12	3.82		26.18	

The compositions of both the raw materials used and the chosen mixes are presented in Table 8.8-11. The raw mixes of the series 1 (S1) are designed to achieve a stoichiometric pure phase, i.e. 100% ye'elimite, whereas the mixes from series 2 (S2) and series 3 (S3) should give a clinker composed of 95% ye'elimite and 5% of excess anhydrite. Higher anhydrite content was targeted to compensate for the potential volatilization of sulphur, observed for S1. The raw mixes of S2 were not analysed and we have no sample left. The differences in the targeted mineralogy of S1 and S3 can be seen by the higher  $Al_2O_3$  content and lower  $CaO$  and  $SO_3$  contents in S1 compared to S3. The excess of 5% anhydrite was targeted to compensate the potential volatilization of  $SO_2$  throughout the sintering. The XRF analyses of the alumina and iron sources are above 100 % as their element contents are out of calibration range for the standardized alumina and iron-carriers.

The PSD of the used raw materials and chosen raw mixes is shown in Figure 8.8-3. Unfortunately, no analyses of the S2 raw mix are available. The alumina and sulphate source are relatively coarse compared to the already fine calcium carbonate or iron oxide. Tests were made with the alumina and sulphate sources as received in the S1 and S2 series. Later the alumina and sulphate sources were ground to a  $d_{90} < 40 \mu m$  for the series S3. The S1 raw mix has a higher content of the fraction above  $10 \mu m$  compared to the S3 raw mix due to the use of the coarse materials.

Annex

**Table 8.8-12 Measured chemical composition of the raw materials (for all synthesis campaigns) and the produced raw mixes in g/100g; L.o.I = loss of ignition at 1050 °C; \* = out of calibration range**

	$CaCO_3$	$Al_2O_3$	$Fe_2O_3$	Bernd Kraft $CaSO_4 \cdot 2H_2O$	Merck $CaSO_4 \cdot 2H_2O$	RM Y S1	RM Fe-Y S1	RM Y S3	RM Fe-Y S3
L.o.I.	43.56	0.05	1.90	20.81	20.54	18.05	18.25	17.78	17.94
$SiO_2$	0.38	0.03	0.25	0.20	0.03	0.10	0.08	0.19	0.30
$Al_2O_3$	0.10	101.35*	0.05	0.00	0.00	43.03	39.06	39.54	37.03
$TiO_2$	0.01	0.00	0.00	0.00	0.00	0.00	0.00	0.00	0.00
$MnO$	0.01	0.00	0.15	0.00	0.00	0.00	0.01	0.00	0.01
$Fe_2O_3$	0.06	0.00	101.46*	0.00	0.00	0.02	4.25	0.32	4.33
$CaO$	56.11	0.00	0.00	32.79	33.54	29.57	29.56	30.1	28.61
$MgO$	0.32	0.01	0.00	0.38	0.01	0.42	0.40	0.12	0.12
$K_2O$	0.03	0.00	0.00	0.01	0.00	0.00	0.01	0.01	0.01
$Na_2O$	0.01	0.08	0.03	0.00	0.00	0.02	0.02	0.01	0.02
$SO_3$	0.04	0.00	0.00	46.04	47.26	9.91	9.87	12.76	11.54
$P_2O_5$	0.07	0.00	0.02	0.00	0.00	0.00	0.00	0.02	0.02

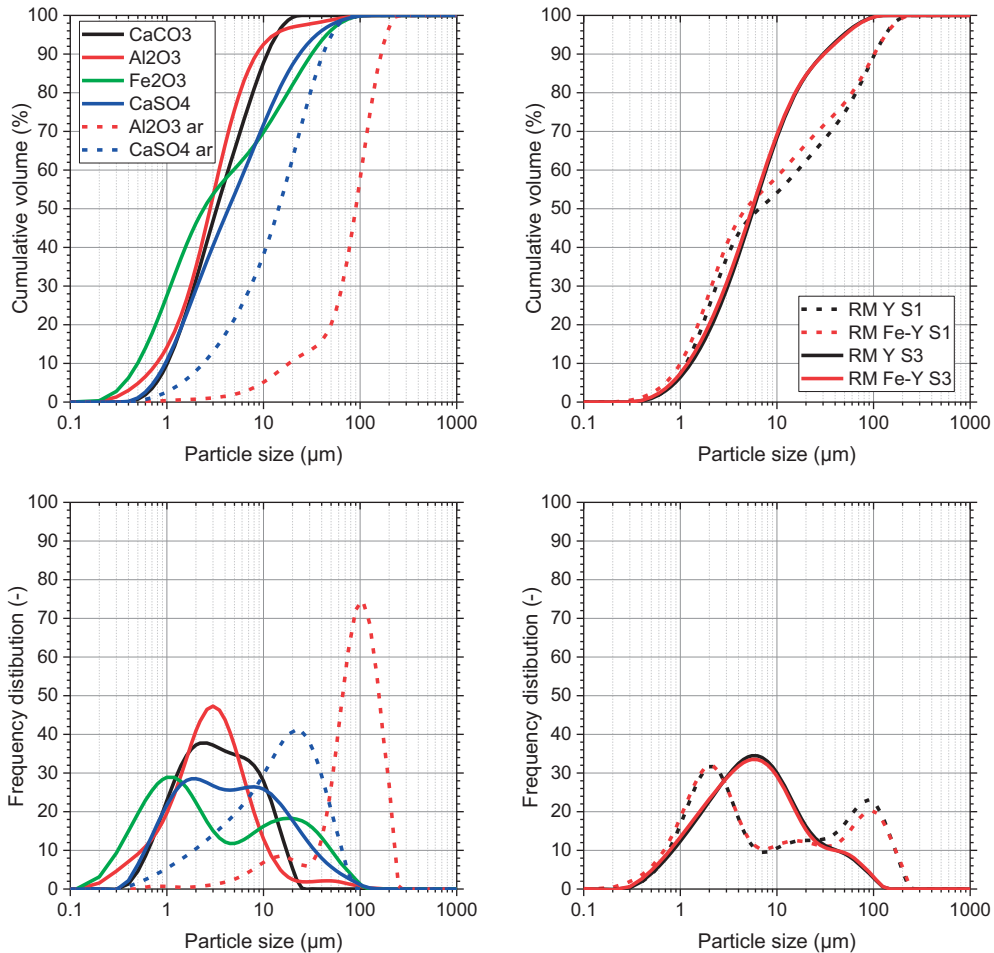


**Figure 8.8-3 Particle size distribution (PSD) of the used raw materials (left) and the prepared mixes (right); ar = used as received**

The **physical characteristics** of the **ye'elimite clinkers** from the several series as described hereafter. The PSD of the ground clinkers is shown in Figure 8.8-4. The clinkers from S1 and S2 were ground dry for 1 minute in a vibration disc mill. The clinkers from S3 were ground dry for 1 minute in a planetary ball mill. The clinker produced in S3 was sintered in a single step without any intermediate grinding. We compared the PSD of the raw mix and the ground clinker of S3 to investigate whether a coarsening of the materials can be observed, e.g. caused by sintering reactions and probably the formation of a liquid phase. Moreover, we try to see whether the addition of iron has any impact such as the densification of the microstructure and the formation of a harder to grind material compared to the stoichiometric ye'elimite. As expected, the coarsening of the materials throughout the sintering process and a higher hardness of Fe-Y compared to Y can be seen. The coarsening is caused by the conversion of the raw materials into the new clinker phases accompanied by the formation of a new microstructure. A higher content of a coarser fraction is presented with increasing iron contents.

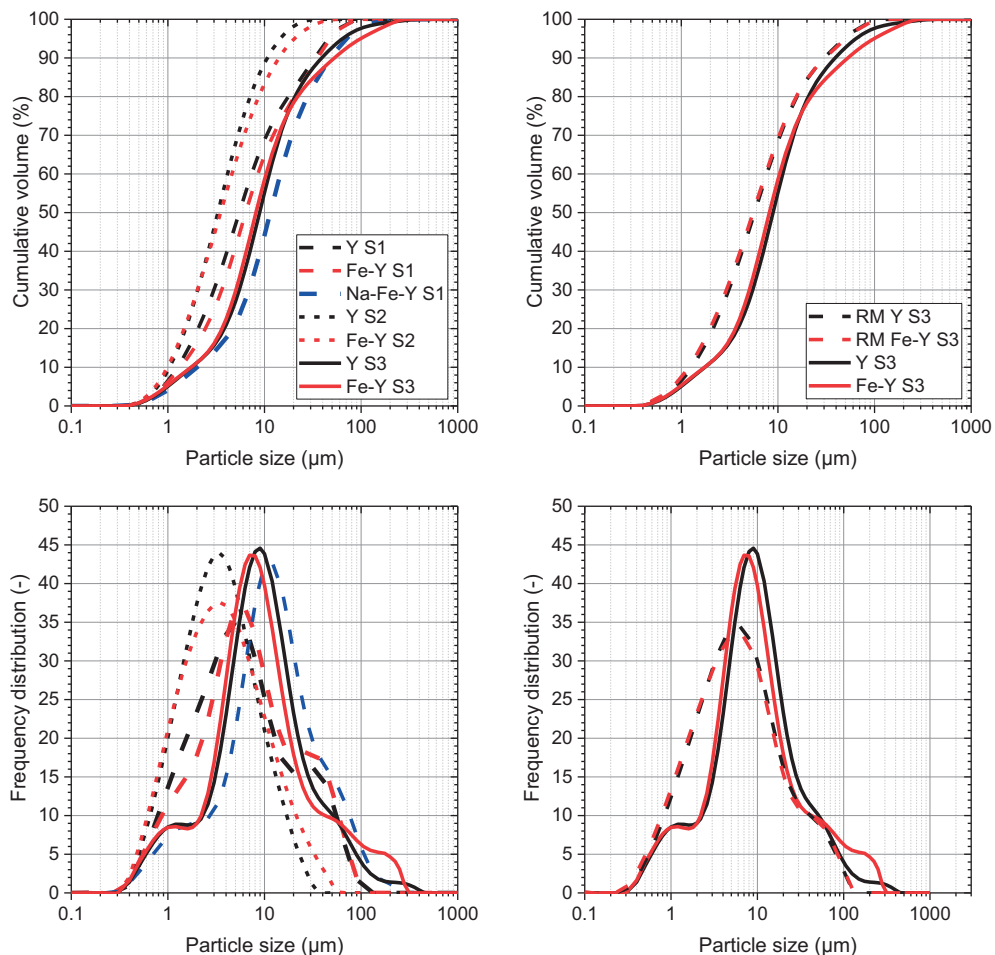


Figure 8.8-4 Cumulative volume distribution (top) and frequency distribution (bottom) of the PSD of the ground clinkers (left) and a comparison of chosen raw mixes and clinkers (right)

Figure 8.8-5 shows the results of the ground clinkers of the S2 series. The samples become coarser, when using the same grinding procedure, with increasing iron contents. The sample 0.80Fe-Y was sintered two times including an intermediate grinding step. The clinker was still much coarser compared to the other ones.

The coarsening coincides with the increasing formation of the ferritic phase contents. This indicates that the impact of iron is amplified in the presence of sodium causes or at least promotes the formation of a coarser fraction. The  $SSA_{BET}$  of all products is shown in Table 8.8-13 below.

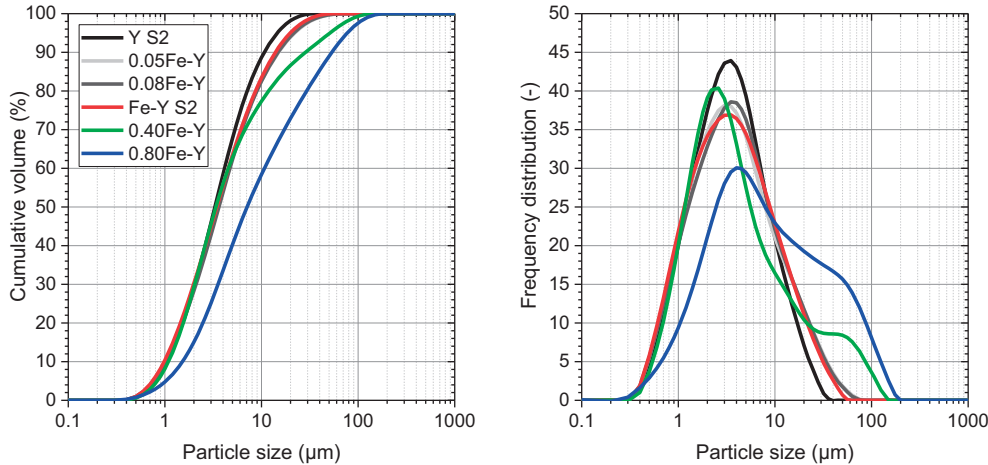


Figure 8.8-5 PSD of the ground clinkers (left) and a comparison of chosen raw mixes and clinkers (right)  
Table 8.8-13 Specific surface area of the ground clinkers

	S1			S2					S3		
	Y	Fe-Y	Na-Fe-Y	Y	Fe-Y				Y	Fe-Y	
$C_4A_{3-x}F_xS$ with $x_{target}$	0	0.2	0.2	0	0.05	0.08	0.2	0.4	0.8	0	0.2
=											
Sintering repetitions (-)	3	3	3	3	2	2	1	1	2	1	1
$SSA_{BET}$ ( $m^2/g$ )	1.43	1.32	0.84	1.50	1.62	1.64	1.77	1.71	1.26	1.16	0.96

The distribution of phases within certain size fractions of selected clinker samples was also investigated. For that purpose Y and Fe-Y clinker was produced using the S3 synthesis protocol. The clinker samples were not ground but instead gently crushed by hand in an agate mortar and sieved to three fraction; 90-125  $\mu m$ , 32-90  $\mu m$  and <32  $\mu m$ . The fractions were characterised by PSD,  $SSA_{BET}$  and QXRD analyses. In addition, the impact of the PSD on the hydration kinetics was assessed by calorimetry. The results of these analyses are presented below.

The **clinker formation** and **achieved composition** is presented. The reaction is incomplete at 1100 °C, 1150 °C and 1200 °C. Raw material phases like anhydrite, corundum and lime together with intermediate krotite, mayenite, grossite and ferrites are present. It is known that the sintering temperature plays an important role for the impact of iron on the kinetics of the ye'elinite formation as well as on the incorporation of iron into the crystal lattice. The main formed calcium aluminate phase at low sintering temperatures like 1100 °C to 1150 °C is krotite ( $\pm$ mayenite). With increasing temperatures grossite is increasingly formed over krotite. However, grossite again reacts with lime to krotite and ultimately to ye'elinite and as a result disappears. This sequence is well demonstrated in the case of stoichiometric ye'elinite (see Chapter 4). The results of the synthesis of stoichiometric ye'elinite (S1) as a function of the sintering temperatures are shown in Table 8.8-14.

Annex

**Table 8.8-14 Mineralogical composition of stoichiometric ye'elimite as a function of the applied temperature**

S1; \* addition of 5%  $C\bar{S}$  before 3<sup>rd</sup> sintering

Target -  $C_4A_3S$  (Y)

Sintering temp. [°C]	1100			1150			1200			1250			1300		
	1	2	3*	1	2	3*	1	2	3*	1	2	3*	1	2	3*
	[%]														
$C_4A_3\bar{S}$	14.4	50.3	53.2	20.4	68.3	68.8	18.8	80.4	82.2	37.8	86.4	93.4	89.4	94.2	96.9
$C_{12}A_7$	0.9	9.8	2.9	1.1	1.6	0.6	0.8	0.7	0.5	2.4	0.9	0.7	0.6	0.8	n.d.
$CA$	12.8	22.4	28.2	10.1	21.7	20.4	9.4	14.5	10.6	9.5	10.6	2.4	2.3	4.7	n.d.
$CA_2$	3.9	1.5	n.d.	14.5	0.6	n.d.	17.4	n.d.	n.d.	14.5	n.d.	n.d.	2.4	n.d.	n.d.
$A$	31.2	4.0	1.5	23.0	n.d.	n.d.	21.7	n.d.	n.d.	14.6	n.d.	n.d.	2.2	n.d.	n.d.
$C\bar{S}$	18.5	11.5	13.7	16.0	7.4	9.9	16.5	4.1	6.4	12.1	1.8	3.2	1.4	n.d.	2.7
$C$	17.5	0.2	0.1	14.3	n.d.	n.d.	14.7	n.d.	n.d.	8.6	n.d.	n.d.	1.4	n.d.	n.d.
$CH$	0.5	n.d.	n.d.	0.4	n.d.	n.d.	0.4	n.d.	n.d.	0.3	n.d.	n.d.	n.d.	n.d.	n.d.
$M$	0.3	0.3	0.4	0.2	0.4	0.3	0.3	0.3	0.3	0.2	0.3	0.3	0.3	0.3	0.4

Table 8.8-15 shows the mineralogical composition  $C_4A_{2.8}Fe_{0.2}\bar{S}$  clinker as a function of the sintering temperatures.

**Table 8.8-15 Mineralogical composition of iron-bearing ye'elimite as a function of the applied temperature**

S1; \* addition of 5%  $C\bar{S}$  before 3<sup>rd</sup> sintering

Target -  $C_4A_{2.8}Fe_{0.2}S$  (Fe-Y)

Sintering temp. [°C]	1100			1150			1200			1250			1300		
	1	2	3*	1	2	3*	1	2	3*	1	2	3*	1	2	3*
	[%]														
$C_4A_3\bar{S}$ -o	17.2	25.2	29.2	21.9	35.4	34.9	36.8	36.8	31.7	48.5	45.0	37.6	36.7	43.4	35.0
$C_4A_3\bar{S}$ -c	n.d.	10.5	22.2	3.6	29.0	36.7	42.2	42.3	53.7	31.1	48.6	55.8	42.2	47.6	59.3
$C_{12}A_7$	5.0	2.3	n.d.	4.8	n.d.	n.d.	0.4	0.4	0.7	1.0	0.7	0.6	0.4	0.5	0.8
$CA$	20.7	36.5	31.9	18.0	24.4	17.5	13.4	13.3	6.8	5.1	2.1	0.3	13.5	4.6	n.d.
$CA_2$	4.0	1.0	n.d.	9.5	n.d.	n.d.	n.d.	n.d.	n.d.	2.5	n.d.	n.d.	n.d.	n.d.	n.d.
$C_4AF$	5.4	4.0	2.5	6.3	2.6	2.2	1.5	1.5	0.7	6.7	3.1	2.4	1.5	3.5	2.7
$C_2F$	5.1	3.6	1.0	4.1	1.1	n.d.	2.0	2.0	1.4	0.6	n.d.	n.d.	2.0	n.d.	n.d.
$A$	17.4	3.0	n.d.	11.4	n.d.	n.d.	n.d.	n.d.	n.d.	1.2	n.d.	n.d.	n.d.	n.d.	n.d.
$F$	n.d.	n.d.	n.d.	n.d.	n.d.	n.d.	n.d.	n.d.	n.d.	n.d.	0.5	0.4	n.d.	0.4	n.d.
$C\bar{S}$	17.7	13.6	13.3	15.7	7.5	8.7	3.7	3.7	5.0	3.3	n.d.	2.8	3.7	n.d.	2.2
$C$	6.9	n.d.	n.d.	4.4	n.d.	n.d.	n.d.	n.d.	n.d.	n.d.	n.d.	n.d.	n.d.	n.d.	n.d.
$CH$	0.2	n.d.	n.d.	n.d.	n.d.	n.d.	n.d.	n.d.	n.d.	n.d.	n.d.	n.d.	n.d.	n.d.	n.d.
$M$	0.4	0.3	n.d.	0.3	n.d.	n.d.	n.d.	n.d.	n.d.	n.d.	n.d.	n.d.	n.d.	n.d.	n.d.

Table 8.8-16 shows the mineralogical composition  $Na_{0.2}C_{3.8}A_{2.8}Fe_{0.2}\bar{S}$  clinker as a function of the sintering temperatures.

Table 8.8-16 Mineralogical composition of sodium-iron-bearing ye'elinite as a function of the applied temperature

S1; * addition of 5% $C\bar{S}$ before 3 <sup>rd</sup> sintering															
Target - $Na_{0.2}C_{3.8}A_{2.8}Fe_{0.2}\bar{S}$ (Na-Fe-Y)															
Sintering temp. [°C]	1100			1150			1200			1250			1300		
	1	2	3*	1	2	3*	1	2	3*	1	2	3*	1	2	3*
Sintering cycle [-]	[%]														
$C_4A_3\bar{S}$ -o	35.8	33.2	36.8	36.8	32.9	40.1	31.2	19.3	36.1	15.6	18.4	19.7	19.2	15.8	19.7
$C_4A_3\bar{S}$ -c	16.1	25.5	26.5	20.7	29.5	26.8	31.4	48.9	40.4	70.0	73.7	71.7	73.1	77.7	73.2
$C_{12}A_7$	1.1	0.7	0.4	0.7	0.8	n.d.	1.3	1.2	0.8	0.9	1.3	0.3	0.5	0.5	0.5
$CA$	29.7	28.4	25.3	28.1	24.9	20.8	23.7	20.3	13.0	5.3	1.4	n.d.	n.d.	n.d.	n.d.
$CA_2$	2.2	0.8	n.d.	0.5	n.d.	n.d.	n.d.	n.d.	n.d.	0.0	n.d.	n.d.	n.d.	n.d.	n.d.
$C_4AF$	11.8	7.0	7.1	8.7	7.4	8.1	11.0	9.6	8.2	6.6	4.5	6.4	6.1	5.5	5.6
$C_2F$	n.d.	2.8	0.7	2.4	3.2	1.3	n.d.	n.d.	n.d.	n.d.	n.d.	n.d.	n.d.	n.d.	n.d.
$C\bar{S}$	0.4	n.d.	0.5	0.4	0.4	0.4	0.4	n.d.	n.d.	0.3	n.d.	0.5	n.d.	n.d.	n.d.
Glauberite $CNS_2$	2.6	1.6	2.7	1.7	0.9	2.5	1.0	0.7	1.5	0.6	0.7	0.9	0.8	0.5	0.7
Jasmundite	n.d.	n.d.	n.d.	n.d.	n.d.	n.d.	n.d.	n.d.	n.d.	0.7	n.d.	0.5	0.3	n.d.	0.3
$M$	0.3	n.d.	n.d.	n.d.	n.d.	n.d.	n.d.	n.d.	n.d.	n.d.	n.d.	n.d.	n.d.	n.d.	n.d.

The **measured elemental composition** of the different **ye'elinite** types is shown in Figure 8.8-6. The plot was adopted from the work of Touzo et al. [193]. Almost all points fall on the theoretical trend line for the  $Al_2O_3/Fe_2O_3$  ratio in the targeted iron-bearing solid solutions of ye'elinite except for the S1 campaign. The compositions in S1 are probably shifted due to too fine intermixing with krotite ( $\pm$  mayenite) and anhydrite originating from the partial decomposition of ye'elinite.

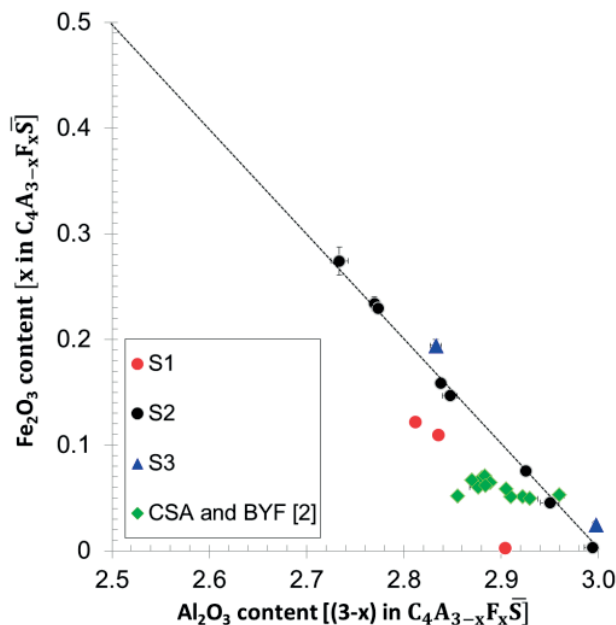


Figure 8.8-6 Plot of the  $Al_2O_3 / Fe_2O_3$  ratio in  $C_4A_{3-x}F_x\bar{S}$  (left); Dotted trend line =  $Al_2O_3 / Fe_2O_3$  ratio of 3, values determined by SEM-EDS analysis (including data for various CSA and BYF from pilot and industrial scale)



The formation and **stability of stoichiometric ye'elimite** will be briefly discussed here. Puertas et al. [198] had shown that the **decomposition** of stoichiometric ye'elimite resulted in the formation of **secondary krotite** and **mayenite**. His findings were supported by the results of the recent study from Tilman Scholten [302] as shown in Figure 8.8-7 (left). Mayenite is only detectable in the sample sintered for 90 minutes at 1350 °C indicating the decomposition of ye'elimite and volatilization of sulphur. In the iron-rich samples (right), mayenite was found at all temperatures but passing a minimum with prolonged dwell times and / or temperatures from around 1250 °C to 1300 °C.

This indicates the presence of two types or origins of mayenite, primary and secondary. The impact of iron on the formation and potential stabilisation of primary mayenite is discussed in Chapter 4, section 4.5.2. In the stoichiometric ye'elimite tricalcium aluminate and some mayenite are formed rather than krotite with increasing dwell times and / or at higher sintering temperatures. The presence of free lime together with tricalcium and monocalcium aluminate indicates too high calcium content in the system which may alter the results. The minor phases present in the solid solution ye'elimite sample are ferrites, mayenite and krotite. The ferrites and mayenite are present in all samples. Monocalcium aluminate was only found initially only at the shortest dwell time and lowest tested sintering temperature (primary phase) but again at 1350 °C as secondary phase from the decomposition of ye'elimite. The increase of the ferritic phase content with increasing temperature indicates the decomposition of iron-bearing ye'elimite. The absence of any  $C_3A$  in the sample with iron should be highlighted. Instead of a single calcium-rich aluminate two phases with intermediate calcium contents, compared to ye'elimite and krotite, are formed.

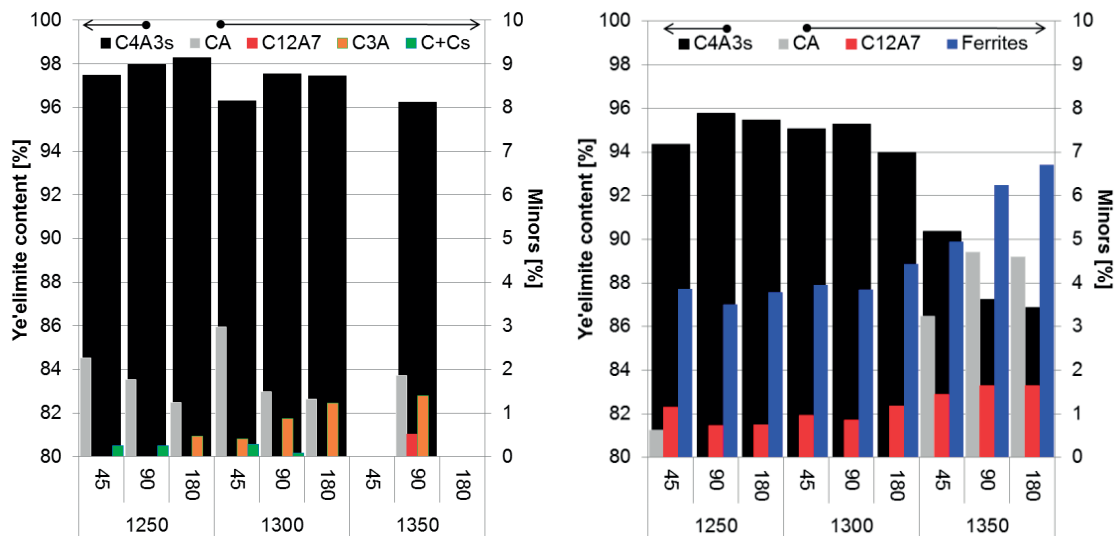


Figure 8.8-7 Mineralogical composition of targeted stoichiometric (left) and an iron-rich solid solution ye'elimite " $C_4A_{2.8}F_{0.2}\bar{S}$ " (right) composition, applying different temperature and sintering dwell time; samples from [302] and evaluated by myself



The microstructure of ye'elimite clinkers from S2 series are shown in Figure 8.8-8.

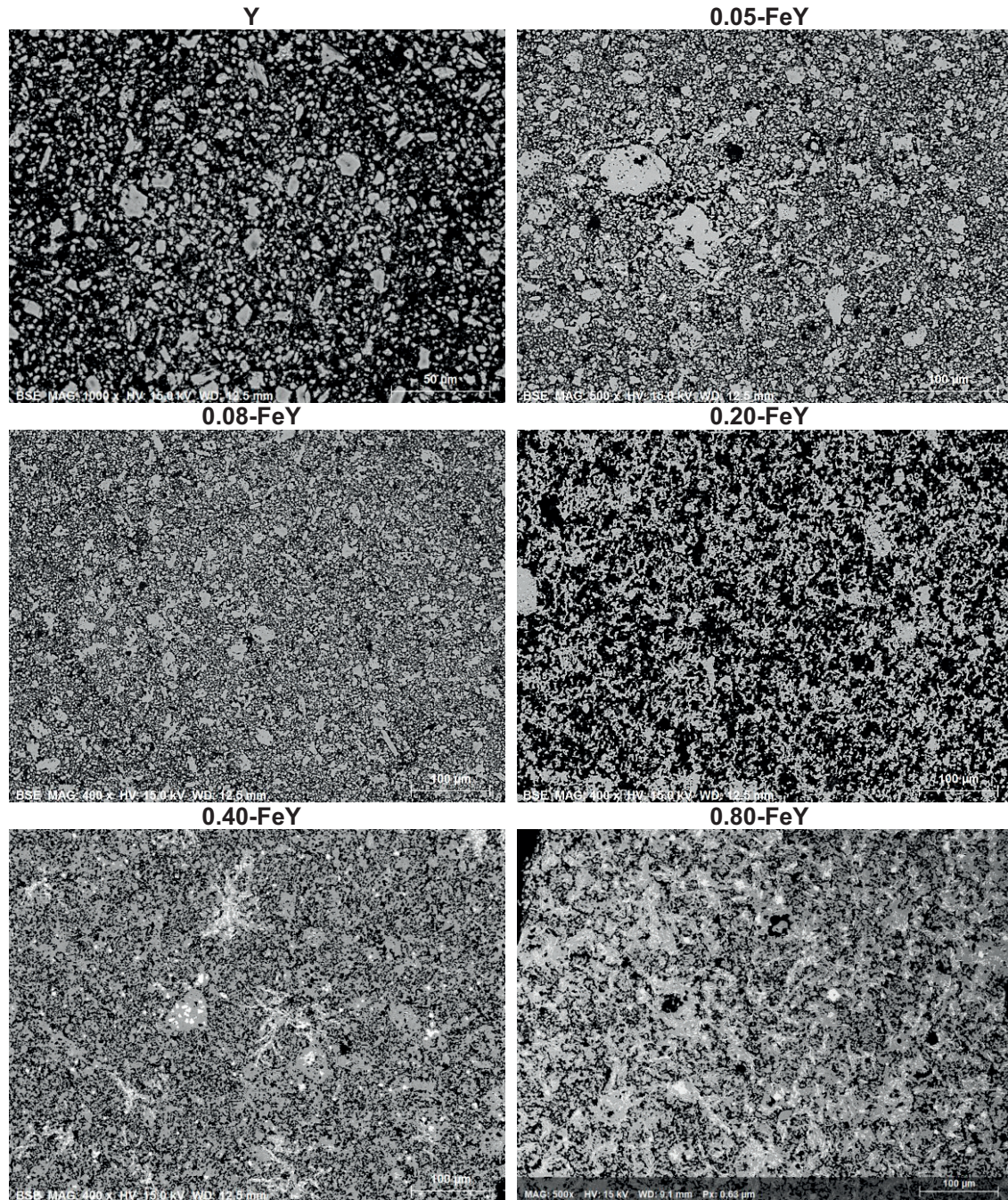


Figure 8.8-8 SEM micrographs of the ye'elimite clinkers from the S2 series



The comparison of the **microstructure of synthetic Na-Fe-Y (S1)** and **industrial BYF clinker** is shown in Figure 8.8-9. The relevance of the liquid phase, not only for the phase formation but as well for the shape of the clinker microstructure, can be seen. The clinker which was produced at industrial scale reveals some similar features as the iron and sodium-bearing solid solution ye'elinite produced in a lab muffle furnace. The ye'elinite particles are embedded or glued together by an interstitial ferritic liquid phase. The rounding of the ye'elinite particles is a typically feature of industrially produced CSA and BYF clinker. It indicates the initiated melting or better dissolution of the ye'elinite into the ferritic liquid phase due to too high sinter zone temperatures and / or too long dwell times. The dissolution of ye'elinite is further indicated by the differences in the ferritic phase composition.

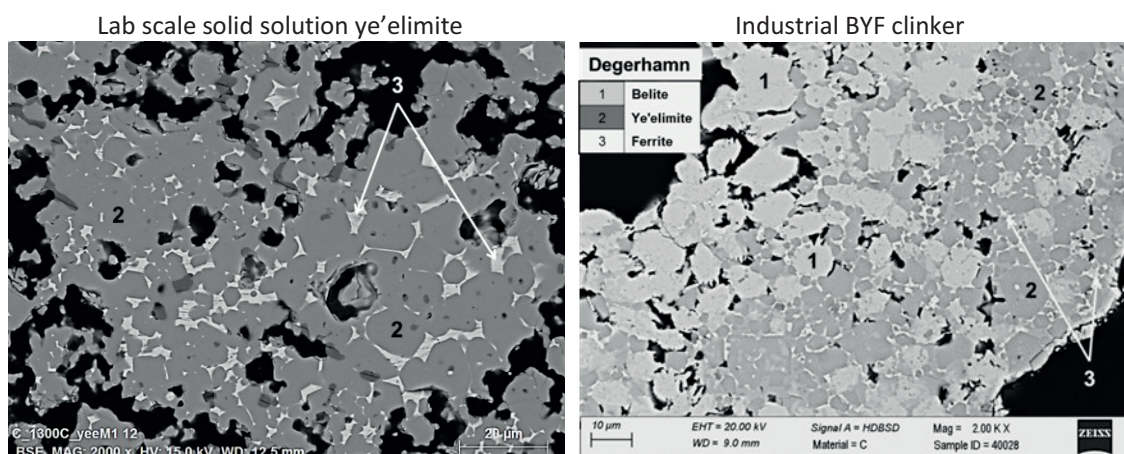


Figure 8.8-9 SEM micrographs of the Na-Fe-Y from the 2013 series and BYF clinker produced at industrial scale

At the same time we can determine the formed **solid solution composition** of the **main minerals** in pilot and industrial **BYF** clinkers. Considering the amount of minor elements present in “stoichiometric” ye'elinite and the investigated solid solutions, it is obvious that all minor elements, i.e. present as impurities in the raw mix like alkali,  $MgO$  and  $SiO_2$ , are at least partly incorporated into the crystal structure of ye'elinite.

**Iron content:** As reported in chapter 4, high substitution levels of above 90% were mainly achieved for low values of  $x$ , i.e. in  $C_4A_{3-x}F_x\bar{S}$ , of about 0.05 to 0.08. A similar value was reported earlier by Schmidt [186] but with the limitation that the maximum synthesis temperature was only 1200 °C. This is below the melting point of srebrodolskite, i.e.  $C_2F$ , in the system  $CaO - Fe_2O_3$  as described by Bergman [87]. Our investigation on the iron-rich clinker of the 2013 series has shown that at 1100 °C and 1200 °C mainly orthorhombic ye'elinite and ferritic phases were formed (see section, appendix). Contrary, at 1250 °C and 1300 °C incrementally the iron-bearing cubic polymorph is formed over the orthorhombic type and the ferritic phase. Therefore we assume that ferrites like brownmillerite and srebrodolskite are formed initially at lower sintering temperatures. With increasing sintering temperatures the melting of these phases occur which enable the incorporation of iron into ye'elinite. **Silica content:** Regarding the  $SiO_2$  content, the same range is covered as for the natural ye'elinite [197], even so that in the natural type was formed in system with an excess of silica present (i.e. present in a so-called *Ca*-rich combustion metamorphic host rock; Hatrurim Formation). Moreover, similar amounts of incorporated  $SiO_2$  were found in ye'elinite present in industrial clinkers (results not presented here). These results indicated that a  $SiO_2$  content of around 1.80 % represent the upper limit under the given synthesis conditions.

Annex

Higher incorporation levels as presented in other studies [35] [38] does not seem to be representative for most of the available CSA and BYF clinkers and are very likely correlated with the high concentration of sodium.

**Table 8.8-17 Minimum and maximum minor elements contents present in synthetic phases and industrial clinker minerals; n.d. = not determined**

	Synthetic ye'elimite		CSA and BYF clinkers from pilot & industrial scale		
	ye'elimite [%]	ferrite [%]	ye'elimite [%]	ferrite [%]	belite
Fe <sub>2</sub> O <sub>3</sub>	0.0 to 8.0	<i>main</i>	1.3 to 1.6	<i>main</i>	0.4 to 0.7
MgO	0.0 to 1.5	0.0 to 1.0	0.5 to 1.0	0.5 to 4.0	0.4 to 0.5
Na <sub>2</sub> O	0.0 to 1.5	0.0 to 1.0	0.1 to 0.5	0.3 to 0.6	0.2 to 0.4
K <sub>2</sub> O	n.d.	n.d.	0.0 to 0.3	0.0 to 0.3	0.0 to 0.5
SiO <sub>2</sub>	0.0 to 0.5	0.0 to 2.0	0.7 to 0.8	1.5 to 4.0	<i>main</i>
TiO <sub>2</sub>	n.d.	n.d.	n.d.	0.5 to 5.0	0.1 to 0.8
SO <sub>3</sub>	<i>main</i>	0.0 to 1.0	<i>main</i>	0.2 to 0.8	0.5 to 2.0

## Annex V – Chapters 5 to 7

The calorimetry results of Y (supplementing the results presented in Chapter 5) at all tested w/b ratios are shown in Figure 8.8-10.

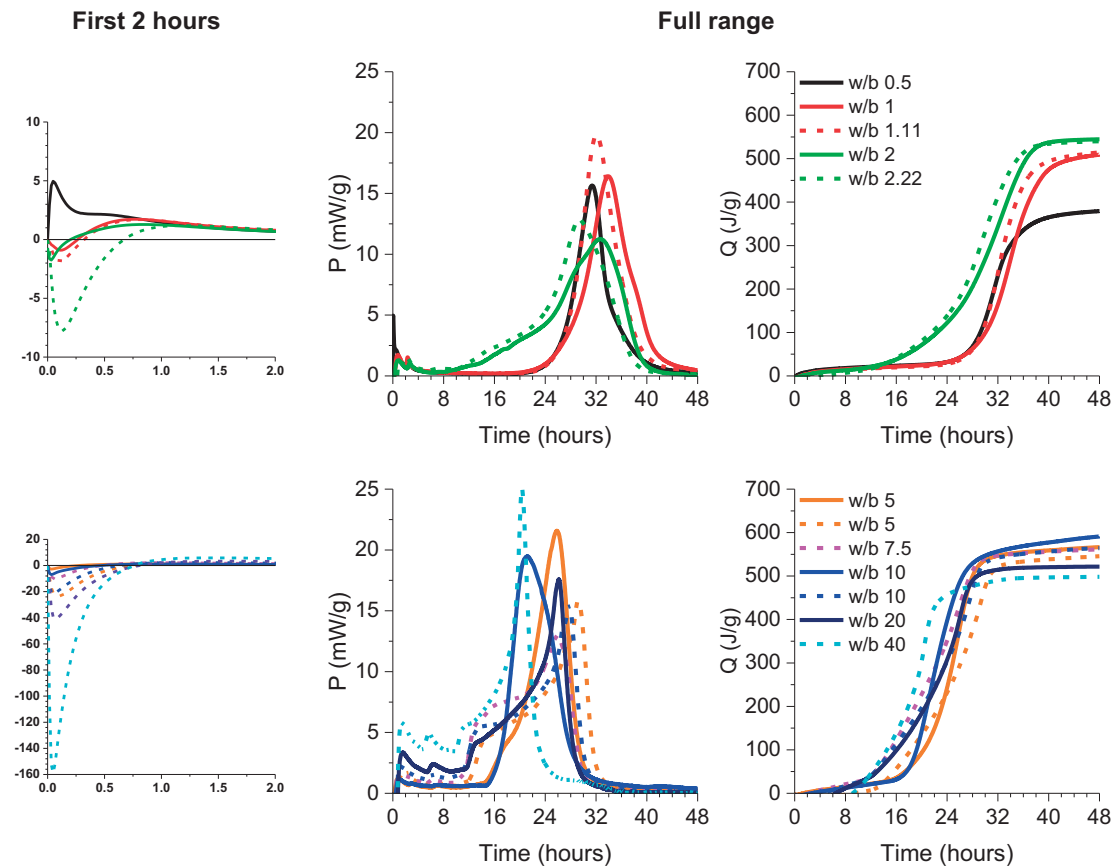


Figure 8.8-10 Rate of heat evolution (left and middle) and cumulative heat (right) of hydrating Y and blends containing quartz expressed per gram of clinker; solid line = neat clinker and dashed line = blend with quartz

The calorimetry results of Fe-Y (supplementing the results presented in Chapter 7) at all tested w/b ratios are shown in Figure 8.8-11. A **summary of all results** with regard to the **hydration degree versus w/b and w/s ratio** is presented hereafter (supplementing the results presented in the Chapters 5 and 7).

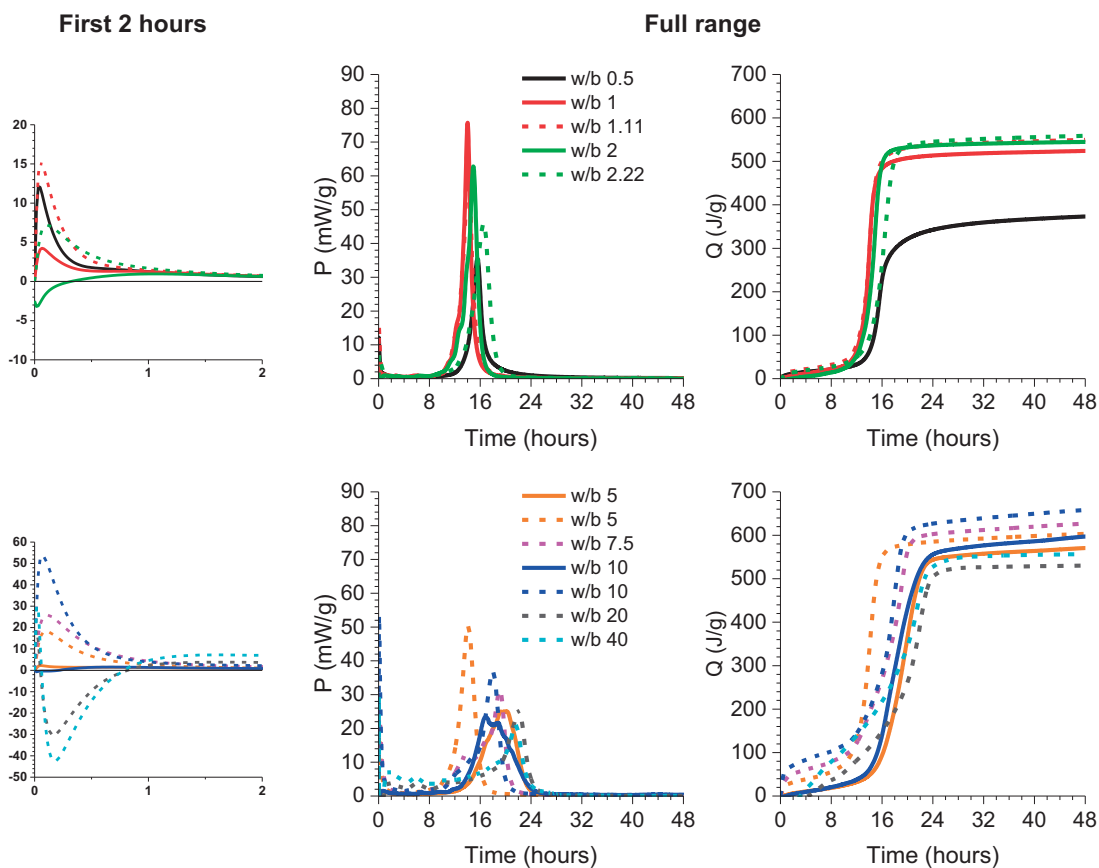


Figure 8.8-11 Rate of heat evolution (left and middle) and cumulative heat (right) of hydrating Fe-Y and blends containing quartz expressed per gram of clinker; solid line = neat clinker and dashed line = blend with quartz

Figure 8.8-12 shows the determined hydration degree of Y and Fe-Y in comparison to the cumulative heat after 48 hours of hydration. In general, increasing the water to cement and solid ratios caused the increase of the achieved hydration degree. For example, the hydration of ye’elinite was incomplete even at high w/c ratios such as 1 or 2. Hence, the presence of sufficient water to theoretically hydrate the whole sample did not guarantee that this will be achieved.

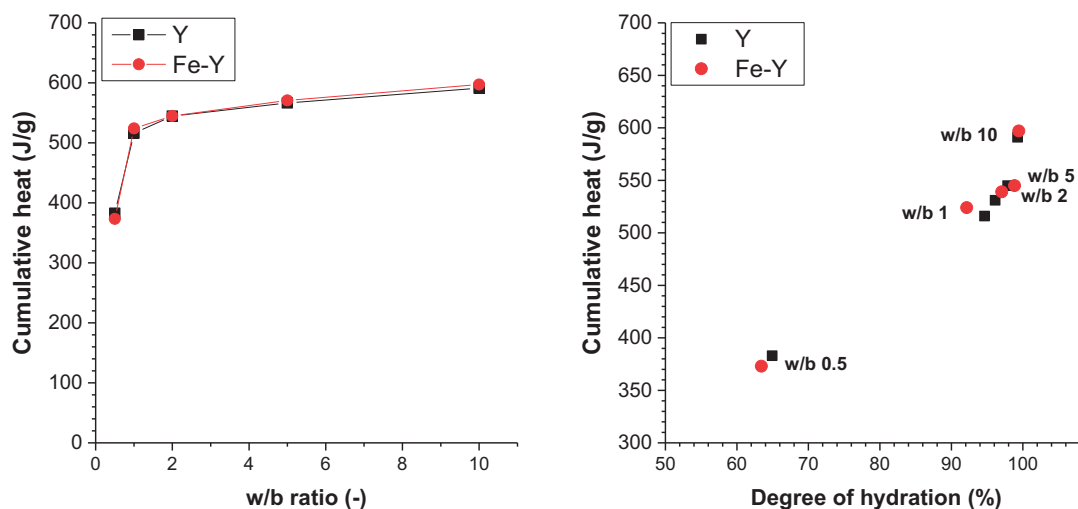


Figure 8.8-12 Hydration degree of Y and Fe-Y versus the cumulative heat

Figure 8.8-13 presents the measured versus targeted quartz content. The results indicated a relatively good fit and hence, accuracy of the derived Rietveld results.

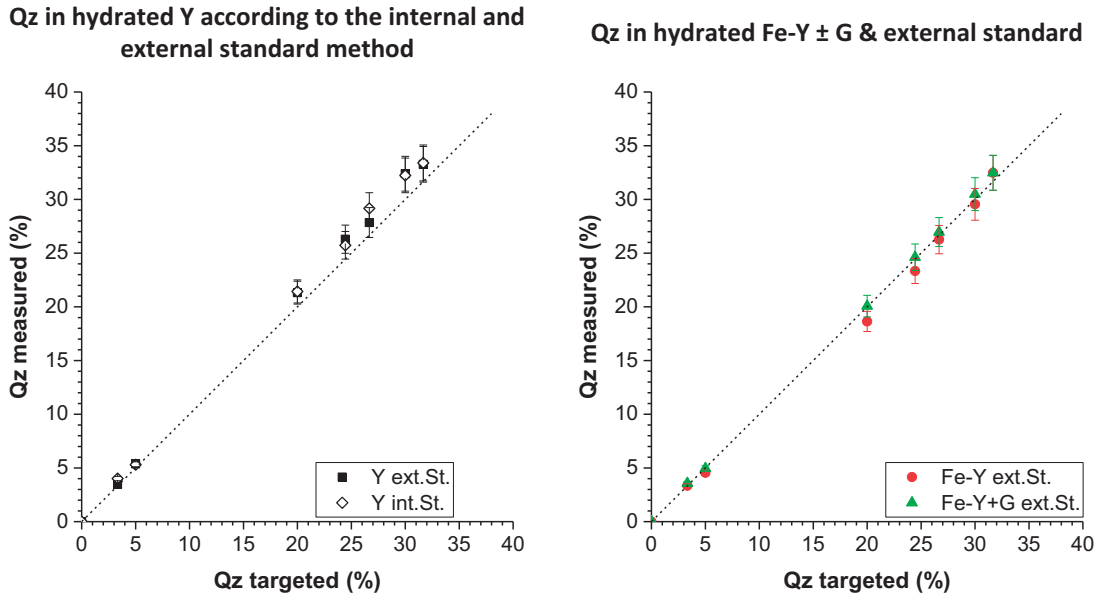


Figure 8.8-13 Measured versus targeted Qz content in paste; error bar represent the relative error of 5%

The derived composition of the hydrates assemblage is shown in Figure 8.8-14. The amount of monosulphate was higher and that of the amorphous phases lower in Y compared to Fe-Y. The quantities of ettringite and aluminium hydroxide were similar in both series. This indicates that iron may have a negative impact of the crystallinity and / or growth of monosulphate.

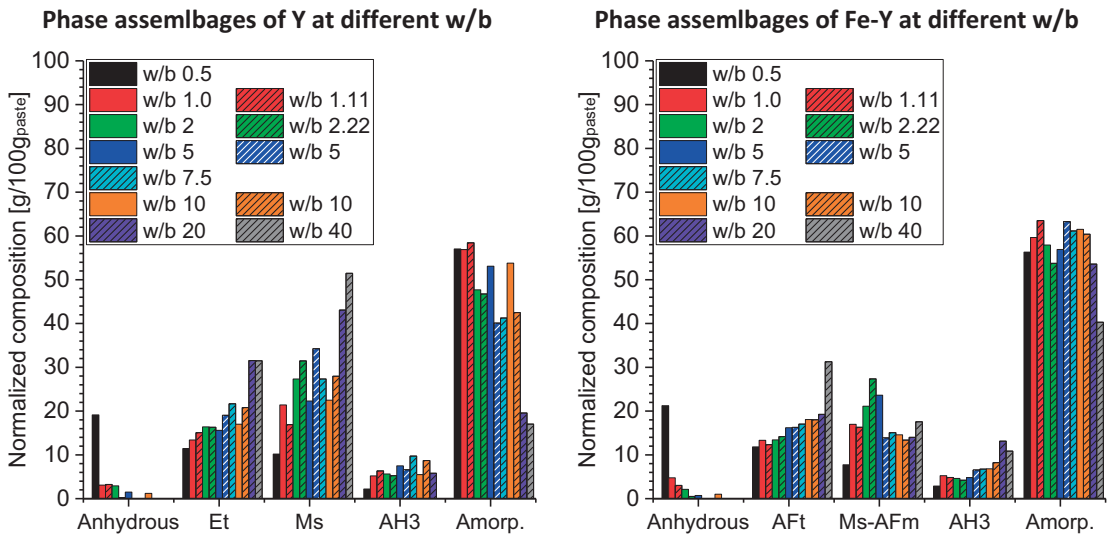


Figure 8.8-14 Normalized phase assemblage per gram of anhydrous and without Qz



The phase assemblage of Fe-Y with gypsum at serval w/b ratios is shown in Figure 8.8-15.

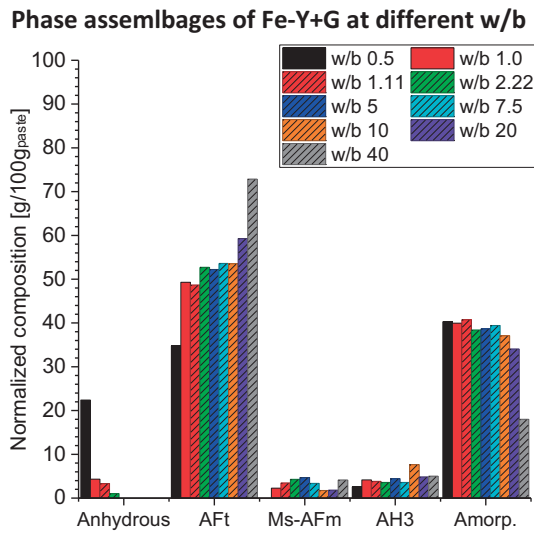


Figure 8.8-15 Normalized phase assemblage per gram of anhydrous and without Qz

The thermogravimetric analyses are shown in Figure 8.8-16 (supplementing the results presented in the Chapters 5 and 7).

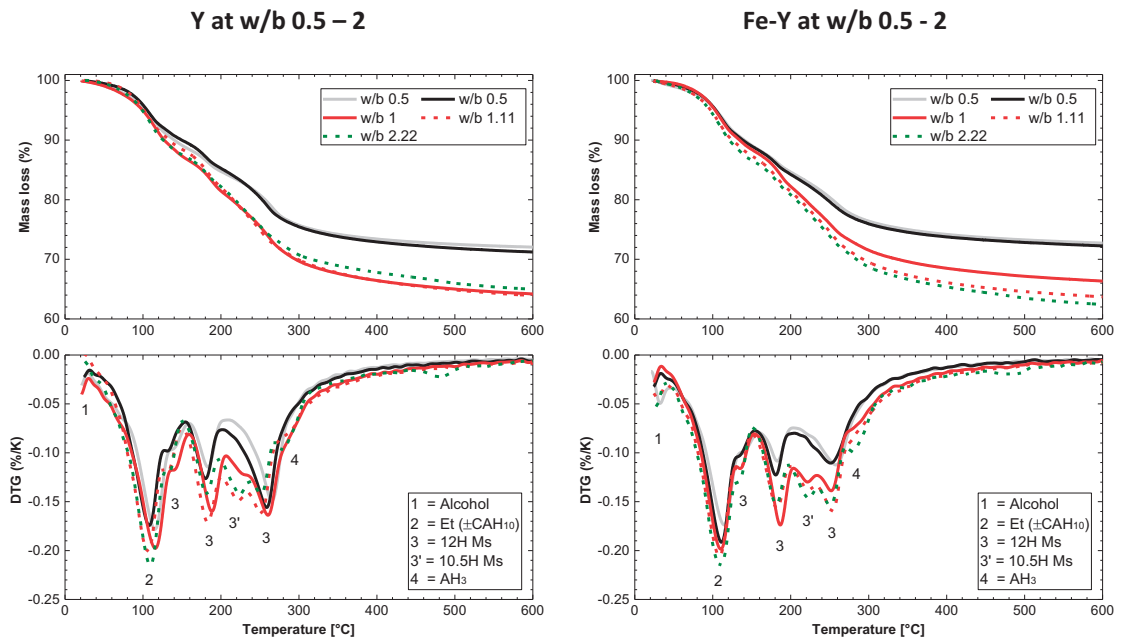


Figure 8.8-16 Normalized TGA analysis of Y and Fe-Y with Qz at w/b from 0.5 to 2 after 2 days of hydration

The normalized (per gram of ye'elimite) thermogravimetric analyses are shown in Figure 8.8-17.

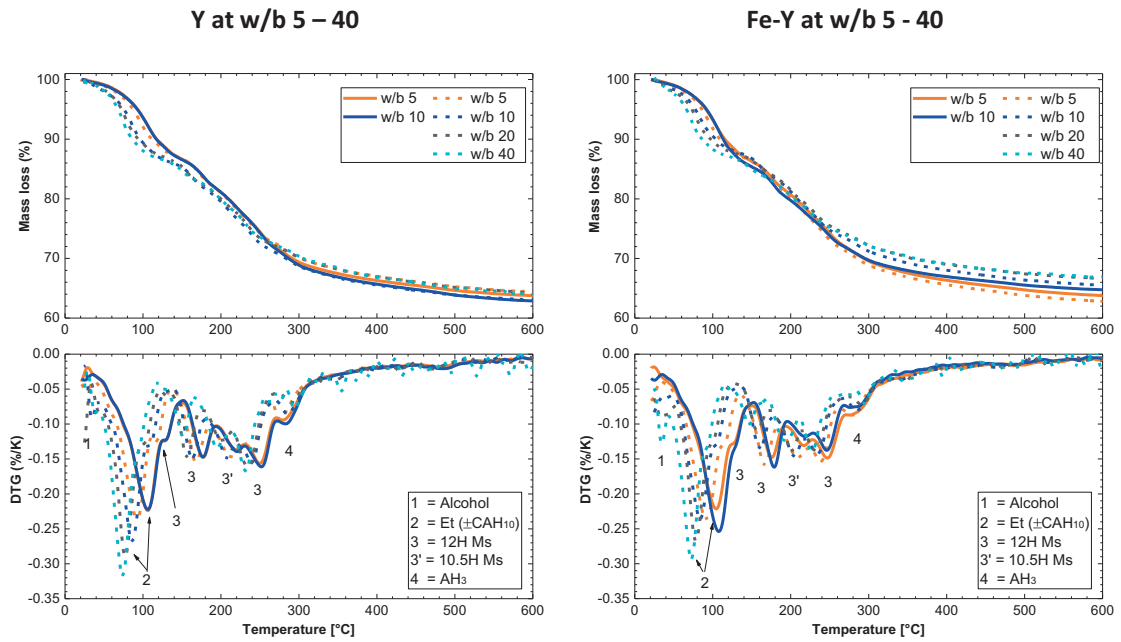


Figure 8.8-17 Normalized TGA analysis of Y and Fe-Y with Qz at w/b from 5 to 40 after 2 days of hydration

We further compared the TG analysis at w/b 0.5 and 2 as shown in Figure 8.8-18. The samples based on Fe-Y show a higher ettringite and lower monosulphate content, consistent with the assumption that mayenite promotes the ettringite formation.

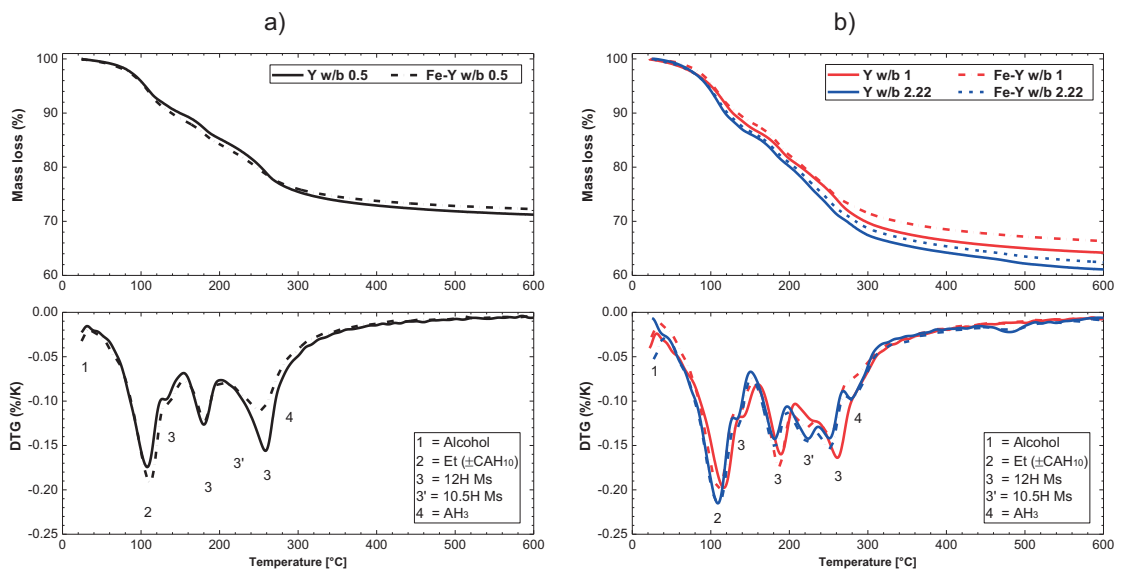


Figure 8.8-18 Comparison of the normalized TGA analysis of Y (solid line) and Fe-Y (dashed line)

Selected XRD plots of the hydrates samples are presented in Figure 8.8-19 (supplementing Chapter 5).

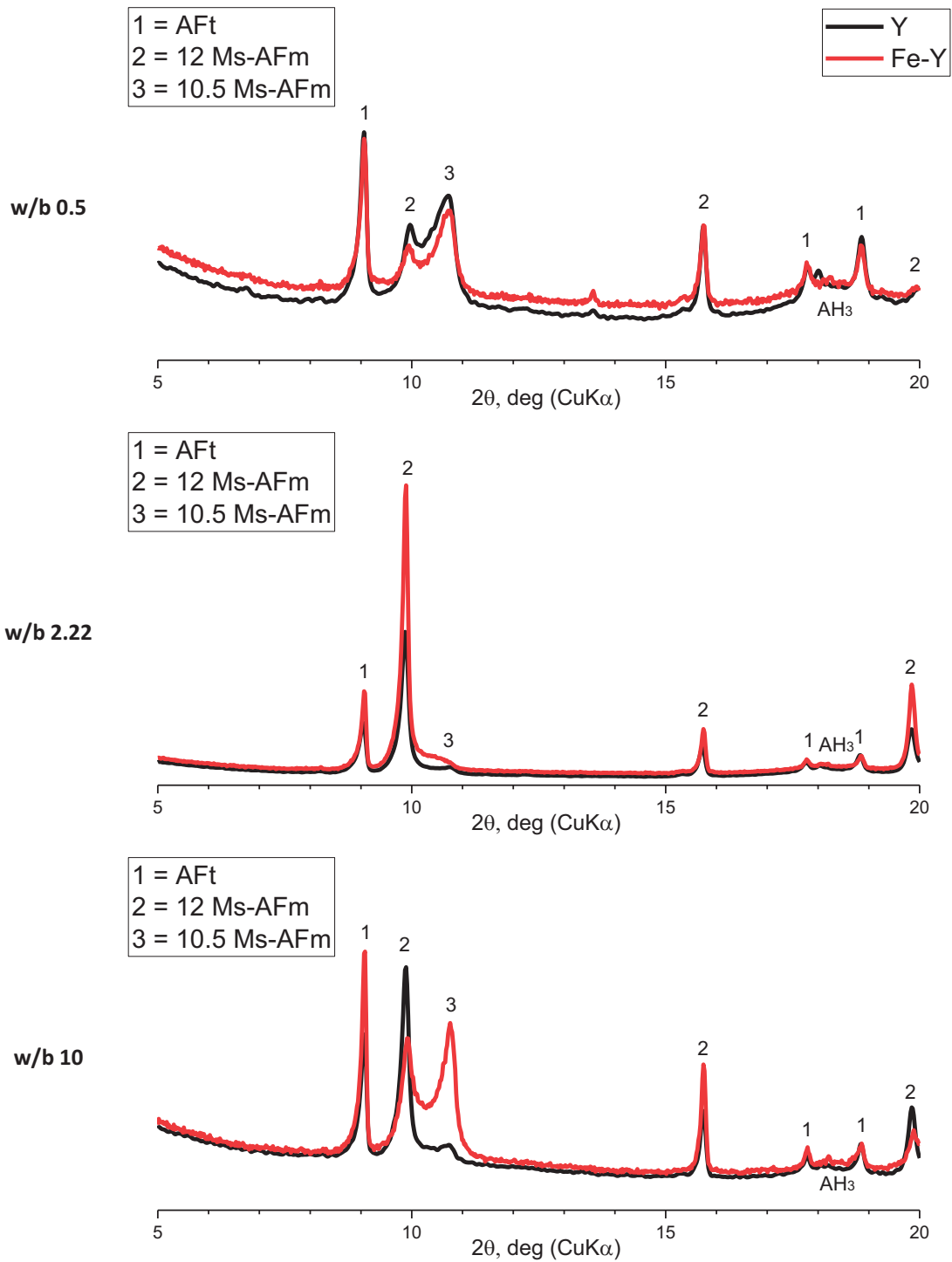


Figure 8.8-19 XRD plot of Y and Fe-Y blends with Qz filler

The chemical **composition of the amorphous phase**, for the paste samples with quartz, was derived from **mass balance** calculations based on QXRD and TGA analyses. The results of the mass balance calculation are shown in Figure 8.8-20 supplementing the results presented in Chapter 5 (Y and compared to Fe-Y) and 6 (Fe-Y+G).

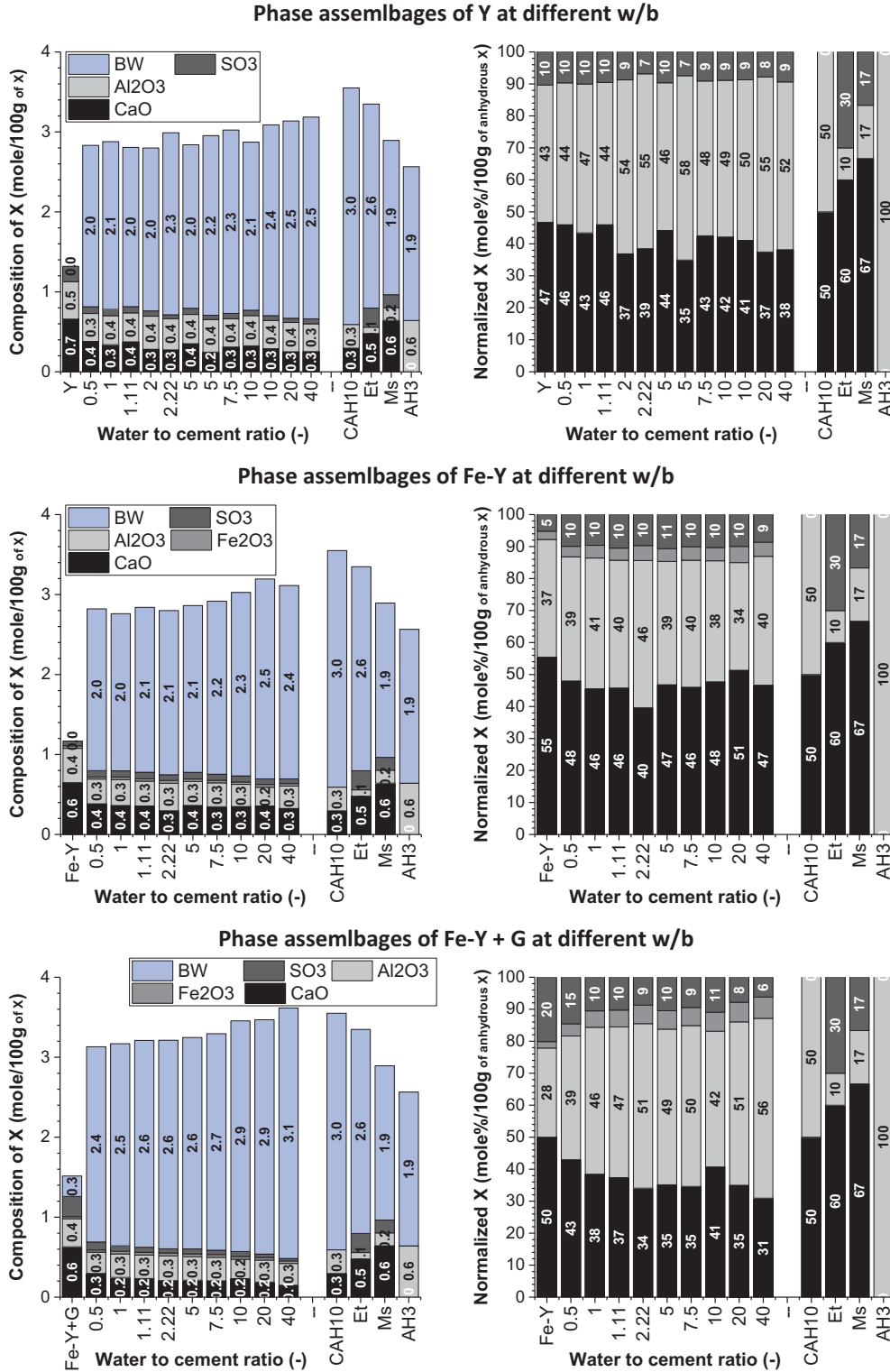


Figure 8.8-20 Normalized phase assemblage per gram of anhydrous and without Qz

The QXRD analyses from the residues of the experiments carried out with Y and Fe-Y at w/b 40 are presented in Figure 8.8-21.

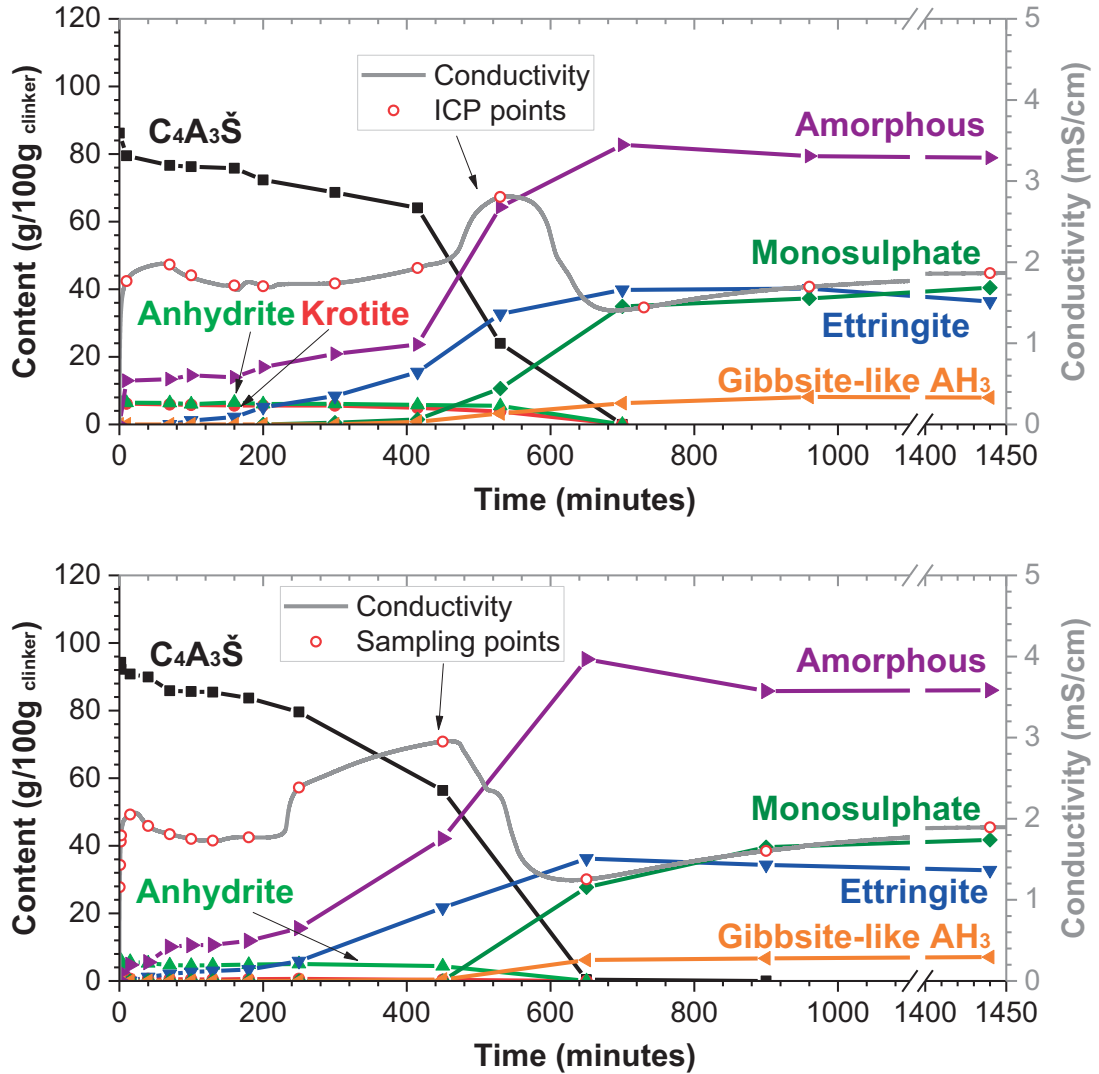


Figure 8.8-21 Evolution of the phase assemblage of the spot samples for Y [303] (left) and Fe-Y (right) at w/b 40 and of the continuous measured conductivity; Et = ettringite and Ms = monosulphate

Supplementary **thermogravimetry** analyses of **Y and Fe-Y hydrated at w/b 40**, as partly presented in **Chapter 5**, are presented in Figure 8.8-22.

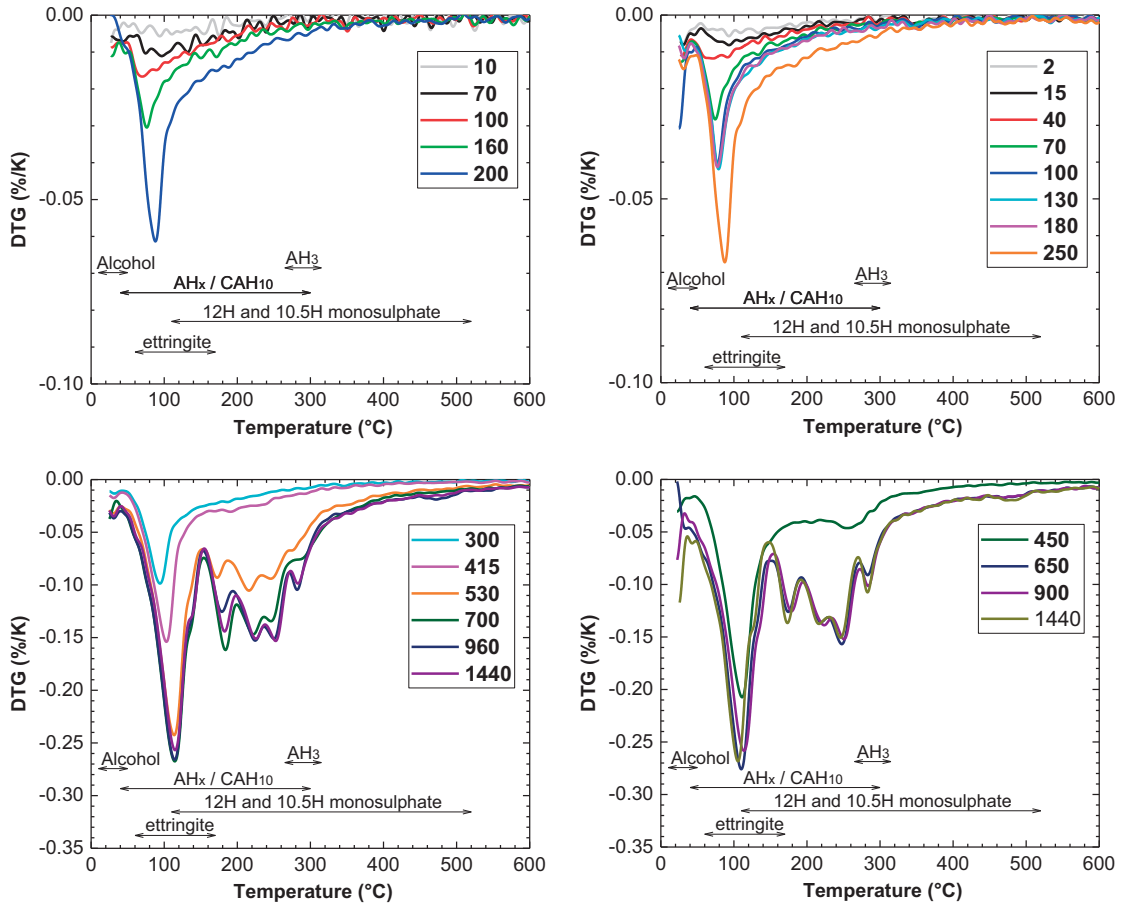


Figure 8.8-22 Differential thermogravimetric analyses for Y [303] (left) and Fe-Y (right) at w/b of 40



The chemical **composition of the amorphous phase**, for the sample from the **experiments in suspensions**, was derived from **mass balance** calculations based on QXRD and TGA analyses. The results of the mass balance calculations are shown in Figure 8.8-23 and supplement the results presented in Chapter 5.

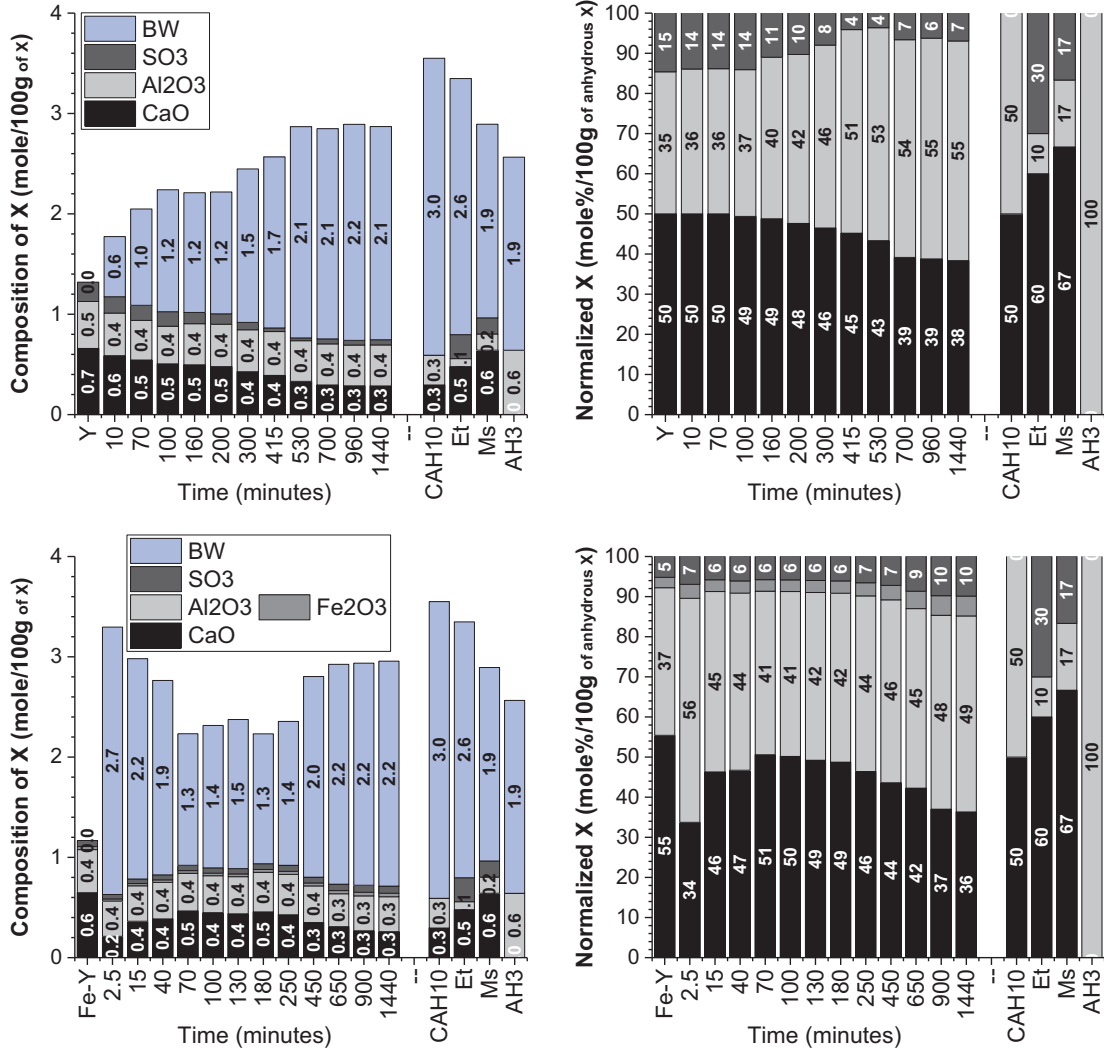


Figure 8.8-23 Mass balance analyses for Y (top) and Fe-Y (bottom) at w/b of 40

The **summary of all experiments carried out with Y and Fe-Y at w/b 100** (supplementing the results presented in Chapter 5 and 7) are presented here (Figure 8.8-24).

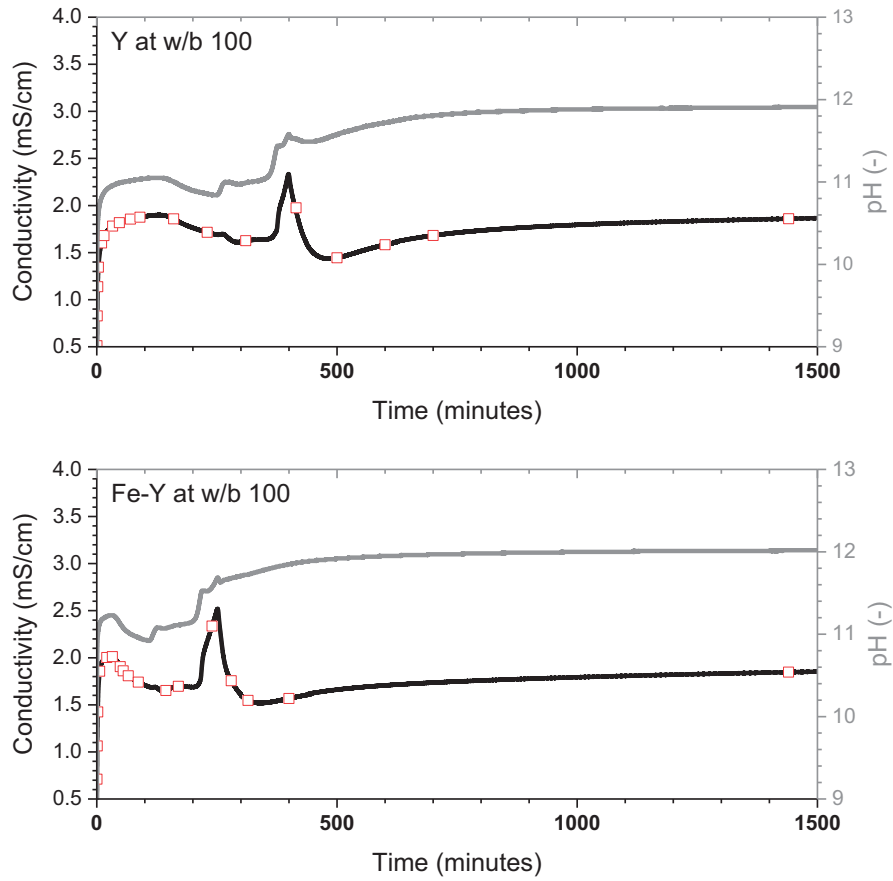


Figure 8.8-24 Evolution of the conductivity and pH;  $\square$  = sampling points

The evolutions of the ion concentration for Y and Fe-Y at w/b 100 are shown in Figure 8.8-25 (supplementing the results presented in Chapter 5 and 7).

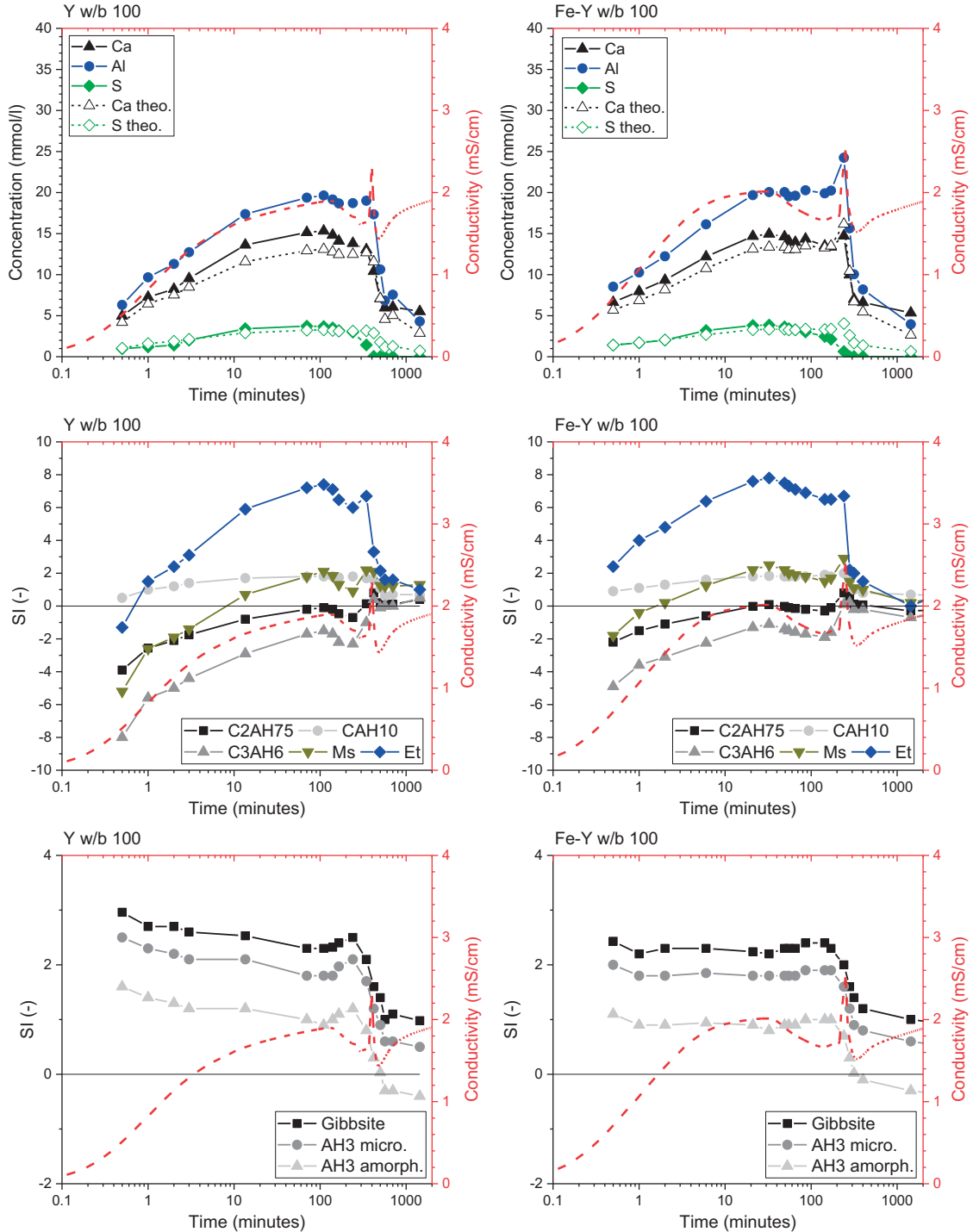


Figure 8.8-25 Evolution of the conductivity (continuous measurement) and concentration (spot samples) including the calculated Ca and S concentrations (dashed lines) for Y (left) and Fe-Y (right) at w/b 100, solubility products from [115] and for AH3am was  $\log K_{S0}$  of 0.24 from [116]

The HR-SEM micrographs of Y and Fe-Y hydrated at w/b 100 after selected hydration periods are shown in Figure 8.8-26 to Figure 8.8-31 (supplementing the results presented in Chapter 5 and 7).



Y at 23 °C and w/b 100 after 90 seconds of hydration

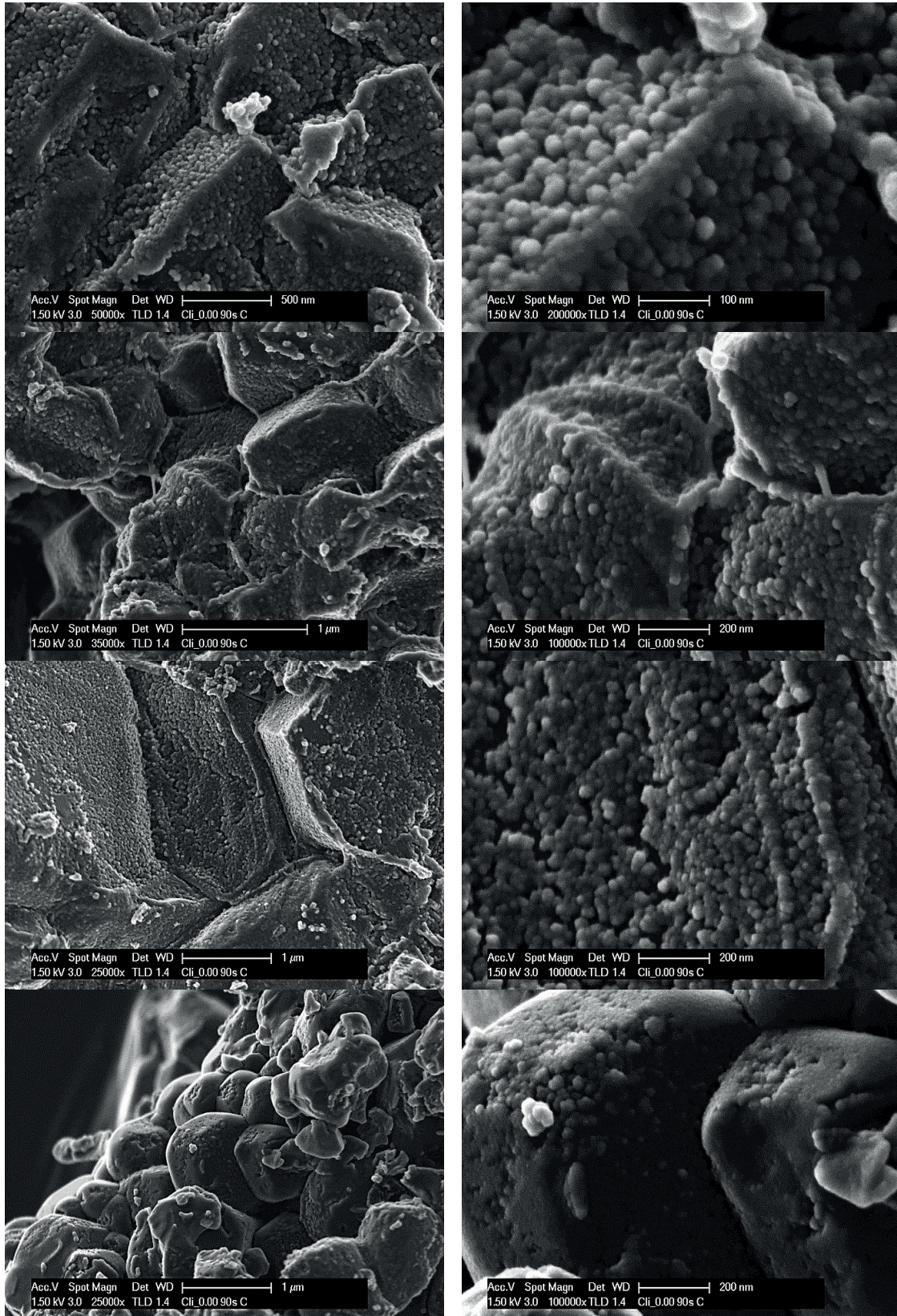


Figure 8.8-26 Morphological characterization of the hydrated Y at 23 °C and a w/b ratio of 100



Y at 23 °C and w/b 100 after 250 seconds of hydration

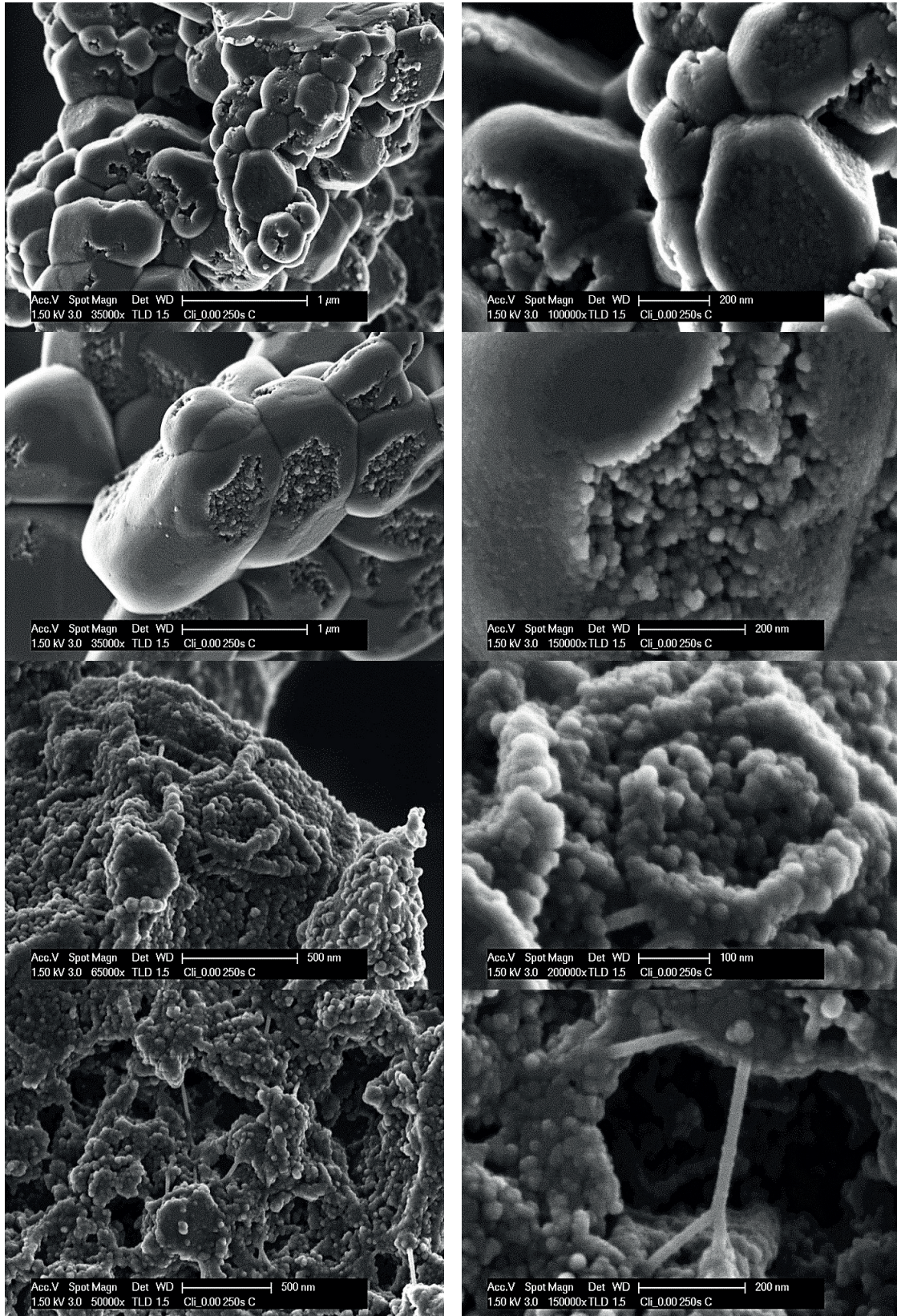


Figure 8.8-27 Morphological characterization of the hydrated Y at 23 °C and a w/b ratio of 100



Fe-Y at 23 °C and w/b 100 after 30 seconds of hydration

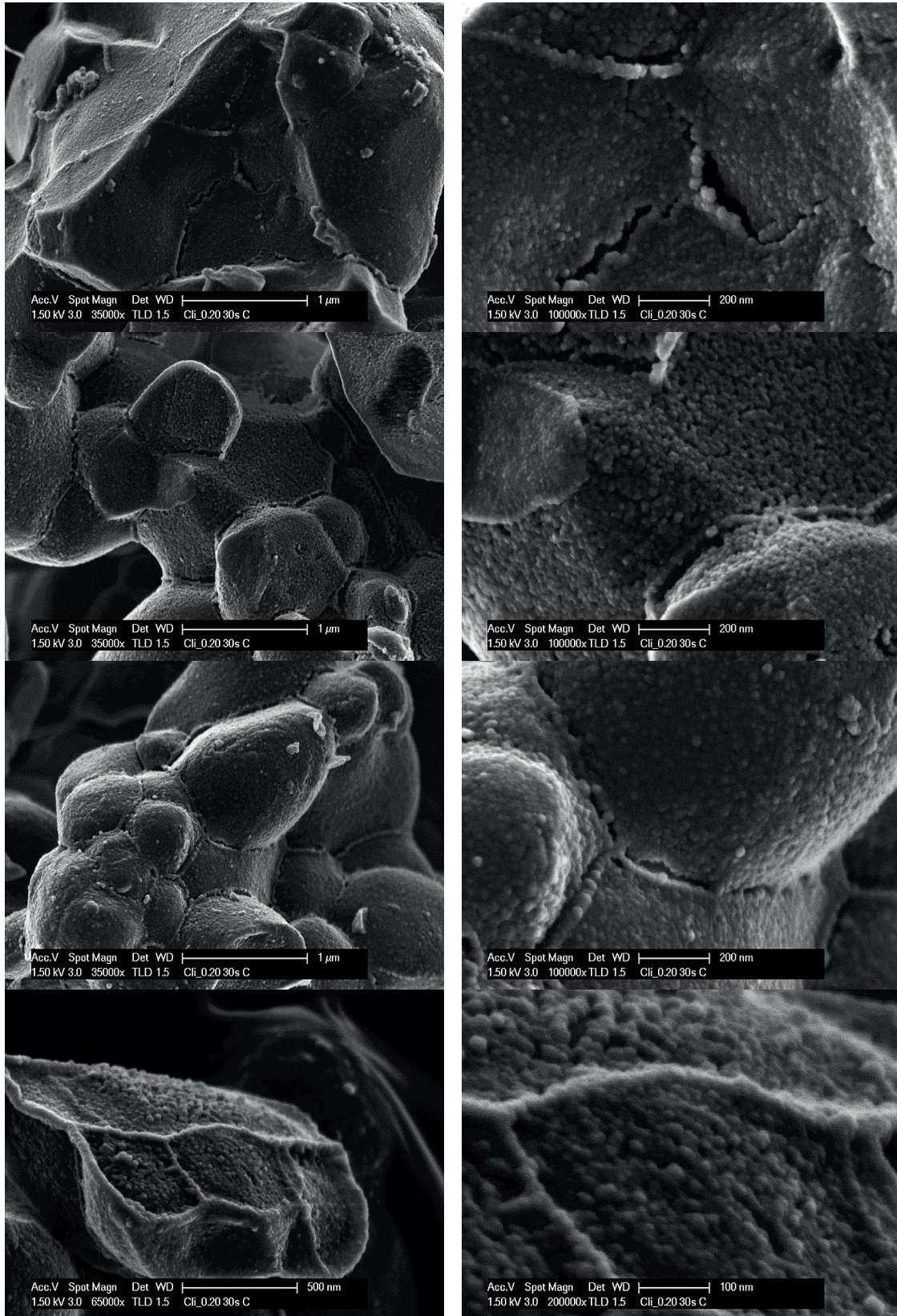


Figure 8.8-28 Morphological characterization of the hydrated Fe-Y at 23 °C and a w/b ratio of 100



Fe-Y at 23 °C and w/b 100 after 90 seconds of hydration

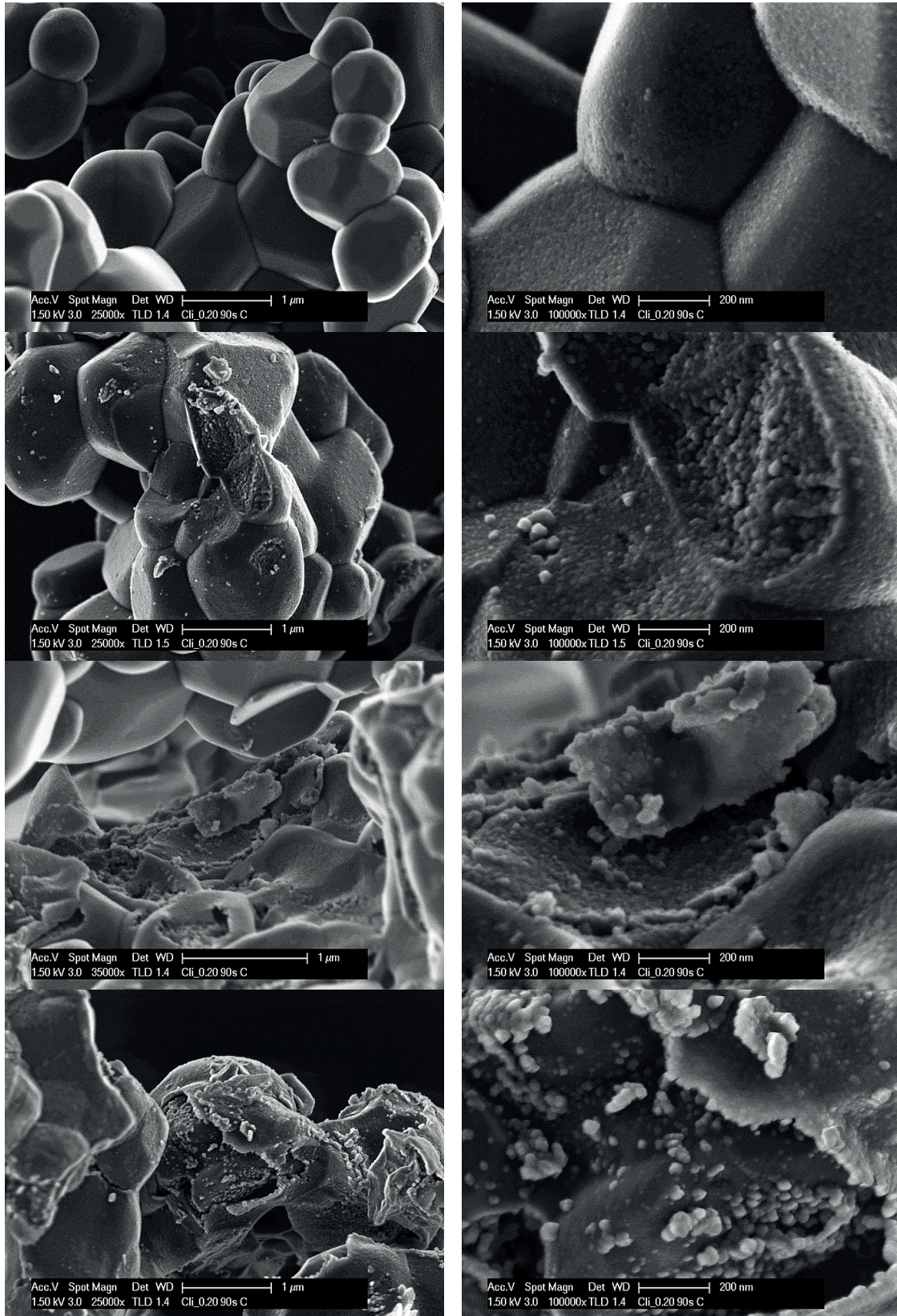


Figure 8.8-29 Morphological characterization of the hydrated Fe-Y at 23 °C and a w/b ratio of 100



Fe-Y at 23 °C and w/b 100 after 120 seconds of hydration

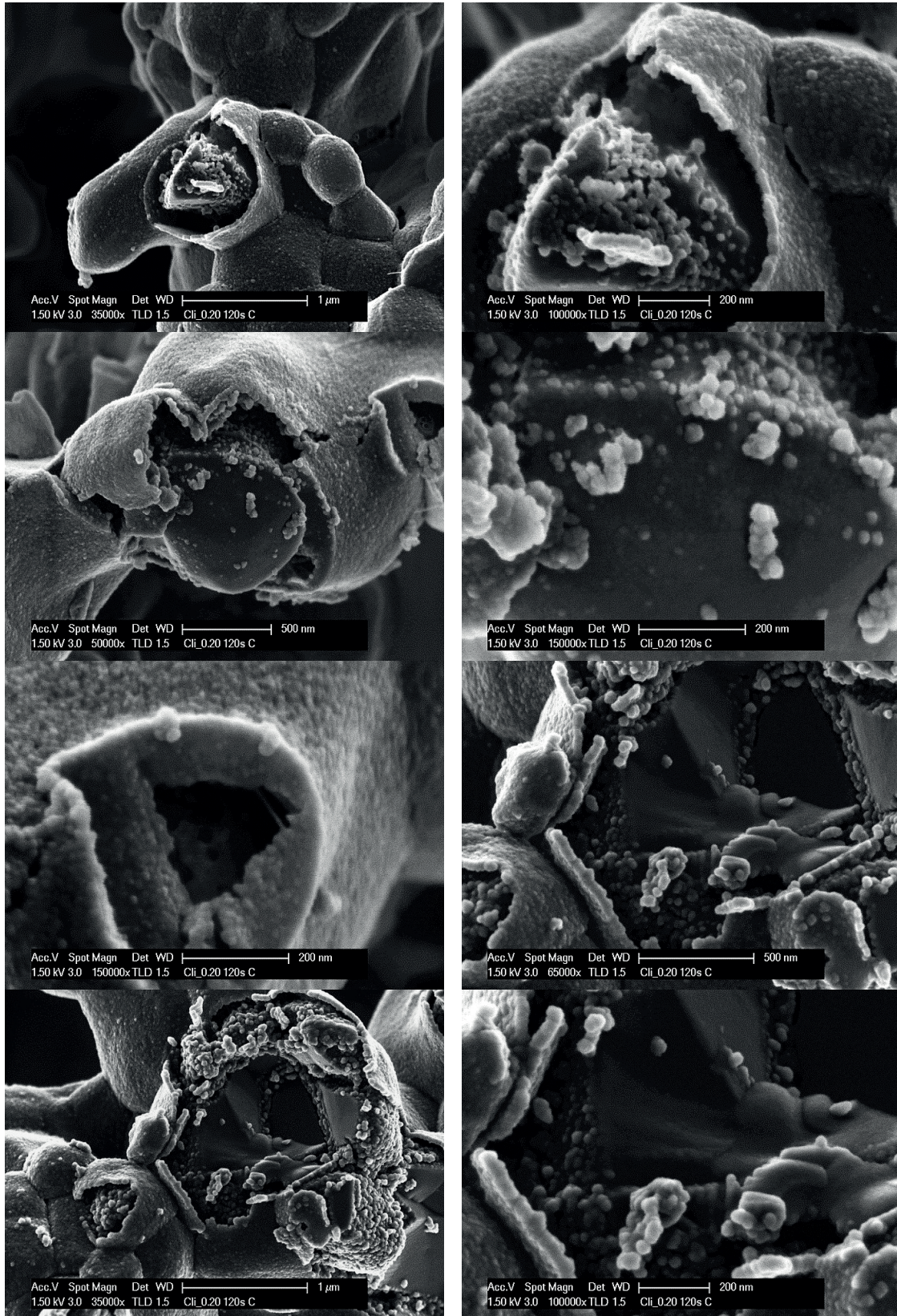


Figure 8.8-30 Morphological characterization of the hydrated Fe-Y at 23 °C and a w/b ratio of 100



Fe-Y at 23 °C and w/b 100 after 7 minutes of hydration

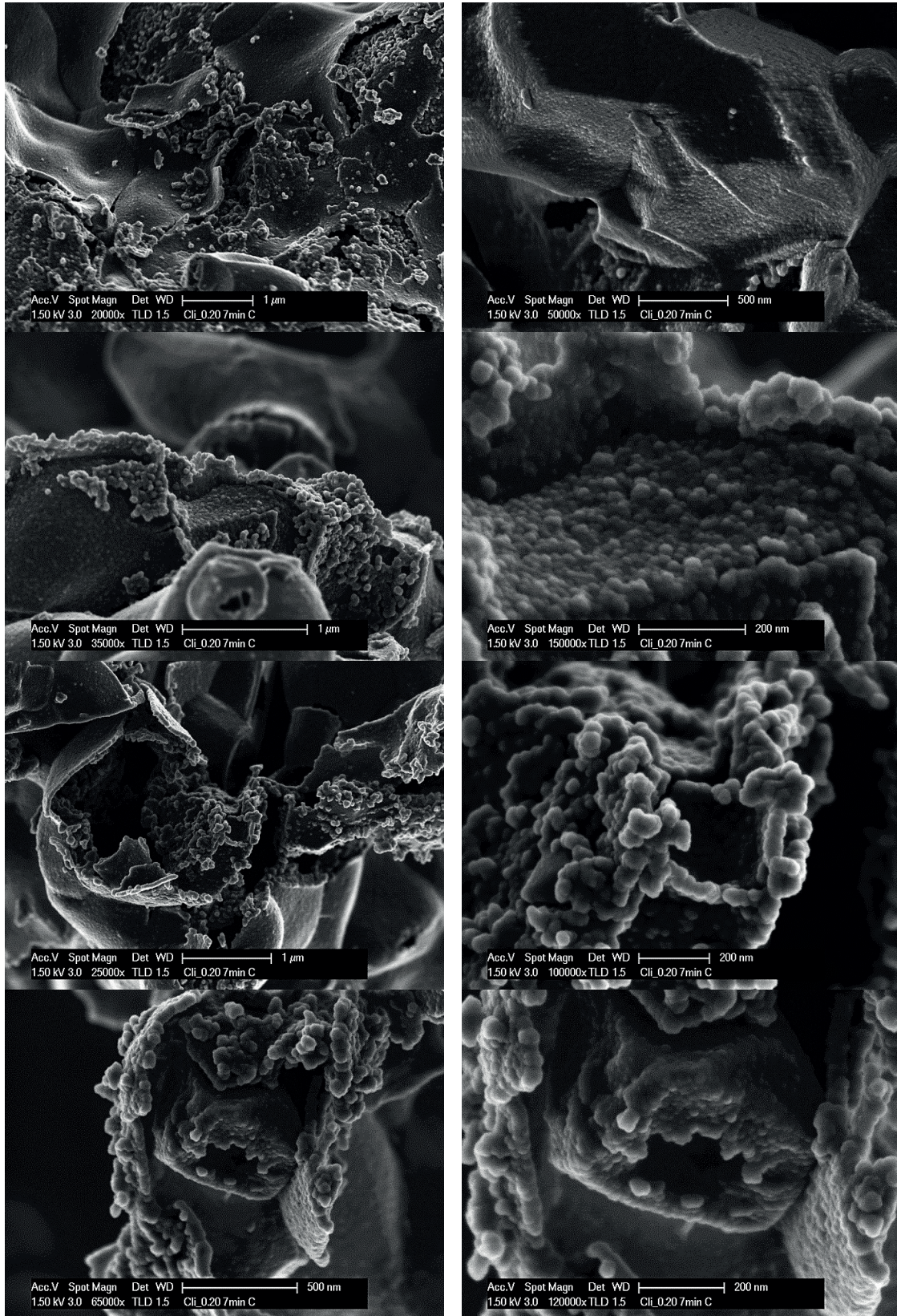


Figure 8.8-31 Morphological characterization of the hydrated Fe-Y at 23 °C and a w/b ratio of 100



Selected STEM micrographs of Y and Fe-Y hydrated at w/b 100 after 7 minutes are shown in Figure 8.8-32 to Figure 8.8-36 (supplementing the results presented in Chapter 5 and 7).

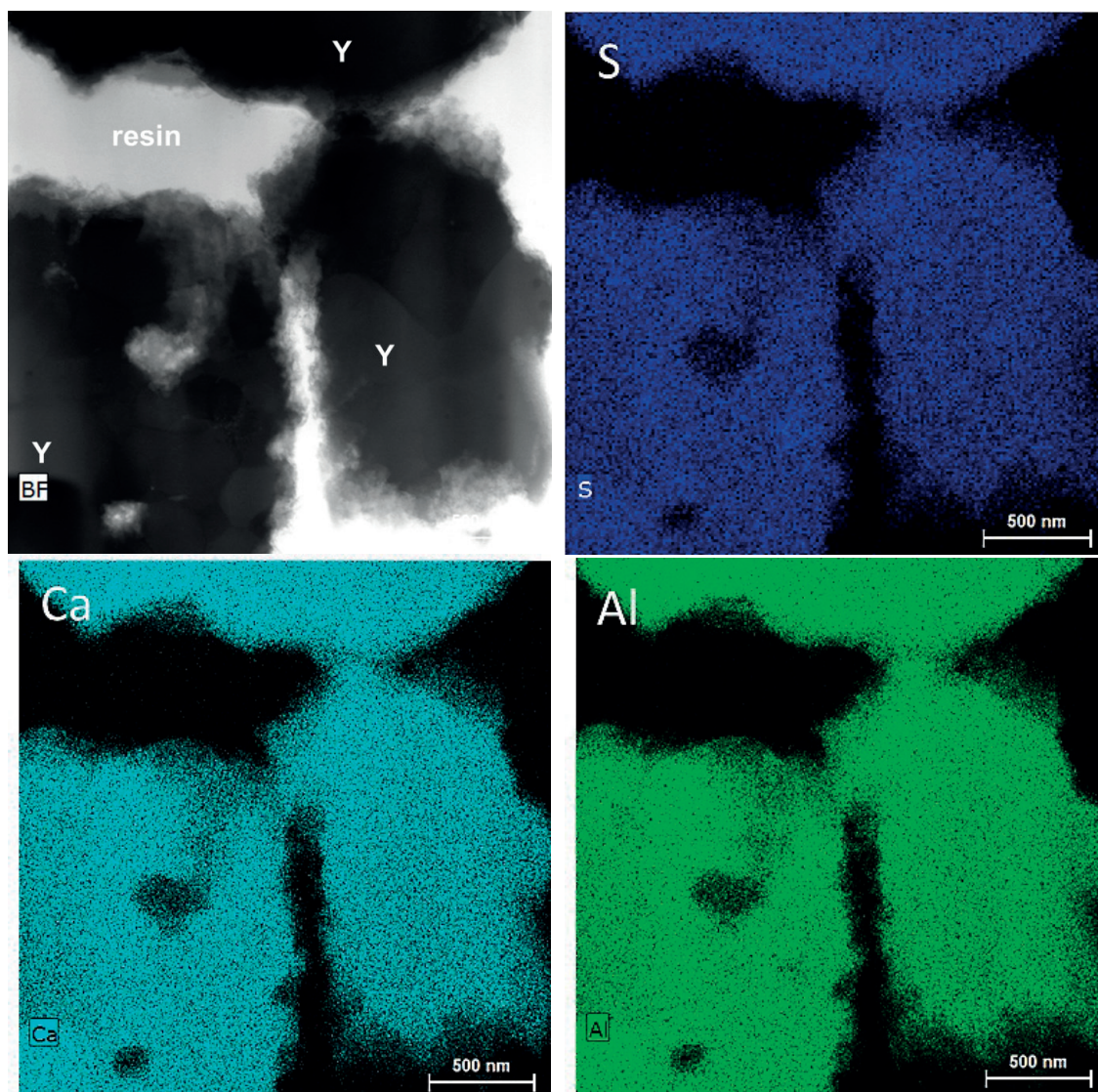


Figure 8.8-32 STEM images (HAADF) of Y after 7 minutes of hydration at 23 °C at w/b 100

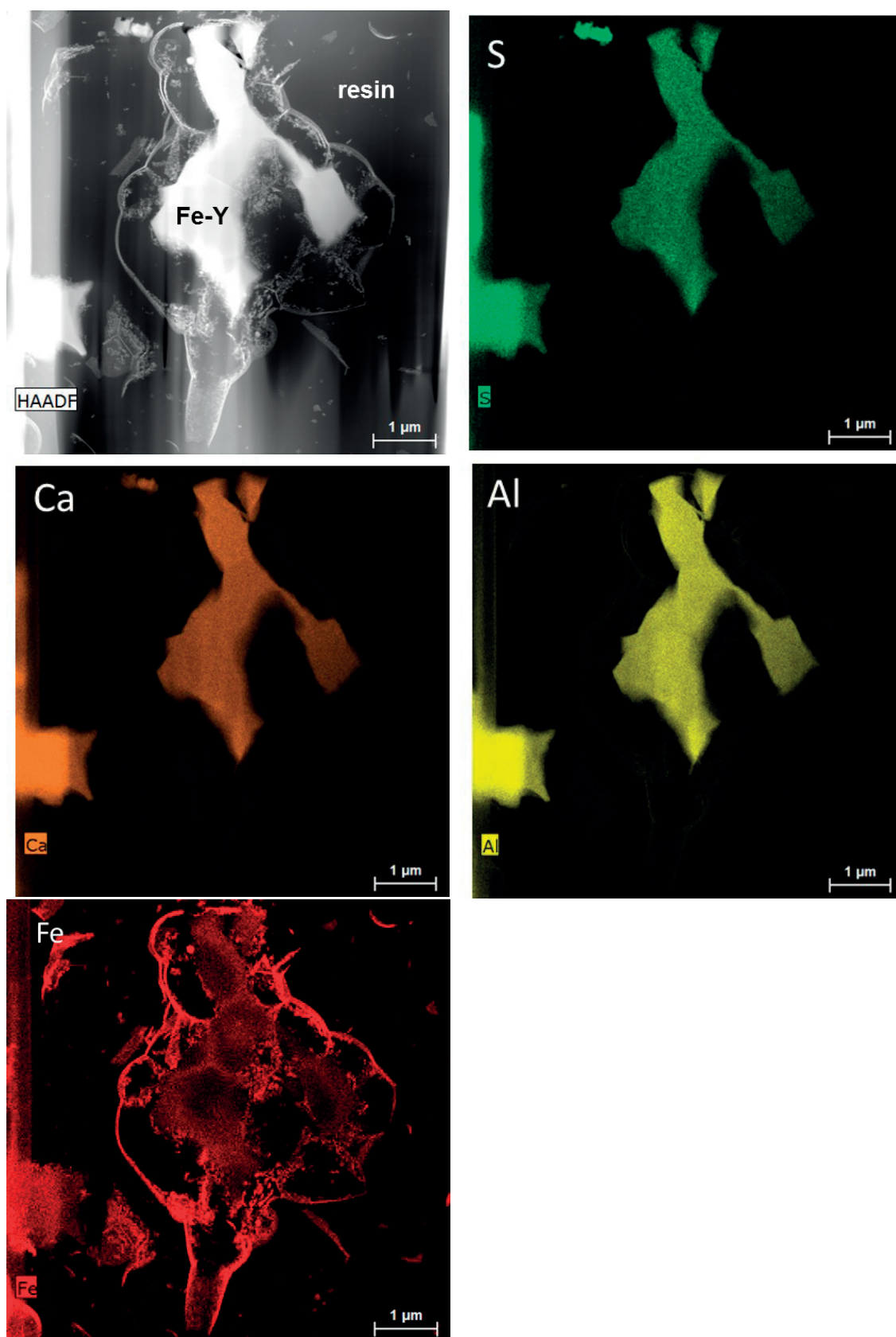


Figure 8.8-33 STEM images (HAADF) of Fe-Y after 7 minutes of hydration at 23 °C at w/b 100



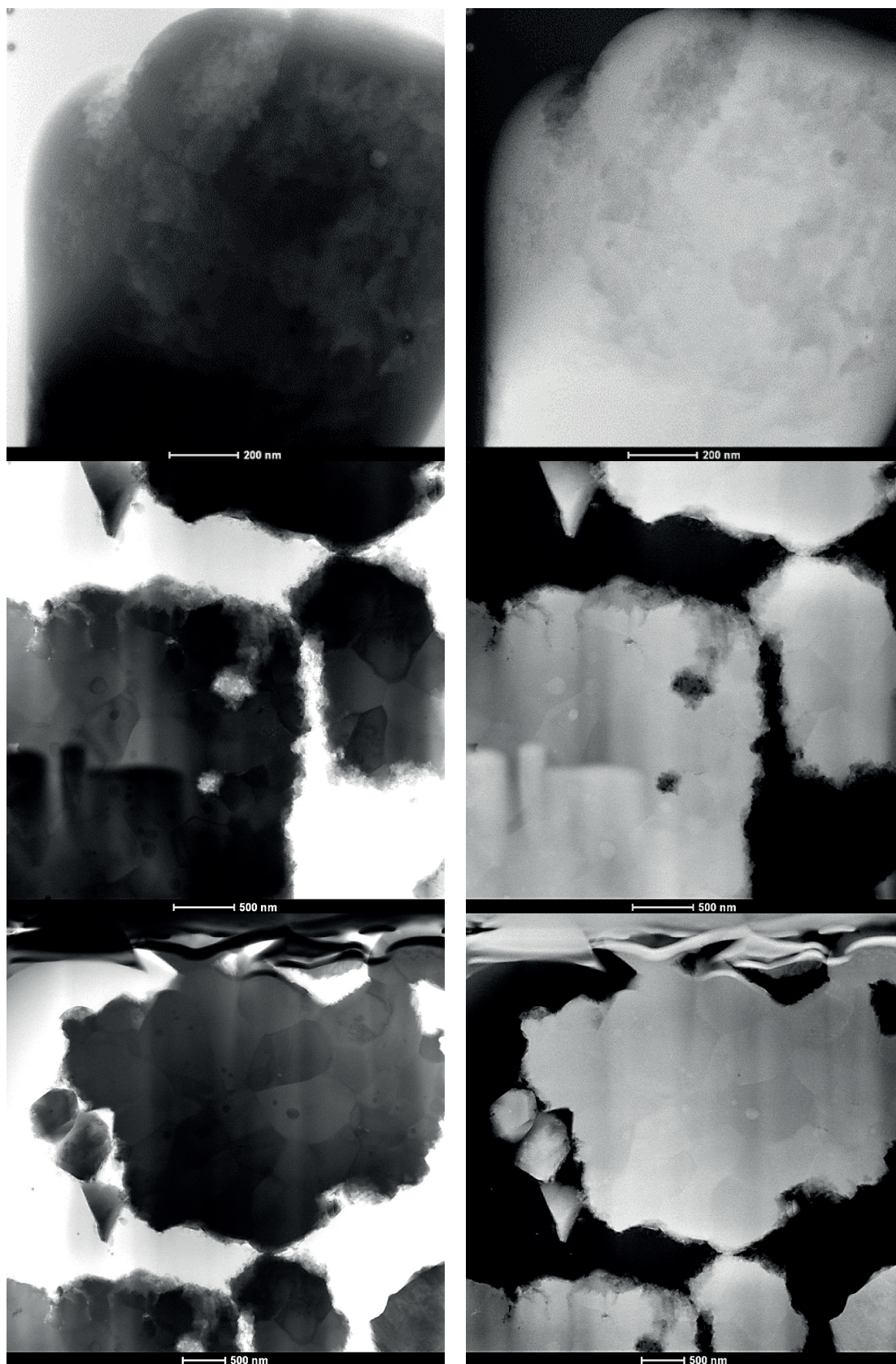


Figure 8.8-34 STEM images (HAADF and BF image) of Y after 7 minutes of hydration at 23 °C at w/b 100



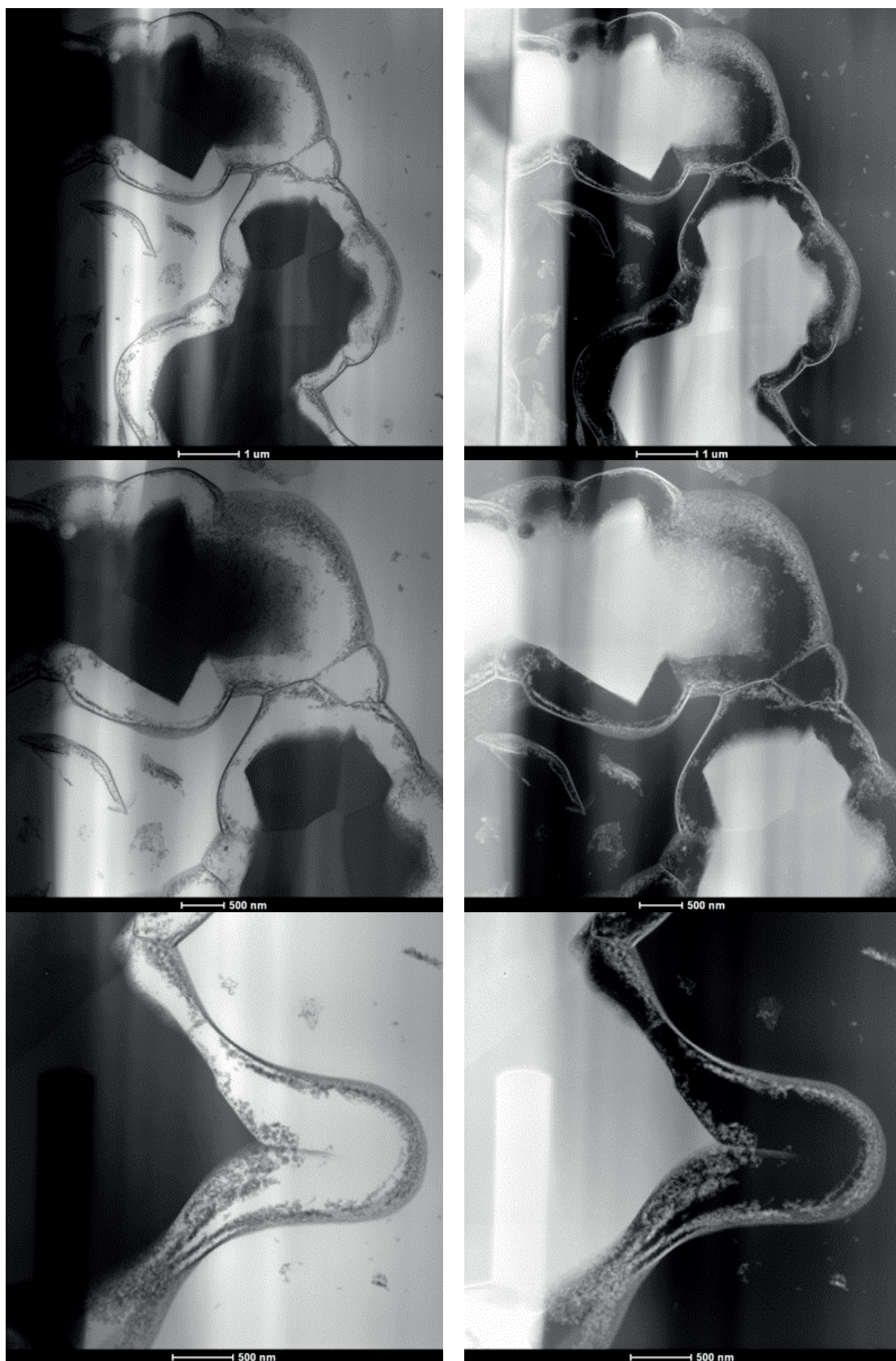


Figure 8.8-35 STEM images (HAADF and BF image) of Fe-Y after 7 minutes of hydration at 23 °C at w/b 100



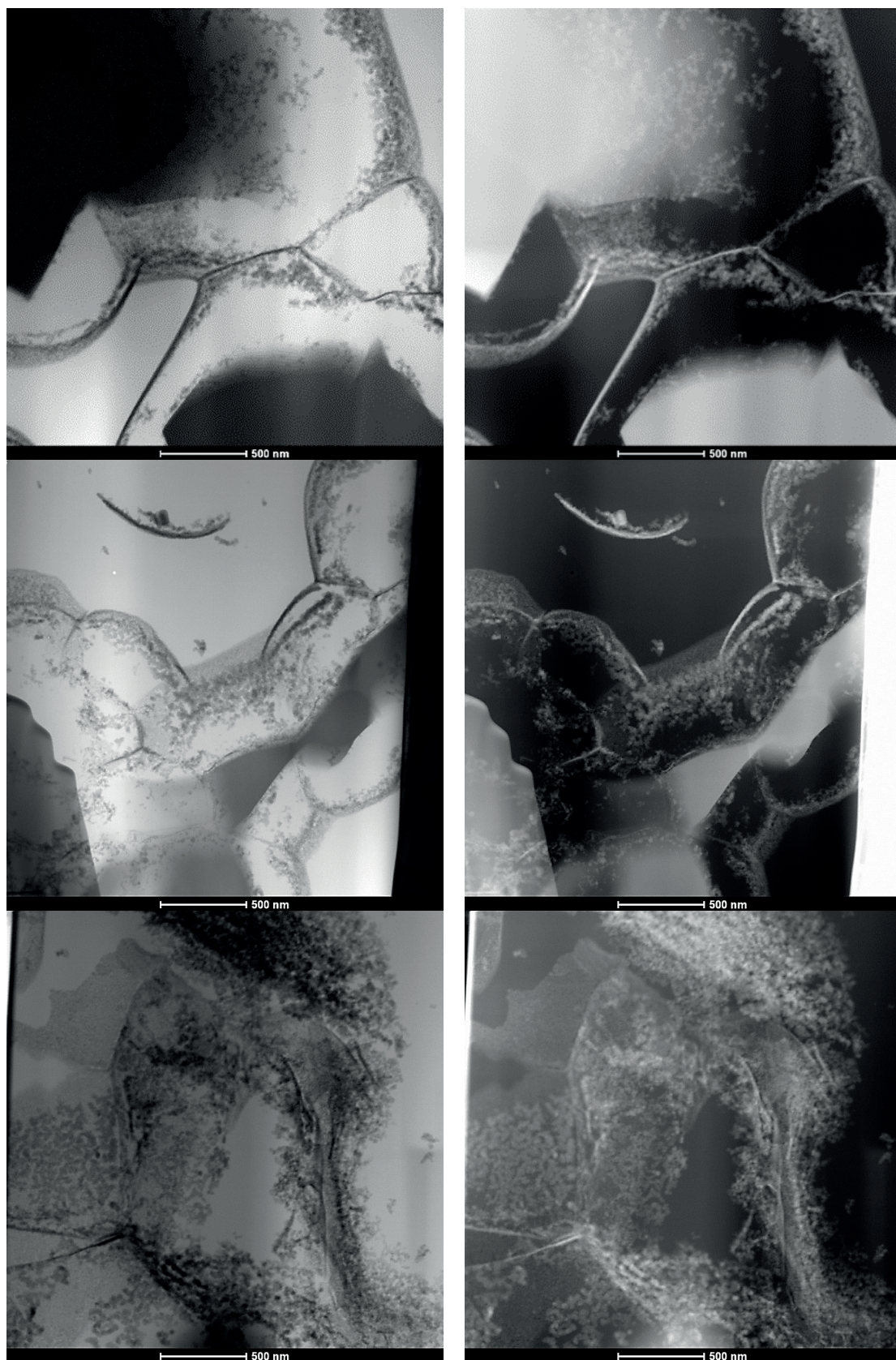


Figure 8.8-36 STEM images (HAADF and BF image) of Fe-Y after 7 minutes of hydration at 23 °C at w/b 100

Selected **STEM micrographs of Y hydrated at w/b 100 after 6 hours** are shown in Figure 8.8-37 and Figure 8.8-38. Selected **STEM micrographs of Fe-Y the hydrated at w/b 100 after 3 hours** are shown in Figure 8.8-39 and Figure 8.8-40 (supplementing the results presented in Chapter 7).

Figure 8.8-39 and Figure 8.8-40 also show that some of the Fe-Y particles form hydrated surfaces with etch pitch-like structures.



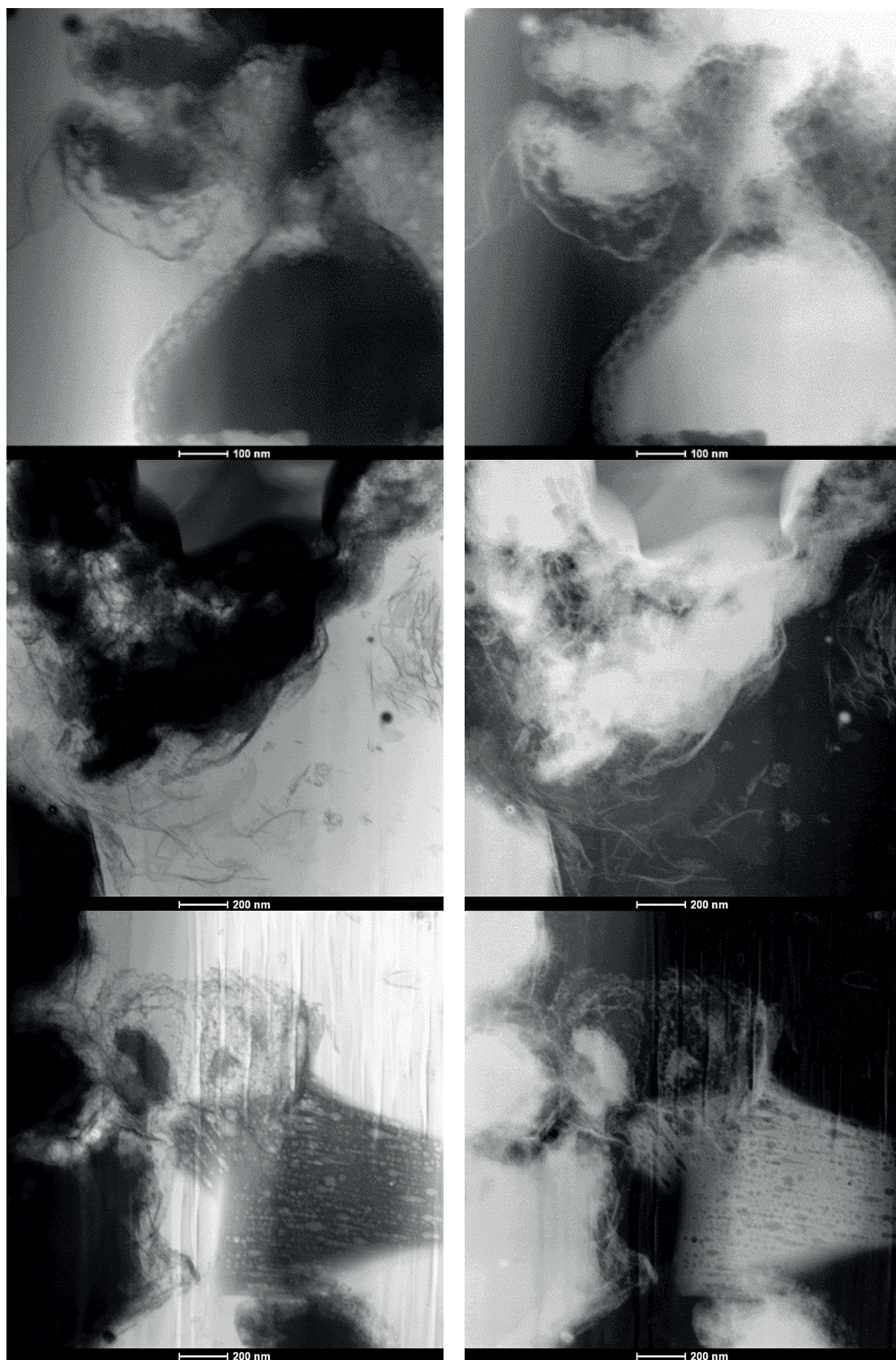


Figure 8.8-37 STEM micrographs (HAADF and BF image) of Y after 6 hours of hydration at 23 °C and w/b 100



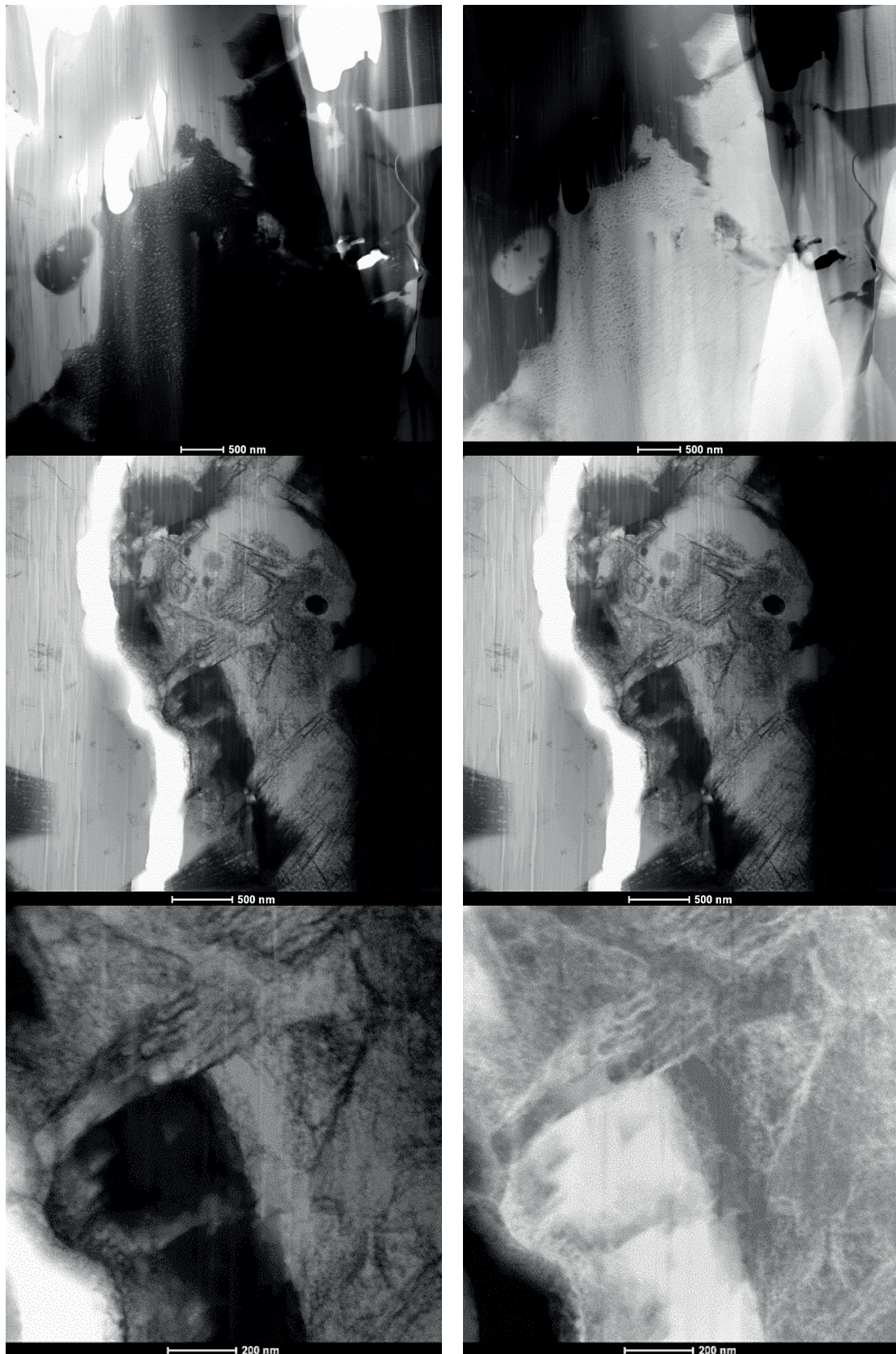


Figure 8.8-38 STEM micrographs (HAADF and BF image) of Y after 6 hours of hydration at 23 °C and w/b 100



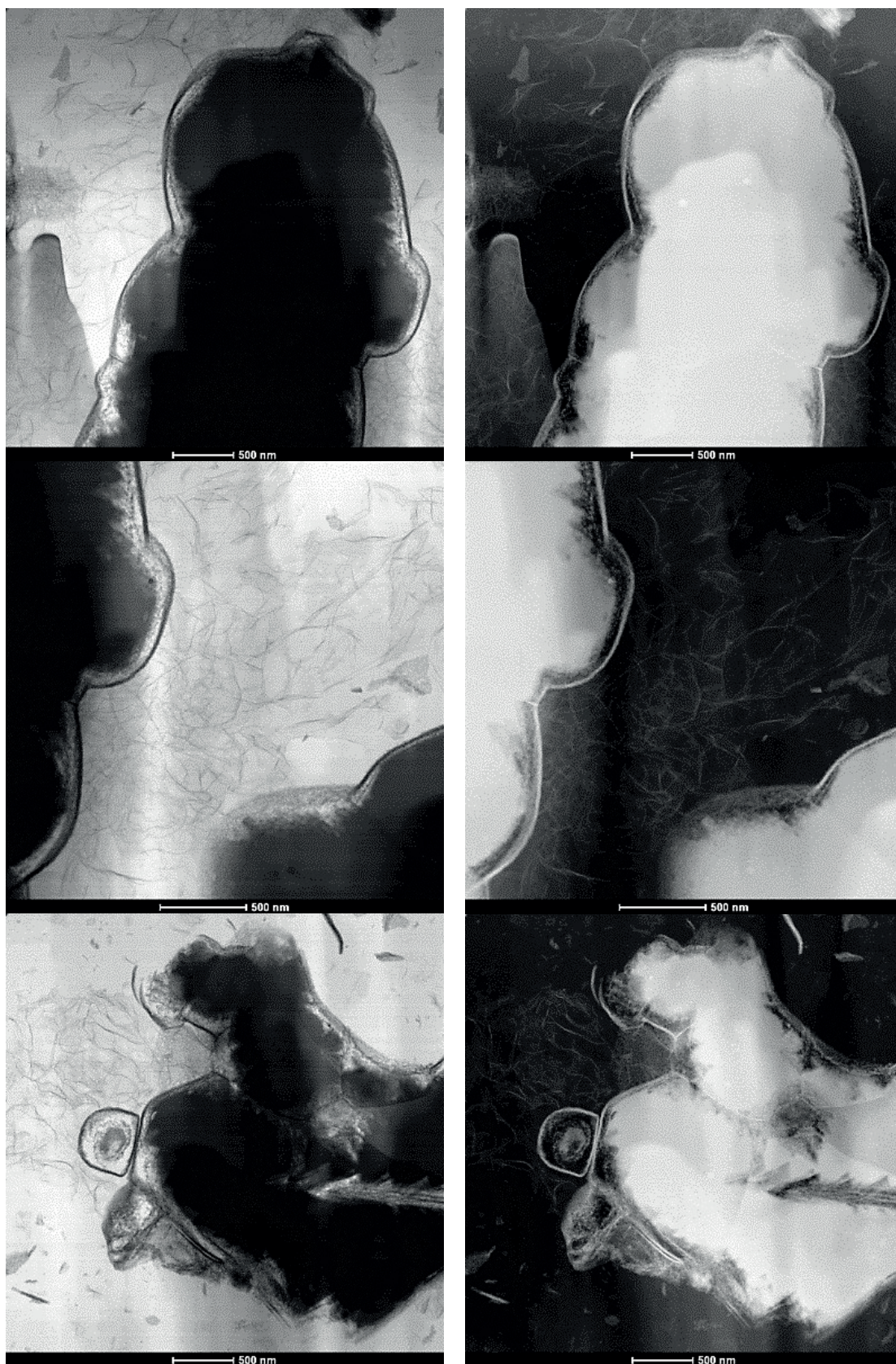


Figure 8.8-39 STEM micrographs (HAADF and BF image) of Fe-Y after 3 hours of hydration at 23 °C and w/b 100



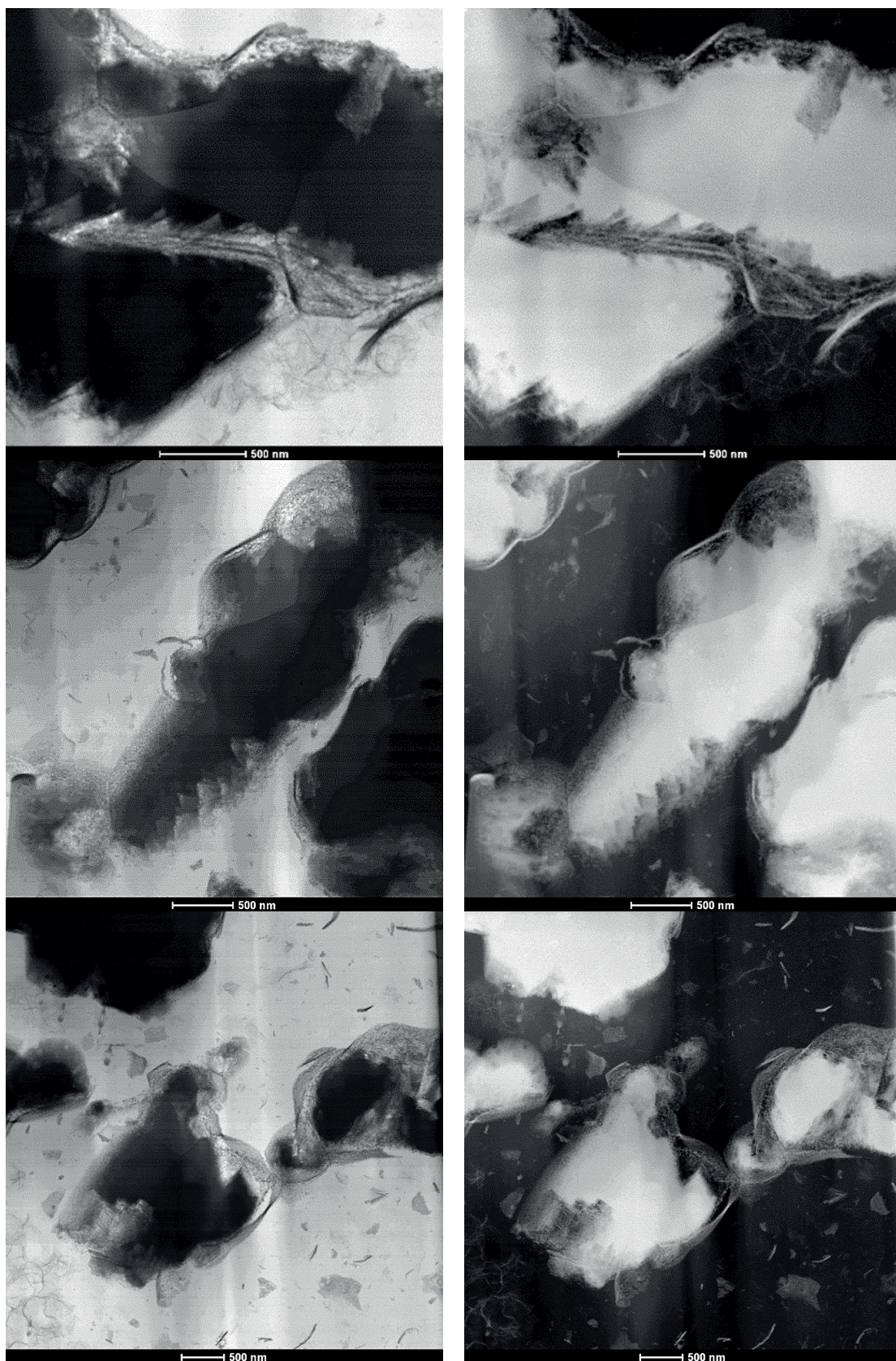


Figure 8.8-40 STEM micrographs (HAADF and BF image) of Fe-Y after 3 hours of hydration at 23 °C and w/b 100

The summary of all experiments carried out on Y and Fe-Y with gypsum at w/b 100 (supplementing the results presented in Chapters 6). The evolution of the ion concentration is shown in Figure 8.8-25.

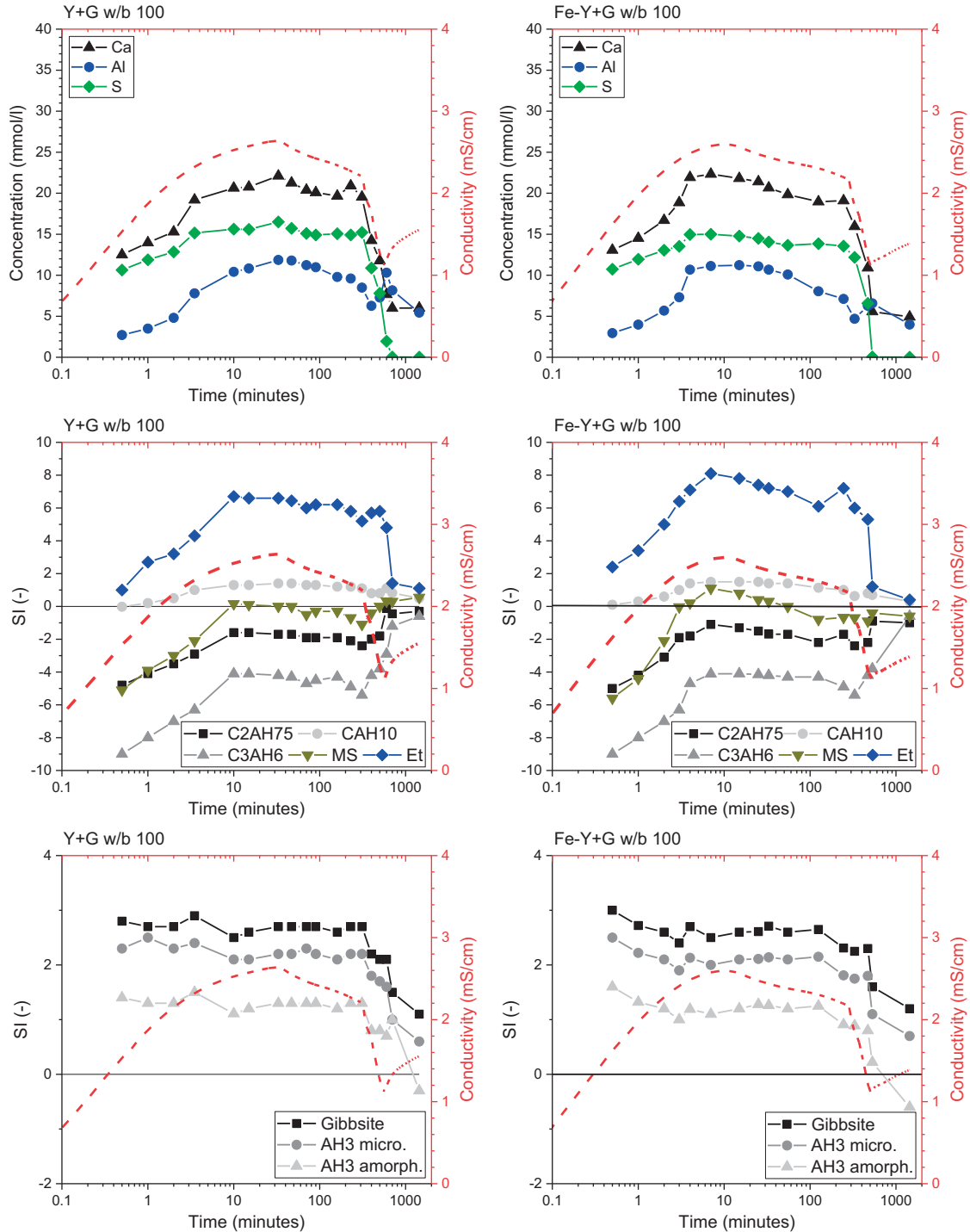


Figure 8.8-41 Evolution of the conductivity (continuous measurement) and concentration (spot samples) including the calculated Ca and S concentrations (dashed lines) for Y (left) and Fe-Y (right) at w/b 100, solubility products from [115] and for AH3am was  $\log K_{S0}$  of 0.24 from [116]



Fe-Y+G at 23 °C and w/b 100 after 30 seconds of hydration

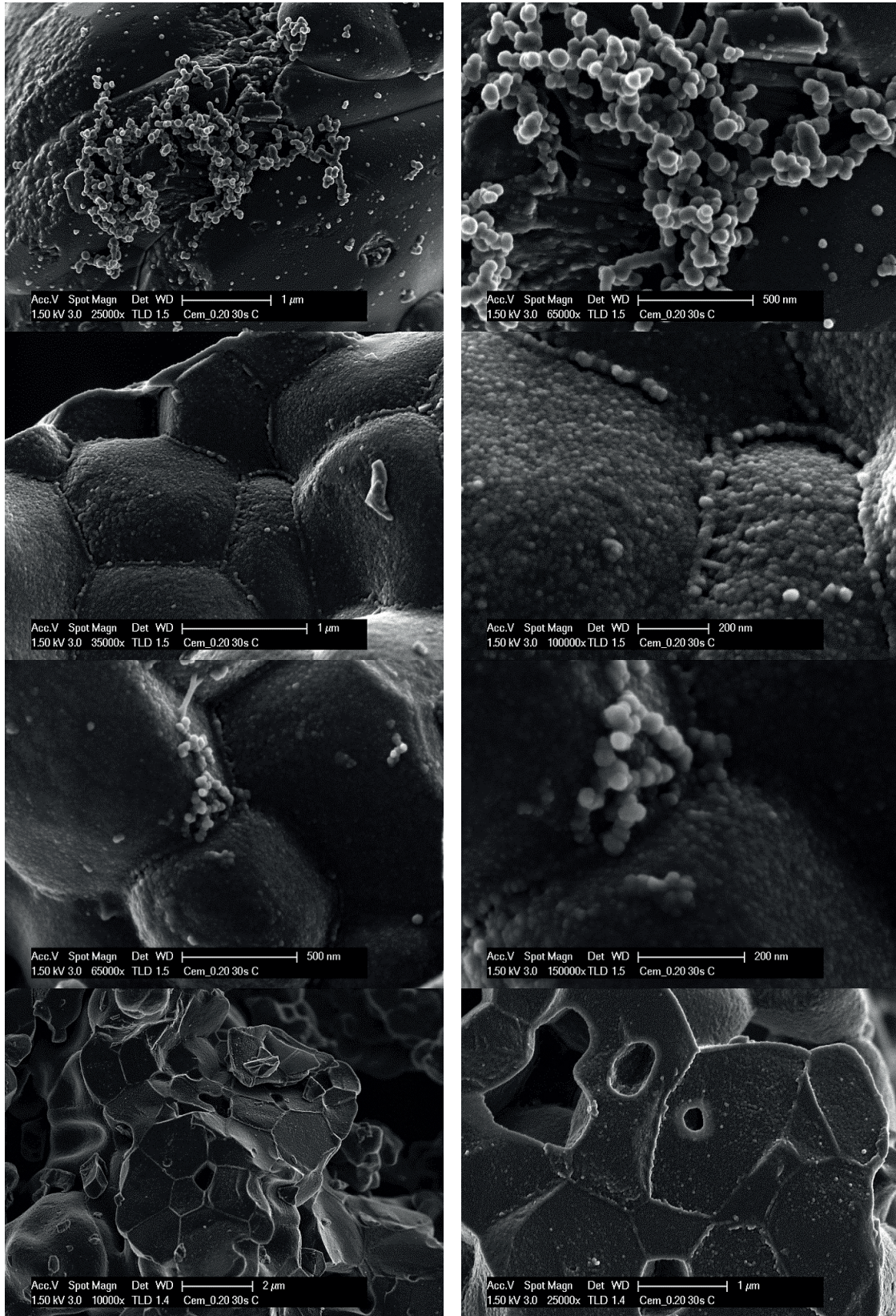


Figure 8.8-42 Morphological characterization of the hydrated Fe-Y+G at 23 °C and a w/b ratio of 100



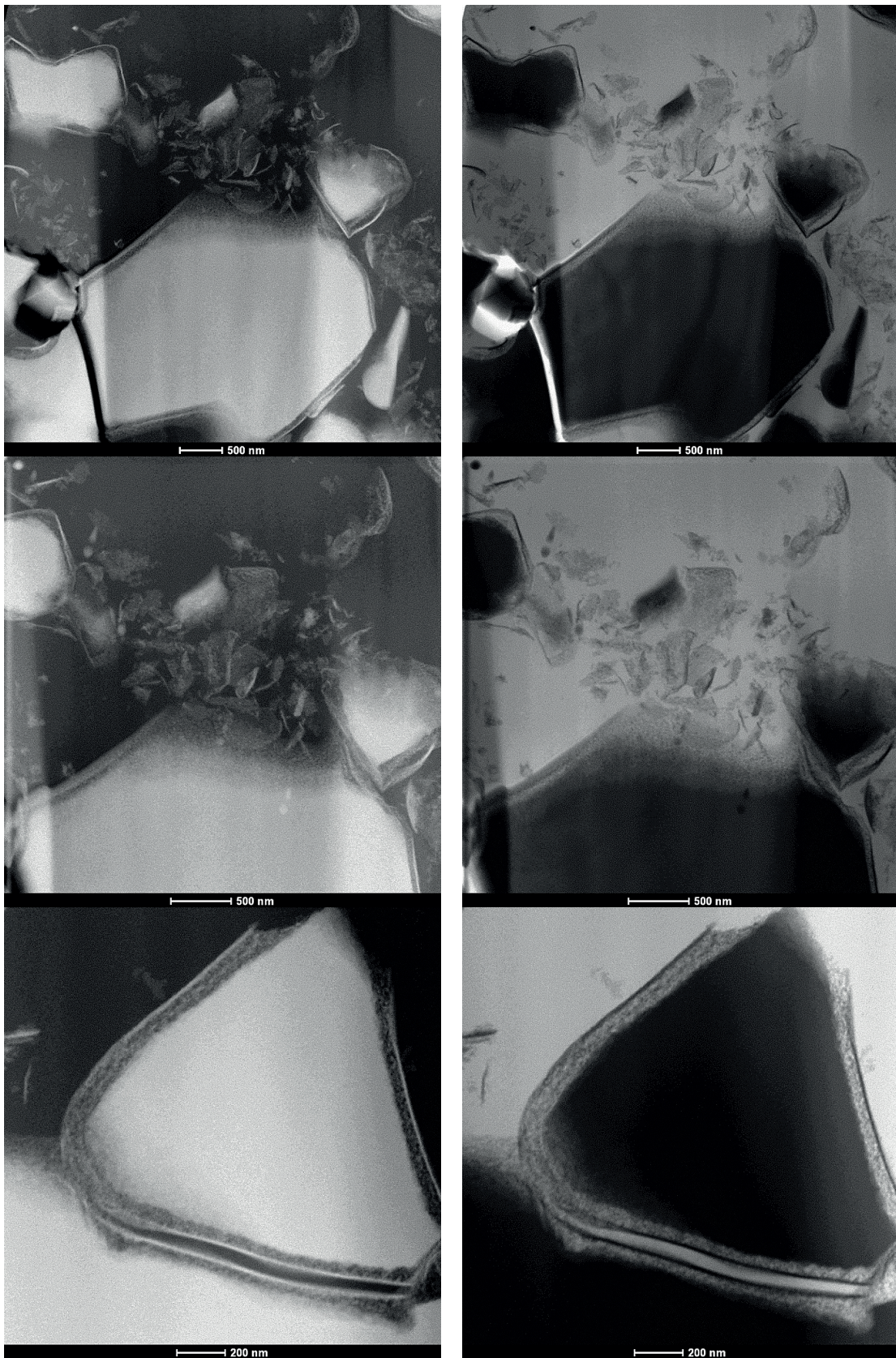


Figure 8.8-43 STEM images (up: HAADF image and down: BF image) of Y+G after 7 minutes of hydration at 23 °C and a w/b ratio of 100; Y = anhydrous ye'elimite particles; hydrates = mix of phases including ettringite



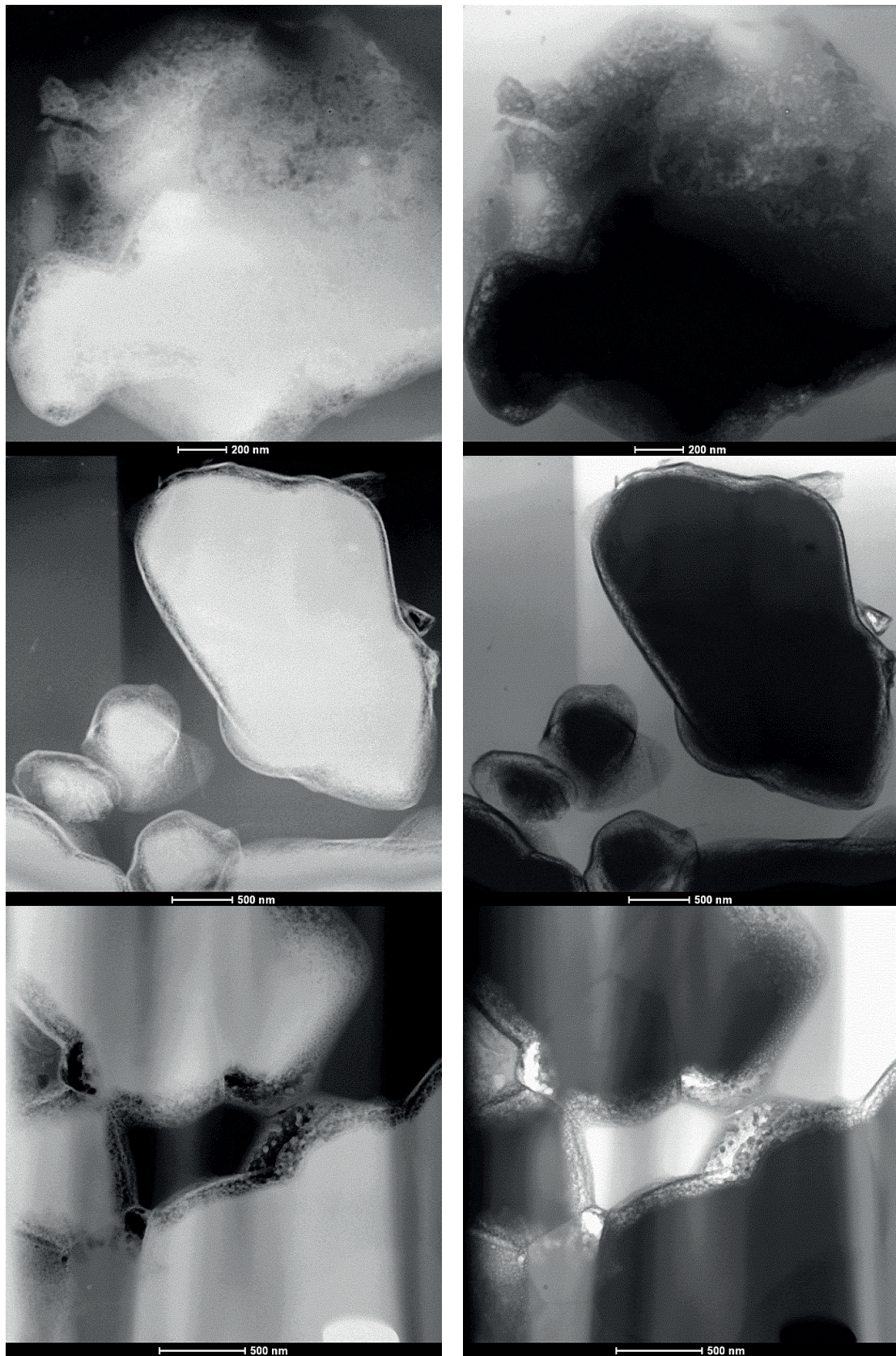


Figure 8.8-44 STEM images (up: HAADF image and down: BF image) of Y+G after 4 hours of hydration at 23 °C and a w/b ratio of 100; Y = anhydrous ye'elimite particles; hydrates = mix of phases including ettringite



The chemical and mineralogical composition of the amorphous phase "X", for the sample from the chemical shrinkage experiments, was derived from mass balance calculations based on QXRD and TGA analyses (supplementing the chemical shrinkage section in Chapter 6). The results of the calculations are shown in Figure 8.8-45 and in Figure 8.8-46.

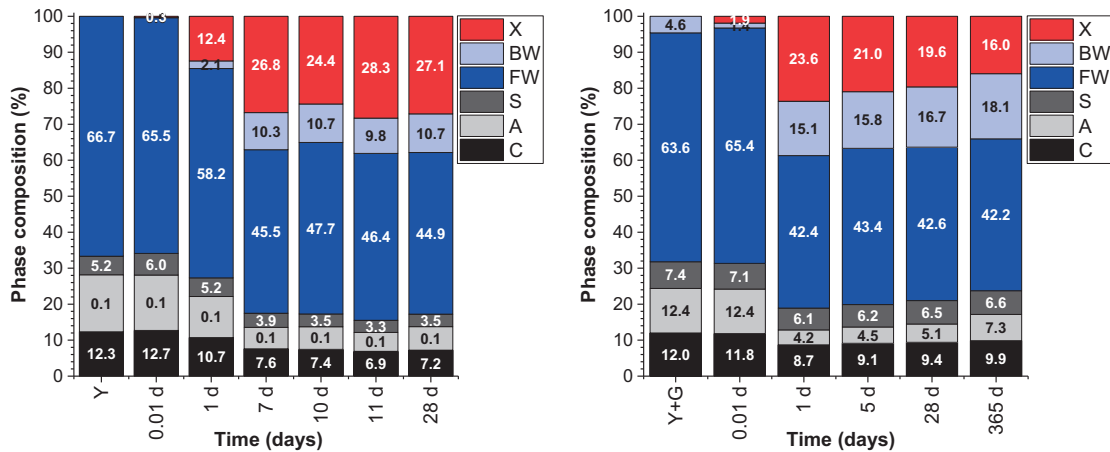


Figure 8.8-45 Chemical composition of the crystalline detectable hydrates assemblage derived by the mass balance calculations for Y and Y+G in paste ; FW = free water and BW = chemically bound water; X = quantity of amorphous fraction; S =  $SO_3$ ; A =  $Al_2O_3$  and C =  $CaO$

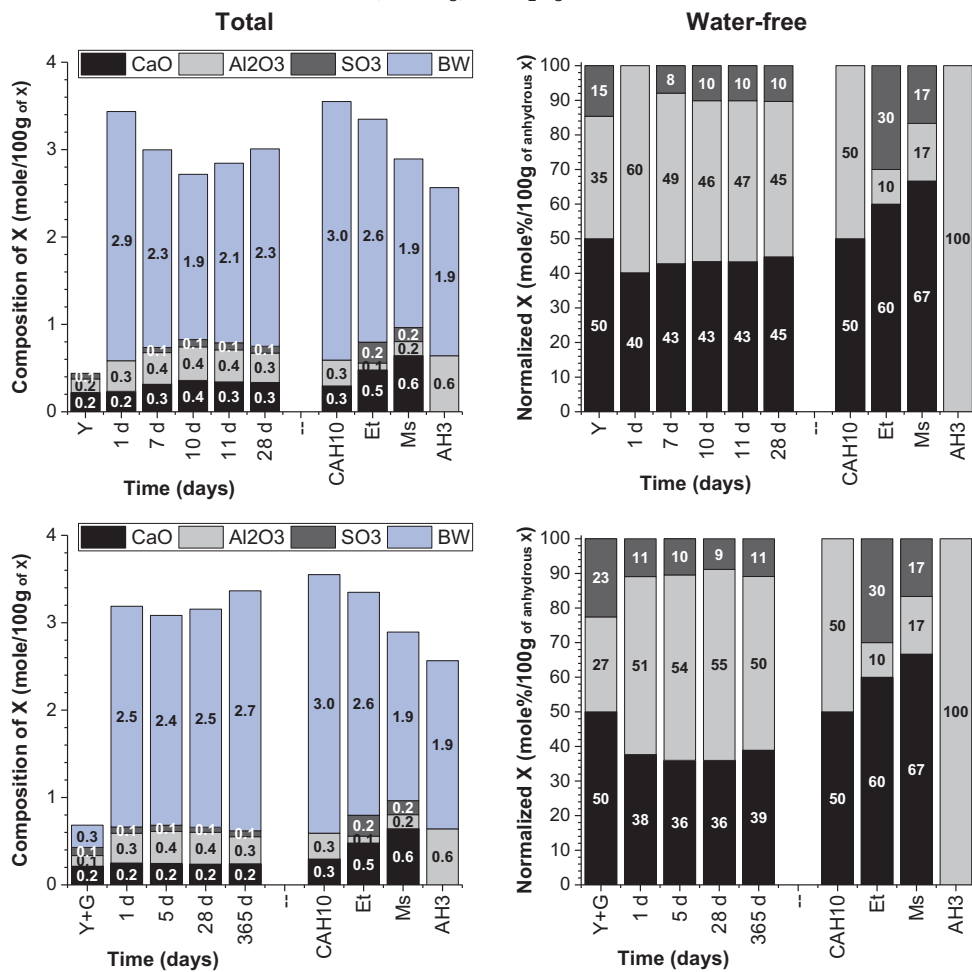


Figure 8.8-46 Chemical composition of the amorphous fraction X in paste

The evolution of the BW content of the amorphous fraction did correlate well with the observed release of BW. The results of these calculations are shown in Figure 8.8-45. Using the results presented above, we could calculate the chemical composition of X which is presented together with these of chosen hydrates in Figure 8.8-46. The water-free results are presented to distinguish whether the observed release of bound water correlates with the change of any of the other elements. Using the known amount and composition of X, we calculated the potential mineralogical compositions. The results are presented in Figure 8.8-47. For the calculations we assumed that X consists of either ettringite or monosulphate together with  $CAH_{10}$ ,  $AH_3$  and water (BW). The precipitation of ettringite in the Y gives negative results for the amount of water and was therefore disqualified. Similarly, monosulphate was disqualified for Y+G for the lack of calcium and water. To summarize, the amorphous fraction of Y is composed of an even mixture of monosulphate and  $AH_3$  with only traces of  $CAH_{10}$ . Contrary for Y+G, it is a relatively even mixture of ettringite,  $CAH_{10}$  and  $AH_3$ . However, it is important to highlight that the SEM-EDS analyses indicated that the amorphous aluminium hydroxide may contain sulphate and some calcium. This impact of course cannot be represented by such simplified calculations. Further the solvent exchange method, to stop the hydration reactions, damage the hydrates.

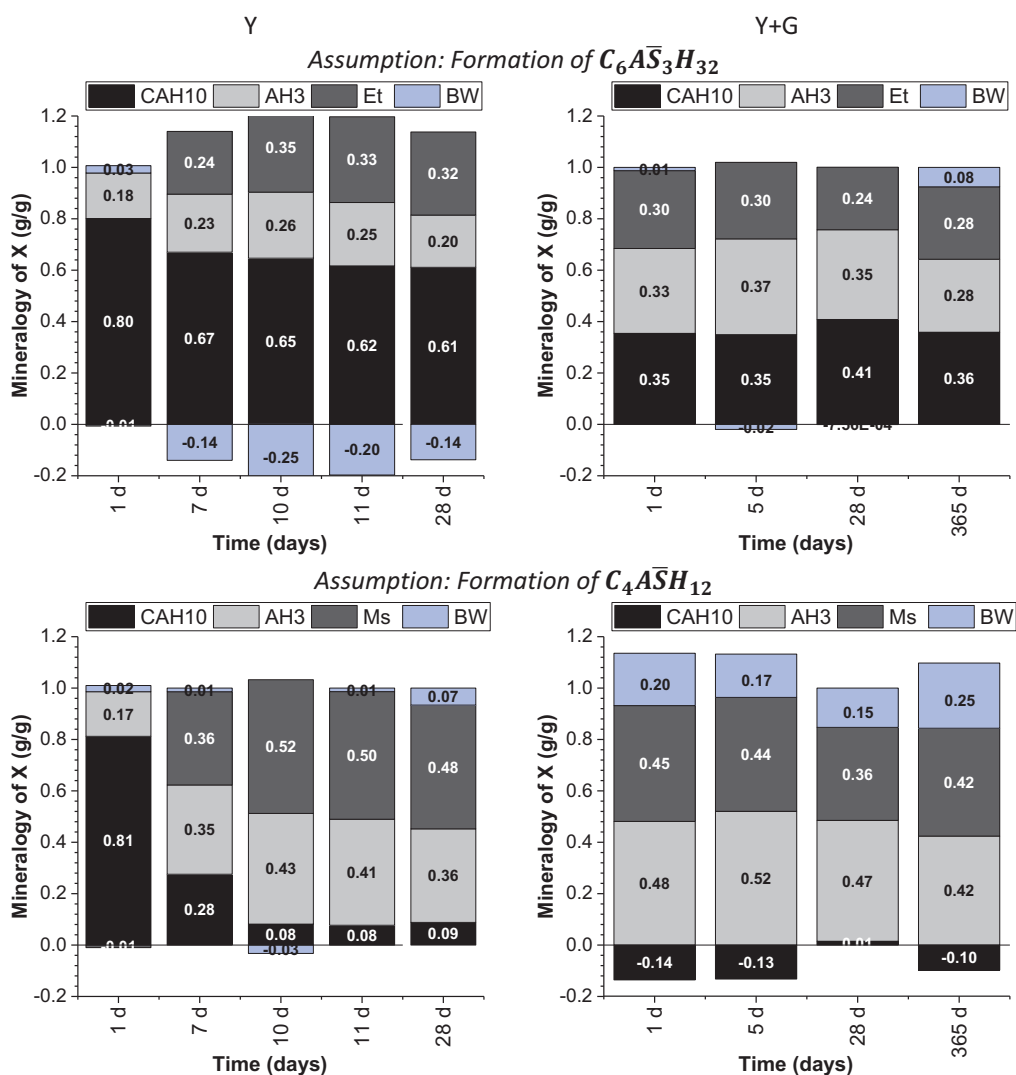


Figure 8.8-47 Calculated mineralogical composition of X in Y and Y+G over time

XRD plots of Y and Y+G after 28 days of hydration are shown in Figure 8.8-48 (supplementing the chemical shrinkage section in Chapter 6).

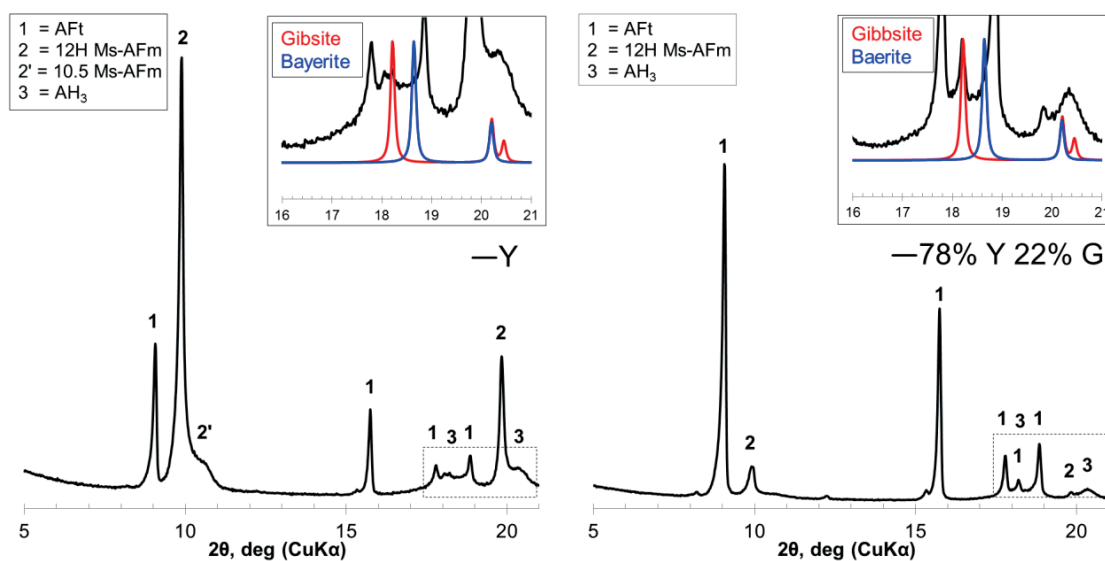


Figure 8.8-48 XRD plot of Y and Y+G at w/b 2 after 28 days of hydration

To investigate the impact of iron on the formed hydrates assemblage, we analysed the samples of the chemical shrinkage after its finalisation of the measurements at 28 days of hydration. For that purpose a “representative” sample was prepared by mixing the five separate samples. The thermogravimetric analyses are shown in Figure 8.8-49.

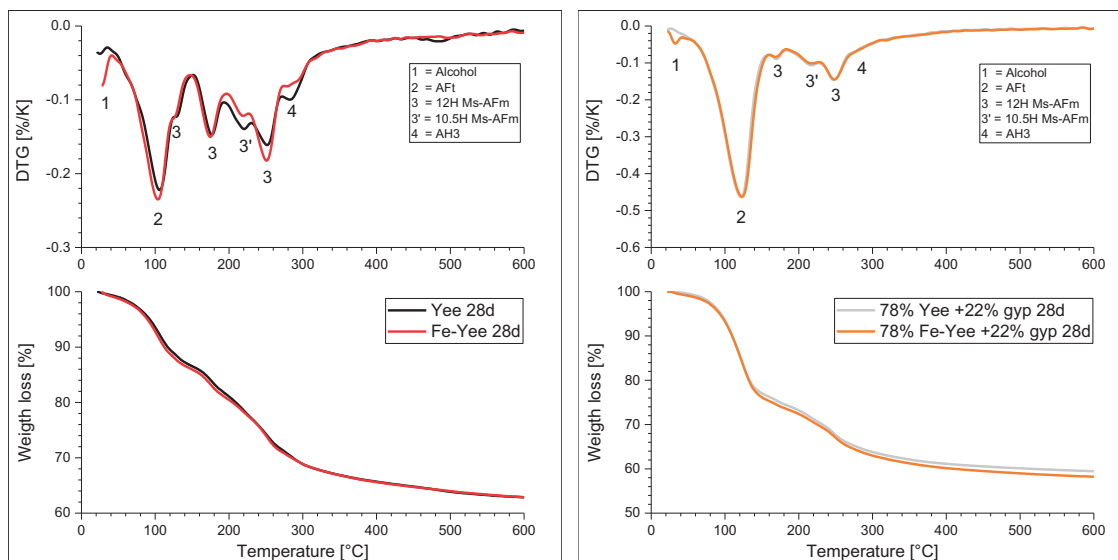


Figure 8.8-49 Differential thermogravimetric analysis (top) and weight loss (bottom) of Y (left) and Y+G (right) after 28 days of hydration; samples taken after the completion of the chemical shrinkage measurements



SEM-EDS micrographs of the samples at selected hydration ages are shown in Figure 8.8-50(supplementing the **chemical shrinkage** section in **Chapter 6**).

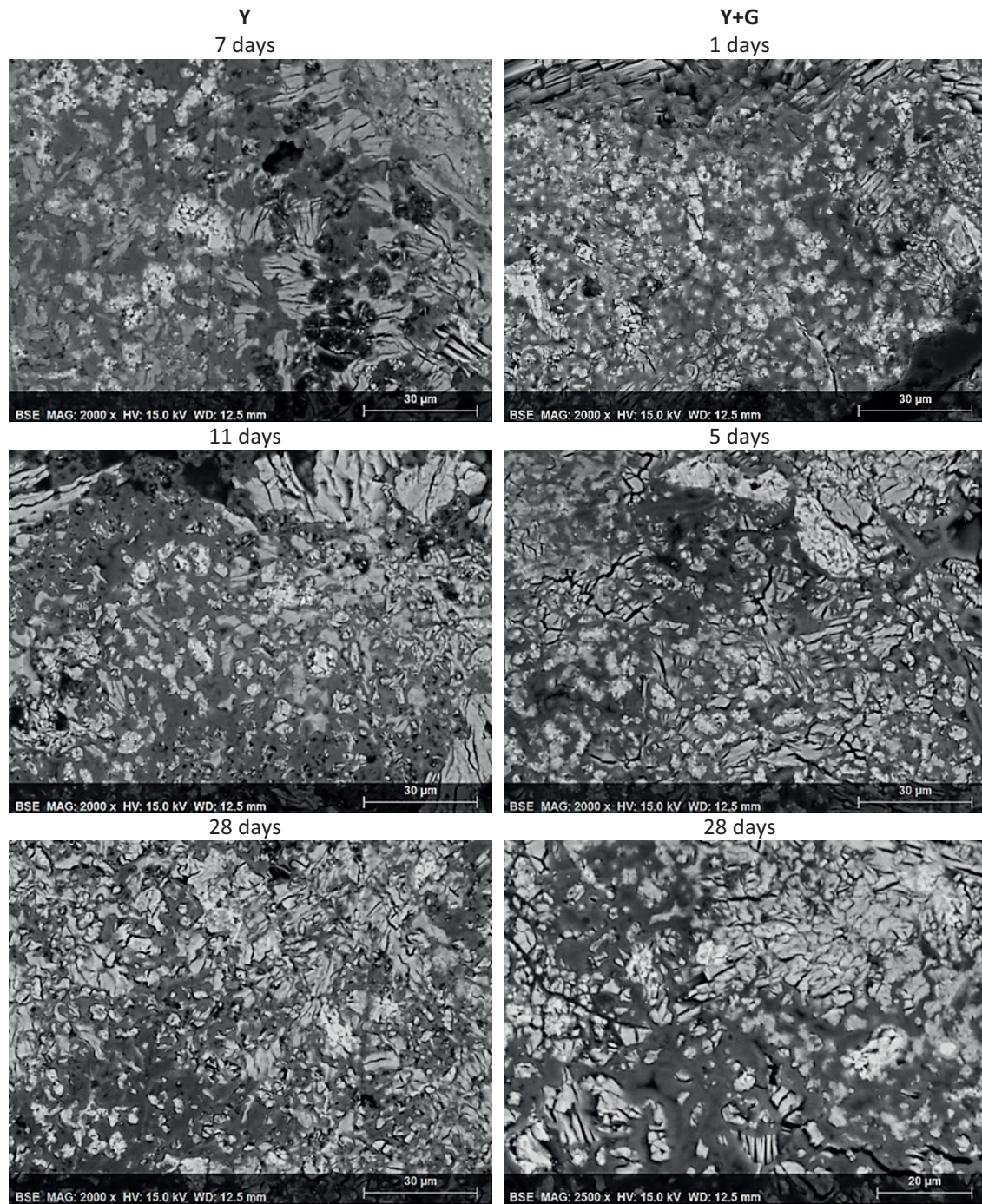


Figure 8.8-50 Backscattered electron micrographs (BSE) of hydrated  $\gamma$  and Y+G

The **chemical shrinkage** of Fe-Y with and without gypsum is shown in Figure 8.8-51.

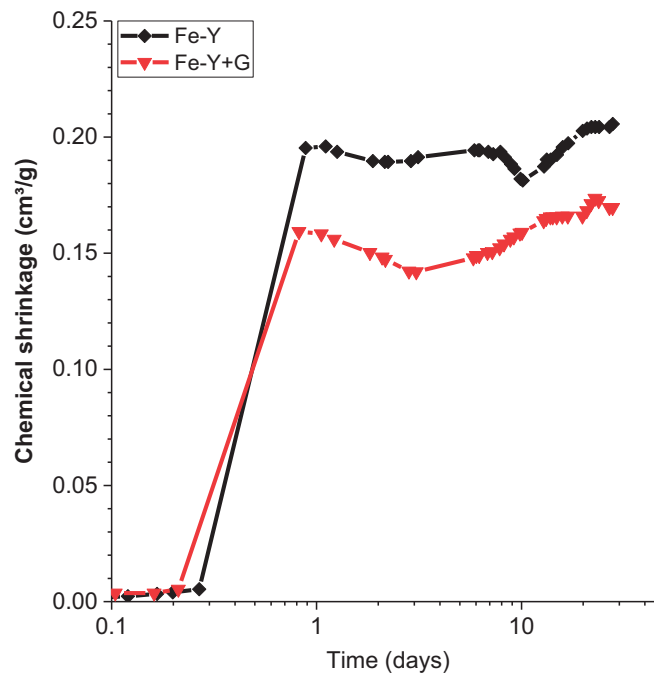
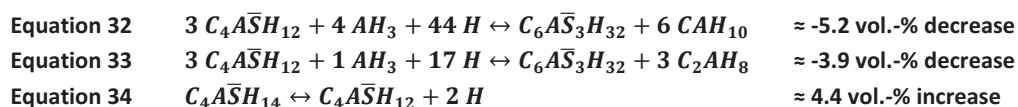


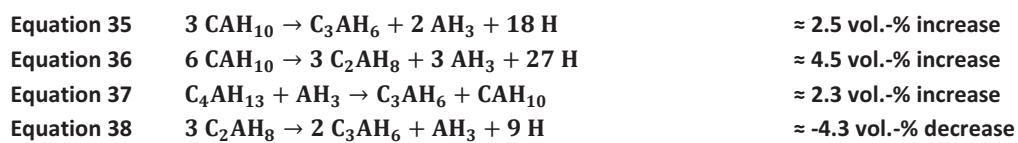
Figure 8.8-51 Measured chemical shrinkage of Fe-Y with and without G at w/b 2; the standard deviation between 5 samples was in average about 0.003

**Other potential crystallisation and transformation reactions** which may occur during the period of the **chemical expansion** are presented hereafter. The impact of potential phase transformation reactions was assessed by the calculation of the resulting volume changes.

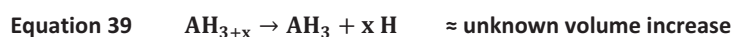
#### Potential conversion reactions between monosulphate and ettringite



#### Potential conversion reactions of calcium aluminate hydrates



The recrystallization of the **X-ray amorphous aluminium hydroxide** and potential released of combined water





The **synthesis protocol** and **raw mix quality** had an **impact** on the **clinker composition** and **hydraulic reactivity**. Figure 8.8-52 shows a comparison of the particle size distribution and hydraulic reactivity of similar ye'elimite clinkers from the three synthesis campaigns. The clinkers from S1 (sintered for 3 times at 1300 °C) revealed the longest dormant period lasting till 12 and 36 hours for Fe-Y and Y, respectively. On the contrary, the hydration of the clinkers from the S2 (x times at 1300 °C but much higher fineness) and S3 (once at 1250 °C) fall into a more narrow range. The main hydration period lasted from about 10 to 20 hours for Fe-Y and 18 to 36 hours for Y. All Fe-Y samples hydrated faster compared to any stoichiometric ye'elimite sample. The endothermic peak was only observed for the samples of the S3 series. One may argue that the **different kinetics** result from **different fineness** and **particle size distributions** of the clinkers. The impact of the ye'elimite fineness on the hydration kinetics was already investigated by Palou and Majling [132] and Sahu et al. [136]. The authors could show that the amount of ettringite formed mainly corresponded with the fineness of ye'elimite, where a high fineness favoured the formation of ettringite rather than monosulphate. The authors related that to the rate at which  $Al(OH)_4^-$  ions were liberated to a solution which contain calcium and sulphate. The rate of its liberation controls the aluminium over calcium and sulphate ratios, which in turn favours either the formation of ettringite or monosulphate. To better understand the role of the PSD on the hydration kinetics and formed products, we produced different size fractions by sieving. For that purpose a new batch of Y and Fe-Y clinkers were produced in accordance to the protocol for S3. The characterisation of the fractions was therefore carried out.

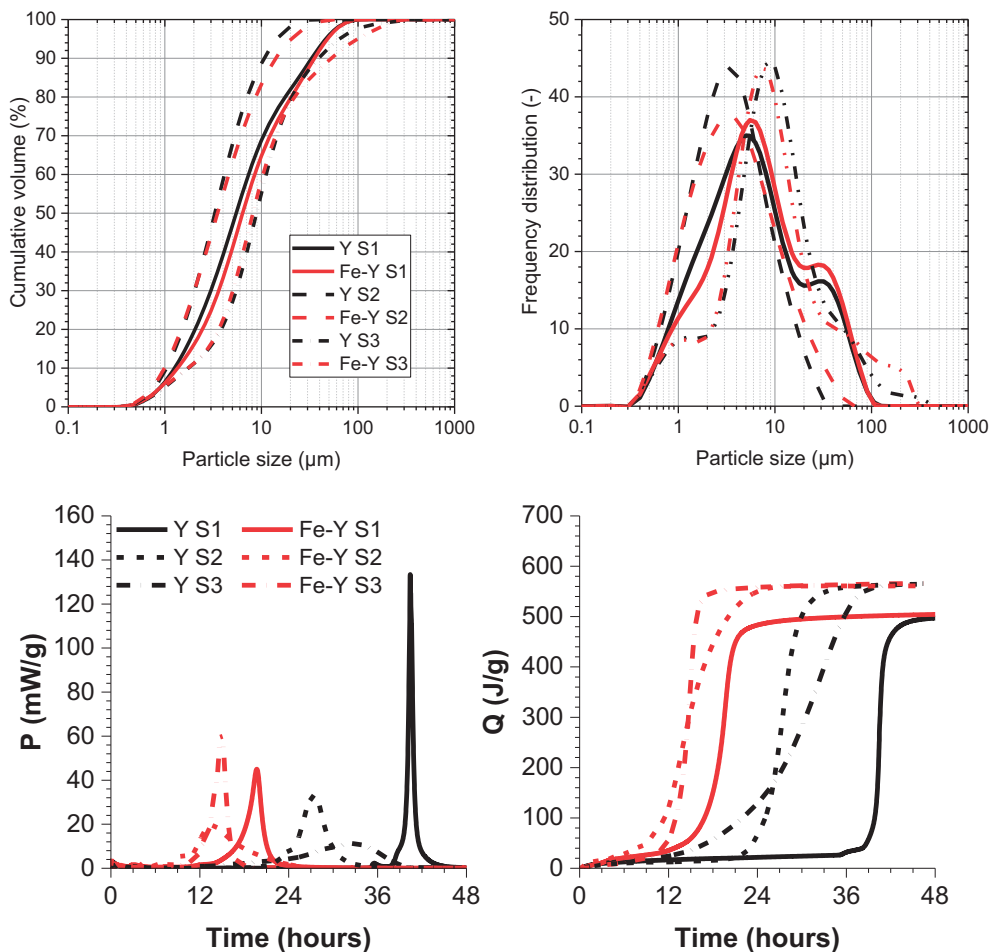


Figure 8.8-52 Particle size distribution (top) and rate of heat evolution and cumulative heat at w/b 2 (bottom)

Figure 8.8-53 (left hand) presents the PSD of the sieved fractions and the comparison of the  $SSA_{BET}$  versus the PSD (right hand). We achieved a very good separation for the size fractions 90-125  $\mu\text{m}$  and < 32  $\mu\text{m}$ , whereas the size fraction 32-90  $\mu\text{m}$  was a mix of both. The  $SSA_{BET}$  further revealed an almost linear correlation between the measured total surface area and the size fraction class. All three Fe-Y fractions showed a measurably lower  $SSA_{BET}$  values compared to those of Y, which very probably correspond to the fluxing effect of iron and the formation of a liquid phase.

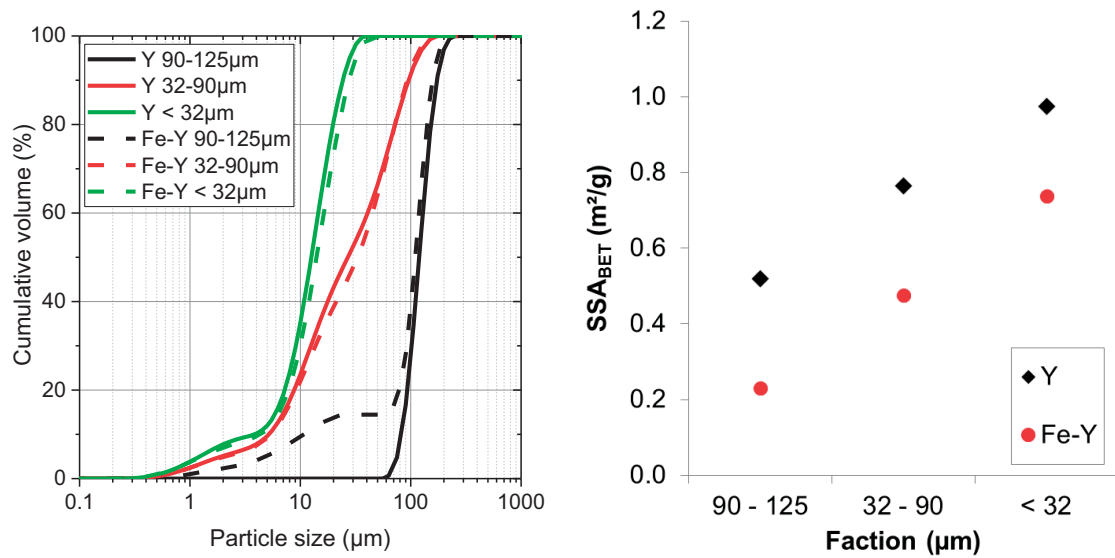


Figure 8.8-53 PSD (left) and SSABET versus PSD (right)

The mineralogy of the fractions is presented in Table 8.8-18. The results demonstrated the measurable enrichment of aluminates phases within the coarse and of anhydrite within the fine fraction. The presence of mayenite and magnesio ferrite ( $MF$ ) was only detected in the Fe-Y sample.

Table 8.8-18 Mineralogy of the sieved fractions

	90-125 $\mu\text{m}$		32-90 $\mu\text{m}$		<32 $\mu\text{m}$		Y	Fe-Y
	Y	Fe-Y	Y	Fe-Y	Y	Fe-Y		
Portion (%)	14.9	16.3	64.9	39.3	20.2	44.4	<b>100</b>	<b>100</b>
	wt. %							
$\Sigma C_4A_3\bar{S}$	80.5	92.8	93.6	93.7	96.4	94.3	<b>92.2</b>	<b>93.8</b>
$CA$	10.5	0.4	2.4	n.d.	0.6	n.d.	<b>3.2</b>	<b>0.1</b>
$CA_2$	7.5	3.8	0.6	1.2	0.3	n.d.	<b>1.6</b>	<b>1.1</b>
$C_{12}A_7$	n.d.	1.4	n.d.	1.0	n.d.	0.9	<b>n.d.</b>	<b>1.0</b>
$MF$	n.d.	0.4	n.d.	0.7	n.d.	0.1	<b>n.d.</b>	<b>0.4</b>
$C\bar{S}$	1.5	1.2	3.4	3.4	2.7	4.7	<b>3.0</b>	<b>3.6</b>

The **hydraulic reactivity** of the fractions was assessed by isothermal conduction calorimetry. With the knowledge about the PSD,  $SSA_{BET}$  and the mineralogical composition of the size fractions we are now able to better characterize the hydration kinetics of those. The hydraulic reactivity of the fractions was assessed at a w/c of 2.0. The PSD had only a little impact on the hydration kinetics, by means of the onset of the acceleration and main hydration period. Mainly the shape of the main peak (which covers the acceleration and main period) was altered. The coarse fraction revealed a slight shift to earlier times, where it was sharper and more intense with increasing fineness. The differences in the cumulative heat are the result from the available amount of ye'elite in each fraction.

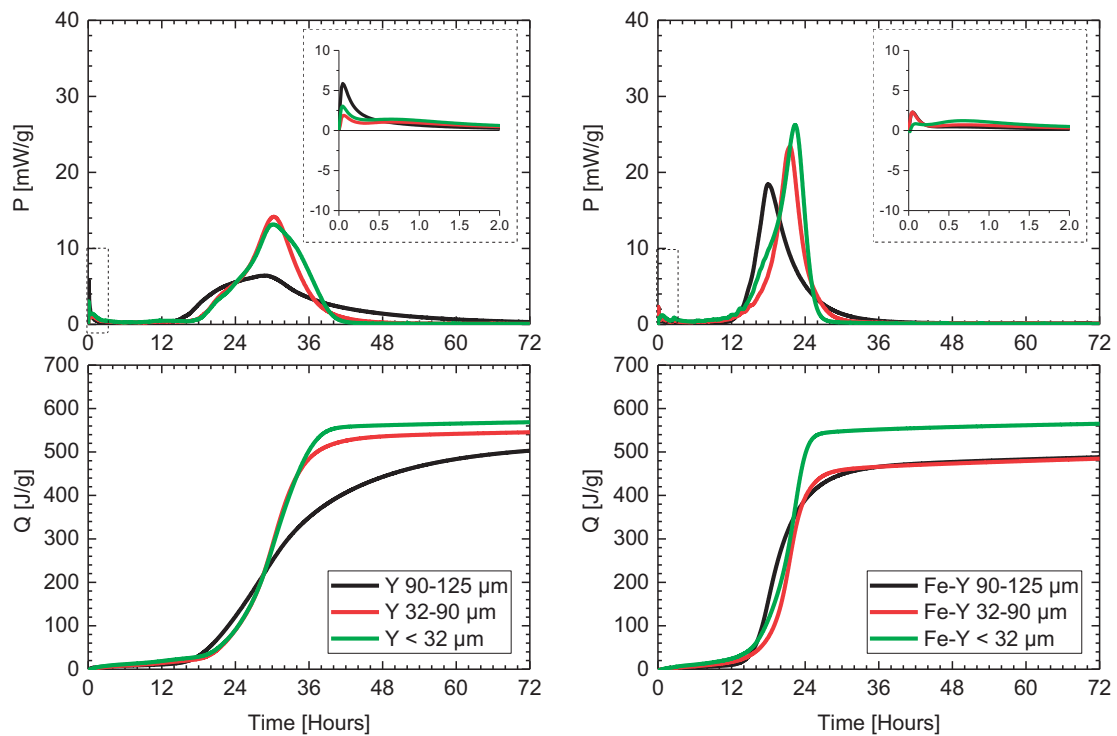


Figure 8.8-54 Rate of heat evolution (top) and cumulative heat (bottom) of the sieved fractions

Figure 8.8-55 shows the PSD and the rate of heat evolution and cumulative heat of the two batches Y and Fe-Y produced according to the S3 protocol. The hydraulic reactivity of Y was very similar even when having a different fineness (for Y S3 2<sup>nd</sup>; i.e. “Y < 32  $\mu\text{m}$ ”). On the contrary, the Fe-Y samples showed a measurable difference in the hydration kinetics (for Fe-Y S3 2<sup>nd</sup>, i.e. “Fe-Y < 32  $\mu\text{m}$ ”).

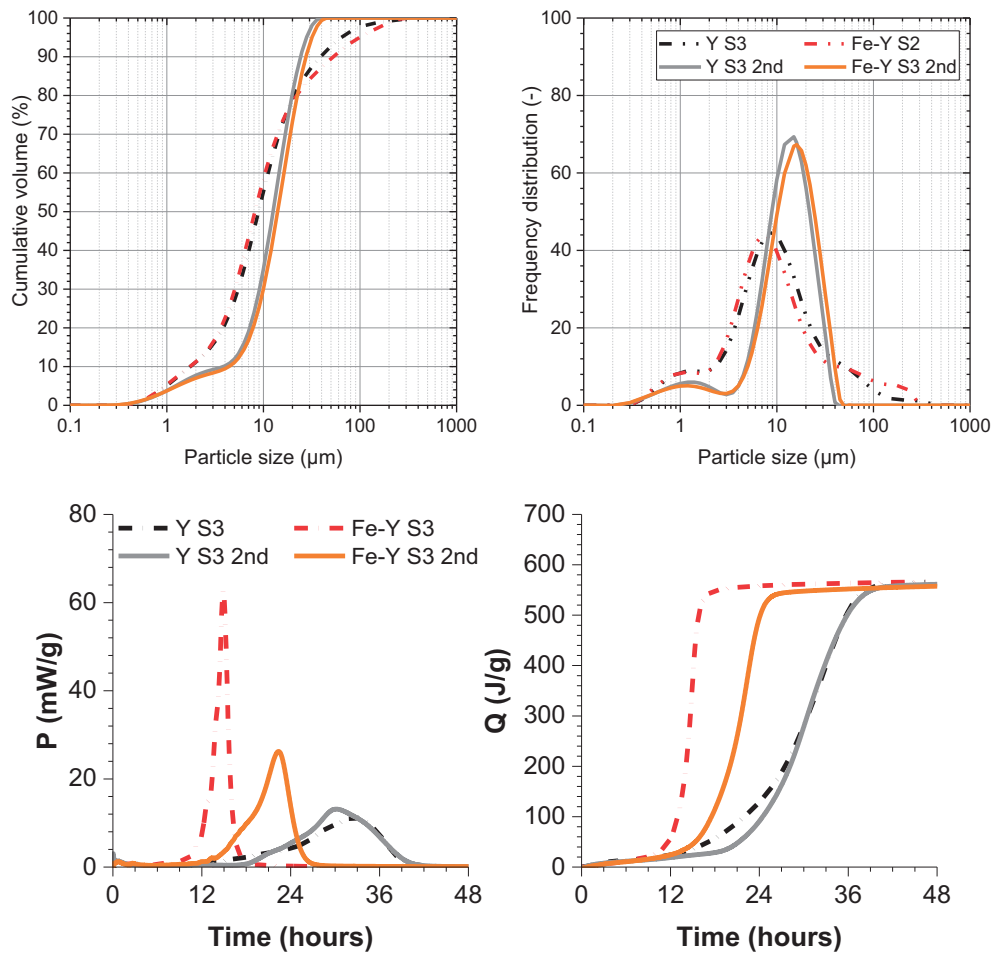


Figure 8.8-55 Particle size distribution (top), rate of heat evolution and cumulative heat (bottom)

The hydration kinetics of the **ye’elinite clinkers** from the **S1** series were analysed to investigate the **effect of sintering temperature, (combined) portlandite and sulphate additions**. The addition of ready soluble anhydrite (tempered at 700 °C) or gypsum caused the acceleration and harmonisation of the hydration kinetics. The addition of hard burnt anhydrite had almost no impact on the hydration kinetics. The addition of ready soluble calcium sulphate resulted in the faster formation of ettringite, almost independent of the ye’elinite type and mitigated the effect of mayenite. The intense and sharp peak at around 13 hours as shown in Figure 8.8-56 resulted from the gypsum depletion, reaccelerated ye’elinite dissolution and monosulphate formation.

Annex

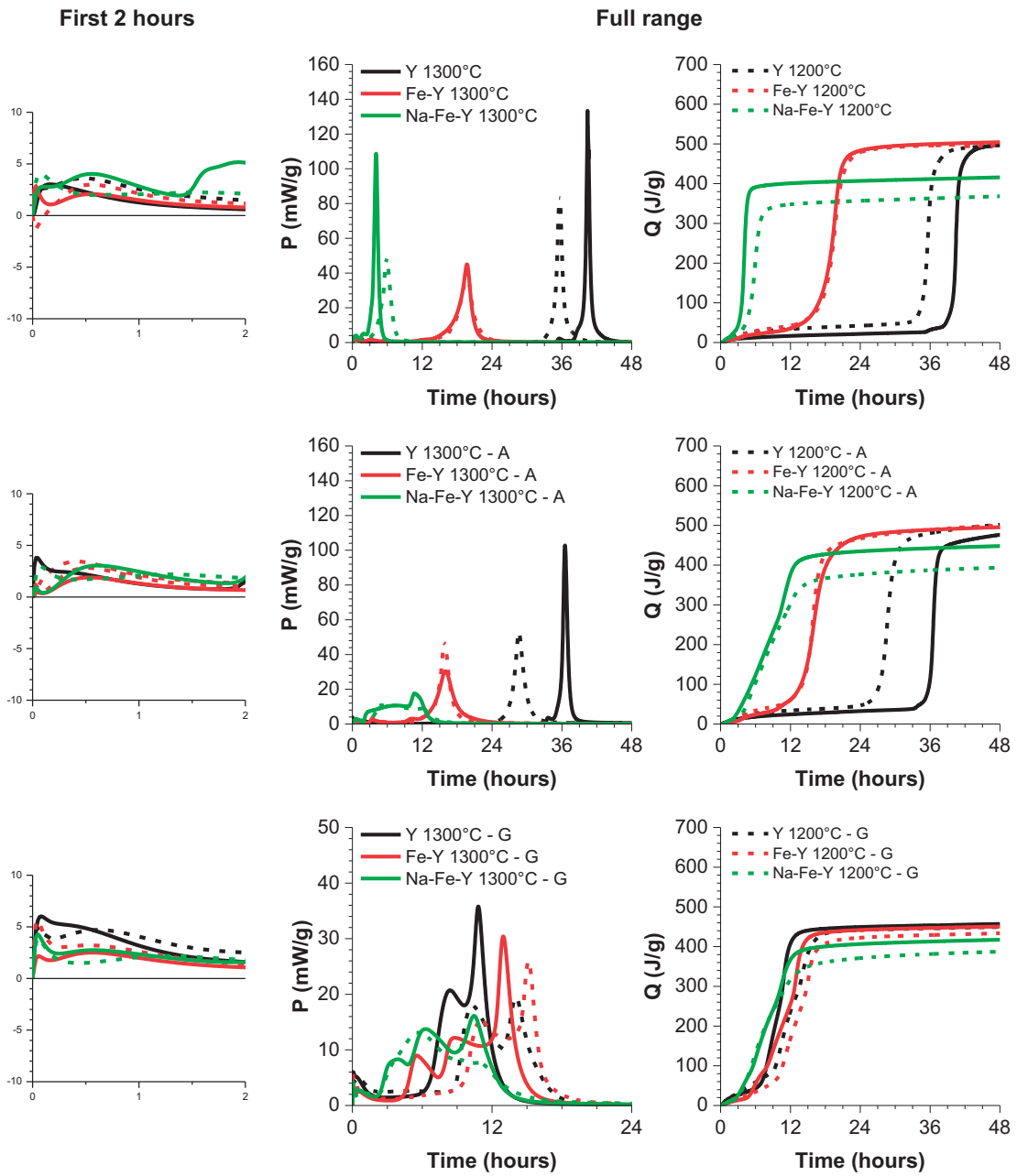


Figure 8.8-56 Rate of heat evolution (left and middle) and cumulative heat (right) of hydrating Y, Fe-Y and Na-Fe-Y from S1 as neat clinker (top), cement with 2M hard burnt anhydrite, 2 h at 1100 °C (middle) and 2M gypsum (bottom) at w/b 1



The hydration kinetics of **ye'elite clinkers** from the **S2 series** were investigated to assess the **effect of gradual Al by Fe substitution, (combined) portlandite and sulphate additions**. We investigated the hydration kinetics of stoichiometric ye'elite and several iron-bearing solid solutions from the S2 series. In addition, we tested the impact of gypsum additions (1 mole ye'elite (64% by weight) to 2 mole gypsum (36% by weight)). The results of those analyses are presented in Figure 8.8-57. The absence of an endothermic peak at early hydration ages remains unclear. We actually assume that this may be related to the very high fineness of the clinkers from the S2 series. The impact of portlandite additions was tested to check whether or not we can simulate the hydration kinetics of the Fe-Y sample.

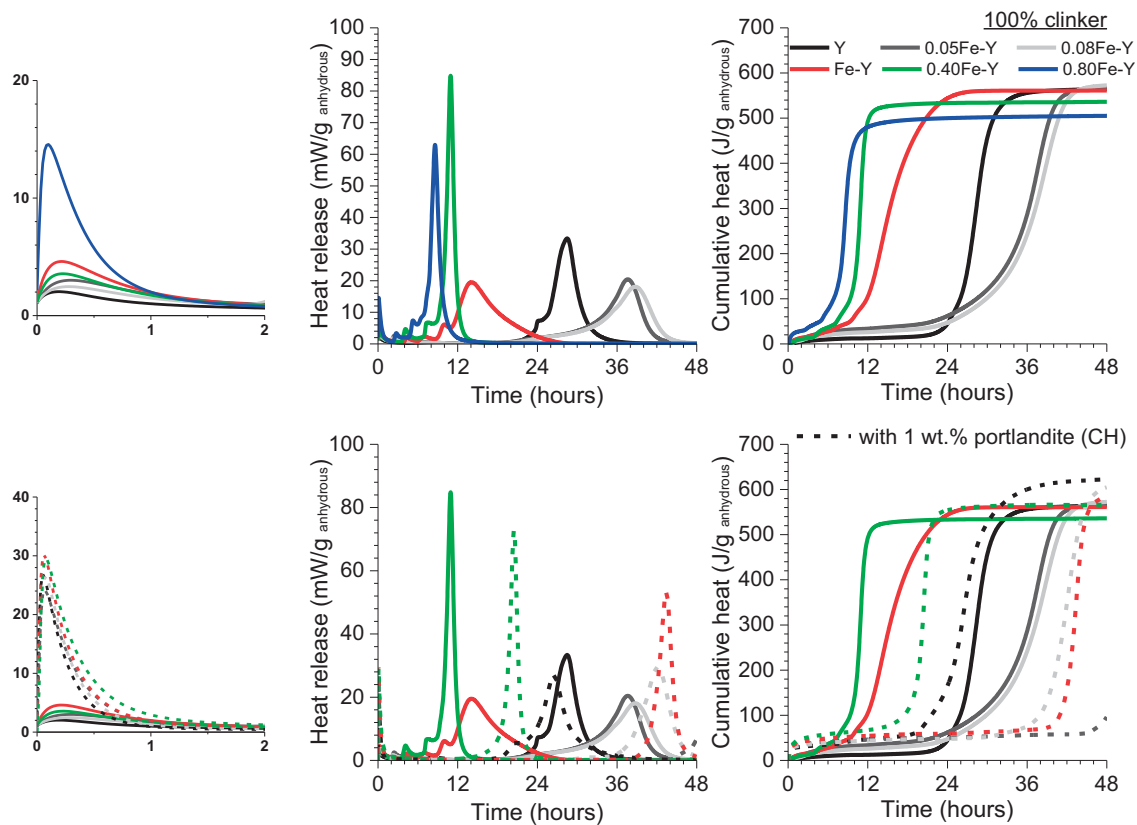


Figure 8.8-57 Rate of heat evolution (left and middle) and cumulative heat (right) of neat clinkers (top) and cements with gypsum (bottom) at a w/b ratio of 2

We further investigated the impact of calcium sulphate, gypsum versus anhydrite, and portlandite additions as shown in Figure 8.8-61.

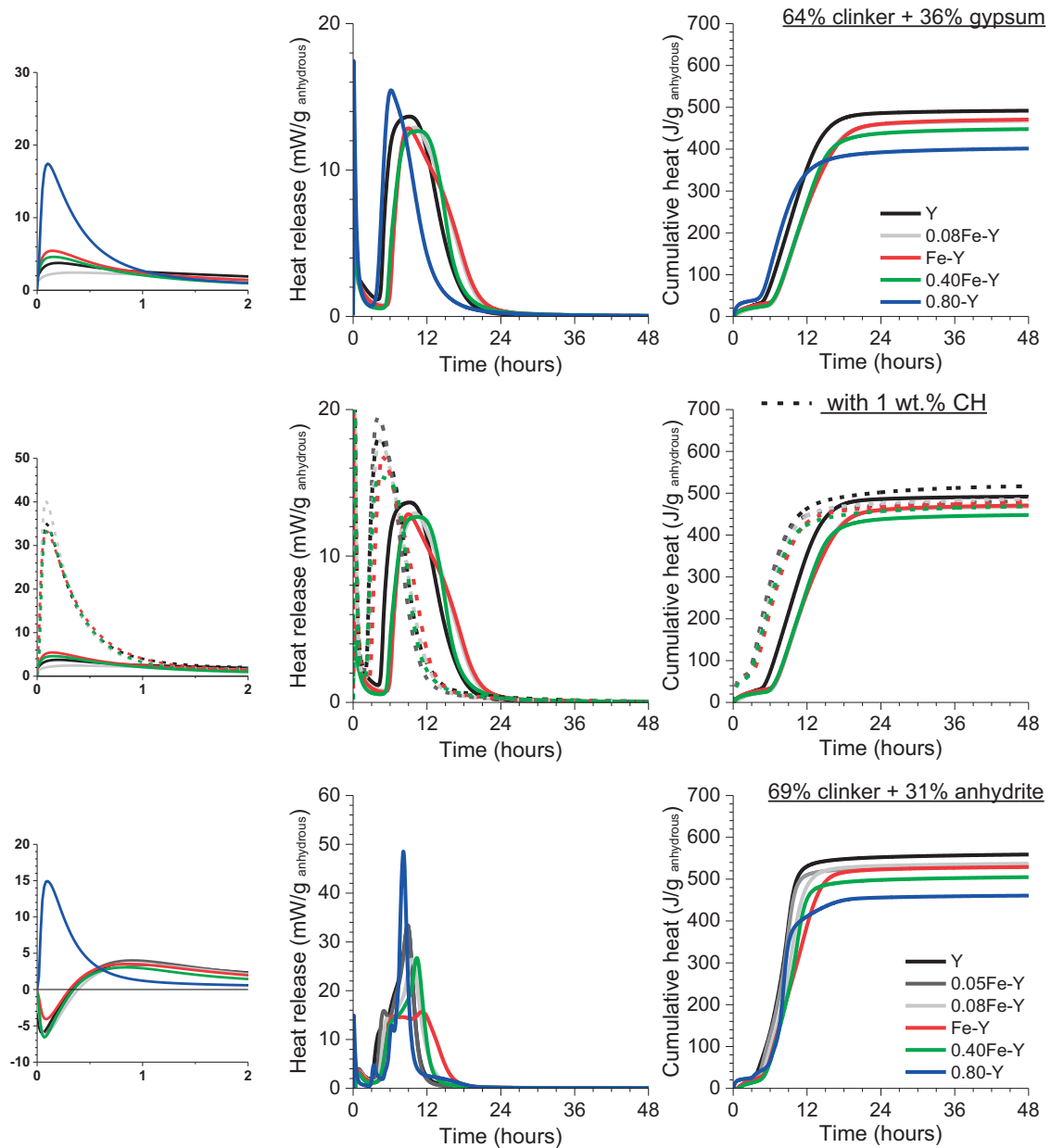


Figure 8.8-58 Rate of heat evolution (left and middle) and cumulative heat (right) of cements with gypsum (top), gypsum and portlandite (middle) and with middle burnt anhydrite, 2 h at 700 °C (bottom) at a w/b ratio of 2

The hydration kinetics of ye'elite clinkers from the S3 series were investigated to assess the effect of (combined) portlandite and sulphate additions. The results are shown in Figure 8.8-60.

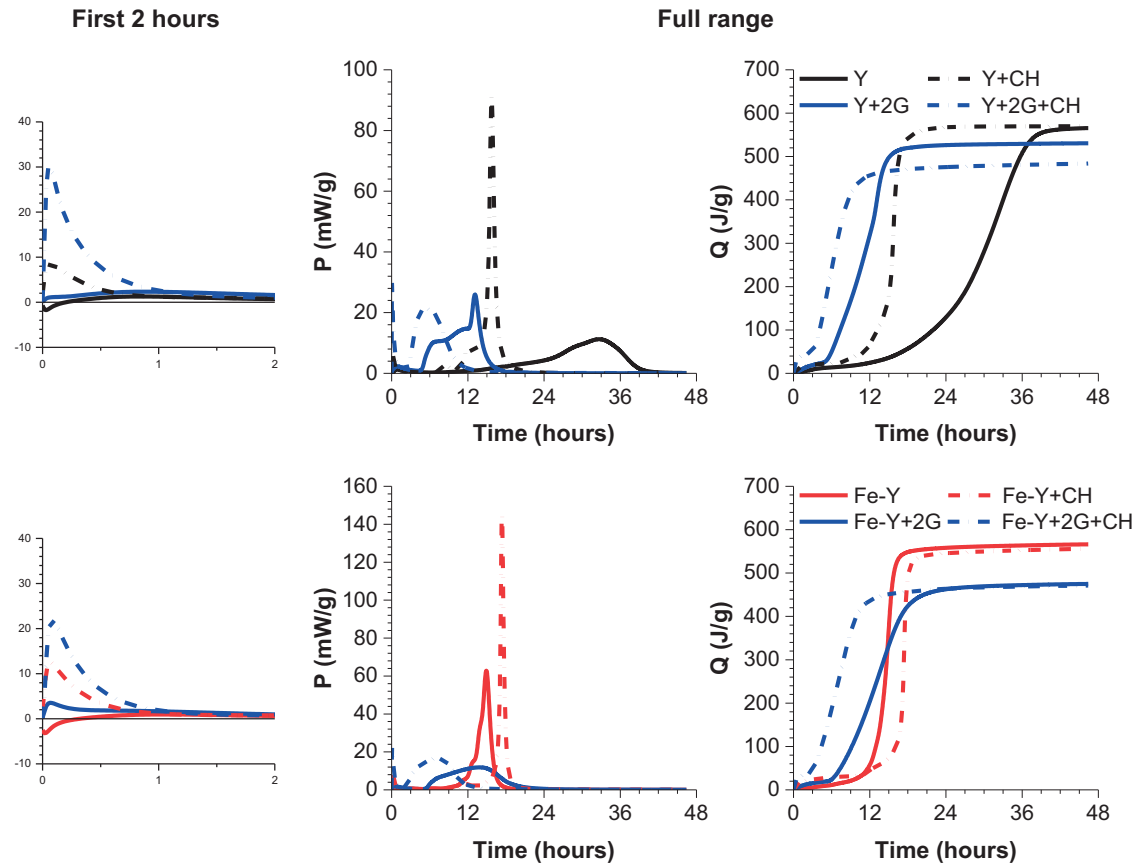


Figure 8.8-59 Rate of heat evolution (left and middle) and cumulative heat (right) of hydrating Y (top) and Fe-Y (bottom) as neat clinker or cement with 2M gypsum with and without 1 wt.% portlandite (CH) at w/b 2,

The dissolution experiments of Y and Fe-Y using w/b ratios from 40 to 1000 are shown in Figure 8.8-60.

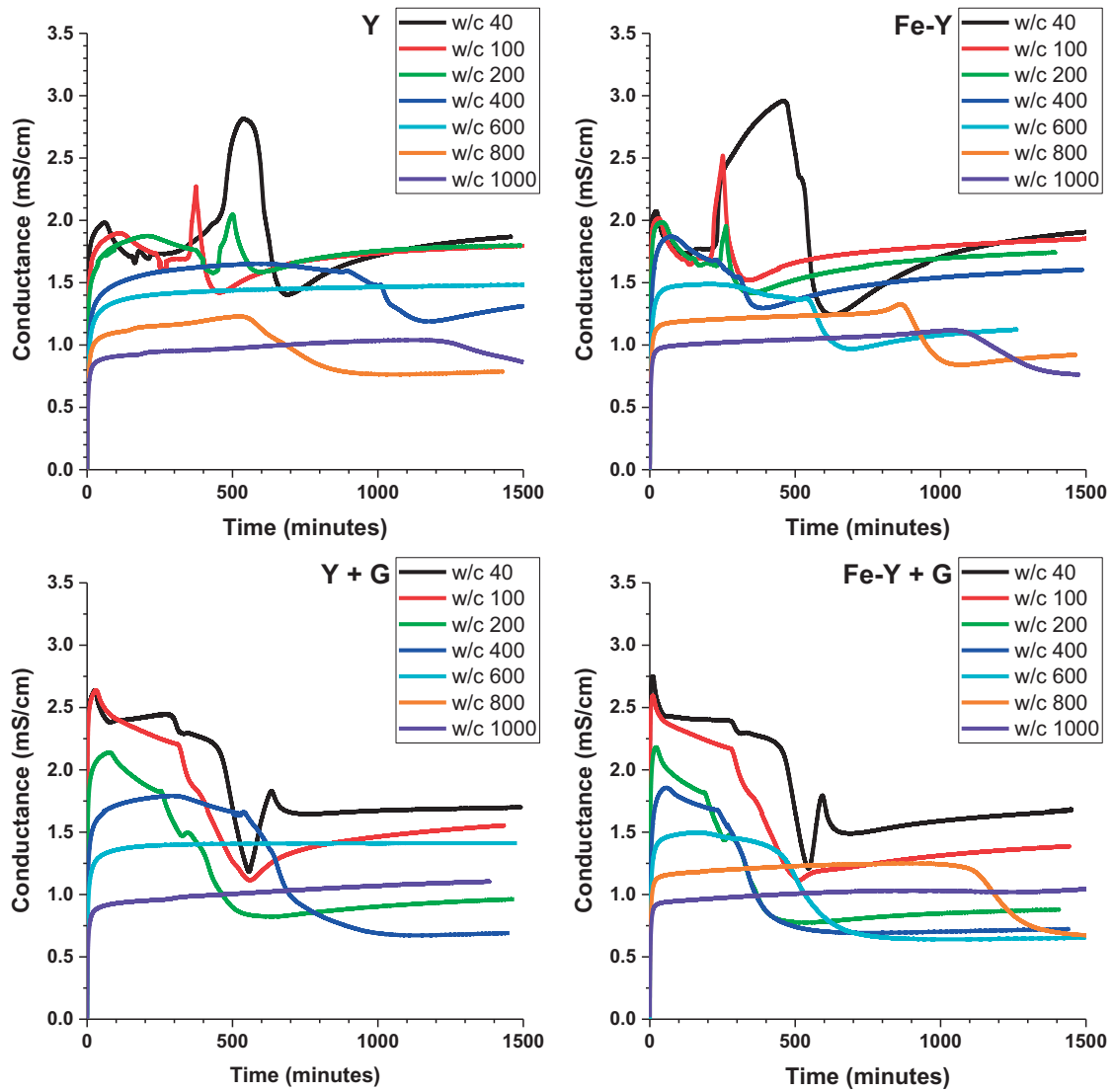


Figure 8.8-60 Evolution of the conductivity of Y and Fe Y with (bottom) and without (top) gypsum at w/b ratios from 40 to 1000

Annex

The dissolution experiments of G and tow anhydrite (A) types at w/b ratios from 40 to 10000 are shown in Figure 8.8-61. This data was used to calculate the slope of the linear dissolution part, e.g. during the first seconds only, which in turn indicates the dissolution rate shown in Figure 8.8-62.

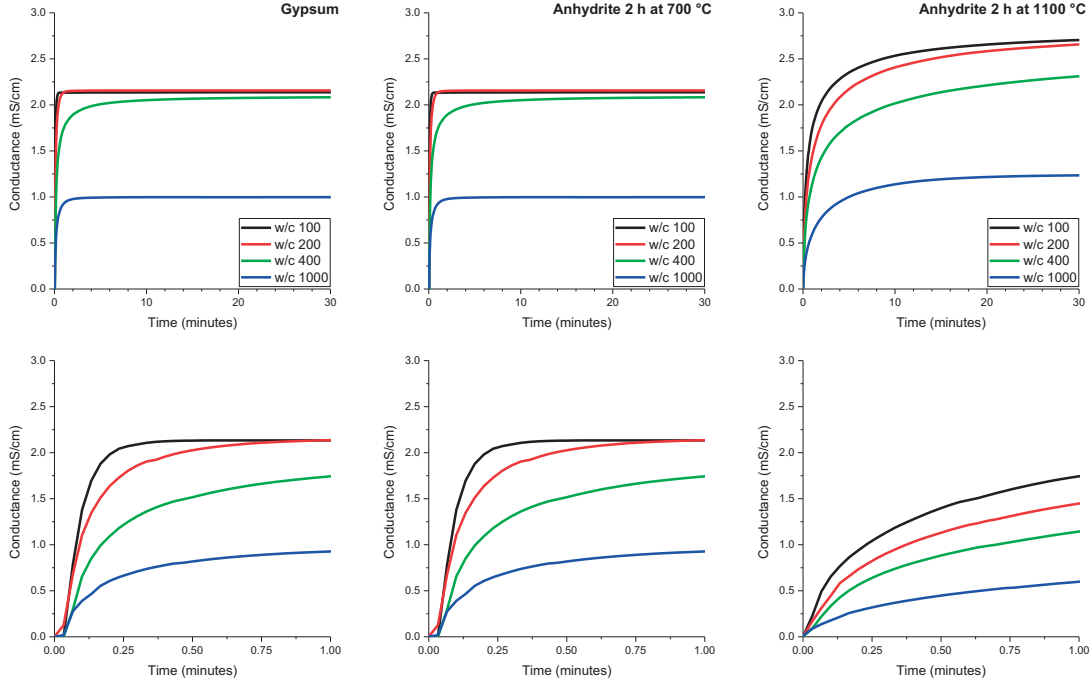


Figure 8.8-61 Evolution of the early conductivity of several calcium sulphates at w/b ratios from 100 to 1000 up to 30 minutes (top) and during the first minute (bottom)

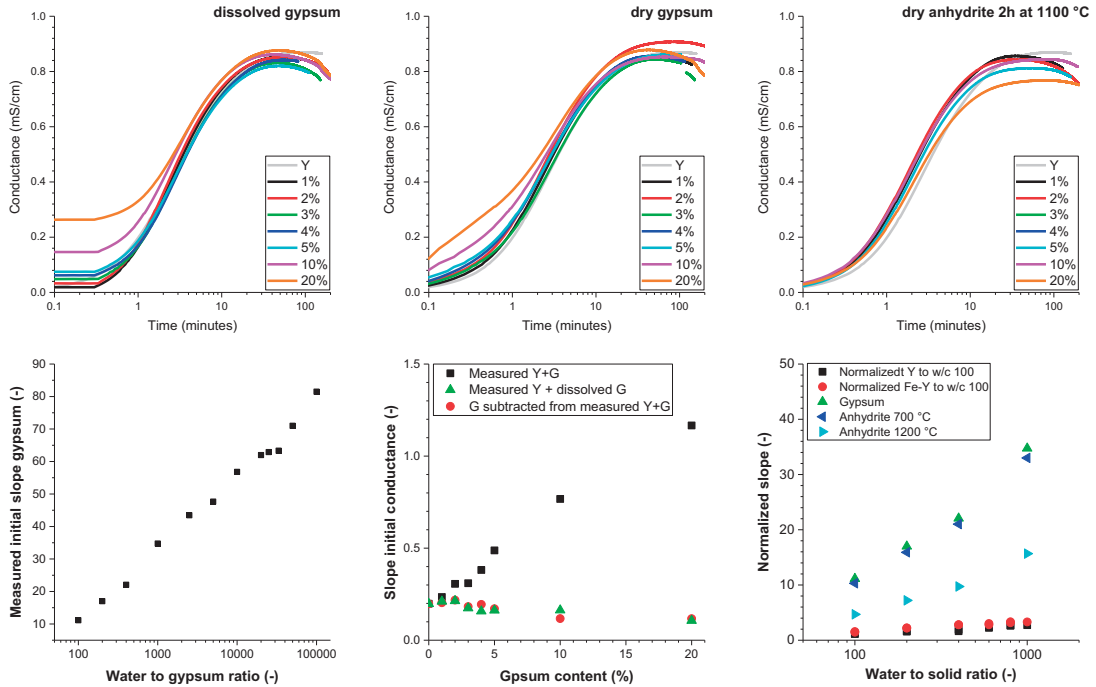


Figure 8.8-62 Evolution of the early conductivity of Y at different calcium sulphates dosages (top) and measured and calculated slope values during the first seconds to minutes for the linear increase of the conductivity (bottom)



The **impact of fillers**, i.e. availability of nucleation sites, **on the hydration kinetics** was also tested in suspension at w/b 100. It was shown that the dissolution of Y caused the instant precipitation of hydrates, which was even more pronounced in the case of Fe-Y. STEM-EDS analyses further indicated the formation of a (calcium) iron hydroxide-rich layer and  $SSA_{BET}$  measurements showed the increased surface area of the hydrated residues for Fe-Y compared to Y. Therefore, we assumed that those first hydration products increased the available surface area which may act as nucleation sites, causing the accelerated kinetics. To investigate this hypothesis 5%, 10% and 20% of gibbsite ( $AH_3$ ) and 5% and 10% of goethite ( $FH$ ) were added. The  $SSA_{BET}$  surface area of gibbsite and goethite was  $4.47 \text{ m}^2/\text{g}$  and  $13.79 \text{ m}^2/\text{g}$ , respectively. The materials were also chosen due their similar chemical and mineralogical composition as the initial hydration products. This should potentially result in a topotactic growth of chosen hydrates and the acceleration of the kinetics. Figure 8.8-63 shows the results of the conductivity and pH measurements. The kinetics were accelerated but the general evolution was very similar to that of Y. The rates of Fe-Y were still not reached. Moreover, the amount of seeding proves to have almost no impact even so that the available surface area was increased significantly.

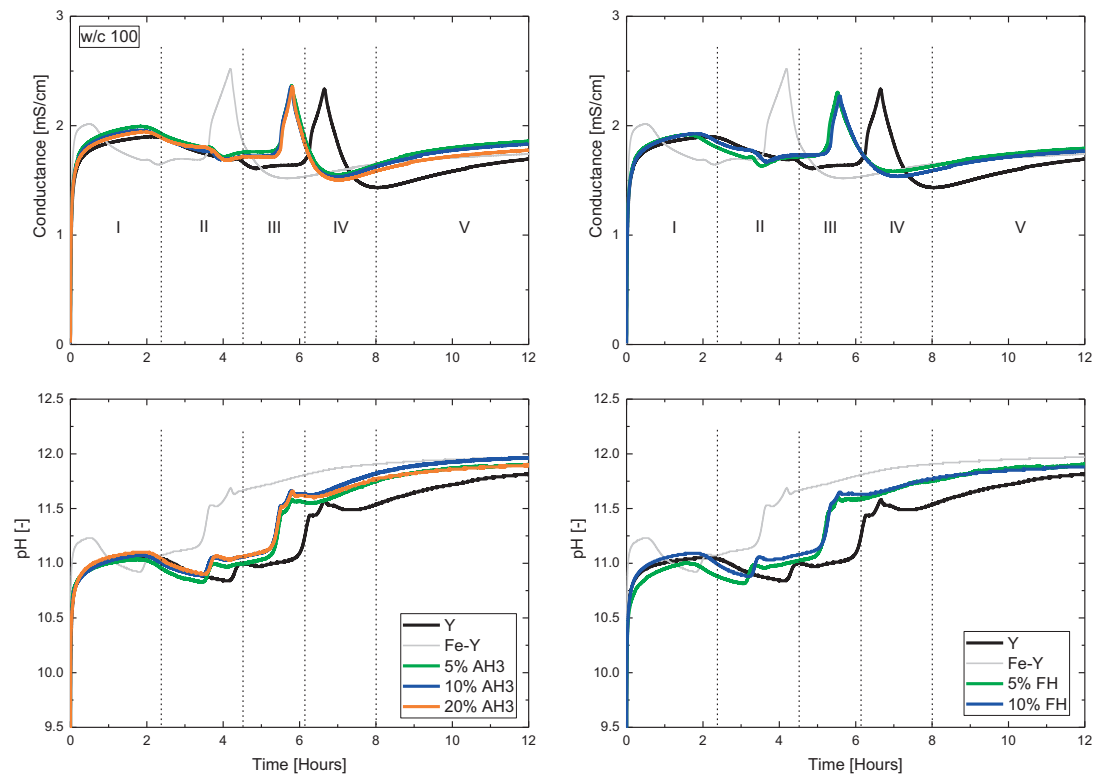


Figure 8.8-63 Evolution of the conductivity (top) and pH (bottom) of Y and Fe-Y with the addition of gibbsite [ $AH_3$ ] (left) and goethite [ $FH$ ] (right); dashed lines represent the five hydration stages for plain Y

The **addition of portlandite to neat Y and Y with 10% of goethite** caused the acceleration of the early reactions and the extension of the main hydration period. However, the presence of portlandite could not reach the same kinetics as Fe-Y.

Annex

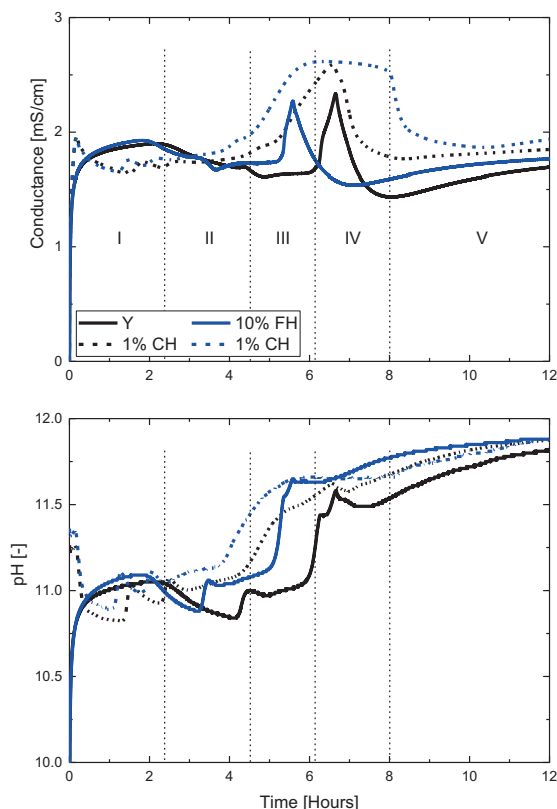


Figure 8.8-64 Evolution of the conductivity (top) and pH (bottom) of Y and Fe-Y with the addition of gibbsite  $[AH_3]$  (left) and goethite  $[FH]$  (right) at w/b 100; dashed lines represent the five hydration stages

The hydrates morphology was investigated using at several hydration ages and using two w/b and w/s ratios. The impact of the applied w/c and w/s ratios (see Chapter 5, section xxx) was further assessed by characterising the hydrates morphology by SEM. The morphology of ettringite is characteristic for the nucleation (initial and acceleration period) and the growth (dormant and final period) hydration periods. The sampling points are highlighted in Figure 8.8-65.

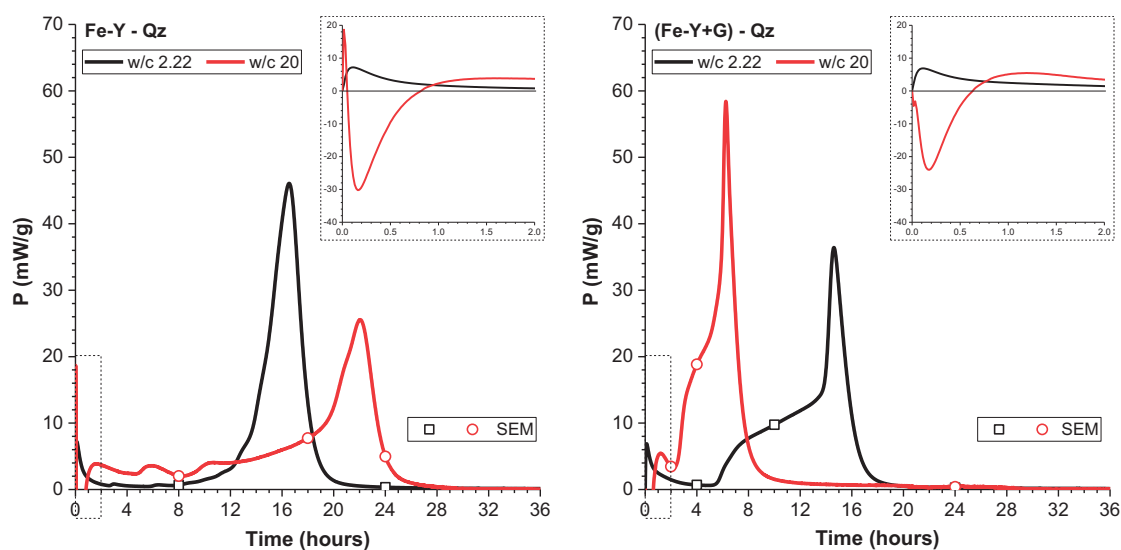


Figure 8.8-65 Rate of heat evolution Fe-Y+Qz with and without gypsum at w/b 2.22 and 20 (w/s 2)

**Hydrates morphology** of at w/c 2: *Dormant period*: Idiomorphic, hexagonal crystals with low aspect ratio of ettringite were formed, independent of the presence of gypsum (see Figure 8.8-66). Rarely some clusters of intermixed AFm phases and aluminium hydroxide phases were determined. The ettringite was intermixed with anhydrous ye'elimite particles that were covered with a shell of hydrates. *Final period*: Several new types of hydrates and morphologies were formed. The initial ettringite crystals continued to grow forming large elongated (several micron) crystals with higher aspect ratios. In addition, a second needle-like ettringite was present. At least two types of AFm-phases were formed; a foil-like lamellar one (probably  $CAH_{10}$ ) and monosulphate hexagonal platelets.

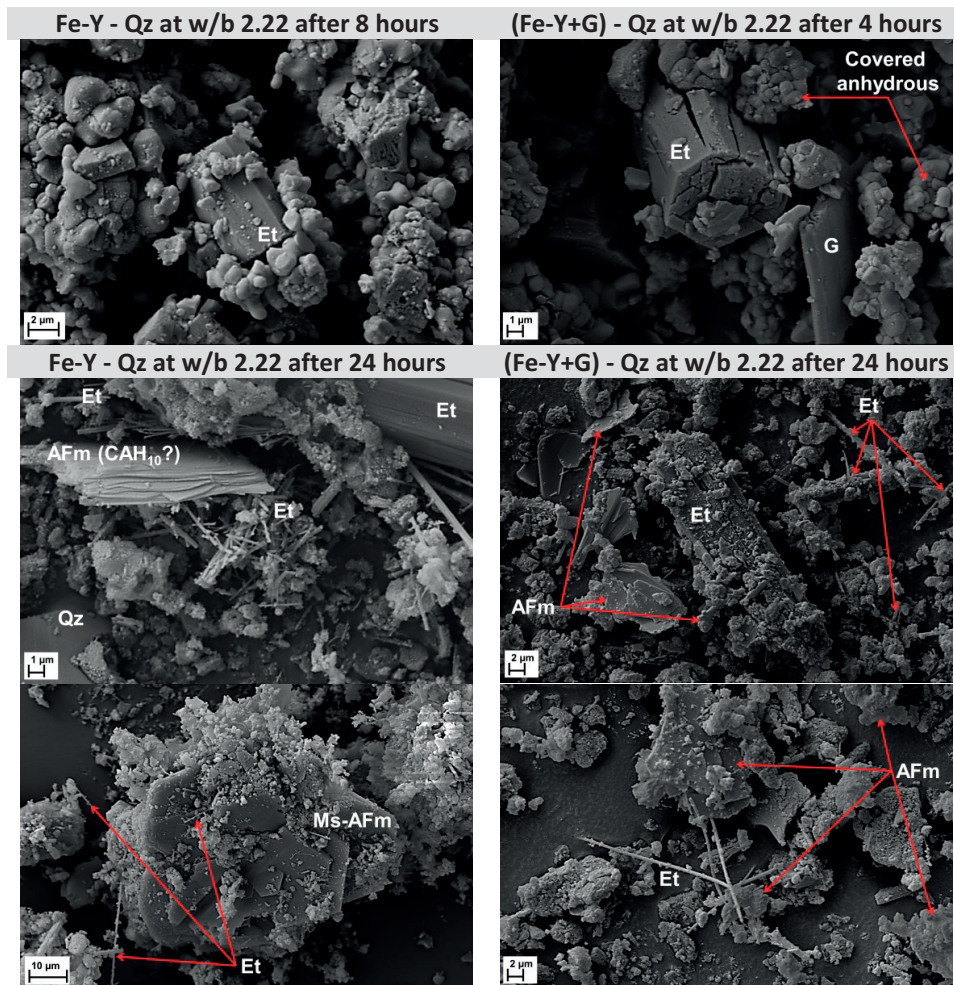


Figure 8.8-66 SEM micrographs; AFm = mixtures of Ms-AFm and e.g.  $CAH_{10}$  (often traces of  $AH_3$ ), Et = ettringite, G = gypsum and Qz = quartz

**Hydrates morphology** of at w/b 20: *Dormant period*: The features of the hydrates were similar to those at a w/b of 2.22 (see Figure 8.8-67). *Acceleration period*: The ettringite crystals continued to grow and the massive formation of AFm phases occurred. The addition of gypsum caused the fast and massive ettringite nucleation, as indicated by the formation of clusters needle-like ettringite. *Final period*: The features of the hydrates are similar to those at a w/b of 2.22.



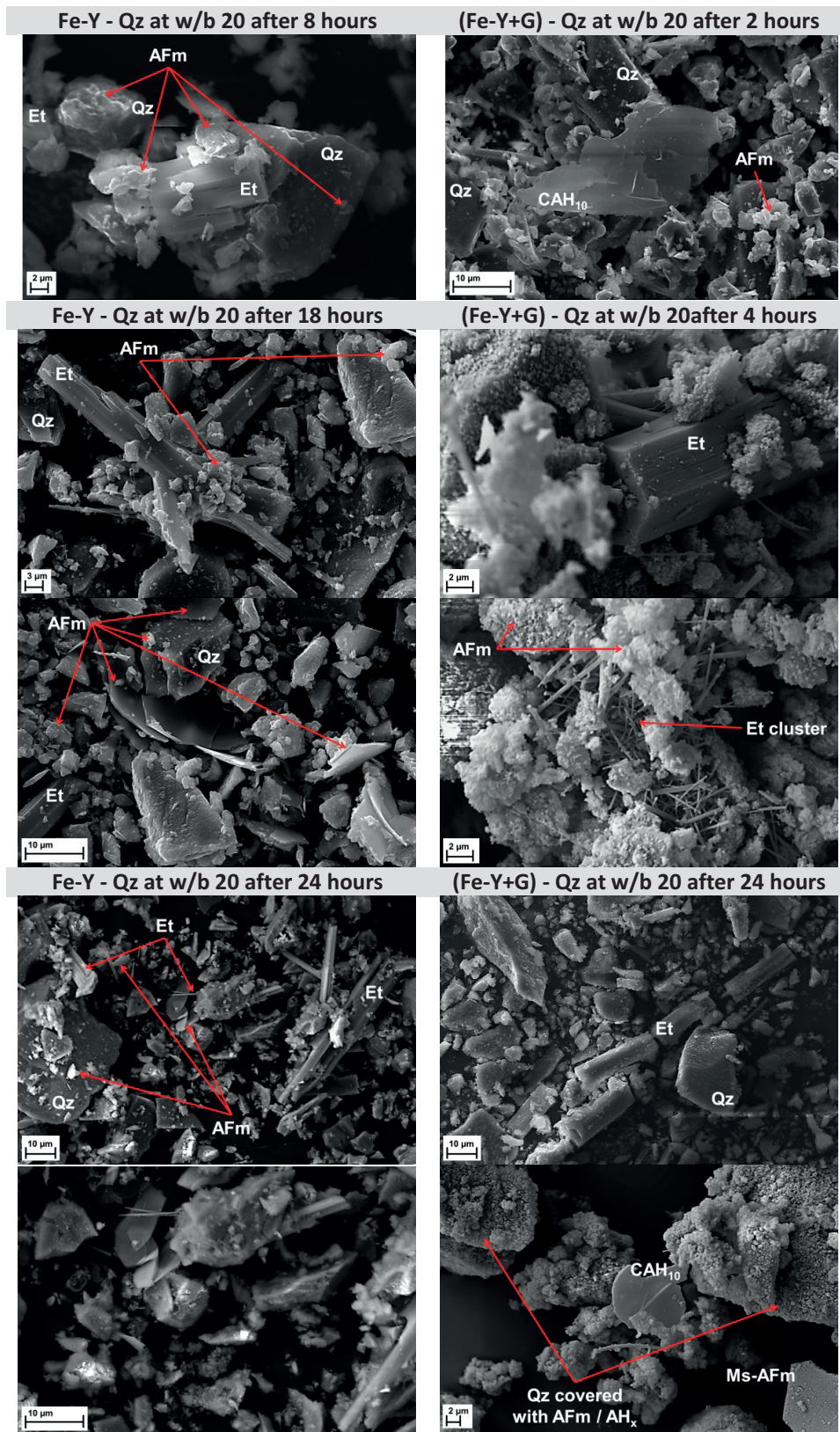


Figure 8.8-67 SEM micrographs; AFm = mixtures of Ms-AFm and e.g.  $CAH_{10}$  (often traces of  $AH_3$ ), Et = ettringite and Qz = quartz

A special feature is the presence or absence of hydrates on the **quartz surfaces** depending on the used binder type and applied w/b ratio. Hydrates morphology of at w/b 2: *Dormant period*: The quartz surfaces were almost free of any hydrate in both samples. (see Figure 8.8-68). *Acceleration period*: Only the sample with gypsum was analysed. The quartz particles were partly and sometimes even fully overgrown with a mix of AFm and  $AH_x$  phases. *Final period*: Most quartz particles in the fully hydrated plain clinker were almost free of any hydrates. On the contrary, the quartz particles in the presence of gypsum were covered with hydrates.

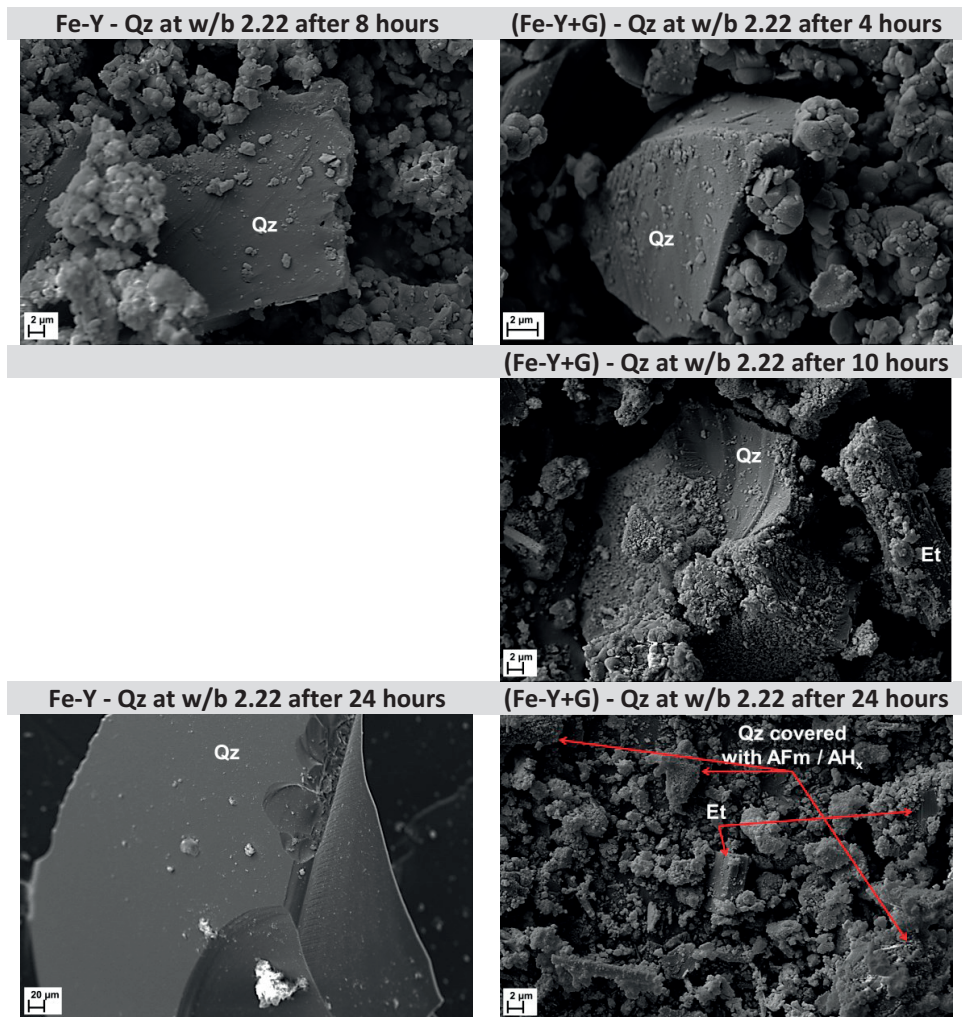


Figure 8.8-68 SEM micrographs; AFm = mixtures of Ms-AFm and e.g.  $CAH_{10}$  (often traces of  $AH_3$ ), Et = ettringite and Qz = quartz

Hydrates morphology of at w/b 20: *Dormant period*: Contrary to the lower w/b ratios, the quartz particles were partly covered with growing hydrates in both samples (see Figure 8.8-69). But those hydrates were more dominant and bigger in the presence of gypsum. *Acceleration period*: The quartz surfaces in the plain Fe-Y sample were slightly more covered compared to those of the dormant period but still clearly visible. On the contrary in the presence of gypsum, all quartz particles were fully covered with a mix of AFm and aluminium hydroxide. *Final period*: The same features as during the acceleration period were present.



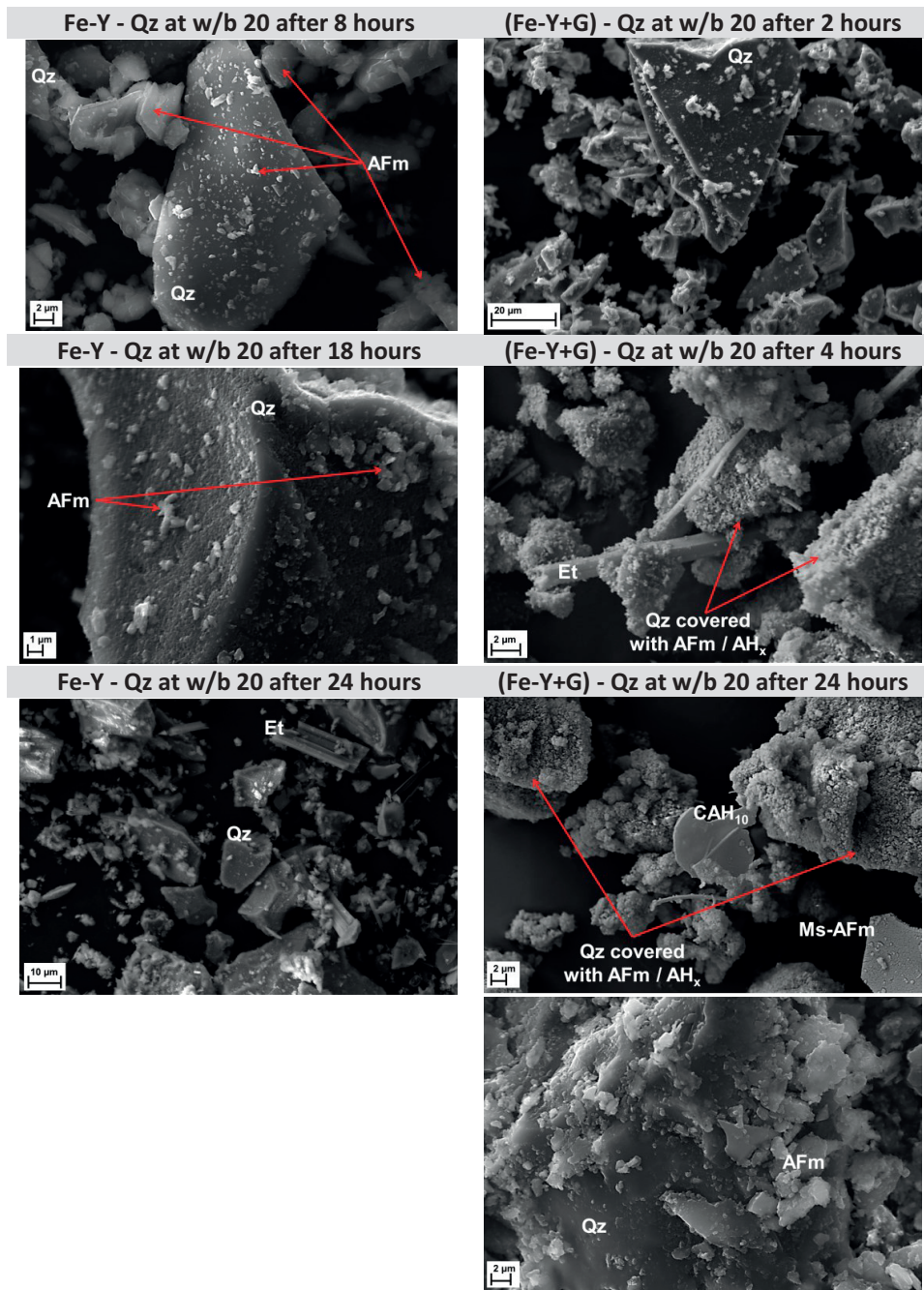


Figure 8.8-69 SEM micrographs; AFm = mixtures of Ms-AFm and e.g.  $CAH_{10}$  (often traces of  $AH_3$ )

The presence of mayenite is also of **industrial relevance** as traces of mayenite are often present in CSA and BYF clinkers [33] [37]. In an internal study we produced four different clinkers from one set of raw materials but in different proportions. The raw mixes were fired for 1 hour at 1250 °C. The achieved mineralogical composition is very similar, except for the absence of mayenite in the BYF 1\* samples, as shown in Table 8.8-19.

Table 8.8-19 Mineralogical composition of CSA and BYF clinker; n.d. = not detected

	CSA	BYF 1	BYF 1*	BYF 2
	Content (%)			
Ye'elimite ortho. / cubic	52.4 / 15.6	23.9 / 25.2	18.7 / 30.1	8.0 / 18.0
Krotite / <b>mayenite</b> / tricalcium aluminate	0.7 / <b>1.7</b> / 0.5	0.7 / <b>1.2</b> / n.d.	n.d. / <b>n.d.</b> / 2.9	n.d. / <b>1.7</b> / n.d.
Brownmillerite	0.9	4.8	n.d.	6.6
Dicalcium silicate / ternesite	24.8 / n.d.	41.4 / n.d.	18.7 / 21.9	56.1 / n.d.
Anhydrite / jasmundite	0.5 / 0.8	n.d. / n.d.	0.4 / n.d.	n.d. / n.d.
Σ minors <sup>#</sup>	2.1	2.8	7.3	9.6

<sup>#</sup> Bredigite, periclase, åkermanite-gehlenite, arcanite and maghemite

All clinkers were ground to the same Blaine fineness of 4000 cm<sup>2</sup>/g. The hydraulic reactivity of the clinkers was tested by calorimetry using w/c ratios of 0.72 for CSA, 0.62 for BYF 1 and 0.52 for BYF 2. In addition, mixes with varying replacement by natural anhydrite were prepared with 15% for CSA, 10% for BYF 1 and 5% for BYF 2. The w/c and anhydrite dosages were chosen to enable the full hydration of the samples and to achieve the maximum ettringite formation for each mix. In the case of the sample BYF 1\* the extra anhydrite was added directly to the raw mix, i.e. before the firing, to investigate the impact on the clinker composition and hydraulic reactivity.

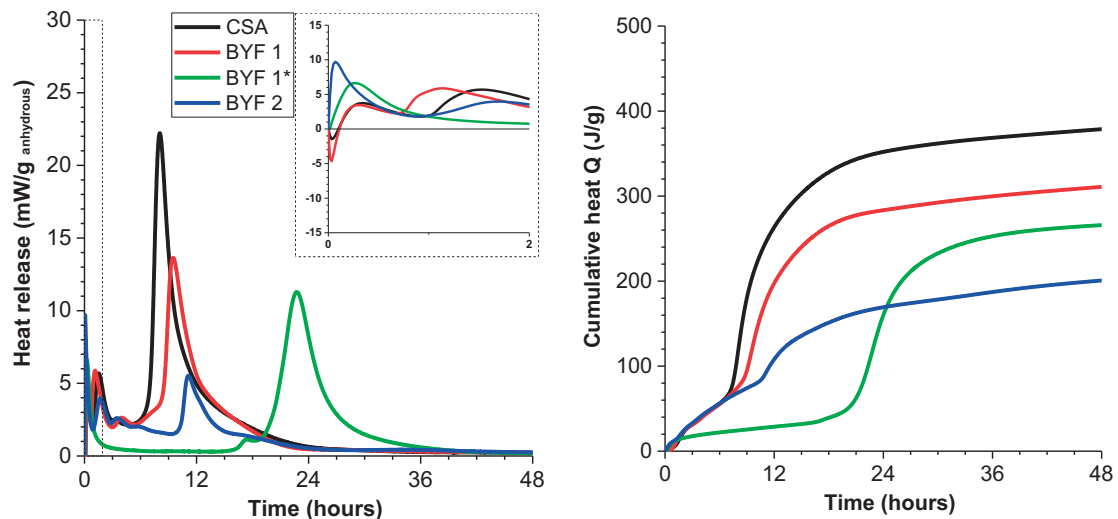


Figure 8.8-70 Rate of heat evolution (left) and cumulative heat (right) of cements



## Curriculum vitae

### Frank Bullerjahn

Date and place of birth 18.07.1983; 06132 Halle; Germany  
 Address Bodelschwingstraße 2, 69181 Leimen, Germany  
 Tel. +49 6221 481 13680  
 Mail [frank.bullerjahn@heidelbergcement.com](mailto:frank.bullerjahn@heidelbergcement.com)

#### PROFESSIONAL EXPERIENCES

---

- |                |  |
|----------------|--|
| 2012 - PRESENT | Research Scientist: Team "Cement&Binder Technology" – Global R&D at HeidelbergCement Technology Center GmbH <ul style="list-style-type: none"> <li>• <i>Development and characterisation of CO<sub>2</sub>-reduced" clinker and cements</i></li> <li>• <i>Project management, scientific publishing and patenting</i></li> </ul>                 |
| 2011 - 2012    | Junior Scientist: Team "Cement&Binder Technology" – Global R&D at HeidelbergCement Technology Center GmbH <ul style="list-style-type: none"> <li>• <i>Development and characterisation of CO<sub>2</sub>-reduced" clinker and cements</i></li> <li>• <i>Project management, scientific publishing and patenting</i></li> </ul>                   |
| 2010 - 2011    | Technical Trainee: Team "Cement&Binder Technology" – Global R&D at HeidelbergCement Technology Center GmbH <ul style="list-style-type: none"> <li>• <i>Development and characterisation of CO<sub>2</sub>-reduced" clinker and cements</i></li> <li>• <i>Support in the field of applied mineralogy and geology</i></li> </ul>                   |
| 2009 – 2010    | Internship: Team "Cement&Binder Technology" – Global R&D at HeidelbergCement Technology Center GmbH <ul style="list-style-type: none"> <li>• <i>Development and characterisation of CO<sub>2</sub>-reduced" binders based on magnesium silicate hydrates</i></li> <li>• <i>Support in the field of applied mineralogy and geology</i></li> </ul> |

#### EDUCATION

---

- |                |  |
|----------------|--|
| 2013 - PRESENT | Ph.D. candidate EDMX Materials Science and Engineering<br>Ecole Polytechnique Fédérale de Lausanne (EPFL) in <i>Laboratory of Construction Materials (LMC), EPFL, Switzerland</i><br>Thesis: Characterisation and hydration of ye'elimité containing cements |
| 2007 – 2009    | M.Sc. Applied Geosciences<br>Martin-Luther-Universität Halle-Wittenberg<br>Thesis: Untersuchungen zur chemischen und mechanischen Stabilisierung eines Mg-Al-LDHs  |
| 2004 – 2007    | B.Sc. Applied Geosciences<br>Martin-Luther-Universität Halle-Wittenberg<br>Thesis: Der Moritzteich bei Döbern - Untersuchung der Pufferungsmechanismen eines stark pyritversauerten Bergbausees des Lausitzer Braunkohlereviere (RL-1223s)                   |

---

**LANGUAGES** German (native language); English (business fluent in speech and writing)

**OTHERS** Expertise in data acquisition and interpretation, including advanced techniques such as quantitative X-ray diffraction and Rietveld analysis; differential heat flow calorimetry and thermo-analytical methods; light (transmitted & reflected light microscope) and scanning electron microscopy coupled with an energy dispersive X-ray analyser; Microsoft office suit, OriginLab